

**An Investigation of Fatigue Crack Growth
In Thermally Cycled Components.**

by

David Charles Kerr.

submitted in partial fulfilment of the requirements for the award of the degree of
Doctor of Philosophy to the University of Glasgow.
August 1993.

Supervisors: Dr. R.C. Hurst and Prof. J.W. Hancock.

This work was conducted at the Commission of the European Communities' Institute of Advanced Materials, Petten, The Netherlands, and completed at the University of Glasgow while the author was a registered student of the Department of Mechanical Engineering in the University of Glasgow.

© D.C. KERR, August 1993.

ProQuest Number: 13815486

All rights reserved

INFORMATION TO ALL USERS

The quality of this reproduction is dependent upon the quality of the copy submitted.

In the unlikely event that the author did not send a complete manuscript and there are missing pages, these will be noted. Also, if material had to be removed, a note will indicate the deletion.



ProQuest 13815486

Published by ProQuest LLC (2018). Copyright of the Dissertation is held by the Author.

All rights reserved.

This work is protected against unauthorized copying under Title 17, United States Code
Microform Edition © ProQuest LLC.

ProQuest LLC.
789 East Eisenhower Parkway
P.O. Box 1346
Ann Arbor, MI 48106 – 1346

Thesis
9716
copy 1

Abstract.

Fatigue Crack Growth In Thermally Loaded Components.

The design of first wall components in a nuclear fusion reactor must take into account thermal cycling, through thickness temperature gradients and the possible presence of surface defects arising during construction or through plasma bombardment during service. This thesis describes the experimental procedures and the analysis performed in an investigation of the thermal fatigue crack growth behaviour of defective tubular components of the fusion reactor first wall material, ICL 167 SPH. To provide a basis for the investigation, a literature review is initially presented. The literature review introduces the process of fatigue failure and the important relationships and equations. Fatigue crack growth rate is identified as the parameter used to determine the component life, while the application of both linear elastic fracture mechanics and post yield fracture mechanics to thermal fatigue is discussed. Finally the metallurgy, both physical and mechanical properties and the behaviour of ICL 167 SPH under cyclic loading is presented.

Both low cycle fatigue and linear elastic fatigue loading experiments were performed on standard specimen geometries to develop the material characteristics at the temperatures of interest. The experimental rigs, specimen development and method of data accumulation are described. The results are compared with available data for the similar Type 316L austenitic stainless steel and coefficients for the fatigue relationships produced. A thermal cycling rig was constructed to simulate the thermal loading of first wall tubular components. The development and instrumentation of the tubular components is described in conjunction with the adaptation of the direct current potential drop method which monitored the thermal fatigue crack growth. Beyond the influence of the crack initiating notches, the thermal fatigue crack growth rates were found to be similar from either the external or the internal surfaces of the components and were in a similar range to the resultant crack growth rates from the mechanical fatigue crack growth experiments.

A thermal strain finite element analysis was performed to determine the values of stress and strain, through the thickness of a defect free, unnotched component, during a number of thermal cycles. The superposition method was applied to calculate the equivalent stress intensity factor at various crack depths through the thickness of the component. The difficulties in analysing thermal cyclic problems and the necessity for post yield evaluation were identified. Finally, it was concluded that mechanical fatigue crack growth rate data could be used to predict thermal fatigue crack growth rates in the thermal cycling loading of first wall tubular components.

List of Contents.

	Page
Contents.	I
Declarations.	V
Acknowledgements.	VI
List of Figures.	VII
List of Tables.	XIV
Nomenclature.	XVI
1.0. Introduction.	1
Section 1.0: Figure.	3b
2.0. Literature Review.	4
2.1.1. Introduction To Fatigue.	4
2.1.2. Monotonic Testing Properties.	6
2.1.3. Mechanical Properties Of Fatigue.	7
2.1.3.1. Stress Cycling Properties.	7
2.1.3.2. Strain Cycling Properties.	10
2.1.3.3. Shakedown and Ratchetting.	16
2.1.3.4. Microstructural Development During Cyclic Loading.	17
2.1.4. Fatigue Life Relationships.	24
2.1.5. Factors Effecting Fatigue Life.	29
2.1.5.1. Surface and Notch Effects.	29
2.1.5.2. Time Dependent Effects on Fatigue Life.	31
2.1.5.3. Irradiation Effects on Fatigue Life.	37
2.1.5.4. Combined Thermal/Mechanical Cycling Effects on Fatigue Life.	37
2.1.5.5. Thermal Cycling Effects on Fatigue Life.	39
Section 2.1: Figures.	44
2.2. Fatigue Crack Growth.	58
2.2.1. Linear Elastic Fracture Mechanics, (LEFM).	58
2.2.2. Elastic-Plastic Solution.	59
2.2.2.1. Application of LEFM to Fatigue Failure.	61
2.2.2.2. Mechanisms of Fatigue Crack Growth.	64
2.2.3. Elastic-Plastic Fracture Mechanics (EPFM) and Fatigue Failure.	69

2.2.4.	Application of Fracture Mechanics to Thermal Fatigue Crack Growth.	77
2.2.4.1.	Finite Element Method.	77
2.2.4.2.	Weight Function and Superposition Method.	78
2.2.4.3.	Elastic-Plastic Equivalent Stress Intensity Method.	80
2.2.5.	Methods of Measuring Thermal Fatigue Crack Growth.	82
	Section 2.2: Figures.	90
2.3.	Material Selection.	107
2.3.1.	Metallurgy and Microstructure of ICL 167 SPH.	108
2.3.2.	Physical Properties of ICL 167 SPH.	110
2.3.3.	Cyclic Behaviour of ICL 167 SPH.	111
2.3.3.1.	Microstructural Development of ICL 167 SPH.	111
2.3.3.2.	Fatigue Properties of ICL 167 SPH.	111
2.3.4.	Fatigue Crack Growth of ICL 167 SPH.	112
	Section 2.3: Figures.	113
3.0.	Experimental Testing Facilities and Techniques.	115
3.1.	Introduction.	115
3.2.	Low Cycle Fatigue Testing.	116
3.2.1.	Experimental Equipment.	116
3.2.2.	Specimen Design, Instrumentation and Assembly.	118
3.2.3.	LCF: Experimental Procedure and Results.	119
	Section 3.2: Figures.	125
3.3.	Mechanical Fatigue Crack Growth Testing.	132
3.3.1.	Introduction.	132
3.3.2.	Centre Cracked Tension Specimen Design, Instrumentation and Test Equipment, Experimental Procedure and Results.	132
3.3.3.	Compact Tension Specimen Design, Instrumentation and Test Equipment, Experimental Procedure and Results.	137
	Section 3.3: Figures.	144

3.4.	Thermal Fatigue Crack Growth Testing.	159
3.4.1.	Design and Development of Thermal Fatigue Experiments.	159
3.4.1.1.	The Cooling Section.	159
3.4.1.2.	The Heating System.	160
3.4.1.3.	The Test Component Section.	162
3.4.1.4.	The Instrumentation, Data Logging and Control System.	168
3.4.2.	Thermal Fatigue Experimental Procedure.	170
3.4.3.	Calibration of the Crack Growth Monitoring System.	176
3.4.3.1.	Calibration For Longitudinal Notched Components.	176
3.4.3.2.	Calibration For Circumferential Notched Components.	178
	Section 3.4: Figures.	179
3.4.4.	Experimental Results.	195
3.4.4.1.	Rectangular Shaped External Surface Notches in the Longitudinal Plane.	195
3.4.4.2.	Rectangular Shaped Internal Surface Notches in the Longitudinal Plane.	202
3.4.4.3.	Semi-Circular Shaped External Surface Notches in the Longitudinal Plane.	205
3.4.4.4.	External Surface Notches in the Circumferential Plane.	210
3.4.4.5.	Internal Surface Notches in the Circumferential Plane.	214
3.4.4.6.	Miscellaneous Experiments: Results Section.	219
	Section 3.4.4: Figures.	223
4.0.	Analysis and Discussion Section.	268
4.1.	Thermal Fatigue Crack Growth.	268
	Section 4.1: Figures.	272
4.2.	Calculation of Cyclic Stress/Strain Field.	285
	Section 4.2: Figures.	295
4.3.	Development of the Thermal Fatigue Stress Intensity Factors.	313
	Section 4.3: Figures.	318
4.4.	Mechanical and the Thermal Fatigue Crack Growth Rates.	322
	Section 4.4: Figures.	326

5.0.	Conclusions.	330
6.0.	Suggestions For Further Work.	332
7.0.	References.	334

Declarations.

I hereby declare that;

- a) this thesis has not been submitted as an exercise for a degree at any other university,
- b) all non-referenced work in this thesis is entirely my own.

Furthermore, I agree that the library of the University of Glasgow, may lend or copy this thesis upon request.

David C. Kerr.

Acknowledgements.

Throughout this project I have been extremely fortunate in obtaining help from a large number of people to whom I am greatly indebted. I would particularly like to offer my thanks:

To my supervisors Dr. R.C. Hurst of the J.R.C., Petten and Prof. J.W. Hancock of the University of Glasgow for their encouragement, support and patience throughout the project.

To Messrs. Brian Eriksson, John Hedderly, Jim Morrissey and Chris McGirl for their help and advice in the design and development of the thermal cycling rig, to Messrs. Ari Schipper and Cees Bobeldijk and the workshop staff for the specimen preparation, to Dr. Tasos Youtos for the introduction to using the finite element analysis, to Mr. Ruudi van Nieuwenhuisen for the excellent photographs, to Messrs. Kurt Schuster and Peter Frampton for the metallography service and to Dr. Johan Bressers and the technicians in the ETL for their help in performing the mechanical fatigue loading experiments.

I would also like to thank Prof. M. van de Voorde for the provision of the facilities of the Materials Characterisations Division of the Institute of Advanced Materials, and the Commission of the European Communities for the award of a generous grant.

I would also like to my fellow students, ex-colleagues and friends at both Petten and the University of Glasgow for helping me to enjoy both the work and the social aspects of performing a research project. I would especially like to thank Dr. Jean-Nic Adami, Mr. Paul Young and Mr. Al Carey for all the laughs and the beers during our expeditions throughout Europe, 1988 to 1992.

Finally, I would like to thank my mother, my father and my sister for their continuous support and their uncanny ability to keep me going when all seems lost. Thanks folks, this one is for all three of you, with all my love.

List of Figures.

Section 1.0.

Figure 1.0.1. Experimental Fusion Reactor NET, (after Merola and Matera,[1991]).

Section 2.1.

Figure 2.1.1. Monotonic Testing Stress/Strain Curves, (after Rice et al.,[1989]).

Figure 2.1.2. Stress Control Test Parameters, (after Miller,[1980]).

Figure 2.1.3. Typical S-N Curves For Ferrous and Non-Ferrous Metals,
(after Colangelo and Heiser,[1974]).

Figure 2.1.4. Modified Goodman Diagram, (after Budynas,[1977]).

Figure 2.1.5. Hysteresis Loop Parameters, (after Rice et al.,[1989]).

Figure 2.1.6. Variation in Stress Amplitude under Strain Control Cycling,
(after Rice et al.,[1989]).

Figure 2.1.7. Cyclic Stress/Strain Behaviour, (after Miller,[1980]).

Figure 2.1.8. Effect of Treatment on Cyclic Stress/Strain Curves, a) Copper and
b) Cu-75%Al, (after Feltner and Laird,[1967]).

Figure 2.1.9. Characterisation of Dislocation Substructure in fcc Metals as a Function
of Strain Amplitude, Temperature and Stacking Fault Energy,
(after Coffin,[1972]).

Figure 2.1.10. Schematic Drawing of Fatigue Life Curves, (after Coffin,[1977]).

Figure 2.1.11. Schematic Representation of Fracture Mode Change With Temperature
and Plastic Strain Range, (after Coffin,[1977]).

Figure 2.1.12. Environment and Frequency Effects on LCF Life of A286 Steel:
Numbered Points are Frequency in cpm, (after Coffin,[1977]).

Figure 2.1.13. Typical Strain Controlled LCF Cycles With Corresponding
Hysteresis Loops, (after Lord and Coffin,[1973]).

Figure 2.1.14. Effect of Varying the Temperature Range on the Fatigue Life of
18Cr-10Ni Steel, (after Kawamoto et al.,[1966]).

Figure 2.1.15. Equivalent Plastic Strain Through the Thickness of a Thermally Shocked
Cylinder, (after Burlet et al.,[1989]).

Section 2.2.

Figure 2.2.1. Body with a Crack of Length $2a$.

Figure 2.2.2. Three Modes of Fracture, (after Colangelo and Heiser,[1974]).

- Figure 2.2.3. Polar Coordinate System For Stresses at the Crack Tip, (after Rice et al.,[1989]).
- Figure 2.2.4. Specimens For Standard Crack Growth Experiments, (after Clark,[1971]).
- Figure 2.2.5. Shape of Plastic Zone at the Crack Tip Through the Body Thickness, (after Klesnil and Lukas,[1980]).
- Figure 2.2.6. Three Regions of a Fatigue Crack Growth Plot, (after Brown,[1988]).
- Figure 2.2.7. Fatigue Crack Growth Curves For a Series of Materials, (after Speidel,[1975]).
- Figure 2.2.8. Two Stages of Fatigue Crack Propagation, (after Klesnil and Lukas,[1980]).
- Figure 2.2.9. Laird's Model of Fatigue Crack Propagation, (after Klesnil and Lukas,[1980]).
- Figure 2.2.10a. Linear Elastic Body Containing a Crack and Loaded by the Remote Load P, (after Webster,[1989]).
- Figure 2.2.10b. Load vs. Load Point Displacement Plot, (after Webster,[1989]).
- Figure 2.2.11. Loaded Body For Calculation of J-Integral, (after Chell,[1981]).
- Figure 2.2.12. Load vs. Load Point Displacement Plot, (after Webster,[1989]).
- Figure 2.2.13. Estimating ΔJ For Cyclic Loading Conditions, (after Chell,[1981]).
- Figure 2.2.14. Stress Through a Thermal Shocked Component, (after Skelton,[1979]).
- Figure 2.2.15. Uncracked and Cracked Bodies For Determination of the Weight Function for use in the Superposition Method, (after Chell,[1981]).
- Figure 2.2.16. Skin Effect in a.c. Potential Drop Technique, (after Rice et al,[1989]).

Section 2.3.

- Figure 2.3.1. NET First Wall Surface Heat Flux, (after Diegele et al.,[1991]).
- Figure 2.3.2. Microstructure of ICL 167 SPH.

Section 3.2.

- Figure 3.2.1. Axial Extension Measurement Extensometer.
- Figure 3.2.2. Low Cycle Fatigue Specimen Dimensions.
- Figure 3.2.3. Stress Amplitudes During LCF Experiments at 0.5% Strain Amplitude.
- Figure 3.2.4(a-b). Hysteresis Loops During LCF Testing.
- Figure 3.2.5. ICL 167 SPH: Cyclic Stress/Strain Results and 316L Comparisons.
- Figure 3.2.6. ICL 167 SPH: Fatigue Life Results with 316L Comparisons.

Section 3.3.

- Figure 3.3.1. CCT Specimen Instrumented with P.D. Probes.
- Figure 3.3.2. CCT: Potential Drop Development Curves.
- Figure 3.3.3. CCT Specimen Fracture Surfaces.
- Figure 3.3.4. CCT: Crack Growth Measurement Curves.
- Figure 3.3.5. Fatigue Crack Growth Rate Data, Type 316L and 316 Stainless Steel.
- Figure 3.3.6. ICL 167 SPH: CCT Fatigue Crack Growth Rate P.D. Calibration and Results.
- Figure 3.3.7. Compact Tension Specimen Dimensions.
- Figure 3.3.8. Long Arm Clevis and Pin Assembly For Gripping CT Specimen.
- Figure 3.3.9. Thermal Gradient CT Specimen.
- Figure 3.3.10. Instrumented CT Specimen in Experimental Testing Position.
- Figure 3.3.11. CT Specimen Fracture Surface: Room Temperature Experiment.
- Figure 3.3.12. CT: Potential Drop Development Curves.
- Figure 3.3.13. CT: Crack Growth Measurement Curves.
- Figure 3.3.14. ICL 167 SPH: CT Fatigue Crack Growth Rate Plots.
- Figure 3.3.15. CT and CCT Results: Fatigue Crack Growth Rates.

Section 3.4.

- Figure 3.4.1. Thermal Cycling Rig.
- Figure 3.4.2. Block Diagram of the Thermal Cycling Rig.
- Figure 3.4.3. Cooling System Expansion Unit.
- Figure 3.4.4. Thermal Gradient Through Tube Thickness During a Cycle.
- Figure 3.4.5. Dimensions of a Tubular Component.
- Figure 3.4.6. Dimensions of the Nozzle Section.
- Figure 3.4.7. Instrumented Specimen Section Containing a Tubular Component.
- Figure 3.4.8. Rubber Moulds of Pre-Test Notch Shape, a) Rectangular, b) Semi-Circular.
- Figure 3.4.9. Tubular Component with Direct Current Input Positions and Potential Measurement Probe Positions.
- Figure 3.4.10. Instrumented Component with a Longitudinal Notch.
- Figure 3.4.11. Instrumented Component with a Circumferential Notch.
- Figure 3.4.12. Surface Temperature Measurements During Thermal Cycling.
- Figure 3.4.13. Aluminium Foil Calibration Curves For External Longitudinal Notched Components.
- Figure 3.4.14. Aluminium Foil Calibration Curves For Internal Longitudinal Notched Components.

Figure 3.4.15. Electro-Erosion Calibration Curves For External Longitudinal Notched Components.

Figure 3.4.16. Electro-Erosion Calibration Curves For Internal Longitudinal Notched Components.

Figure 3.4.17. Aluminium Foil Calibration Curves For Circumferential Notched Components.

Figure 3.4.18. Potential Measurements in Expt.#4.

Figure 3.4.19. Potential Measurements in Expt.#12.

Figure 3.4.20. Normalized Potential Measurements in Expt.#4.

Figure 3.4.21. Normalized Potential Measurements in Expt.#12.

Figure 3.4.22. Crack Growth along the External Surface from the Notch, Expt.#11.

Figure 3.4.23. Crack Growth along the Internal Surface, Expt.#23.

Figure 3.4.24. Transgranular Crack from External Longitudinal Notch, Expt.#4.

Figure 3.4.25. Internal Surface Crack Initiation, Expt.#5.

Figure 3.4.26. External and Internal Crack Coalescence, Expt.#23.

Figure 3.4.27a Calibration Curves for 1mm Deep External Longitudinal Notched Components: Established by Different Methods.

Figure 3.4.27b. Calibration Curves for 2mm Deep External Longitudinal Notched Components: Established by Different Methods.

Figure 3.4.28a. Calibrated Crack Depths in 1mm Deep External Longitudinal Notched Components.

Figure 3.4.28b. Calibrated Crack Depths in 2mm Deep External Longitudinal Notched Components.

Figure 3.4.29. Development of Calibrated Crack Depths in Expt.#11.

Figure 3.4.30. Heat Tinted Half Fracture Surface, Expt.#11.

Figure 3.4.31. Crack Front Development and Experimental Results, Expt.#11.

Figure 3.4.32. Potential Measurements in Expt.#9.

Figure 3.4.33. Potential Measurements in Expt.#17.

Figure 3.4.34. Normalized Potential Measurements in Expt.#9.

Figure 3.4.35. Normalized Potential Measurements in Expt.#17.

Figure 3.4.36. Transgranular Crack from an Internal Longitudinal Notch, Expt.#2.

Figure 3.4.37a Calibration Curves for 1mm Deep Internal Longitudinal Notched Components: Established by Different Methods.

Figure 3.4.37b. Calibration Curves for 2mm Deep Internal Longitudinal Notched Components: Established by Different Methods.

Figure 3.4.38a. Calibrated Crack Depths in 1mm Deep Internal Longitudinal Notched Components.

Figure 3.4.38b. Calibrated Crack Depths in 2mm Deep Internal Longitudinal Notched Components.

- Figure 3.4.39. Calibrated Crack Depths in Expt.#17.
- Figure 3.4.40. Half Fracture Surface, Expt.#2.
- Figure 3.4.41. Crack Front Development and Experimental Results from Expt.#17.
- Figure 3.4.42. Normalized Potential Difference for 1mm Deep External Longitudinal Semi-Circular Notched Components.
- Figure 3.4.43. Normalized Potential Difference for 2mm Deep External Longitudinal Semi-Circular Notched Components.
- Figure 3.4.44. Surface Cracking from 2mm Radius Notch, Expt.#5.
- Figure 3.4.45. Surface Cracking from 2mm Radius Notch, Expt.#19.
- Figure 3.4.46. Transgranular Crack from 2mm Deep Semi-Circular Notch, Expt.#13.
- Figure 3.4.47. Calibrated Crack Depths in External Longitudinal Semi-Circular Notched Components.
- Figure 3.4.48. Potential Measurements During Expt.#3 and Expt.#15.
- Figure 3.4.49. Normalized Potential Measurements in Expt.#3 and Expt.#15.
- Figure 3.4.50. Transgranular Crack in 1mm Deep External Circumferential Notched Component, Expt.#3.
- Figure 3.4.51. Circumferential Crack Fracture Surface, a) Expt.#3, b) Expt.#15.
- Figure 3.4.52. Calibration Curves for 1mm Deep External Circumferential Notched Components: Established by Different Methods.
- Figure 3.4.53. Calibrated Crack Depths in 1mm Deep External Circumferential Notched Components.
- Figure 3.4.54. Potential Measurements in 1mm Deep Internal Circumferential Notched Components.
- Figure 3.4.55. Normalized Potential Measurements in 1mm Deep Internal Circumferential Notched Components.
- Figure 3.4.56. Transgranular Crack in 1mm Deep Internal Circumferential Notched Component, Expt.#6.
- Figure 3.4.57. Circumferential Crack Fracture Surface, Expt.#6.
- Figure 3.4.58. Calibration Curves for 1mm Deep Internal Circumferential Notched Components: Established by Different Methods.
- Figure 3.4.59. Calibrated Crack Depths in 1mm Deep Internal Circumferential Notched Components.
- Figure 3.4.60. External Surface Crack from a Spot Weld, Expt.#7.
- Figure 3.4.61. Pre-Test Laser Welded Spot with a Short Crack, Expt.#21.
- Figure 3.4.62. Post-Test Laser Welded Spot with a Longer Crack, Expt.#21.
- Figure 3.4.63. Crack Growth from Laser Welded Spot, Expt.#21.

Section 4.1.

- Figure 4.1.1a. Thermal Fatigue Crack Growth Rates in a 1mm Deep External Longitudinal Notched Component.
- Figure 4.1.1b. Thermal Fatigue Crack Growth Rates Through a 1mm Deep External Longitudinal Notched Component.
- Figure 4.1.1c. Thermal Fatigue Crack Growth Rates in a 2mm Deep External Longitudinal Notched Component.
- Figure 4.1.1d. Thermal Fatigue Crack Growth Rates Through a 2mm Deep External Longitudinal Notched Component.
- Figure 4.1.1e. Thermal Fatigue Crack Growth Rates in a 1mm Deep Internal Longitudinal Notched Component.
- Figure 4.1.1f. Thermal Fatigue Crack Growth Rates Through a 1mm Deep Internal Longitudinal Notched Component.
- Figure 4.1.1g. Thermal Fatigue Crack Growth Rates in a 2mm Deep Internal Longitudinal Notched Component.
- Figure 4.1.1h. Thermal Fatigue Crack Growth Rates Through a 2mm Deep Internal Longitudinal Notched Component.
- Figure 4.1.1i. Thermal Fatigue Crack Growth Rates in an External Circumferential Notched Component.
- Figure 4.1.1j. Thermal Fatigue Crack Growth Rates Through an External Circumferential Notched Component.
- Figure 4.1.1k. Thermal Fatigue Crack Growth Rates in an Internal Circumferential Notched Component.
- Figure 4.1.1l. Thermal Fatigue Crack Growth Rates Through an Internal Circumferential Notched Component.
- Figure 4.1.2. Thermal Fatigue Crack Growth Rates Through Each of the Notched Components.

Section 4.2.

- Figure 4.2.1. Model of Tubular Component for Finite Element Analysis.
- Figure 4.2.2a. Hoop Stress Through a Section of an Unnotched Component.
- Figure 4.2.2b. Axial Stress Through a Section of an Unnotched Component.
- Figure 4.2.2c. Total Strain Through a Section of an Unnotched Component.
- Figure 4.2.3(a-b). Stress Distribution Through an Unnotched Component During a Thermal Cycle.
- Figure 4.2.4(a-d). Stress Distribution Through an Unnotched Component During a Thermal Cycle.

**Figure 4.2.5. Plastic Strain Distribution Through an Unnotched Component
During a Thermal Cycle.**

Figure 4.2.6. Fatigue Crack Growth From a Spot Weld in Expt.#11.

Figure 4.2.7. Surface Cracking from a Spot Weld in Expt.#7.

Figure 4.2.8,(a-b). Notch Effect on Hoop Stress Profile, (after Andritsos,1991[a-b]).

Figure 4.2.9,(a-d). Notch Effect on Maximum Stress Profiles During a Thermal Cycle.

Section 4.3.

Figure 4.3.1(a-b). Stress Intensity Factors for Longitudinal Cracked Components.

Figure 4.3.2(a-b). Stress Intensity Factors for Circumferential Cracked Components.

Section 4.4.

**Figure 4.4.1a. Thermal Fatigue Crack Growth Rates in External Longitudinal Notched
Components.**

**Figure 4.4.1b. Thermal Fatigue Crack Growth Rates in External Longitudinal Notched
Components.**

**Figure 4.4.1c. Thermal Fatigue Crack Growth Rates in Internal Longitudinal Notched
Components.**

**Figure 4.4.1d. Thermal Fatigue Crack Growth Rates in Circumferential Notched
Components.**

List of Tables.

Section 2.1.

Table 2.1.1. Cyclic Hardening Constants and Coefficients for Annealed Type 316L.

Table 2.1.2. Coefficients from Coffin-Manson Equation for Type 316L.

Section 2.3.

Table 2.3.1. Specifications of First Wall Operating Conditions.

Table 2.3.2. Chemical Composition of Type 316 Stainless Steels.

Table 2.3.3. Physical and Mechanical Properties of ICL 167 SPH.

Section 3.2.

Table 3.2.1. Modulus of Elasticity.

Table 3.2.2a. LCF Results 80°C.

Table 3.2.2b. LCF Results 350°C.

Section 3.3.

Table 3.3.1. Centre Cracked Tension Specimen, Experimental Matrix.

Table 3.3.2. CT Specimen Thermal Gradient.

Table 3.3.3. Maximum Loads for Grips and CT Specimen.

Table 3.3.4. Compact Tension Specimen, Experimental Parameters.

Table 3.3.5. Constants for Paris Law Equations.

Section 3.4.

Table 3.4.1a. Experimental Matrix for Thermal Cycle Fatigue of Tubular Components Containing Longitudinal Rectangular Shaped Notches in the External Surface.

Table 3.4.1b. Experimental Matrix for Thermal Cycle Fatigue of Tubular Components Containing Longitudinal Rectangular Shaped Notches in the Internal Surface.

Table 3.4.1c. Experimental Matrix for Thermal Cycle Fatigue of Tubular Components Containing Longitudinal Semi-Circular Shaped Notches in the External Surface.

- Table 3.4.1d. Experimental Matrix for Thermal Cycle Fatigue of Tubular Components Containing Circumferential Notches in the External Surface.
- Table 3.4.1e. Experimental Matrix for Thermal Cycle Fatigue of Tubular Components Containing Circumferential Notches in the Internal Surface.
- Table 3.4.1f. Experimental Matrix for Thermal Cycle Fatigue of Various Unnotched Tubular Components.
- Table 3.4.2. External Surface Rectangular Notches in the Longitudinal Direction: Experimental Results.
- Table 3.4.3. Internal Surface Rectangular Notches in the Longitudinal Direction: Experimental Results.
- Table 3.4.4. External Surface Semi-Circular Notches in the Longitudinal Direction: Experimental Results.
- Table 3.4.5. External Surface Notches in the Circumferential Plane: Experimental Results.
- Table 3.4.6. Internal Surface Notches in the Circumferential Plane: Experimental Results.
- Table 3.4.7. Miscellaneous Experimental Results.

Section 4.2.

- Table 4.2.1. Reduction in Stress Concentration Factors from Notch Root.

Section 4.3.

- Table 4.3.1. Correction Factor, ω , as a Function of a/t and a/c .

Nomenclature.

Symbol	Description	Units
A	cyclic strength coefficient	KNmm ⁻²
A _f	specimen area at fracture	mm ²
A _o	original specimen area	mm ²
A _n	polynomial coefficients, equation 2.2.35	
A _t	normalized crack depth, equation 2.2.32	mm
a	half-crack depth in Figure 2.2.1, equation 2.2.3	mm
a _{cal}	calibrated crack depth	mm
a _f	final crack depth	mm
a _m	mean crack depth	mm
a _o	original crack depth	mm
a _{op}	optical measurement of crack depth	mm
a _{pd}	potential drop measurement of crack depth	mm
b	fatigue strength exponent	
B	body thickness	mm
C	coefficient in Paris Law, equation 2.2.10	
CH1	p.d. measurement channel number 1	
C _N	plastic compliance, equation 2.2.24	
C _s	specimen compliance, equation 2.2.18b	
c _f	final half-crack surface length	mm
c _o	original half-notch surface length	mm
da	change in crack depth, equation 2.2.10	mm
dN	increase in number of cycles, equation 2.2.10	cycles
E	modulus of elasticity	GPa
E'	plane stress modulus of elasticity	GPa
E _B	cracked body energy, equation 2.2.18e	J
e	engineering strain	
e _n	nominal, smooth specimen, strain	
f _{ij}	non-dimensional functions in equation 2.2.1	
G	strain energy release rate	J/m ²
J	J-integral, equation 2.2.21	N/m
k	exponent in equation 2.1.22	
k _f	theoretical fatigue concentration factor at the notch root	
k _t	theoretical stress concentration factor at the notch root	
k _s	strain concentration factor at the notch root	
k _σ	stress concentration factor at the notch root	

K	stress intensity factor, equation 2.2.14	MPa√m
K_{eff}	effective stress intensity factor, equation 2.2.11	MPa√m
$K_{I,II,III}$	stress intensity factor for each mode of fracture	MPa√m
K_{IC}	material fracture toughness	MPa√m
K_{max}	maximum stress intensity factor, equation 2.2.9	MPa√m
K_{min}	minimum stress intensity factor, equation 2.2.9	MPa√m
ΔK	range of stress intensity factor	MPa√m
ΔK_{eq}	equivalent stress intensity factor, equation 2.2.30	MPa√m
ΔK_{th}	threshold stress intensity factor	MPa√m
ΔK_c	strain intensity factor, equation 2.2.29	
l	crack length (in equation 2.1.12)	mm
l_0	original specimen gauge length	mm
Δl	change in specimen gauge length	mm
L	strength coefficient, equation 2.1.6	KNmm ⁻²
m	coefficient in Paris Law, equation 2.2.10	
$m(A_i, X_i)$	weight function, equation 2.2.32	
n	strain hardening exponent, equation 2.1.6	
n'	cyclic strain-hardening exponent	
N	number of fatigue cycles	cycles
N_f	number of fatigue cycles to failure	cycles
P	load	KN
P_f	load at fracture, equation 2.1.4	KN
P_{max}	maximum load	KN
Q	coefficient in equation 2.2.24	
q	coefficient of crack opening, equation 2.2.29	
r	crack tip radial coordinate, equation 2.2.1	mm
r_i	internal radius of tubular component	mm
r_o	external radius of tubular component	mm
r_y	plastic zone size at the crack tip, equation 2.2.6	mm
R	load ratio, $\sigma_{min}/\sigma_{max}$	
REF.	p.d. measurement reference channel	
S	engineering stress	KNmm ⁻²
S_e	endurance strength	KNmm ⁻²
S_n	nominal smooth specimen stress	KNmm ⁻²
S_u	engineering ultimate tensile strength	KNmm ⁻²
S_y	engineering proof strength	KNmm ⁻²
T	temperature	°C
T_{av}	volume average temperature	°C

\underline{T}	stress vector, equation 2.2.21	KNmm ²
t	thickness of thermally shocked component	mm
u	load point displacement, equation 2.2.18b	mm
U_a	strain energy of a crack, equation 2.2.33	J
V_a	potential difference over a crack of depth, "a"	mV
V_o	potential difference over the original crack depth	mV
V^*	normalized potential difference, $(V_a - V_o)/V_o$	
W	specimen width	mm
W_e	strain energy density, equation 2.2.21	J/m ³
W_f	final specimen width	mm
W_o	original specimen width	mm
X_t	normalized distance, x/t , equation 2.2.32	
x	distance, equation 2.2.33	mm
Y	compliance function, equation 2.2.9	
Y_n	magnification factor, equation 2.2.35	
Z	constant in equation 2.1.12	cycles ⁻¹
α	coefficient of thermal expansion	K ⁻¹
β	exponent in the Coffin-Manson equation.	
δ	crack tip opening displacement, equation 2.2.13	mm
δ_c	critical crack tip opening displacement	mm
δU	crack extension energy, equation 2.2.18a	J
ΔU_p	change in plastic work, equation 2.2.25	J
ϵ	strain rate	sec ⁻¹
ϵ_a	strain amplitude during a cycle	
ϵ_e	elastic strain	
ϵ_{eb}	elastic biaxial strain	
ϵ_{eu}	elastic uniaxial strain	
ϵ_f	fracture ductility	
ϵ_f'	tensile ductility in the Coffin-Manson equation.	
ϵ_p	plastic strain	
ϵ_{pb}	plastic biaxial strain	
ϵ_t	total strain	
ϵ_{tb}	total biaxial strain	
ϵ_{tu}	total uniaxial strain	

ϵ_1	maximum local principal strain at the notch root	
$\Delta\epsilon_e$	elastic strain range	
$\Delta\epsilon_e/2$	elastic strain amplitude	
$\Delta\epsilon_p$	plastic strain range	
$\Delta\epsilon_p/2$	plastic strain amplitude	
$\Delta\epsilon_t$	total strain range	
$\Delta\epsilon_t/2$	total strain amplitude	
σ	stress	KNmm ⁻²
σ_a	stress amplitude	KNmm ⁻²
σ_{eqb}	equivalent equibiaxial stress, equation 2.2.37	KNmm ⁻²
σ_f	engineering fracture strength	KNmm ⁻²
σ_{fs}	flow strength, equation 3.3.2	KNmm ⁻²
σ_f'	fatigue strength coefficient	KNmm ⁻²
σ_{ij}	stress tensor at the crack tip in equation 2.2.1	KNmm ⁻²
σ_m	mean stress	KNmm ⁻²
σ_{max}	maximum tensile stress	KNmm ⁻²
σ_{min}	maximum tensile stress	KNmm ⁻²
σ_o	maximum quenched surface stress	KNmm ⁻²
σ_T	average deformation zone stress, equation 2.2.12	KNmm ⁻²
σ_u	ultimate tensile stress of the material	KNmm ⁻²
σ_{ys}	yield stress of the material	KNmm ⁻²
$\sigma_{1,2,3}$	principal components of stress, equation 2.2.5	KNmm ⁻²
$\sigma(X)$	function of stress gradient, equation 2.2.32	KNmm ⁻²
$\sigma(x)$	function of stress gradient, equation 2.2.33	KNmm ⁻²
$\Delta\sigma$	stress range	KNmm ⁻²
$\Delta\sigma_{eq}$	pseudo elastic stress range, equation 2.2.30	KNmm ⁻²
$\Delta\sigma/2$	stress range amplitude	KNmm ⁻²
$\Delta\eta_p$	coefficient in equation 2.2.25	
$\tau_{xy,yz,zx}$	shear stress near a crack tip, equation 2.2.2	KNmm ⁻²
π	3.147	
ν	frequency of fatigue cycles	Hz
ν_p	Poisson's ratio	
θ	polar coordinate in equation 2.2.1	°
$\Phi(x)$	displacement between crack surfaces, equation 2.2.33	mm
ω	crack shape development factor	
%RA	reduction in area of the gauge section	

1.0. Introduction.

Engineering materials are an important commodity in the development of modern society. Engineers use the diverse properties of different materials in the design of products and systems to meet society's needs. Beyond the basic requirements of survival, (food, shelter and clothing), energy must rank as the greatest of modern society's needs. The greatest demand is for the generation of electricity. There is increasing awareness of the ecological damage involved in the burning of fossil fuels therefore the requirements for alternative sources of energy has never been greater. Extended use of the waves, wind and the force of gravity on water to generate electricity, produces visions of a clean, efficient and cheap energy source in the twenty-first century. However, in reality, the most developed method of generating ecological friendly electricity, a hydro-electric power station, can only produce one tenth of the present demand of a coal burning power station.

A solution is required which does not have the limited life of fossil fuels but can generate electricity in a large enough quantity to meet the demand for power. Generation of electricity using the thermal product of nuclear reactions has increased over the last forty years. However, the combined problems associated with the radioactive waste from nuclear fission and the threat of radioactive contamination of the atmosphere as a consequence of a reaction chamber melt-down has turned public opinion away from nuclear power as the preferred source of energy. Consequently, a greater interest has been placed on the development of a power station which generates electricity from a fusion reaction. The physics involved is beyond the scope of this thesis. However, a fusion reaction occurs as a chain reaction to produce energy, a helium nucleus and gamma radiation. The continuous use of reaction products to initiate further reactions reduces the quantity of radioactive waste. Therefore a significant problem for the engineer, is to design a structure that can house a fusion reaction while safely supporting the necessary components under in service loading conditions.

Thus the engineer has the unenviable task of designing a large structure and selecting materials which will be subjected to loads that can only be speculated during the design phase. Therefore, since the early 1980's, a number of European and international committees have been formed to investigate the material requirements of the components of a fusion reactor, [Harries,1986]. The Next European Torus, (NET), is the nuclear fusion project of the European Communities. The basic design of the NET experimental fusion reactor contains a thermonuclear plasma within a pulsed electromagnetic field, as illustrated in Figure 1.0.1. The structure is supported by a first wall with divertor plates, to maintain the purity of the plasma, and a breeding blanket, which is a system for heat

recovery and tritium production.

The original candidate materials for the first wall components were ICL 167 SPH, which is a batch of Type 316L austenitic stainless steel, and the martensitic steel, DIN 1.4914. The three main damaging processes of the first wall in service conditions have been identified as thermal fatigue, plasma disruptions and irradiation creep, [Merola and Matera,1991]. Both materials have been compared under the proposed loading conditions, [Harries and Zolti,1986], and the austenitic stainless was selected, mainly due to the large industrial and nuclear experience acquired on this material.

Within the framework of the NET project, an investigation into the integrity of first wall components is being made at the Commission of the European Communities' Institute for Advanced Materials, at Petten in The Netherlands. The project was divided into two parts. The first was an experimental simulation of the behaviour of first wall components when subjected to the proposed thermal cycling out-of-pile, which forms the subject of this thesis. The task of developing this experimental rig and analysing the results, was designated to the components testing section of the material characterisations group. The second part of the NET first wall project is to investigate the thermal cyclic loading of similar components within the high flux fission reactor, at Petten. The components testing section is in an expert position to investigate the behaviour of first wall components due to their previous success in developing unique component testing rigs, [Hunter and Hurst,1989], combined with the available knowledge in the behaviour of steels and alloys under loading conditions within the power generation industry.

With the continuous development in the design of the fusion reactor, both the structural design and the first wall loading parameters have been specified, [Merola and Matera,1991]. The thinnest designed sections of the first wall are 10mm in thickness, from the plasma facing surface through to the internal surface of the coolant flow channel. The most life diminishing effect has been predicted to be the thermal fatigue crack growth resulting from the combination of the thermal cycles and defects in the first wall components. Manufacturers and operators of structural components have learned to live with the problems of in service fatigue loading using information available on material properties and the effects of cyclic stresses, environmental conditions and surface quality. However the majority of fatigue lifetime predictions have been produced using standard specimen geometries under controlled loading conditions. Complications arise when the shape of actual components differs greatly from that of the test specimen and when the component is subjected to a combination of loading such as variable cycling, internal surface pressure and axial stress at high temperatures. When thick-walled tubular components are subjected to a combination of external heating and

internal cooling, thermal gradients will develop through the thickness of the component. Cycling the external surface temperatures will produce transient secondary stresses within the component, the magnitude of which will depend upon the range in temperatures, the material characteristics and the geometry of the component. the difficulty in calculating the magnitude of such stresses is increased further when a defect or a crack is situated within the thickness of the component.

A combination of these factors govern the effective lifetime of the first wall components. It is normally considered impossible to predict the lifetime of such components from available mechanical fatigue data for similar austenitic stainless steels. Research is required into the behaviour of components under conditions which simulate the most damaging first wall loading conditions.

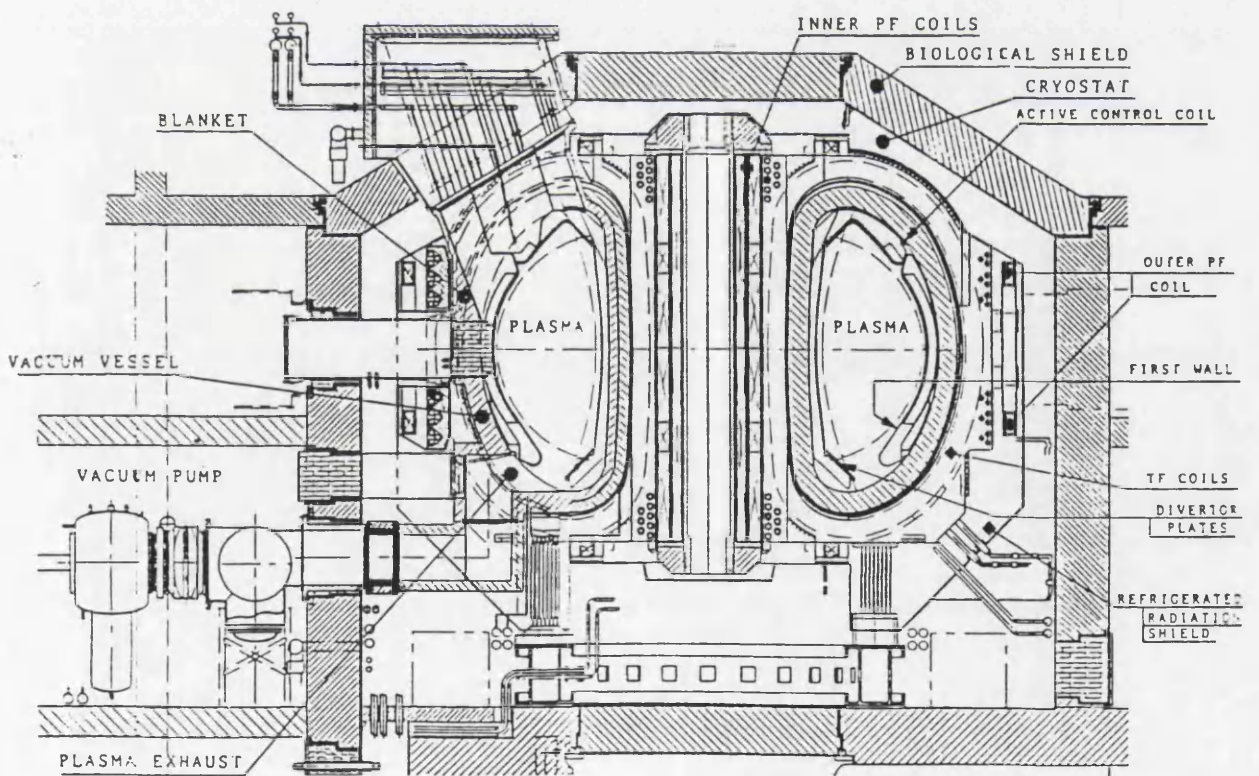


Figure 1.01. Experimental Fusion Reactor NET, (after Merola and Matera,[1991]).

2.0. Literature Review.

The aim of the following sections is to introduce the important terms in the study of fatigue behaviour of metals with reference to the findings of previous investigations. Following an introduction to the process of fatigue failure a section will be devoted to the various methods which have been employed to determine the fatigue behaviour of metals and the relationships developed to relate the behaviour of metals to the test conditions. The effects of external parameters on the mechanical fatigue behaviour of metals will introduce the effect of increased and varying temperature which in turn will lead on to the study of thermal fatigue behaviour of metals.

Interest will then be diverted to the study of fracture mechanics and the methods of determining the behaviour of metals in relation to fatigue crack growth under mechanical loading. This section will be extended to crack growth under thermal fatigue loading and the significance that this has on the development of electricity generating power stations.

From this position the material of interest ICL 167 SPH will be introduced, its similarity to other 316 type stainless steels will be described and the relevant fatigue and fatigue crack growth relationships produced from the available literature on austenitic stainless steels. Specific interest will be made to the proposed conditions of application of the components of the first wall of a nuclear fusion reactor and the necessary data required to perform thermal cycling tests and analyse the resultant data will be discussed.

2.1.1. Introduction To Fatigue.

In engineering terms, fatigue is the failure of a component at a stress concentrating region through the propagation of a crack under cyclic loading. The amplitude of cyclic stress is often below that of the yield strength of the material, which is determined from increasing tensile load tests, which are often expressed as monotonic load tests. The process of fatigue failure is a combination of three stages; local deformation, crack initiation and crack propagation to failure. In engineering terms;

- 1) Dislocation movement produce microcrack initiation within the grains of the material's substructure. The cracks are relative in dimensions to grain size.
- 2) Coalescence of microcracks to form and initiate a macrocrack.
- 3) The crack propagates in a perpendicular direction to the applied load and final fracture occurs when the crack is very long and the remaining ligament cannot support

the load.

The process of fatigue contributes to the failure of components in many industrial applications. Engineering theory is applied at many of the cornerstones that support the national economies, including energy generation, manufacturing processes and methods of transportation. In each application there are requirements for the safe and economical use of materials for manufacture of both structures and working parts. During service, load carrying components can experience vibrations, cyclic movements, shutdowns, start-ups, heating and cooling resulting in cyclic loading. The resultant cyclic stresses and strains enhance the fatigue failure of the components. For simplicity the origins of the damaging stresses can be separated and the term fatigue can be described as;

1) mechanical fatigue in which direct loading produces primary stresses in components in the automotive industry, air and space travel, offshore structures and power generation.

2) thermal fatigue in which thermal differences produce secondary stresses in components in advanced gas cooled reactors, engine blades, sodium-cooled fast reactors, proposed fusion reactors, military gun barrels and steam turbines.

To design components for such industrial applications the engineer needs to know the operating load conditions and which materials can perform satisfactorily under these conditions. Therefore knowledge of the material properties data and the behaviour of materials under the actions of various loading conditions are required. The term "fatigue" was originally used by Braithwaite,[1854], in an address to the Institution of Civil Engineers in 1854, to describe the failure of various pieces of industrial equipment including railway carriage axles and manufacturing equipment used in brewing beer. With continued failures in both railway bridges and wheel axles investigations into the fatigue behaviour of iron and steel became very important for both safe designs and liability cases. In Germany, Wöhler,[1871], investigated the fatigue behaviour of railway axle steels with decreasing stress amplitudes and found that failure occurred at cyclic stress levels which were less than the yield strength of the material as determined from uniaxial tensile tests. From the early experiments to the present day the study of fatigue has expanded and has become a very complex subject. Using the history of fatigue as a guideline the following sections will describe the important relationships which relate the fatigue process and the experimental techniques used to explain them. It is worthwhile to introduce monotonic testing as the behaviour of materials from such tests are constantly used as comparisons with the behaviour of materials under cyclic loading.

2.1.2. Monotonic Testing Properties.

In a tension test a smooth specimen with either a cylindrical gauge section or a flat sheet section is subjected to an increasing uniaxial tensile load while the resultant elongation is measured. Two stress/strain curves can be developed from this testing technique, Figure 2.1.1. The engineering stress/strain curve is a direct measurement of applied load, P , divided by original specimen area, A_o , plotted against change in specimen gauge length, Δl , divided by original specimen gauge length, l_o . The modulus of elasticity is the slope of this curve in the initial linear regime and is given by the equation;

$$E = \frac{S}{e} = \frac{\left(\frac{P}{A_o}\right)}{\left(\frac{\Delta l}{l_o}\right)} \quad (2.1.1)$$

The engineering proof strength of the material is the stress at which an offset line, (normally 0.2% strain), with slope E , intersects the stress/strain curve. The engineering ultimate tensile strength is the stress at maximum load, and is given by the equation;

$$S_u = \frac{P_{\max}}{A_o} \quad (2.1.2)$$

When the reduction in area of the gauge section is taken into account then the true engineering stress/strain curve is developed. At all tensile stresses, the true stress continues to increase due to increasing load. The reduction in area is given by the equation;

$$\%RA = \left(\frac{A_o - A_f}{A_o}\right) \times 100 \quad (2.1.3)$$

The true engineering fracture strength, σ_f , is given by the equation;

$$\sigma_f = \frac{P_f}{A_f} \quad (2.1.4)$$

while the true fracture ductility, ϵ_f , is given by the equation;

$$\varepsilon_f = \ln\left(\frac{A_o}{A_f}\right) \quad (2.1.5)$$

where the subscript, f, represents values at fracture and the subscript, o, represents original values. From Figure 2.1.1, the relationship between true stress and true plastic strain is developed which includes the strain hardening exponent, n, and the strength coefficient, L;

$$\sigma = L(\varepsilon_p)^n \quad (2.1.6)$$

Equation 2.1.6 can be used to compare with the cyclic stress/strain behaviour of the material and will be discussed in greater detail in the following sections.

2.1.3. Mechanical Properties Of Fatigue.

2.1.3.1. Stress Cycling Properties.

The first systematic fatigue testing was carried out by Wöhler,[1871], between 1852 and 1875 on smooth and notched specimens of railway axle steels. He performed the experiments on a rotating bending stress machine under stress control. Stress control tests can be performed using axial loading, (tensile-compression), rotating bending or alternate bending. Stress control is obtained by cycling the specimen between a pre-determined load. Figure 2.1.2. displays the important stress parameters. Wöhler,[1871], was the first to perform a series of experiments on similar specimens, each at a different stress amplitude, and to display the results as stress-range/life plots. He also found that the number of cycles required to cause failure of a steel specimen decreased when a notch was introduced and the specimen was tested at the same nominal stress range. Through the development of fatigue testing both the specimen geometry and testing techniques have been standardised. Experiments are performed on solid section specimens with circular or rectangular cross-sections with or without machined notches. With notches, the circular cross-section specimen normally has a circumferential notch while the rectangular cross-sectioned specimen normally has side notches. The different testing techniques produce different results due to the stress gradients through the specimen. Uniaxial tests produce a uniform stress gradient across the whole cross section while bend test specimens experience large stresses at the outer surface and zero stress in their centres.

From Wöhler's original experiments the first S/N curves were developed, Figure 2.1.3, which displayed that with decreasing stress, steels are subjected to increasing cycles to

failure until a certain stress at which fatigue failure does not occur. The investigation of the fatigue behaviour of iron and steels was continued in Germany by Bauschinger,[1886], who invented a mirror extensometer which measured small inelastic strains. Bauschinger confirmed Wöhler's findings that at low stresses there existed a "natural elastic limit" below which fatigue would not occur. This was termed as the fatigue limit of the ferrous metals. With non-ferrous alloys and aluminium the rate of decreasing stress amplitude with increasing number of cycles is less and there is no definite fatigue limit. This led to the recognition of an endurance limit of 10^7 cycles, therefore avoiding infinite life tests. In the early years of the 20th century, Basquin,[1910], was investigating endurance testing and described fatigue failure during tests in which the stress amplitude was the same for each cycle by a relationship of the following form;

$$\Delta\sigma = \sigma'_f (N_f)^{-b} \quad (2.1.7)$$

where $\Delta\sigma$ is the stress range, σ'_f is the fatigue strength coefficient given by extrapolation of the S/N curve to $N=1$, N_f is the number of cycles to failure and b is called the fatigue strength exponent which is the slope of the line on a $\log\Delta\sigma$ vs. $\log N_f$ plot. This coefficient is often within the range $-0.12 < b < -0.05$. As recently as the 1960's, Morrow,[1965], took mean stress, σ_m , into account and developed equation 2.1.7 into;

$$\Delta\sigma = (\sigma'_f - \sigma_m) (N_f)^{-b} \quad (2.1.8)$$

This relationship displays a decrease in fatigue life with a tensile mean stress and an increase in fatigue life with a compressive mean stress. When a specimen is subjected to a state of stress that combines a mean stress, σ_m , with a cyclic stress amplitude, σ_a , failure by fatigue fracture may be predicted from a Goodman diagram. The Goodman diagram contains the modified Goodman line which relates the mean stress, on the x-axis, to the stress amplitude, on the y-axis, by the equation;

$$\frac{\sigma_m}{S_u} + \frac{\sigma_a}{S_e} = 1 \quad (2.1.9a)$$

where S_u is the tensile strength of the material and S_e is the endurance strength of the material. If the plotted point, (σ_m, σ_a) , lies between the line represented by equation 2.1.9a and the x-axis, then it may be assumed that fatigue failure will not occur. Upon yielding, the modified Goodman line is altered to take the yield strength, S_y , of the material into account;

$$\frac{\sigma_m}{S_u} + \frac{\sigma_a}{S_e} = 1 \quad \text{for} \quad \frac{\sigma_a}{\sigma_m} \geq \frac{S_e}{S_u} \left(\frac{S_u - S_y}{S_y - S_e} \right) \quad (2.1.9b)$$

and

$$\sigma_a + \sigma_m = S_y \quad \text{for} \quad \frac{\sigma_a}{\sigma_m} \leq \frac{S_e}{S_u} \left(\frac{S_u - S_y}{S_y - S_e} \right) \quad (2.1.9c)$$

To take into account the more detrimental effect of tensile mean stresses in comparison to compressive mean stresses, the Goodman diagram may be altered to that shown for the yield criteria in Figure 2.1.4. Goodman diagrams can also be constructed for conditions of bending and torsion loading and those of general biaxial states of stress, [Budynas,1977].

Ewing and Humfrey,[1903], performed microscopic studies, at 1000 times magnification, of the same region of a flat fatigue specimen of annealed steel at various intervals during stress cycling. After a few cycles they observed slip lines on some of the crystals. The slip lines were similar to those observed on a specimen after static tensile loading beyond the yield stress. After more cycles the density of slip lines increased. Further cycling and the slip lines appeared as wide bands with tangled boundaries. With increasing number of cycles the breadth of the bands increased and dark markings were observed on the surface. The broad bands had formed as crystals and cracking was observed along the broad slip bands and in some cases on a single crystal. More cycling and individual cracks across the crystals coalesced to form one long crack which grew to fracture. This investigation described the basics of the fatigue failure process.

During the first twenty years of the 20th century cyclic strain was identified as an important factor in the process of fatigue failure. Bairstow,[1911], measured cyclic plastic strains during axial push-pull tests on iron and steel. He observed cyclic softening in axle steel at stress levels well below the yield point on the monotonic stress-strain curve. He also recognised that the endurance limit was at a stress level corresponding to predominately elastic strains. During 1915 Smith and Wedgewood,[1915], presented stabilized cyclic stress-strain hysteresis loops which were later analysed by Jenkins,[1923], who presented a model which described the effects of stress amplitude, mean stress and previous loading history on the cyclic stress-strain curves.

During the 1920's Griffith,[1921], presented his classic paper, which demonstrated that when a crack grows to a critical length then depending on the magnitude of the applied load, brittle fracture occurs. This is exactly the same as the last cycle of a fatigue failure

at a critical crack length. However it was not until forty years later that interest in fatigue related fracture mechanics began. Modern fatigue fracture mechanics is to be discussed in detail in a later section. During the forty years following the introduction of Griffith's fracture theory, research into fatigue was mainly performed to determine the effects of various factors on long-term fatigue life. However many theoretical studies were made on the elastic thermal stresses resulting from temperature differences in tubes, [Barker,1927], spheres and cylinders, [Kent,1932], flat plates, thin and thick-walled cylinders, [Goodier,1937], and in the case of periodic surface temperatures on cylinders, [Jaeger,1945]. Although these studies did not indicate the effects of cyclic thermal stresses on the various geometries they did display the large magnitude of stresses that could be generated through heating components.

In 1954 two simultaneous, independent investigations into the effects of cyclic thermal stresses on ductile materials by Coffin,[1954], and Manson,[1954], led to the confirmation that cyclic plastic strain was the basic cause of fatigue failure. Both parties performed experiments under cyclic temperature conditions and related the fatigue life to the plastic strain range. Coffin suggested that even at very low ranges of total plastic strain a fatigue crack would propagate and that the endurance limit, as observed in ferrous metals, was a strain ageing effect due to the diffusion of impurity atoms which prevent the reverse motion of dislocations. If the range of applied stress is low then it could be impossible for dislocations to cross-slip to a neighbouring plane. Therefore microcracks can not nucleate and the stress level remains constant with the increasing number of cycles. The investigations of Coffin and Manson brought about a renewed interest in cyclic strain and the initiation for the development of fatigue life relationships based on strain control.

2.1.3.2. Strain Cycling Properties.

During strain controlled experiments a specimen is cycled between pre-determined strain amplitudes over the specimen's gauge length. Simultaneous recording of the stress and strain amplitudes produces a hysteresis loop. The changes in the hysteresis loop during a test produce a graphical representation of the process of fatigue. Figure 2.1.5 is a typical hysteresis loop displaying the stress range, $\Delta\sigma$, and the total strain range, $\Delta\varepsilon_t$, which is the sum of the elastic strain range, $\Delta\varepsilon_e$, and the plastic strain range, $\Delta\varepsilon_p$. During a strain controlled experiment the initial change in stress range of the hysteresis loop displays whether the material cyclic hardens or cyclic softens and when a stable stress range is reached corresponds to the number of cycles at which saturation occurs. Towards failure the stress range changes once more, normally the stress range decreases over the last number of cycles however with some materials the stress range increases. The behaviour

of the stress range during a strain controlled test is clearly observed in a plot of stress against number of cycles, Figure 2.1.6. The number of cycles corresponding to hardening/softening, saturation and failure are easily identified.

During the saturation period the hysteresis loops produced during each cycle are identical. Plotting the total strain range against the stress range, as defined in Figure 2.1.7, for a number of tests which were performed at different strain ranges produces the cyclic stress/strain curve for the material under the conditions of testing. The cyclic stress strain curve is described by a relationship between the cyclic plastic strain range and the steady state stress range in the following form;

$$\Delta\sigma = A(\Delta\varepsilon_p)^{n'} \quad (2.1.10)$$

where n' is the cyclic strain-hardening exponent and A is a constant, sometimes called the cyclic strength coefficient. Values of A and n' have been developed for type 316L stainless steel, in terms of the saturated stress amplitude, $\Delta\sigma/2$, and the saturated plastic strain amplitude, $\Delta\varepsilon_p/2$, and are presented in Table 2.1.1, [Gorlier et al., 1984], [Brun et al., 1976].

Temperature (°C)	A	n'
20	1300	0.21
300 ($\Delta\varepsilon_p \leq 10^{-3}$)	460	0.13
300 ($\Delta\varepsilon_p \geq 10^{-3}$)	4400	0.53
600	1500	0.29
20	1720.5	0.294
300	1267.4	0.2619
450	1042.1	0.2147

Table 2.1.1 Cyclic Hardening Constants and Coefficients for Annealed Type 316L.

When the cyclic stress-strain curve is compared with the monotonic curve the cyclically induced changes in deformation resistance are observed. If the cyclic stress-strain curve lies above the monotonic curve, the material cyclically hardens, if the cyclic curve is below the monotonic the material cyclically softens. Pre-cycling treatment of a metal can result in either hardening or softening. Typically, metals which have been cold worked, (a percentage reduction in area by straining), display softening upon cycling while metals which have been annealed, (held at a high temperature before natural cooling), display hardening upon cycling. In metals which have a face centred cubic, (f.c.c.), lattice such as copper, aluminium and nickel the cyclic stress-strain curve stabilises to the same value independent of the prestrain, as shown for copper in Figure 2.1.8., Feltner and Laird, [1967]. The copper was pre-strained up to 50% in tension at room temperature and the greatest annealing was for 24 hours at 450°C. A similar behaviour was observed with cold-worked and annealed pure aluminium. In contrast to these observations with OFHC copper, Lukas and Klesnil,[1973], have shown the above statement to be true for prestrains up to 20%. For prestrains above 20% the cyclic stress-strain curves lie slightly above the corresponding curves for the annealed material. For Cu-7.5%Al, (f.c.c.), the cyclic stress-strain curve from the cold worked material always lies above that of the annealed material. Thus indicating that the material maintains a degree of the initial hardening effects of the cold-working.

Under cyclic loading at room temperature, Type 316L in the annealed condition hardened to such an extent that the cyclic stress-strain curve sat well above the monotonic stress-strain curve, especially at high strain amplitudes, while the same batch of material pre-strained to a 20% cold-work condition softened, [Lieurade et al.,1986]. Cyclic softening of Type 316 stainless steel, which was cold-worked to a 20% reduction

in area, produced a cyclic stress-strain curve below the corresponding monotonic stress-strain curve at room temperature, [Manjoine and Landerman,1982]. While 40% cold-worked Type 316, cycled over a wide range of strain amplitudes, softened at both room temperature and 600°C, [Plumbridge et al.,1980]. Cyclic hardening occurred with annealed Type 316L at both room temperature and 600°C, although the stabilized stress magnitude decreased with increasing temperature, [Degallaix et al.,1988].

Landgraf et al.,[1969], have demonstrated four quick methods of obtaining the cyclic stress strain curve, for several metals, each using only one specimen. These methods include;

1) multiple step tests; in which a smooth specimen is cycled for about 20% of the life at high strain until saturation: A point for the cyclic stress strain curve is obtained, the stress and strain are brought to zero and another block of cycling is carried out at a lower strain amplitude than the first block and so forth.

2) incremental step tests; in which a smooth specimen is subjected to blocks of 20 or so gradually increasing then decreasing strain amplitudes. After a small number of these blocks the material stabilises resulting in a series of superimposed hysteresis loops with a clearly easily observed locus of tips corresponding to the cyclic stress strain curve.

3) monotonic tension after cyclic straining; in which a specimen is cycled to saturation by one of the previous two methods and is tested to fracture in tension. The resultant monotonic tension curve was observed to almost lie over the locus of loop tips for an aluminium alloy.

4) individual hysteresis loop; in which the cyclic stress strain curve is estimated from a stabilized hysteresis loop by measuring the corresponding stress and strain from the loop tip and dividing these values by two.

Agreement between the incremental, multiple step cycling data and the series of specimen results was achieved at large strains with three different pre-treated specimens of OFHC copper. However with various alloys the results from the four different methods produced very similar values to the multiple specimen cyclic stress-strain curves. Both the cyclic stress-strain and incremental step technique displayed the expected shape relative to the monotonic stress-strain curves for quenched and tempered SAE 1045 and SAE 4142 steels with four different values of original hardness. For each steel an increasing degree of cyclic softening was observed with decreasing original hardness.

The cyclic stress strain curves can vary if the temperature or the strain rate at which the test is performed are changed. Mowbray and McConnelee,[1973], have investigated the effect of increasing temperature from room temperature to 285°C on the cyclic stress strain response of three different steels. With 2¼Cr.1Mo steel a slight decrease in the cyclic yield stress and a slight increase in the following hardening rate were observed. With a low carbon steel there was a marked change in both the yield stress and the following strain hardening. Both increased well with the increase in temperature which was due in part to a strain ageing phenomena. With 304 austenitic stainless steel the yield stress was difficult to determine at room temperature however the number of curves from the first cycle to a shakedown beyond 100 cycles indicated that the yield stress would be greater at room temperature than at and 285°C. However the corresponding strain hardening rate would have been greater at the higher temperature.

Cyclic stress-strain curves have been produced by Jaske et al.,[1973], for annealed Type 304 and solution-annealed iron-nickel-chromium Alloy 800 over a range of temperatures using both the increment step technique and the standard multiple specimen technique. As with the results of Mowbray and McConnelee, Jaske and co-workers found that the yield stress of the Type 304 decreased with increasing temperature between room temperature and 649°C. However they also found the resulting cyclic hardening to decrease with increasing temperature. With Alloy 800 both the yield stress and the resulting cyclic hardening increased between room temperature and 427°C then simultaneously decreased with increasing temperature between 427°C and 760°C. At the higher temperature range Jaske and co-workers found that decreasing the strain rate from 4×10^{-3} to 4×10^{-5} sec⁻¹ increased the cyclic hardening at 538°C and decreased it at 649°C. These results indicated that there was a time dependent factor on the cyclic stress-strain behaviour at high temperatures. This could possibly be a creep crack growth or creep interaction effect which brings in the effect that hold times at maximum or minimum strain have on the cyclic stress strain curve.

Abdel-Raouf et al.,[1973], have also produced cyclic stress-strain curves for low carbon steel at different strain rates at a range of temperatures between room temperature and 540°C. At room temperature the hardening increased with strain rate however at 205°C the hardening decreased with increasing strain rates. At both of these temperatures secondary hardening was observed. Secondary hardening occurs after a saturation period following the initial hardening. Secondary hardening occurred in tests performed at 370°C where decreasing strain rate produced greater hardening. The secondary hardening was due to strain ageing effects except for the tests performed at 540°C in which no secondary hardening occurred and the amount of hardening increased with

strain rate. At the lowest strain rate, $4 \times 10^{-4} \text{ sec}^{-1}$ no primary hardening was observed for the range of strain amplitude investigated. Low carbon steels have a high interaction energy between dislocations and impurity atoms which encourages secondary hardening.

A 40% cold-worked Type 316, which was cycled over a wide range of strain amplitudes, softened at both room temperature and 600°C , [Plumbridge et al.,1980]. Cyclic hardening occurred with annealed Type 316L at both room temperature and 600°C , although the stabilized stress magnitude decreased with increasing temperature, [Degallaix et al.,1988]. Previous ageing at 600°C produced no differences in the hardening nature of the material although the stabilized stress magnitude decreased with longer aged material at the high strain ranges and high temperature. With annealed 316L an increase in nitrogen content produces cyclic softening at low strain ranges and hardening at high strain ranges and room temperature. An increase in temperature to 600°C and hardening was observed with high nitrogen contents although the degree of hardening is less at lower strain ranges than at the higher strain ranges of 1%. The effect of increased ageing on Type 316LN with increased nitrogen content produces fatigue softening at lower strain ranges and hardening at higher strain ranges when tested at both 20°C and 600°C .

For nuclear reactor applications, Grossbeck and Liu, [1981,1982,1985], irradiated samples of 20% cold-worked Type 316 stainless steel and found similar magnitudes of irradiation resulted in cyclic hardening when tested at 430°C , cyclic softening when tested at 550°C and no change when tested at 650°C . All fatigue tests were performed in a vacuum. Vandermeulen et al.,[1988], also observed a hardening effect of irradiated Type 316L when tested in air at 430°C . Following hardening the flow stress of the irradiated material was twice that of the unirradiated material.

Cycling annealed Type 316L specimens in a vacuum displayed little difference from the cyclic hardening behaviour in air at both room temperature and 600°C , [Driver et al.,1988]. The increasing temperature resulted in a decrease in the saturated stress amplitude in both vacuum and air. With low strain range tests at 300°C , the saturation stress values in a vacuum were larger than the corresponding values in air. This resulted from a secondary hardening behaviour of the steel in a vacuum, which appeared as the specimen in air failed and the vacuum specimen continued to harden during its extended fatigue life. With single crystals, very little hardening was observed at low temperatures, $\leq 300^\circ\text{C}$, and low plastic strain ranges, $\leq 0.3\%$, while at higher strains and higher temperatures, the crystals display large proportions of cyclic hardening which produce higher saturation stresses at 600°C than at both 300°C and 20°C . Following the rapid hardening at 600°C a long period of cyclic softening occurred. In a vacuum the fatigue

life of the single crystals was over three times that in air and the cyclic hardening continued to failure and produced a saturation stress that was twice the value of that in air.

Gorlier et al.,[1984], developed cyclic stress-strain curves from the data of Driver et al.,[1988], for polycrystal and single crystal Type 316L in air. On a log-log scale, a straight line relationship was obtained between the saturation stress amplitude, $\Delta\sigma/2$, and the saturated plastic strain amplitude, $\Delta\varepsilon_p/2$, at both 20°C and 600°C for both the polycrystal and the single crystal material. At 300°C a break in the straight line plots was observed, with an increase in hardening at plastic strain amplitudes above 2×10^{-3} . The higher rate of hardening at both 300°C and 600°C corresponded with the required temperature and plastic strain range conditions for the Portevin-Le Chatelier effect to occur. This dynamic strain ageing effect occurs from successive yielding and ageing during the test and results in slightly larger stress amplitudes at stabilization.

The material also displayed a memory effect, that is the influence of high strain pre-cycling on a subsequent low strain level in a two step test, [Gorlier et al.,1984]. The specimen was cycled to saturation at $\Delta\varepsilon_p/2 = 2\%$, then the remainder of the test was performed at a total strain amplitude of 0.3% at which the resultant saturation stress amplitude was compared with that of a specimen cycled continuously at a total strain amplitude of 0.3%. At room temperature the two step saturation stress amplitude was 120MPa greater than that of the continuous test. Identical two step tests at 300°C and 600°C resulted in greater saturation stress amplitudes of 90MPa and 50MPa respectively.

2.1.3.3. Shakedown and Ratchetting.

The transition period of cyclic strain is not confined to loading above the yield stress. It is possible for a structure to experience an applied load above yielding during the initial cycling, followed by purely elastic loading. This process is known as shakedown and depends on the magnitude of the residual stress field that develops in the structure following the initial applied loading. If the maximum applied tensile stress does not exceed twice the yield stress then the resulting compressive residual stress may be large enough to prevent the structure from being subjected to further tensile yielding, [Rose and White,1987]. It may be difficult to determine the magnitude of residual stress when separate mechanical or thermal loadings are applied, as occur in components within the electricity generating industry. Furthermore, a material that displays a low yield strength combined with cyclic hardening characteristics, such as 316L stainless steel, may complicate the shakedown process, [Rose and White,1987]. It is possible for the

maximum strain to increase with strain hardening while the strain range decreases, with shakedown into the elastic strain range. Further complications arise at higher temperatures when creep can occur. The resulting stress relaxation and re-distribution may prevent the possibility of calculating the magnitude of the residual stress. Therefore it may be impossible to determine whether shakedown will occur or not.

Shakedown can also occur in components that are subjected to thermal cycling, [Skelton,1983]. Regions of plastic and elastic strain ranges have been determined within tubular components which were subjected to thermal cycling. A region of plastic strain was calculated to shakedown to elastic strain loading following the first half cycle, [Burlet et al.,1989]. Regions of plastic strain were calculated to occur at the heated external surface during the cooling part of a thermal cycle and at the internal surface of a tubular component during the heating part of the cycle. Shakedown was shown to occur in each case, [Skelton,1983]. Shakedown may also occur in part of the cross-section of a component which yields when subjected to a combination of a steady and a cyclic stress, [Beer,1971].

When primary and secondary stresses combine such that the complete cross-section is strained beyond yield, then a certain amount of progressive deformation can occur during each cycle. This process of incremental collapse is known as ratchetting and can reduce fatigue life without crack propagation. During ratchetting, the regions undergoing yield, alternately on each side, overlap and the cycle does not settle down. With each subsequent cycle, the strain increases further by a finite amount and the continuously yielded zone increases in size. Ratchetting has produced plastic increases in the diameter of cylindrical shell components within a steam turbine plant, [Beer,1971]. Although the inclusion of a notch or a crack would enhance the possibility of ratchetting the overall effect would be an increase in ratchetting rate as ratchetting has been shown to have little effect on crack growth rates of 10^{-4} mm/cycle, [Skelton,1983].

Following the transition period, the fatigue life may be described by relationships which are based on the saturation stress-strain behaviour and the number of cycles to failure. However, before introducing these relationships an indepth study of the micromechanics of the transition period is required. This should help to explain the hardening and softening behaviour of different materials.

2.1.3.4. Microstructural Development During Cyclic Loading.

With the renewed interest in strain cycling in the 1950's and the developments in electron microscopy over the past twenty-five years, a number of important

investigations have been made based on the original findings of Ewing and Humfrey in 1903. The work of Feltner and Laird,[1967], Lukas and Klesnil,[1973], and Magnin et al.,[1988], and many others have been referenced in a number of reviews of cyclic loading and the transition period of the fatigue process, Ham,[1967], Coffin,[1972], Grosskeutz,[1971] and Hatanaka,[1990].

The number of cycles spent in the transition period and the corresponding magnitude of cyclic hardening or softening depend on a number of factors including the initial microstructure of the material, the magnitude of the strain loading and the temperature. When a metal is subjected to plastic straining, dislocations within the microstructure slip along and/or across the crystallographic planes. The cyclic hardening of an annealed metal occurs because of the interaction of dislocations to produce barriers to further dislocation movement. Therefore an increase in stress is required for further plastic deformation. Cycling between low strain limits may produce hardening that continues for the entire duration of the test. With increased cyclic loading the dislocations form a substructure suitable for supporting the load at a saturated stress level. The cyclic loading of cold-worked material breaks-down the dislocation tangles and loops which existed in the substructure following prestraining. The resultant softening of the metal stabilises to a saturated value when a lower stress level is reached which can still accommodate plastic deformation.

The ease with which screw dislocations can cross slip from one plane to another is a major factor in the process of cyclic hardening or softening. The appearance of the surface slip markings which develop from the plastic deformation make it possible to categorise all metals into one of two slip modes. Metals in which screw dislocations cross slip easily display a wavy slip mode, examples including copper, iron, nickel, aluminium and low-carbon steels. While metals that witness a rare and difficult cross slip are termed planar slip metals, such as Fe-Si alloy, austenitic steels, α -brass, magnesium and nickel-base super alloys. Generally the number of cycles spent in the transition period is lower in the case of wavy-slip materials than in planar-slip materials as observed by Klesnil and Lukas,[1980], with the hardening of pure copper, (wavy-slip) and Cu-31%Zn alloy, (planar-slip), under identical loading conditions.

In single phase face centre cubic, (fcc), metals the resultant saturated substructure can be related to the amplitude of plastic strain, the temperature and the energy stored in the stacking faults, (Figure 2.1.9). Grosskreutz and Hancock,[1969], have shown the microstructural changes in a single crystal of copper during the hardening process. Initially the dislocations appear as groups of long, straight, bundles or loops. With repeated strain cycling the density of the groups of dislocations increase and the longer

dislocations break up into short tangled bunches. At saturation a cell structure of dislocation walls exist which can support the plastic strain without further increase in the dislocation density. This mechanism of dislocation of a single copper crystal is typical for wavy-slip f.c.c metals with a high stacking fault energy when subjected to large strain amplitudes. Figure 2.1.9 is also a suitable approximation for pure bcc metals. Klesnil and Lukas,[1980] have shown a similar behaviour in the microstructural development of iron during high strain amplitude cyclic hardening. A saturation cell structure developed within 1000 cycles, which was 2% of the fatigue life. As strain amplitude is increased the saturation cell size decreases. Feltner and Laird observed the increase in dislocation density within the cell walls, and the corresponding decrease in cell size, in the saturated substructure of polycrystalline copper, with increasing strain range. Furthermore, this cell size change was observed to be reversible with change in the strain level, Feltner and Laird,[1967]. The cell size increases with an increase in temperature.

With low strain amplitudes, loops and dipoles of dislocations form instead of a cell structure. Klesnil and Lukas,[1980] produced microstructures of polycrystalline iron during the transition period when cycled at low cyclic strain amplitudes. Within 10 cycles an abundance of dislocations were observed throughout the material which was almost dislocation free at the test onset. After 200 cycles the dislocations were assembled in dense bands around areas which contained the occasional string of dislocations and some small dislocation loops. After 2000 cycles, 0.2% of the fatigue life, saturation stress was reached and the bands of dislocations were greater in density while the area between the bands contained less dislocations. Furthermore polycrystalline copper cycled in the low strain amplitude region also exhibited irregular bands of dislocations with relatively dislocation free areas in between. This phenomena is observed in Figure 2.1.9 for high stacking fault energy metals at low strain amplitudes. With an increase in strain amplitude the density of the dislocations within the bands increases and with further increase in strain a cell structure develops. Cell structures that develop under high strain cycling cannot be reversed to a sub-structure of loops and dipoles, even if the cyclic strain amplitude is significantly reduced.

Some confusion exists over the microstructure development of fcc polycrystals such as Type 316L austenitic stainless steel which has been identified to have a the stacking fault energy which is in a critical region, between 20 and 30 mJ/m², [Magnin et al.,1989]. Persistent slip bands do not form in materials with lower stacking fault energies. Persistent slip bands of dislocations have been observed in 316L polycrystals while a more planar slip of dislocation bundles were observed in 316L with an increased volume of nitrogen, [Magnin et al.,1989]. When deformation amplitudes and the number of applied cycles are low the dislocations appear in planar arrays. While at high strain

amplitudes and with increasing numbers of cycles the planar arrays are transformed into well-defined veins and cells, [Lieurade et al.,1986]. A memory effect was observed when the dislocation twins formed at high strain remained in the microstructure even when the material was cycled at lower strains which correspond to typical planar-array dislocation microstructures. However when cycled from a period at low strain to a period at high strain the dislocation tangles transformed to veins, cells and dislocation twins, [Lieurade et al.,1986].

In comparison, with bcc single crystals of 26Cr-1Mo-4Ni ferritic steel, labyrinth and wall structures of dislocations developed through cyclic hardening while the polycrystal 26Cr-1Mo-4Ni ferritic steel developed a wall structure of dislocations throughout the specimen, [Magnin et al.,1989]. No persistent slip bands of dislocations developed and it was tentatively concluded that, in the ferritic steel, plastic activity in the grains is fairly uniform throughout the specimen.

The development of dislocation bundles and bands in 316L austenitic stainless steel is typical of the saturation microstructure of planar slip materials, which have a low stacking fault energy, at all strain amplitudes, as shown in Figure 2.1.9. Similarly, Klesnil and Lukas,[1980], observed planar arrays of dislocations in the saturated structure of α -brass which were cycled from the annealed state at low strain amplitudes while Feltner and Laird,[1967], observed bands of dislocations with a lower density of faults and dislocations between the bands of Cu-7.5%Al which were cycled from the annealed state at a higher strain range. The planar array of dislocations are formed because the dislocations are restricted to the primary plane due to the difficult cross slip mechanism. Therefore planar slip materials cannot form bands or walls no matter the magnitude of the strain amplitude. Although Lukas and Klesnil,[1973], could not find any change in the substructure of α -brass with a change in the strain amplitude, Grosskreutz stated that the density of the bands of dislocations increases with the increasing plastic strain amplitude. This increase in number of bands and the corresponding decrease in band spacing has been observed in Cu-7.5%Al by Laird and Feltner,[1967]. Increasing the temperature of cycling increases the band spacing in planar slip materials while the density of dislocation bundles and bands increases as the plastic strain amplitude increases.

Cyclic softening is a common occurrence during the transition period of a material which has been hardened through a pre-testing process such as cold-working. During cold-working the sample is strained to a desired reduction in area under a tensile or a torsional load. Reversed plastic strain is required to move dislocations, decrease dislocation densities thus decrease the stress required to maintain the same amplitude of

plastic strain.

Following cold-working, hardened wavy-slip metals display a cell structure with a high density of dislocations in the cell walls and a lower density of dislocations within the actual cells, as observed in 20% cold-worked Cu by Lukas and Klesnil,[1973]. During cyclic softening the dislocations move, reducing the dislocation density in both the cells and the cell walls. The cell walls appear sharper as the width of the walls decrease and the size of the cells increase, as shown on 20% cold-worked Cu by Feltner and Laird,[1967]. At saturation the cell size of annealed wavy-slip metals is almost identical to that of the same metal after pre-deformation and cycling at the same strain amplitude. Therefore the saturation stress amplitudes are the same. Feltner and Laird,[1967], observed this with copper pre-strained to 23% however Lukas and Klesnil,[1973], observed 30% and 40% pre-strained copper to retain the hardening effects with slightly greater saturated stress levels over a range of low amplitude strain levels.

Following pre-strain, such that the material was 20% cold-worked, the dislocation microstructure of the hardened material displayed small ill-defined cells and large number of dislocation twins. During low strain amplitude cycling little change appeared, however with increased cycling, at a total strain amplitude of 1.8%, larger well defined cells developed, [Lieurade et al.,1986].

With the planar slip alloys, α -brass and Cu-7.5%Al, the greater the percentage cold-work the greater is the saturation stress. At each plastic strain amplitude the saturation stress is always lower for the material originally in the annealed condition than it is for the same material originally cold-worked. Observations have been made of the corresponding microstructures. Following cold-working a planar slip material displays a planar array of bands with a high density of dislocations. Cycling does not change the structure, it merely decreases the density of dislocations within the bands, although not to the extent of the planar array of the annealed material following the same plastic strain cycling.

Fatigue softening also occurs in materials which were hardened by methods other than cold-working. Phase transformations may occur when quench-aged low-carbon steels are plastically cycled, and small iron-carbide particles re-solute into the steel. Softening occurs in a variety of precipitation hardened alloys. The precipitates harden the material by creating obstacles for the dislocation slip. In some alloys the density of the particles is low and the dislocations move freely thus cyclic softening occurs. When the density of precipitate particles is great then the dislocations have to split through the particles and reduce their physical size until the particles revert to solid solution. The speed of this

process increases with plastic strain range. With a decrease in the density of precipitates, the required stress amplitude to maintain the plastic strain decreases. This irreversible softening was observed to occur along active slip planes during the cyclic loading of Fe-C alloys which were previously quenched and aged, Feltner and Laird,[1967]. With Type 316L an increased nitrogen content, 0.25 wt% N, reduced the dislocation movement to such an extent that planar slip dislocation tangles formed during high strain cycling. In contrast, cellular microstructures which were observed with lower nitrogen contents, 0.8 wt% N, [Lieurade et al.,1986]. The planar slip of dislocations to form the tangled arrays requires greater stress amplitudes thus the greater magnitude of cyclic hardening with high nitrogen content Type 316L steel.

In a vacuum and at room temperature, annealed Type 316L steel initially hardens followed by a longer period of softening to failure except when cycled at higher strain amplitudes, $\Delta\epsilon_p > 1\%$, [Gerland et al.,1989a]. At the lower strain ranges, $\Delta\epsilon_p = 0.12\%$, the microstructure consisted of typically planar arrays of dislocation tangles and dipoles. At a mid-strain range, $\Delta\epsilon_p = 0.4\%$, the microstructure consisted of a mixture of wavy-slip dislocation patterns, such as cells, veins and labyrinths, and typical planar array dislocation patterns such as microtwins, planar slip bands and dislocation tangles. At the highest strain range, $\Delta\epsilon_p = 2\%$, the microstructure consisted of a mainly wavy-slip dislocation patterns especially cells and wall channels. Similar proportions of dislocation structures were observed with increasing cyclic strain ranges in air, [Gerland et al.,1989a]. A series of vacuum tests at $\Delta\epsilon_p = 1\%$ were stopped after a different number of cycles corresponding to the end of primary hardening, end of softening thus the beginning of the stress saturation period, failure in air and finally failure in a vacuum. The findings from these tests concluded that the initial hardening promotes the formation cells, wall channels and dislocation tangles. As cycling continues the percentage volume of cells increase slightly while the greatest transformation is from dislocation tangles to wall-channels. With further cycling the percentage of wall channels decreases while the percentage of cells increase. At the later stages the cell walls are well defined with condensed dislocation structures.

At 300°C a secondary hardening is observed in vacuum testing of Type 316L stainless steel which is more extensive at lower cyclic strain amplitudes, [Gerland et al.,1989b]. The hardening continues to failure, well beyond the corresponding fatigue life in air, and is typified at low strain ranges by alternate black and white bands, which are composed of very small dislocation loops, in the microstructure. At higher strain ranges, these bands are not so prominent and cell structures dominate the microstructure. The bands, like the cells, are a very hard, stable structure which continue to develop up to the beginning of failure softening and are responsible for the marked secondary hardening.

When Type 316L in the solution annealed state is cycled in a vacuum at 600°C the development of the microstructure and the corresponding hardening behaviour are dependent on the cyclic strain amplitude. At low strains the stable microstructure is never obtained as the material continuously hardens at a slow rate and only 20% of the microstructure at failure displays a cellular structure. With higher strain amplitudes the microstructure consists mainly of walls and labyrinths at saturation and cell structures at failure. It is the transformation from walls to cells which requires the increased stress amplitude and produces the secondary hardening effect.

At saturation of the hardening or softening process, nucleation of microcracks occurs. In the majority of cases microcracks nucleate at a free surface. Examples of nucleation sites are where fatigue slip bands intersect the surface, where grain boundaries intersect the surface or in certain alloys where inclusion particles intersect the surface. Microcrack nucleation can occur below the surface at regions of maximum shear stress due to contact fatigue and the resultant fretting. However in all cases of near surface deformation, it is the plastic strain concentration that controls the nucleation process of microcracks. Nucleation at slip bands is very important as slip band formation often precedes nucleation at grain boundaries or at surface inclusions. For each of the three dislocation substructures which develop during the transition period, a distinctive marking is produced during the saturation cycling which in turn promotes microcrack nucleation.

With wavy-slip materials at low strain amplitude cycling the dislocation bundles form into distinct ladders within persistent slip bands while surrounded by a substructure of dislocation veins at the near surface. Dislocation motion within the bands produces coarse slip markings on the surface during saturation cycling. The dislocation motion is reversible within the bands however when the bands intersect the free surface the motion is irreversible and results in deep extrusions and intrusions at the surface.

With wavy-slip materials at high strain amplitude cycling a cell structure is formed within the bands which create a separate cell structure at the surface. Surface extrusions and intrusions appear as crests and troughs at the intersection of the slip band and the surface. Plastic strain concentrates at the bottom of the inclusions and microcracks nucleate with continuous cycling.

The difficult slip process associated with planar slip metals requires the plastic strain cycling to continue well into the saturation period for almost slip band like substructures to develop and produce areas of shallow extrusions and intrusions on the surface. With

increased plastic strain concentration at the deepest point of the inclusions microcrack nucleation occurs. If a grain boundary intersects the surface at an area of slip band surface relief then it is possible for intrusions to develop at the grain boundary and the corresponding microcrack to nucleate within the grain boundary. Furthermore localised slip can concentrate around surface breaking inclusion particles in certain alloys. Even at stress levels too low to produce slip at inclusion free areas surface relief around inclusions can result in microcrack nucleation at the site of maximum plastic strain.

With increasing temperature and corrosive environments, oxides form over the surface breaking slip bands and can act to protect the metal or alternatively enhance microcrack nucleation. If the applied stress is below the fracture stress of the oxides then the oxides act as a protective cover and suppress the surface deformation. However upon cracking of the oxides at a higher stress localised plasticity occurs in the metal surface at the highly strained slip bands. Voids and surface scratches are also sites for microcrack nucleation while fretting at joints can result in surface erosion and fatigue crack nucleation due to the rubbing of the two surfaces.

Microcracks which grow beyond nucleation often coalesce and produce stage I macrocracks which grow along the planes of maximum shear stress. This mechanism of fatigue crack growth will be discussed at length in a later section. However as the plastic strain amplitude has been identified as the controlling factor in fatigue crack initiation it is of great importance to discuss the relationships developed, through strain cycling analysis, which relate the plastic strain cycling to the fatigue life during the saturation period.

2.1.4. Fatigue Life Relationships.

Following the transition period the majority of the fatigue life of a metal component is spent in the saturation period until rapid final fracture. From the saturation hysteresis loops, values of stress range, total strain range, plastic strain range and elastic strain range are measured. Apart from cyclic stress/strain relations, values from the hysteresis loops are often plotted against the number of cycles to failure from a series of experiments on similar specimens to develop fatigue life plots.

Over the last twenty-five years, the cyclic stress/strain behaviour has generally been obtained under cyclic strain control. Cyclic strain control is preferred to cyclic stress control as it produces a greater approximation of the deformation within the plastic zone, which in turn controls fatigue failure, [Coffin,1972]. However a small number of investigations have performed experiments to describe the fatigue life behaviour of

Types 316L and 316 stainless steel under cyclic stress control in the high cycle fatigue range. The fatigue life of both Types 316L and 316 stainless steels increases with decreasing stress amplitude at both 700°C and 800°C, [Driver,1971]. At both temperatures the fatigue life of Type 316, at a given stress amplitude, is greater than that of Type 316L at 800°C. The fatigue life decreases with increasing temperature until 2×10^7 cycles at which point an endurance limit was observed for Type 316 at both temperatures and Type 316L at 700°C. At 800°C, Type 316 failed within 5×10^6 cycles at the lowest stress amplitude of 40MPa. Endurance limits of 10^8 cycles were observed in two different heats of Type 316 stainless steel over the temperature range of 20°C to 700°C, [Yoshida et al.,1977]. The material that had been annealed for 1 hour longer at 1100°C always failed at lower stress amplitudes over the entire test temperature range. The stress amplitudes at which endurance occurred decreased with increasing test temperature from 245MPa at 20°C to 139MPa at 700°C.

When experiments are performed under strain control, the resultant saturation plastic strain range is plotted against the number of cycles to failure on a log-log scaled diagram. The data is represented by a straight line. the equation of the line is known as the Coffin-Manson equation;

$$\Delta \epsilon_p = \epsilon_f' (N_f)^\beta \quad (2.1.11)$$

The exponent β is the slope of the line and is in the range of -0.5 to -0.7 for most materials at room temperature and ϵ_f' is the tensile ductility which corresponds to the plastic strain range at $N = \frac{1}{4}$. Values of β and ϵ_f' were determined to describe the fatigue life of annealed Type 316L in terms of the plastic strain amplitude, $\Delta \epsilon_p / 2$, over a range of temperatures, [Driver et al.,1988], and are presented in Table 2.1.2.

Temperature (°C)	ϵ_f'	β
20	0.456	-0.542
300	0.6039	-0.582
600	0.2114	-0.5496

Table 2.1.2. Coefficients from Coffin-Manson Equation for Type 316L.

The Coffin-Manson equation was developed from experiments performed to 10^6 cycles. However a major finding in the investigation of Coffin was the non-existence of an

endurance limit. In fact this investigation confirmed the earlier ideas of Bairstow that the endurance limit is a natural elastic limit at which there is no reversed plastic flow. This relationship has been confirmed by numerous investigators and by the mid 1960's Boettner, Laird and McEvily,[1965], had developed a relationship to describe the crack growth rate, which was measured from striations on the fracture surface of highly strained copper, with the corresponding plastic strain range;

$$\frac{dl}{dN} = Z(\Delta\epsilon_p)^2 l \quad (2.1.12)$$

The crack length is represented by l and N the number of cycles. When integrated between the initial crack length and the final crack length and the corresponding number of cycles to failure, the above equation produces the Coffin-Manson equation with β equal to 0.5. Thus the Coffin-Manson equation describes the plastic behaviour of a material in the near vicinity of the crack tip and the reversed plastic strain amplitude is the dominant factor in both the progression of a fatigue crack and in the resultant fracture of a component. This should be expected since the process of fatigue failure is controlled by the various stages of crack growth.

Driver et al.,[1988], observed microcrack initiation along slip bands in polycrystalline Type 316L following fatigue at 20°C and 300°C, in both air and vacuum. Observations were made on a scanning electron microscope, SEM, and revealed that many microcracks initially follow intense slip bands across grain boundaries and after crossing two or three grains either coalesce or arrest. The microcracks that coalesce and propagate in a general direction normal to the applied stress. Crack propagation during continuous cycling at temperatures below 450°C is generally transgranular, producing a fracture surface with ductile striation patterns perpendicular to the direction of crack growth, [Wareing and Vaughan,1979], [Yamaguchi et al.,1978].

In single crystals of Type 316L crack nucleation occurred in the slip bands which are perpendicular to the applied stress at the surface, [Driver et al.,1988]. Microcracks continued to propagate through the crystals by jumping from one slip band to another. A similar crack jumping process occurred in the initial process of microcrack propagation within the grains of the polycrystalline Type 316 stainless steel.

Significant differences in crack initiation and propagation occur at higher temperatures. Driver et al.,[1988] observed crack initiation to be both transgranular and intergranular in air at 600°C and purely intergranular in a vacuum. Crack propagation under continuous cycling at 625°C produced creep voids along slip bands within the predominantly ductile transgranular fracture surface of unirradiated, 20% cold work

Type 316 stainless steel, [Grossbeck and Liu,1985]. Likewise, mixed intergranular voids and transgranular striations were observed in the fracture surface of Type 316L which had been aged for 2000 hours at 600°C prior to continuous cycling at 600°C, [Degallaix et al.,1988]. The same material aged for 10000 hours at 600°C displayed a greater quantity of intergranular crack propagation following identical cycling conditions. While investigating the reduction in fatigue life of Type 316L at 600°C with increasing tensile hold times, Clavel et al.,[1979], found that intergranular damage was not only in the vicinity of the advancing crack tip but was also in the bulk of the material. This process of cracking before the crack, results in both the increased growth rate and the decreased fatigue life associated with intergranular crack growth. Intergranular fracture, in Type 316L, must be considered as a creep damage phenomenon that takes place, at a temperature above 450°C, during long tensile hold times in the fatigue cycle and not as an environmental process of oxidation at the crack tip. Reduced fatigue lives in sodium with increasing tensile hold times confirm this, [Ardellier,1981].

By the early 1970's the improved testing machines and strain controlled specimen instrumentation enabled Lukas, Klesnil and Polak,[1974], to show the Coffin-Manson relationship to be true for both polycrystalline copper, α -brass and three carbon steels over the high cycle, (10^5 - 10^7 cycles), fatigue range. The high cycle fatigue data was obtained through plastic strain controlled cycling at a high frequency of 80Hz. With each of the materials an endurance limit appeared at 10^7 cycles when the plastic strain range was 1×10^{-4} for both the copper and the α -brass and 8×10^{-5} for the carbon steel. Klesnil and Lukas,[1980], have tabulated stress and plastic strain fatigue limits for a number of materials and has found that as the stress limits vary by a factor of 24 the plastic strain range limits are always in the order of 10^{-4} . Recently, Hatanaka and Fujimitsu,[1984], have found a similar endurance limit in normalized medium carbon steel JIS S35C while the straight line in a log-log plot Coffin-Manson law held for annealed copper up to 2×10^7 cycles at plastic strain range of 6×10^{-5} . However with quenched then tempered SCM 435 chromium-molybdenum alloy steel the plastic strain range diminished to 7×10^{-6} at a fatigue life of only 10^5 cycles which corresponds to the stress based fatigue life. In fact all of the fatigue data above 3×10^4 cycles, in Hatanaka's review,[1990], was generated under stress control which could result in higher or lower plastic strain ranges due to cyclic softening or hardening. However an important observation that was made for each of the previous three materials was that when the fatigue life was plotted against the corresponding plastic, elastic and total strain ranges then total strain life was best represented by the plastic strain up to a point, approximately 10^4 cycles and a plastic strain range of 4×10^{-3} , beyond which the elastic strain was a better representation.

This was observed with Type 316L over a wide range of temperatures, [Brun et

al.,1976] and for 20% cold worked Type 316 stainless steel, [Manjoine and Landerman,1982]. Type 316 stainless steel displayed similar fatigue life in both the 20% cold worked and the annealed condition at both 20°C and 600°C, in terms of the total strain range, [Plumbridge et al.,1980]. However in terms of the plastic strain range the cold worked material displayed reduced fatigue lives at both temperatures. Although explained as a softening effect this phenomenon was not clearly described due to the lack of comparable data available. The lack of comparable data results from the differences in test techniques from one investigation to another and due to the cast-to-cast variations in Type 316 and Type 316L stainless steels.

The point on a Coffin-Manson plot where the plastic strain range equals the elastic strain range is known as the transition fatigue life and is schematically displayed in Figure 2.1.10. At strain values higher than the transition point the failure is one of low cycle fatigue, (LCF), which is characterised by high strain crack propagation. At strain values lower than the transition point the failure is one of high cycle fatigue, (HCF), which is characterised by a great number of cycles spent in crack nucleation while the resultant crack growth is determined by linear elastic fracture mechanics. There is no set number of cycles defined as the transition point however the low cycle fatigue regime is regarded to be generally less than 50000 cycles for most ductile materials, Rice et al.,[1989]. From Figure 2.1.10 the elastic strain range over both the HCF and LCF regions is represented by the number of cycles to failure using Basquin's equation;

$$\Delta\mathcal{E}_e = \frac{\Delta\sigma}{E} = \left(\frac{\sigma'_f}{E} \right) N_f^{-b} \quad (2.1.13)$$

while the plastic strain range is given in the Coffin-Manson equation. The representation of fatigue life in terms of the total strain amplitude, (the sum of the elastic and plastic strain), is of practical importance as the strain measurements taken from working components are obtained in the form of total strain measurements. Using the following equation;

$$\Delta\mathcal{E}_t = \Delta\mathcal{E}_e + \Delta\mathcal{E}_p \quad (2.1.14)$$

Manson and Hirschberg,[1965], developed the Universal Slopes Equation which related the total strain range to the number of cycles to failure;

$$\Delta\mathcal{E}_t = \left(\frac{3.5\sigma_u}{E} \right) N_f^{-0.12} + (\mathcal{E}'_f)^{0.6} N_f^{-0.6} \quad (2.1.15)$$

where the fatigue strength coefficient equals 3.5x the ultimate tensile stress and the slopes for the elastic and plastic lines were given as -0.12 and -0.6 for all materials. Recently, Manson and Muralidharan,[1988], have improved the Universal Slopes Equation from the analysis of the fatigue life behaviour of 47 different materials;

$$\Delta \varepsilon_t = \left[0.0266D^{0.155} \left(\frac{\sigma_u}{E} \right)^{-0.53} N_f^{-0.56} \right] + \left[1.17 \left(\frac{\sigma_u}{E} \right)^{0.832} N_f^{-0.09} \right] \quad (2.1.16)$$

where D is the ductility of the material and σ_u is the ultimate tensile strength of the material. The advantages of the modified equation are improved estimates of fatigue life, over the range 10-10⁶ cycles, from data provided from static tensile tests and a lower slope in the elastic fatigue life line produces longer fatigue life at very low strains.

2.1.5. Factors Effecting Fatigue Life.

2.1.5.1. Surface and Notch Effects.

Wareing and Vaughan,[1979], have identified the damaging effect of the surface finish and the importance of time spent on crack initiation on the fatigue life of Type 316 at 400°C. Fatigue lives of finely electropolished specimens were found to exceed those of specimens with either ground or turned surface finishes, by a factor of four. Crack nucleation was limited to discrete sites on the electropolished surfaces while machined surfaces displayed crack nucleation sites all around the test section.

The total strain based fatigue life equation is often used to determine the fatigue life of working components, the geometry of which often contains grooves and shaped features at which stress concentrates and the initiation of fatigue crack occurs. Originally stress controlled fatigue testing of notched specimens revealed that the inclusion of a notch decreased the fatigue life at the same stress range. Coles et al.,[1967], have shown a similar behaviour when the fatigue life of unnotched and notched specimens were compared with the total strain range. However they did observe that there was little further reduction in fatigue endurance with increasing severity of notch geometry. The severity of notch geometry was measured as the theoretical stress concentration factor which was defined by Neuber,[1961], as;

$$k_t = (k_s k_\sigma)^{1/2} = \left[\left(\frac{\varepsilon_1}{\varepsilon_n} \right) \left(\frac{\sigma_1}{S_n} \right) \right]^{1/2} \quad (2.1.17)$$

where;

k_ϵ is the strain concentration factor at the notch root,

k_σ is the stress concentration factor at the notch root,

ϵ_1 is the maximum local principal strain at the notch root,

σ_1 is the maximum local principal stress at the notch root,

e_n is the corresponding nominal, smooth specimen, strain, and

S_n is the nominal smooth specimen stress.

Equation 2.1.16 may be used to determine notch root strains from the known stress/strain behaviour of the material. Furthermore, Morrow et al.,[1969], further developed Neuber's rule to produce a relationship between the nominal stress range, ΔS , and the notch root cyclic stress and strain ranges, $\Delta\sigma$ and $\Delta\epsilon$, respectively,

$$\frac{[(\Delta S)(k_f)]^2}{E} = (\Delta\sigma)(\Delta\epsilon) \quad (2.1.18)$$

k_f is the theoretical fatigue concentration factor. Using a combination of the elastic stress/strain rule and the cyclic stress/plastic strain equation, the total strain range can be represented in terms of the stress range and substituted into equation 2.1.18 such that the local stress range at the notch root is a function of the nominal stress range;

$$\frac{(k_f \Delta S)^2}{E} = \Delta\sigma \left[\frac{\Delta\sigma}{E} + \left(\frac{\Delta\sigma}{A} \right)^{1/n'} \right] \quad (2.1.19)$$

Through a process of trial and error, the local stress range is calculated and substituted into the equation for the total strain range;

$$\Delta\epsilon_t = \frac{\Delta\sigma}{E} + \left(\frac{\Delta\sigma}{A} \right)^{1/n'} \quad (2.1.20)$$

After the notch strain amplitude has been calculated the corresponding fatigue life may be obtained from equation 2.1.15. Using a combination of equations 2.1.17 to 2.1.19 Stadnick and Morrow,[1972], found the fatigue life of unnotched specimens, of two different aluminium alloys, which were cycled at an applied stress range identical to the calculated notch stress range, to compare well with the resultant life of notched specimens. In both investigations the similarity in results was observed for two different load histories. In one of the load histories, a reversed overload, initially in tensile

yielding, prior to smaller amplitude cycling produced a tensile residual stress at the notch root and was detrimental to fatigue life. Conversely, a reversed compressive yielding overload, before smaller amplitude cycling, produced a compressive residual stress at the notch root which was beneficial to the fatigue life. Potter,[1973], confirmed these findings with 2024-T4 aluminium alloy. From the early 1970's elastic plastic finite element analyses have been performed to determine the notch root stress and strains. Mowbray and McConnelee,[1973], displayed a good agreement between notch root strains calculated from an elastic-plastic finite element analysis with values measured during fatigue experiments on three different steels. Comparisons with calculations, which were made using the Neuber formula with a correction factor to account for the biaxial plastic strains at the notch root, indicated that the theoretical method over-predicted the notch root strains at stress levels beyond yielding. However for each of the three steels a good comparison was made between the fatigue crack initiation life of smooth and notched specimens and a stress-strain function instead of the plastic strain range;

$$f(N_i) = (E\sigma_{\max}\epsilon_a)^{1/2} \quad (2.1.21)$$

where σ_{\max} and ϵ_a are the maximum tensile stress and the strain amplitude during a cycle, respectively. Although fatigue initiation life based on the plastic strain range produced a reasonably good correlation the above mentioned function was favoured as it takes into account the effects of the biaxial stress fields at the notch root and the mean stress during zero-to-tension loading. James et al.,[1989], proposed a numerical technique to determine plastic strains at the notch root which compared well with calculations with plastic strains from a plain strain finite element analysis. The technique produced acceptable predictions of fatigue crack initiation life from notched specimens using a Coffin-Manson fit through smooth specimen data. Hatakana has also reviewed notch and smooth specimen fatigue crack initiation and life plots and observed that a better representation was obtained in terms of both equivalent stress and equivalent plastic strain amplitudes than with the corresponding axial stress amplitudes. The calculated axial stresses at the notch root were overestimated.

2.1.5.2. Time Dependent Effects on Fatigue Life.

Apart from mean stress and notch effects a number of well documented time dependent factors exist which have an effect on the fatigue life of metals. Unfortunately most fatigue life data exist in the format of Coffin-Manson equations and relate to LCF conditions. Therefore to make a brief discussion of the various time dependent factors which have an effect on the fatigue life of metals it is better to concentrate on the LCF

region. In the following sections reference will be made to the HCF region whenever appropriate information can be found or when known differences from the LCF region occur.

Engineering components are subjected to fatigue loading over a wide range of temperatures from the sub-zero temperatures of the Alaska pipeline to temperatures beyond half of the melting point of the alloys as experienced in jet engines. Temperature is one of the most important external parameters influencing fatigue life. Many reviews have been written, [Coffin,1974, Lundberg and Sandstrom,1982, and White,1970], which display the differences in fatigue life from experiments which were performed at various constant temperatures. Below room temperature most of the data is from stress controlled tests however the Coffin-Manson equation has been shown, [Coffin,1977], to hold under LCF strain controlled conditions with a low carbon steel. From room temperature to -125°C the relationship between plastic strain range and fatigue life was temperature independent and was explained to be due to an absence of mechanism changes with the decreasing temperature. This phenomenon is very important in the fatigue life relationships at temperatures above room temperature.

The general effect of temperature is to cause a reduction in fatigue life with increasing temperature. Berling and Slot,[1969], found this behaviour occurred for three austenitic stainless steels, in the 300 series, at temperatures between 430°C and 816°C over a plastic strain range of 0.2% to 3.0%. Edmunds and White,[1966], observed a similar reduction in the fatigue life of 2¼Cr-1Mo steel at 600°C in comparison to the fatigue life at room temperature. They regarded the fracture surface oxidation, observed on the specimens tested at 600°C , to be the main cause of reduced fatigue life. Increasing the test temperature led to reductions in the fatigue life for both polycrystalline and single crystals of Type 316L, which were strained under identical cyclic strain amplitudes, [Driver et al.,1988]. The decrease in fatigue life was not as great between 20°C and 300°C as it was at the higher temperatures of 450°C and 600°C , [Driver et al.,1988], [Brun et al.,1976]. As the crack growth through single crystals is transgranular at all temperatures, the increased crack growth, and subsequent decrease in fatigue life, can be explained as an oxidation effect during both crack initiation and propagation, [Driver et al.,1988]. This opinion was enhanced further by the increased and similar fatigue lives of Type 316L, over a wide range of plastic strain amplitudes, at 20°C , 300°C and 600°C , in a vacuum in comparison with the fatigue life in air, [Driver et al.,1988]. A similar increase in fatigue life was observed with Type 316L in sodium in comparison to that in air at both 450°C and 600°C , especially at the lower plastic strain ranges, [Ardellier,1981].

Coffin,[1977], modelled this environmental effect on the plastic strain range/fatigue life plot, (Fig. 2.1.11.) Coffin explained that the break in the slope of the $\Delta\epsilon_p-N_f$ plot, with increasing temperature, represented a change in the mode of crack propagation. At low temperatures the crack propagates transgranularly through the grains. At lower strains, this is a time consuming process due to the large amount of energy required for a crack to break across the grain boundaries. At high temperatures the crack propagates through the grain boundaries which often include prime fracture sites such as precipitates. A combination of precipitates and oxidation of the exposed crack tip surface with every cycle promotes rapid crack growth. This intergranular crack growth leads to reduced fatigue life. At high strains the crack growth is large enough at all temperatures to revoke the effects of oxide-damage.

Degallaix et al.,[1988], observed that an increased in nitrogen content, up to 0.12 wt%, produced an increase in fatigue life at both room temperature, [Vogt et al.,1984], and 600°C. The increased nitrogen content stabilized the austenite phase, decreases the stacking fault energy and encouraged planar arrays of dislocations which required a greater stress amplitude to form crack nucleation sites. In the same investigation, ageing of the material at 600°C for 2000 and 10000 hours, before testing was found to be detrimental on the fatigue life of the steel with both a low and a high nitrogen content. Grain boundary precipitation and high stresses produced intergranular rupture and rapid failure. However, at low strain amplitudes the increased nitrogen still increased the fatigue life even in the longest aged material when tested at 600°C. Driver,[1971], observed that increased carbide precipitates at grain boundaries increased the fatigue life, at low cyclic stress amplitudes, by restricting grain boundary sliding and by preventing crack growth through the grain boundaries.

The strong temperature dependence of the Coffin-Manson plots at high temperature decreases when cycling is performed in a vacuum, [Coffin,1972], or an inert gas, [Wood et al.,1977]. Figure 2.1.12 displays the removal of the temperature effect when the austenitic stainless steel A286 was cycled in a vacuum at both room temperature and 593°C. In vacuum the fracture tended to be transgranular and the fracture surfaces at both temperatures displayed no trace of oxides. In comparison with the results from the tests performed in air at 593°C, the vacuum tests display an increase in fatigue life and a decrease in the slope of the fatigue life plot. Wood et al. also observed an increase in fatigue life with the removal of an oxidation environment for both a 9%Cr ferritic steel at 525°C and type 316 steel tested at 625°C in a helium mixture.

Another factor which effects the fatigue life at high temperature and is displayed in Fig. 2.1.12 is the reduction in fatigue life with a decrease in the frequency of cycling. It is

suggested that at lower test frequencies in air there is sufficient time for a localized oxidation to occur at the crack tip, which, if the oxidation occurs adjacent to grain boundaries, promotes the faster intergranular crack growth, [Coffin,1977]. The numbered points on Fig. 2.1.12 indicate that the vacuum environment removes the frequency sensitivity of fatigue life. Therefore fatigue at high temperature can be regarded as a time-dependant process, such that the longer the time available for oxidation to occur, the shorter the fatigue life. Coffin,[1972], took the high temperature frequency effect into account by introducing the frequency, ν , into the Coffin-Manson equation;

$$\Delta \mathcal{E}_p = \left(\mathcal{E}'_f \right)^\beta \left(N_f \nu^{(k-1)} \right)^{(-\beta)} \quad (2.1.22)$$

The fatigue effect at high temperature has been further incorporated into the original universal slopes curve to produce an expression for the total strain fatigue life which contains the frequency of cycling;

$$\Delta \mathcal{E}_t = \frac{3.5 \sigma_u}{E} \left(\mathcal{E}'_f \right)^{(\beta n)} N_f^{(-\beta n)} \nu^{[k_1 + (1-k)\beta n]} + \mathcal{E}'_f{}^\beta N_f^{-\beta} \nu^{[(1-k)\beta]} \quad (2.1.23)$$

Other authors such as Kanazawa and Yoshida,[1973], prefer to describe the high temperature time dependent fatigue life in terms of the strain rate, $\dot{\mathcal{E}}$, however as the frequency and the strain rate are principally the same parameter related by the equation;

$$\dot{\mathcal{E}} = 2(\Delta \mathcal{E}_t) \nu \quad (2.1.24)$$

They will be treated together. Kanawaza and Yoshida observed no strain rate dependence of the fatigue life, for a given plastic strain range, of four austenitic stainless steels from the 300 series at room temperature. However with increasing temperatures between 450°C and 800°C a decrease in strain rate produced a decrease in fatigue life, although the magnitude of decrease in fatigue life was material dependent at all temperatures. Therefore to describe the fatigue life of a material in terms of strain rate and total strain range, using a combination of equations 2.1.23 and 2.1.24, would require a large number of experiments at each temperature of interest to generate the coefficients of the equation. Equation 2.1.23 can also describe the strain rate in terms of the time for one cycle since the frequency is the inverse of the time to complete one cycle.

Varying the waveshape can also have an effect on the fatigue life. Numerous waveshapes can be generated using the modern testing machines. In order to simulate some service conditions which include a certain amount of creep fatigue interaction, a period of

constant strain at either or both the maximum and minimum strain values, is introduced in low cycle fatigue testing. Figure 2.1.13 displays four strain controlled cycles and the corresponding hysteresis loops and stress relaxation cycles. During periods of constant strain the stress relaxes and elastic strain transforms into plastic strain. Kanazawa and Yoshida have observed that periods of constant strain at both the maximum tensile and compressive strains during strain cycling produce similar fatigue life at corresponding plastic strain ranges as the continuous cycle. This was observed with three austenitic stainless steels at temperatures ranging from 450°C to 800°C. Both the continuous cycling and the cycles containing 2.5 minutes of maximum tensile and compressive strain were performed at the same high strain rate of 6.7×10^{-3} /sec. Yamaguchi and Kanazawa,[1980], observed a decrease in the fatigue life of 316 steel at both 600°C and 700°C when the continuous cycling was at a lower strain rate of 6.7×10^{-5} /sec, however greater reductions were observed when the waveshape was altered to include a slow tensile part followed by a fast compressive part and also when the cycle contained hold times at maximum strain only. In each of these cycles the resultant crack growth was intergranular in nature while the later two cycles produced extensive interior grain boundary microcracks especially at triple points.

Yoshida et al., [1977], observed a decrease in fatigue life of Type 316 stainless steel with decreasing rate of applied cyclic strain at tests temperatures above 450°C. At room temperature and 450°C the fracture mode was transgranular with clear striation patterns, [Yamaguchi et al., 1978], while at 600°C and a high strain range, 2%, the fracture mode was mainly intergranular. The decrease in fatigue life at 450°C was due to a mechanical effect of cyclic hardening depending on the strain rate while the decreased fatigue life at 600°C was due to the increased crack initiation and propagation of an environment-creep-fatigue interaction. Similar decreases in the fatigue life of Type 316L were observed by Ardellier,[1981], at 600°C with increasing tensile dwell periods, although the magnitude of the degradation was reduced when the hold time tests were performed in a non-oxidising environment, liquid sodium. Jaske et al.,[1973], also observed a decrease in fatigue life of Type 316 with increasing tensile hold times, 0 to 10 hours, at both 566°C and 649°C while compressive hold periods or combined tensile and compressive hold periods during the cycle had little effect on the cyclic life.

Cycles containing a fast tensile part and a slow compressive part displayed similar fatigue life to continuous cycling, which in conjunction with the findings of Kanazawa and Yoshida, display that periods of compressive strain help to deter fatigue crack growth in austenitic stainless steels. The simple explanation of these findings is that at constant levels of high plastic strain the length of time at which the crack is opened is long enough for creep damage and oxidation of the crack tip to occur. Conversely

periods of constant levels of compressive strain prevent oxidation and creep damage occurring and can cancel the effects of previous periods of constant tensile strain. Surprisingly, Udoguchi et al.,[1973], have observed decreasing fatigue life when a 1%Cr-0.2%Mo steel has been cycled with increasing lengths of hold time at both the maximum tensile and the compressive strains at 550°C. Clearly, the effect of waveshape on fatigue life is material dependent.

Consideration of the idea that creep damage is the governing factor which produces the drastic failure of materials under cyclic loading with tensile hold times at high temperatures has been investigated in a number of apparently non-oxidising environments. White,[1970], observed a decrease in the fatigue life of ½%Mo steel cycled in a vacuum at 500°C with 30 minutes hold times in comparison with continuous cycling. Furthermore, a greater reduction in the fatigue life was observed when the material was cycled with hold times in air. Therefore it was suggested that the oxidation at the crack tip, during the creep-fatigue loading in air, had a greater effect on the endurance of the material than purely creep-fatigue loading. While Wood et al.,[1977], observed identical fatigue endurance of type 316 steel when cycled in both air and a helium mixture at 625°C with tensile hold times. The length of hold times was thought to be long enough for oxidation to occur in each case, as fractographs of the fracture surfaces revealed. Ardellier,[1981], found reduced fatigue life of 316L stainless steel when cycled in air with increasing hold times between zero and 100 minutes in comparison with similar cycling, also at 600°C, in a sodium environment. The fatigue life decreased with increasing tensile hold times in both environments although the increased fatigue life in sodium, in comparison to that in air, was attributed to the lower oxidization rate in sodium. However periods of maximum compressive strain during the fatigue cycle also decrease the fatigue life as observed by Lord and Coffin,[1973], with the nickel based super alloy Rene 80 at 817°C. Continuous cycling and cycling with equal hold periods produced similar fatigue life while strain cycles with tensile hold periods were beneficial to fatigue life. The decrease in fatigue life at compression hold periods was due to the tensile mean stress resulting from stress relaxation at the hold period. At 817°C, the transition fatigue life of Rene 80 was very low, about 100 cycles, while the experiments performed all lasted longer than 170 cycles. Therefore they were all performed at strain levels in which the elastic strain was greater than the plastic strain and the resultant mean stresses from the stress relaxation had a dominant effect. Similarly compressive mean stresses at the tensile hold periods helped to deter fatigue crack propagation.

2.1.5.3. Irradiation Effects on Fatigue Life.

A further important factor which may have an effect on the fatigue life of nuclear reactor components is the effect of irradiation on the material behaviour. Grossbeck and Liu,[1981, 1982, 1985], have carried out a number of investigations into the fatigue life of type 316 steel in both the cold worked and the irradiated form at a range of temperatures from 430°C to 650°C. The results displayed a decrease in fatigue life of the irradiated material at 430°C by a factor of 3 to 10 in comparison with the cold worked material. Two possible reasons for the decrease in fatigue life were enhanced precipitation of the carbide phases and formation of helium bubbles along the slip bands. Further studies at both 550°C and 650°C displayed similar fatigue life to the corresponding tests on cold-worked material and no trace of helium embrittlement. Therefore the results at 430°C were explained to be due to fracture of carbide phases precipitates on slip bands resulting from the cold-work rather than irradiation induced embrittlement. However Brinkman and Korth,[1974], observed tensile hold times to decrease the fatigue life of type 316 steel specimens at 593°C with intergranular fatigue cracking while further decrease in fatigue life of material that was previous irradiated and then cycled with tensile hold times indicated that irradiation induced damage had an effect on the fatigue life. Vandermeulen et al.,[1988], found a slight decrease in the fatigue life of solution annealed 316L when tested at 430°C following irradiation exposure in comparison to the same material unirradiated. A decrease in the frequency of the strain cycling from 0.5Hz to 0.005Hz had little effect on both the unirradiated and the irradiated material.

2.1.5.4. Combined Thermal/Mechanical Cycling Effects on Fatigue Life.

An important variation on the strain controlled cycle which has relevance in many industries, including the power generation industry and the aero-industry, is the addition of thermal cycles to the mechanical cycle or thermal cycles only with the specimen either fixed or free to expand. When thermal strain cycles are performed with mechanical strain cycles such that the maximum temperature corresponds to the maximum mechanical strain the process is termed in-phase thermo-mechanical fatigue, (TMF). Conversely out-of-phase TMF cycles are performed when the minimum temperature occurs at the maximum mechanical strain. Jaske and Leis,[1979], have clearly described methods of performing both in-phase and out-of-phase TMF, using an induction heating system for rapid heating, internal water cooling for thin-walled tubular specimens or forced air cooling for solid specimens combined with mechanical strain control as in LCF tests. It would be very useful for the design engineer to describe the endurance of a TMF test on the same diagram as the fatigue life during LCF tests, however the effects

of combined temperature and strain cycling on the fatigue life of a component are varied. Laboratory experiments have shown that lifetime under conditions of TMF is dependent on a number of factors including, the material, the temperature range, the mean temperature, the waveshape and the length of hold times at both maximum temperature and strain. The material aspect has been covered in reviews such as those by Skelton,[1983], and Lundberg and Sandström,[1982], who have discussed that while the fatigue life of austenitic stainless steels is severely reduced when tested under in-phase TMF conditions, where high temperature effects combine with tensile loading, superalloys such as IN 738, experience equally damaging effects under conditions of both in-phase and out-of-phase TMF. Out-of-phase cycling would be expected to cause the greatest reduction in fatigue life, as found in AISI 1010 steel, [Jaske and Leis,1979], due to the combined tensile strains at both minimum temperature, (maximum thermal strain), and maximum mechanical strain, however Degallaix et al.,[1990], have found similar fatigue lifetimes for 316L stainless steel with out-of-phase cycling between 150°C and 500°C and isothermal LCF tests at 500°C. Furthermore Jones, Bourcier and Van Avyle,[1988], found reduced fatigue life for both type 316 stainless steel and Alloy 800 under both in-phase and out-of-phase TMF with temperatures cycled between 360°C and 649°C in comparison with isothermal tests at 649°C. With both steels, all out-of-phase cycling produced striation patterns on the fracture surfaces while in-phase cycling produced mixed mode intergranular and transgranular crack growth featuring cleanly split grains separated by ductile tearing with void formation.

Another effect which has been observed to decrease the fatigue life is to increase both the range of the cyclic temperatures and the mean temperature by increasing both the minimum and the maximum temperatures, Fig 2.1.14. Kawamoto et al.,[1966], have shown that the induced creep effects of a combined maximum tensile stress and increasing maximum temperature of a TMF cycle lead to greater reductions in the fatigue strength of 18Cr-10Ni steel. It appears that comparisons between the isothermal Coffin-Manson law and TMF fatigue life have to be considered separately for each material under the conditions of interest.

Crack growth rates during thermal fatigue have been calculated from the striations on the fracture surfaces of 12%Cr-Mo-V-W steel and low alloy Cr-Mo cast steel by Okazaki and Koizumi,[1983]. Similar crack growth rates were calculated for a number of notched specimens of the 12%Cr-Mo-V-W steel which were cycled out-of-phase between 300°C and 550°C and 350°C and 600°C at several strain ranges. Similar crack growth rates were also calculated for the Cr-Mo steel which was cycled in-phase and out-of-phase between 300°C and 550°C. In each case crack growth was transgranular with striation patterns on the fracture surface. Jones, Bourcier and Van Avyle,[1988], found crack

growth rate during out-of-phase TMF cycling of 316 stainless steel to be less than that of isothermal cycling at the maximum temperature and concluded that the decrease in the corresponding TMF life with respect to the isothermal fatigue life was due to the damage cause by TMF during initiation.

Further reductions in TMF life are observed when periods of maximum tensile or compressive strain hold are introduced into the TMF cycle. Jones, Bourcier and Van Avyle,[1988], introduced periods of 5 minutes maximum or minimum temperature into the thermal cycling of a constrained Alloy 800 specimen which resulted in compressive or tensile hold times in the out-of-phase TMF cycling. The samples cycled with the 5 minute maximum temperature, compressive hold period showed the shortest cycle lives. Cracking was transgranular with the formation of a clear striation pattern. The decrease in endurance was explained due to the development of large tensile mean stresses following gross stress relaxation at the high temperature compressive hold time. Hold time effects during in-phase cycling of Type 304 stainless steel were investigated by Westwood,[1979], who incorporated tensile strain hold times at the maximum temperature during cycling between 350°C and 700°C. Specimens which experienced TMF with a one hour hold period failed due to intergranular cracking.

2.1.5.5. Thermal Cycling Effects on Fatigue Life.

The difficulties in assessing the failure of components under thermo-mechanical fatigue conditions are further complicated when the temperature and the resultant stress field varies through the thickness of the material. This situation often occurs in components within jet engines, gas cooled reactors, and other components which are subjected to thermal cycling. It is impractical to perform realistic tests on working components which are subjected to in-service thermal fatigue due to both the physical dimensions of the components and the time between each cycle, therefore a number of different methods to develop similar thermal stresses within practical size specimens have been developed. Thermal fatigue tests are often performed as repeated thermal shock tests in which unconstrained specimens are heated to a uniform temperature then one face of the specimen is subjected to rapid cooling or one face of the specimen is rapidly heated and then the whole specimen is immersed in a cooling medium. In each case a temperature gradient is developed through the thickness of the specimen which results in a complex thermal stress field which varies with depth and time. For aero-engine and high temperature turbine applications thermal shock tests are performed on double-edge wedge or tapered disk specimens of nickel based super-alloys, Marchand, Dorner and Ilschner,[1988], or cobalt based superalloys, Mowbray and Trantina,[1978], while investigations into the thermal shock behaviour of heat-exchangers and components for

power stations are often performed on steel plates, Newton,[1976], Bethge et al.,[1988], Marsh,[1981], or cylindrical tubes of stainless steels and other iron based alloys, Skelton,[1990], and Burlet et al.,[1989].

In general, thermal shock tests are performed as a repeated thermal cycle which may vary depending on the application that the thermal shock test is attempting to model. An upshock is a combination of rapid heating of one surface of a specimen until the temperature is uniform throughout the specimen followed by a longer period of cooling. Similarly a downshock is obtained by rapidly cooling one surface of a specimen which has been at a uniform high temperature. The length of time spent in heating and cooling is varied depending on the application that the test is intended to model. Mowbray and Trantina,[1978], have performed alternate heating and cooling shock tests, to model the start-up and shutdown experience of high temperature turbine components, by immersing tapered disk specimens of the cobalt based alloy FSX 414 into fluidized baths which were either at a minimum temperature of 21 °C or a maximum temperature between 816 °C and 1038 °C. Downshock tests were performed on 2¼ %Cr-1%Mo steel plates, [Newton,1976], to simulate the effects of cleaning the heavy soot deposits from boiler's superheater tubes, within coal fire burners, by firing waterjets at the tubes which are at operating temperatures above 500 °C and working pressures above 10MPa. An increasing number and depth of cracks were observed to grow with increasing original temperature, from the quenched face of plate specimens. Bethge et al.,[1988], found cracks to grow from a machined notch within the face of a plate of reactor vessel steel which was quenched to simulate the shutdown or possible accident conditions as experienced within parts of the pressure vessel and the piping system of a light water reactor. Similarly Marsh,[1981], investigated the effects of shutdown cooling on the structural components above the core of a liquid metal fast reactor by quenching the faces of Type 316 and 304 austenitic stainless steel plates from various temperatures between 500 °C and 250 °C for differing durations resulting in a range of minimum temperatures. Other investigations have been performed to observe thermal fatigue crack growth in plates of 316L steel over a wide range of temperatures, [Shimizu et al.,1983].

A number of investigations into the effects of start-up and shutdowns on the components within power plants, such as valve chests, turbine casings and rotors, have involved downshock testing of cylindrical components. Skelton and Nix,[1987], observed multiple crack initiation in the bore of ferritic and austenitic steel cylinders following water quenching of the internal surface from a uniform temperature of 550 °C. Metallurgical inspection revealed that the crack propagation was transgranular with clear striation patterns beyond the region of initiation. The striation spacing indicated a short period of crack acceleration to a peak followed by deceleration as the crack grew towards the

centre of the tube. The decrease in the elastic stress gradient from the bore was calculated in the equation;

$$\sigma = \frac{E\alpha(T - T_{av})}{1 - \nu_p} \quad (2.1.25)$$

where E is the modulus of elasticity, α is the coefficient of thermal expansion, T is the temperature at a point radius, T_{av} is the volume average temperature and ν_p is Poisson's ratio. Skelton and Miles,[1984], also used high frequency induction heating to obtain a uniform temperature of 550°C before quenching the bore of ½Cr-Mo-V steel cylinders and found the pre-test heat treatment and the resultant microstructure to have a large effect on the endurance of the material. Similar to the findings of Skelton and Nix, the as received material displayed craze crack initiation from the quenched bore and subsequent transgranular crack growth which was observed to arrest before reaching half the thickness. However the tests were terminated before the crack was long enough to be detected from the external surface using the potential drop technique. This technique of monitoring crack growth during an experiment will be discussed in greater detail in section 2.2.5. When the ferritic steel had been quenched and tempered before thermal cycling the microstructure consisted of large and coarse grains which promoted crack growth to ¾ of the thickness from multiple cracks initiated at the bore while a circumferential crack was observed to grow through the thickness of the two specimens each of which contained an internal circumferential semicircular notch, from which the cracks initiated. Calculations of the stress gradient identified the small region of yielding at the internal surface, a portion of which would be subjected to reversed plastic straining throughout the test while the remainder towards the external surface would shakedown from yielding during the initial shock to cyclic elastic straining.

This phenomena of yielding over a small region from the shocked surface was observed when Burlet et al.,[1989], subjected internally water-cooled 2¼%Cr-1%Mo steel cylinders to external surface upshocks, between room temperature and 600°C in 10 seconds, using an induction heating system. The crack growth rate from machined notches on the external surface was calculated using the interrupted test technique and the resultant fracture surfaces displayed a transgranular mode of fracture with an oxide coating which obscured the striation patterns. The equivalent plastic strain through the thickness of an unnotched cylinder, Fig. 2.1.15, was calculated from an elastic-plastic thermal-strain finite element analysis. The analysis indicated that the crack growth rate decreased as the crack grew from the cyclic plastic zone into the elastic domain in the middle of the cylinder. However the stress concentrating effect of a notch was neglected. This effect has been calculated by Kussmaul and Stegmeyer,[1989], to influence the cyclic strain up to the centre of an externally notched thick-walled cylinder when

subjected to thermal upshocks at the notched surface. The presence of the notch also increased the plastic deformation at the internal surface. Furthermore care had to be taken in the choice of elastic modulus, coefficient of thermal expansion, and the strain hardening rule for the material characteristics which were used in the finite element analysis. Using values corresponding to the average temperature of the thermal cycle resulted in underestimation of the calculated strains. However taking into account the hardening, yielding and equivalent strain at the notch tip enabled comparisons to be made between the number of cycles required to initiate a crack to a length of 1mm over a range of thermal strains and mechanical strains in axially loaded experiments at the maximum temperature of the thermal cycle.

The effects of hold periods at the maximum and/or minimum temperature during a thermal cycle have been investigated with regards to both the initiation of cracks from notches and the resultant crack propagation. Love and Hoddinott,[1983], found endurance limits to initiation, during thermal cycles with hold times below ten minutes at high strains, to compare well with the total strain initiation life relationship for uniaxial cycling at the maximum temperature of the thermal cycle, 625°C, of type 316 stainless steel. With increased hold times, one hour at 625°C during upshock testing, the number of cycles to initiation decreased and the crack growth was observed to be intergranular with a single longitudinal crack growing to $\frac{3}{4}$ of the 20mm cylinder thickness. This increase in crack growth was explained as an effect of the concentration of bending stresses at the crack tip or local overheating due to the radio frequency current being diverted by the presence of the crack. However, Cordwell,[1990], has also observed increased crack growth rates with maximum temperature hold times during the upshocks of type 316 stainless steel. The faster growing intergranular cracks were observed to follow grain boundary ferrite stringers due to both the reduced energy required to propagate the crack through the weak matrix/stringer interface and because the straight grain boundaries of the stringers would allow propagation without the energy consuming meandering of the crack.

It is likely that components which are subjected to thermal cycling may also be subjected to end loads, due to constraints on longitudinal expansion from joining components, or the induced hoop stresses from pressurized fluids which are flowing through the components. Both Skelton,[1983], and Shimizu et al.,[1983], have observed that increasing tensile end stresses tends to increase the crack growth rate, on a plane perpendicular to the end stress, during downshock thermal cycling of type 316 stainless steel. Although multiple cracks, in the axial plane, initiated from the quenched bore of a cylinder they all arrested before reaching half way through the thickness regardless of the end stress, which was applied in the axial direction. However within the same

specimen a circumferential crack was observed to propagate, perpendicular to the applied end stress of 60MPa, and penetrate through the thickness of the cylinder in 32,000 thermal cycles. The cracking was transgranular, indicating that the induced mean stress prevented the crack from arresting, while the thermal cycles controlled the fatigue crack growth. However Shimizu et al.,[1983], showed that the crack growth rate in downshocks from 860°C with an end stress of 38MPa compared well with the corresponding creep crack growth rates, beyond the initial creep damage accumulation period, at 860°C. Unfortunately no indication was given to the mode of the fracture, however it must be stated that as the specimen had been held at such a high temperature, in order to obtain a uniform temperature before cooling, then the possibility of creep damage occurring must be considerably large.

Before discussing the methods used to analyse the crack growth rate through the complex strain gradients which are developed in thermal fatigue it is worthwhile to review the study of fracture mechanics and the methods of determining the behaviour of metals in relation to the study of fatigue crack growth under mechanical loading. The resultant relationships can then be applied to describe the fatigue crack growth under thermal cyclic loading.

Monotonic Tension Properties

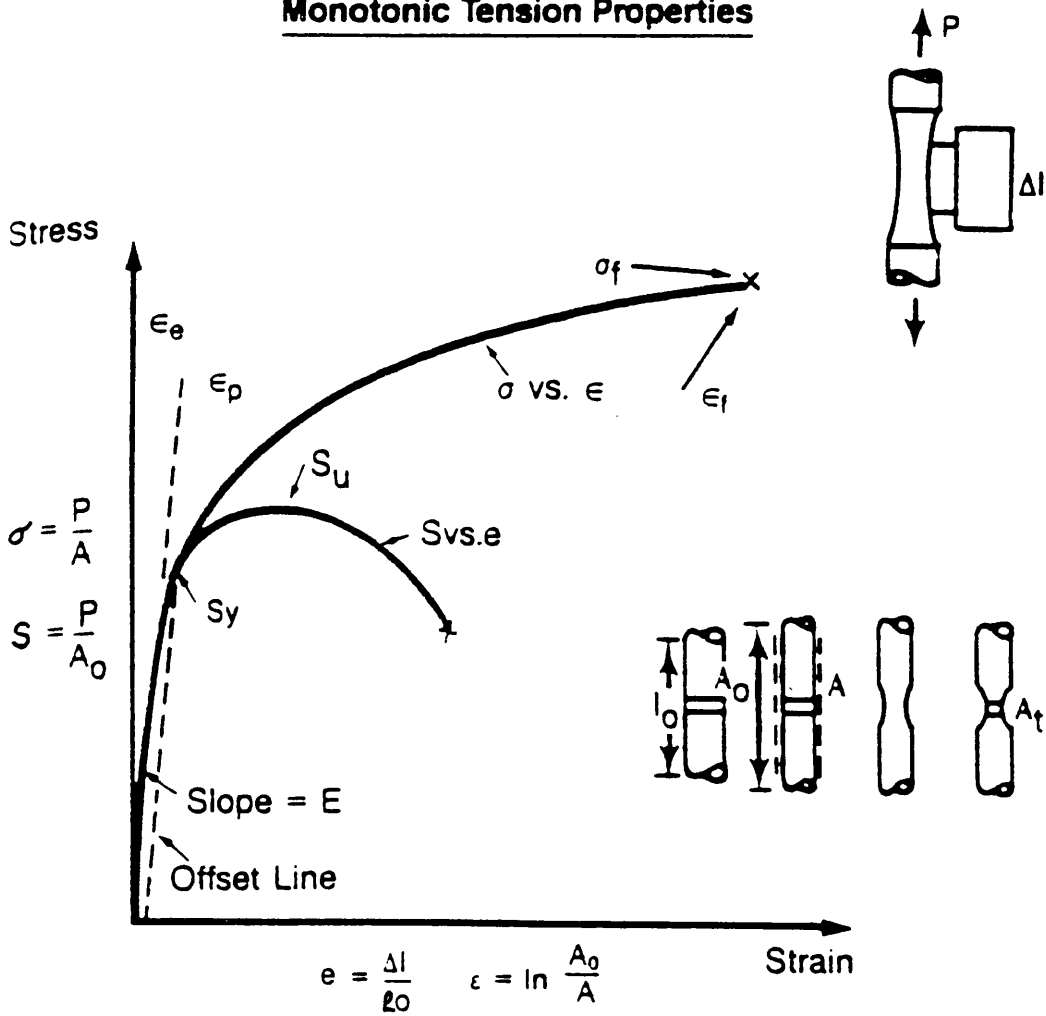


Figure 2.1.1. Monotonic Testing Stress/Strain Curves, (after Rice et al., [1989]).

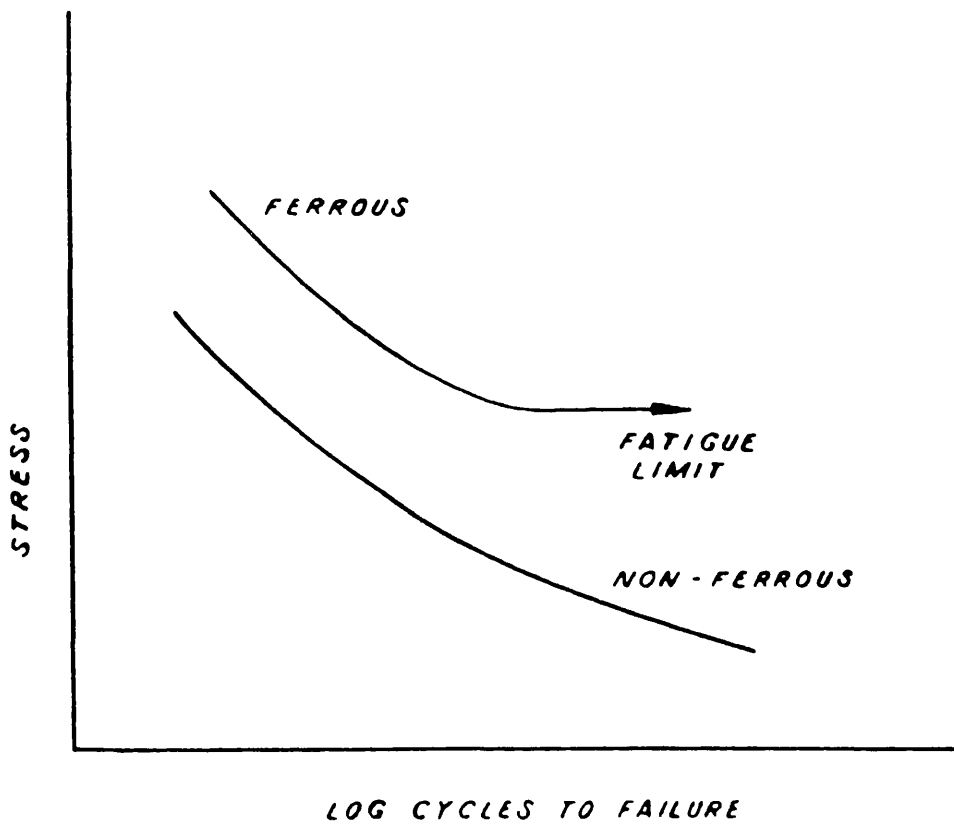


Figure 2.1.3. Typical S-N Curves For Ferrous and Non-Ferrous Metals, (after Colangelo and Heiser,[1974]).

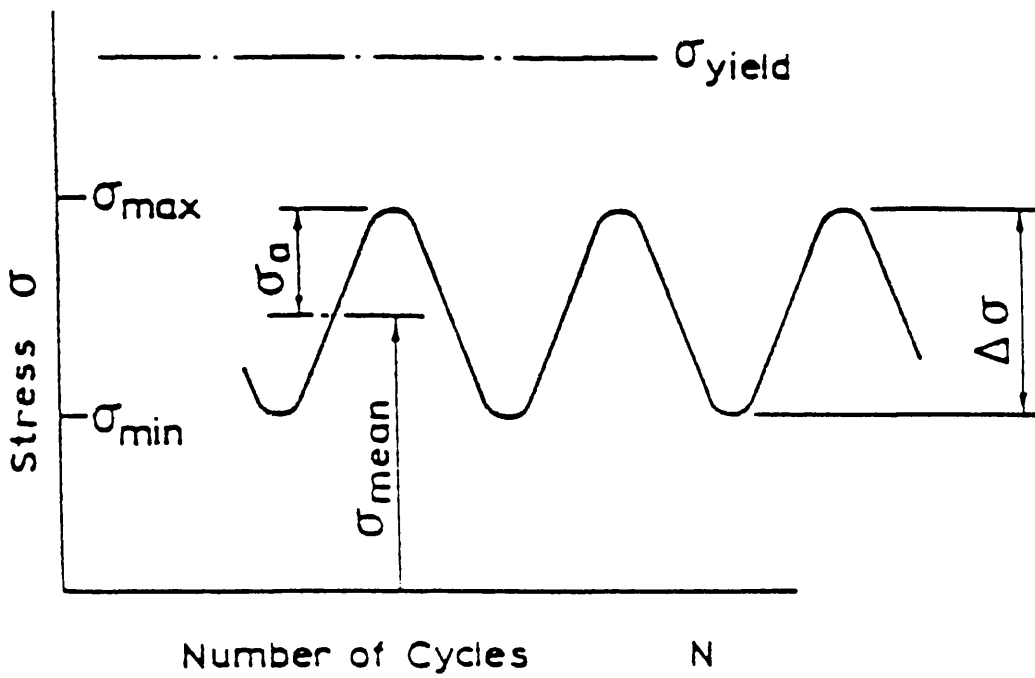


Figure 2.1.2. Stress Control Test Parameters, (after Miller,[1980]).

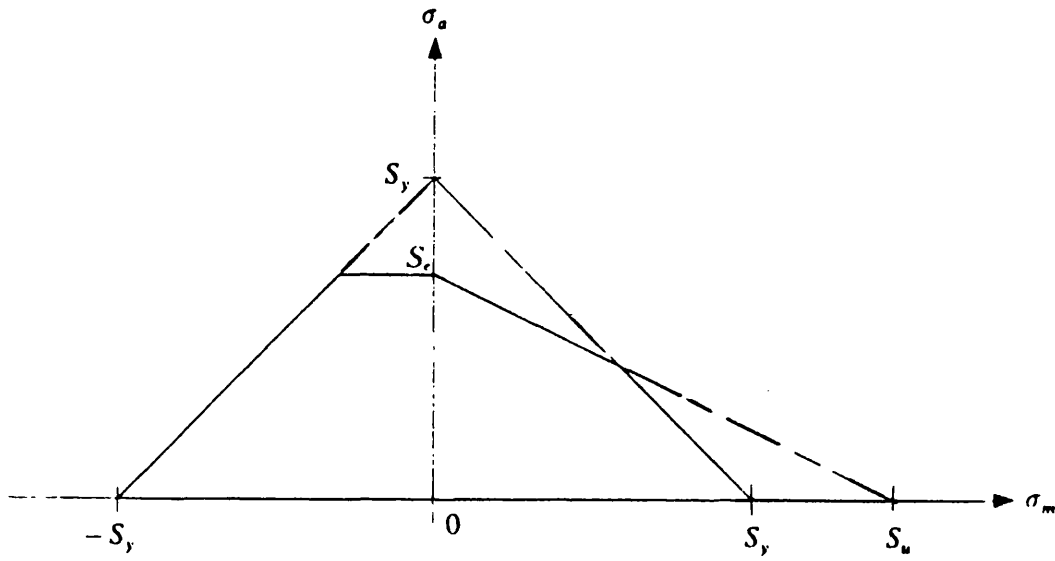


Figure 2.1.4. Modified Goodman Diagram, (after Budynas,[1977]).

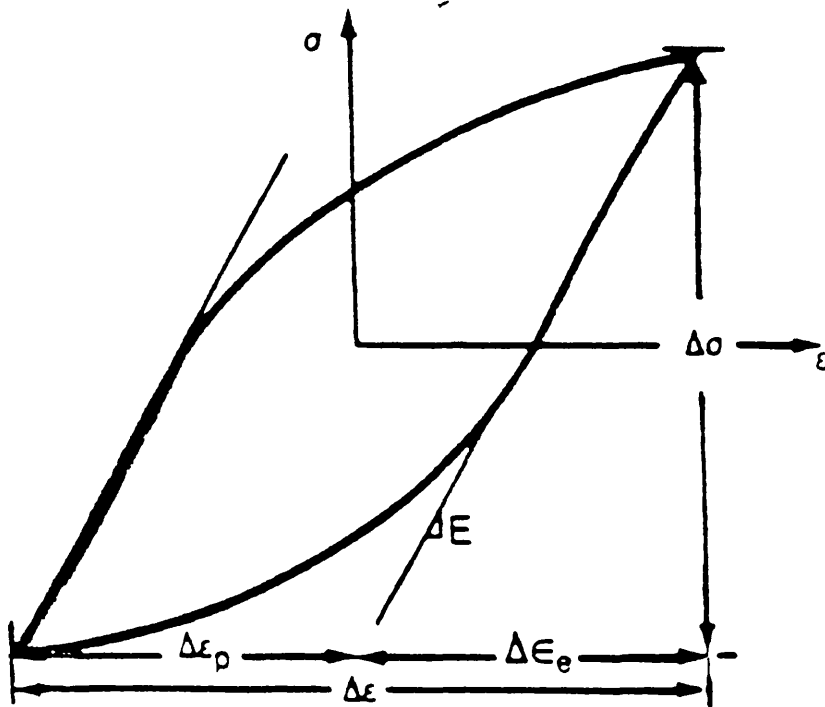


Figure 2.1.5. Hysteresis Loop Parameters, (after Rice et al.,[1989]).

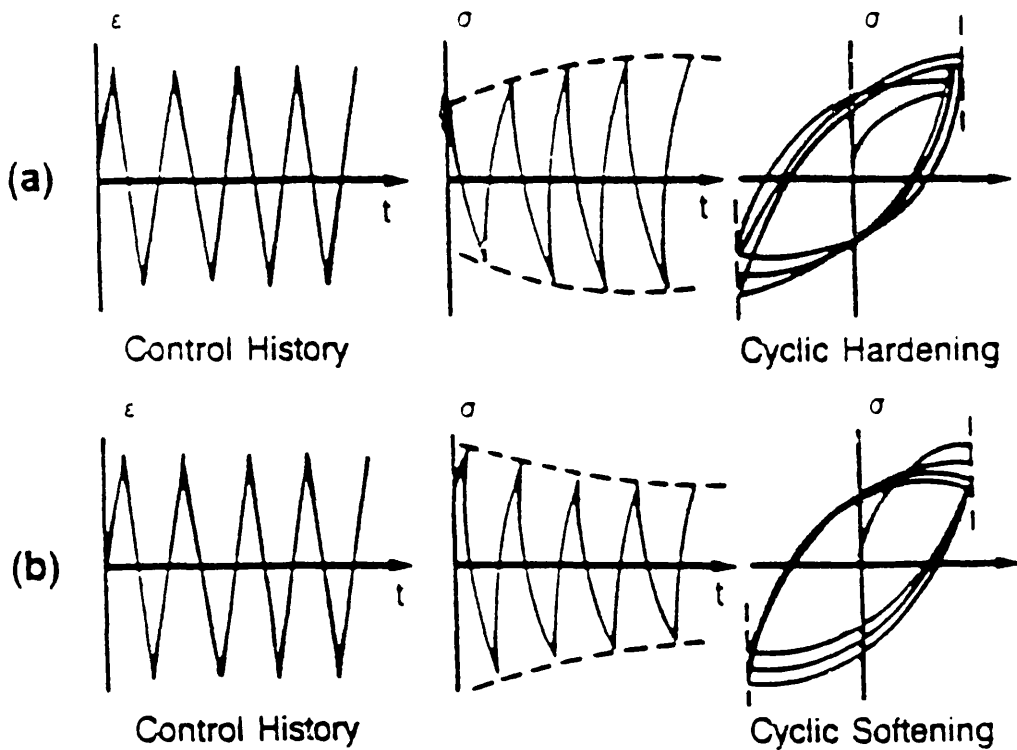


Figure 2.1.6. Variation in Stress Amplitude under Strain Control Cycling, (after Rice et al., [1989]).

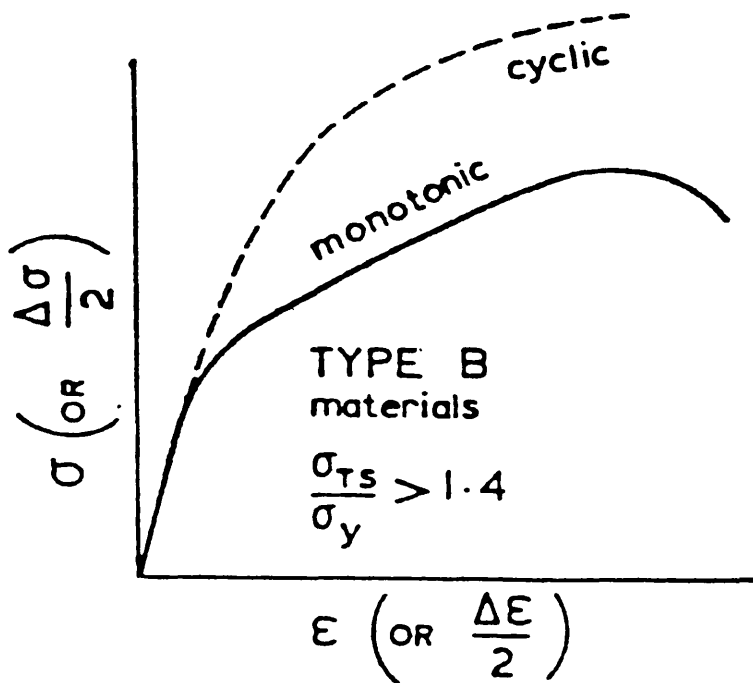
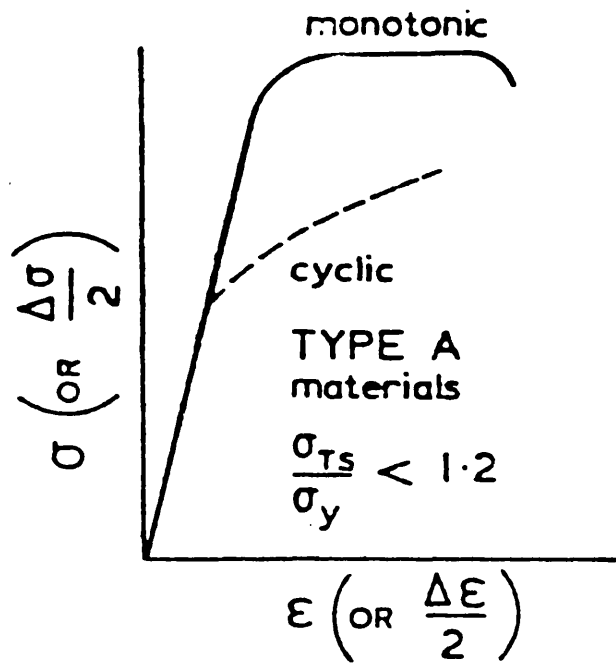


Figure 2.1.7. Cyclic Stress/Strain Behaviour, (after Miller,[1980]).

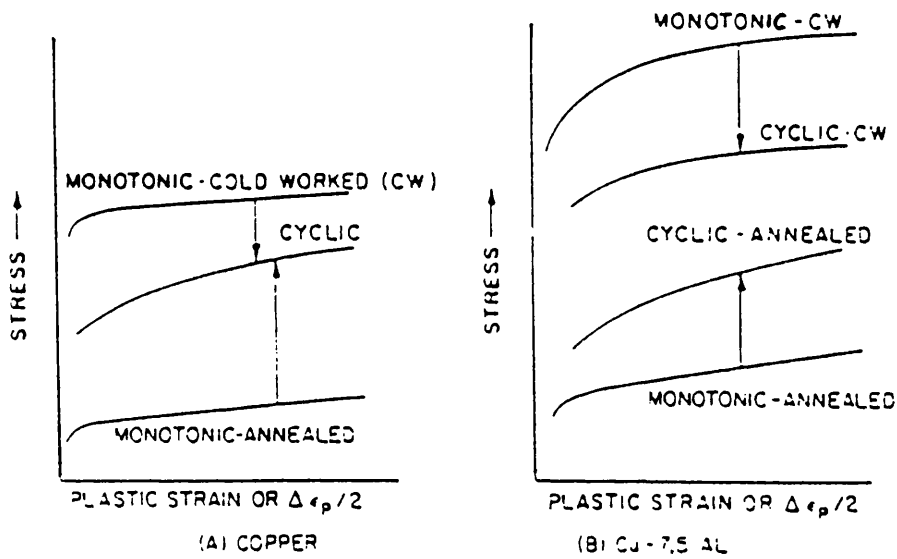


Figure 2.1.8. Effect of Treatment on Cyclic Stress/Strain Curves, a) Copper and b) Cu-7.5%Al, (after Feltner and Laird,[1967]).

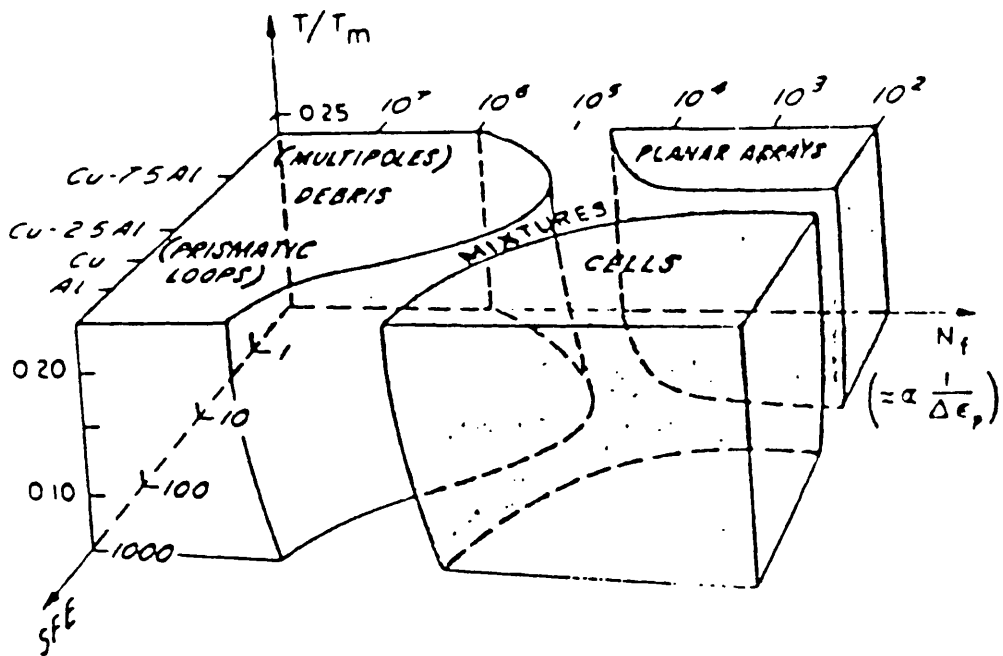


Figure 2.1.9. Characterisation of Dislocation Substructure in fcc Metals as a Function of Strain Amplitude, Temperature and Stacking Fault Energy, (after Coffin,[1972]).

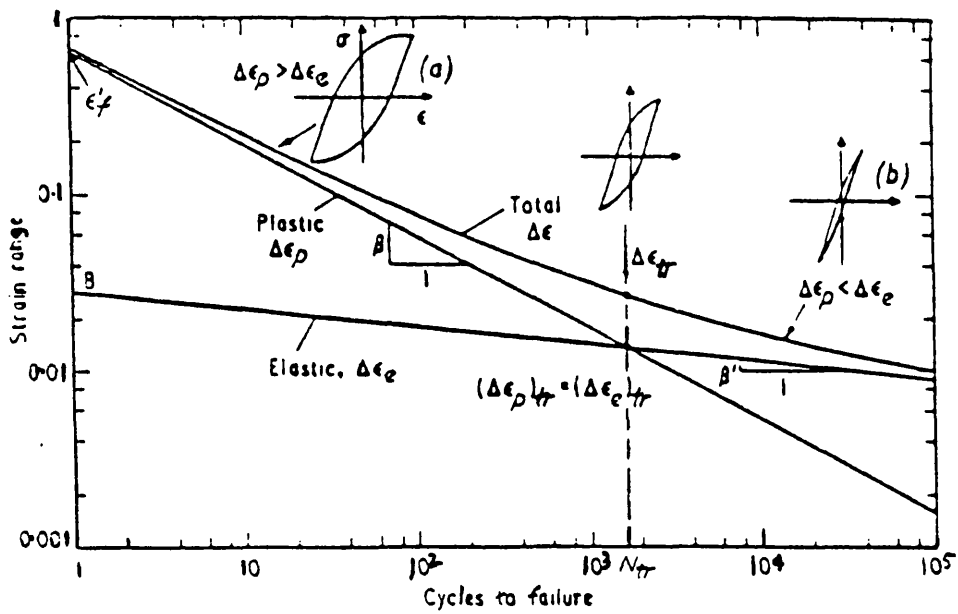


Figure 2.1.10. Schematic Drawing of Fatigue Life Curves, (after Coffin,[1977]).

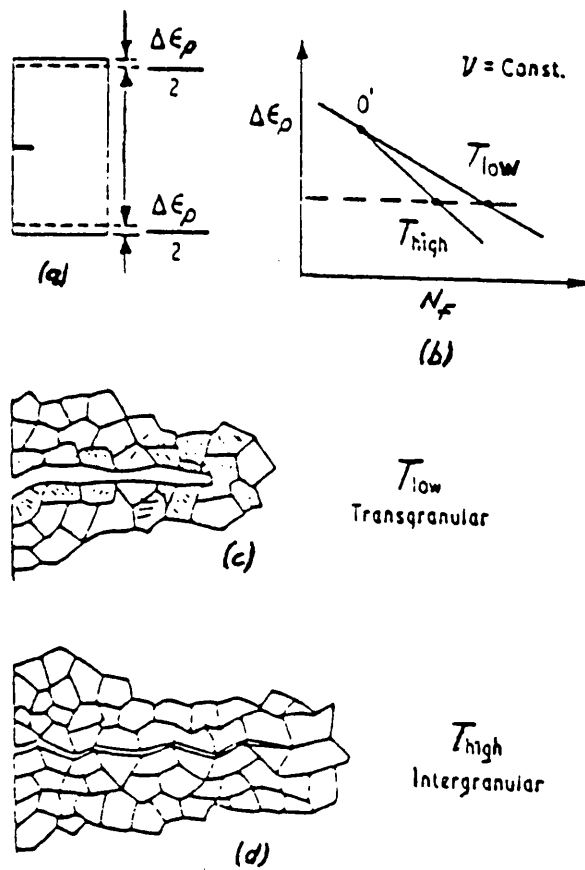


Figure 2.1.11. Schematic Representation of Fracture Mode Change With Temperature and Plastic Strain Range, (after Coffin,[1977]).

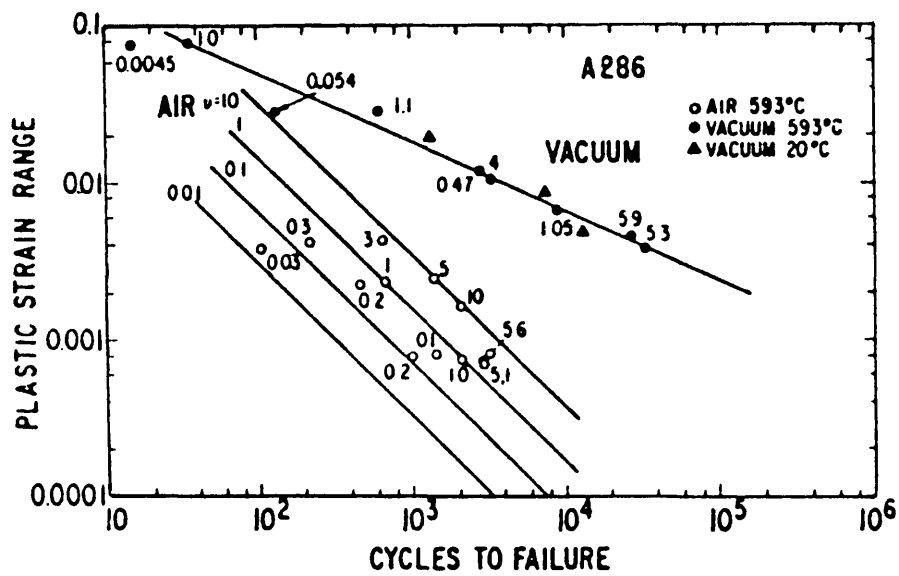


Figure 2.1.12. Environment and Frequency Effects on LCF Life of A286 Steel: Numbered Points are Frequency in cpm, (after Coffin,[1977]).

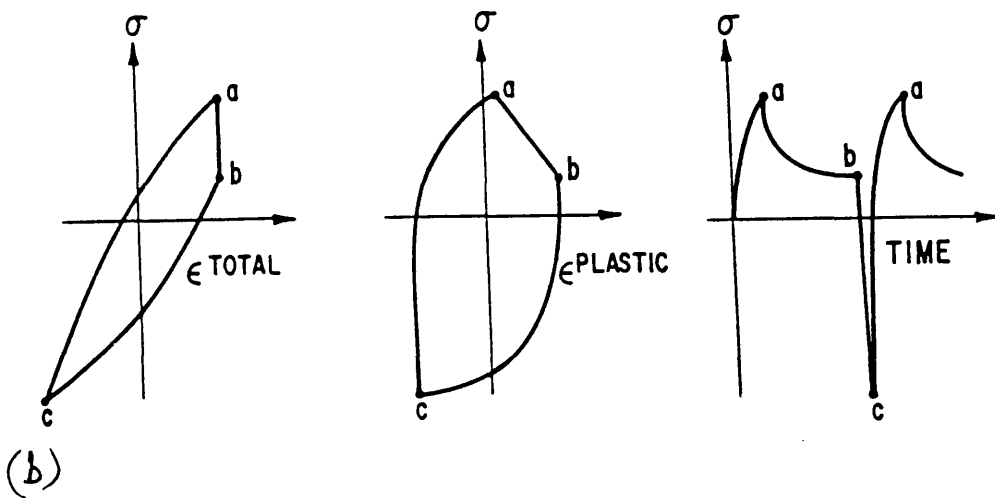
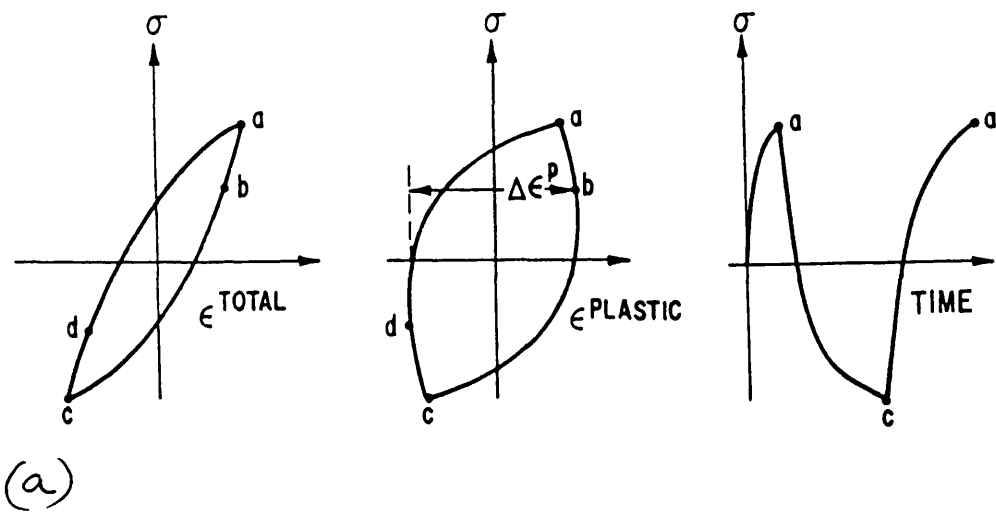


Figure 2.1.13,(a-b). Typical Strain Controlled LCF Cycles With Corresponding Hysteresis Loops, (after Lord and Coffin,[1973]).

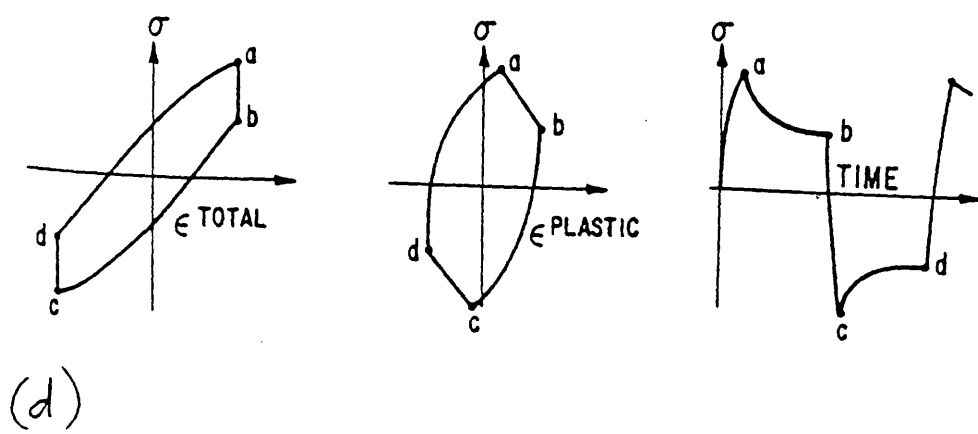
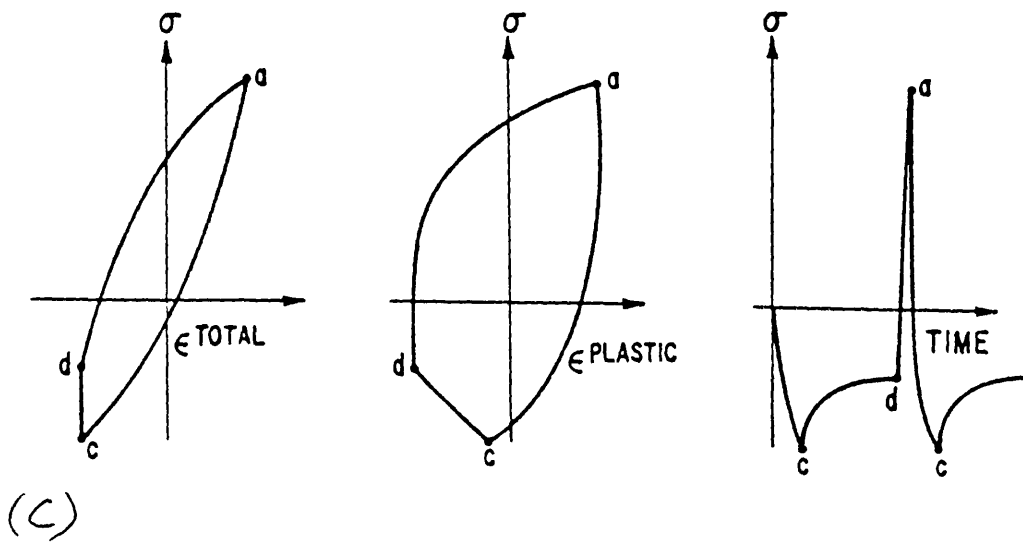


Figure 2.1.13,(c-d). Typical Strain Controlled LCF Cycles With Corresponding Hysteresis Loops, (after Lord and Coffin,[1973]).

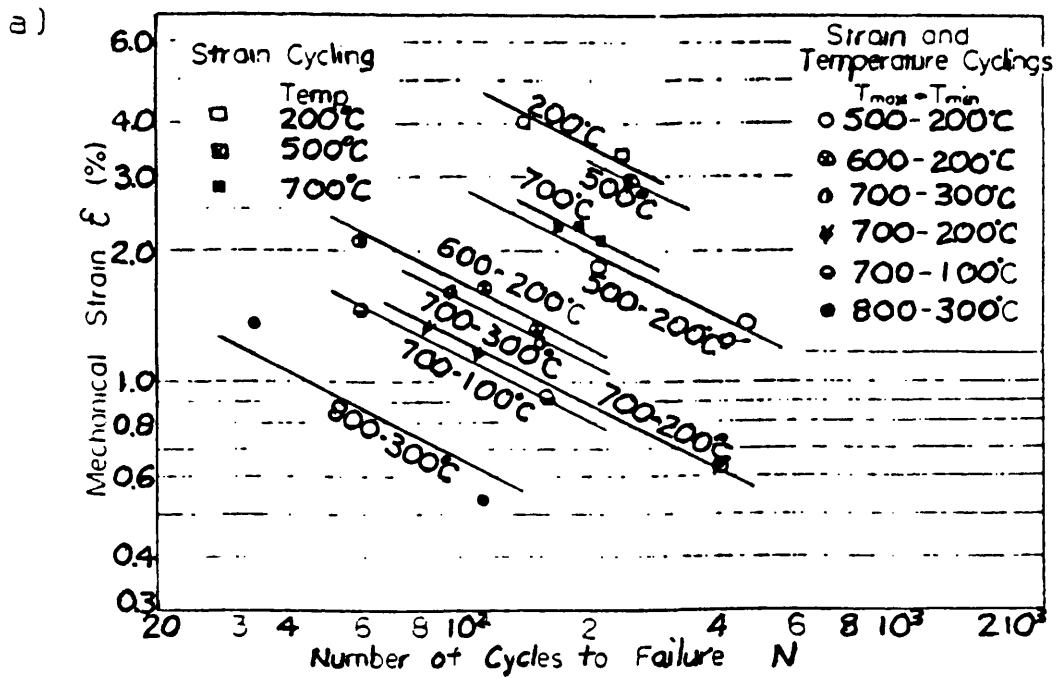


Figure 2.1.14. Effect of Varying the Temperature Range on the Fatigue Life of 18Cr-10Ni Steel, (after Kawamoto et al., [1966]).

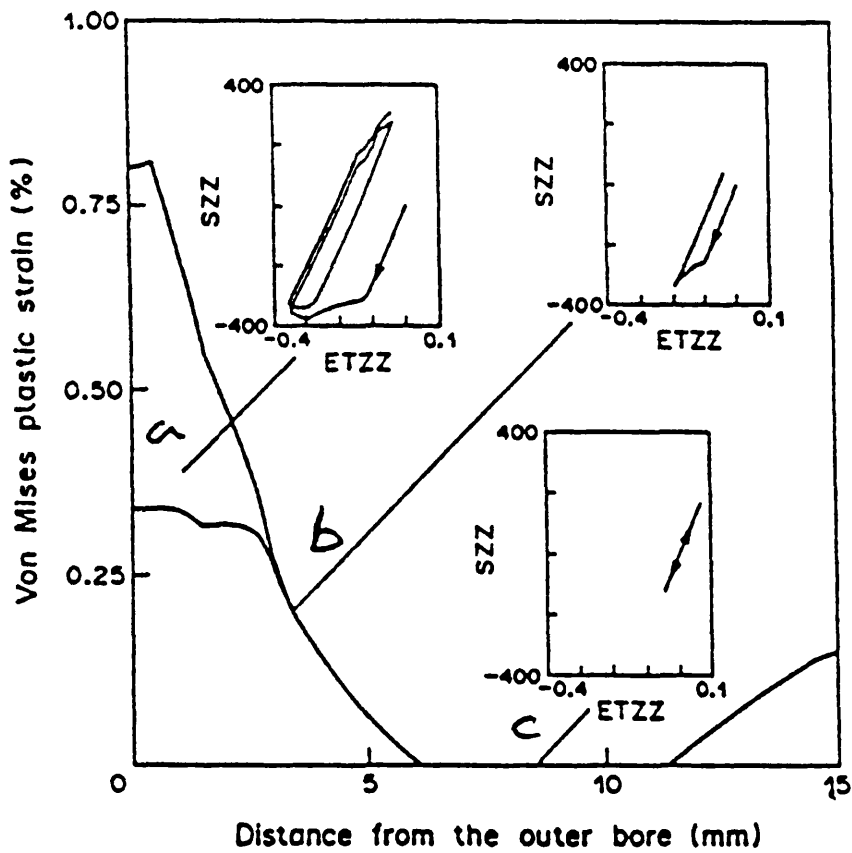


Figure 2.1.15. Equivalent Plastic Strain Through the Thickness of a Thermally Shocked Cylinder, (after Burlet et al., [1989]).

2.2. Fatigue Crack Growth.

2.2.1. Linear Elastic Fracture Mechanics, (LEFM).

Failure of a component due to fatigue loading arises from a combination of initial changes in the microstructure of the material, followed by crack initiation, followed by crack propagation then final fracture. The last fatigue cycle before failure was identified to be the same as the complete fracture of a body due to the presence of a crack which was subjected to a critical load, [Griffith, 1921]. The mechanics of the fracture process contribute greatly to fatigue failure.

If a homogeneous body containing a sharp crack of length $2a$, (Fig.2.2.1), is loaded by external forces then the elastic solutions of the stress tensor at the crack tip is expressed in terms of the polar co-ordinates r and θ ;

$$\sigma_{ij} = r^{-1/2} [K_I f_{ij}^I(\theta) + K_{II} f_{ij}^{II}(\theta) + K_{III} f_{ij}^{III}(\theta)] \quad (2.2.1)$$

The stress intensity factors K_I , K_{II} , K_{III} , are function of the crack length, geometry of the body and the geometry of the external forces. It is possible for the crack to fracture the material in one or a combination of three modes, Fig. 2.2.2, depending on whether the load is tensile, (mode I), shearing, (mode II), or anti-plane shearing which is often termed as tearing, (mode III). The non-dimensional f_{ij} functions in equation 2.2.1 depend solely on θ . Assuming that the load is of a magnitude such that the material behaves in a fully elastic manner then linear elastic fracture mechanics, (LEFM), can be used to characterise the crack tip stress field. The principles of LEFM are discussed here assuming that the body is subjected to tensile, mode I, loading with a more complete study of the subject being given by Knott,[1973]. The stresses near the tip of a crack can be represented as indicated in equations 2.2.2a-c, which are based on the co-ordinate system shown in Figure 2.2.3.

$$\sigma_x = \frac{K_I}{\sqrt{2\pi r}} \cos \frac{\theta}{2} \left(1 - \sin \frac{\theta}{2} \sin \frac{3\theta}{2} \right) + \dots \quad (2.2.2a)$$

$$\sigma_y = \frac{K_I}{\sqrt{2\pi r}} \cos \frac{\theta}{2} \left(1 + \sin \frac{\theta}{2} \sin \frac{3\theta}{2} \right) + \dots \quad (2.2.2b)$$

$$\tau_{xy} = \frac{K_I}{\sqrt{2\pi r}} \cos \frac{\theta}{2} \sin \frac{\theta}{2} \cos \frac{3\theta}{2} + \dots \quad (2.2.2c)$$

$\tau_{xy} = \tau_{yz} = \sigma_z = 0$ for plane stress, $\sigma_z = (\sigma_x + \sigma_y) \nu_p$ for plane strain.

These equations display that the stresses around the crack tip are characterized by K_I . To describe the stresses further away from the crack tip, additional terms relating to the distance from the crack tip, r , must be included, however near the crack tip the $r^{-1/2}$ parameter holds. When the body in Figure 2.2.1 is loaded by a remote external stress, σ_y , which is perpendicular to the crack plane, then the stress intensity factor is given by the expression;

$$\underbrace{K_I}_{r \rightarrow 0} = \sigma_y \sqrt{2\pi(a+r)} \quad (2.2.3)$$

Stress intensity values are normally calculated for standard specimens such as finite centre-notched specimens, three-point bend specimens and compact tension specimens, Figure 2.2.4, [Clark,1971] for which stress intensity calculations can be made using standard procedures, [ASTM E647,1988], and fracture mechanics handbooks, [Rooke and Cartwright,1976], [Tada et al.,1985], which also contain geometry factors for some typical component crack-type geometries. In the purely elastic case, the stress intensity factor is used to describe the crack propagation rate. However, in reality, a zone of plastic deformation occurs at the crack tip. The size of this plastic zone is determined using an elastic-plastic solution.

2.2.2. Elastic-Plastic Solution.

The plastic zone is a region at the crack tip in which the local stress is greater than the yield stress of the material, σ_{ys} . If the plastic zone size is large enough then it can have an effect on the stress distribution within the elastically loaded material adjacent to the plastic zone. However, when the plastic zone size is small in comparison to both the crack length and the dimensions of the body then the stress distribution further away from the crack tip is identical to the elastic solution. This is termed as small scale yielding.

In equation 2.2.1 it was shown that the crack tip stress state is three dimensional. Considering an ideal elastic-plastic material as a material that behaves elastically at stresses up to σ_{ys} , beyond which it yields without hardening, then the Von Mises criterion states that the material yields when the equivalent stress equals σ_{ys} ;

$$\sigma_{ys} \geq 2^{-\frac{1}{2}} \sqrt{[(\sigma_1 - \sigma_2)^2 + (\sigma_2 - \sigma_3)^2 + (\sigma_3 - \sigma_1)^2]} \quad (2.2.4)$$

σ_1 , σ_2 , and σ_3 are the principal components of stress and are derived from equations 2.2.2(a-c) in the form;

$$\sigma_1 = K_I (2\pi r)^{-\frac{1}{2}} \cos \frac{\theta}{2} \left(1 + \sin \frac{\theta}{2} \right) \quad (2.2.5a)$$

$$\sigma_2 = K_I (2\pi r)^{-\frac{1}{2}} \cos \frac{\theta}{2} \left(1 - \sin \frac{\theta}{2} \right) \quad (2.2.5b)$$

$$\sigma_3 = K_I (2\pi r)^{-\frac{1}{2}} 2\nu_p \left(\cos \frac{\theta}{2} \right) \quad \text{for plane strain} \quad (2.2.5c)$$

$$\sigma_3 = 0 \quad \text{for plane stress} \quad (2.2.5d)$$

Combining equations 2.2.4 and 2.2.5(a-d) gives the plastic zone size, r_y , in terms of the polar angle θ , for conditions of plane stress and plane strain respectively;

$$r_y = \frac{1}{2\pi} \left(\frac{K_I}{\sigma_{ys}} \right)^2 \cos^2 \left(\frac{\theta}{2} \right) \left(1 + 3 \sin^2 \left(\frac{\theta}{2} \right) \right) \quad (2.2.6a)$$

$$r_y = \frac{1}{2\pi} \left(\frac{K_I}{\sigma_{ys}} \right)^2 \cos^2 \left(\frac{\theta}{2} \right) \left(1 + 3 \sin^2 \left(\frac{\theta}{2} \right) - 4\nu_p (1 - \nu_p) \right) \quad (2.2.6b)$$

The component of stress perpendicular to a free surface is zero, therefore plane stress conditions prevail at the crack tip on the surface of the body. However, at the crack tip in the centre of the body plane strain conditions dominate. The differences are observed in the change in shape of the plastic zone from the external surface through to the centre and on to the opposite surface of a thick body, Figure 2.2.5. The values of plastic zone size along the direction of the propagating crack, $\theta = \theta$, for conditions of plane stress and plane strain respectively are expressed as;

$$r_y = \frac{1}{2\pi} \left(\frac{K_I}{\sigma_{ys}} \right)^2 \quad (2.2.7a)$$

$$r_y = \frac{1}{2\pi} \left(\frac{K_I}{\sigma_{ys}} \right)^2 (1 - 2\nu_p)^2 \quad (2.2.7b)$$

For $\nu_p=0.3$, equations 2.2.7(a-b) calculate the plane stress plastic zone size to be greater than the plane strain plastic zone size by a factor of 6.25. However, the general approximation is that the plane strain plastic zone in the direction of crack propagation is 1/3 of the plane stress plastic zone, [Klesnil and Lukas,1980], [Tada et al.,1985]. Therefore it is desirable to calculate the stress intensity values using thick specimens to assure that a large proportion of the crack front is under plane strain loading. Recommended ratios of specimen width to thickness are given in the standard testing procedures, [ASTM E399,1978]. Considering the applied stress to be in the region of half of the yield stress, or smaller, then:

$$r_y \leq \frac{1}{6\pi} \left[\frac{0.5\sqrt{\pi a}}{2} \right]^2 \quad (2.2.8)$$

Therefore the plastic zone radius is less than one hundredth of the crack depth and maybe neglected. However at higher applied stresses the plasticity at the crack tip causes redistribution of the stress within the elastically loaded region to maintain equilibrium. It was observed that equilibrium could be satisfied by advancing the origin of the coordinates, (r,θ) , in Figure 2.2.3 ahead of the crack tip and into the plastic zone, [Irwin,1960]. An effective crack size of $a+r_y$ is often used as a correction, [Tada et al.,1985].

2.2.2.1. Application of LEFM to Fatigue Failure.

The range of stress intensity factor, ΔK , upon cyclic loading is described in terms of the applied stress range, $\Delta\sigma$;

$$\Delta K = Y \Delta\sigma \sqrt{\pi a} = K_{\max} - K_{\min} \quad (2.2.9)$$

where Y is a specimen geometry dependent factor.

Paris and Erodogan,[1963], showed the rate of fatigue crack growth to be related to the range of stress intensity factor for two aluminium alloys. This has become known as the

Paris Law of fatigue crack growth;

$$\frac{da}{dN} = C(\Delta K)^m \quad (2.2.10)$$

where C and m are material constants which are obtained by experiment, da is the change in crack depth during a corresponding increase in the number of cycles, dN , and the stress intensity range, ΔK , is the difference between the maximum and the minimum values of stress intensity factor during a fatigue cycle, $K_{\max} - K_{\min}$. Although the K_{\max} term in equation 2.2.9 corresponds to the maximum stress σ_{\max} and has a positive value, the corresponding minimum stress intensity cannot be represented by a negative value, as compressive loads are carried by the faces of the crack. Consequently the K_{\min} term in equation 2.2.9 should be given the value of K at which the crack opens during the tensile/compressive cycle. However factors which affect the crack closure such as fracture surface roughness and oxide formation within the crack are very difficult to account for numerically. Therefore, on the assumption that the crack will close at zero load, K_{\min} is given the value of zero for all cycles when the load ratio, $R = \sigma_{\min} / \sigma_{\max}$, is less than zero.

A typical crack growth curve has three distinct regions, as illustrated in Figure 2.2.6. Equation 2.2.10 describes the fatigue crack growth behaviour during the region II. Region I is a low growth rate region in which the range of stress intensity factor approaches the threshold stress intensity factor, ΔK_{th} , below which crack growth does not occur. Region III is a region of high growth rate in which the maximum stress intensity factor approaches the fracture toughness of the material, K_{IC} , and crack growth involves stable ductile tearing. Pickard et al., [1975], have clearly defined the three regions on a log-log scaled plot for Type 316L stainless steel. The ΔK_{th} was calculated to be $6 \text{ MPa}\sqrt{\text{m}}$ when the crack growth rate was less than 10^{-7} mm/cycle . Deviation from the Paris Law occurred at $\Delta K = 52 \text{ MPa}\sqrt{\text{m}}$ and K_{IC} was calculated to be $65 \text{ MPa}\sqrt{\text{m}}$. Both the crack growth rates and the threshold stress intensity factor were similar in Type 316L tested at 25°C and -196°C , [Mahoney and Paton, 1974], while increased crack growth rates were observed, at 649°C , over the same range of stress intensity factors.

Standard test procedures and specimen geometries for development of the Paris Law are available, [ASTM E647, 1988] while values of m , in equation 2.2.10, vary from 2 to 5 for most structural materials. Paris, [1964], displayed similar slopes, $n=4$, on the $\log \Delta K$ vs. $\log(da/dN)$ plots for various materials including steel, molybdenum, titanium, magnesium and the aluminium alloys 2024-T3 and 7075-T6, while Speidel, [1975], has shown that the fatigue crack growth rates in a given stress intensity range can differ considerably for different materials when tested in a vacuum, Figure 2.2.7. Furthermore

when the cyclic stress intensity range is divided by the appropriate value of modulus of elasticity, the power law regions of many different materials come together within a single band. Therefore the strain crack growth parameter, $\Delta K/E$, determines the crack growth rate irrespective of other material properties. The temperature effect of increasing the crack growth rate with increasing temperature was observed to disappear when the data from vacuum tests on Type 316 steel at 25, 427 and 593 °C, was plotted against ΔK_e , [Sadananda and Shahinian,1980].

Amzallag et al.,[1981], observed that an increase in the load ratio-R produced a decrease in the corresponding ΔK at low crack growth rates in Type 316 stainless steel. Other factors such as specimen thickness, specimen type, crack length, waveform and environment had no effect at such low crack growth rates. Ermi et al.,[1981] found an increased crack growth rate with increasing R-ratio at low ΔK values and used an effective stress intensity factor, K_{eff} , equation 2.2.11, to describe the crack growth rate as a Paris Law equation;

$$K_{eff} = K_{max}(1 - R)^m \quad (2.2.11)$$

where $m=0.667$ for annealed Type 316 at room temperature and K_{max} is the maximum stress intensity factor during a cycle. Slightly higher crack growth rates were observed in miniature centred cracked tension, CCT, specimens in comparison to standard compact tension, CT, specimens. This phenomenon was also observed by Rickerby et al.,[1984], with data from CCT specimens of solution annealed Type 316 steel in comparison with the data obtained from single edge notch, SEN, specimens as a result of the high plastic deformation in CCT specimens at relatively low values of ΔK .

The greater number of cycles were required to initiate a fatigue crack in notched specimen of irradiated, annealed Type 316 stainless steel over the entire range of temperatures, from 100 °C to 500 °C, in comparison to the same material in the unirradiated state, [Fenici and Suolang,1991]. For both materials the required number of cycles, $R=0.1$, to crack initiation decreased with increasing temperature. Irradiation induced defects blocked the dislocation glide thus increasing the resistance of the material to crystallographic plane slip and crack initiation. The corresponding fatigue crack growth rate of the irradiated material was always lower than that of the unirradiated material over the entire temperature range. The fatigue crack growth rate was found to increase with increasing temperature for both materials while the threshold stress intensity factor of the irradiated material was greater than that of the unirradiated Type 316 steel.

2.2.2.2. Mechanisms of Fatigue Crack Growth.

Following microcrack nucleation, fatigue crack propagation appears in two stages, Figure 2.2.8. Stage I cracking appears in the form of microcracks inclined to the direction of the applied load along the slip planes of maximum shear stress. With further cycling the microcracks either arrest or grow and combine to produce a dominant stage II macrocrack which propagates in a direction approximately perpendicular to the applied load. The stage II cracks propagate across the grains or through the grain boundaries until final fracture of the remaining ligament ahead of the crack. The number of cycles necessary for stage I propagation in sharply notched or pre-cracked bodies becomes negligible and the total fatigue crack propagation is stage II type.

At ambient temperatures, continuous cycling produces fatigue cracks which are usually transgranular, that is the crack propagates through the grains, and the resultant fracture surface consists of the fractured grains which are often patterned with fatigue crack markings, known as beach-marks or striations. The striations can display the crack initiation point, the development of the crack shape and the point at which stage II cracking becomes final fracture. Striations have also been used to measure the crack growth on the basis that each striation spacing corresponds to a cycle. Therefore the spacing between the striations is the distance the crack has developed in one cycle. Paris,[1964], observed that during random loading of aluminium alloys, a periodic single cycle overload produced a marked ring on the fracture surface which was far greater than the other marks, the number of which corresponded to the number of cycles between each overload. Striation markings have been measured to give fatigue crack growth rates which when plotted against the corresponding values of ΔK produced similar Paris Law plots to the crack growth measurements made during the tests on Type 316L, [Pickard et al.,1975]. Similar experiments in air and in vacuum, [Sadananda and Shahinian,1980], have shown that the formation of striations is dependent on the environment. The fracture surfaces from the vacuum tested material appeared to be featureless in comparison to the striation formation on the material tested in air. However striations on material tested in a vacuum have been observed to be shallower with less space between them than those produced during a test in air.

The crack growth rate at ambient temperature is influenced by the environment, while the effects of both the load ratio and the pre-test treatment of the material on the crack growth rate, vary for different materials, [Speidel,1975], [Amzallag et al.,1981]. Different samples of the nickel based superalloy, Nimonic 105, were treated to produce both a brittle and a ductile version of the material before LEFM fatigue testing in either vacuum or air, [Speidel,1975]. In the ductile condition the crack growth rate in air was

two-to-three times higher than that in the non-aggressive environment. At the lower ranges of stress intensity factors the material in the brittle condition behaved similarly, however at higher ranges the crack growth rate in both vacuum and air were far greater. Intergranular cracking through the brittle material increased the crack growth rates and similarities between the crack growth rates in both water and air indicated that the intergranular crack growth was influenced more by the increased mechanical mean stress than by environmental effects. With the ductile materials, 2¼Cr-1Mo steel and SA 542 pressure vessel steel, there was no effect of increasing load ratio, (mean stress), on the fatigue crack growth rate, between 10^{-6} and 10^{-3} mm/cycle, at room temperature, [Ritchie,1986]. In non aggressive environments and at the same ΔK range, crack growth rates were independent of cyclic frequency, waveshape and the thickness of specimens.

Crack growth rate at 649°C was greater than that at 25°C , [Mahoney and Paton,1974], although the mode was predominantly transgranular even with the increased carbon content in Type 316, and the increased distribution of M_{23}C_6 carbides in the aged Types 316L and 316. The M_{23}C_6 carbides raise the transition temperature from 600°C to 800°C for transgranular to intergranular fatigue failure by preventing grain boundary sliding, [Driver,1971].

The fatigue crack growth rate of annealed Type 316 stainless steel is slightly lower in a vacuum than in air at 25°C , 427°C and 593°C , although this effect decreases with increasing stress intensity range at the higher temperatures, [Sadananda and Shahinian,1980]. The mode of fracture was transgranular in the regime of low crack growth rates, ($da/dN < 10^{-3}$ mm/cycle), at both 25°C and 593°C , as the low stacking fault energy restricted slip from one crystallographic plane to another. With 20% cold worked Type 316 the crack growth rates at 593°C in both air and vacuum were similar and far greater than that in air at 25°C , over the corresponding range of ΔK . A one minute tensile hold period during the fatigue cycle at 593°C increased the crack growth rate, both in air and vacuum, by two orders of magnitude over that of the continuous cycling. Fatigue crack growth was predominately intergranular with and without hold times at 593°C in a vacuum. In air at 593°C , continuous cycling continued to display transgranular striations while the introduction of the one minute hold time produced intergranular cracking. When the crack growth rate was plotted on a time basis as mm/hour, both data from cycles with one minute hold times and static load data displayed higher crack growth rates than the corresponding continuous cycling tests at 593°C . The enhanced crack growth rate due to creep-fatigue interaction and the similar crack growth rates in both air and vacuum means that the increased crack growth in this material is not completely due to a time dependent process. If the local stress is below the increased yield stress of the cold-worked material then plastic relief at the grain

boundary junctions ahead of the main crack is prevented and microcrack nucleation is possible. Therefore the crack growth rate increased. Other material factors which increase the fatigue crack growth rate in Type 316L stainless steel include the increased size, concentration and nature of multiple phase inclusions and the increased grain size in Type 316L welds, [Pickard et al.,1975].

With an increase in temperature from room temperature to 538°C the crack growth rate of type 304 steel, in air, increased over the mid range, [Speidel,1975]. At low stress intensity ranges, $< 12 \text{ MPa}\sqrt{\text{m}}$, no effect of decreasing frequency was observed on the crack growth rate at 538°C. However with increasing ΔK and decreasing frequency, the crack growth rate increases. Such an effect was also observed with a cobalt based superalloy, HS 188, at 600°C, [Speidel,1975], which displayed a critical frequency of 0.01Hz below which the fracture mode changed from transgranular to intergranular cracking. The corresponding crack growth rate increased and was found to be similar to creep crack growth rates at 600°C. It can only be assumed that in aggressive environments, decreasing the frequency also increases the crack growth rate.

The environmental effect on striation formation has been taken into account in Laird's plastic blunting model, [Laird,1967]. Using Figure 2.2.9 as a guideline, the fatigue crack propagation during one cycle is basically described in terms of the local plastification, along the planes of maximum shear stress, at 45° to the crack tip. Initially, the zero load condition represents a well developed stage II crack with a striation pattern on the fracture surfaces behind the crack tip, (a). Under the initial tensile load the material yields, (b), then the crack tip blunts and increases in size to a semi-circular configuration with the increasing tensile load, (c). When the maximum tensile load is applied, oxides from the air quickly form on the exposed surface of the crack tip. On application of the compressive part of the cycle, the process of rewelding of the crack tip surfaces is inhibited by the oxide layers therefore the surfaces are only partly folded by buckling into a double notch at the crack tip, (d). Upon continued compression, the crack tip sharpens and the double notch becomes the troughs of the striation pattern, which are a length of Δl in front of the previous markings, (e). In a vacuum the oxides do not develop on the fracture surface, a greater degree of cold rewelding of the crack tip occurs during the compressive phase. The striation pattern does not appear to develop and the extension of the crack tip is reduced over the cycle. Therefore the crack growth rate is reduced in a non-aggressive environment.

Kaplan and Laird, [Klesnil and Lukas,1980, ref.#126], observed no propagation from sharp notches in the planes of maximum shear stress in single copper crystals loaded in repeated zero-compression cycling. Taking this into account, they developed two models

to describe stage I crack growth. The first model refers to the frequent cross-slip in wavy slip materials. The maximum shear stress component in the plane of the crack produces a repeated process of plastic blunting and reshaping of the crack tip. An increment of crack extension occurs with each cycle. The second model is also based on repeated plastic deformation at the crack tip. However in this model the crack extension is due to the upper part of the crystal slipping with respect to the lower part. The slip occurs along the crack plane, which is identical to the active slip plane. This mechanism does not require a normal component of stress, is believed to be particularly applicable to metals with limited cross slip.

A recommended procedure for determining the threshold stress intensity factor is given in ASTM E647,[1988], and is defined as the ΔK for which the corresponding crack growth rate is equal to or below 1×10^{-7} mm/cycle. Experimentally, the threshold range in stress intensity factor is determined by decreasing the stress amplitude, and the corresponding stress intensity range, while the load ratio, R , remains constant until crack propagation stops. However Klesnil and Lukas,[1980], found that the threshold value was dependent on the magnitude of the stress intensity factor at which the crack was propagating before the stress amplitude was reduced. Figure 2.2.8 revealed that the early stage of fatigue crack growth was a combination of modes I and II and that the cracking was of a crystallographic nature and dependent on microstructure. Brown and Miller,[1985], found ΔK could describe the fatigue crack growth in both the near threshold region and Paris Law region for type 316 stainless steel measured under three different types of biaxial stress fields. Tables of results, [Klesnil and Lukas,1980], have shown threshold stress intensity factors to range from 0.5 to 8.0 $\text{MPa}\sqrt{\text{m}}$ depending on the type of material and the load ratio. The value of threshold stress intensity factor decreases with increasing load ratio during tension-tension cycling. Growth rates increase as the mean stress and the corresponding threshold ΔK_{th} are reduced. Ritchie,[1986], also observed that near-threshold growth rates were greater with increasing strength of steels and were generally slower in coarse grained microstructures. In general, aggressive environments reduce the threshold ΔK_{th} as Amzallag et al.,[1981], observed with 2618 aluminium alloy in argon when compared to air. However with type 316 stainless steel environmental effects were negligible. At ultra-low load ratios, ($R=0.05$), the near threshold growth rates of 2¼Cr-1Mo steel in dry hydrogen were significantly faster than in moist air, [Ritchie,1986], also in lower strength steels seemingly aggressive environments such as water and wet hydrogen produced marginally slower near threshold crack growth rates than in supposed inert environments like dry helium. The reduction in near threshold crack growth rate in wet environments was explained as an effect of oxide induced crack closure. However at higher load ratios the effects of environment on the near threshold crack growth rates are largely absent since the crack is opened to such an

extent that oxide fretting does not occur. Specimen type, thickness of specimen, crack length, waveform and frequency of cycling have no influence on the low crack growth rate region, [Amzallag et al.,1981].

At high ΔK values, region III, the crack tip stresses reach a critical condition resulting in rapid crack growth rates to failure. For mode I loading and brittle plane strain conditions, the critical value of stress intensity at which rapid failure occurs is designated as K_{Ic} . Furthermore, since the crack tip stresses required to produce rapid failure are material dependent, then K_{Ic} can be used as a parameter to describe the material's resistance to failure. This parameter is referred to as the fracture toughness of the material. Therefore if the stress intensity factor of a cracked body is calculated to be less than the known fracture toughness of the material then it is possible to calculate either the maximum allowable stress or crack depth within a factor of safety of component failure.

Values of material fracture toughness are calculated from experiments on standard specimen geometries. During region III, the crack growth rate, which is transgranular in region II, is increased due to addition of or replacement by static modes of fracture such as cleavage, intergranular cracking and microvoid coalescence. Resulting failure is either through brittle fracture or unstable ductile tearing. The growth rate is sensitive to microstructure, mean stress and specimen thickness. The higher mean stresses, resulting from increased load ratios, have been observed, [Ritchie,1986], to decrease the critical stress intensity factor, K_{Ic} , from $50\text{MPa}\sqrt{\text{m}}$ to $25\text{MPa}\sqrt{\text{m}}$ in a low toughness, (temper-embrittled), low-alloy steel. Although both microvoids in the microstructure and intergranular cracking influence the high crack growth rates, the actual magnitude of the velocity of the cracking is so great that corrosion and other environmental effects are negligible.

When the applied stress level increases towards the yield stress of the material then the region of fast fracture increases and the principles of linear elastic fracture mechanics no longer hold. Brown et al.,[1988], measured the fatigue crack growth rate in stainless steel specimens which were cycled at four different stress ranges from 67MPa to near yield stress and beyond to 560MPa which was almost $1\frac{1}{2}$ times the yield stress. The applied stress ranges which were near or above the yield stress produced higher crack growth rates and the characteristics of the Paris Law were not observed. For engineering components which may be subjected to fatigue stresses above the yield stress, such as thermal fatigue of power plant components, a method has to be developed which can describe the fatigue crack growth in terms of both the elastic and the plastic behaviour of the material.

2.2.3. Elastic-Plastic Fracture Mechanics (EPFM) and Fatigue Failure.

Tomkins,[1968], developed a model which described the crack propagation process in a ductile material under tension-compression straining unlike earlier models which were restricted to tensile loading, [Dugdale,1960], [Bilby, Cottrell and Swinden,1963]. Tomkins' theoretical model of the fatigue crack propagation under conditions of crack-tip plasticity and high strain fatigue was based on plane strain conditions. He replaced the crack tip plastic zone, [Dugdale,1960], by accommodating the plastic deformation during the tensile part of the cycle, along two narrow shear stress bands at $\pm 45^\circ$ to the crack tip. Increasing the load to the tensile strain limit produced a new crack surface along the inner surface of the flow bands. Although the load is reversed into compression the deformation is largely irreversible, therefore the crack closes with both an extension to the crack tip and a surface ripple in the cracked material behind the crack tip. The resulting fatigue crack growth rate was described in terms of the applied plastic strain range, $\Delta \epsilon_p$;

$$\frac{da}{dN} = \frac{\pi^2}{8} \left(\frac{A}{2\sigma_T} \right)^2 \Delta \epsilon_p^{(2n'+1)} a \quad (2.2.12)$$

where σ_T is the average deformation zone stress, (the flow stress of the material), and is greater than twice the value of the maximum applied stress. Tomkins,[1968], observed that the integral of equation 2.2.12 produced the Coffin-Manson equation and that the fatigue life data for four metals lay between upper and lower limits of equation 2.2.12 when the average deformation zone stress, (σ_T), was represented by the true tensile fracture stress of the material, (σ_f) and the ultimate tensile stress, (σ_u), respectively. Variations of equation 2.2.12, [Skelton,1982], which were based on striation counting, compare well with the growth rates of short cracks in a number of materials under high strain fatigue conditions at high temperatures. However when cracks propagate from a region of high plastic strain into a region of elastic shakedown the relationships based on equation 2.2.12 predict that crack propagation ceases when $\Delta \epsilon_p = 0$, yet under conditions of thermal fatigue, [Burllet et al.,1989], this is not the case. Therefore a fracture mechanics approach is required to determine the crack growth rate through a complete component in terms of both the plastic and the elastic strains.

A number of parameters have been developed to relate to the crack growth rate under conditions of post yield monotonic tensile loading. The crack tip opening displacement, CTOD, was developed in the early 1960's by Cottrell,[1961], as a method of relating the crack extension with the displacement between the surfaces of the crack at a position

corresponding to the original crack tip. Experimentally, the CTOD is determined from measurements of the surface displacement across the notch from which the crack has initiated. Fracture is considered to occur when a critical crack tip opening displacement, δ_c , is attained and is related to the applied stress, in plane stress conditions, by the equation;

$$\delta = \frac{8\sigma_y a}{\pi E} \ln \left[\sec \left(\frac{\pi \sigma}{2\sigma_{ys}} \right) \right] \quad (2.2.13)$$

where σ_{ys} is the yield stress. For low values of σ/σ_{ys} , equation 2.2.13 is reduced to;

$$\delta = \frac{\sigma^2 \pi a}{E \sigma_{ys}} = \frac{K^2}{E \sigma_{ys}} = \frac{G}{\sigma_{ys}} \quad (2.2.14)$$

where G is the strain energy release rate. Following his analysis of crack growth due to plastic strain, Tomkins,[1984], extended the crack tip opening displacement approach to include the contribution of the both the elastic and the plastic strain ranges during the fatigue crack propagation of a crack in an infinite plate loaded in tension;

$$\Delta \delta = \frac{\pi \Delta \sigma^2 a}{2 \sigma_r E} + \frac{\pi \Delta \sigma \Delta \epsilon_p a}{\sigma_r (1+n')} \quad (2.2.15)$$

From equation 2.2.15 values of CTOD are calculated for the corresponding crack depth and plots of Δ CTOD vs. da/dN are generated. During cyclic loading the crack opens under tensile loading, it extends with increasing tensile strain, thus creating new crack surfaces which are not cohesively closed during the compressive part of the cycle. Therefore a crack extension of half of the CTOD would be expected per cycle. However Brown,[1988], has found the $\Delta\delta/2$ relationship to be an upper bound to measured crack growth rates which indicates that the crack depth extension is less than half the crack tip opening displacement each cycle. For work hardened materials, the crack flanks accommodate some of the crack opening because they are involved in crack tip plasticity, [Rice and Rosengren,1968], therefore the crack extension is reduced while other factors such as the nonuniformity of crack advancement and crack closure could also contribute to the discrepancies.

Another parameter which relates the crack tip stress/strain field to the crack depth is the plastic zone size, r_p . In the small scale yielding regime, in which only the crack tip is subjected to plastic loading the corresponding plastic zone size can be calculated using equation 2.2.7. In the presence of large scale plastic deformation, both the CTOD,

equation 2.2.13, and the plastic zone size have been determined in terms of the crack depth a , using the strip yielding model of Bilby, Cottrell and Swinden,[1963]. In this model, the yielding is confined to the plane of the crack, of length, $2a$, in an infinite body which is subjected to a uniform tensile stress, σ , such that the plastic zone size is;

$$r_y = a \left[\sec \left(\frac{\pi \sigma}{2 \sigma_{ys}} \right) - 1 \right] \quad (2.2.16)$$

where σ_{ys} is the yield stress. Brown,[1988], altered equation 2.2.16, to describe the fatigue crack growth rate of type 316 stainless steel in terms of the cyclic plastic zone size. The applied stress was replaced by a stress range, $\Delta\sigma$, which was the difference between the maximum stress and the crack opening stress, and the yield stress was taken as $2\sigma_u$, the tensile strength of the material after strain hardening. From three candidate elastic-plastic fracture mechanics parameters, $\Delta\delta$, Δr_y and the cyclic J-integral, ΔJ , the cyclic plastic zone size was the most successful in describing the fatigue behaviour of type 316 stainless steel. Furthermore, Brown produced an equation which described the crack growth rate in terms of the plastic zone size with respect to the elastic and the plastic components of strain;

$$\frac{da}{dN} = C \left(4\beta\pi\sigma_u^2 r_y \right)^{m/2} + \frac{r_y \Delta \epsilon_p}{1+2n'} \quad (2.2.17)$$

where β is 2 or 6 depending on the stress regime and r_y must be evaluated from the tensile strength. Unfortunately, no data was found to confirm equation 2.2.17 and as the plastic zone size can vary across the crack front through the thickness of a component it is worthwhile to investigate other EPFM parameters which can be determined from both component and standard specimen tests and compared with available data.

The third EPFM parameter that Brown,[1988], described the fatigue crack growth rate of type 316 stainless steel in terms of was the cyclic J-integral, ΔJ . The cyclic J-integral was developed from the J-integral concept of Rice,[1968], which was basically a non-linear approach to the crack growth energy theory of Griffith,[1921], in which a linear elastic body, of thickness B , containing an edge crack of length a , is subjected to a remote load P , Figure 2.2.10a.

The difference between the corresponding lines of elastic load, P , and load point displacement, u , Figure 2.2.10b, for similar bodies with crack of lengths a and $a+\delta a$ respectively is the shaded area dU . This is the energy required to extend the crack a distance of δa . The corresponding energy release rate G , becomes;

$$G = -\frac{1}{B} \frac{\partial U}{\partial a} \quad (2.2.18a)$$

where B is the thickness of the body. As $\delta a \rightarrow 0$ the shaded area is difficult to measure. However the load and the displacement are related by the expression;

$$C_s = \frac{u}{P} \quad (2.2.18b)$$

where C_s is the reciprocal of the load-displacement slope and is known as the specimen compliance, which is a constant for a given crack length. The change in displacement, δu , is represented by;

$$\delta u = C_s \delta P + P \delta C_s \quad (2.2.18c)$$

However, with a constant load, $\delta P = 0$, therefore the change in displacement;

$$\delta u = P \delta C_s \quad (2.2.18d)$$

The energy stored within the body is $E_B = \frac{1}{2} Pu$, therefore the change in energy is;

$$\delta E_B = \frac{1}{2} u \delta P + \frac{1}{2} P \delta u \quad (2.2.18e)$$

With $\delta P = 0$, the energy stored in the body is given by;

$$\delta E_B = \frac{1}{2} P \delta u \quad (2.2.18f)$$

Combining equations 2.2.18d and 2.2.18f produces an equation for the change in energy δU ;

$$\delta U = \delta E_B = \frac{1}{2} P^2 \delta C_s \quad (2.2.18g)$$

As a crack advances forward by an increment δa the change in energy is given by;

$$G \delta a B = \frac{1}{2} P^2 \delta C_s \quad (2.2.18h)$$

Therefore the energy release rate due to an increment of crack growth is expressed as;

$$G = \frac{P^2}{2B} \frac{\partial C_s}{\partial a} \quad (2.2.19)$$

Knott,[1973], recommended that allowances must be made for yielding at the loading points and that fracture toughness of a material can be determined using this method assuming that the specimen is relatively small. This energy theory approach to crack growth has been shown, [Knott,1973], to relate to the stress intensity factor;

$$G = \frac{K^2}{E'} \quad (2.2.20)$$

where E' is the elastic modulus for plane stress or $E/(1-\nu_p^2)$ for conditions of plane strain.

When yielding occurs the load-displacement relationship is no longer linear and some of the energy is released without contributing to the crack growth. Rice,[1968], developed the theory for the J-integral in the late 1960's to determine the toughness of a cracked body, subjected to yield loading, in terms of the strain energy density. He considered an edge crack in a two dimensional body of unit thickness with an arbitrary contour, Γ , which begins along the bottom surface of the crack and ends along the top surface, Figure 2.2.11.

In the co-ordinate system shown, ds is an increment of the arc length along the contour, \underline{T} is the stress vector exerted on the material within the contour, u is the displacement and with the strain energy density, W_e , the line integral J around the crack tip is given by;

$$J = \int_{\Gamma} \left(W_e dy - \underline{T} \frac{\partial u}{\partial x} ds \right) \quad (2.2.21)$$

The strain energy density $W = \int \sigma_{ij} d\epsilon_{ij}$ where σ_{ij} and ϵ_{ij} are the stress and strain tensors respectively and the traction vector $T_i = \sigma_{ij} n_{ij}$ acting along the normal unit vector n_{ij} from the arc section ds along the contour Γ . Rice,[1968], has shown that the J-integral is path independent and is equivalent to a change in potential energy corresponding to the extension, da , of either a notch or a sharp crack, in a non-linear elastic material. With small scale yielding confined to the crack tip in an infinite elastic body, the J-integral becomes identical to the strain energy release rate, G , for a linear elastic body, with a plane strain plastic zone correction in the calculation of K ;

$$J = G = \frac{K^2}{E} (1 - \nu_p^2) = \frac{\sigma^2 \pi (a + r_y)}{E} (1 - \nu_p^2) \quad (2.2.22)$$

The J-integral can be evaluated in the elastic plastic regime using a finite element stress analysis, however a number of simpler estimation schemes exist, [Chipperfield,1978]. Rice et al.,[1973], have shown that the J-integral can be determined from the load-load pin displacement diagram of a cracked body as previously shown for G, Figure 2.2.12. The shaded area represents the work done in crack extension, dU and;

$$J = \frac{-1}{B} \frac{\partial U}{\partial a} \quad (2.2.23)$$

For power law hardening materials the plastic compliance of the cracked body, $C_N = u/P^Q$, varies with crack length and is used to determine dU in terms of P and u to give;

$$J = \frac{P^{(Q+1)}}{(Q+1)B} \frac{dC_N}{da} \quad (2.2.24)$$

This equation is valid for any path of the load displacement curve corresponding to the difference between the original crack length and the increased crack length and can be altered in terms of P(du) and u(dP) to account for crack extension at constant load or constant load point displacement respectively.

Although Brown,[1988], has argued that the J-integral was developed to describe crack extension with increasing tensile load and that no unloading of the stress can be accounted for, a number of estimations of a cyclic J-integral, ΔJ , have been developed to take into account the non-linear cyclic loading that occurs in high strain fatigue. Chell,[1981], has described an estimation of ΔJ in terms of an elastic and a plastic component, ΔU_p , the irreversible plastic work expended on unloading, as shown in Figure 2.2.13. Compared to the monotonic version, the cyclic J-integral depends on the change in elastic strain energy, equation 2.2.25, as the cyclic plastic work, ΔU_p is a reduction on the plastic work in tension.

$$\Delta J = \frac{(\Delta K)^2}{E'} + \frac{\eta_p \Delta U_p}{B(W-a)} \quad (2.2.25)$$

where E' depends on the stress state, B and W are specimen thickness and width respectively, a is crack depth and η_p is a function of specimen, the plastic collapse load and a/W and commonly has the value of 1 for centre cracked panels and 2 for bend

specimens in plane strain. Dowling,[1976], and Taira et al.,[1979], have also developed relationships using the ΔJ to describe the fatigue crack growth in centre cracked plates, CCP, in terms of elastic and plastic parameters at low and high temperatures respectively. Dowling's method employed the load-load point displacement plot with the origin at the compressive stress level at which the crack closed. The original model was for deep notched CCP specimen however modifications were made to produce an expression for ΔJ which relates the stress and strain ranges to a thumbnail shaped crack in a CCP specimen;

$$\Delta J = \left(\frac{\pi(\Delta\sigma)^2}{E'} + \frac{2\pi\Delta\sigma\Delta\varepsilon_p}{1+n'} \right) a \quad (2.2.26)$$

where n' is the cyclic strain hardening exponent. Equation 2.2.26 is related to the Δ CTOD relationship of Tomkins, equation 2.2.15, by the relationship;

$$\Delta J = 2\sigma_T\Delta\delta \quad (2.2.27)$$

Taira et al.,[1979], produced a similar relationship, with a temperature dependent elastic modulus, for a CCP specimen with a shallow crack. Using the area enclosed in the cyclic load versus crack centre opening displacement loop the plastic work term was derived and the resultant equation produced a straight line relationship between da/dN and ΔJ , on a log-log scale, for 316 stainless steel at both 600°C and 650°C over a wide range of stress levels;

$$\frac{da}{dN} = 1.18 \times 10^{-4} (\Delta J)^{1.32} \quad (2.2.28)$$

Dowling's equation has been shown, [Tomkins,1981], to describe the growth rate of deep cracks in Type 304 steel, under high strains at room temperature. However short crack growth data differs from the line. This was observed in A533B pressure vessel steel, [Tomkins,1981], at room temperature. Skelton,[1983], has compared crack growth rates of various materials under high strain fatigue at high temperatures using the ΔJ equation of Tomkins, and has found a similar relationship to equation 2.2.28. Hatanaka et al.,[1989], used a finite element analysis to determine the stress-strain hysteresis loops at the notch and calculated ΔJ values for cracks propagating in both smooth and notched specimens of the medium carbon steel S35C. For crack growth rates below 10^{-5} mm/cycle the ΔJ - da/dN equations were observed to overestimate crack growth rates for short cracks in comparison to long cracks at a similar ΔJ . Leis,[1982], also found differences between long crack and short crack predictions and results in steel plates

when the ΔJ parameter underestimated the crack growth rate for short cracks in high strain fields. This behaviour was explained as a notch effect on the local plastic fields which had a greater effect on short cracks in comparison to longer cracks which propagate in a stress field beyond the effects of the notch. No crack growth relationships or experimental data were found to relate the ΔJ parameter to fatigue crack growth in tubular components.

The requirement for a simpler parameter to describe the fatigue crack growth in both high strain and linear elastic fields results from problems with the options available. These include the uncertainty of the ΔJ parameter to successfully model the fatigue crack growth of short cracks propagating from notches in a plastic strain field, and the necessity to perform a three dimensional block finite element analysis to determine the stress and strain fields around a notch in a tubular component.

One such parameter is the strain intensity factor, ΔK_ε , which has been shown to be represented in terms of both the elastic and the plastic strain ranges, [Haigh and Skelton,1978];

$$\Delta K_\varepsilon = (\Delta \varepsilon_p + q\Delta \varepsilon_e) \sqrt{\pi a} \quad (2.2.29)$$

where $q=1/2$, and is the coefficient of crack opening. Haigh and Skelton,[1978], determined this value with crack opening displacement tests with a typical high strain fatigue, HSF, cycle in both air and vacuum. The electrical potential readings across the crack decreased as the crack closed. This behaviour was observed more with the vacuum tests than the tests in air as the electrical conduction across the crack faces was reduced by oxidation. The term $(\Delta \varepsilon_p + q\Delta \varepsilon_e)$ is called the equivalent elastic strain and describes the part of a hysteresis loop in which the crack opened, it ignores the compressive component of elastic strain. Upon multiplication by the elastic modulus, E , the equivalent elastic strain becomes a pseudo elastic stress, $\Delta \sigma_{eq}$, which leads on to the equivalent stress intensity factor, ΔK_{eq} ;

$$\Delta K_{eq} = E\Delta K_\varepsilon = E(\Delta \varepsilon_p + q\Delta \varepsilon_e) \sqrt{\pi a} \quad (2.2.30)$$

Although it is a strange practise to multiply the plastic strain range by the elastic modulus, it should be observed that the equivalent stress intensity factor is merely an assumed parameter which has been developed in an attempt to account for both the elastic and the plastic strain components, [Burlet et al.,1989]. In comparison with crack growth data for Type 1018 steel at room temperature in relation to a total strain based parameter, the equivalent stress intensity factor, equation 2.2.30, displayed a reduced

scatter of data at the lower strains and a good agreement at the high plastic strains. Haigh and Skelton found the spread of results in the HSF regime, using equation 2.2.30, to sit between the upper limit of tension-compression testing, ($R=-1$), in LEFM and a lower limit of the tension only mode, ($R=0$), with $\frac{1}{2}$ CrMoV steel in a vacuum at 550°C . A similar trend was observed with Type 316 steel in air at 625°C with LEFM data, ($0.2 \leq R \leq 0.6$), and HSF data, ($0.001 \leq \Delta \epsilon_p \leq 0.005$). Skelton, [1983], has shown that there is a relationship between the effective stress intensity and the J-integral;

$$\Delta K_{eq} = \sqrt{E \Delta J} \quad (2.2.31)$$

where ΔJ is given by equation 2.2.26 with a semi-stress range since the crack is closed in compression. However in comparison a greater scatter was observed using a ΔJ -stress intensity factor derived from equation 2.2.26 in comparison with same data obtained using the equivalent stress intensity, equation 2.2.31.

The accuracy of the equivalent stress intensity to describe the fatigue crack growth in both LEFM and HSF regimes and the knowledge that a finite element analysis is required to determine the stress and strain fields for a ΔJ analysis has made the equivalent stress intensity the most attractive method to use when attempting to model the fatigue crack growth under conditions of thermal cycling.

2.2.4. Application of Fracture Mechanics to Thermal Fatigue Crack Growth.

Under conditions of thermal cycling, the stress field through a component will vary with respect to both the thickness of the material and the time following the thermal shock, [Skelton, 1979]. With the initiation and propagation of a crack during the thermal cycling, the process of analysis of the fatigue crack propagation, through the complex stress field, using the stress intensity factor becomes very difficult. There are a number of methods of calculating stress intensity factors. The decision of which to use depends on the complexity of the problem, the time available to perform the calculation, the accuracy of results required and the availability of computing software which can perform the calculations.

2.2.4.1. Finite Element Method.

In the finite element method the component is modelled as a mesh of regions or elements. The elements are built up of lines which connect points or nodes, which are located at the corners and mid-side positions. Complicated three dimensional components can be analysed while symmetry may be taken into consideration to reduce the actual size

of the computer model. The basic field variables, such as stress and displacement, are assumed to be constant, or vary simply within the elements. Material characteristics and boundary conditions, such as applied stress, temperature changes and restricted nodal displacement are defined before the analysis is performed. Continuity of the basic field variables across the elements is maintained throughout the analysis. Therefore, nodal displacements are calculated to coincide with the reduction in potential energy of the system. Values of stress and strain may be calculated at specified elements for increments of the analysis. Cracked surfaces are modelled using elements with load carrying restrictions. Accurate values of the stress intensity factor, at special crack tip elements, are obtained from either the calculated nodal displacements, evaluating the calculated J-integral or by differentiating the calculated potential or strain energy.

2.2.4.2. Weight Function and Superposition Method.

The elastic stress distribution through an uncracked thermal shocked component is calculated using equation 2.1.25. Depending on the magnitude of the temperature difference and the elastic properties of the material, a yielded zone can develop over a small distance from the shocked surface, Figure 2.2.14. Assuming the stress gradient through the thickness of the material to be purely elastic then it can be represented as a function of the maximum quenched surface stress, σ_0 , and the normalized distance from the quench face with respect to the component thickness, a/t , [Skelton,1979]. This stress gradient equation can be used to develop a function of the maximum stress intensity at the tip of a crack which is propagating through the component;

$$K = \int_0^a \sigma(X_i) m(A_i, X_i) dx \quad (2.2.32)$$

where X_i is the distance from the shocked surface, A_i is the crack depth, $\sigma(X)$ is the stress gradient function of the thickness of the component and $m(A_i, X_i)$ is the weight or influence function. The principles of the weight function are described in greater detail elsewhere, [Chell,1981], however, a basic description of the method can be given by reference to Figure 2.2.15.

When an uncracked body, Figure 2.2.15a, is subjected to an external traction, T_i , external displacement, u_i , body forces, X_i , and initial internal strains, ϵ_{ij} , induced tractions, T_i^* , and corresponding stresses, $\sigma(x)$, are applied normal to a plane AA', of length x , positioned anywhere within the body. Assuming that a plane AA' becomes a crack then the applied stresses produce a relative displacement between the crack surfaces, $\Phi(x)$. Upon removal of the external tractions and displacements and internal

stresses and strains, the displacement of the crack surfaces corresponding to the stress profile, $\sigma(x)$, would only be possible if tractions $-T_i^*$ were applied to the surface AA' to maintain the equilibrium. Therefore the displacement of the crack surfaces and the corresponding strain energy of the crack, U_a , depend on the total of the uncracked body stresses, $\sigma(x)$, the crack length and the geometry of the body. Thus for a two-dimensional body of thickness B containing an external crack of depth, a, in combination with equation 2.2.20, the stress intensity is given by equation 2.2.33. The second term in the equation is the weight function, $m(a,x)$ from equation 2.2.32, in terms of the crack length and the distance from the surface of the body upon which the stress is acting.

$$K = \frac{E'}{BK} \frac{\partial U_a}{\partial a} = \int_0^a \sigma(x) \frac{E'}{2K} \frac{\partial \Phi(x)}{\partial a} dx \quad (2.2.33)$$

The weight function depends on the crack depth and shape, the geometry of the component and is independent of loading therefore once $m(a,x)$ is known for a component then the stress intensity factor can be calculated from a stress analysis of the uncracked component. Weight functions for various geometries are available from the literature, [Tada et al.,1985], and have been calculated for cylinders using analytical methods, [Oliveira and Wu,1987], and finite element analysis, [Raju and Newman,1979]. Equation 2.2.32 can be used to determine the stress intensity factor using weight function values, which are a function of the normalized crack depth.

Another method used to determine the stress intensity factors within a cracked component, for which only the external loading is known, is the superposition method. The superposition method draws very similar comparisons to the weight function method. The superposition method states that a section through an uncracked component is subjected to a stress profile, $\sigma(x)$, which results from the external loading. If a crack is propagating through the component, then an assumption is made that the crack surface is subjected to the same stress profile, $\sigma(x)$, which is perpendicular to the plane of crack propagation. The stress profile is represented by a polynomial equation as a function of the normalized crack depth through the component section, equation 2.2.34, [Parker and Andrasic,1984];

$$\sigma(x) = \sum_{n=0}^6 A_n x^n \quad (2.2.34)$$

While the stress intensity factor at the crack tip is calculated from the integrated form of equation 2.2.32, that can be expressed as a polynomial of order six to give;

$$K = \sqrt{\pi a} \sum_{n=0}^6 A_n Y_n \alpha^n \quad (2.2.35)$$

A_n are the coefficients of the polynomial expression representing the stress profile in the uncracked section, Y_n are magnification factors corresponding to the crack shape in the geometry analysed and have been developed for various geometries, [Parker and Andrasic,1984] and tabulated for different shaped cracks, for $0 \leq n \leq 4$, [Chell,1981]. The magnification factors are independent of the type of loading and can be determined using any arbitrary stress profile over the cracked surface. Values of Y_n have been calculated at increments of increasing crack depth and have been tabulated, with respect to the normalized crack depth, for thin-walled tubular components containing either longitudinal or circumferential cracks, [Buchalet and Bamford,1976]. Analysis of cracked surfaces which were subjected to uniform, linear, quadratic and cubic stress distributions have been performed to determine the values of Y_n , [Buchalet and Bamford,1976]. Magnification factors have been presented in the form of dimensionless stress intensity factors, to the sixth order polynomial, for a variety of thick-walled tubular components with longitudinal cracks, [Parker and Andrasic,1984]. The crack depths were in the ranged of $0.01 \leq a/t \leq 0.8$. The superposition method is valid for elastic loading conditions with boundary conditions corresponding to an external load. However it can be extended, within a first approximation, for boundary conditions corresponding to imposed displacement which are closer to those associated with thermal loading, [Burlet et al.,1989].

Values of the stress intensity factors are calculated, using equation 2.2.35, for increasing increments of crack depth and are plotted against a/t to produce a stress intensity profile. Using the superposition method, Skelton,[1982] developed the stress intensity profile from a profile of the elastic stress, Figure 2.2.14, through a small thick-walled cylinder of Type 316 stainless steel. When the values of stress intensity factors were applied to the Paris Law equation very conservative values of crack growth rate were calculated in comparison to experimental thermal fatigue crack growth rates.

2.2.4.3. Elastic-Plastic Equivalent Stress Intensity Method.

The effects of yielding over the shaded area, Figure 2.2.14, were taken into consideration and the elastic-plastic stress profile was represented by a polynomial. Using the superposition method the resultant stress intensity profile and the corresponding crack growth rates were calculated and were found to underestimate the crack growth rate in comparison to the experimental results.

Both the superposition method and the weight functions cannot be used under conditions

of yielding. It is possible to determine the J-integral for increasing crack depths but this requires an expensive, time consuming three dimensional block finite element analysis. Alternatively an equivalent stress profile through an uncracked component may be developed and used to calculate an equivalent stress intensity profile, equation 2.2.30.

Burlet et al.,[1989], assumed that the crack propagation occurred due to the single thermal stress field which was perpendicular to the crack plane. Therefore only one of the components of stress was of interest for a crack in a specific plane. Skelton,[1982], developed an equivalent stress profile which took into account the cyclic stress strain data for the same material and temperature conditions while restricting the yield zone in the thermal cycling tests to the yielded region following thermal shakedown. Furthermore the uniaxial cyclic stress-strain data was converted to equibiaxial values, to take into account biaxial stress/strain field developed during thermal cycling, using;

$$\epsilon_{tb} = \frac{1}{2} [\epsilon_{tu} + (1 - 2\nu_p)\epsilon_{eu}] \quad (2.2.36)$$

where the first subscripts refer to total and elastic values and the second subscripts refer to biaxial and uniaxial values. The corresponding equibiaxial elastic and plastic strain values were determined for the elastic-plastic stress profile in the reduced yield zone following thermal shakedown and the equivalent equibiaxial stress profile was developed using;

$$\sigma_{eqb} = \frac{(\epsilon_{pb} + 0.5\epsilon_{eb})E}{(1 - \nu_p)} \quad (2.2.37)$$

where the first subscripts refer to equivalent, plastic and elastic values and the second subscripts refer to equibiaxial values, [Haigh and Skelton,1978].

Following a polynomial fit, the equivalent equibiaxial stress profile, was superimposed into the appropriate equation of the superposition method and the resultant equivalent stress intensity profile compared well with experimental results for short cracks and high crack growth rates. However for longer cracks and experimental crack growth rates below 10^{-4} mm/cycle, the equivalent stress intensity factor overestimated the crack growth rate when applied to the Paris Law equation.

When it is not possible to determine the elastic stress profile in an unnotched cylinder using the thermal shock elastic stress, equation 2.1.25, due to the high frequency of thermal cycling, then the elastic-plastic stress and strain profiles may be calculated using

a thermal-strain finite element analysis, [Burlet et al.,1989]. The finite element analysis was performed with an external heat flux applied to the elements at the external surface of the components. The resultant cyclic temperature gradients throughout the component were compared to those measured experimentally and were used as the input file for a thermal stress/strain analysis. The analysis was performed for a number of cycles to allow for cyclic hardening to reach a saturated value. Profiles of stress, total, elastic and plastic strain, through the central section of the component, at various increments of the thermal cycles, were produced. The stress profiles were adjusted to give an equivalent stress profile and the superposition method was applied to calculate the equivalent stress factor profile.

2.2.5. Methods of Measuring Thermal Fatigue Crack Growth.

Most investigations use the interrupted test techniques, in which a number of similar tests are performed for different numbers of cycles, the tests are stopped and the fracture surfaces are broken under load in liquid nitrogen, or sectioned, polished and etched to clearly display the crack through the thickness of the material. Estimations are then made of the development of the crack during the period between different tests at which no test has been stopped. A number of thermal fatigue investigations have observed fracture surfaces that indicated that the cracks had stopped growing, arrested, [Skelton and Miles,1984]. From the crack growth rate calculations, it was estimated that the crack propagation had decreased to growth rates that were in the range of 10^{-7} to 10^{-8} mm/cycle, which are sub-threshold growth rates for most metals and alloys.

Other methods to try and measure crack growth during testing include test interruption methods such as visual inspection and measurement, magnetic particle analysis, ultrasonics, eddy current technique, dye penetrant and both a.c. and d.c. potential drop techniques.

Visual measurements are very useful if the specimen is flat, [Marsh,1981], or the thermal cycles are conducted by immersing the specimen from a hot medium into a cold medium, [Cordwell,1990], or vice versa, such that the shocked surface is easily observed and the extension in crack growth can be measured with each thermal cycle. However surfaces are often under conditions of plane stress while through the thickness the crack propagates under conditions of plane strain which can produce crack curvature. Therefore the crack surface must be observed to determine the relationship between the mid-crack depth and the surface crack depth during cycling. Thus the interruption of tests is required to determine a function to describe the development of the crack front shape with the thermal cycles. If the crack grows away from the shocked face towards

the unshocked face, [Bethge et al.,1988], then a relationship has to be obtained between the growth rate of the crack length on the shocked surface with the growth rate of the crack depth through the thickness. Differences here occur at the surface as the crack grows through a plastic strain field, while through the thickness the crack grows towards an elastic strain regime. Other problems with visual inspections include thermocouples on the specimen surface which block the view of the crack as it propagates past them and if the specimen is heated within a furnace or an induction heating coil then the specimen cannot be observed at all. This would also be a problem if a dye penetrant was employed to detect surface cracks. The process of crack detection using a dye penetrant involves, cleaning the surface and coating the surface with a liquid which contains a dye. Excess penetrant is then removed from the surface and a detector is applied to the surface to draw the penetrant out of the surface defects through a capillary action. The bright colour of the penetrant, red or yellow, clearly marks the site of the defect. Therefore it is a useful technique to employ to determine the position of the surface defects while presenting the opportunity to measure the surface crack length. However both the depth and the shape of the defect cannot be determined using the dye penetrant technique. Furthermore, the presence of mid-thickness defects that do not break the inspection surface, cannot be determined using the technique.

The magnetic particle technique is frequently used for inspection of tubular welded joints on offshore structures, [Kerr,1988]. Basically the inspection area of the ferromagnetic component is cleaned, the component is placed within a magnetic field, fine ferromagnetic particles are distributed over the surface then the surface is scanned to detect regions at which the particles have congregated. Defects and cracks act as breaks in the magnetic field and hold the ferromagnetic particles which are visually detected. The particles are available in various colours for easy detection with the contrasting surface of the component. Problems with this method include test interruption to make measurements, having to clean oxides from heated surfaces to make measurements and altering the test set up and handling the specimen during testing to make measurements. If cracks initiate at the internal surface of a tube and propagate towards the external surface, as occurs with internal quenching of cylinders and in gun barrels, or if the material is not ferromagnetic, such as austenitic stainless steel then the magnetic particle detection method cannot be used.

Ultrasonic inspection is used to detect surface and internal defects in both metals and composites, [Rice et al.,1989]. Basically, the detection technique involves directing high frequency sound waves into the material and recording the reflected signal. The detector may be positioned on either the same surface as the transmitter or on the opposite surface, through the thickness of the component. With both transmitter and receiver on

the same surface, an echo of the transmitted signal is detected after a time, t , which is dependent on the velocity of sound through the material. Any echo that occurs before this signal indicates the presence of a flaw. The distance from the surface to the flaw in comparison to the thickness of the component is proportional to the ratio of the time between the echo from the flaw and the back wall echo. The detected echo is converted into an electrical signal, amplified and displayed on a computer. The amplitude of the reflected signal depends on the defect size, the orientation of the defect relative to the sound waves and the acoustic impedance of the interface between the material and the defect. Therefore the angle at which the sound waves are sent through the specimen may have to be varied in a trial-and-error technique until the most prominent signal is received. Another requirement of this technique is that a layer of water, oil or grease is required between the signal receiving transducer and the specimen surface to avoid loss of signal due to the high acoustic impedance of an interface between the specimen material and an air gap.

The eddy current method of defect detection is performed by creating a rapidly changing electromagnetic field in a component made from an electrically conducting material, [Granville,1991]. Eddy currents, which are generated in the material to oppose the changing magnetic field, flow in a set pattern which is interrupted by the presence of a defect and produces a change in the impedance of the sensing coil around the component. It is possible to use probe type coils to scan the surface of complex shaped components however care must be taken to avoid changes in the probe-to-surface distance as a lift-off effect can produce changes in the signal which may be interpreted as changes corresponding to defects. The eddy current method has been used to determine the depth and direction of crack growth on thermally shocked tubes, [Love,1990]. At intervals of 100 cycles the tests piece was removed from the rig and scanned using a probe coil which was part of a balanced bridge circuit. As the probe crossed a defect, the impedance of the system changed, which produced an unbalance in the bridge circuit and the resultant change in signal was recorded. Maps of the surface were simultaneously produced and the position, size and direction of the cracks determined. From calibration tests, cracks of 0.1mm were detectable while the maximum crack depth before saturation of signal was 3mm. Each inspection took $\frac{1}{2}$ hour therefore the period of one test was greatly increased. Unfortunately, on going inspection requires special instrumentation to inspect either the internal or external surface of a cylinder. This would not be practical if the component is positioned within an induction heating coil, or a furnace and if the internal surface has to be periodically quenched or constantly cooled with a cooling fluid.

Other methods of detecting the presence of defects, such as holographic detection, and to determine the crack growth rate, such as acoustic emission, X-ray inspection and

oxide/gel electrodes technique, have the disadvantage of requiring the use of complex equipment especially near the specimen surface. Details concerning these techniques may be found in literature on non-destructive testing and fatigue, [Rice et al.,1989].

A more practical method would be to have only instrumentation probes on the surface of the component and measurements corresponding to the crack growth taken out with the experimental set-up. The electrical potential drop technique is used to detect the growth rate of a pre-determined crack through an electrical field. Basically, the potential drop method involves developing an electric field in a specimen by passing either a direct current, (d.c.), or an alternating current, (a.c.), through the specimen and measuring the voltage across a crack growing through the field. For practical reasons the potential is measured across the machined notch at the surface of a standard specimen. Therefore the position of crack initiation and the plane of crack propagation are determined before fatigue or creep loading, [Li and Wei,1966], [Hayashi et al.,1985], [Aronson and Ritchie,1979] and [Hunter et al.,1992]. As a crack of depth a grows, the potential difference between two points spanning the crack, V_a , increases due to the reduction in the uncracked area ahead of the crack and the corresponding increase in the electrical resistance. In comparison to a reference potential, V_0 , which corresponds to the original notch or crack depth, a_0 , the crack depth-to-specimen-width ratio, a/W , is determined from a calibration curve for the specimen geometry. Calibration curves are usually given in the form of V_a/V_0 versus a/W , [Aronson and Ritchie,1979], or $(V_a-V_0)/V_0$ versus a/W , [Wei and Brazill,1981], and can be determined in a number of ways.

Experimentally, [Li and Wei,1966], developed potential drop calibration curves from centre-notched specimens by interrupting fatigue tests at suitable intervals and measuring the potential, operating current and the crack depth from plastic replicas of the specimen surface with a microscope at X100. The advantage of normalizing the potential drop measurements is that scaled models of the specimens can be used to produce the calibration curves. Such models range from the simplistic thin aluminium foil specimen cross section model, through which the increasing crack is cut through the model using a razor blade, to plastic moulds of the test component which are filled with an electrical conducting fluid, through which a plastic plate is positioned at increasing depths to represent the crack growth. With all calibration models both the current input and potential measurement lead locations must be accurately positioned, relative to the test condition, as differences in both the magnitude and the sensitivity as well as errors in the accuracy of the potential measurements have otherwise been observed, [Aronson and Ritchie,1979]. Another problem with the calibration determination from interrupted experiments is that a limited number of tests are performed and calibrations corresponding to very short cracks are often produced using best-fit line techniques,

[Clark and Knott,1975]. In general the interrupted test potential drop calibrations are accurate to crack growth measurements of 0.1mm, [Gangloff,1981].

Analytical methods of determining the potential drop calibration involve complex mathematical functions, [Clark and Knott,1975], in which the current density is often modelled as a two-dimensional fluid flow problem. The analytical methods are used primarily for simple specimen geometries, such as edge cracked plates, [Hayashi et al.,1985]. However for more complex geometries difficulties are thought to arise when using this method of analysis, [Wei and Brazill,1981].

A numerical method which is used to determine the calibration curve for a potential drop analysis is to model the specimen in a finite element analysis, [Aronson and Ritchie,1979]. By specifying the electrical conductivity of the material and using fine element meshes at both the current input leads and the potential measurement probe positions, the specimen edges and at the crack tip, accurate changes in potential drop were determined for increases in crack depth. Interrupted experiments confirmed the finite element calibrations, although coarse meshed models are thought to yield relatively crude results, [Wei and Brazill,1981]. Both the numerical and the analytical method of determining the crack growth calibration curve do not take into account the possibility of specimen heating from the current supply or the effects of crack tunnelling and the conductivity of the cracked surfaces touching. During experimental calibrations with identical test conditions these effects can be neglected.

From the early investigations of crack growth behaviour during the 1960's, [Wei and Li, 1966], the direct current potential drop technique has been a very popular method of determining the crack growth rate. The advantages of the d.c. technique are that it is easy to use due to the limited requirements of a power supply, connection leads, potential measurement probes, amplifier and a data logging and measurement system. The direct current supply also produces a uniform current density over the thickness of the component. However problems have been found when dissimilar metals have been used for the p.d. probes and the specimen material during tests at increased temperatures, [Wei and Brazill,1981]. Induced thermocouple effects, due to electromotive forces, can occur producing noise on the measured signal and interference due to high frequency, (R.F.), heating is also common. Possible solutions would be to use shielded or coaxial cables, avoid electrical loops, measure specimen potential under test condition with no d.c. supply and compensate for any unavoidable signals and during thermal cycling take all p.d. measurements when the induction heating system is off.

From the late 1970's an alternative to d.c. potential drop is a similar process using an

alternating current supply. This technique has the advantage that a relatively small current is required, the signal is insensitive to disturbances from thermal emf or R.F. induction heating and the crack length resolution is greater than that of d.c systems operating at a similar potential. However to measure crack growth using the a.c. potential drop technique requires a complex system which can tune the frequency of the supply to reduce the skin-effect by producing a more uniform current density through the specimen thickness, [Wei and Brazill,1981], Figure 2.2.16. Although the skin-effect is beneficial to the measurement of short surface crack growth the effect of producing a non-uniform current density through the thickness of the specimen increases the effective resistance of the specimen, and hence for a given current, increases the potential measurement. The potential measurement from an a.c. supply system may also contain effects from the reactive components of the specimen, such as the capacitance and inductance of the material. However with increasing crack growth these effects become negligible.

The d.c. potential drop technique has been successful in monitoring the crack growth in tubular components of alloy 800H under creep loading conditions, [Hunter et al.,1992], with a calibration curve developed from interrupted experiments which were performed in the laboratories at JRC Petten. Under thermal fatigue loading, the technique has not been applied with such great success, [Skelton,1979], with small 4.5mm thick-walled cylinders under constrained thermal cycling recorded circumferential crack growth from the internal surface to breakthrough using a reverse face calibrated potential drop technique, while longitudinal cracks which arrested at 0.46 of the thickness were not detected by the potential drop system. With longer and thicker, 20.5mm, cylinders found that d.c. potential drop, on the external surface, could only detect cracks once they had penetrated half-way through the wall-thickness from the internal surface, [Skelton and Miles,1984]. The measurement of crack growth from the opposite face, relative to the p.d. probes, was shown to be possible in a plate, [Hayashi et al.,1985], however both the magnitude of the signal and the sensitivity for short cracks were low in comparison to measurement across the cracked edge. The potential drop technique was also used to measure the crack growth during thermo-mechanical fatigue of compact tension specimens, [Burlet et al.,1989]. Measurements of experimental data were taken at the same temperature and load during each cycle to avoid errors. However later comparison tests on tubular components which were subjected to thermal cycling could not use potential drop as the specimen were too large and a very high current was required to detect cracks, [Skelton and Nix,1987].

Marchand, Dorner and Ilschner,[1988], developed an a.c. potential drop system to measure the thermal fatigue crack growth in double-edged wedge specimens of nickel

based superalloys. Calibrations were obtained using a thin saw cut to represent the crack extension. Graphs of the potential drop during the crack initiation phase indicated three zones. In zone I thermal shakedown of the specimen occurred, the potential probes achieved thermal stability and the potential drop decreased for 100-200 cycles. Zone II corresponded to microcrack initiation and the potential drop either increased or decreased smoothly depending on whether initiation occurred at the edge where the potential drop measurements were taken or at the opposite edge respectively. In zone III the potential drop significantly changed due to crack growth. Other investigations, [Marsh,1981], [Bethge et al.,1988], refer to using a potential drop technique to monitor the thermal fatigue crack growth through steel plates but determine the crack propagation rates from post-test analysis of the fracture surfaces.

In general the difficulties in performing thermal fatigue tests, such as transferring specimens from fluidized beds, using induction heating and jet cooling, [Lieurade et al.,1986], and the dimensions of the specimens, such as large, thick cylinders, hinder the use of the potential drop method to measure the crack growth rates. Following testing, specimens are either sectioned, polished and etched in a reagent or broken in liquid nitrogen to reveal the nature of the crack growth or the fracture surface markings. In some investigations, the thermal cycles are periodically altered or a mechanical cycle periodically is induced on the thermal cycle to leave a clear beach mark over the thermal fatigue fracture surface. Under microscopic examination the fracture surfaces may display striation patterns which give an estimation of the crack advancement during each cycle. However crack surfaces are often covered in oxides following thermal fatigue and the striation patterns are not easily visible, [Burlet et al.,1989]. Therefore a number of investigations include a series of experiments under identical conditions for a varying number of cycles to produce cracks of different depths to give an average crack growth rate over the series of experiments.

Crack growth rates in the region of 10^{-3} to 10^{-4} mm/cycle have been measured using p.d. measurement on small Type 316 stainless steel specimens, quenched from 625°C , [Skelton,1979]. Similar crack growth rates occurred between 860 and 580°C in downshock tests, [Shimizu et al.,1983] on Type 316 steel plates, [Shimizu et al.,1983]. Marsh,[1981], has shown that decreasing the temperature range, the maximum temperature and the quench time correspondingly decreases the thermal fatigue crack growth rate in 316 stainless steel plates from maximum growth rates of 1.5×10^{-3} mm/cycle, with $T_{\text{max}}=500^{\circ}\text{C}$, $\Delta T=288^{\circ}\text{C}$, $t_{\text{quench}}=4\text{sec}$ to 4×10^{-5} mm/cycle, with $T_{\text{max}}=300^{\circ}\text{C}$, $\Delta T=172^{\circ}\text{C}$, $t_{\text{quench}}=4\text{sec}$. Bethge et al.,[1988], have found similar crack growth rates with a reactor pressure vessel steel which was quenched from a range of maximum temperatures, 306°C to 414°C with a change in temperatures from 271°C to

391 °C. Overall the thermal fatigue crack growth rates are found to fall in the range of mechanical crack growth data, yet vary with different temperature cycles, different specimen geometries, different materials and different cycle waveshapes. In general crack growth is transgranular although the presence of embrittled material or the introduction of end loads with high maximum temperatures have encouraged faster intergranular cracking.

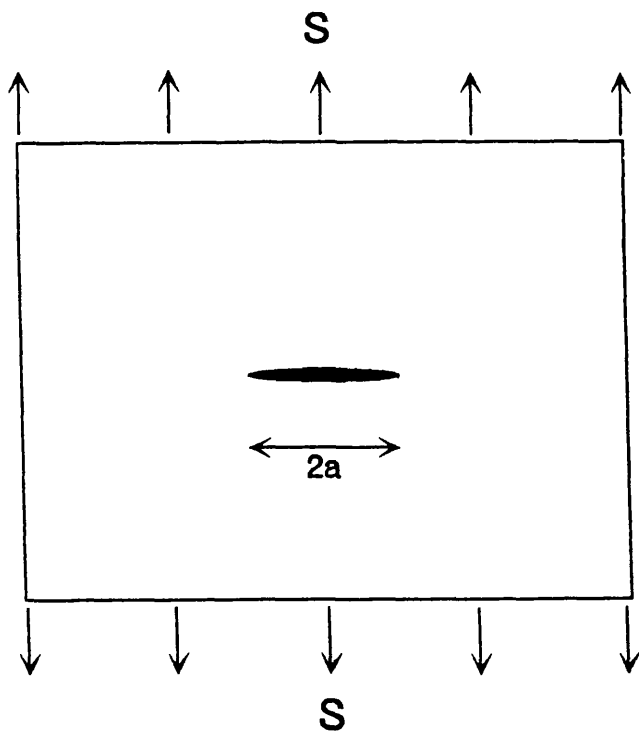


Figure 2.2.1. Body with a Crack of Length $2a$.

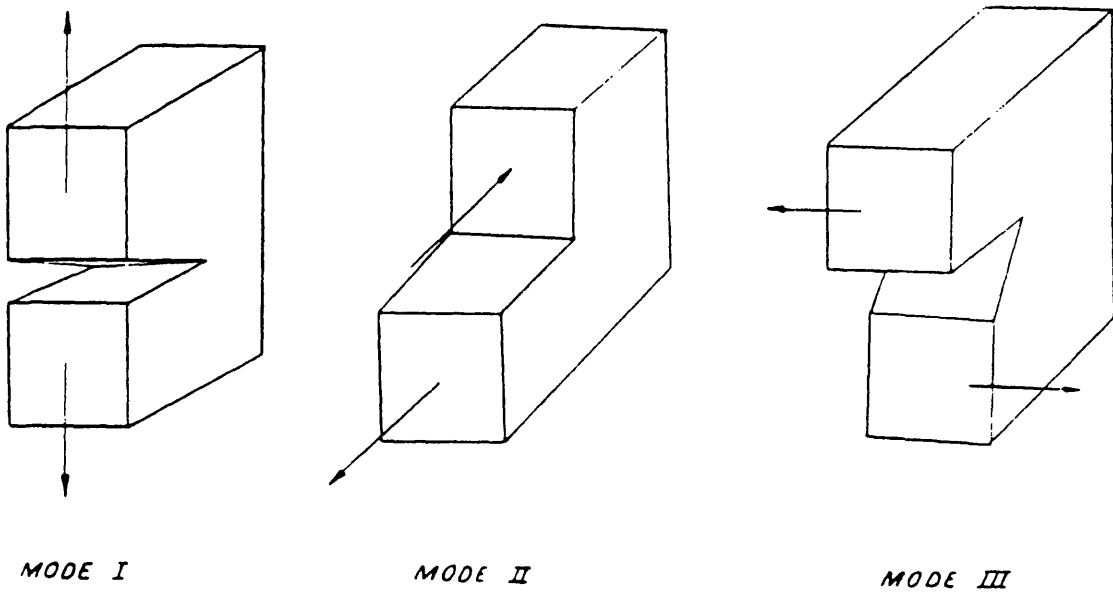


Figure 2.2.2. Three Modes of Fracture, (after Colangelo and Heiser,[1974]).

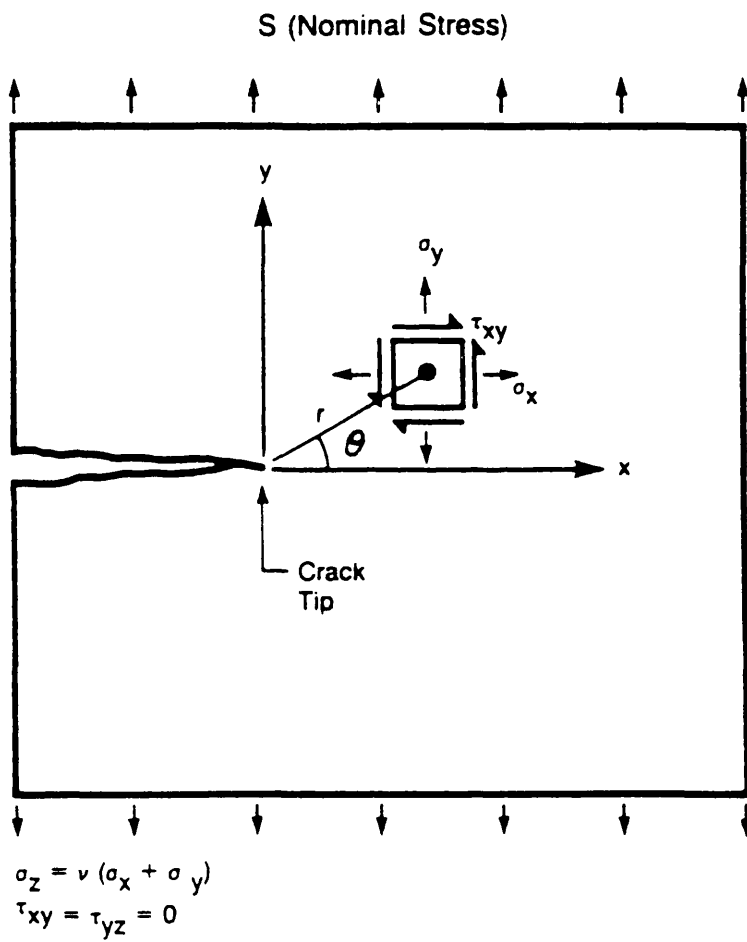
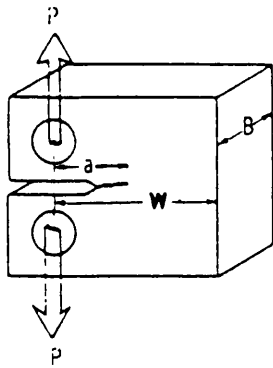
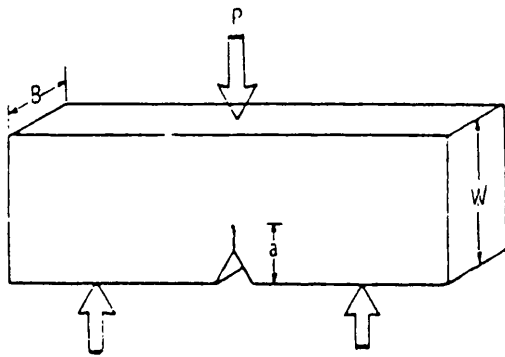


Figure 2.2.3. Polar Co-ordinate System For Stresses at the Crack Tip, (after Rice et al., [1989]).



Compact Tension Specimen

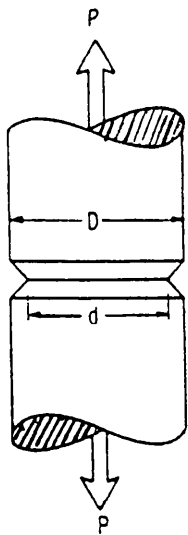
$$K_I = Y_1 \frac{P\sqrt{a}}{BW}$$



Bend Specimen

$$K_I = Y_2 \frac{6M\sqrt{a}}{BW^2}$$

M = Bending Moment



Notched Round Specimen

$$K_I = \frac{P}{D^{3/2}} \left[1.72 \left(\frac{D}{d} \right) - 1.27 \right]$$

Figure 2.2.4. Specimens For Standard Crack Growth Experiments, (after Clark,[1971]).

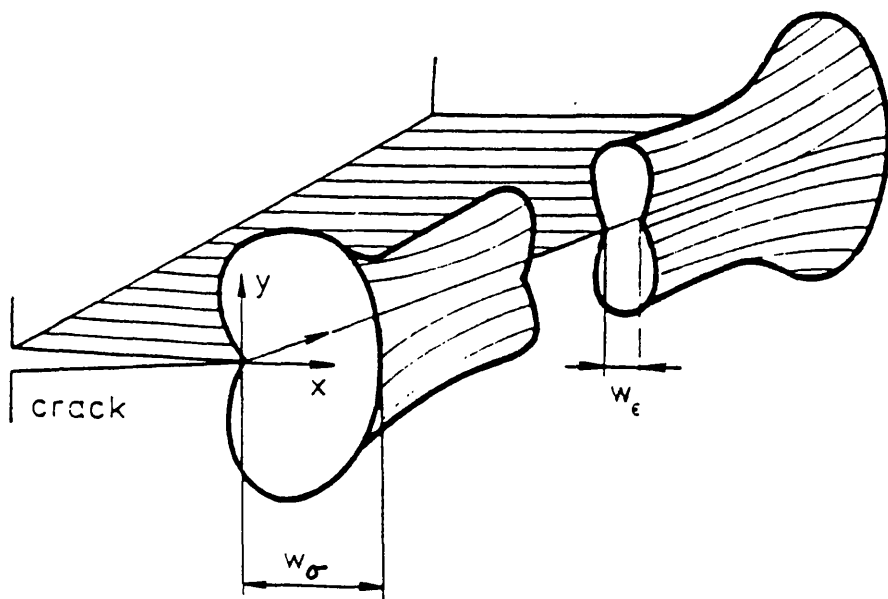


Figure 2.2.5. Shape of Plastic Zone at the Crack Tip Through the Body Thickness, (after Klesnil and Lukas,[1980]).

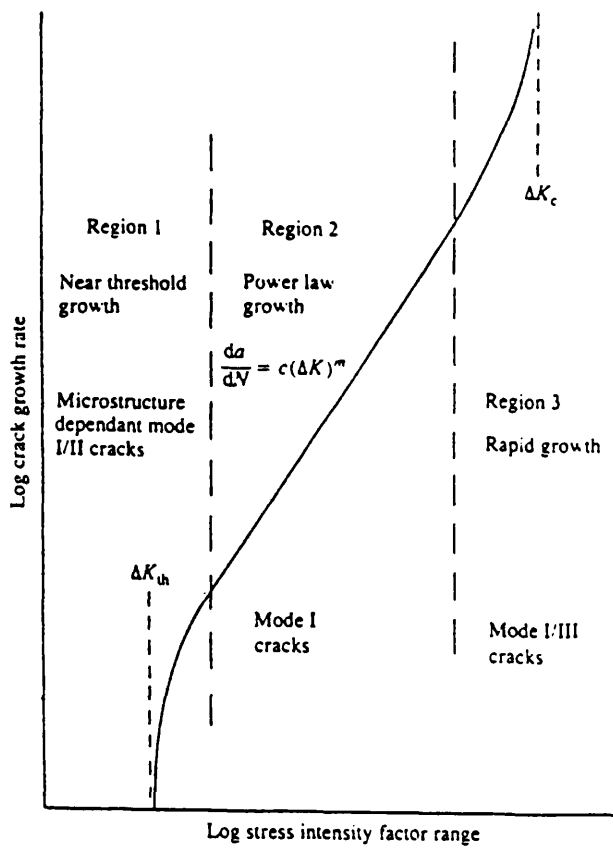


Figure 2.2.6. Three Regions of a Fatigue Crack Growth Plot, (after Brown,[1988]).

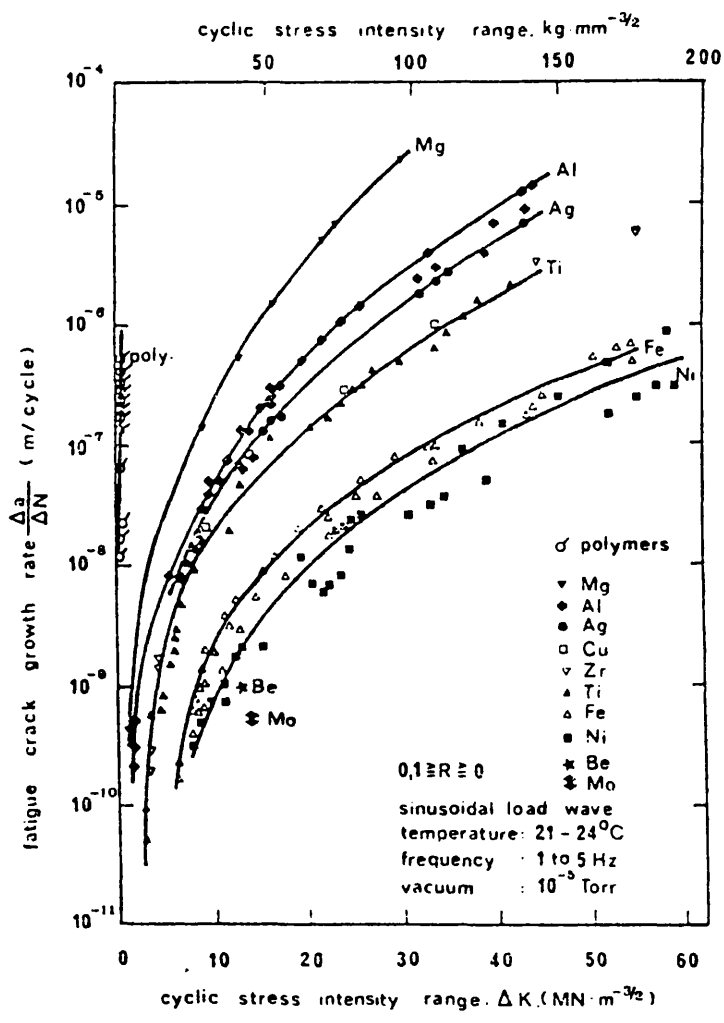


Figure 2.2.7. Fatigue Crack Growth Curves For a Series of Materials, (after Speidel,[1975]).

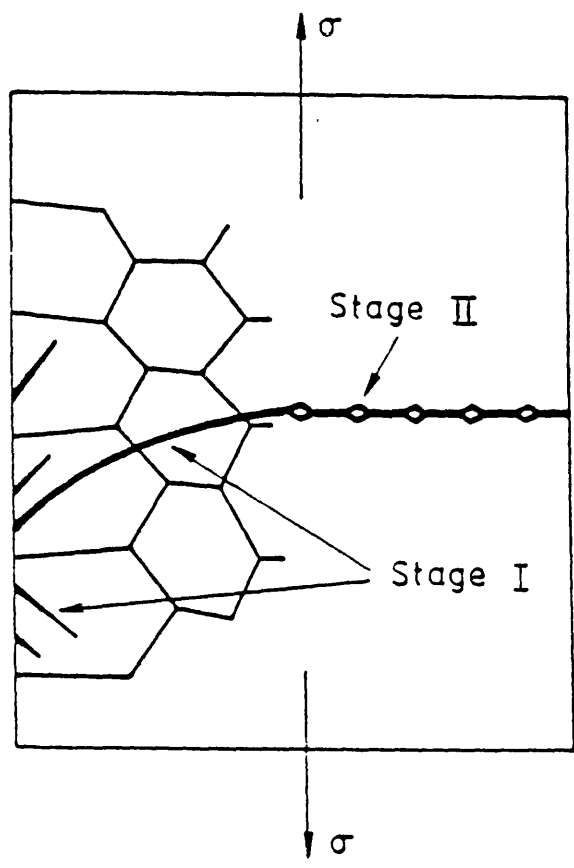


Figure 2.2.8. Two Stages of Fatigue Crack Propagation, (after Klesnil and Lukas,[1980]).

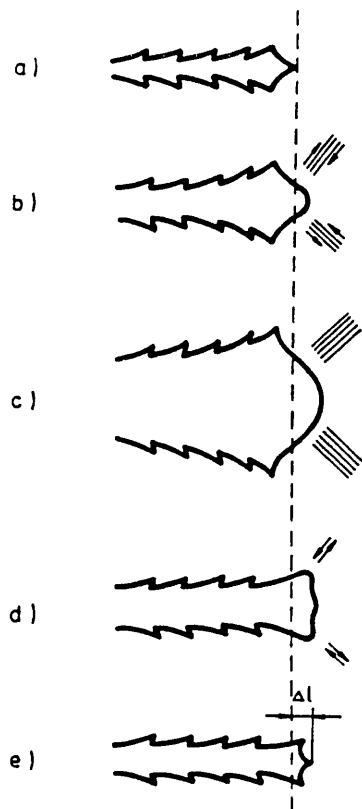


Figure 2.2.9. Laird's Model of Fatigue Crack Propagation, (after Klesnil and Lukas,[1980]).

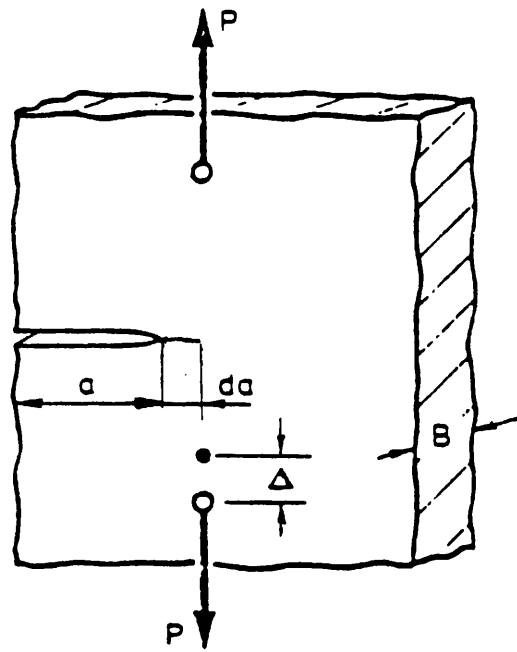


Figure 2.2.10a. Linear Elastic Body Containing a Crack and Loaded by the Remote Load P , (after Webster,[1989]).

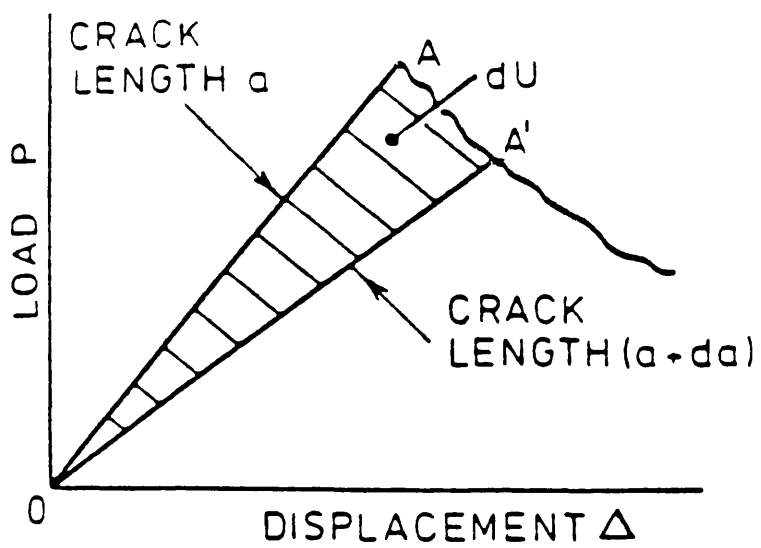


Figure 2.2.10b. Load vs. Load Point Displacement Plot, (after Webster,[1989]).

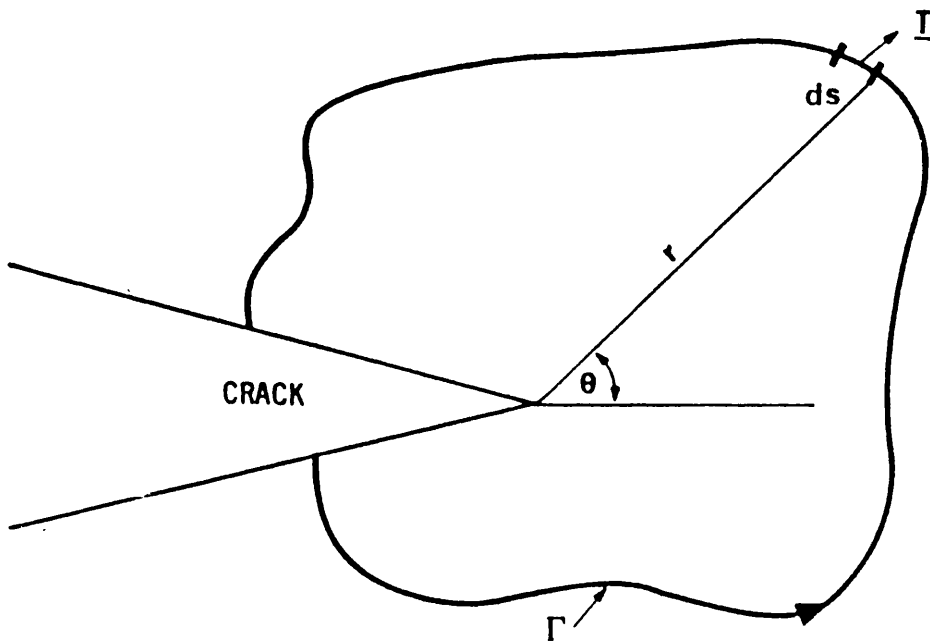


Figure 2.2.11. Loaded Body For Calculation of J-Integral, (after Chell,[1981]).

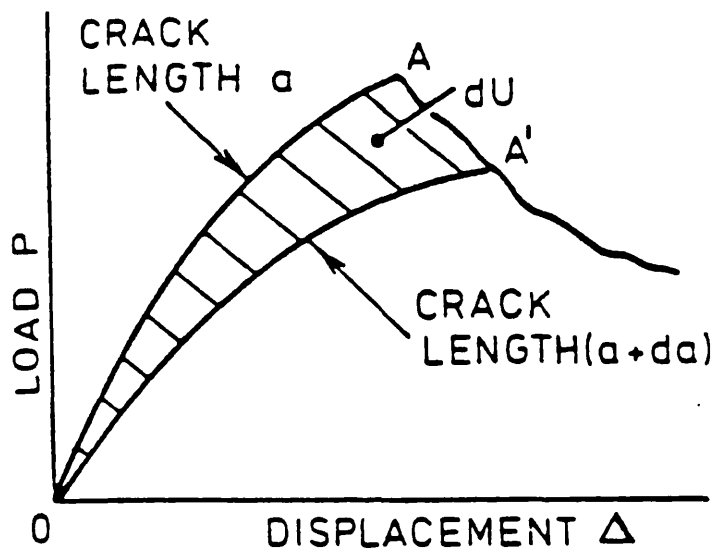
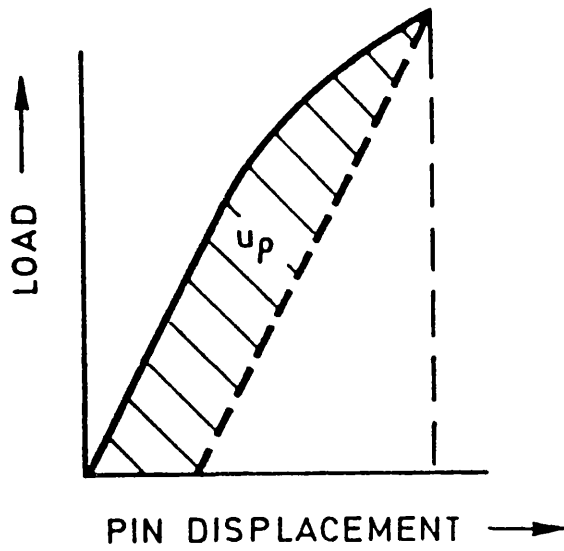


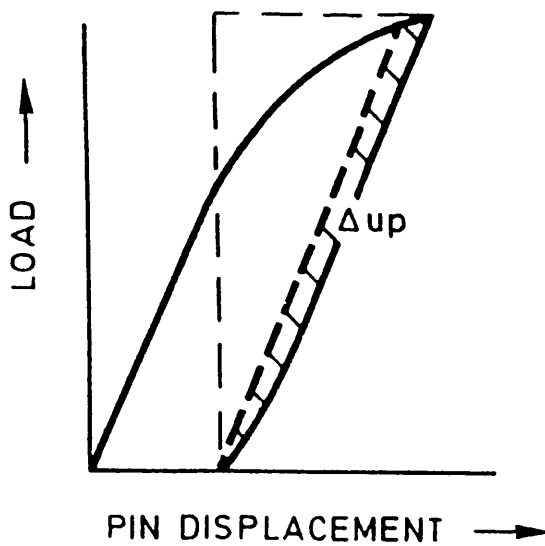
Figure 2.2.12. Load vs. Load Point Displacement Plot, (after Webster,[1989]).

$$J = \frac{k^2}{E'} + \frac{\eta p u_p}{B(t-a)}$$



(a) LOADING CYCLE

$$\Delta J = \frac{(\Delta k)^2}{E'} + \frac{\eta p \Delta u_p}{B(t-a)}$$



(b) UNLOADING CYCLE

Figure 2.2.13. Estimating ΔJ For Cyclic Loading Conditions, (after Chell,[1981]).

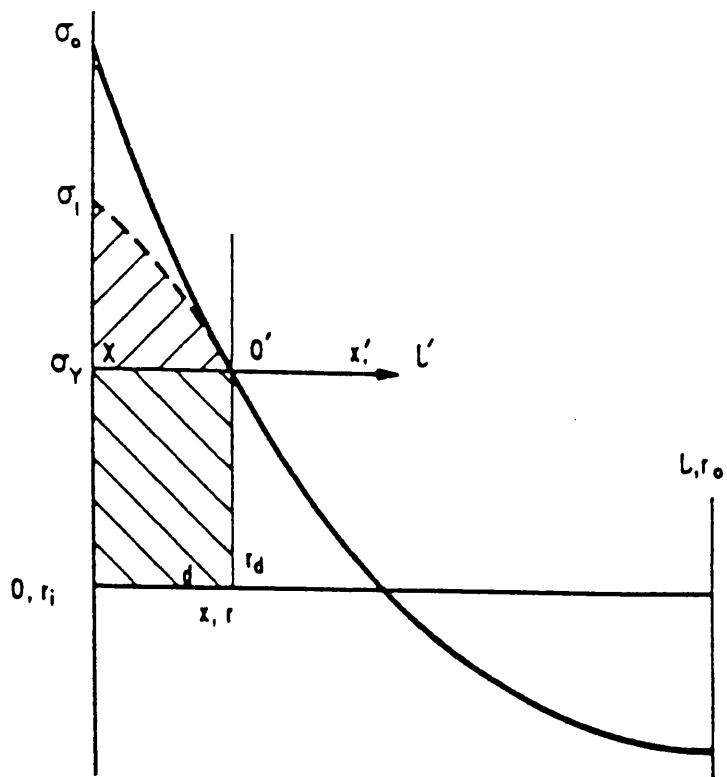


Figure 2.2.14. Stress Through a Thermal Shocked Component, (after Skelton,[1979]).

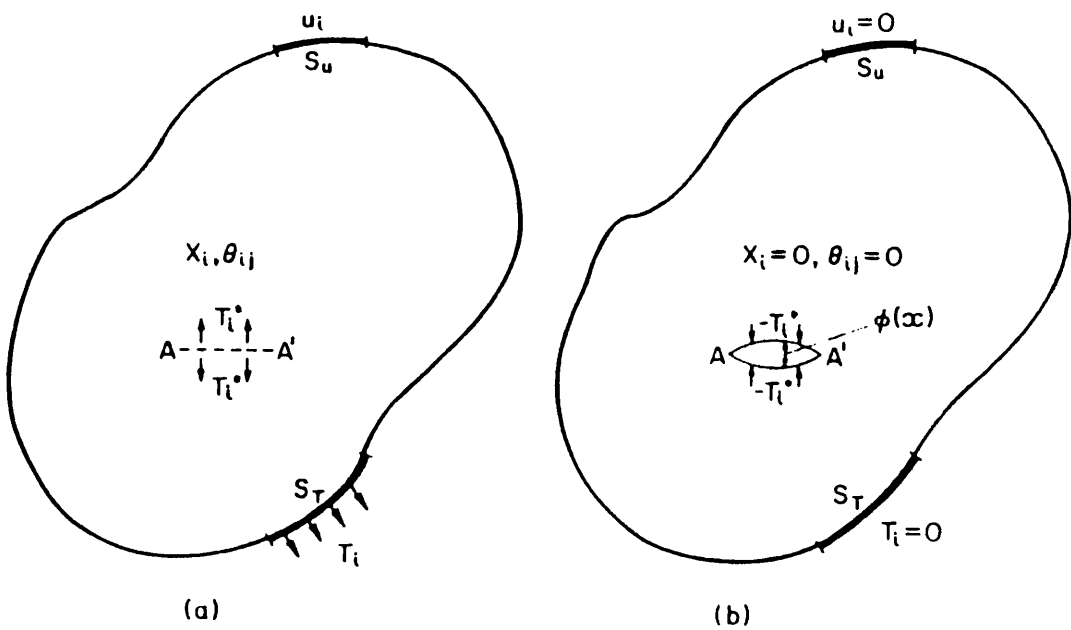


Figure 2.2.15. Uncracked and Cracked Bodies For Determination of the Weight Function for use in the Superposition Method, (after Chell, [1981]).

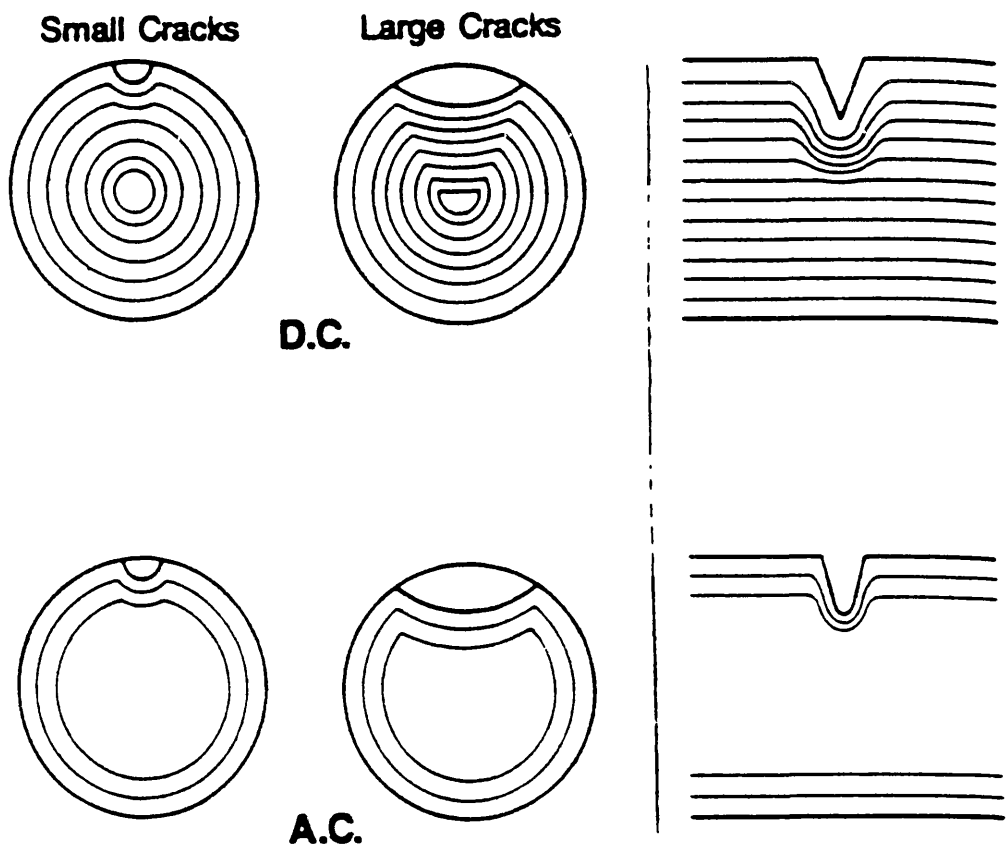


Figure 2.2.16. Skin Effect in a.c. Potential Drop Technique, (after Rice et al.,[1989]).

2.3. Material Selection.

The candidate materials for the Next European Torus, NET, first wall and breeder structural components were the martensitic steel, 1.4914, and ICL 167 SPH, which is a variation of the austenitic stainless steel Type 316L, [Harries,1986]. Two preliminary designs for the first wall have been produced, one consisting of a steel shell on the plasma facing side with brazed coolant tubes on the opposite side and the other being a steel box structure containing coolant tubes, [Harries and Zolti,1986]. Although the operating conditions for NET have not been finalised, initial estimations suggested that the first wall components would be subjected to the conditions of Table 2.3.1, [Harries,1986];

Average Neutron Wall Loading	1 MW/m ²
Peak Surface Heat Flux	≤0.5 MW/m ²
Average Neutron Fluence	0.8 MW.yr/m ²
Burn Pulse Length	50 → 1000 sec.
Number of Pulses	0.9x10 ⁵
Coolant Inlet Temperature	250 °C
First Wall Operational Temp. Range	260 °C ≤ T ≤ 500 °C

Table 2.3.1 Specifications of First Wall Operating Conditions.

However, with a coolant inlet temperature greatly reduced to that of water at room temperature, [Tartaglia,1989], and the surface heat flux represented as a cycle, Figure 2.3.1., [Diegele et al.,1991], the external surface operating temperature range has been calculated to be between 63.3 °C and 385.6 °C, [Merola,1991]. In this calculation, the first wall was modelled as a 10mm thick plate with a 8mm diameter internal coolant tube constructed from the austenitic stainless steel. The variation in temperature at the coolant surface during the cycle was between 20.7 °C and 81.1 °C.

Components of the first wall will be subjected to a variety of potentially damaging loadings during service, [Harries,1986]. Thermal cycling will produce through thickness temperature gradients and alternating secondary thermal stresses. Disruptions in the plasma current will change the magnetic field and induce localised heating and stresses on the first wall. Covering the surface of the components with graphite tiles will reduce the maximum temperatures and protect against plasma disruptions. Although the thermal creep strength of Type 316L is very favourable at temperatures below 480 °C, inelastic deformation of the material can occur due to irradiation creep. Irradiation creep also

relaxes the maximum thermal stress and changes the mean stress during the cycle, which can reduce fatigue life. Further irradiation damage includes the development of helium and hydrogen within the austenitic microstructure, which promotes intergranular cracking. Irradiation induced void swelling may result in the distortion of first wall components to such an extent that flow of the coolant may be restricted which encourages failure through a thermal controlled process. Bombardment of ions and energetic neutral atoms from the plasma reaction will result in sputtering and erosion of the first wall, which will encourage initiation of cracks. However graphite tiles will help to reduce if not prevent the damaging effect of the bombardment, [Merola and Matera,1991].

The austenitic stainless steel, ICL 167 SPH, has been selected as the first wall material due to a combination of the availability of the large data base for similar Type 316 austenitic stainless steels due to their extensive use for reactor applications, [Harries,1986], and the advantageous characteristics of ICL 167 SPH in comparison to Types 316 and 316L. It has the same intergranular corrosion resistance as Type 316L with the greater high temperature strength properties of Type 316H. Resistance to embrittlement after long time exposure over 500°C is guaranteed while the restricted variation of chemical analysis and mechanical properties ensures reproducibility of the material properties, [Creusot-Loire Industrie,1984].

2.3.1. Metallurgy and Microstructure of ICL 167 SPH.

The material of interest was produced by the French company Creusot-Loire by hot forming in a neutral or slightly oxidising atmosphere between 1150°C and 900°C. Treatment consisted of solution annealing between 1050°C and 1150°C followed by rapid cooling in air or water. This produced an austenitic microstructure with an average grain size of 60µm and ferritic stringers, Figure 2.3.2. The material was supplied in the form of a 52mm thick hot rolled plate. It could be machined and welded by different processes without the requirement of pre-welding heat treatment. The composition of ICL 167 SPH is displayed in comparison with other examples of the austenitic stainless steel Types 316L and 316 in Table 2.3.2.

MAT	C	Mn	Si	S	P	Cr	Ni	Mo	N	Co
ICL 167 SPH	0.024	1.77	0.33	.0006	0.023	17.28	12.07	2.41	0.071	0.064
316L (a)	≤0.03	≤2.0	≤1.0	≤0.03	≤ 0.045	16→ 18	10→ 14	2.0→ 3.0	—	—
316 (a)	≤0.08	≤2.0	≤1.0	≤0.03	≤ 0.045	16→ 18	10→ 14	2.0→ 3.0	—	—

balance is Fe, values are given in wt%.

(a) denotes values taken from *The Making, Shaping and Treating of Steel*, [1971].

Table 2.3.2. Chemical Compositions of Type 316 Stainless Steels.

The quantities of each alloy within the stainless steel are predetermined to combine with both the iron and the carbon to produce a material with certain properties. Small quantities of carbon are dissolved into the iron lattice, at high temperatures, to produce steels with increased strength and resistance to plastic deformation. However increasing percentages of carbon reduce the toughness and the ductility of the material. ICL 167 SPH contains only 0.024wt% carbon which would have dissolved into the iron completely during the solution state. The 1.77wt% manganese is present to counteract the brittling effects of sulphur. Nickel, like manganese is an austenite phase former and when such a high quantity of nickel as 12.07wt% is combined with chromium then the resulting steel displays heat resistant properties. Chromium stabilizes the austenizing effect of nickel and in contents as high as 17.28wt% promotes both heat-resistance and corrosion-resistance. The ferrite-phase promoting molybdenum, 2.41wt%, is included to increase the elevated temperature strength of the steel while enhancing the corrosion resistance. Nitrogen is added in a small quantity, 0.071wt%, to reduce the amount of nickel required to assure austenite while the solubility of the nitrogen is maintained.

The material has been annealed at a temperature range which produces the austenite phase and which would dissolve any constituents that may be present, in the forged material, into the solution state. Such constituents include carbon which will remain in solution if the steel is rapidly cooled following the annealing period. However during welding or high temperature applications, such that the steel is sensitized, carbide precipitation may occur, although a prolonged period at a high temperature is required when the carbon content is less than 0.03wt%.

Ferrite stringers developed in the supplied material due to either prior exposure at higher

temperatures or because of the addition of ferrite forming alloys like silicon and molybdenum. The material is regarded to have a greater resistance to embrittlement than standard Type 316 and 316L during long term exposure at temperatures between 500°C and 900°C. It is non-magnetic and may be work-hardened but cannot be hardened by heat treatment, [Creusot-Loire Industrie,1984].

2.3.2. Physical Properties of ICL 167 SPH.

Both the mechanical and the physical properties of the material compare well with standard data, [Peckner and Bernstein,1977,], and are presented in Table 2.3.3

Temperature (°C)	20	300	500	700
Density (kg/m ³)	8000	7870	7780	7680
Thermal Expansion (20°C to T°C 10 ⁻⁶ /K)	16	17	18	19
Electrical Resistivity (10 ⁹ Ωm)	760	950	1040	1120
Tensile Modulus of Elasticity (KN/mm ²)	195	175	155	140
Thermal Conductivity (W.m ⁻¹ .K ⁻¹)	14.5	18	20	23
Specific Heat (J.kg ⁻¹ .K ⁻¹)	480	550	580	600
Tensile Strength (N/mm ²)	525	425	400	270
Proof Stress 0.2% Offset (N/mm ²)	220	133	112	104

Table 2.3.3. Physical and Mechanical Properties of ICL 167 SPH

With reference to Table 2.3.3, the following notes can be made on the physical and mechanical properties of ICL 167 SPH.

The coefficient of thermal expansion increases with temperature up to 723°C at which point it tails off at a value corresponding to 19x10⁻⁶ K⁻¹. The thermal conductivity increases linearly with increasing temperature while the thermal diffusivity decreases with increasing temperature, for values of temperature below room temperature, then it increases almost linearly with increasing temperature. The specific heat increases as a

function of increasing temperature, initially fast, then a great deal slower at temperatures greater than 300°C. The electrical resistivity increases linearly with increasing temperature to 600°C, beyond which the value increases at a slower rate. Both Young's modulus of elasticity and the 0.2% offset proof stress, (yield strength), of the material decrease with the increasing temperature.

2.3.3. Cyclic Behaviour of ICL 167 SPH.

With the limited data available from literature on ICL 167 SPH, [Driver et al.,1988], [Gerland et al.,1989(a-b)], [Levaillant and Pineau,1982], the following review of the microstructure development, lifetime characteristics and crack growth behaviour under cyclic loading, will compare with that of similar austenitic stainless steels from the 300 series, Types 316L and 316, at temperatures of interest.

2.3.3.1. Microstructural Development of ICL 167 SPH.

The average grain size of the supplied material was 60µm, although grains as large as 200µm have been observed in ICL 167 steel following a double annealing treatment at 1070°C, [Levaillant and Pineau,1982].

Some confusion exists over the microstructure development of ICL 167 SPH due to the stacking fault energy for the material, 28mJ/m² which is in a critical region, between 20mJ/m² and 30mJ/m², below which persistent slip bands do not form. Therefore dislocation structures were observed to be either typical of wavy-slip behaviour and formed cells or that of planar-slip behaviour and formed planar arrays of dislocation tangles, [Gerland et al.,1989a]. When deformation amplitudes and the number of applied cycles are low the dislocations appeared in planar arrays while at high strain amplitudes and with increasing numbers of cycles the planar arrays are transformed into well-defined veins and cells.

2.3.3.2. Fatigue Properties of ICL 167 SPH.

Under cyclic loading up to plastic strain amplitudes of 2×10^{-3} at room temperature, ICL 167 SPH displayed a similar stress-strain behaviour as the monotonic curve which was developed from the first quarter cycle of each fatigue test, [Gerland et al.,1989a]. Beyond 2×10^{-3} the stabilised cyclic stress amplitude hardened to a value of up to 50% greater than the corresponding monotonic stress. Cyclic hardening of ICL 167 SPH was observed in both air and vacuum at room temperature with slight softening before saturation. The saturation period was prolonged in a vacuum leading to increased fatigue

lives, [Driver et al.,1988]. Similar hardening behaviours were observed at both 300°C and 600°C, although the saturation stress amplitudes decreased with increasing temperature. The only significant difference was the extended fatigue life at 300°C in a vacuum and the secondary hardening to failure.

The fatigue life of ICL 167 SPH decreased with increasing strain amplitude whether it was under total strain amplitude control, [Levaillant and Pineau,1982], or plastic strain amplitude cycling, [Driver et al.,1988]. A decrease in fatigue life was observed with increasing test temperatures from 20°C to 300°C to 600°C, [Driver et al.,1988]. Testing in a vacuum increased the fatigue lives at each of the three temperatures with the most significant increase at lower plastic strain amplitudes and at the greater temperatures.

2.3.4. Fatigue Crack Growth of ICL 167 SPH.

No fatigue crack growth data has been found from available literature for ICL 167 SPH under either mechanical or thermal cycling. Therefore an assumption has to be made that the fatigue crack growth rate can be described in terms of the stress intensity factor using the coefficients of the Paris Law as developed for similar Type 316L stainless steels. However with availability of both the supplied material and fatigue testing machines, it is possible to determine both the LCF and the Paris Law characteristics of ICL 167 SPH at the temperatures of interest in first wall applications.

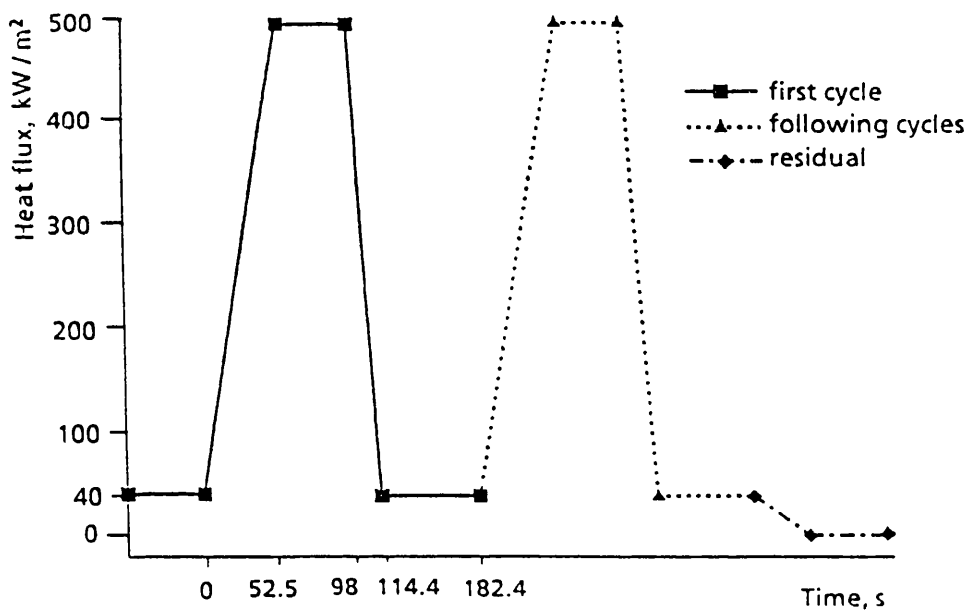


Figure 2.3.1. NET First Wall Surface Heat Flux, (after Diegele et al.,[1991]).

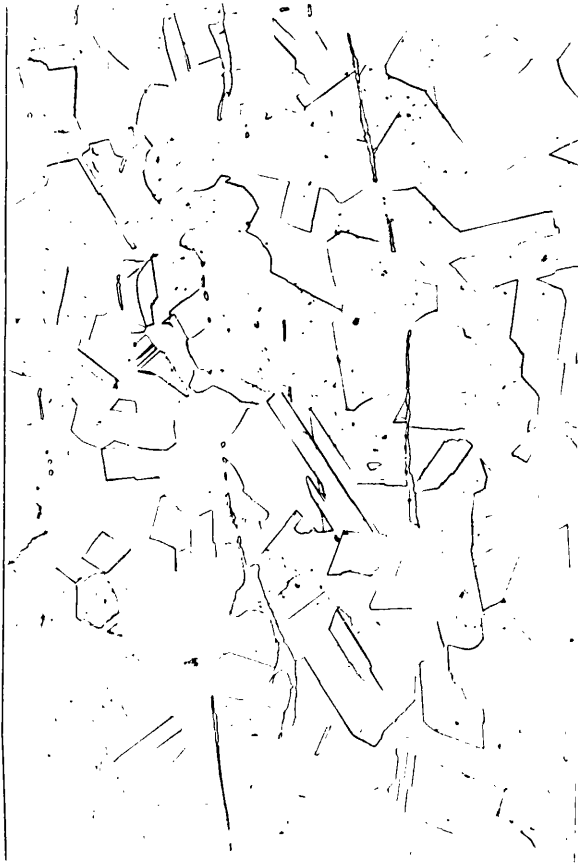


Figure 2.3.2. Microstructure of ICL 167 SPH, (Mag.X250).

3.0. Experimental Testing Facilities and Techniques.

3.1. Introduction.

An investigation into fatigue crack growth within a component subject to thermal cycling requires knowledge of both the crack growth behaviour within the material under linear elastic conditions and the behaviour of the material under cyclic strains above yield. It is not always possible to find relevant equations which describe the characteristics of the material of interest under conditions similar to those of the application in question. In the present study, the proposal of the NET team, [Merola,1991], is that the components of the first wall shall be subjected to thermal cycles between 80°C and 350°C due to plasma bombardment. The candidate material for construction of the first wall components is ICL 167 SPH which is an austenitic stainless steel similar in composition to type 316L. The experimental investigation in this study has been divided into three sections;

1. Low Cycle Fatigue (LCF) Testing: to develop relationships which describe the behaviour of ICL 167 SPH under total strain control and in the plastic regime at the temperatures of interest, 80°C and 350°C.

2. Mechanical Fatigue Crack Growth Testing: to develop relationships which describe the crack growth behaviour of ICL 167 SPH under conditions of Linear Elastic Fracture Mechanics, (LEFM), at the temperatures of interest, 25°C, 80°C and 350°C.

3. Thermal Fatigue (TF) Crack Growth Testing: to produce data to model the crack growth behaviour within tubular components of ICL 167 SPH being subject to the Thermal Cycling (TC) and Thermal Gradients (TG) expected of First Wall components.

The relationships developed from the standard specimen testing, (1 and 2), will be used in the modelling of the data produced from the tubular component testing, (3). All experimentation was performed in the Environmental Testing Laboratory, ETL, at the Commission of the European Communities' Institute of Advanced Materials in Petten. This laboratory is divided, geographically, into two main sections which are split into areas of separate group's activities. ETL North is dedicated to creep and corrosion testing of standard type specimens. ETL South is divided into a standard specimen testing section and a tubular component testing facility. The standard specimen testing section contains six closed loop testing machines upon which fatigue and creep testing of engineering materials are performed at various temperatures in either air or a vacuum. Both the LCF and LEFM testing were carried out in this area of the ETL South. The

tubular component testing facility contains four concrete cells in which tubes are tested under complex loading with the possibility of aggressive environments. There was also a large area of this facility, separate from the cells, in which a special rig has been constructed to carry out the thermal fatigue testing of tubular components.

In the following sections the experimental details are discussed, including the equipment used, the design and assembly of the specimens, the data measurement systems employed and the results obtained.

3.2. Low Cycle Fatigue Testing.

3.2.1. Experimental Equipment.

Uniaxial testing of solid section specimens under cyclic strain control is widely practised, [Driver et al.,1988], to determine the fatigue characteristics of austenitic stainless steels. Cyclic stress/strain curves, hardening/softening behaviour, fatigue life/strain relationships and the elastic modulus of the material can all be determined from this method of testing. To develop these relationships for ICL 167 SPH at the two temperature extremes of the thermal cycling tests, 80°C and 350°C, a series of uniaxial low cycle fatigue tests have been carried out on a Schenck Treble II 100KN electro-mechanical closed loop testing machine.

The Schenck Treble II has three possible control modes, force, strain and stroke, which operate in a closed loop system. In each case a voltage/time signal is sent through a servo controller to a servo valve which controls the movement of the load train through a mechanical gear system. In each of the three control modes the response of the machine is measured and sent back to the servo-controller through a calibrated measurement device. Thereafter the response signal is matched to the limits set at the control panel and the test continues. Under stroke control a linear variable differential transformer, (LVDT), measures the actual axial displacement of the load train, a load cell measures the axial displacement of the load train which is calibrated to the selected load range and under strain control the axial displacement of the load train is measured relative to the selected gauge length of the specimen. In each case the signals sent through calibrated sensors can be measured directly from the control panel on the testing machine.

All LCF testing was performed under total strain control. Continuous cycling was performed over a range of total strain amplitudes at a constant total strain rate of $4 \times 10^{-3} \text{sec}^{-1}$ to enable comparison with LCF data on types 316 and 316L stainless steels over similar temperature ranges and strain rates, [Driver et al.,1988]. The triangular

waveform was developed using a MTS digital function generator and the response was measured using a spring balanced extensometer. The extensometer, Figure 3.2.1, consists of an assembly of two alumina arms, each 20cm long, fixed into two aluminium blocks which are supported by a thin sheet of steel which can bend like a spring. In the end of each block is a v-shaped groove into which the knife edges of a LVDT are positioned. When the end points of the arms are positioned at a set gauge length on the specimen surface, any axial movement of the specimen results in a corresponding movement of the blocks which is detected by the LVDT. The extensometer is housed within a copper tube cooling chamber with a constant flow of water to avoid overheating of the extensometer during testing. The whole assembly was mounted on a displacement table which could be moved to and from the specimen using a screw and spring mechanism allowing the end points of the extensometer arms to be held in position.

The gauge section of the specimen was heated using a Celes 6KW Induction Heating System, which operated in a closed loop. Both the heat-up time to temperature and hold time at temperature were programmed into a Eurotherm thermal response controller. A copper tubing induction heating coil was manufactured to uniformly heat the test section while giving the opportunity to position the extensometer arms against the side of the specimen and allow optical inspection of the specimen surface during testing. The copper tubing was 1mm thick with an external diameter of 6mm, and was shaped to produce a coil consisting of three loops, each 20mm internal diameter, a 16mm wide gap and another three loops. The coil, which was covered with an insulating sock to avoid direct contact with the specimen, was positioned around the gauge length of the specimen. With the gauge length of the specimen in the 16mm wide gap between the loops of the coil, the gauge surface was clearly visible and the extensometer arms were positioned through the centre of the loops onto the side of the specimen. The temperature measurement and control was realised using K-type, NiCr/NiAl, thermocouples which were spot welded onto the specimen. Throughout the present study all thermocouples have been calibrated before testing in a calibration furnace. The measurements of one of the thermocouples were supplied to the Eurotherm controller for comparison and alteration of the supply signal to the heating system. The induction heating system induces voltages in both the specimen and the copper coil, therefore cooling water was pumped through the heating coil, the induction heating capacitance box, the induction heating generator, the extensometer housing and the specimen grips in a closed loop through a refrigerated reservoir to maintain a cooling water temperature of 18°C.

The number of cycles were continuously recorded on a counter on the control panel of the test machine. The system also featured an interlock switch enabling the machine to be stopped after the desired number of cycles. Voltage output readings corresponding

to load, total strain, plastic strain and temperature were recorded on a W&W chart recorder while stress/strain hysteresis loops were drawn on a X-Y recorder. To avoid damage to the fracture surface limit switches were set to hold the specimen under tension when failure of the specimen occurred. In the event of reduced cooling water flow the induction heating system has a shutdown system to avoid overheating and damage to the system.

3.2.2. Specimen Design, Instrumentation and Assembly.

The dimensions of the specimens tested under LCF loading are shown in Figure 3.2.2. The total length of the specimen was 112mm long including a test gauge section which was 9mm long, 12mm wide and 3mm thick. At each of the ends an axial length of 13.7mm was threaded to M16 for gripping of the assembly rings. The gripping rings were manufactured with a M16 bore and eight holes, 6mm diameter, concentric around the same diameter. In the bottom surface of the rings a 2mm deep groove was machined to match the 2mm deep flange on both the upper and lower facing pistons of the load train. To position the specimen the gripping rings were screwed onto the ends of the specimen with the grooved ends facing away from the gauge section. With the machine under stroke control the specimen and gripping assembly was positioned onto the lower piston, the eight tightening screws were slightly fastened and the actuator was raised until the top of the specimen met the top piston face. The upper ring was positioned to match the upper piston and the eight fastening screws were tightened. Under load control, the specimen was compressed to a 0.5KN load and the sixteen screws were fastened. To avoid induced bending loads an initial specimen was instrumented with six strain gauges and the screws were tightened to a position when the bending strains across the specimen were similar in the range of 5% to 7%. Each screw was marked with its corresponding hole and depth. It was practically impossible to strain gauge every specimen due to both the limited number of strain gauges available and need to have uncovered specimen surfaces for both optical inspection and extensometer contact points. The removal of strain gauges from the surface with the specimens in position was a very tedious operation which often resulted in the separation of a spot welded thermocouple and occasionally the scratching of the surface. Re-spot welding thermocouples onto the specimen while the specimen was positioned in the machine was also a very difficult procedure which could also result in damage to the specimen.

The induction heating coil was connected to the capacitance chamber which was supported on a displacement table to enable the coil to be positioned in two directions. The final position of the coil around the specimen, the temperature gradient over the test section and the ideal positions of the control thermocouples on the specimen were all

determined using an instrumented pre-test specimen. Within a flow of Argon gas, K-Type thermocouples were spot welded in a line around the specimen at the centre of the gauge surface. Further thermocouples were positioned 5mm either side of the centre in the axial direction and at the side of the specimen 19mm either side of the centre of the gauge section. Over the gauge surface the temperature was found to vary by $\pm 1^\circ\text{C}$ at 80°C and by $\pm 5^\circ\text{C}$ at 350°C . Microscopic inspection of the spot welds indicated possible crack initiation sites within the gauge section therefore control thermocouples were limited to positions 19mm above and below the centre of the gauge section, with all thermocouples removed from the test sections of the specimen. The corresponding control temperatures at the control thermocouples were 69°C and 293°C when the centre of the test section was 80°C and 350°C respectively.

The extensometer arms were placed through the loops of the induction coil, with the machined tips resting against the side of the specimen. No positioning edges or pits to support the edge points were machined into the side of the specimen therefore the tips were accurately positioned 9mm apart along the axial direction in the middle of the 3mm side of the specimen using a travelling microscope. The extensometer had been calibrated at room temperature giving a linear relationship in both compression and tension in the range of 0 to 10 volts over 200 microns displacement corresponding to 2% strain.

3.2.3. LCF: Experimental Procedure and Results.

Before testing the specimen was held in low tension at 0.5KN and measurements of the gauge width, thermocouple positions and the point of contact of the extensometer arms, (the gauge length) were made. At room temperature, the specimen was loaded to 4KN under tensile then compressive loading and the corresponding values of extension were recorded on the X-Y recorder. The specimen was heated to the test temperature and the procedure was repeated giving data for the calculation of Young's modulus of elasticity.

The experiments were performed over a range of total strain amplitudes, ($0.2\% < \Delta\epsilon_t/2 < 1.5\%$), at a constant strain rate, $\dot{\epsilon}$, of $4 \times 10^{-3} \text{sec}^{-1}$. In each case the gauge length displacement in μm was calculated to give the total strain range, $\Delta\epsilon_t$, and the corresponding voltage for the MTS digital signal generator was set. The frequency, f , of the cycles was calculated from the equation;

$$f = \frac{\dot{\epsilon}}{2\Delta\epsilon_t} \quad (3.2.1)$$

The specimen was held under total strain control at the test temperature and the signal generator was started producing a triangular waveform, cycling between the tensile and compressive strain amplitudes at the frequency calculated. During the experiment the surface was observed for evidence of cracking and the experiment was terminated when complete fracture of the gauge section occurred. The number of cycles to failure was recorded, the induction heating system was stopped and the recording equipment was switched off. The fractured specimen pieces were removed from the grips, the thermocouples were broken off from the specimen and the specimen was stored for photographs and metallurgical examination. The pistons of the load train were returned to a neutral position under stroke control.

The calculated values of Young's modulus of elasticity over the experimental temperature range are compared with values produced by suppliers of the material, [Creusot-Loire Industrie,1984] in Table 3.2.1.

Temperature (°C)	Measured Modulus of Elasticity (GPa)	Modulus of Elasticity (GPa)
25	198	195
80	186	190.7
350	163	170

Table 3.2.1. Modulus of Elasticity.

The modulus of elasticity was found to decrease with increasing temperature. The similarity between the calculated values of E and those supplied by the suppliers verify the experimental technique and measurement system used in the present study.

Continuous stress plots during experiments at both temperatures, (Fig. 3.2.3), display the initial hardening, then a saturation region followed by softening to failure. The plots indicate that the degree of hardening increases with both temperature and strain range. This behaviour has been observed in 316 stainless steels at room temperature, [Vogt et al.,1984], and up to 600°C, [Driver et al.,1988] and in Type 321 at 450°C, [Yamaguchi et al.,1978]. Yamaguchi et al.,[1978] compared the hardening effect with the fracture surface. Hardening which was represented by an increase in the load range over the initial 100 cycles corresponded to a region of flat facets of the grains depicting stage I crack growth. Fatigue crack propagation was represented by striation patterns for 400 cycles which corresponded to the period of saturated load range. Over the last 50 cycles

the softening of the load corresponded to a rapid failure dimple pattern on the fracture surface.

The hardening behaviour is also observed in the hysteresis loops, (Figs.3.2.4a-b), from which the values of total, plastic and elastic strain were measured. Little change occurred in the plastic strain ranges during the tests therefore values for plastic and total strain ranges were taken from the saturation periods when the stress amplitudes were constant. The values from the saturation periods from each experiment are tabulated along with the number of cycles to failure, N_f , Tables 3.2.2a-b.

Expt. #	Total Strain Amplitude ($\Delta\epsilon_t/2$)	Plastic Strain Amplitude ($\Delta\epsilon_p/2$)	Elastic Strain Amplitude ($\Delta\epsilon_e/2$)	Stress Amplitude ($\Delta\sigma/2$) (MPa)	Cycles To Failure (N_f)
B5	0.002	0.00088	0.00112	220	104900
A10	0.005	0.00335	0.00165	322	9240
A6	0.0095	0.00745	0.00205	353	3124
A7	0.0115	0.0092	0.0023	389	1572
A8	0.014	0.0117	0.0023	455	1025

Table 3.2.2a: LCF Results 80°C

Expt #	Total Strain Amplitude ($\Delta\epsilon_t/2$)	Plastic Strain Amplitude ($\Delta\epsilon_p/2$)	Elastic Strain Amplitude ($\Delta\epsilon_e/2$)	Stress Amplitude ($\Delta\sigma/2$) (MPa)	Cycles To Failure (N_f)
B3	0.00186	0.0009	0.0009	188	182346
B6	0.003	0.002	0.001	208	21650
B4	0.0039	0.0027	0.0012	239	9659
B2	0.00497	0.00353	0.00144	267	5995
B1	0.0099	0.0078	0.0021	381	1274

Table 3.2.2b: LCF Results 350°C

For each of the experimental temperatures, values of the saturation period stress amplitude were plotted against the corresponding plastic strain amplitudes giving the cyclic stress/strain curves for the ICL 167 SPH, (Fig. 3.2.5). The results compare well with those of Gorlier et al., [1984], at 20°C and 300°C.

Plotted as $\log\Delta\sigma/2$ vs. $\log\Delta\epsilon_p/2$ the cyclic stress/strain curve is a straight line. At 20°C the straight line is continuous for all values of strain amplitude, however at 300°C the gradient of the line increases for plastic strain amplitude values greater than 2×10^{-3} . The gradient of the line is the cyclic strain hardening exponent and the results of Gorlier et al., [1984], show that the gradient at 300°C and plastic strain amplitudes below 2×10^{-3} is similar to that at 20°C while at plastic strain amplitudes above 2×10^{-3} the gradient of hardening is nearer the higher value at 600°C.

The experimental results can be represented by the following equations;

80 °C;

$$\frac{\Delta\sigma_s}{2} = 1331.3 \left(\frac{\Delta\epsilon_t}{2} \right)^{0.269} \quad (3.2.2a)$$

$$\frac{\Delta\sigma_s}{2} = 1024.7 \left(\frac{\Delta\epsilon_p}{2} \right)^{0.202} \quad (3.2.2b)$$

350 °C;

$$\frac{\Delta\sigma_s}{2} = 2234.1 \left(\frac{\Delta\epsilon_t}{2} \right)^{0.39} \quad (3.2.3a)$$

$$\frac{\Delta\sigma_s}{2} = 1639.0 \left(\frac{\Delta\epsilon_p}{2} \right)^{0.311} \quad (3.2.3b)$$

Fatigue life plots of the experimental results, (Fig.3.2.6), show that an increase in temperature results in a decrease in number of cycles to failure for plastic strain amplitudes greater than 10^{-3} . However at a plastic strain amplitude of 9×10^{-4} the lifetime at 350 °C was greater than the corresponding lifetime at 80 °C. The experimental results compare well with those of Driver et al., [1988], from experiments on Type 316 stainless steel at both 20 °C and 300 °C. On a $\log(\Delta\epsilon_p/2)$ vs. $\log(N_f)$ plot a straight line through the data gives the Coffin-Manson equation which is a useful relationship to describe the fatigue lifetime behaviour of the material.

Unfortunately the extended lifetime of the 1.86×10^{-4} total strain amplitude test carried out at 350 °C has a great effect on the gradient of the Coffin-Manson relationship for the series of 350 °C tests. Therefore Coffin-Manson equations have been developed for each of the plots of the experimental results, as shown in Figure 3.2.6;

80 °C ($\Delta\mathcal{E}_t/2 > 0.001$);

$$\frac{\Delta\mathcal{E}_t}{2} = 0.269(N_f)^{-0.426} \quad (3.2.4a)$$

$$\frac{\Delta\mathcal{E}_p}{2} = 0.621(N_f)^{-0.567} \quad (3.2.4b)$$

$$\frac{\Delta\mathcal{E}_e}{2} = 0.0074(N_f)^{-0.164} \quad (3.2.4c)$$

350 °C ($\Delta\mathcal{E}_t/2 > 0.001$);

$$\frac{\Delta\mathcal{E}_t}{2} = 0.094(N_f)^{-0.333} \quad (3.2.5a)$$

$$\frac{\Delta\mathcal{E}_p}{2} = 0.138(N_f)^{-0.418} \quad (3.2.5b)$$

$$\frac{\Delta\mathcal{E}_e}{2} = 0.0064(N_f)^{-0.172} \quad (3.2.5c)$$

350 °C ($\Delta\mathcal{E}_t/2 > 0.002$);

$$\frac{\Delta\mathcal{E}_t}{2} = 0.209(N_f)^{-0.429} \quad (3.2.6a)$$

$$\frac{\Delta\mathcal{E}_p}{2} = 0.251(N_f)^{-0.489} \quad (3.2.6b)$$

$$\frac{\Delta\mathcal{E}_e}{2} = 0.0141(N_f)^{-0.265} \quad (3.2.6c)$$

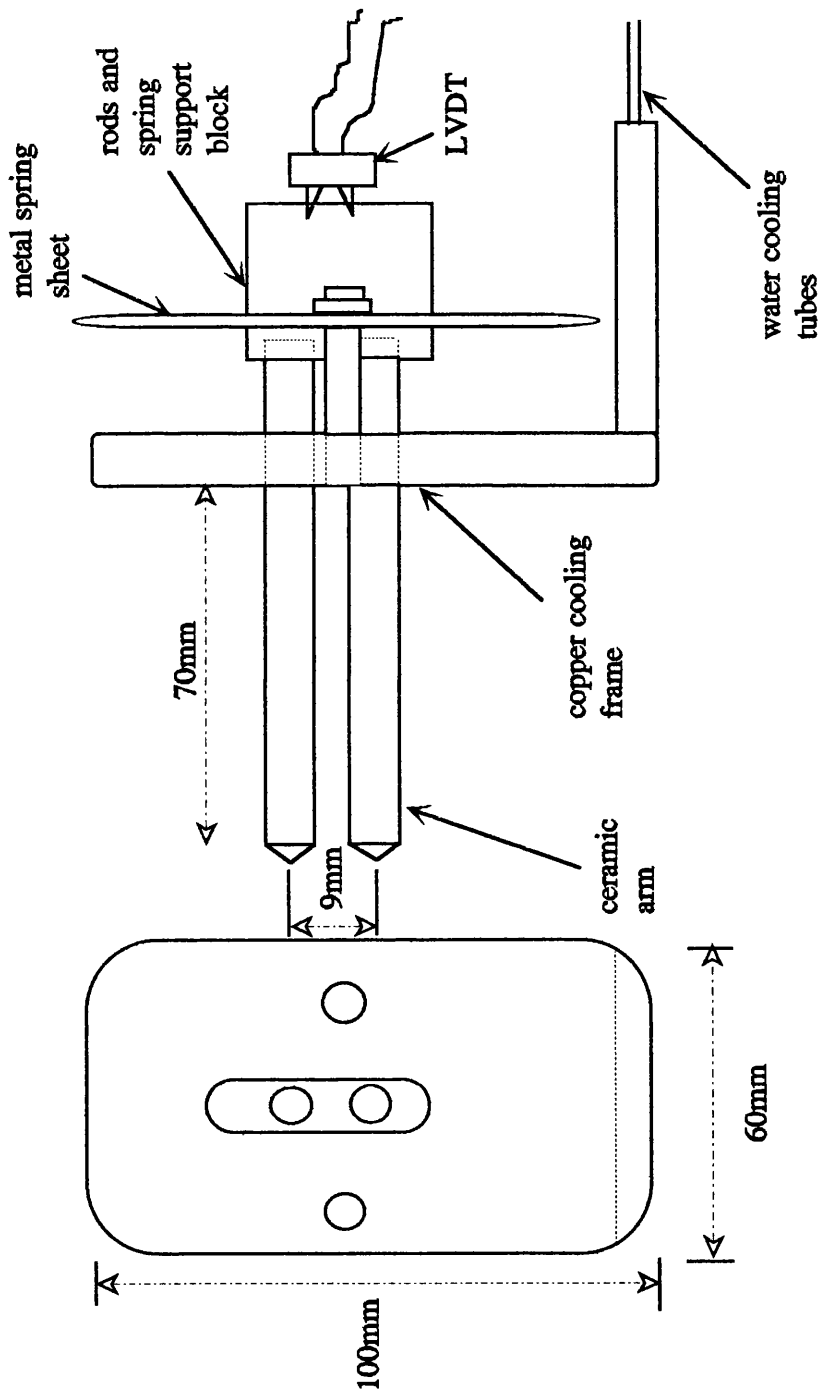


Figure 3.2.1. Axial Extension Measurement Extensometer.

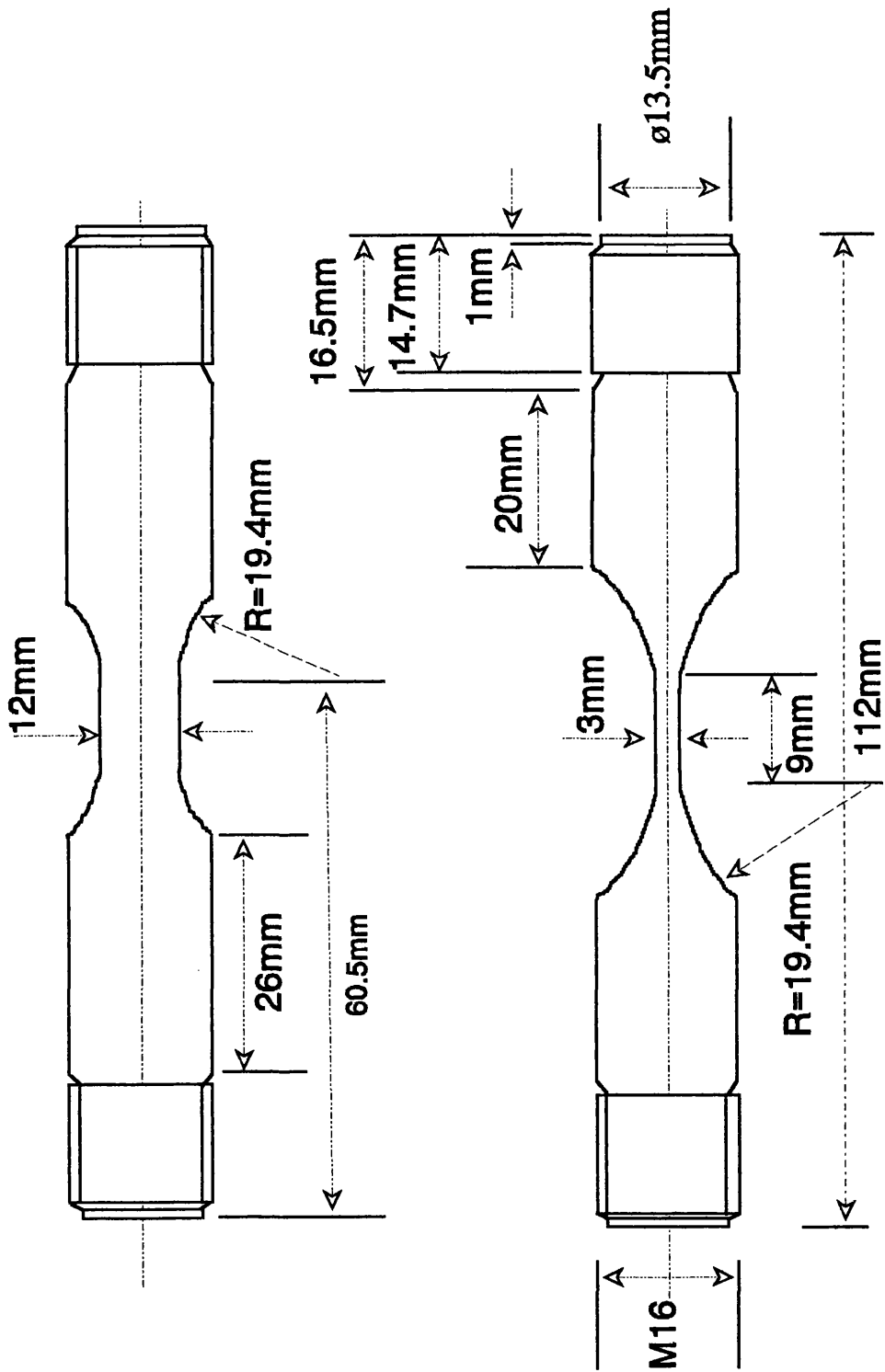


Figure 3.2.2. Low Cycle Fatigue Specimen Dimensions.

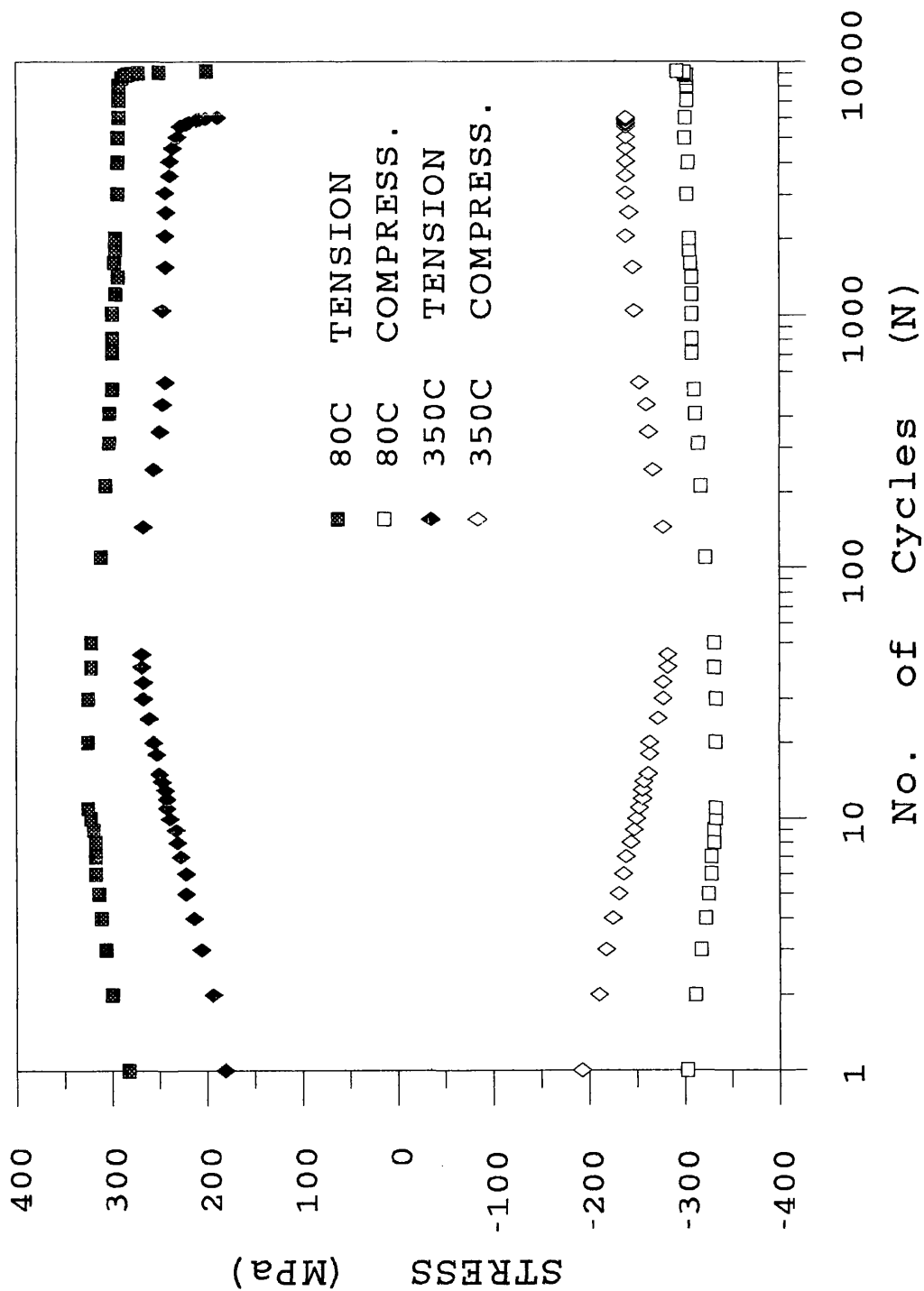


Figure 3.2.3. Stress Amplitudes During LCF Experiments at 0.5% Strain Amplitude.

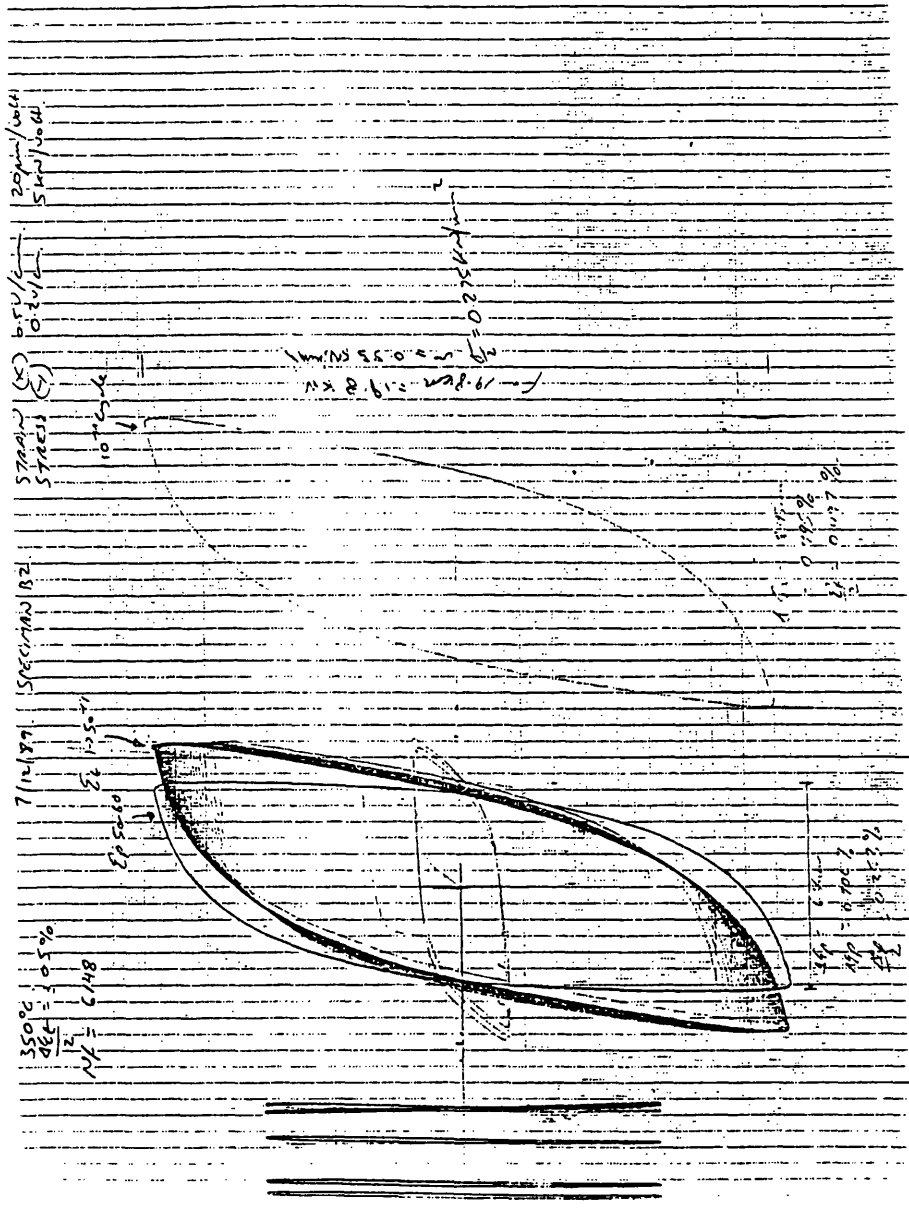


Figure 3.2.4b. Hysteresis Loops During LCF Testing at 350°C, $\Delta\epsilon_t/2=0.5\%$.

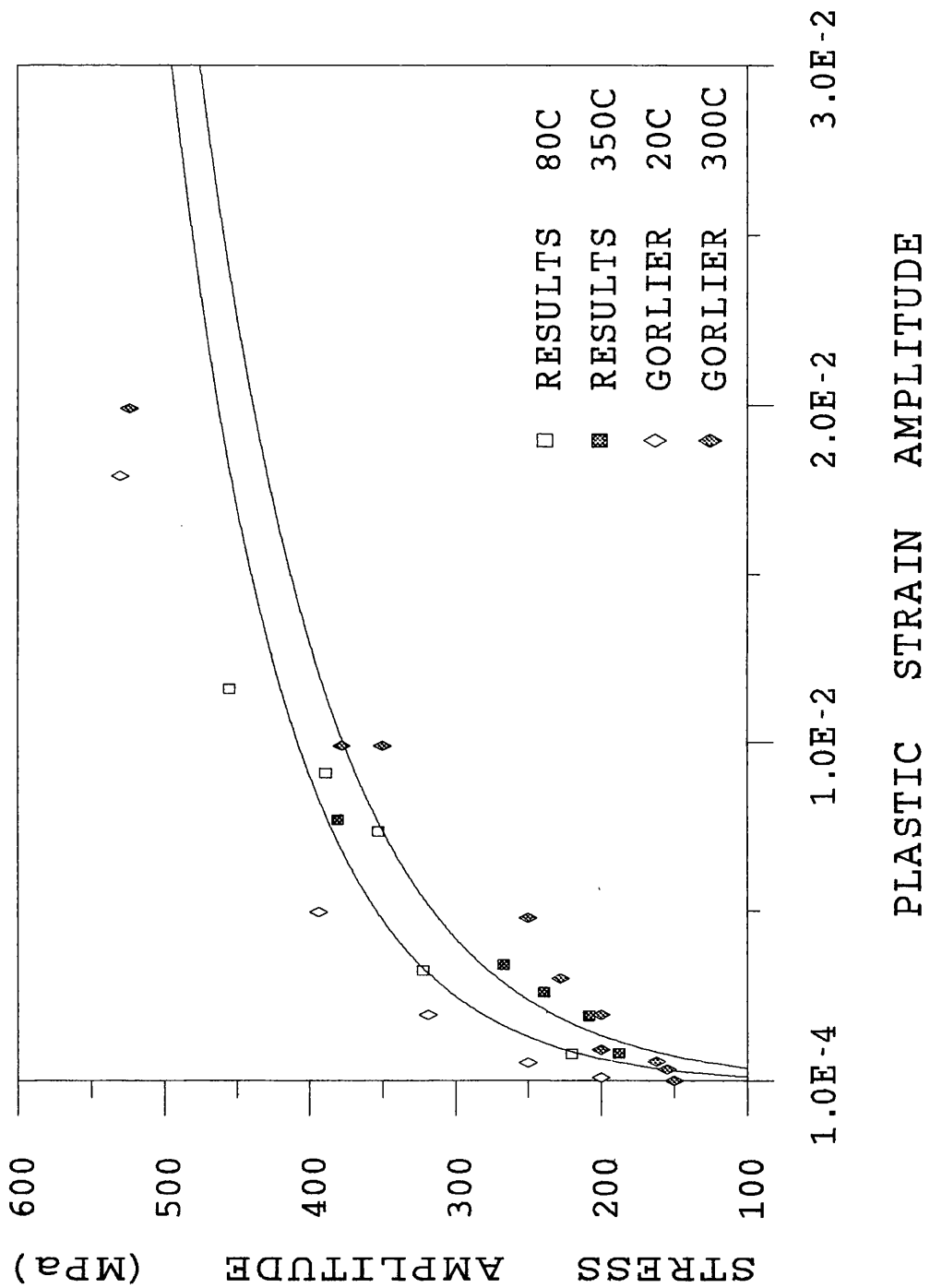


Figure 3.2.5. ICL 167 SPH: Cyclic Stress/Strain Results and 316L Comparisons.

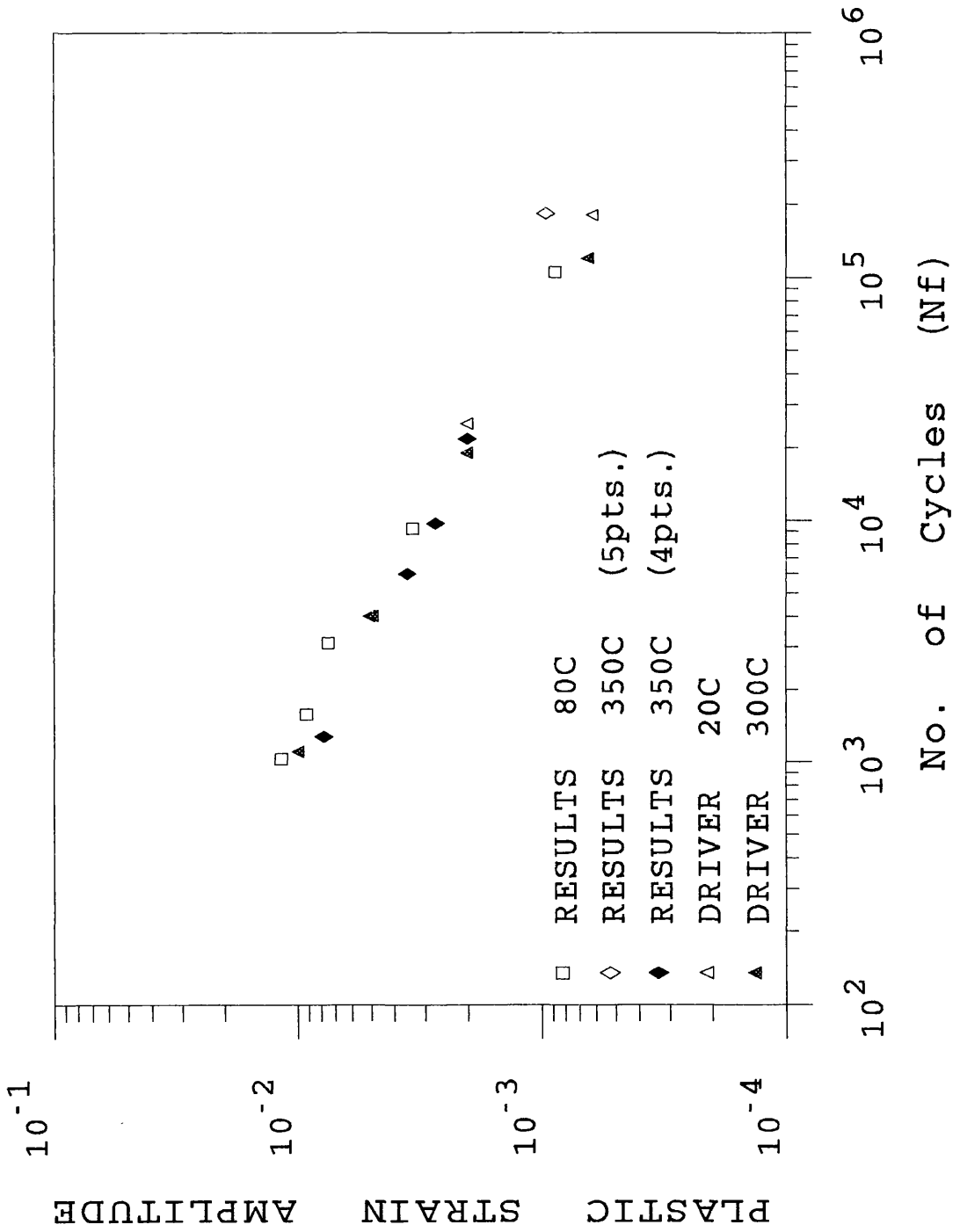


Figure 3.2.6. ICL 167 SPH: Fatigue Life Results with 316L Comparisons.

3.3. Mechanical Fatigue Crack Growth Testing.

3.3.1. Introduction.

The complex cyclic stress field through a tube wall subjected to thermal cyclic loading generates various problems. Previous investigations have shown that the stress field through the thickness of the tube is made up of regions of cyclic plastic strain, plastic-elastic shakedown and purely elastic stresses, [Skelton and Nix,1987], [Burllet et al.,1989]. With knowledge of the material characteristics upon yielding, it is possible to describe the stress field as an equivalent elastic stress field. However linear elastic crack growth relationships for ICL 167 SPH at temperatures below 350°C had to be developed. The initial experiments were performed on centre cracked tension, CCT specimens in the uniaxial Schenck Treble II testing machine. This decision was made due to the supply of prepared solid section specimens and the previous success in developing fatigue crack growth rate data, from CCT specimens, in the same laboratory.

3.3.2. Centre Cracked Tension Specimen Design, Instrumentation and Test Equipment, Experimental Procedure and Results.

The initial mechanical fatigue crack growth experiments were conducted under linear elastic fracture mechanics loading and were performed on solid section specimens with the same geometry and dimensions as the LCF specimens described in section 3.2.2. To initiate and grow a crack through the centre of the gauge section a 0.5mm diameter hole was bored through the 3mm thickness giving 34.5mm² load bearing cross section. Each of the faces were lightly polished, using an electric motor driven polishing wheel and brasso, then cleaned in an ultrasonic bath, to simplify crack growth detection.

The specimens were instrumented to both measure and control the temperature and record direct current, (d.c.), potential drop, (p.d.), across the hole. K-type thermocouples were spot welded at the same control positions as with the LCF specimens. Three 0.5mm diameter 316 stainless steel wires were spot-welded onto the gauge surface to continuously measure the potential drop across the hole. The three wires were spot-welded in a line, along the specimen axis, across the hole on the front face of the specimen. One was positioned 1mm below the centre of the hole and another 1mm above the centre of the hole. The third wire was positioned 3.5mm above the centre of the hole. Millivolt signals were recorded across the two wires over the hole to detect crack initiation/growth and across the two wires above the hole for reference.

The experimental set up on the Schenck Treble II was similar to that of the LCF tests

except that the extensometer was removed and the experiments were performed to ASTM E647,[1988], under load control. Before the experiments could begin it was required that cracks were pre-fatigued to a length of 0.5mm on both faces either side of the hole. Specimens were pre-fatigued under push-pull axial loading of $\pm 7.6\text{KN}$, in a triangular waveform at a frequency of 1Hz. After three failed attempts to initiate pre-fatigued cracks of valid dimensions either side of the hole, the specimen geometry was altered by machining 0.2mm wide starter notches a distance of 0.5mm either side of the holes perpendicular to the direction of the applied load. The test programme was continued on a Schenck 100KN Hydro-Pulse closed loop uniaxial testing machine. The Schenck Hydro Pulse closed loop testing machine operates along the same principles as the Schenck Treble II. However the axial displacement of the load train is powered by a hydraulic power supply which is controlled by the servo valve. Although all linear elastic fracture mechanic crack growth tests were performed under load control the hydro-pulse also presents the possibility of both strain and stroke control. The control signal sent to the servo valve was set on the control panel by defining a static point, a dynamic range, a waveform and a frequency. The load train axial displacement of the initial pulse was detected by the load cell and the corresponding signal was sent back to the control panel. The PID of the system was automatically changed to match the response of the machine with the input signal. Both the signal and the response waveforms were displayed on an oscilloscope.

The specimen was held in the load train by two MTS hydraulic pressure grips. To match the smooth surface of the grips the specimen had to be machined to a diameter of 12mm over a length of 15mm at each end. The specimen was heated within a copper tubing induction heating coil powered by a 50kW Celes induction heating system which was controlled in a closed loop by a Eurotherm controller. The thermal response measurement, K-type thermocouple positioning on the specimen and selection of heating coil geometry were carried out as described in section 3.2.2. Thermocouple readings were taken in millivolts on a Keithley digital voltmeter and were converted to $^{\circ}\text{C}$ from tables.

Throughout the experiments the crack growth was monitored using a 5amps direct current potential drop measurement system. The change in voltage across the crack penetrating ligament was measured through 0.5mm diameter 316 stainless steel wires positioned on the face of the specimen as shown in Figure 3.3.1. The current input lead was connected to the upper grip which was insulated from the machine and the output lead was positioned on the lower grip which was electrically grounded. A filter system was developed to remove interference on the amplified signals which were recorded on a W&W chart recorder.

The instrumented specimen was positioned in the lower grip and visually aligned with a travelling microscope. Under stroke control the load train was raised and the specimen was secured in the grips to a pressure of 200 bar. The control mode was changed to load control and the specimen was held under tension at 0.5KN. The heating coil was positioned as in the LCF experiments and the 5amps direct current was introduced through the specimen.

The specimen was pre-fatigued at room temperature under tensile-compression loading to the specifications of ASTM E647,[1988]. The experiments were performed at room temperature, 80 °C and 350 °C with a tensile load ratio of 0.1, in a triangular waveform at a frequency of 10Hz, Table 3.3.1. For the results to be valid with the principles of linear elastic fracture mechanics, LEFM, the following relationship for the uncracked ligament, (W-2a), was required;

$$(W - 2a) \geq \frac{1.25P_{\max}}{B \sigma_{ys}} \quad (3.3.1)$$

The thickness of the specimen, B, was 3mm, σ_{ys} is the 0.2% offset yield strength at the test temperature and P_{\max} is the maximum applied load during a cycle. When the material supplier's values of σ_{ys} were applied to equation 3.3.1, the calculated values of P_{\max} required to maintain validity, over the entire range of uncracked ligaments, did not produce crack propagation. Therefore an effective yield strength, termed the flow strength, σ_{fs} , was calculated, as described in ASTM E647,[1988], for high strain hardening materials, ($\sigma_u/\sigma_{ys} \geq 1.3$);

$$\sigma_{fs} = \frac{(\sigma_{ys} + \sigma_u)}{2} \quad (3.3.2)$$

where σ_u , is the ultimate tensile strength. The corresponding values of flow strength were applied to equation 3.3.1 to calculate the applied maximum load and ensure validity over the entire range of 2a/W, Table 3.3.1. Unfortunately, use of this alternative size requirement allows mean plastic deflections to occur in the specimen therefore increased crack growth rates by as much as factor of two can be expected, [ASTM E647,1988].

During the experiments the specimen surfaces were monitored with a travelling microscope between 20 and 60 times magnification at the standard specified intervals. Furthermore the fracture surfaces were heat tinted for a series of decreasing temperatures

with increasing crack growth under a 2KN static tensile load for 1 minute. Heat tinting temperatures ranged from 375 °C to 550 °C.

Expt. #	Temp. (°C)	Pre-fat (KN)	$2a_o/W_o$	Applied Load P_{min}/P_{max}	$2a_f/W_f$	# Applied Cycles
A11	RT	± 5.16 to ± 4.5	0.2028	$\frac{+0.45}{+4.50}$	0.73	546416
C8	80 °C	± 6.55	0.211	$\frac{+0.655}{+6.55}$	0.66	176590
B10	80 °C	± 6.55	0.20	$\frac{+0.655}{+6.55}$	0.62	123430
A4	80 °C	± 5.16	0.233	$\frac{+0.516}{+5.16}$	0.66	332600
A6	350 °C	± 5.16 to ± 4.30	0.17	$\frac{+0.43}{+4.30}$	0.65	350000
A7	350 °C	± 5.00 to ± 4.30	0.17	$\frac{+0.43}{+4.30}$	0.625	396000
A8	350 °C	± 5.00 to ± 4.30	0.172	$\frac{+0.43}{+4.30}$	0.74	257200

Table 3.3.1: Centre Cracked Tension Specimen, Experimental Matrix.

The potential drop readings were normalised against the initial readings, V_o , and plotted against the corresponding number of cycles for each of the test temperatures, Figure 3.3.2. Values of the crack length with respect to the width of the specimen, $2a/W$, were determined from the potential drop readings using the calibration curves produced by Gilbey and Pearson,[1966], for centre crack specimens of similar geometry, current input position and potential drop probe locations.

Upon completion of the experiments, the specimen was separated across the remaining ligament to reveal the heat tinted fracture surface, Figure 3.3.3. The different colours of each heat tint clearly display the development of the crack front. When crack front curvature occurred then an average crack length was calculated using a five point variation of the three point through thickness average crack length measurement technique as described in ASTM E399,[1978]. Measurements of the maximum crack

length were also taken. Comparison of the calibrated crack length from the p.d. readings with both the optical crack length, (a_o), and the average crack length, (a_m), from the fracture surface measurements, produce no consistently better method of measuring the crack length. Figure 3.3.4 displays a set of results for one experiment from each of the experimental temperatures.

From the room temperature experiments the normalised crack growth was similar to that observed on the surface of the specimen during the tests for $a/W < 0.62$. With $a/W > 0.62$ the calibrated value was lower. Both the average and maximum value from the fracture surface measurements were always greater than both the p.d. and optical values due to the amount of crack curvature. From the 80°C experiments the p.d. values appeared to be similar to the values measured on the surface of the gauge section for $a/W < 0.3$, but for $a/W > 0.3$ the calculated crack depths from the p.d. measurements were greater than both the optical measurements and average values from the fracture surface measurements. Only the maximum values from the fracture surface measurements compare well with the p.d. values and beyond $a/W = 0.52$ the p.d. values are greater. From the 350°C experiments with $a/W < 0.32$ the p.d. values were low. For $0.32 < a/W < 0.6$ there was a similarity between all measured values, but with $a/W > 0.6$ the p.d. values increase rapidly. This rapid increase could result from differences between the experimental p.d. and the calibration probe positions. However the differing percentage of crack tunnelling, as observed in the amount of crack front curvature, must also have had an effect on the potential drop readings.

Using both the calibrated a/W and the average a_m/W values from the fracture surface measurements, the elastic crack growth rate and the corresponding crack tip stress intensity range have been calculated for each of the experimental temperatures using the compliance coefficient equation given in the test procedure, [ASTM E647, 1988].

$$\Delta K = \frac{\Delta P}{B} \sqrt{\frac{\pi \varpi}{2W} \sec \frac{\pi \varpi}{2}} \quad (3.3.X1)$$

where $\varpi = 2a/W$ and equation 3.3.X1 is valid is $2a/W < 0.95$.

Existing data for Type 316 stainless steels has been gathered from experiments performed between 20°C and 427°C on various specimen geometries. When this data is plotted on a $\log(\Delta K)$ vs. $\log(da/dN)$, Figure 3.3.5, a large scatter of results is observed. However both the room temperature data of Mahoney and Paton, [1974], on CT specimens of 316L and the 427°C data of Shahinian et al., [1973], on single edged notched, (SEN), specimens of Type 316 stainless steel, will be employed as data limits

for comparison with the experimental results from the present study. The data limits are plotted as perpendicular and diagonal crosses in Figure 3.3.6. Plotted against these data limits, both the measured and calibrated results from the CCT experiments, display higher crack growth rates at range of stress intensity factors greater than $18\text{MP}\sqrt{\text{m}}$. If best-fit lines were drawn through the data limits, then the crack growth rates in the CCT experiments would be greater at all range of stress intensity factors greater than $10\text{MP}\sqrt{\text{m}}$.

Increased crack growth rates were observed by Bucci,[1981], when comparisons were made between results from CCT and SEN specimens of non stress-relieved aluminium alloy from an extruded rod. The lower values of ΔK required for the same crack growth rate in CCT than in SEN specimens was due to the resultant residual stress field from the manufacturing technique. Tensile residual stresses were produced at the core of rod after heat treatment and rapid quenching while the external surface was subject to compressive residual stresses. However Amzallag et al.,[1981], observed no specimen geometry effect on the low fatigue crack growth rates using the load shedding procedure on 316 steels. Their results from a number of tests under the same loading conditions have displayed crack growth rates four times the value over the same range of ΔK . This phenomenon was observed more so with 316 steel than with 2618 aluminium alloy and was related to crack front curvature.

3.3.3. Compact Tension Specimen Design, Instrumentation and Test Equipment, Experimental Procedure and Results.

To investigate the possible effects of different specimen geometries on the crack growth rate behaviour of ICL 167 SPH a series of mechanical fatigue crack growth tests were performed on compact tension, CT, specimens which were machined from the same block of material with the notch positioned in the same direction relative to the rolling direction of the material. The compact tension, specimen dimensions, tolerance of dimensions, surface finish and test procedure followed the guidelines of the ASTM standard E647,[1988]. The specimen dimensions are given in Figure 3.3.7.

To perform fatigue crack growth rate experiments on CT specimens within the Schenck Hydro Pulse 100KN testing machine, modifications were made to both the specimen gripping system and the specimen heating system. A long arm clevis and pin assembly for gripping the CT specimen was designed, (Fig.3.3.8), and machined from stock 316 stainless steel bar. The end of each clevis was roughly finished to 30mm diameter to give a secure hold within the pressurised MTS grips at 210 bar. The long arms were designed to support the specimen with a loading pin while containing the minimum

volume of material as possible to keep the volume of conducting material within the induction heating field to a minimum. A different induction heating coil was designed to give an even thermal gradient over the entire CT specimen. The coil was supported and controlled in the same method as discussed in section 3.3.2.

To determine both the thermal gradient across the specimen and the ideal position to control and monitor the temperature during the experiments a specimen was instrumented with seven K-type thermocouples, (Fig.3.3.9). Thermocouples #1,#2,#6 and #7 were positioned along the proposed line of cracking on both faces to assure that the positioning of the coil would give a consistent temperature along the crack front as the crack grew. Thermocouples #3 and #4 were positioned 5mm above and below the proposed line of cracking at a distance of 19.5mm from the notched end of the specimen. When the signal from these two thermocouples matched then it was assumed that the coil was positioned correctly in the vertical direction. Finally thermocouple #5 was spot welded onto the long arm of the clevis, below the upper pin position from which the specimen was held in position within the load train.

The thermal calibration specimen was assembled into position in the same way as the actual specimen was for the experiments. Initially the upper long armed clevis was placed into the upper MTS collet grip such that the two holes in the long arms were concentric when viewed from the front of the machine. The grip was secured to a pressure of 5 bar and the instrumented specimen was carefully positioned between the arms with the upper hole on the specimen concentric with the holes in the arms of the clevis. A pin was positioned through the holes thus holding the specimen in place. Under stroke control the lower clevis was raised until the holes of the clevis were concentric with the lower hole in the specimen and a pin was passed through the holes. With the specimen held between the arms the grips were pressurized to 200 bar and the specimen was held at 0.5KN tension under load control. The induction heating coil was positioned around the specimen and thermocouple #2 was plugged directly into a two channel input zero point reference with the output going to the Eurotherm controller. The other six thermocouples were plugged into a six channel selector switch box, with the output going to the zero point reference then on to a digital voltmeter. The corresponding temperatures were read from standard K-type tables. The readings obtained at 80°C and 350°C are given in Table 3.3.2.

Thermocouple #	350 °C	80 °C	POSITION
1	351	80	FRONT
2	350	80	BACK
3	351	80.5	ABOVE
4	349	80.3	BELOW
5	290.8	65.6	GRIP
6	351	80.5	FRONT
7	351	81	FRONT

Table 3.3.2: CT Specimen Thermal Gradient.

The temperatures measured indicate that the coil position produced a very favourable thermal gradient over the specimen and that the grip was always cooler than the specimen. Therefore the temperature of the clevis grips nearer the water cooled MTS collet grips was lower than that of the specimen. Before the clevis with the long arms were machined, calculations were made to compare the maximum load that the clevis grips could support with the required loading for both pre-fatigue crack growth at room temperature and experimental loading at room temperature, 80 °C and 350 °C. The results are given in Table 3.3.3.

Temp (°C)	σ_{vs} (MPa)	P _{GRIP} (KN)	P _{TEST} (KN)
RT	220	5.28	3.20
80	195	4.68	3.00
350	126.5	3.04	2.80

Table 3.3.3: Maximum Loads for Grips and Test Specimen.

From the calculations it was possible to grow a pre-fatigue crack 1.56mm in length from the tip of the machined notch in the long arm clevis pin assembly with a maximum tensile load of +5.28KN. However the length of time to grow the pre-fatigue crack could be greatly reduced by pre-fatiguing each specimen in thicker grips at room temperature with a maximum load of +7.0KN. Therefore each specimen was pre-fatigued at room temperature along the guidelines of ASTM E647,[1988]. Pre-fatigue loading was tension-tension with a constant load ratio of 0.1, in a triangular waveform at a frequency of 10Hz. Originally the maximum load was +7KN to encourage crack

initiation. However upon crack propagation the load was sequentially reduced at specified intervals until the maximum load of the experiments was reached.

Throughout the pre-fatigue loading the specimen faces were monitored with a travelling microscope, with a magnification of 20 to 60 times. Following pre-fatigue the specimen was removed from the machine, the faces were polished, thermocouples were spot welded onto the faces at positions 3 and 4 and the specimen instrumented for the detection of crack growth using the direct current, (d.c.), potential drop, (p.d.), measurement technique.

Three pairs of 0.5mm diameter 316 stainless steel wires were spot welded across the machined notch at the side of the specimen. The current input connections were positioned in two 5mm deep holes, which were tapped to M4, each one positioned 9mm in from the unnotched side of the specimen in the mid-thickness of the upper and lower surfaces of the specimen. When both the specimen and the induction heating coil were in position, Figure 3.3.10, a current of 10amps was supplied through the specimen and the signals from the p.d. probes and the thermocouples were checked. Before testing, the specimen was held at +1KN and 450 °C for 1 minute to mark the pre-fatigue crack front with a heat tint.

The experiments were performed in a triangular waveform with a tensile-tensile load ratio of 0.1 at a frequency of 10Hz. An example of the experimental parameters for each temperature of testing are given in Table 3.3.4;

Temp (°C)	a_0/W_0	Load (KN)	a_f/W_f	# Cycles
25	0.291	0.32/3.2	0.706	1,152,541
80	0.314	0.30/3.0	0.741	808,000
350	0.294	0.28/2.8	0.686	674,316

Table 3.3.4: Compact Tension Specimen Experimental Parameters.

Validity with the LEFM procedures was maintained throughout each experiment such that the value of the specimen's uncracked ligament satisfied the following requirement, [ASTM E647,1988];

$$(W - a) \geq \left(\frac{4}{\pi}\right) \left(\frac{K_{max}}{\sigma_{ys}}\right)^2 \quad (3.3.3)$$

During the experiments, the signals from the three potential drop channels were recorded on a W&W chart recorder. Both optical measurements of the surface crack length and the corresponding p.d. readings were made under static tensile loads of +1.5KN at intervals of normalised crack length, (a/W), as specified in the standard. The number of cycles between each interval was recorded from the counter on the control panel of the machine. The experiments were terminated when either the final normalised crack length, $a_f/W = 0.7$, or plasticity around the crack tip increased to such an extent that it became impossible to identify the crack tip. Upon completion of the experiment, the specimen was held under a static tensile load of +1.5KN. The induction coil was placed away from the specimen, all instrumentation wires were removed from the specimen surface and the static tensile load was increased to pull apart the remaining ligament. The resultant half-specimens were removed from the test machine and the fracture surfaces, (Figure 3.3.11), were observed under a microscope.

Each of the fracture surfaces revealed curvature of the pre-fatigue crack front which straightened out as the fatigue crack increased in length. Measurements were made at five points over both the pre-fatigue crack front and the final crack front. Linear regression was used to determine the crack length over the crack front for each of the surface measurements made at the various intervals during the test. Values of both the mean crack growth length and the maximum crack growth length were calculated. The potential drop readings were normalised to either the initial potential drop reading corresponding to the pre-fatigue crack length or to the potential drop reading when $a/W=0.3$.

The normalised readings from the three pairs of probes from the 80°C experiment are shown in Figure 3.3.12. Three pairs of the p.d. probe were positioned across the notch on the notched side of the specimen. One pair were positioned directly across the centre of the notch, a distance of 6.125mm from the side of the specimen which was viewed during testing, while the other two pairs were positioned 3mm and 4.5mm either side of the centre pair respectively. The consistency of the similarity in the readings from the three channels indicates that the crack front was straight for the duration of the experiment. However inspection of the fracture surface has indicated that the pre-fatigued crack front displayed curvature which straightened out with crack growth. This could be due to the current input position which was towards the unnotched side of the specimen to avoid contact with the clevis gripping system. It is possible that the current was so far away from the notch tip that no difference could be detected in the curvature of the front of a crack less than 2mm in length. The other two curves in Figure 3.3.12 show that the potential drop across the centre of the CT specimens tested at room

temperature and 350° C developed similarly to that of the measurements at 80° C.

The data from both the room temperature and the 350° C experiments were normalised to the potential drop reading when $a/W = 0.315$, to correspond with the potential drop calibration curves developed by Aronson and Ritchie,[1979], for a compact tension specimen using a finite element model. The dimensions of the calibration model were twice those of the experimental specimen and the current input/output position on the calibration model was directly half way along the top surface. These were the only differences between the calibration model and the experimental specimen in the present study. From the calibration curves values of normalised crack growth, (a_{pd}/W) , corresponding to the number of load cycles, have been calculated from the p.d. measurements and are compared, for each experimental temperature, with both the normalised crack growth from the optical measurements, a_{op}/W , and from the average of the fracture surface crack front calculations, a_m/W , (Figure 3.3.13). For each temperature of interest the trend of the results is similar. Initially the average crack growth depths from the fracture surface are greater than the p.d. calculations which are greater than the corresponding values measured during the experiment.

Each method of crack growth measurement displayed similar crack growth rates until approximately the last 15% of the experiment when the measurements from the p.d. calculations displayed an increase in crack growth rate. It is possible that the current input position on the specimen produced a higher sensitivity in the potential drop reading to longer cracks. Therefore the corresponding calibrated crack length was greater than the actual crack length.

Using both the calibrated a/W and the average a_m/W values from the fracture surface measurements, the elastic crack growth rate and the corresponding crack tip stress intensity range have been calculated for each of the experimental temperatures, using the compliance coefficient equation given in the test procedure, [ASTM E647,1988].

$$\Delta K = \frac{\Delta P}{B\sqrt{W}} \frac{(2 + \varpi)}{(1 - \varpi)^{3/2}} [0.886 + 4.64 \varpi - 13.32 \varpi^2 + 14.72 \varpi^3 - 5.6 \varpi^4] \quad (3.3.X2)$$

where $\varpi = a/W$ and equation 3.3.X2 is valid is $a/W \geq 0.2$.

The p.d. calculations and fracture surface measurements produced similar results at low crack growth rates, as shown in Figure 3.3.14. However the calculated range in stress intensity factors from the p.d. measurements was greater than that from the fracture surface measurements at crack growth rates above 10^{-4} mm/cycle. Therefore the results

from the mean fracture surface measurements have been used for comparison with both the results from the CCT specimen experiments and the data available from literature.

In Figure 3.3.15 it is observed that over the same range of crack growth rates the corresponding range in stress intensity factors was greater for the CT specimens than for the CCT specimens. Furthermore the results from the CT specimen experiments were found to sit between the limits of the data from other investigations into the fatigue crack growth behaviour of 316 type stainless steels. From the experiments performed on the CT specimens the following values for C and m, the constants of the Paris Law, have been determined;

Temp (°C)	C	m
25	1.614E-09	3.3497
80	2.195E-09	3.1788
350	4.584E-09	3.2948

Table 3.3.5: Constants for Paris Law Equations.

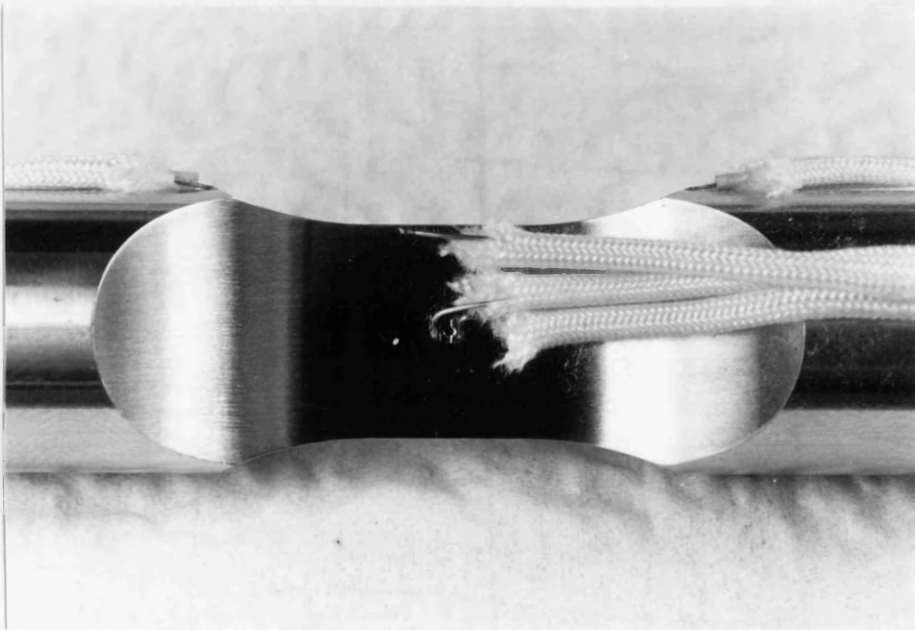
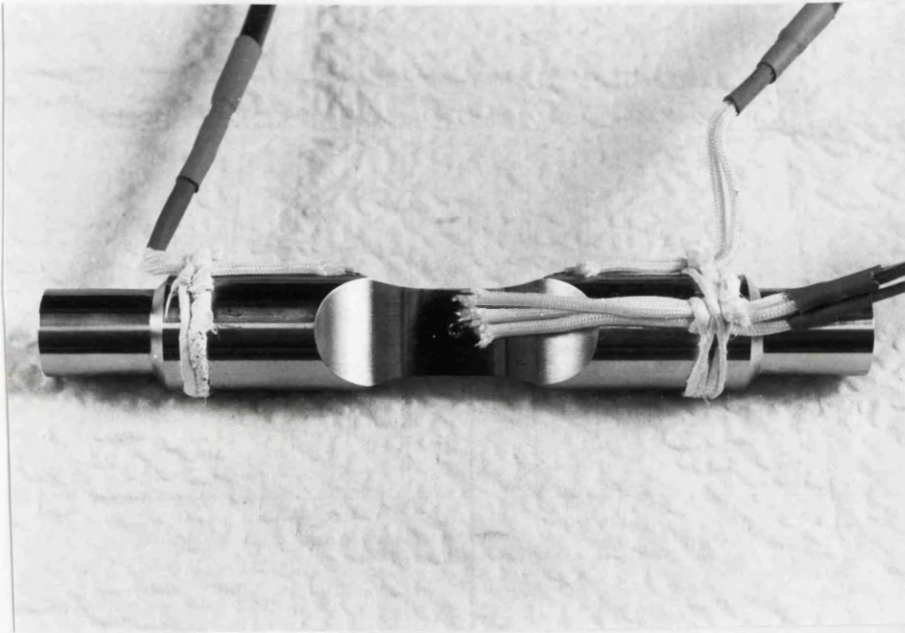


Figure 3.3.1. CCT Specimen Instrumented with P.D. Probes, (Mag.X0.92), Insert, (Mag.X2.4).

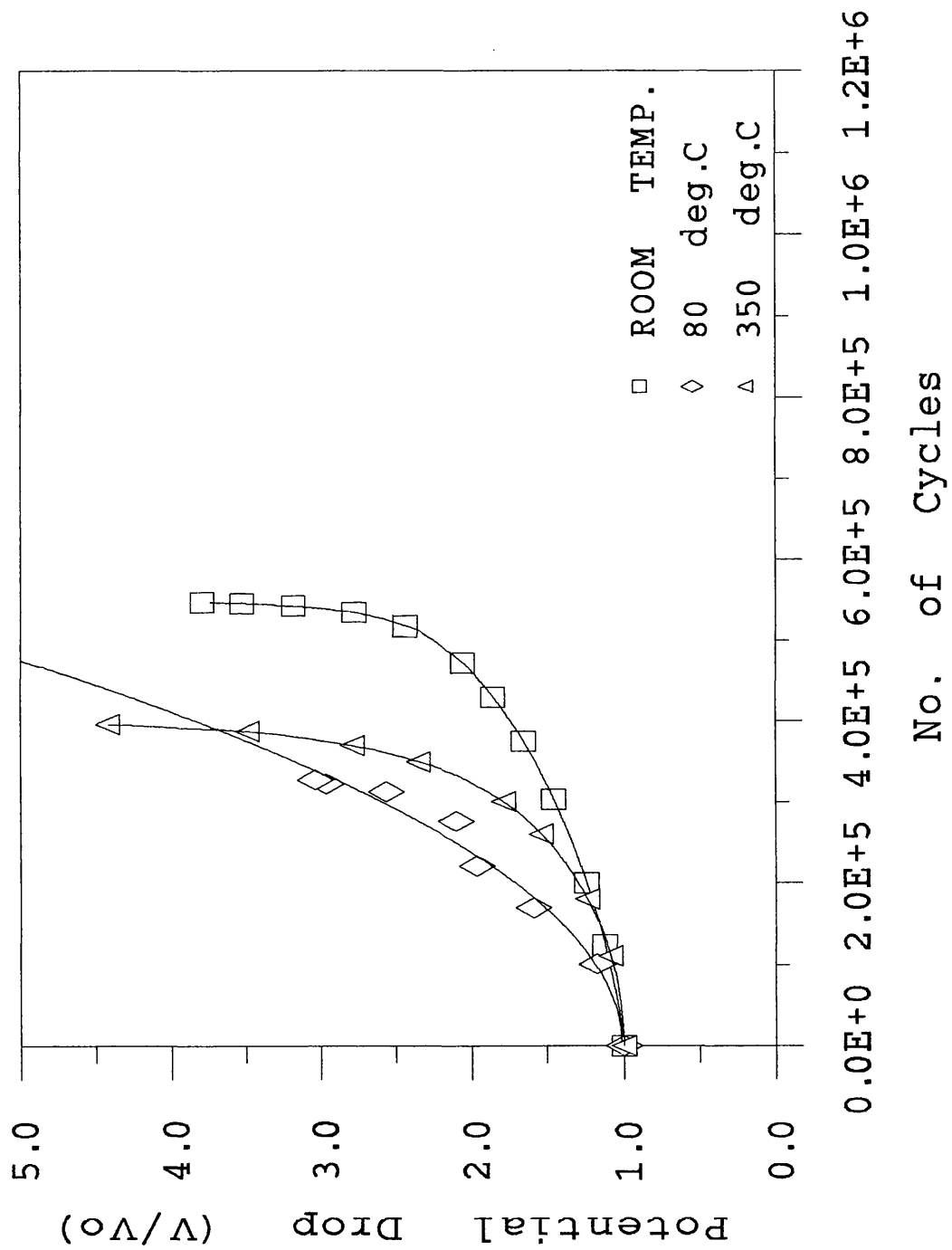


Figure 3.3.2. CCT: Potential Drop Development Curves.



Figure 3.3.3. CCT Specimen Fracture Surfaces, (Mag.X10).

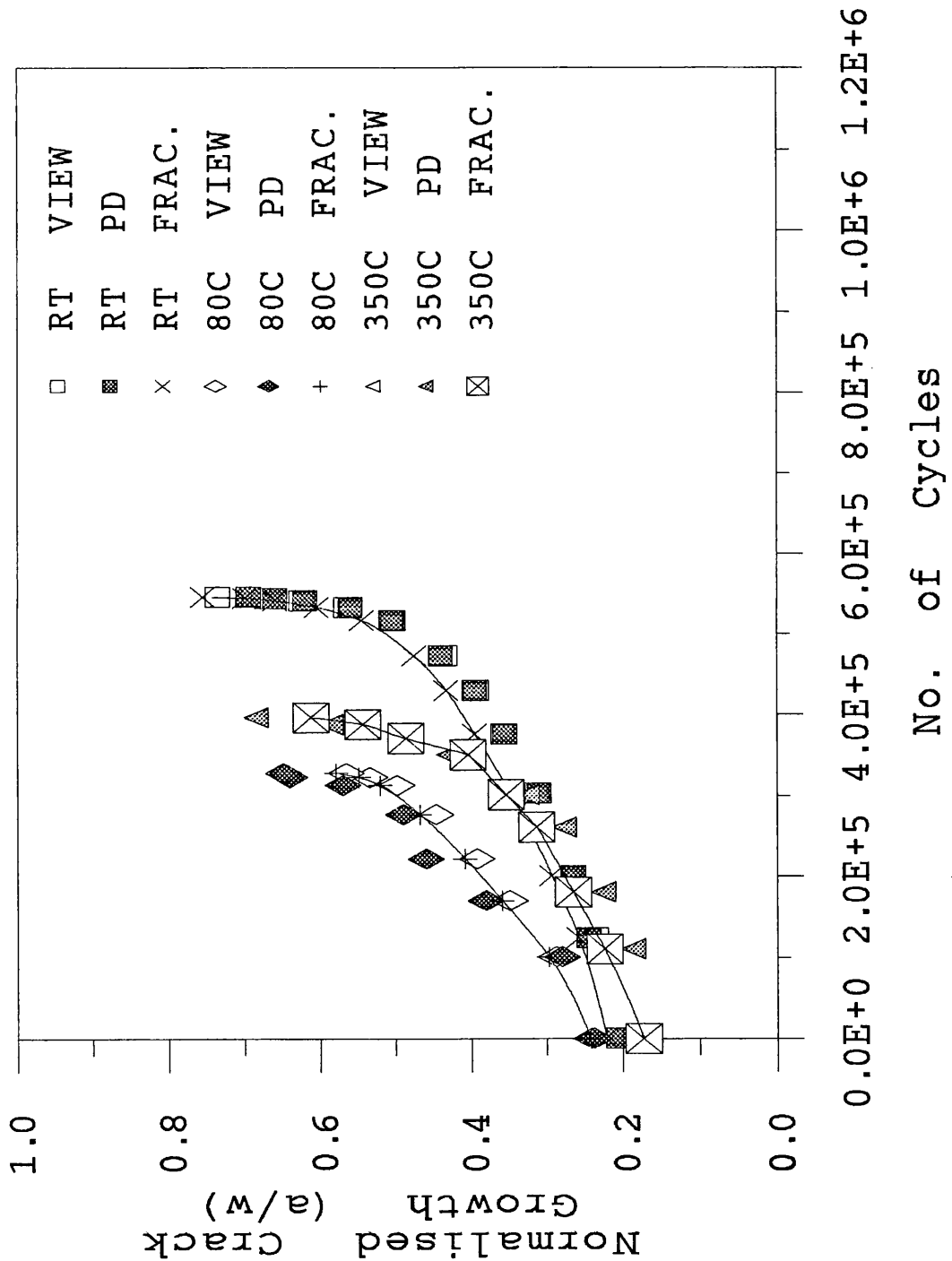


Figure 3.3.4. CCT: Crack Growth Measurement Curves.

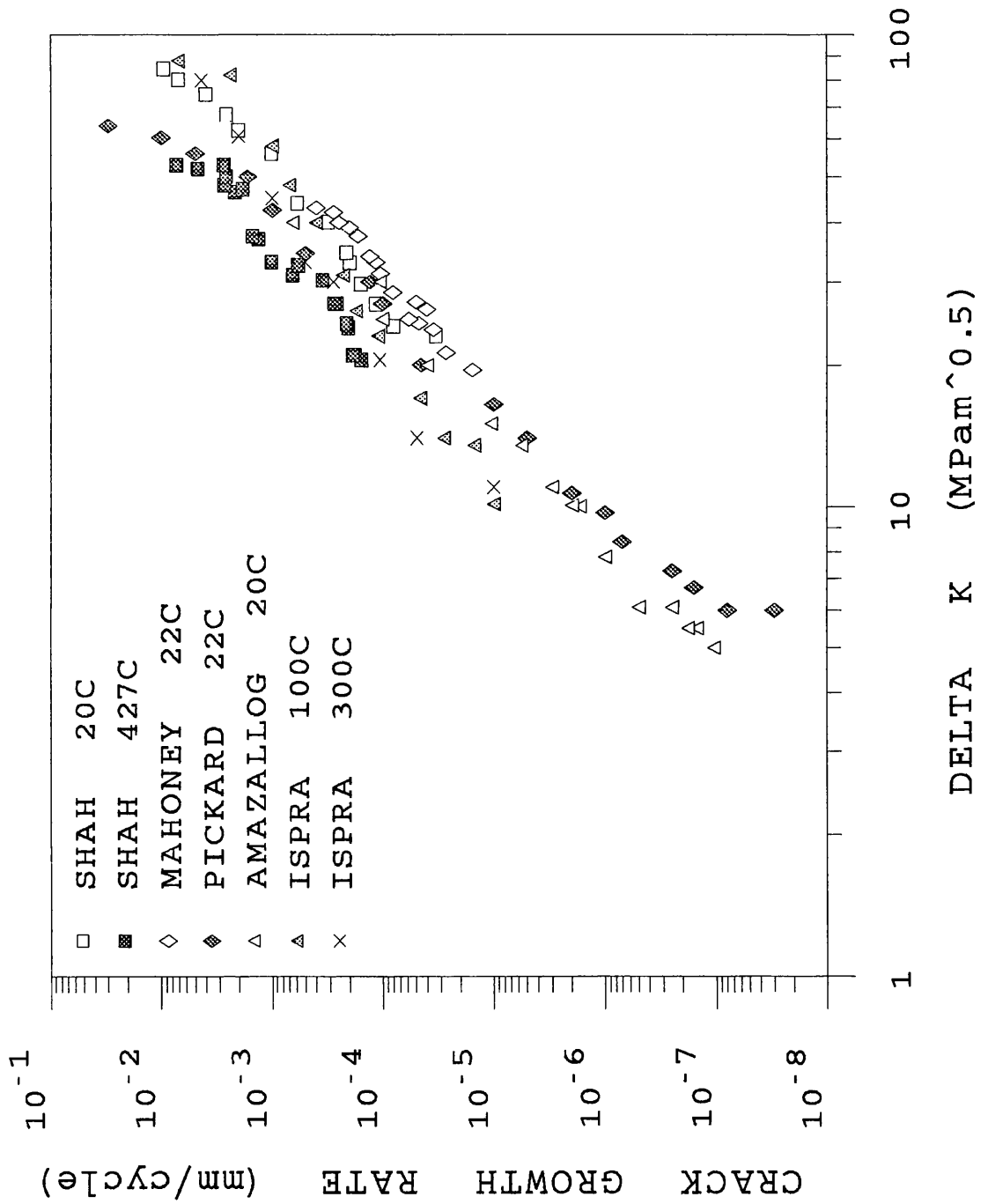


Figure 3.3.5. Fatigue Crack Growth Rate Data, Type 316L and 316 Stainless Steel.

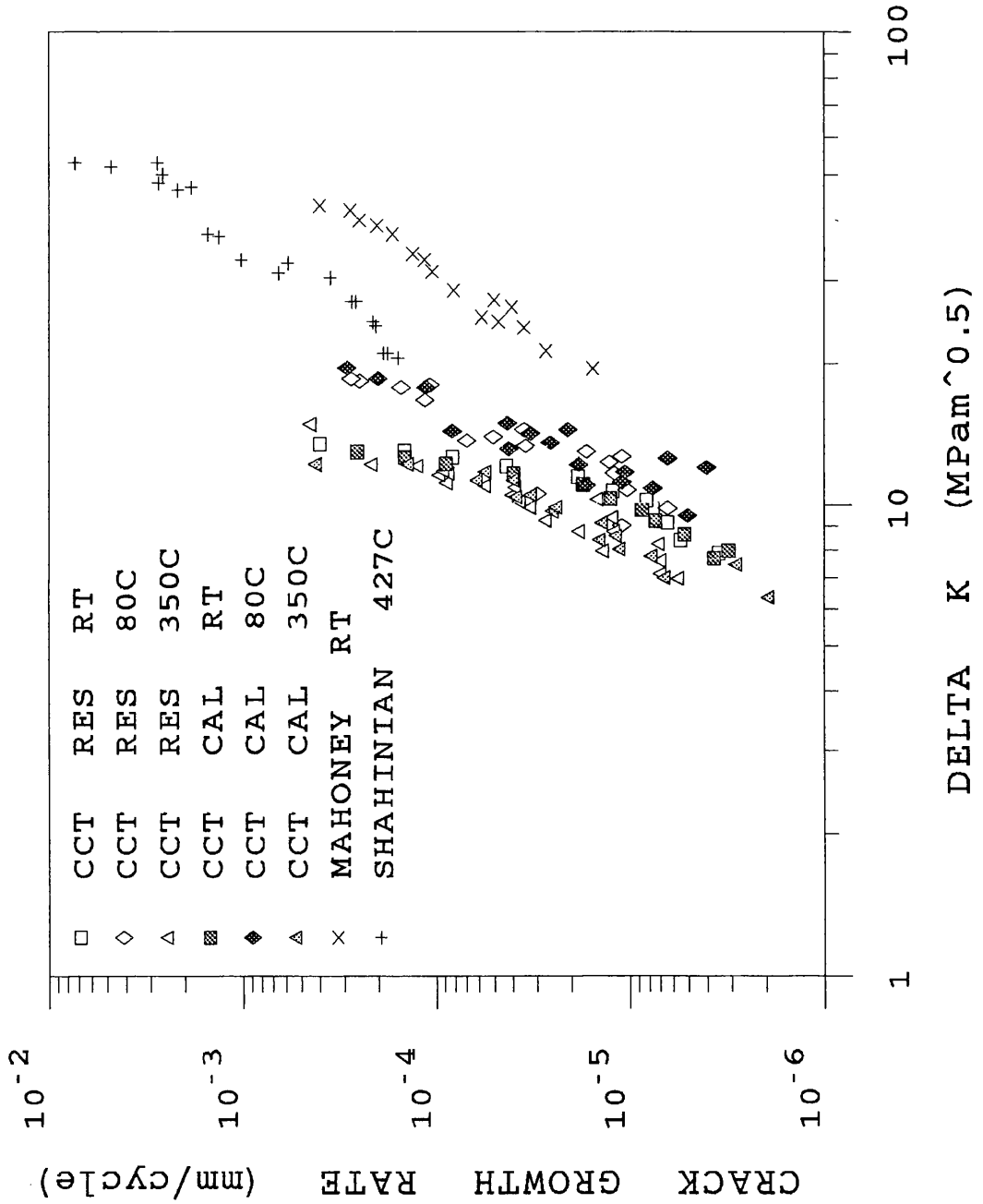


Figure 3.3.6. ICL 167 SPH: CCT Fatigue Crack Growth Rate P.D. Calibration and Results.

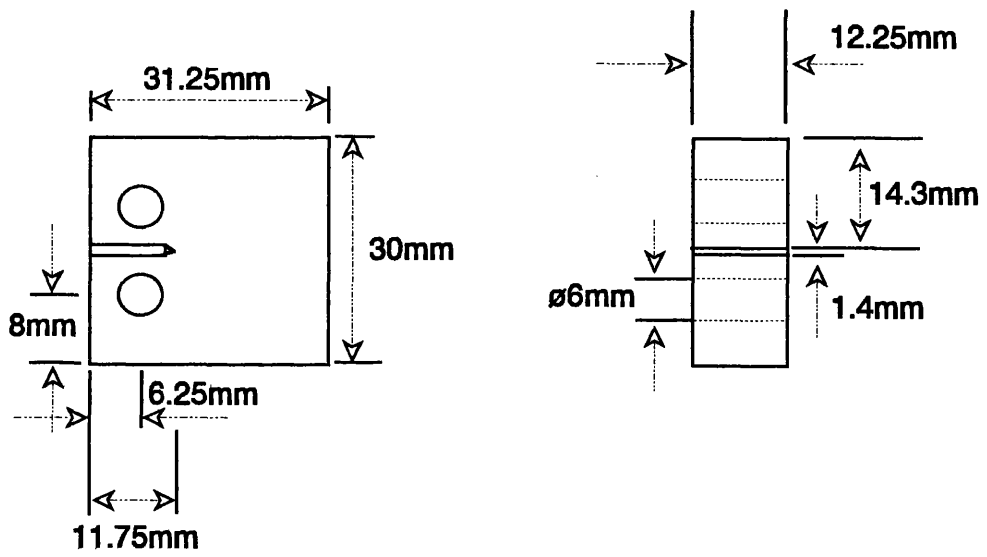


Figure 3.3.7. Compact Tension Specimen Dimensions.

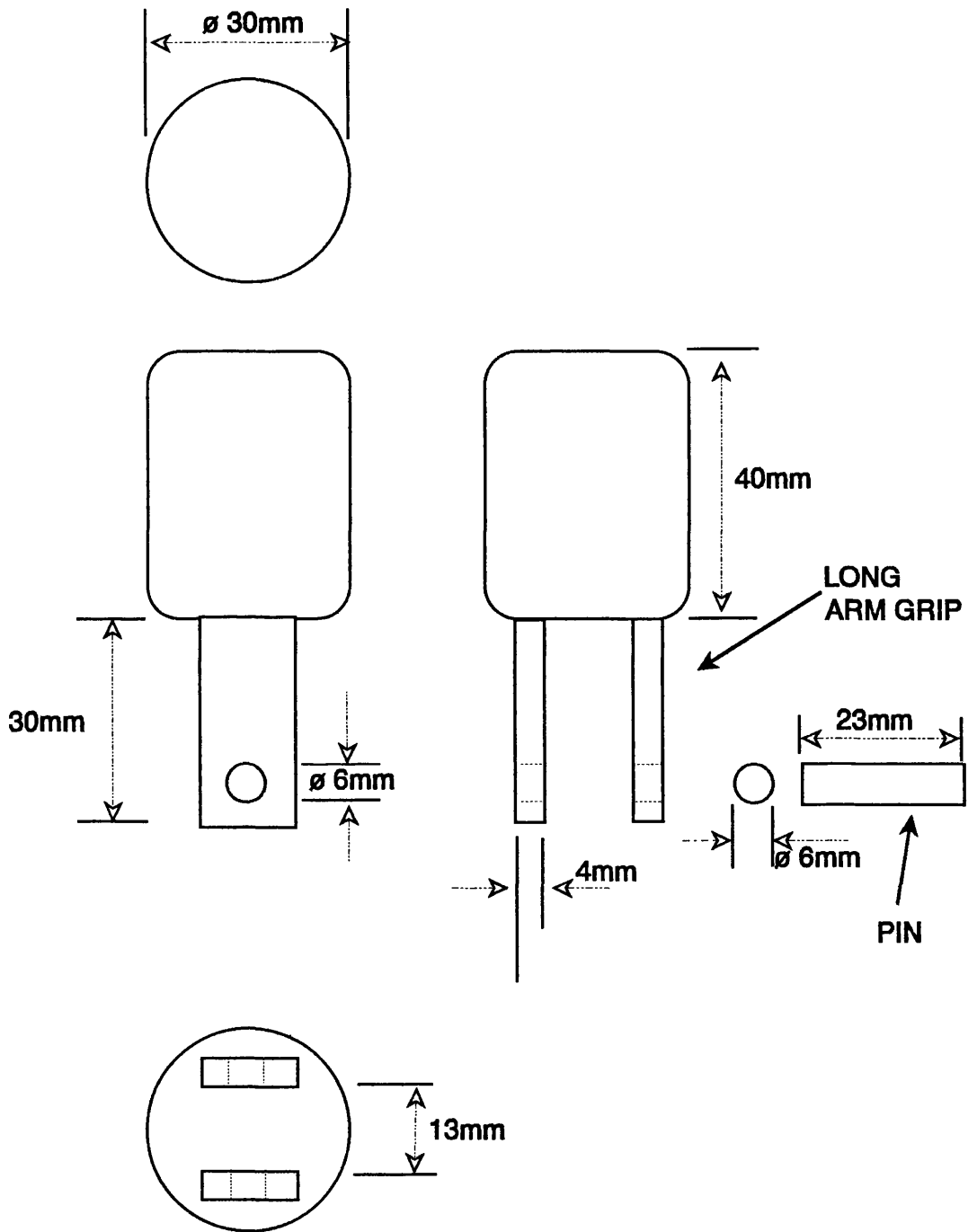


Figure 3.3.8. Long Arm Clevis and Pin Assembly For Gripping CT Specimen.

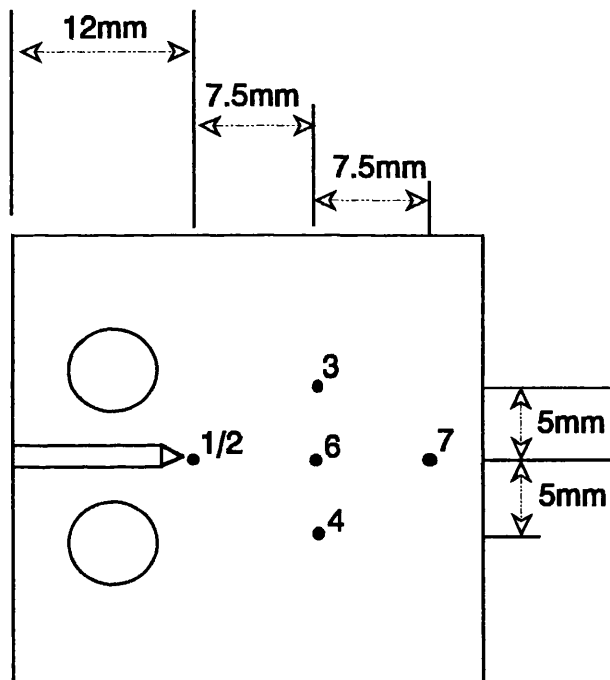


Figure 3.3.9. Thermal Gradient CT Specimen.



Figure 3.3.10. Instrumented CT Specimen in Experimental Testing Position.

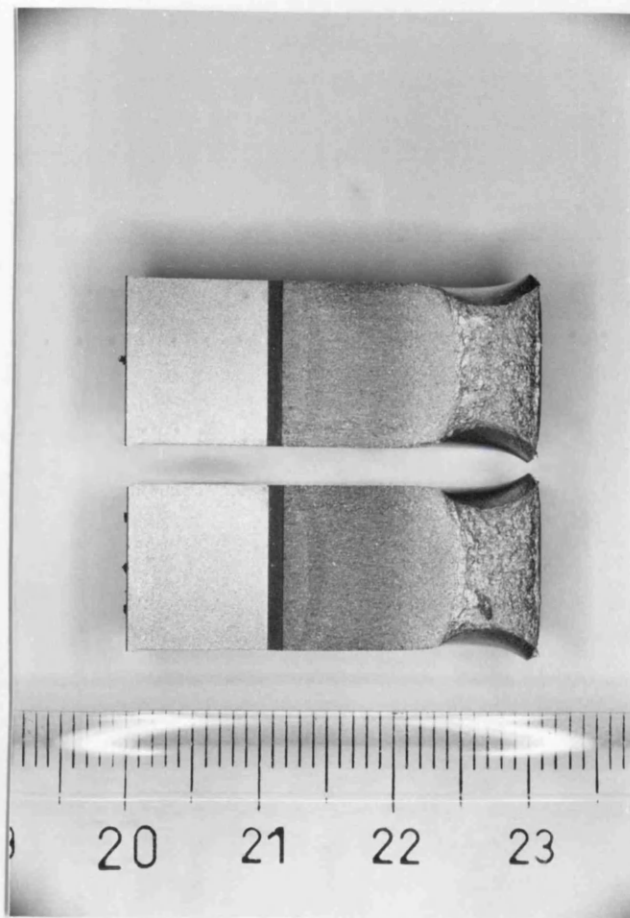


Figure 3.3.11. CT Specimen Fracture Surface: Room Temperature Experiment, (Mag.X1.76).

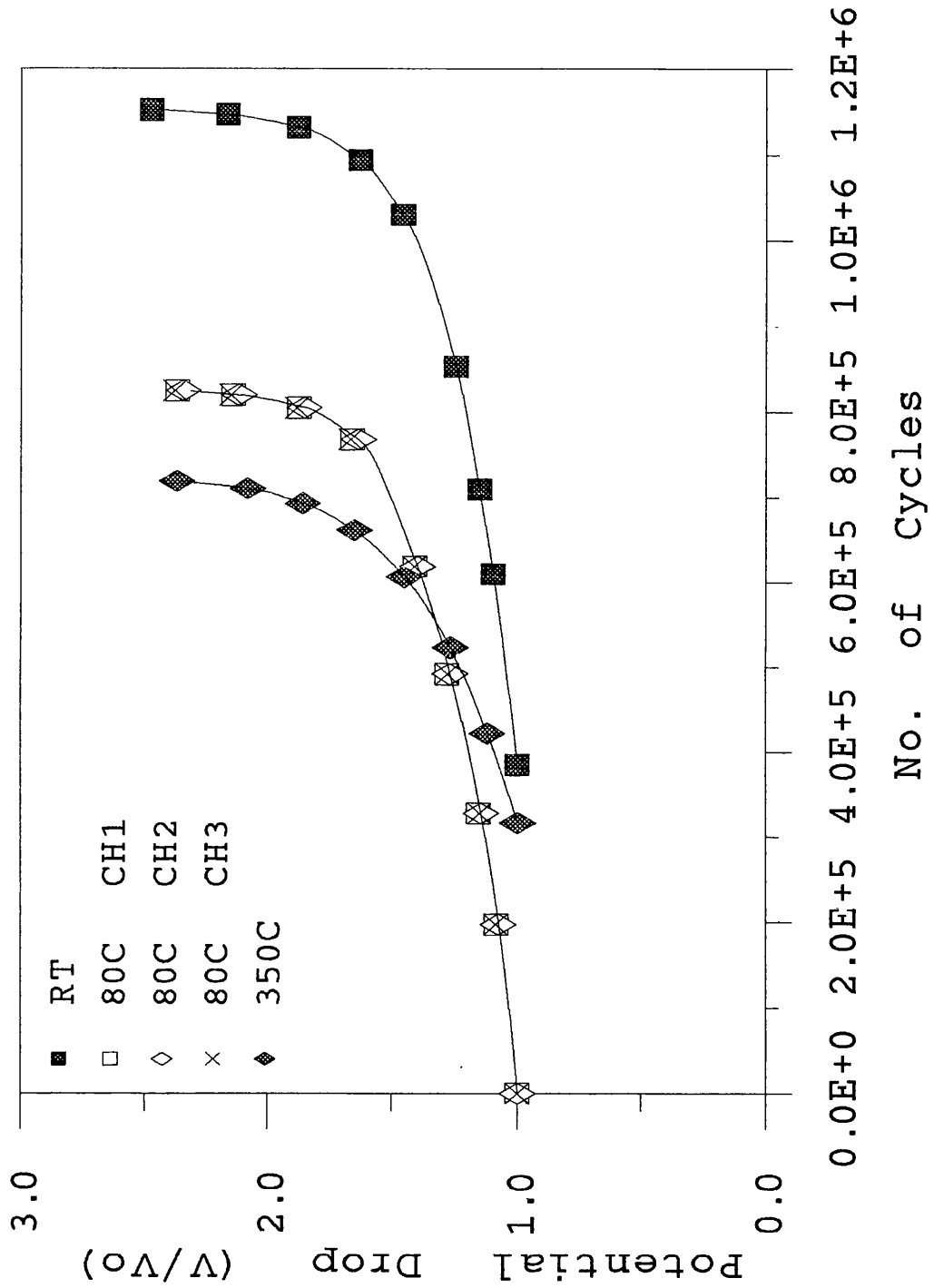


Figure 3.3.12. CT: Potential Drop Development Curves.

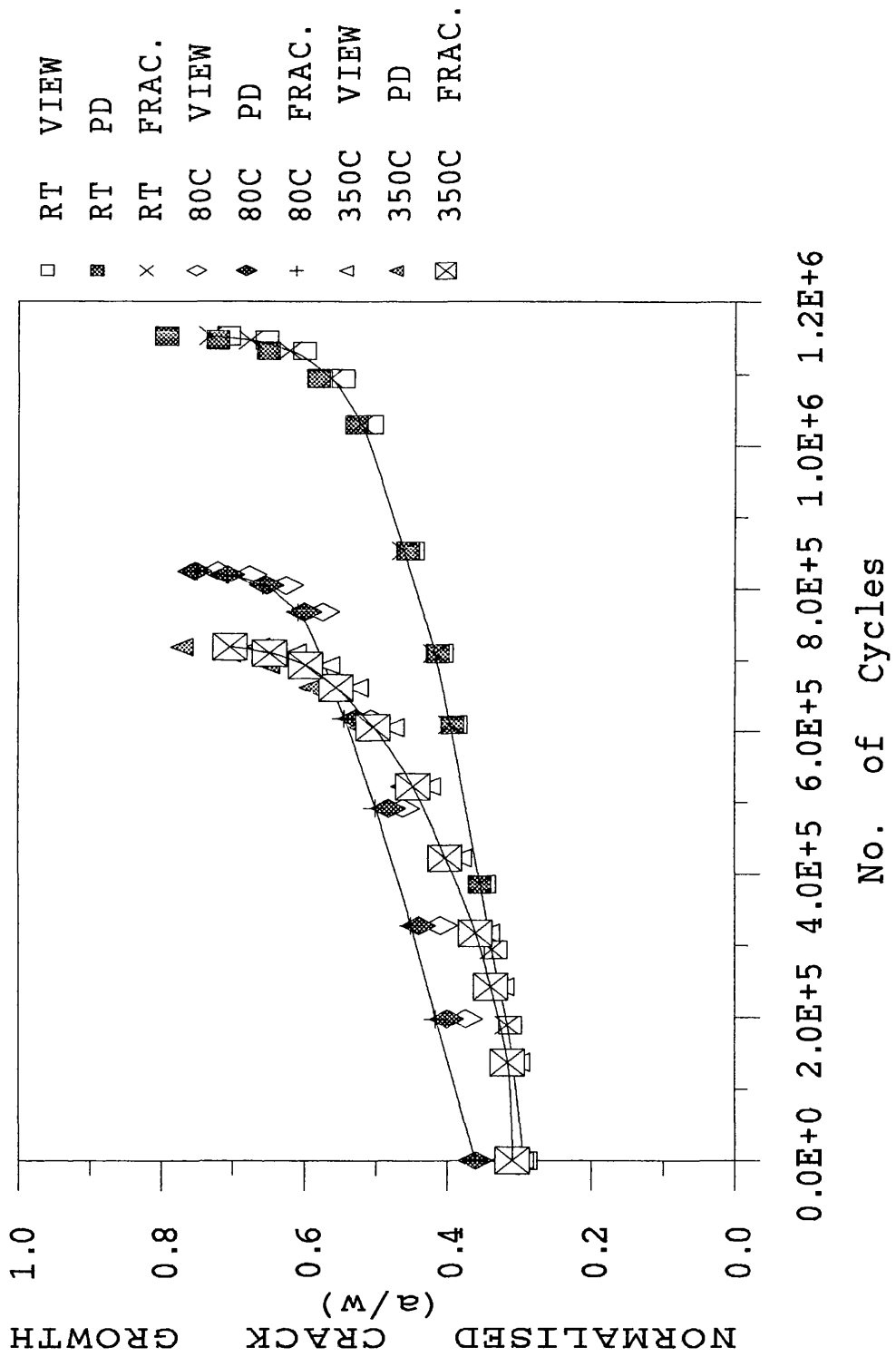


Figure 3.3.13. CT: Crack Growth Measurement Curves.

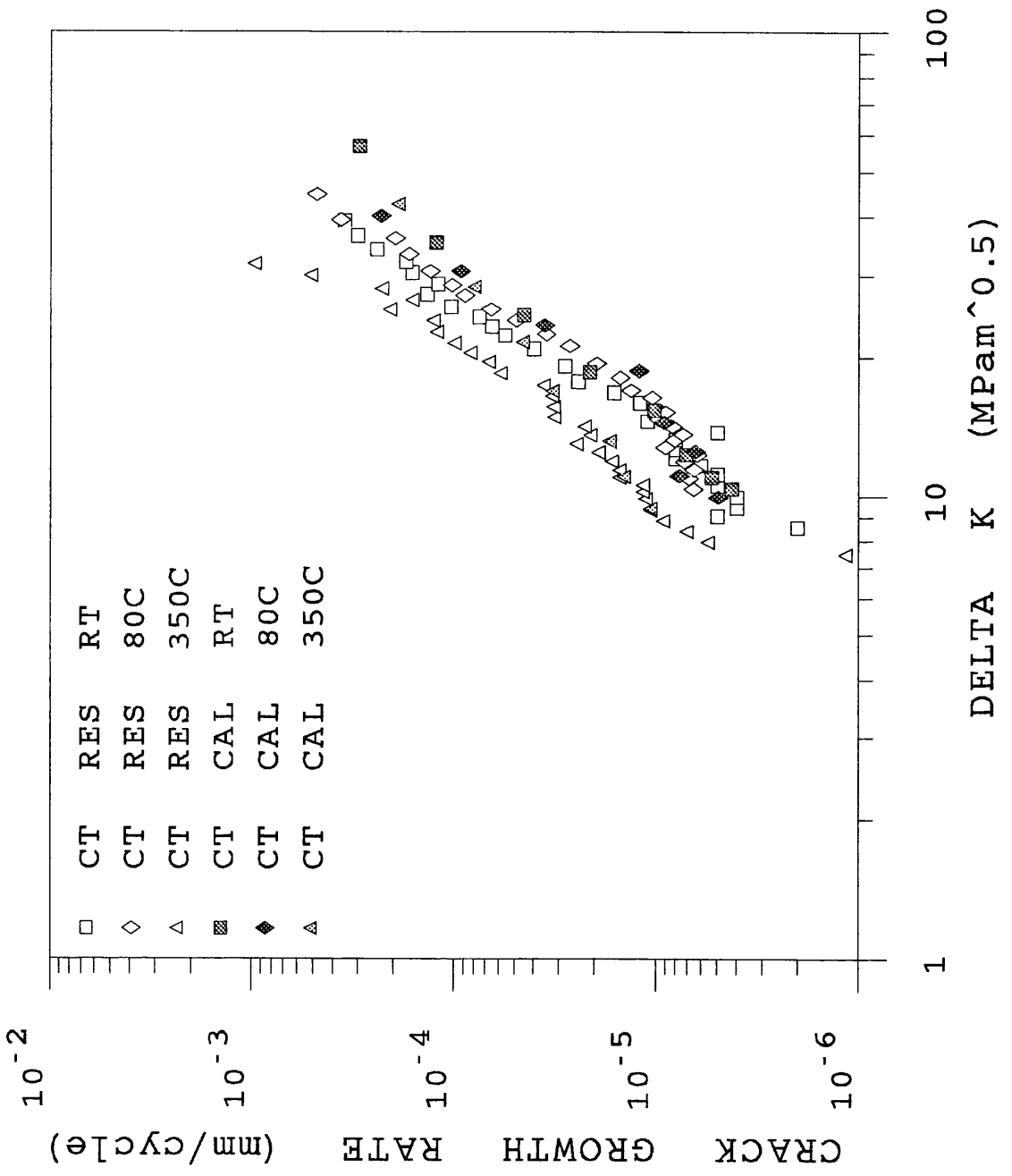


Figure 3.3.14. ICL 167 SPH: CT Fatigue Crack Growth Rate Plots.

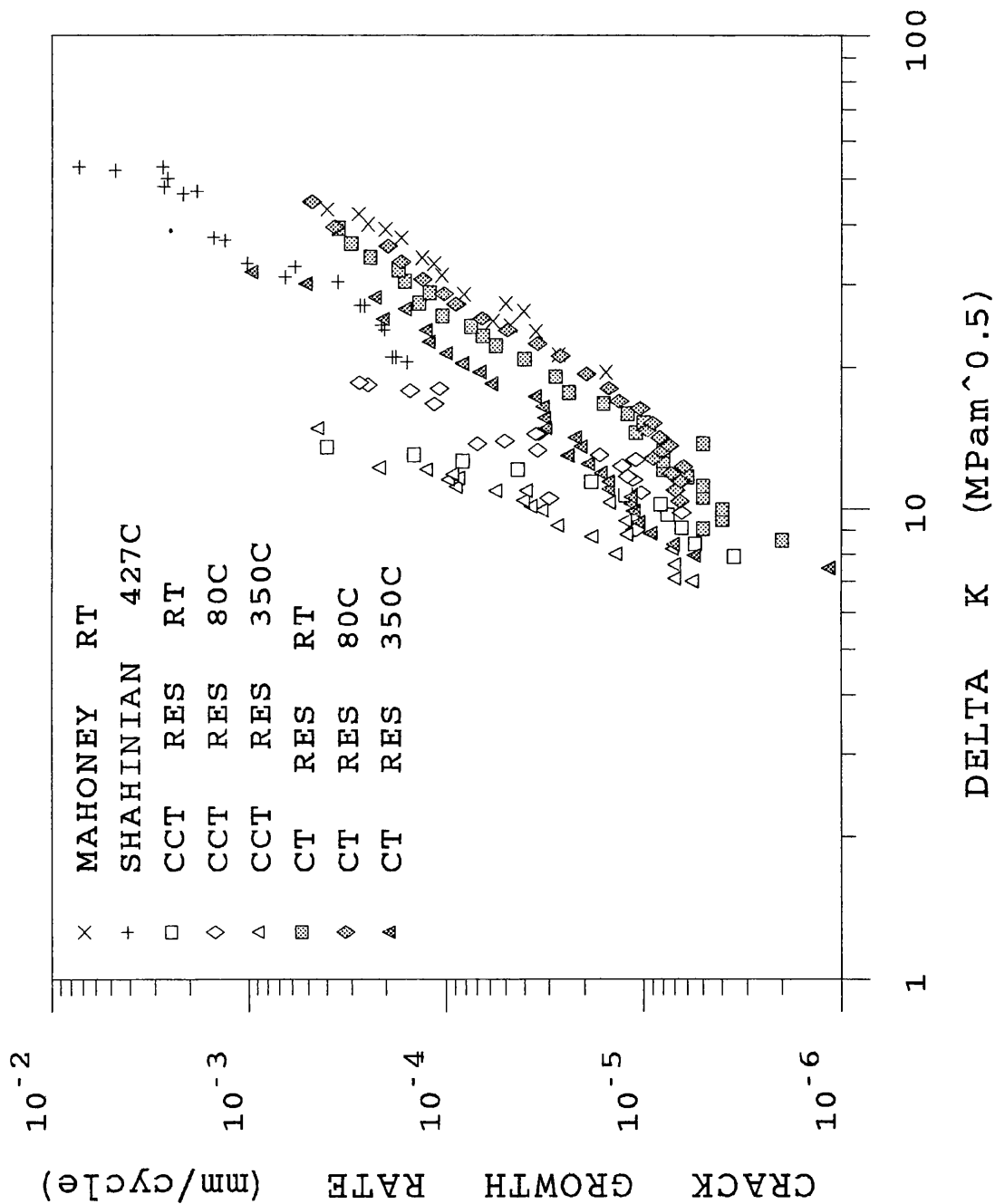


Figure 3.3.15. CT and CCT Results: Fatigue Crack Growth Rates.

3.4. Thermal Fatigue Crack Growth Testing.

3.4.1. Design and Development of Thermal Fatigue Experiments.

The thermal cycling rig was designed to externally heat a tube through a cycling function while internally cooling the tube with a flow of water, as illustrated in Figure 3.4.1. A basic block diagram of the rig was drawn up during the design phase and the main sectors of the rig were identified as;

1. The cooling section
2. The heating system
3. The test component section and
4. The Instrumentation, data logging and control system

Continuous development of each of these sections during both the construction and the commissioning stage resulted in the final experimental set up which is shown in block diagram format in Figure 3.4.2. A box frame was built to support the pipe network, water tank, heating system, specimen section and electronic cables for control and data logging.

3.4.1.1. The Cooling Section.

The purpose of the cooling section was to continuously cool the internal surface of the cylindrical specimen by flowing water through the rig in a closed loop. The cooling section comprises of a water storage tank with an internal pump, which pumps the cooling water through a network of steel pipes (50mm internal diameter, 1mm thickness) to the specimen section. Positioned at significant points throughout the pipe network are flow restricting valves, a flow meter, and a cross-flow heat exchanger, which contains refrigerated freon, as shown in Figure 3.4.2.

The water was pumped from within the buffer tank to the specimen section by-pass valve. Whenever this valve was opened, the flow was directed back to the buffer tank. With the by-pass valve closed the water continued through the main channel towards another switch valve which when closed prevented flow into the specimen section. This valve was closed at pump start-up to avoid a sudden rush of water into the specimen section. With the pump on, the valve was opened slowly to indicate if there were any leaks in the system. If the system was water tight then the valve was completely opened allowing the full flow of the water to continue towards the lowest part of the pipe network where a water discharge valve was situated. With this valve opened, the pipe

network could be drained and when closed the water flow was through a flow meter at 1litre/sec.

The pipe network situated above the flow meter was supported by a horizontal bar clamped between two steel rods running parallel to the specimen section in the frame of the rig. Beyond the specimen section the water flow was through the expansion unit and on to a Y-junction. The expansion unit, (Figure 3.4.3), was designed to allow the specimen section to expand up to 4mm in the vertical direction. Two greased O-rings were positioned within the casing of the expansion unit. The cooling flow pipe from the specimen section was not restricted to travel through the greased O-rings. The contact between the external surface of the flow tube and the O-rings prevented leakage as the system moved. This freedom of expansion prevented end loads being applied upon the test section. The expansion unit was held rigid by another horizontal plate between the two steel support rods. The Y-junction was inserted into the network to allow internal instrumentation without interference to the flow of the water. A long tube barometer and long shielded thermocouples were positioned, through a swage lock fitting at the top of the Y-junction, to measure the water pressure and temperature at the centre of the specimen section. Water flow through the centre of the test specimen section was at a pressure of 2 bars and a temperature less than 30°C.

Beyond the Y-junction the pipe network continued through the adjoining junction of the specimen by-pass and on into the cross-flow heat exchanger. The heat exchanger cooled the water flow through convection of the heat onto a closed-loop flow of refrigerated freon. This unit was controlled by two thermostats, the first of which measured the temperature of the water flowing into the heat exchanger. If the water temperature was below 6°C, the heat exchanger tripped, preventing the water from freezing. The second thermostat measured the water temperature at the outlet of the buffer tank. If the water temperature was higher than required to cool the specimen, then the heat exchanger switched on and the temperature of the freon was reduced to decrease the temperature of the water in the buffer tank.

3.4.1.2. The Heating System.

The basic requirement of the heating system was to produce rapid thermal cycles resulting in a homogeneous temperature profile both around the circumference and along a desired longitudinal length of the specimen. A Celes 50KW Induction Heating System was favoured over alternative methods to produce the rapid heating of the external surface of the specimen. The advantages of this system were the fast heating response, the ease of creating thermal cycles and the adaptability for uniform heating.

The induction heating system contained a 50KW vacuum tube oscillator, a control panel, a step down transformer box and an induction heating coil. The oscillator generated the alternating current to power the system. The control panel contained circuit breakers which could cut the current supply to the coil if either the oscillator has closed down or if the flow rate of cooling water to either the oscillator or the step-down transformer box has decreased. The magnitude of both the voltage and the current supply to the coil was read from a voltmeter and an ammeter on the front of the control panel. The front of the control panel also contained an emergency stop button, which when pressed, immediately cut the current supply to the coil. A voltage supply line was connected to the induction heating control panel from the control system such that the thermal cycle could be programmed from a computer. A relay switch was connected to the flow meter in the cooling system to shutdown the heating system in event of a decrease in cooling water flow to the specimen. Upper and lower flow limits were set at 1.5 and 0.5 litre/sec. If the specimen cooling water flow rate reached the limits then a flow safety switch would be activated to shut down the heating system thus preventing possible overheating of the specimen. The step-down transformer was tuned to give a maximum power of 25KW to the induction coil which was supported at electrical connections on the step down transformer box.

The induction heating coil was manufactured from 1mm thick copper tubing with an external diameter of 6mm. The induction heating coil comprised of six concentric loops, each with an internal diameter of 54mm, to allow space for the positioning of an instrumented tubular component with a suitable gap between the component and the internal surface of the coil. The alternating current flowing through the coil produced a varying magnetic field which induced voltages in both the specimen and the turns of the heating coil. A flow of cooling water was pumped, in a closed loop, through the coil and on through the capacitor banks within the step down transformer box. For further prevention of contact between the coil and the test component, the copper tubing was placed within an insulating sock. The coil was designed to produce a uniform temperature gradient around the circumference and along a length of 20mm at the centre of the component. The length of the coil, which surrounded the test section of the component, from the top loop to the bottom loop, was 41mm. The coil was designed such that the ends of the tubing ran parallel to each other, for a length of 30mm, perpendicular to the external surface, at the centre of the coil. A tapered, conical end feature was soldered on to each of the free ends of the coil, which were screw into position on the step-down transformer box, to give a water tight connection. The transformer box was supported on the main frame of the rig and could be both raised and manoeuvred on PTFE blocks to position the coil accurately, with respect to the

specimen.

The induced current in the testpiece depended on the frequency of the induction heating coil. A supply frequency of 94.5KHz. was selected to produce the desired external surface heating with an appropriate thermal gradient through the testpiece wall thickness.

3.4.1.3. The Test Component Section.

The test component section contained the tubular test section, which was positioned within the induction heating coil, and the necessary end pieces which were required to match the 50mm internal diameter network piping with the test section without disturbance to the cooling water flow.

A thermal analysis performed using a finite difference program, 2DT, [Tartaglia,1989], indicated that the thickness of the material required to obtain the desired thermal gradient was between 7mm and 10mm. A calibration tubular component was manufactured from stock Type 316L stainless steel. The component was 500mm long, 9.5mm thick with a 25mm internal diameter and a 44mm external diameter. A threaded flange was electron beam welded onto each end of the long tube and conical sections were attached to the end flanges to match both the 50mm internal diameter flow meter output and the expansion unit inlet pipes to that of the component. The component was instrumented with 1mm diameter shielded K-type thermocouples which were positioned at various depths around the circumference at the centre of the heated test area. The thermocouples were held in position by nickel brass brazing. An additional number of K-type thermocouples were spot welded onto the external surface, both in rows on the longitudinal direction and around the circumference at the centre of the test area. When an acceptable longitudinal gradient was obtained, the coil was concentrically positioned to obtain a uniform temperature around the external surface. The thermal gradient, (Figure 3.4.4), through a 80°C to 350°C cycle was obtained with 70% power to the induction heating for 5 seconds and a further 20 seconds at zero power.

The thermocouples and potential drop sensing wires often broke away from the external surface, at the spot welds, while the original test section was being placed within the rig. To overcome this problem, the specimen was re-designed to a total length of 120mm, as shown in Figure 3.4.5, of which 100mm remained as a tube with the identical diametric dimensions to that of the 500mm long tube. The heated area remained ± 25 mm from the central circumference with the grip fixings being far enough away to avoid any large change in temperature during the test. The end features were 10mm long at both the top and bottom of each specimen and were machined to match the inner shape of a Leybold

flange clamp, which were used to join the nozzle and diffuser to the specimen. The end features of both the nozzle and the diffuser were identical to those of the specimen. The nozzle, (Figure 3.4.6), was machined from stainless steel tube to merge the network piping to the tubular component, over a length of 89mm, with the minimum possible disturbance to flow. At the 50mm internal diameter, the end features were threaded and contain an O-ring, to give a water-tight match with the screw flange joints of the network piping.

When positioning the specimen, the upper specimen section was raised to the maximum position of the expansion unit and the specimen was positioned within the induction coil. The position of the coil was adjusted so that the component was concentric with the coil over the entire length of the coil. Before clamping the component into position, a 6mm long steel ring of internal diameter 25mm and thickness 1mm was placed in a machined groove in both of the matching surfaces of the nozzle end and the end feature of the test specimen. Ideally this ring should have been made of a stiff, low-conductivity material, such as ceramic, to avoid loss of the potential drop system's input current, from the specimen to the network piping. However the contact area was very small in comparison to the volume of the material. An O-ring was positioned around the outside of the ring and held under compression when the specimen was clamped in place by the Leybold flange clamp.

An identical method was used to connect the upper end feature of the specimen to the diffuser which was positioned below the expansion unit. Once the component was fixed into position, the coil was accurately positioned to develop the desired thermal gradient over the external surface of the component. A fully instrumented specimen section is shown in Figure 3.4.7.

Above the diffuser, an extra section of network piping was inserted to keep continuity within the cooling pipe system. This system has many advantages. At the end of each experiment, the necessary valves in the pipe network were operated to drain the specimen section which allowed the specimen to be replaced with a new fully instrumented specimen. Furthermore, it was possible to test another specimen geometry with the difference in length being taken into account by altering the length of network pipe between the diffuser and the expansion chamber and by raising the position of the induction coil. If the length of the specimen was greatly reduced then the length of the heating coil had to be reduced to avoid heating both the ends of the specimen and the Leybold clamps.

Components with the same geometry and the dimensions, as shown in Figure 3.4.5,

were used for each of the experiments performed. The instrumentation of each component varied as required for each experiment of interest. For both experimental control and continuous monitoring of the thermal cycles each specimen had three K-type thermocouples spot welded at 120° to each other around the centre at the thermal gauge length. A further two K-type thermocouples were spot welded 7.5mm either side of one of the central thermocouples along the axial direction. Before starting the experiment the coil was positioned to give a circumferential gradient of $\pm 1^\circ\text{C}$ at the maximum experimental temperature of 350°C . A corresponding longitudinal gradient of -15°C over the 7.5mm distance either side of the central circumference was produced due to the coil design.

Measurement of the internal surface temperature was obtained with two shielded 1.5mm diameter K-type thermocouples which were spot welded to the internal surface. Two 1.6mm diameter holes were drilled through the thinnest part of the end feature of the component. The thermocouples were fed through and spot welded into positions diametrically opposite at 90° to the fatigue crack initiating notch. To spot weld the thermocouples into position, 5mm of the two wires were exposed and the end was sealed using epoxy resin. Once the thermocouples were spot welded and held in position, the holes at the top of the component were sealed with epoxy resin, thus both the thermocouples were supported and the system was water tight. The temperature of both the water and the ends of the specimen was generally less than 30°C , therefore the epoxy resin could be used without melting. To avoid excessive stresses on the spot welds the external thermocouples were tied to the specimens using thermal resistant string and all of the thermocouples were kept to a maximum length of 100mm from the spot welded junction to a connection plug.

Notches, of approximately 1 or 2mm depths, were machined into either the external or internal surface of the tubular components to encourage crack initiation and to pre-determine the crack growth plane. The notches were located in either the longitudinal or the circumferential plane at the centre of the test specimen. Rectangular or semi-circular notches were electro-eroded along the axial length in the external surface while each of the corresponding longitudinal notches which were electro-eroded into the internal surface were rectangular in shape. The electro-erosion electrode was made from 0.4mm wide copper sheet which produced a notch width of $0.45\text{mm} \pm 0.05\text{mm}$ along the length of the notches. After notching, the specimens were cleaned in an ultrasonic bath and measurements were taken along the length of the notch at a number of positions.

During the course of the experiments matrix rubber moulds of the pre-test notches were produced, using a rubber mixture from Rhodosil Silicones. To prepare the moulds the

specimen was cleaned in an ultrasonic bath, then the rubber compound was poured into the notch under vacuum conditions. After 30 minutes in a vacuum flask the specimen was placed in an oven at 100°C for 2 hours for the rubber compound to thermally set. It was possible to allow the compound to set at room temperature, however this would take up to 48 hours. The moulds were easily removed from the notches, giving an accurate model of the pre-test notch, as shown in Figures 3.4.8a and 3.4.8b. The depth of external notches were found to be in the tolerance of -0.05mm from the desired 1 or 2mm. With internal notches electro-erosion was found to be a difficult process and the tolerance was found to be ± 0.15 mm with 1mm deep notches and ± 0.12 mm with 2mm notches.

Each of the external surface rectangular notches were approximately 15mm long while the lengths of the semi-circular notches were twice the radial depths. One of the components, expt.#12, contained a 2mm deep rectangular notch which was 4mm in length while the 15mm long notch in expt.#8 was electro-eroded to a depth of 4mm. The internal rectangular notches had surface lengths of 16mm and 17mm for the 1mm and 2mm deep notches respectively.

To investigate crack propagation due to the resulting axial stress component of the thermal cycling, fully circumferential notches of approximately 1mm depth were machined into the centre of the test specimen at either the internal or the external surface. Rubber moulds of the pre-test notches displayed the notch cross-section geometries to be semi-circular in shape. In one of the external surface tests, experiment #3, a small section of the notch was spark eroded further to a depth of 2.5mm to investigate whether the crack would grow evenly around the circumference.

For coil positioning and temperature measurement, thermocouples were spot-welded in the same configuration as with the longitudinal notches. Around the central circumference of the gauge length, the thermocouples were positioned at 120° to each other either 0.2mm above or below the external surface notch to avoid the possibility of crack initiation from a thermocouple spot weld. With internal circumferential notches the thermocouples were spot-welded to the internal surface as close to the notch as possible without acting as crack initiation sites.

The potential drop technique has become a widely used method to monitor crack growth in fracture mechanics studies of conventional CT specimens, [Pickard et al.,1975], and tubular components [Hunter et al.,1992]. To monitor the change in potential across the growing crack, the current has to flow perpendicular to the crack. In the tubular components containing a longitudinal notch this entails applying the current across the

diameter of the tube. The original idea was similar to that used by Hunter,[1990], of welding current input rods, 5mm diameter, of Type 316 stainless steel onto the external surface at 90° to the longitudinal fatigue crack initiation notch within the gauge length. Although this method produced an even current distribution across the notch, localised heating, ($+30^\circ\text{C}$), at the rods produced an uneven thermal gradient. Therefore the rods were replaced by curved plates of 3mm thickness which ran the 100mm gauge length with a connection point at the ends of the component for the current supply. Although the localised heating was reduced, the thermal cycling produced stresses between the full length plates and the component resulting in cracking of the welds. The growth of these cracks altered the current field resulting in changes in the potential drop not related to crack propagation from the notch. Therefore the current had to be supplied at a position some distance from the area of heating.

Bench tests were performed to determine the optimum current input positions. Specimens were mapped with a pattern of longitudinal lines every 10° around the circumference and circumferential lines every 10mm along the 100mm tubular section. The 80A direct current, d.c., was supplied at various points between the extremes of the coil and the ends of the tubular section. A uniform flow across the centre of the gauge length was obtained by introducing the current at two points 10mm from the top and bottom of the 100mm long tubular section of the component. For constant current across the longitudinal notches, the negative current leads were positioned 180° around the tube from the positive input leads. For constant current across the circumferential notches, the negative current leads were positioned at the bottom of the component with the positive input leads at the top. To avoid direct flow of current across the upper and lower thirds of the tube, the current input leads were positioned diagonally opposite as shown in Figure 3.4.9. Similarly, diagonal connections were made to produce an even current field across the circumferential cross section with the positive supply leads at the top and the negative leads at the bottom of the component.

To simplify the connection of the current supply leads, four 5mm deep holes were bored into the tubes at the marked positions and were threaded to M5. From stock stainless steel rods, 15mm long pieces were cut and threaded to match the input holes. The current supply leads were fastened onto the threaded rods with copper nuts and washers.

Specimens were isolated at one end and grounded at the other to insulate from the frame. To monitor potential 0.5mm diameter 316L stainless steel probes were spot welded at discrete intervals along the axial length of the longitudinal notch such that two or three probes were attached 5mm either side of the notch itself. The probes were welded onto the external surface to monitor potential change over internal or external notches. Pairs

of probes were welded 2.5mm beyond the notches to detect crack growth in the axial direction from the notch.

The current was introduced at the pre-determined positions and was directed diagonally across the tube. To monitor potential, 0.5mm diameter, Type 316 stainless steel p.d. probe wires were spot welded 10mm apart, across the longitudinal notch. Generally three p.d. probe pairs were positioned across the 15mm long notch, one pair at the centre and the other two 5mm either side. Another pair were often positioned 2.5mm below the notch to monitor crack growth along the surface from the notch in the axial direction. A pair of probes were positioned away from the notch but within the uniform current field for reference p.d. measurements. The p.d. channel numbering system is shown in Figure 3.4.9. A component with two longitudinal notches, positioned 180° around the circumference from each other, could have ten p.d. probe pairs on the external surface. The corresponding p.d. measurements were referred to as CH1, CH2,..., CH10. In later experiments, only eight pairs of p.d. probes were monitored therefore a number of components contained notches with only three pairs of p.d. probes across the notch. Each notch was referred to by a number, i.e. notch number 18/4, in which the first number corresponds to the experiment number and the second number corresponds to the number given to the notch with respect to the number of notches in the component. An instrumented, external, longitudinal notched component is shown in Figure 3.4.10.

For measurement of potential across both internal and external circumferential notches, the direct-current was supplied at the pre-determined positions and directed diagonally from the top to the bottom of the component. The component was instrumented with seven pairs of probes positioned 10mm apart across the notch at equal intervals around the circumference of the component. An additional pair, also 10mm apart, positioned above the notch in the region of constant current, for measurement of the reference potential, as shown in Figure 3.4.11. Each p.d. probe pair were numbered in an identical way to the longitudinal notches, i.e. CH1, CH2,..., CH7 measured the potential across the notch while CH8 measured the reference potential.

To avoid excessive stresses on the welded connections the probes were kept to a minimum length, 100mm, however they were long enough such that the connection plugs were away from the induction coil and the heated region. The length of probes which ran along the length of the specimen through the heated region were covered by insulating socks. The probes were tied to the bottom of the specimens, away from the heated region, to support the probes and to avoid the probes touching the induction heating coil. Similar methods were used to support the probes over circumferential notches.

3.4.1.4. The Instrumentation, Data Logging and Control System.

The data logging and control system consisted of two elements, the thermal cycling and temperature response section and the direct current supply and electrical potential measurement section. A Siemens PCD-2 personal computer was programmed to read the temperatures and potential measurements, save the data on diskettes and control the heating system.

The thermal and temperature response section operated in a closed loop incorporating the instrumented specimen, a Keithley 500A data logger, the computer and the induction heating system. Flexible shielded K-type compensating cables connected the specimen section to the Keithley 500A data logger. Each thermocouple was individually numbered corresponding to an input position on the electronic card within the Keithley 500A which could be directly addressed in the control programme. A series of low pass filters, containing resistor and capacitor circuits, were positioned between the compensating cables and the Keithley 500A data input cards to filter the noise induced upon the signals from the high frequency induction heating system.

The original control program was written in the Basic programming language. This required the percentage power of the induction heating coil to be specified and the computer would send a voltage signal from the Keithley 500A to the induction heating control panel for a specified time interval, in seconds. Six thermocouples were continuously measured by the Keithley 500A, monitored on the visual display unit, VDU, and written to a datafile on a diskette. At the end of the power on period the signal to the induction heating system was cut and the reduction in temperature, due to the internal water cooling of the component, was displayed for a specified power off period. At the end of the power off period, the signal to the induction heating control panel was supplied again and a new thermal cycle began. Before the thermal cycles started a maximum value in temperature was specified in the program, above which the power supply to the heating system would stop and the system shut down.

The direct current for the p.d. measurement was supplied to the component along copper conducting cables from two delta-electronic SM1540-D power packs each capable of generating 40amps direct current. The resistance across the supply terminals was continuously monitored to detect any fluctuations in the supply current. The potential drop measurement probes on the components were connected to the data logging and control system through electrically shielded coaxial cables. Originally the hardware consisted of a combination of a Keithley 197 auto-ranging microvolt digital voltmeter,

which was used to measure the millivolt signals from 10 pairs of potential probes, and a Keithley 196 scanning device which displayed the voltages as an average of ten readings. The scanning device was controlled from the computer. During the heating part of the cycle high frequency interference was observed on the voltage readings therefore the control programme was written to measure potential drop values during the cooling part of the cycle when the induction heating system was off. Arrays of data were written to datafiles on both diskette and the hard disk of the computer for backup. During the initial experiments problems arose when an electrical shutdown occurred and over 5,000 cycles worth of data was lost, expt.#2, and in a very rare instance, a fault in the data diskette forced the program to stall during the heating part of the cycle and the specimen was held at high temperature for a period of time during the night, expt.#5. Therefore the control program was developed to include a command that would cut the signal to the induction heating system if the external surface temperature exceeded a specified value.

During the course of the experiments, an electronic card for the Keithley 500A was purchased which enabled the voltage readings to be logged by the Keithley 500A via an eight channel d.c. amplifier. With a reduction in the number of p.d. channels, the opportunity arose to increase the number of measurements during a cycle the control programme was altered and rewritten in the Quick Basic language to enable faster temperature control.

The Quick Basic language enabled the constant monitoring of three thermocouples, one of which was selected to control the thermal cycles at the external surface, along with the measurements from eight p.d. channels at two specified temperatures during the cooling part of the cycle. For each pair of p.d. probes, the mean of the p.d. values every 100 cycles were written to a high temperature and a low temperature data file on a diskette. Every 1000 cycles the data files were closed and new data files were opened, therefore if an electrical failure occurred the maximum amount of data lost would be less than 1000 cycles worth. The thermal control avoided any possibilities of overheating of the component at the position of the control thermocouple. Two other K-type thermocouples, positioned around the centre circumference of the tube were monitored for comparison. Other internal and external surface thermocouples were randomly checked using a Eurotherm multichannel digital thermometer.

If error commands were to occur, due to either data disk problems, electrical components failure or measurement of p.d. or voltage from thermocouples beyond the specified range, then a string in the control program could stop the power supply to the induction heating system. This prevented the rig from continuing to run with faulty measuring instruments. Following necessary repair work to the instrumentation, the

program could be restarted and the thermal cycling would continue. The error commands prevented the program from stalling during the power on part of the cycle and holding the component at maximum temperature for a period of time. Unfortunately nothing could prevent the loss of data due to a break in the mains electricity supply as no back-up to the electrical power supply was available. A string was written into the program enabling the diskette to be changed during the cooling part of the cycle. Thus the possibility of the program crashing when trying to write data to a full diskette was avoided.

3.4.2. Thermal Fatigue Experimental Procedure.

The method of experimentation was the same whether the component was unnotched or notched. Before assembly, the component was instrumented with thermocouples in the specified locations for positioning the coil and controlling the thermal cycles and with potential drop measurement probes. The instrumented component was fed through the induction heating coil and both were carefully positioned such that the component was in line with the lower nozzle in the specimen section.

The cooling water pump was switched on and if no leakage was detected then the current input leads were fastened into position and the thermocouples and p.d. probes connected to their respective data logging cables. The 80amps direct current power pack was switched on. After fifteen minutes values of the resistance across the supply leads were recorded and the connections of both the p.d. probes and the thermocouples were checked by measuring the values from each. The taps for the cooling water to the induction heating generator, the capacitance chamber and the induction coil were opened, the generator was switched on and the control panel was switched to stand by. The safety trip switch, relayed by either the flow meter or the computer programme was switched on. The induction coil was positioned such that it appeared concentric around the component.

Both the Siemens computer and the Keithley 500A were switched on and an empty formatted data disk was placed in the disk drive. The control programme was started, cycling the external surface temperature between 22°C and 26°C and recording potential drop measurements at 23°C and 25°C. This produced pre-test room temperature readings and indicated if all thermocouples and p.d. probes were reading properly.

With these criteria satisfied another control programme was started which produced real time displays of selected thermocouple readings on the screen. Using this programme the coil was positioned to give both an even longitudinal, (axial), thermal gradient and an

axisymmetric thermal gradient around the circumference at the centre of the gauge length. Each thermocouple was recorded through a number of experimental cycles, as shown in Figure 3.4.12., for an internal and an external surface measurement. A micrometer was positioned above the extension unit to measure axial extension during cycling.

For the experimental programme to run a number of important criteria had to be specified both for providing the required simulation of the fusion reactor first wall thermal cycle and for acquiring the experimental data;

1. Required percentage power of Induction Heating Power: 70%.
2. Maximum temperature of heating cycle at external surface: 350°C.
3. Minimum temperature of cooling cycle at external surface: 80°C.
4. High temperature to record 8 p.d. channels during cooling cycle: 275°C.
5. Low temperature to record 8 p.d. channels during cooling cycle: 95°C.
6. External surface control thermocouple #: 12.
7. Thermocouple #. to monitor for comparison: 13.
8. Thermocouple #. to monitor for comparison: 14.
9. Number of cycles at which test starts: 0.
10. Data file identification: T#a.

Upon pressing the enter command the experiment would begin with the measurements and the corresponding number of cycles performed continuously displayed on the VDU. The external surface test temperature was controlled to 350°C \pm 2°C at high temperature and 80°C \pm 1°C at the low temperature, while the internal surface temperature was recorded to \pm 1°C over range of readings from 40°C to 80°C.

With computer control the experiment could be terminated whenever required, such as after a certain number of cycles or when a desired change in potential drop calibrated to a certain crack depth was reached. In the rare event of a shutdown due to either a reduction in cooling water flow, to either the specimen section or the induction heating coil, or an electrical failure or a disk failure, the fault could be repaired and the programme restarted with the number of cycles performed specified and a new data file name given.

As a consequence of the investment of the extensive effort described in designing the thermal cycling experiment, the reliability of the equipment was unusually high for such a complex experiment. Although considerable time was required before the experiments could commence, once started, the equipment could run unabated allowing a total of twenty-five experiments to be performed in the time available. A summary of the

experiments performed have been grouped in terms of the initial notch shape, location and position within the component, Tables 3.4.1a-e, while the experimental conditions in the miscellaneous experiments performed on unnotched components are given in Table 3.4.1f.

Expt. Number	Notch Number	Notch Depth (mm)	Notch $\frac{1}{2}$ Length (mm)	Number of Thermal Cycles	Remarks
2	2.1	0.94	7.50	52,236	
4	4.1	0.97	7.50	51,740	
4	4.2	0.94	7.50	51,740	
11	11.1	1.00	7.50	81,000	Heat Tint at 50,500 Cycles
18	18.1	1.04	7.50	40,500	
18	18.2	1.01	7.50	40,500	
18	18.3	1.08	7.50	40,500	
18	18.4	1.03	7.50	40,500	
22	22.1	0.99	7.62	16,200	Heat Tint at 7,000 Cycles
23	23.1	1.03	7.50	79,000	
24	24.1	1.00	7.59	4,000	
5	5.1	1.95	7.5	42,400	Over Heat at 26,090 Cycles
12	12.1	1.98	7.50	55,000	
12	12.2	1.98	2.01	55,000	
22	22.2	2.00	7.5	16,200	Heat Tint at 7,000 Cycles
23	23.2	1.94	7.5	79,000	
24	24.2	2.00	7.59	4,000	
8	8.1	4.00	7.50	50,705	

Table 3.4.1a Experimental Matrix for Thermal Cycle Fatigue of Tubular Components Containing Longitudinal Rectangular Shaped Notches in the External Surface.

Expt. Number	Notch Number	Notch Depth (mm)	Notch $\frac{1}{2}$ Length (mm)	Number of Thermal Cycles	Remarks
1	1.1	0.88	8.00	34,118	
2	2.2	0.90	8.00	52,236	
9	9.1	0.85	7.99	50,080	
16	16.1	0.97	8.01	22,000	
17	17.1	0.95	7.96	64,600	
1	1.2	1.88	8.25	34,118	
16	16.2	1.22	8.01	22,000	
17	17.2	1.97	8.69	64,600	

Table 3.4.1b Experimental Matrix for Thermal Cycle Fatigue of Tubular Components Containing Longitudinal Rectangular Shaped Notches in the Internal Surface.

Expt. Number	Notch Number	Notch Depth (mm)	Notch $\frac{1}{2}$ Length (mm)	Number of Thermal Cycles	Remarks
8	8.2	0.92	0.92	50,705	
13	13.1	1.00	1.00	31,000	
19	19.1	1.00	1.00	69,620	Heat Tint at 43,000 Cycles
5	5.2	1.97	1.97	42,400	Over Heat at 26,090 Cycles
13	13.2	2.00	2.00	31,000	
19	19.2	2.00	2.00	69,620	Heat Tint at 43,000 Cycles

Table 3.4.1c Experimental Matrix for Thermal Cycle Fatigue of Tubular Components Containing Longitudinal Semi-Circular Shaped Notches in the External Surface.

Expt. Number	Notch Number	Notch Depth (mm)	Number of Thermal Cycles	Remarks
3	3.1	0.98	39,300	Heat Tint at 26,300 Cycles
3	3.7	2.44	39,300	1mm Notch Eroded to 2.5mm
15	15.1	1.00	81,600	

Table 3.4.1d Experimental Matrix for Thermal Cycle Fatigue of Tubular Components Containing Circumferential Notches in the External Surface.

Expt. Number	Notch Number	Notch Depth (mm)	Number of Thermal Cycles	Remarks
6	6.1	0.90	72,785	
20	20.1	1.00	52,000	
25	25.1	1.00	25,000	

Table 3.4.1e Experimental Matrix for Thermal Cycle Fatigue of Tubular Components Containing Circumferential Notches in the Internal Surface.

Expt. Number	External Surface Treatment	Number of Thermal Cycles	Remarks
7	One Spot Welded Zone	16,700	Cycled Between 80 °C and 600 °C
10	Laser Welded Zones: Spots and a Longitudinal Line	55,100	Cycled Between 80 °C and 350 °C
14	Laser Welded Zones: Spots and a Longitudinal Line	14,010	Cycled Between 80 °C and 450 °C
21	a) Laser Welded Spots With Small Cracks b) 1mm Deep Hole With Diameter of 1mm c) 2mm Deep Hole With Diameter of 2mm	65,105	Cycled Between 80 °C and 350 °C

Table 3.4.1f Experimental Matrix for Thermal Cycle Fatigue of Various Unnotched Tubular Components.

With externally notched specimens there was the possibility of interrupting the experiment to heat tint the fracture surface at a higher temperature, 500 °C, for a short time (1min.). Before restart potential drop reading were recorded at room temperature for comparison with the pre-test and pre-heat tint values, which could be compared to the marked crack depth on the fracture surface. As indicated in Table 3.4.1f, a number of experiments were carried out on specimens with no electro-eroded notches. Experiment #7 was performed to investigate the effects of cycling to a higher temperature since no crack initiation had occurred from the free surface of a tube cycled between 80 °C and 350 °C, external surface temperatures. Experiment #10 was performed to investigate the possibility of crack growth from a line or spots of the external surface which were melted and re-solidified using a laser beam. This test was continued as experiment #14 at a higher temperature range. Experiment #21 was performed to investigate the effects of thermal cycling on a tube containing bored holes and laser welded spots which had been produced using a high powered beam for a short space of time resulting in cracking of the surface of the laser welded spot.

When the experiment was completed a simple procedure was carried out in each case.

Room temperature readings of potential drop were taken before the induction heating system was closed down and the current supply was switched off. All cooling water flow was stopped and the specimen section was drained. The power supply cables were disconnected along with the plugs connecting the probes and thermocouples on the specimen to the data logging and control system. The specimen was removed for surface inspection, photography and post-test metallographic investigations. The specimen was sectioned, mounted and polished across the p.d. probe positions. The sections were etched and the crack depths were measured to plot against the corresponding values of normalised potential difference. With an instrumented specimen ready it was possible to stop one test and have another running within the same day.

3.4.3. Calibration of the Crack Growth Monitoring System.

To relate the experimental potential measurements across the notch to the depth of the fatigue crack, a series of calibration curves were required for each individual notch position and orientation.

3.4.3.1. Calibration For Longitudinal Notched Components.

The initial calibrations were performed on sheets of aluminium foil which were cut to a shape of the circular cross section of the tubular component at a scale ten times that of the actual component. The 3amps d.c. supply leads were attached to the external surface, at positions 180° apart. At 90° to the current supply positions, a radial cut was made with a blade in increments from either the external or internal surface of the model, to represent the crack growth. The corresponding potential measurements for each cut were taken on the external surface across the cut line, with the p.d. probe pairs positioned a scaled distance apart to represent the actual probe positions across the centre of a longitudinally notched specimen. The calibration curves for both the internal and external cuts were plotted in terms of a normalized potential difference, $V^*=(V-V_0)/V_0$, where V is the potential drop across a cut of depth "a", in mm, and V_0 is the initial potential drop at a depth of cut corresponding to the depth of the electro-eroded notch, Figure 3.4.13 and 3.4.14.

The advantage of this method of generating calibration curves is simplicity. It is not always favoured, [Aronson and Ritchie,1979], due to inaccuracies in measurements, especially at shorter crack lengths, however it does produce an initial estimate of crack depth from p.d. measurements. A combination of the current input positions, the complex current field around the longitudinal notch and the 2-dimensional nature of the

aluminium foil model in comparison to the 3-dimensional test components brought about the necessity to additionally examine actual test specimen geometries for calibration.

A calibration of the potential drop measurements with the increasing depth of a rectangular electro-eroded notch was performed on an unnotched tubular component within an electro-erosion machine. The specimen was held in position within a bath of electrolyte fluid while the 0.5mm thick copper electrode was forced through the thickness of the component from the external surface. The 80amps d.c. current was supplied through identical copper leads at identical positions on the specimen as performed in the thermal fatigue experiments. Four pairs of p.d. probes were spot welded across a longitudinal line drawn on the external surface of the component and the 15mm long electrode was positioned onto the line between the probe pairs as accurately as possible. Following each 0.5mm increment of electro-erosion, the electrode was removed from the specimen and potential measurements across the notch were recorded. Potential measurements were made at various depths of electro-erosion through the thickness of the specimen to represent increments of crack propagation. Following the final measurement, the tube was removed from the electro-erosion machine, sectioned across the notch, polished and the depth of the notch was found to be less than that indicated by the digital display on the electro-erosion machine, as is usual due to erosion of the copper electrode. The values of eroded depths were multiplied by the fraction of difference between the actual final depth and the indicated value on the digital display, then plotted against the normalized potential difference, (Figure 3.4.15). A similar technique was employed to produce the calibration curves for the eroded notch depth from the internal surface of a tubular component, (Figure 3.4.16).

With the internal surface calibration method, difficulties arose both in eroding a deep notch through the tube, a section had to be removed from the component to allow access of the electro-erosion plate to the internal surface and in assuring that the direction of the notch remained within the p.d. probe pairs on the external surface. The increased current field through the reduced volume of the component had to be taken into account when determining the normalized potential difference for each increment of notch erosion.

The electro-erosion calibration did give an indication of the performance of the potential drop equipment with the given geometry and displayed an increase in the potential difference with increasing notch depth. Similarities with the aluminium foil calibration curves were observed at very short notch depths, however differences appeared due to the greater potential change in the aluminium foil model with a deeper crack. although it is possible that the electro erosion calibration did not accurately simulate the progression of a fine fatigue crack growing from a notch, it was decided to use the calibration curve

from the electro-eroded component to estimate the crack depth during the initial thermal fatigue experiments. The calibration curves from the aluminium foil calibration were retained for comparison with the experiments if the resultant normalized potential differences were greater than expected following the electro-erosion calibration.

In order to introduce the p.d. dependence of real cracks into the calibration it was decided to perform a number of tests with similar notches, identical current paths and p.d. probe positions under the same testing conditions, each for a different number of cycles for direct comparison with the electro-erosion and foil calibrations.

3.4.3.2. Calibration For Circumferential Notched Components.

An idea to perform an electro-erosion calibration of a circumferential notch through a tubular component was abandoned due to problems in accurately representing the increasing curvature of the crack front as a crack propagates from the external surface through the thickness of the component. It would have been practically impossible to do likewise with an electro-eroded circumferential notch from the internal surface therefore it was decided to create calibration curves using aluminium foil models. A thin aluminium foil, 600mm long and 47.5mm wide, was cut to represent a longitudinal section of the tube at a scale of 5 to 1. A direct current of 3A was introduced through leads attached at the corresponding positions across the plane of the notch. Potential measurements were recorded from the external surface over the centre of the foil as a cut was made in increments from either the external or the internal surface to represent the crack propagation. The resultant calibration curves are shown in Figure 3.4.17.

The advantage of the circumferential notch experiments is that up to seven pairs of p.d. probes may be positioned around the notch during each experiment, therefore only a small number of experiments were required to produce many values of normalized potential difference with the corresponding measurements of actual crack depth.



Figure 3.4.1. Thermal Cycling Rig.

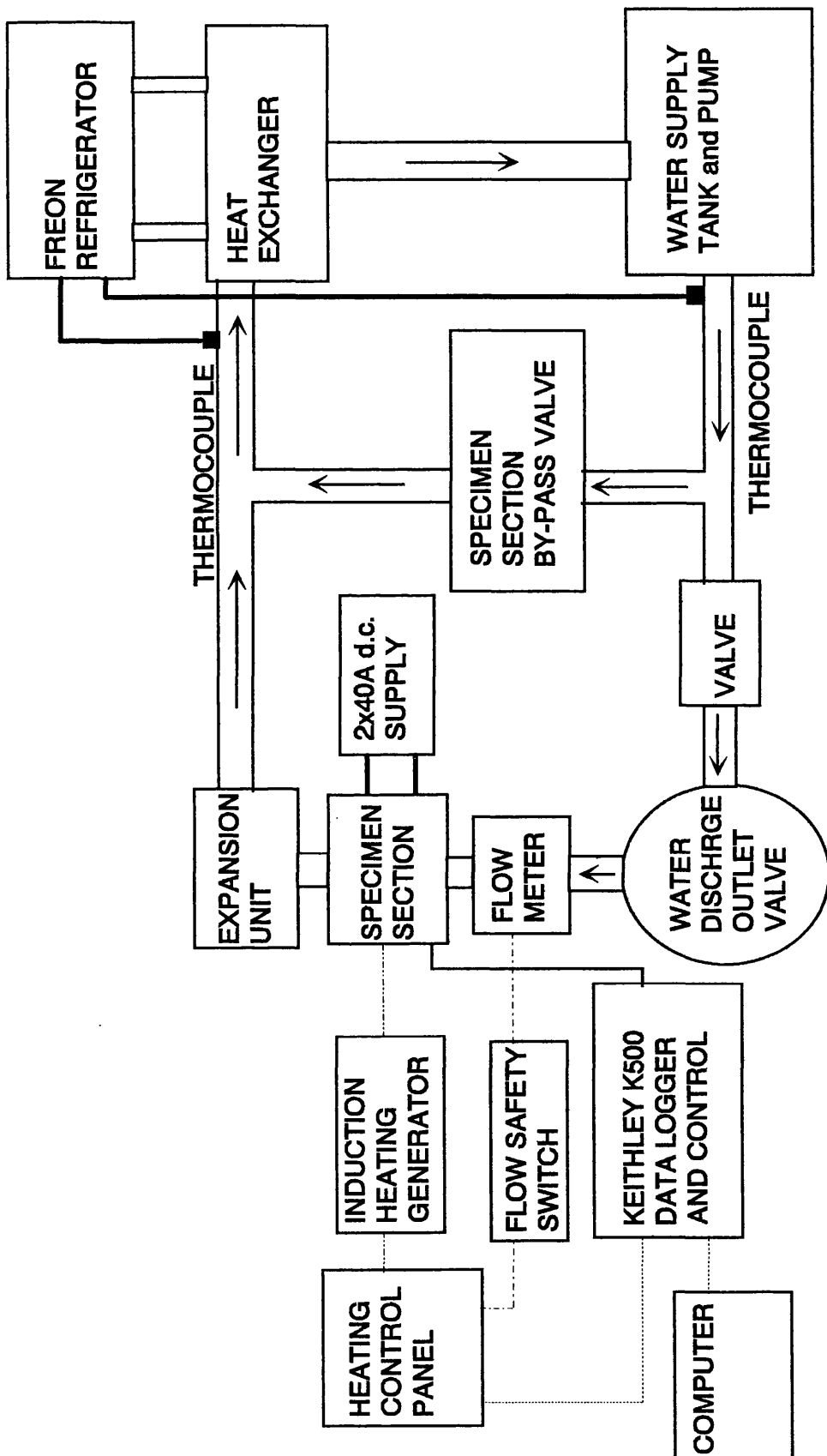


Figure 3.4.2. Block Diagram of the Thermal Cycling Rig.

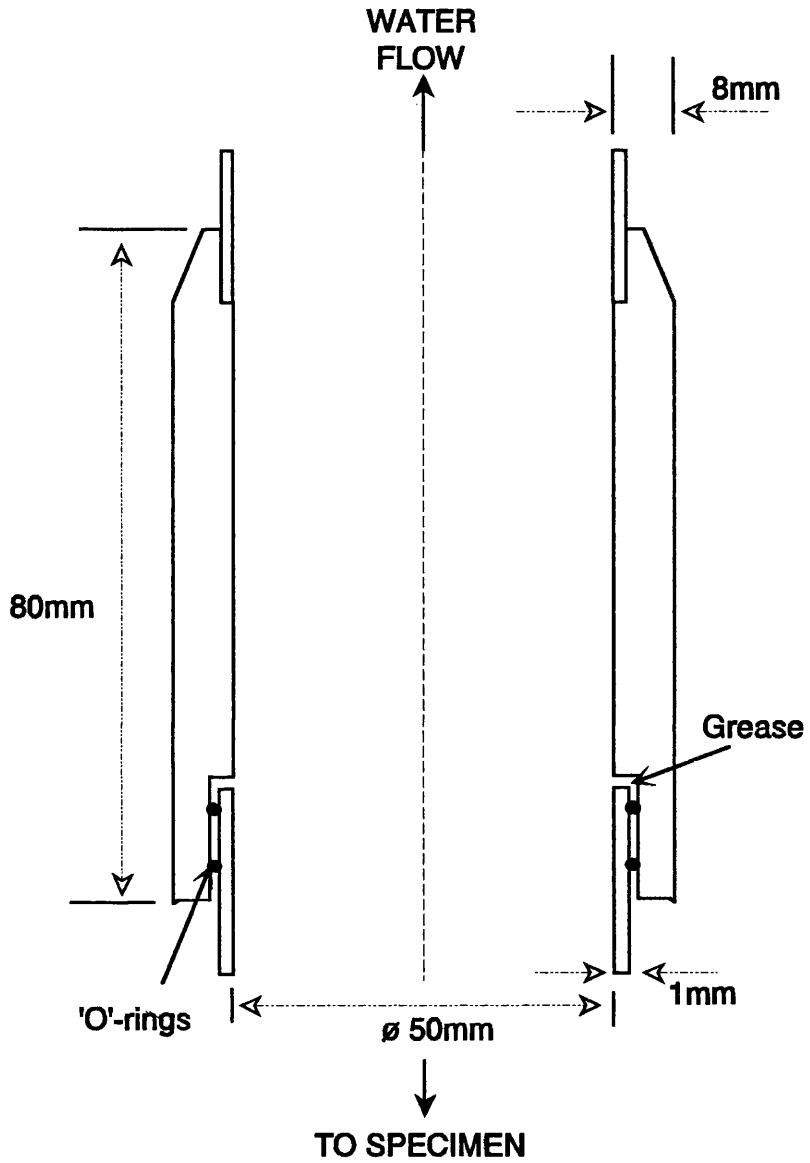


Figure 3.4.3. Cooling System Expansion Unit.

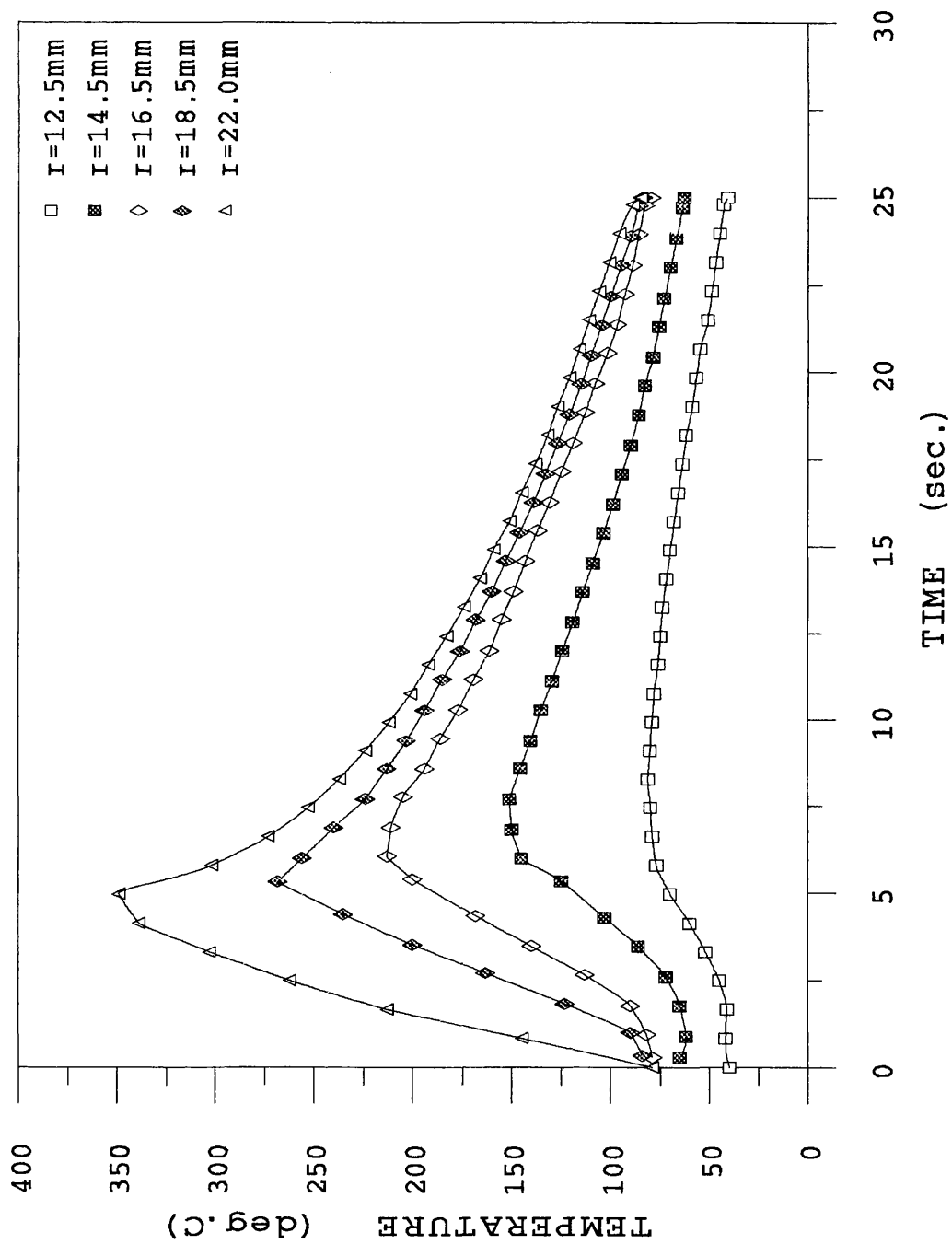


Figure 3.4.4. Thermal Gradient Through Tube Thickness During a Cycle.

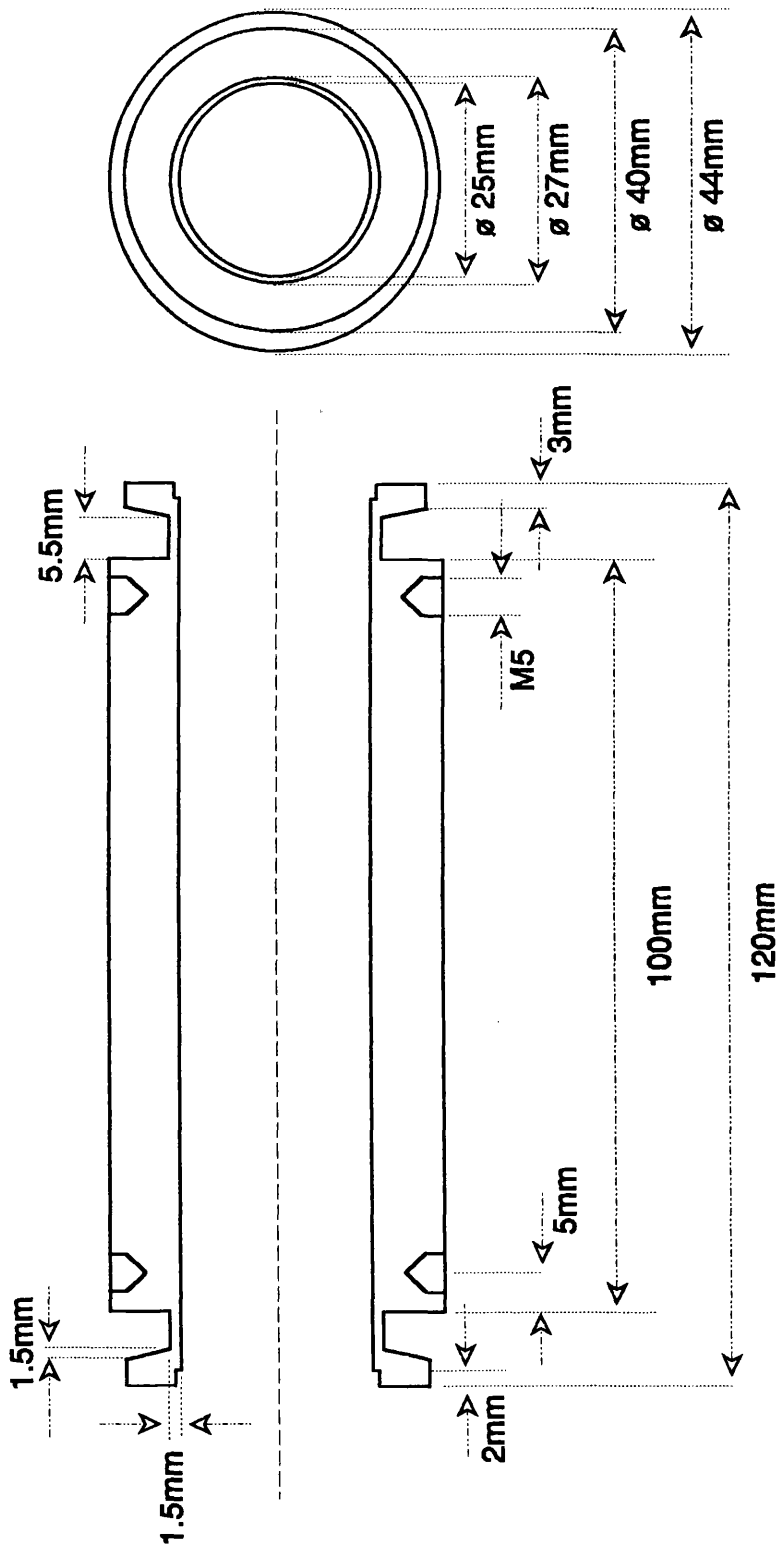


Figure 3.4.5. Dimensions of a Tubular Component.

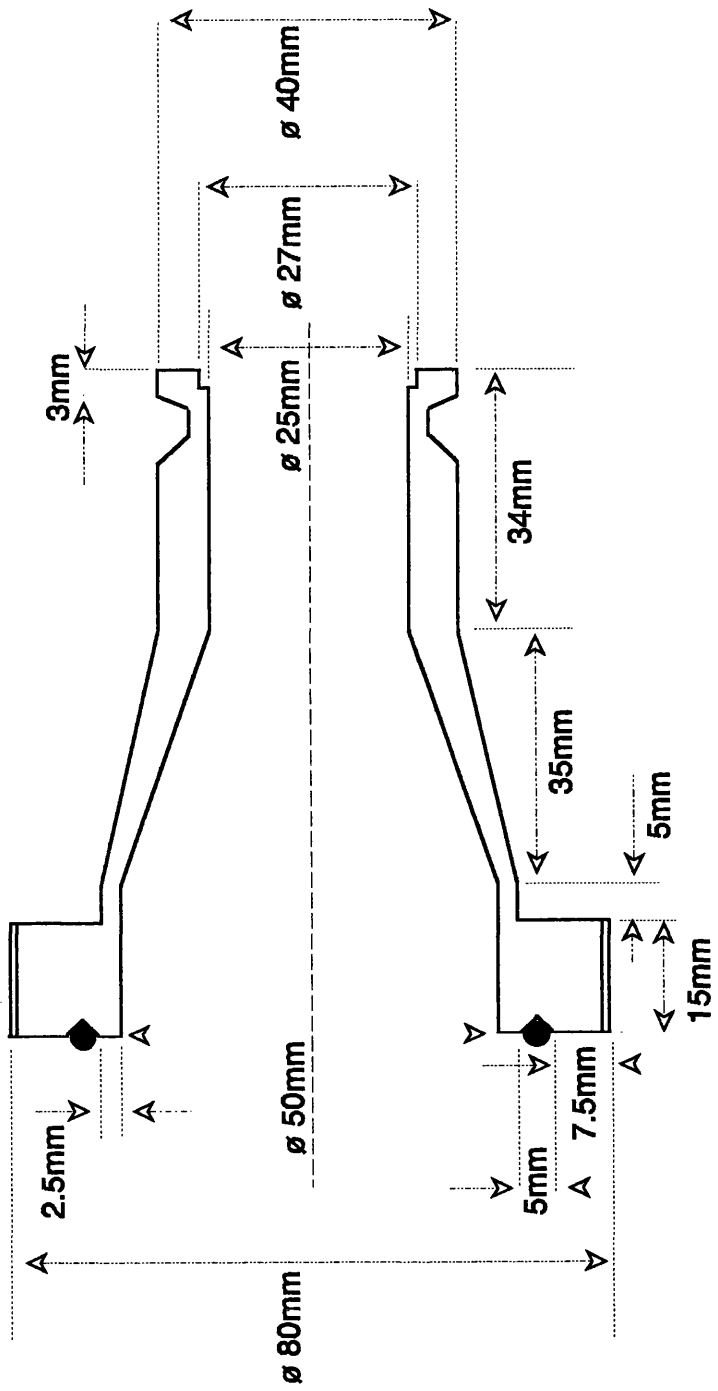


Figure 3.4.6. Dimensions of the Nozzle Section.

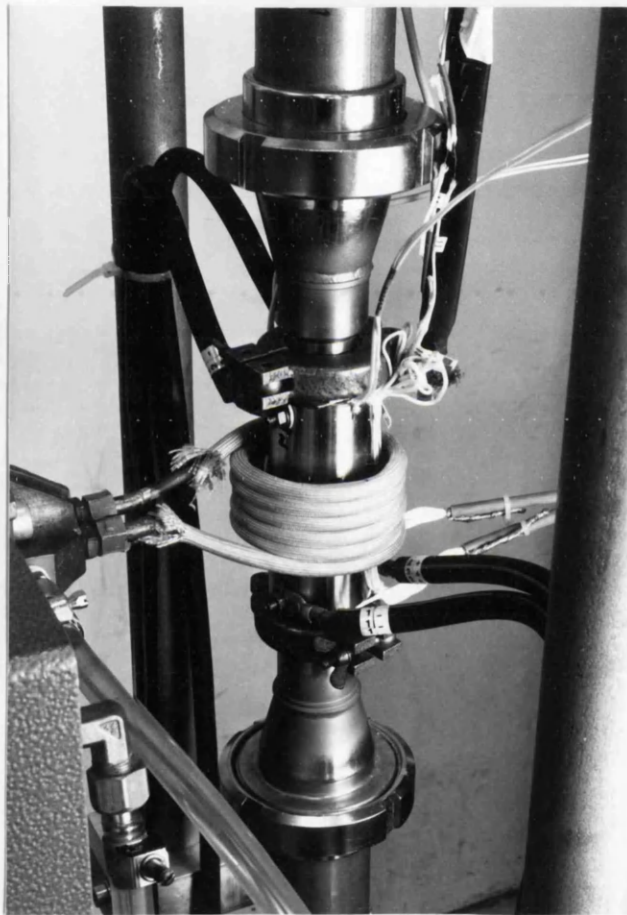


Figure 3.4.7. Instrumented Specimen Section Containing a Tubular Component.

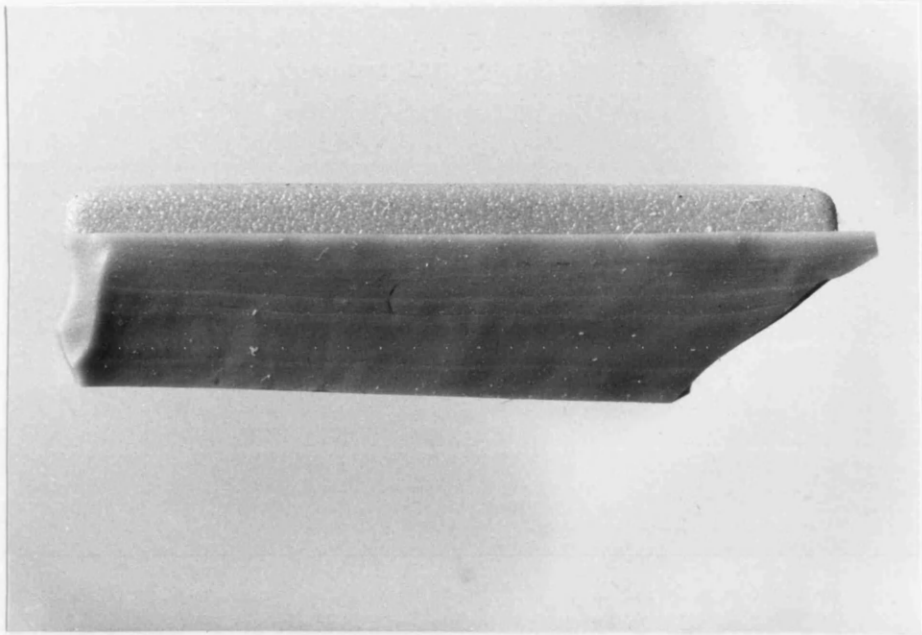


Figure 3.4.8a. Rubber Mould of Pre-Test Rectangular Notch Shape, (Mag.X6.9).

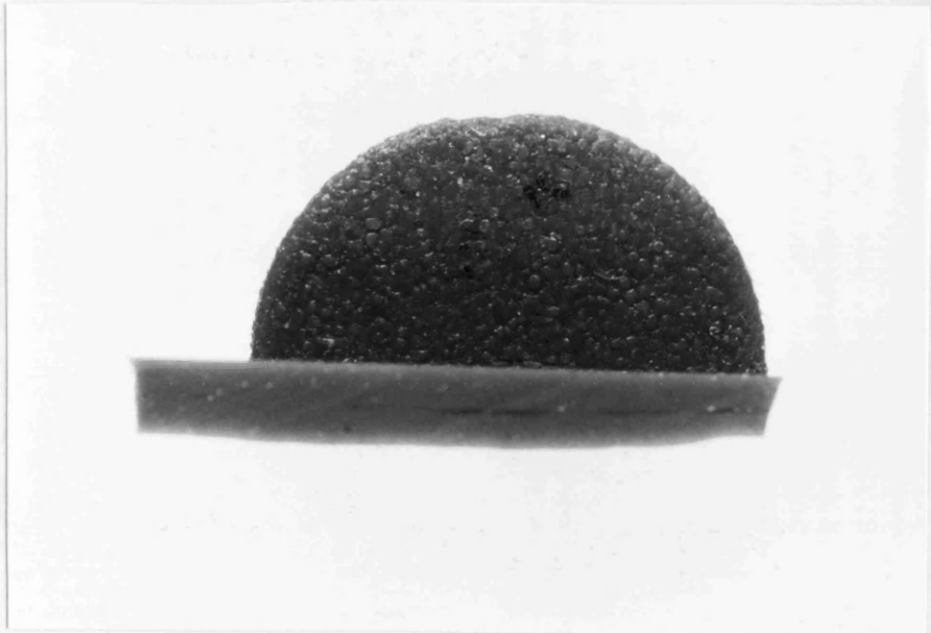


Figure 3.4.8b. Rubber Mould of Pre-Test Semi-Circular Notch Shape, (Mag.X16.9).

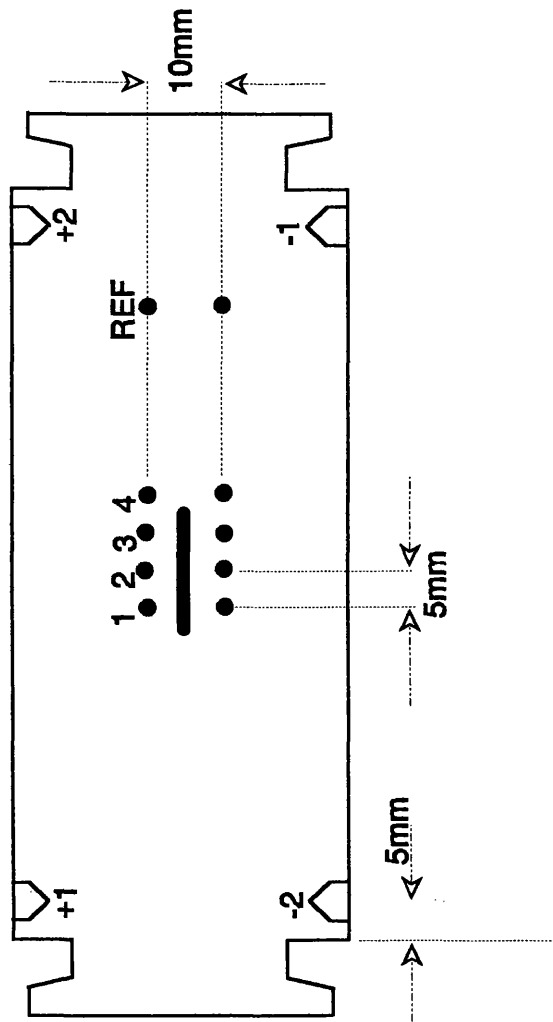


Figure 3.4.9. Tubular Component with Direct Current Input Positions and Potential Measurement Probe Positions.

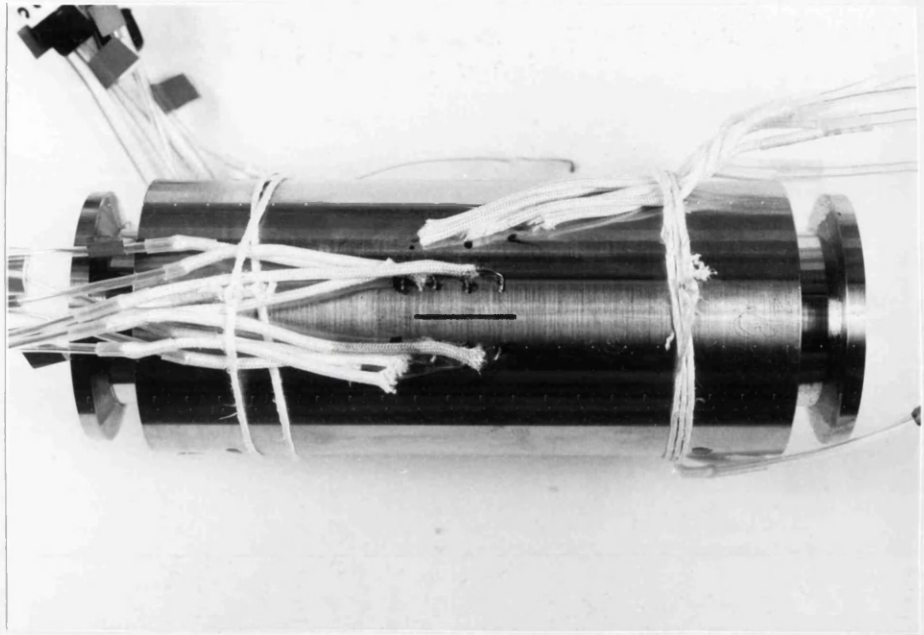


Figure 3.4.10. Instrumented Component with a Longitudinal Notch, (Mag.X0.88).



Figure 3.4.11. Instrumented Component with a Circumferential Notch, (Mag.X0.57).

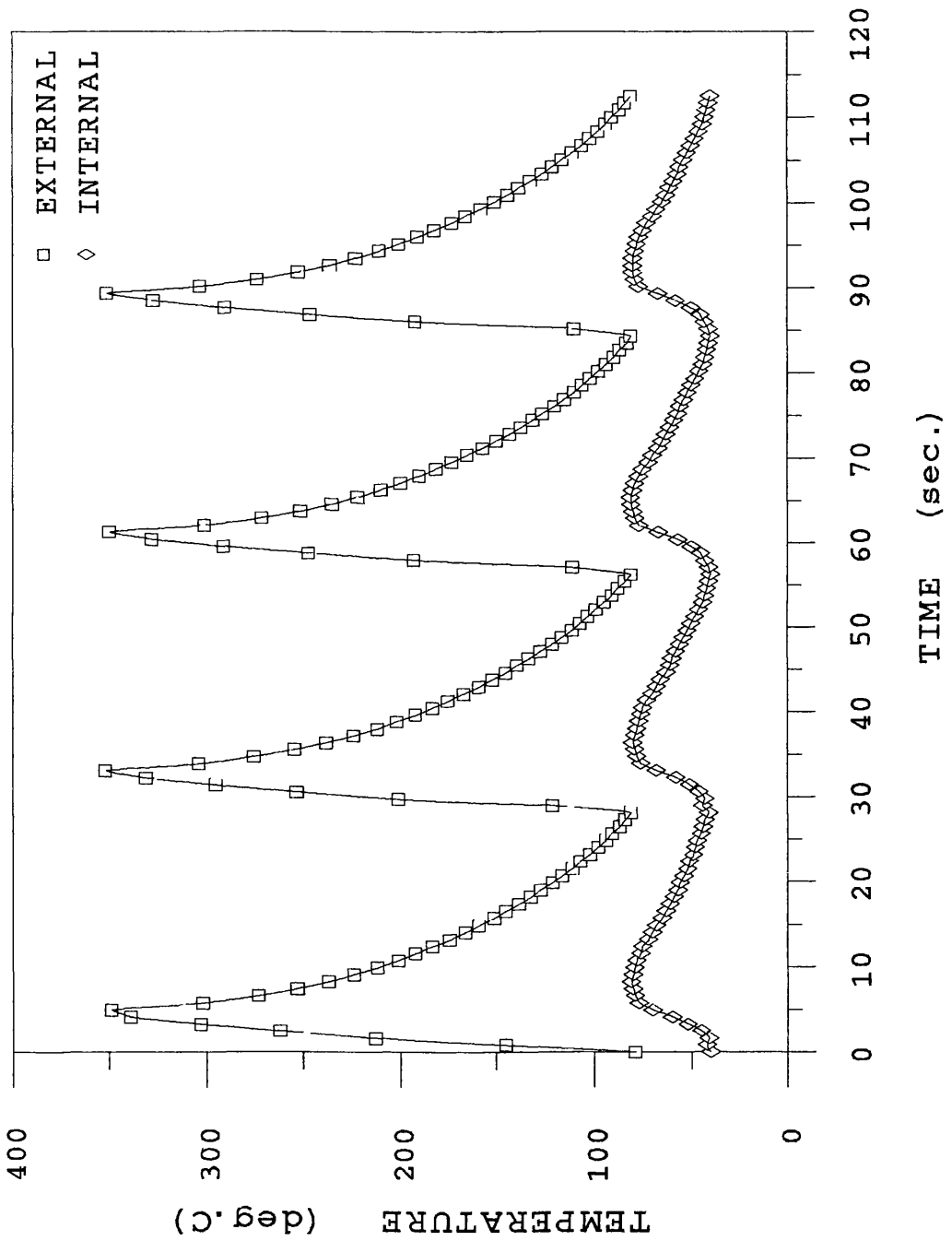


Figure 3.4.12. Surface Temperature Measurements During Thermal Cycling.

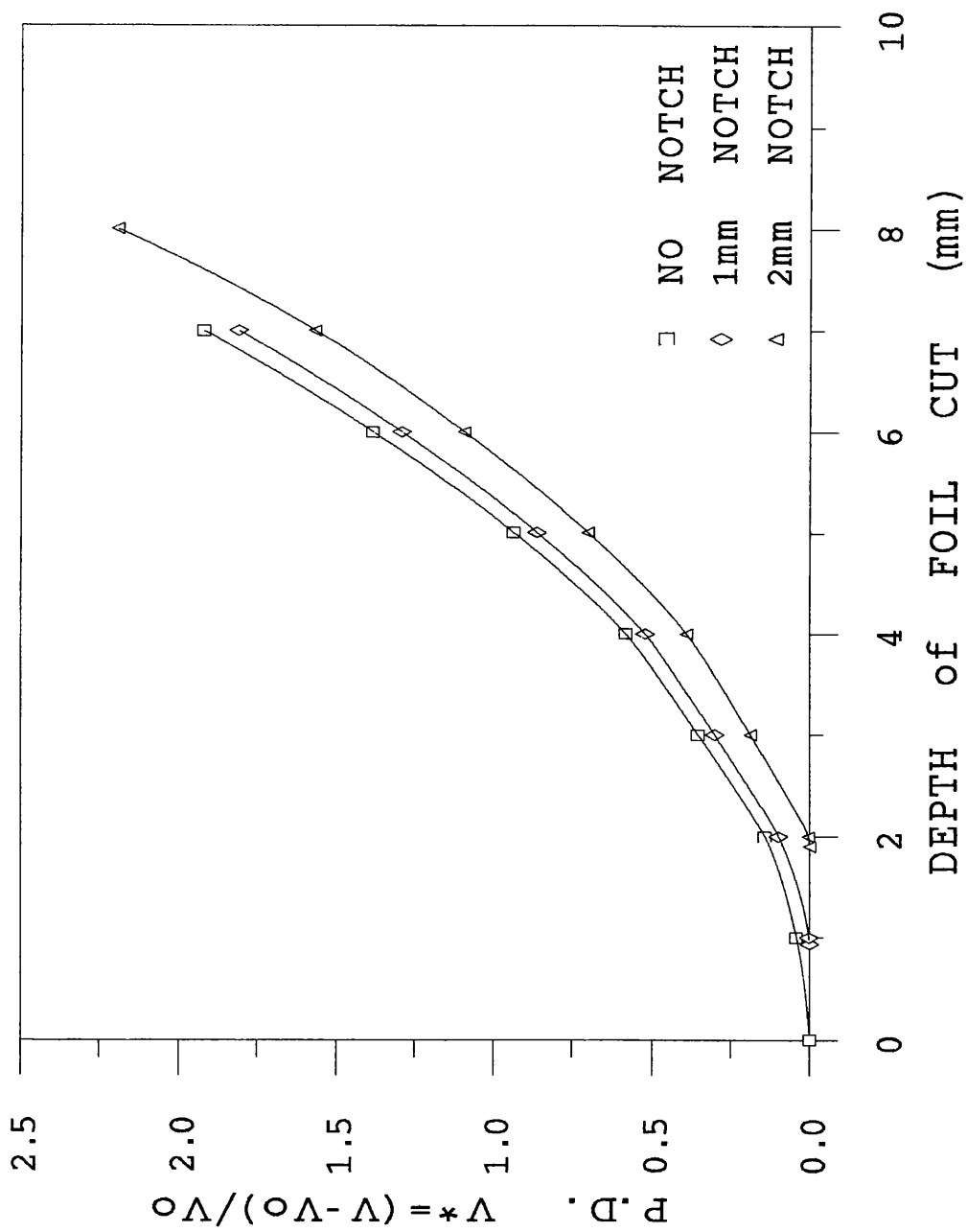


Figure 3.4.13. Aluminium Foil Calibration Curves For External Longitudinal Notched Components.

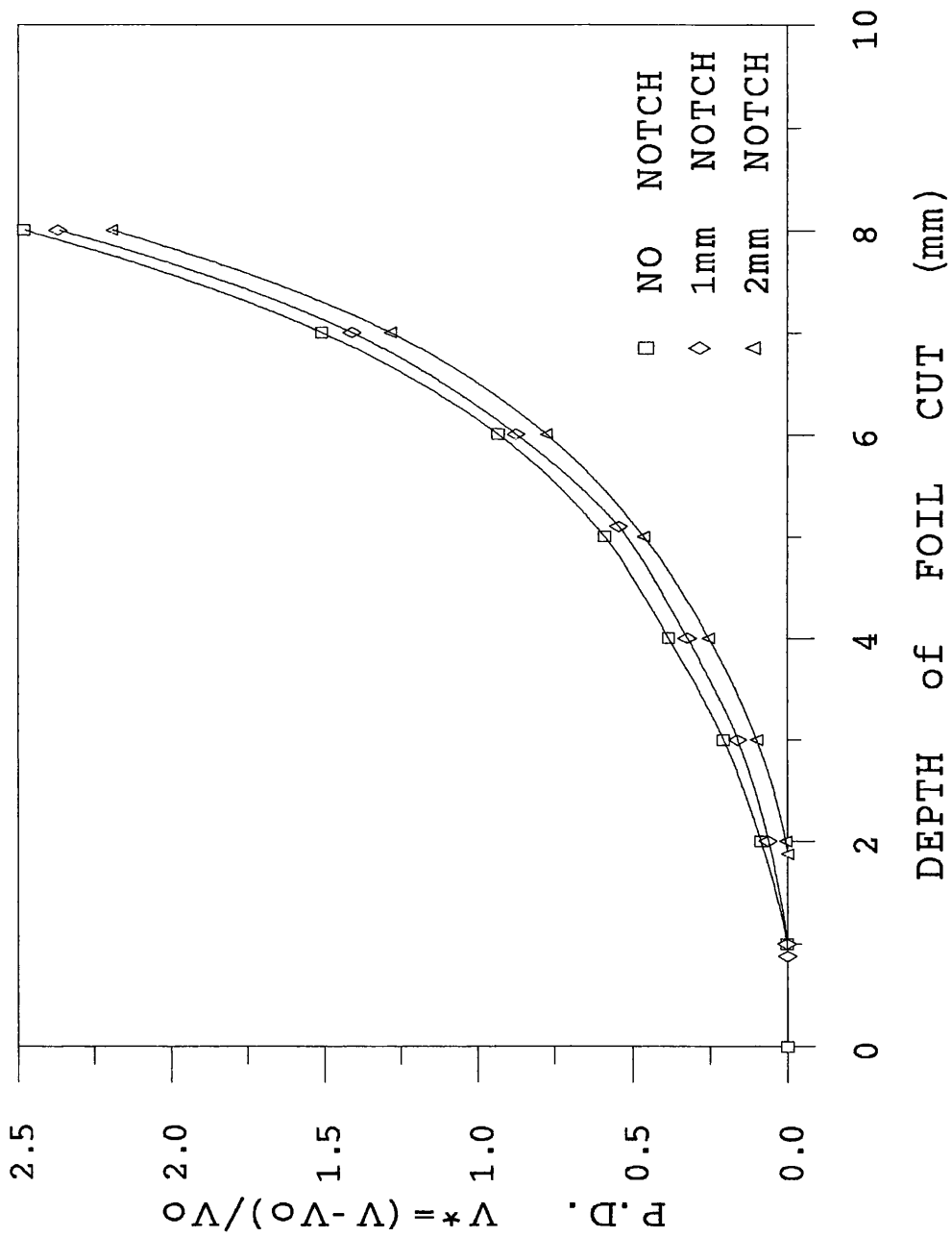


Figure 3.4.14. Aluminium Foil Calibration Curves For Internal Longitudinal Notched Components.

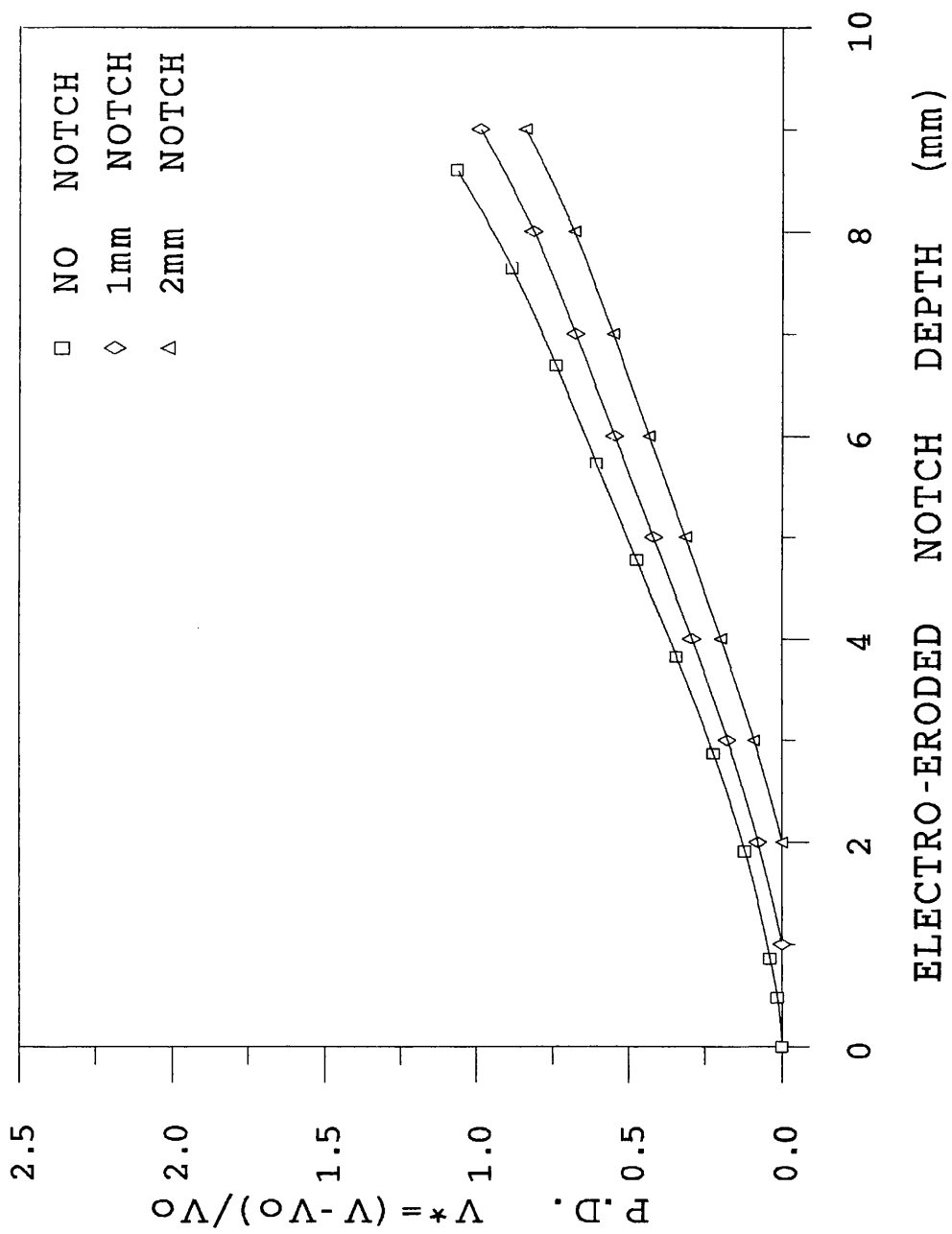


Figure 3.4.15. Electro-Erosion Calibration Curves For External Longitudinal Notched Components.

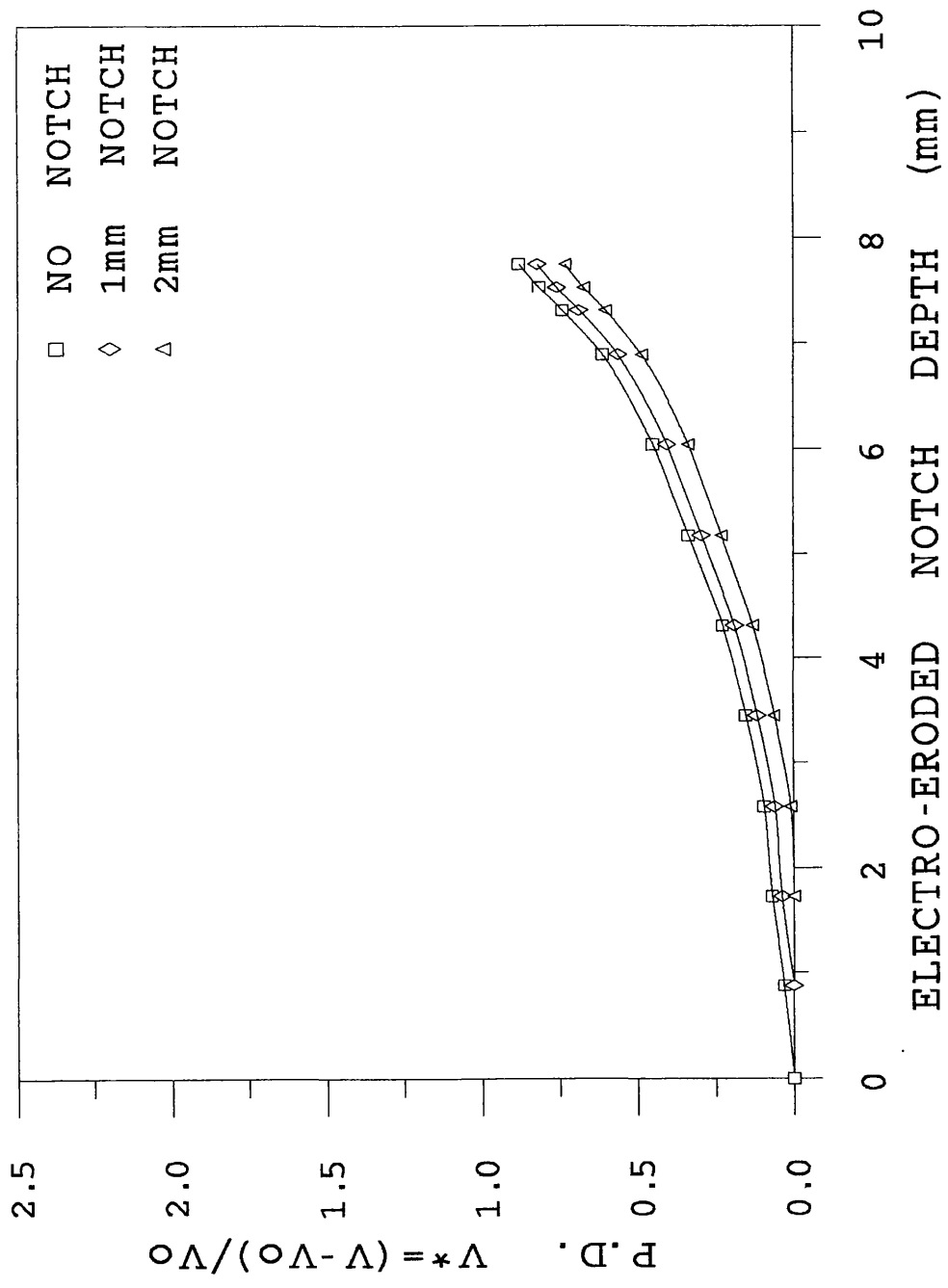


Figure 3.4.16. Electro-Erosion Calibration Curves For Internal Longitudinal Notched Components.

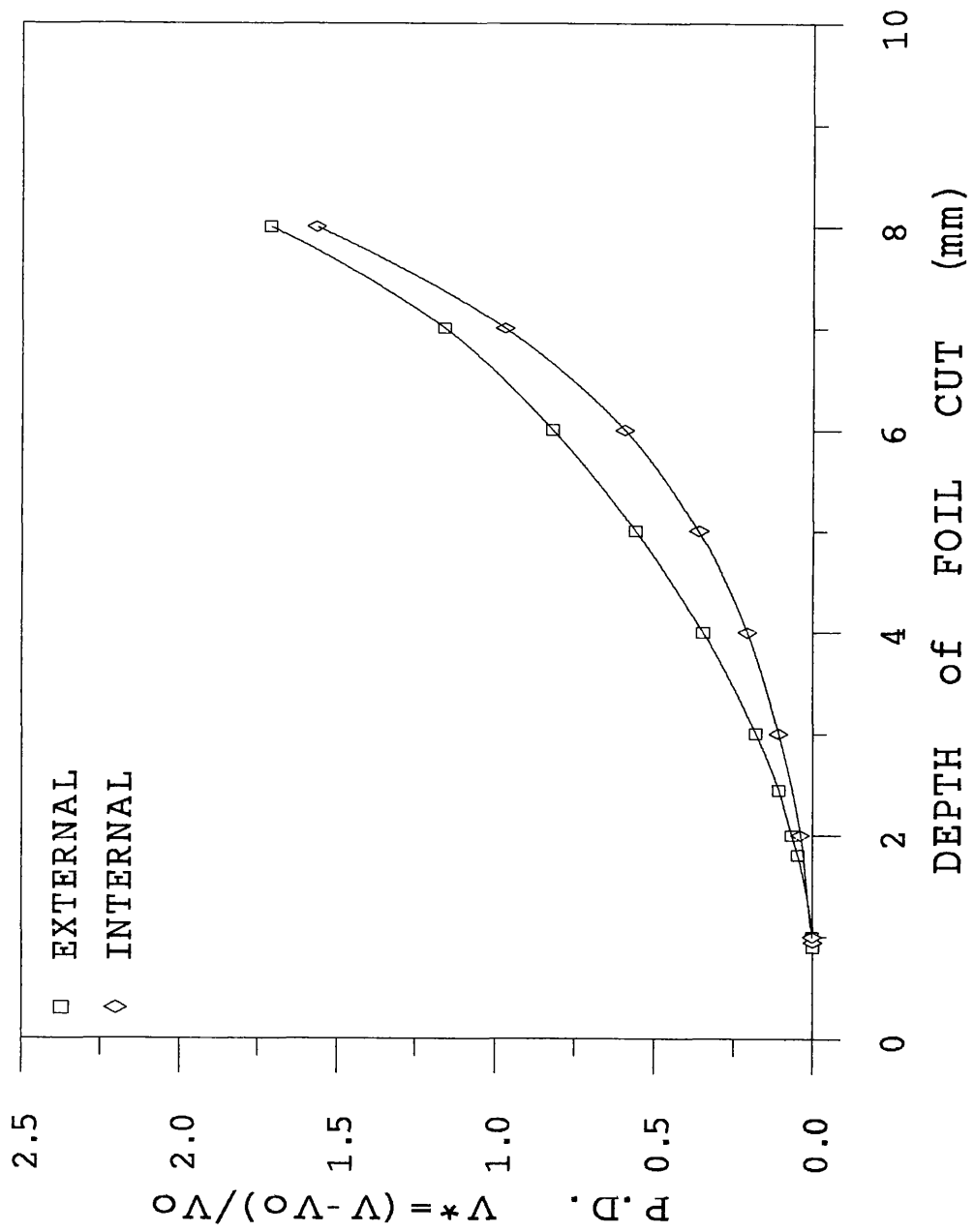


Figure 3.4.17. Aluminium Foil Calibration Curves For Circumferential Notched Components.

3.4.4. Experimental Results.

In the fusion reactor first wall defects may be present, or form on the heated, or water cooled surface. Both the size and orientation of these defects are unknown therefore a wide range of defects have been studied in the present project to give a general consideration to all possibilities. In the majority of the experiments, pre-machined notches have been employed as it is assumed that cracks will not initiate at the free surface in the first wall and hence a crack starter will be required. This has the advantage that the plane of the crack growth is pre-determined which simplifies the procedure of measuring the crack growth. The results from the large number of experiments performed will be presented in the following groups;

- | | | |
|------------------------------|---------------------------|---------------|
| 1. External Surface Notches; | Longitudinal Direction; | Rectangular |
| 2. Internal Surface Notches; | Longitudinal Direction; | Rectangular |
| 3. External Surface Notches; | Longitudinal Direction; | Semi-Circular |
| 4. External Surface Notches; | Circumferential Direction | |
| 5. Internal Surface Notches; | Circumferential Direction | |
| 6. Miscellaneous Test. | | |

Whenever possible each of the series of experimental results will be followed through in the following procedure;

1. A table of resultant crack dimensions for all tests in the series.
2. A typical electrical potential vs number cycles curve.
3. A typical normalized p.d., $[(V-V_0)/V_0]$, vs number of cycles.
4. A photograph of a crack section over p.d. probes.
5. Calibration curve for all tests in series and the best fit equation.
6. Calibrated crack depth vs number of cycles for all tests in series.
7. Aspect ratio development curves and the best fit equation.
8. Photo of typical post-test aspect ratio.
9. Aspect ratio development plots, including a comparison of the estimate and the actual results.

3.4.4.1. Rectangular Shaped External Surface Notches in the Longitudinal Plane.

Thermal fatigue experiments were performed on components with electro-eroded notches on the external surface in the longitudinal direction to investigate the crack growth behaviour in the cyclic hoop stress field. The advantage of having a notch is that the

stress concentrates at the root of the notch, crack initiation occurs therefore the exact plane of the crack growth is pre-determined. The notch is also assumed to model the worse case situation of very deep defects due to plasma bombardment, as is expected in the first wall of the fusion reactor, [Harries,1986]. Another advantage of having a notch in the component is the simplification of monitoring the crack growth with the potential drop method when the position of crack initiation is pre-determined.

After the first two experiments, which were performed to determine if a crack would initiate and propagate from such a notch, the depth of the notches were varied to investigate the effects of notch depth on the crack growth rate. In total seven experiments were performed with approximately 1mm deep rectangular notches, five experiments with approximately 2mm deep rectangular notches and one test, (expt.#8), with a 4mm deep notch. In general the notches were 15mm long however one experiment was performed, in which one of the notches was 2mm deep and 4mm long, (expt.#12), to investigate the effects of original notch shape on the resultant crack growth rate.

In general, experiments were performed with two notches in the components, however one component contained only one notch, (expt.#11), while another had four notches, (expt.#18), to investigate the possibilities of one crack growing faster than another and the effect a single notch has on resultant crack growth rate. In experiment #5, a fault on the data disk forced the programme to stall during the heating phase and the component was held at high temperature overnight. The experiment was restarted, however the final fracture surface revealed a marked band resulting from the period of overheating. This method of heat tinting the fracture surface was developed for shorter periods of time and used in later experiments, (expt.#11 and expt.#22), to observe the crack shape aspect ratio development during the experiments. Unfortunately, even a one minute heating period at 500°C, produced a period of increased crack growth rate during the subsequent thermal cycling. Although it was not possible to use the p.d. data following the heat tint for calculations of the crack growth rate the final measurements following could be used for either calculation of the construction of an experimental p.d. calibration curve. Values of the final crack depths, a_f , final half-surface lengths, c_f , and the final normalized potential difference, $V^*=(V-V_0)/V_0$, across the centre of the notches are given in Table 3.4.2. Potential drop measurements were not taken over notches 18.2 and 18.4 while the magnitude of the potential measurements in the very short experiment, (expt.#24), was so small that a clear value of V_0 could not be determined from the scatter on the signal. Therefore no values of V^* were calculated over notches 18.2, 18.4, 24.1 and 24.2.

Expt. Number and Notch Number	Notch Dimension a_0, c_0 , (mm)	Crack Dimension a_f, c_f , (mm)	Max. Depth P.D. $(V-V_0)/V_0$	Number of Thermal Cycles	Aspect Ratio (a_f/c_f)
2, 2/1	0.94, 7.5	5.76, 14.3	0.4995	52,236	0.403
4, 4/1	0.97, 7.5	5.24, 12.8	0.4647	51,740	0.409
4, 4/2	0.94, 7.5	5.10, 12.7	0.4735	51,740	0.402
11, 11/1	1.00, 7.5	6.26, 14.6	0.5057	50,500	0.429
11, 11/1	1.00, 7.5	7.47, 20.6	0.9047	81,000	0.363
18, 18/1	1.04, 7.5	5.26, 12.9	0.3586	40,500	0.408
18, 18/2	1.01, 7.5	3.90, 10.3	-	40,500	0.377
18, 18/3	1.08, 7.5	4.97, 11.9	0.302	40,500	0.419
18, 18/4	1.03, 7.5	4.92, 11.2	-	40,500	0.438
22, 22/1	0.99, 7.62	2.26, 8.49	0.079	7,000	0.266
22, 22/1	0.99, 7.62	4.03, 9.44	0.230	16,200	0.427
23, 23/1	1.03, 7.5	9.50, 17.5	1.15	79,000	0.543
24, 24/1	1.00, 7.59	1.73, 7.81	-	4,000	0.222
5, 5/1	1.95, 7.5	4.44, 12.41	0.359	26,090	0.358
5, 5/1	1.95, 7.5	7.27, 18.92	0.879	42,400	0.384
12, 12/1	1.98, 7.5	6.36, 17.69	0.613	55,000	0.360
12, 12/2	1.98, 2.01	5.10, 10.57	0.326	55,000	0.483
22, 22/2	2.00, 7.5	3.54, 8.49	0.073	7,000	0.417
22, 22/2	2.00, 7.5	4.75, 10.9	0.268	16,200	0.436
23, 23/2	1.94, 7.5	9.5, 21.0	2.65	79,000	0.453
24, 24/2	2.00, 7.59	3.23, 8.74	-	4,000	0.370
8, 8/1	4.00, 7.5	9.5, 19.575	0.8773	50,705	0.485

Table 3.4.2. External Surface Rectangular Notches in the Longitudinal Direction: Experimental Results.

The general development of the potential measurements during the experiments are typified by the plots in Figures 3.4.18 and 3.4.19 for components containing a 1mm deep notch, (expt.#4), and a 2mm deep notch, (expt.#12), respectively. Channels 1 to 3 are the measurements from the p.d. probe pairs positions over the 15mm long notches with channel 2 at the centre in both experiments. Channels 1 and 3 were each positioned 5mm either side of channel 2 along the length of the notch. The p.d. probe pair corresponding to channel 4 were positioned 2.5mm along the longitudinal length from the end of the notch. The p.d. probe pairs measuring the reference signal were generally positioned a further 20mm along the longitudinal length from the edge of the notch.

In each case, the potential values decreased very slightly during the initial 500 cycles, possibly due to the initial plastic straining at the notch tip, followed by a steady increase. The initial decrease may have been the result of electrical changes within the potential measurement probes, due to thermal hardening. Initially, the potential values increased most rapidly over the centre of the notch, (channel 2), however as the experiment continued, the three potential values over the notch, (channels 1, 2 and 3), converged. The change in potential at channel 4 was initially less than that observed over the notch and then increased at a similar rate to the other three. Very little change occurred over the reference potential measurement probes, (channel 5). To eliminate both specimen and probe position dependent effects on the potential measurements, the lowest value of potential measurement at the beginning of the experiment was used as a zero crack reference potential, V_0 , and the crack growth was related to a normalized potential, V^* . With the current field, p.d. probe pairs positions and cycling conditions remaining constant, the normalized potential was only dependent on changes in the resistance of the component produced by crack extension. The development of the normalized potential through the course of the experiment is typified by Figures 3.4.20 and 3.4.21, for a 1mm and a 2mm deep notch respectively.

At the end of each experiment, both the internal and external surfaces of the components were inspected for signs of crack growth. Both measurements and photographs were made of the crack growth along the surface from the notch, Figure 3.4.22, (expt.#11 or expt.#12). In some cases where the external crack had penetrated close to the inner wall, crack initiation occurred due to the restricted load bearing ligament, as shown in Figure 3.4.23., this occurred in experiment #24.

The components were sectioned across the notches and polished to reveal the nature and depth of crack growth adjacent to the p.d. probe positions and to enable calibration of the crack depth and modelling of the crack shape. The cracking was transgranular with secondary cracking at an angle less than 90° to the direction of propagation of the main crack. The secondary cracking was also transgranular but usually arrested within a couple of grain diameters from the main crack. In the longer experiments, $>40,000$ cycles, the cracks propagated well beyond half the thickness of the components and the cracking at the notch root widened to such an extent that matching crack surfaces for 1mm below the notch were misaligned.

In general, the deepest section of the crack was observed across the p.d. probes at the centre of the notch, Figure 3.4.24. The crack depths at these positions were used to create the experimental potential drop calibration curves.

All of the experiments were terminated at a number of cycles before any of the cracks had propagated through the thickness of the component. However, crack initiation occurred at the internal surface in experiment #5, as shown in Figure 3.4.25. Crack initiation at the internal surface also occurred during experiment #8, in which the component contained a 4mm deep notch and experiment #23, which was performed for 79,000 cycles. The internal surface initiation in the accidentally overheated component, (expt.#5), was at surface breaking grain boundaries and stringers and the resultant cracks propagated transgranularly with bridging and secondary cracking, before arresting at a maximum depth of 0.25mm. In this case the internal crack initiation appears to be related to the overheating of the component. In both experiment #8 and experiment #23, the internal surface crack propagation was transgranular with the crack propagating towards the main crack from the external surface notch. In both cases, sections of the fracture surfaces were separated, after exposure to liquid nitrogen, to reveal a semi-elliptical crack that had propagated from each surface. The larger crack had propagated from the notch at the external surface and the two cracks coalesced at the deepest point of the external crack. The internal cracking in experiment #8 was very straight with very little secondary cracking and bridging. The corresponding internal cracking in experiment #23, which propagated towards the cracks from both the 1mm and the 2mm notches, displayed many secondary cracks, the angle of which helped to determine the point of crack coalescence to be when the external crack was 6.7mm deep, Figure 3.4.26.

From the 2mm deep notch, the point of coalescence between the external and the internal crack was also distinguishable by an area of altered material substructure and the fact that as the crack tips approached, the crack growth lines were parallel and 0.1mm apart. The width of the cracks at the point of coalescence was approximately 0.025mm. Therefore a volume of material, four times the width of the cracks, had to fail for the cracks to coalesce, which possibly explains the area of altered material substructure at the point of coalescence. The final potential drop data cannot be used for calibration purposes from the experiments with internal surface cracking due to the effects that the internal surface crack had on the current field. However enough experiments were performed with external notches to develop experimental calibration curves for comparison with the original calibration curves which were developed from the aluminium foil and electro-eroded tubular components techniques, Figures 3.4.27a-b.

The experimental results compared well with the electro-erosion calibration at low values of crack depth but with increasing crack depth the normalized p.d. from the experiments increased more than the electro-eroded calibration. This could be an effect of the differences between the wide notch and the fine crack tip and the errors in measurement

of the electro-eroded depth due to erosion of the copper electrode. The calibration from the aluminium foil model produced greater values of normalized p.d. than the experimental results over the entire range of crack depths of interest. The simplicity in the 2-dimensional model, the differences in both the current supply positions and the resultant current field around the cut in the aluminium foil produced a greater change in potential drop with the increasing depth of the cut through the thickness of the model.

With the unrealistic calibration curves from the original foil and electro-erosion techniques, the preference was to develop the calibration curves from the p.d. measurements of the probe pairs, which were positioned over the centre of each notch in the experiments. Later, the measurements from all three p.d. probe pairs positioned over each notch were included with no great change in the experimental results calibration curves. To develop a relationship of the total notch and crack depth, a_{cal} , as a function of the normalized potential difference, V^* , polynomials and power law equations were drawn through the experimental data. Unfortunately, it was not possible to develop such a smooth, continuous relationship, therefore a more complex mathematical equation was developed using the Tablecurve software package. Although over one hundred equations were developed, the selection of best equation to describe the experimental results was based on the continuous shape of the curve even although the accuracy at very low values of a_{cal} was prone to errors of ± 0.04 mm. Equations were developed from the experimental results from both the 1mm and the 2mm deep notches respectively, in which a_{cal} is in millimetres, (mm), and the normalized potential difference, V^* , is non-dimensional:

$$a_{cal} = -110.2 + 146.7(V^*) - 69.9(V^*)^{3/2} + 111.1e^{-V^*} \quad (3.4.4.1)$$

$$a_{cal} = -131.8 + 166.7(V^*) - 76.2(V^*)^{3/2} + 133.7e^{-V^*} \quad (3.4.4.2)$$

Equations 3.4.4.1 and 3.4.4.2 were applied to the normalized potential development curves for the central positioned p.d. probe pairs in each of the experiments to show the development of the calibration crack depth with the number of thermal cycles for all the 1mm and 2mm deep notches which were monitored, Figures 3.4.28a-b. For each experiment with a 1mm deep notch, the cracks were observed to initially grow fast in depth, for approximately 20,000 cycles, then the rate in crack growth decreased. A similar crack depth behaviour was observed with cracks from 2mm deep notches except that the decrease in crack growth rate occurred earlier, at approximately 16,000 cycles. The actual crack growth rate, da/dN with continuous thermal cycles will be discussed in greater detail in the analysis and discussions, presented in section 4.1.

The crack shapes and current field distributions require that similar calibration equations were developed for the p.d. probe positions 5mm either side of the centre of the notch and for the surface p.d. probe pairs measurement position 2.5mm below the notch. The resultant calibrated crack depth development curves for the four p.d. probe pair positions in, (for example, expt.#11), Figure 3.4.29, indicate that the crack initially propagates at the centre of the notch at a greater rate than 5mm either side of the centre. With continuing thermal cycles, the crack front across the notch straightens and cracking appears between the p.d. probe pair across the free surface 2.5mm below the notch. The crack clearly appears to develop in a semi-elliptical shape. The photograph of the heat tinted half fracture surface from experiment #11 displays the semi-elliptical shape of the crack front development, Figure 3.4.30.

In general, the cracks were observed to initially grow in depth rather than length, until the ratio of crack depth to half surface length, the aspect ratio, was greater than 0.25 from the 1mm notch and 0.36 from the 2mm notch. With longer experiments, therefore increasing number of cycles, the cracks were observed to grow in both length and depth with a steady aspect ratio in the range of 0.4 to 0.44. The final values of half surface crack length and aspect ratio were plotted against the corresponding values of final crack depth, from Table 3.4.2, and equations relating both to the crack depth were developed again, using the Tablecurve software package. A program was written in the Basic programming language to calculate the development of the crack shape from the calibrated crack depth data. The shape of the crack front was determined from the potential drop measurements for different number of cycles throughout experiment #11 and compared with the measured crack fronts from experiments #11, #18 and #22. The calculations from the computer program, represented by the small squares, triangles and diamonds in Figure 3.4.31, produced a good estimation of the crack front and displayed the tendency for the crack to develop as a semi-ellipse.

This method could also be developed to roughly estimate the crack depth from measurements of the axial extension of the surface crack. If an experiment was interrupted, and a dye penetrant applied to the external surface of the specimen, then an accurate measurement of the surface crack length would produce a corresponding crack depth from the previous experiments. this technique could be very useful if the advanced technique of potential drop was not available.

The transgranular nature of the crack growth was observed when the fracture surfaces were viewed in a scanning electron microscope. Unfortunately, both the meandering of the crack growth and corrosion products covering the fracture surfaces prevented accurate measurement of the striation spacing to determine the crack growth rate.

3.4.4.2. Rectangular Shaped Internal Surface Notches in the Longitudinal Plane.

Thermal fatigue experiments were performed on components with electro-eroded notches on the internal surface in the longitudinal direction to investigate the crack growth from the internal surface due to the cyclic hoop stress field.

The initial experiment, (expt.#1), was performed to determine if a crack would indeed initiate and propagate from internal notches which were again approximately 1mm and 2mm deep. In total five experiments were performed on components containing a rectangular notch which was approximately 1mm deep. Three components contained a second notch which was greater than 1mm deep, while the component in experiment #2 contained both an internal and an external notch. In general, the 1mm deep notches were 16mm long, while the 2mm deep notches were 17mm long. Values of the final crack depths, a_f , final half-surface lengths, c_f , and the final normalized potential difference, $V^*=(V-V_0)/V_0$, across the centre of the notches are given in Table 3.4.3.

Expt. Number and Notch Number	Notch Dimension a_0, c_0 , (mm)	Crack Dimension a_f, c_f , (mm)	Max. Depth P.D. $(V-V_0)/V_0$	Number of Thermal Cycles	Aspect Ratio (a_f/c_f)
1, 1/1	0.88, 8.0	4.65, 12.2	0.2466	34,118	0.382
2, 2/2	0.90, 8.0	3.96, 10.5	0.1843	52,236	0.377
9, 9/1	0.85, 7.99	4.74, 11.6	0.194	50,080	0.409
16, 16/1	0.97, 8.01	2.50, 9.60	0.026	22,000	0.26
17, 17/1	0.95, 7.96	5.75, 14.02	0.340	64,600	0.410
1, 1/2	1.88, 8.25	4.72, 12.8	0.219	34,118	0.369
16, 16/2	1.22, 8.01	3.32, 11.7	0.045	22,000	0.284
17, 17/2	1.97, 8.69	6.55, 16.89	0.44	64,600	0.388

Table 3.4.3. Internal Surface Rectangular Notches in the Longitudinal Direction: Experimental Results.

The general development of the potential measurements during the experiments are typified by the plots in Figures 3.4.32 and 3.4.33 for components containing a 1mm deep notch, (expt.#9), and a 2mm deep notch, (expt.#17), respectively.

In comparison to the potential measurements from the external notched experiments, the magnitude of the potential measurements in Figures 3.4.32 and 3.4.33 were greatly

reduced due to measuring from the external surface. This phenomenon was especially clear at short crack depths, (expt.#16), and in the other experiments with 1mm deep notches. Another difference was in the absence of the initial decrease in the potential measurements which was observed for the external notches, which implies that the decrease could be due to thermal induced changes in the material at the root of the notch. In general, the change in potential measurement with increasing number of cycles was greater over the 2mm notch than the 1mm deep notch. For each notch the change in potential measurements were similar at the probes positioned over the notch. Initially no change was observed in the potential measurement at the p.d. probes positioned over the free surface below the notch, however a small increase occurred after approximately 14,000 cycles with a greater increase beyond 40,000 cycles. The change in reference potential was taken into account before the normalized potential difference, V^* , was calculated. The development of the normalized potential with continuous thermal cycles for both a 1mm and a 2mm deep notch is given in Figures 3.4.34 and 3.4.35 respectively.

The normalized potential increased more over the 2mm than the 1mm notch with a greater change at the central probe positions, (channels #2 and #6), in each case. The probes positioned over the free surface displayed a faster change in normalized potential with the 2mm notch, beginning at 6,000 cycles compared to the 1mm notch when a change was observed at 14,000 cycles. In each case it is possible that the change in potential at the free surface could be an effect of the current field changing around the crack from the notch and not from a direct measurement from a crack between the free surface probes. Therefore individual calibrations of crack depth with the normalized potential are required for each probe pairs position as for the external cracks.

Post-experiment inspections of both the external and the internal surfaces of the components revealed that none of the cracks had penetrated through to the external surfaces and that the cracks grew along the internal surface from the ends of the notches. Measurements of the surface crack lengths were made and the components were sectioned across the notches and polished to observe the depth and the nature of the crack growth across the p.d. probe positions. In each experiment a number of cracks initiated at the root of the notch and either arrested within three grain diameters or coalesced with other cracks to form one dominant crack. The sections were etched to clearly display the transgranular crack growth which was in the general direction of a straight line from the notch root towards the external surface. The main crack tended to meander across the grain boundaries with secondary cracks which arrested within two grain diameters from the main crack, Figure 3.4.36, (expt.#2). During the longer experiments, >50,000 cycles, the cracks propagated to depths beyond the mid-thickness of the component. In

each experiment, the deepest section of the crack was observed across the p.d. probes at the centre of the notch, Figure 3.4.36. The crack depths at these positions were used to develop the experimental potential drop calibration curves for comparison with the aluminium foil and electro-eroded component calibration curves, Figures 3.4.37a-b.

Equations to represent the calibrated crack depth, a_{cal} , in terms of the normalized potential, V^* , were developed, using the Tablecurve software package, from the experimental results for the 1mm and the 2mm deep notches respectively:

$$a_{cal} = -7.67 + 8.98(V^*)^{3/2} + 9.73\sqrt{V^*} + 8.53e^{-V^*} \quad (3.4.4.3)$$

$$a_{cal} = -2.85 - 3.44(V^*)^3 + 4.73e^{V^*} + 3.7\sqrt{V^*} \quad (3.4.4.4)$$

Equations 3.4.4.3 and 3.4.4.4 were applied to the normalized potential development curves for the central positioned p.d. probe pairs in each of the experiments to develop the calibrated crack depth with the number of thermal cycles for all the 1mm and 2mm deep notches which were monitored, Figures 3.4.38a-b. For each experiment with a 1mm deep notch, the cracks were observed to initially grow fast in depth, for approximately 4,000 cycles, then the rate in crack growth decreased. A similar crack depth behaviour was observed with cracks from 2mm deep notches.

Similar calibration equations were developed for the p.d. probe positions 5mm either side of the centre of the notch and for the surface p.d. probe pairs measurement position 2.5mm below the notch. The resultant calibrated crack depth development curves for the four p.d. probe pair positions in experiment #17, Figure 3.4.39, indicate that the crack initially propagates at a greater rate from the centre of the notch than 5mm either side of the centre. However, with continuing thermal cycles, the depth of the crack front develops at a similar rate across each pair of p.d. probes with the depth at the central probe pairs always slightly greater, ($< 0.3\text{mm}$). The calibration predicts that cracking appeared at the free surface, across the p.d. probe pair positioned 2.5mm below the notch, after 5,000 cycles and was initially very slow. After 28,000 cycles the growth rate increased to be similar to the calibrated growth rate over the notch, which was 3.8mm deep. The crack appears to have developed in a semi-elliptical shape.

The semi-elliptical shape of the crack front development was observed when the half fracture surface from a notch in experiment #2, was exposed to liquid nitrogen and separated, Figure 3.4.40.

Over the series of experiments, a similar crack shape development to that of external

longitudinal cracks was observed, although the overall depth of cracks from internal longitudinal notches was reduced in comparison with the depths of cracks from external longitudinal notches for the same number of cycles. In general, the cracks initially grew in depth rather than length, until the aspect ratio was greater than 0.25 and 0.36 for the 1mm and the 2mm deep notches respectively. Further cycling saw the cracks grow in both length and depth with a steady aspect ratio in the range of 0.39 to 0.41.

Equations relating both the half surface length and aspect ratio to the final crack depths from Table 3.4.3 were developed using the Tablecurve software package and were incorporated in a Basic Language program, as for the external cracks, to calculate the development of the semi-elliptical crack shape from the calibrated crack depth data. The shape of the crack front was determined from the potential drop measurements for different number of cycles throughout experiment #17 and compared with the measured crack fronts from experiments #9, #16 and #17. The calculations from the computer program, represented by the small squares, triangles and diamonds in Figure 3.4.41, produced a good estimation of the crack front and displayed the tendency for the crack to develop as a semi-ellipse.

The transgranular nature of the crack growth was observed when the fracture surfaces were viewed in a scanning electron microscope, although a clear measurement of the striation spacing was not possible.

3.4.4.3. Semi-Circular Shaped External Surface Notches in the Longitudinal Plane.

Thermal fatigue experiments were performed on components with semi-circular shaped electro-eroded notches on the external surface in the longitudinal direction to compare both the resultant crack growth rate and the crack shape development with that found in section 3.4.3.1. Using the same equipment as in the previous sections, potential measurements were recorded across the centre of the 1mm and 2mm deep notches. Due to the limited surface length of the notches, 2mm and 4mm respectively, no other p.d. probe pairs were positioned across the notches, however in each experiment probe pairs were positioned above and below the notches to monitor crack extension from the ends of the notches. In total four experiments were performed on components containing at least one semi-circular shaped notch. In experiment #5, a notch of radius 2mm was electro-eroded into the external surface on the opposite side of the component from a 2mm deep rectangular notch to investigate if crack propagation was possible from a semi-circular notch. Similarly a semi-circular notch with a 1mm deep radius was positioned on the opposite side to a 4mm deep notch in experiment #8. With crack

growth observed, a further two experiments, (#13 and #19), were performed, each with a 1mm and a 2mm deep semi-circular notch. Values of the notch radius, final combined notch and crack depths, a_f , final half notch and crack surface lengths, c_f , and the final normalized potential difference, $V^*=(V-V_0)/V_0$, across the centre of the notches are given in Table 3.4.4.

Expt. Number and Notch Number	Notch Dimension Radius (mm)	Crack Dimension a_f, c_f , (mm)	Max. Depth P.D. $(V-V_0)/V_0$	Number of Thermal Cycles	Aspect Ratio (a_f/c_f)
8, 8/2	0.92	2.47, 2.69	0.053	50,705	0.918
13, 13/1	1.00	1.59, 1.61	0.015	31,000	0.988
19, 19/1	1.00	-	0.0164	43,000	-
19, 19/1	1.00	2.81, 3.59	0.044	69,620	0.783
5, 5/2	1.97	3.25, 3.75	0.0718	26,090	0.867
5, 5/2	1.97	5.92, 11.0	0.458	42,400	0.537
13, 13/2	2.00	2.86, 2.91	0.033	31,000	0.983
19, 19/2	2.00	3.15, 3.57	0.056	43,000	0.882
19, 19/2	2.00	4.16, 7.2	0.141	69,620	0.578

Table 3.4.4. External Surface Semi-Circular Notches in the Longitudinal Direction: Experimental Results.

During experiment #5 the component was held at high temperature, as previously mentioned in section 3.4.3.1, which produced a heat tint on the fracture surface of the crack propagating from notch 5.2. Following the period of over heating, the potential measurement increased rapidly, resulting in a very high value of normalized potential difference which will not be considered in the analysis of the crack growth rate from semi-circular notches. However the potential measurement was recorded at the point of over heating and the crack front was clearly marked on the fracture surface at that point in the experiment. The method of heat tinting the fracture surface was used to develop two potential measurements and cracks depths for each notch in experiment #19.

Unfortunately, an accurate measurement of crack depth at the mark corresponding to the heat tint was not possible as no clear crack front was observed on the fracture surface which developed from the 1mm deep notch. However from the p.d. measurements, an estimation of the total notch and crack depth is 1.76mm deep at the heat tint with a corresponding half surface crack length of 1.79mm.

The general development of the normalized potential differences, V^* , during the experiments are typified by the plots in Figures 3.4.42 and 3.4.43 for components containing both a 1mm and a 2mm deep notch, (expt.#13 and expt.#19).

In comparison to the potential measurements from the rectangular shaped external notched experiments, the magnitude of the normalized potential differences in Figures

3.4.42 and 3.4.43 were greatly reduced and the rate of change of V^* at the centre probe position was lower than that observed with the rectangular notches. The lower magnitude of potential measurements exaggerates the scatter of the data especially with the short term experiments. However a general trend was observed with the normalized potential measurements increasing from a low number of cycles and continuing at a steady rate until each test was stopped. The normalized potential increased more over the 2mm than the 1mm notch with a greater change at the central probe positions, (channels #2 and #6), in each case. Calibrations of crack depth with the normalized potential were performed for the probe pairs positioned over the centre of each notch.

Post-experiment inspections of both the external and the internal surfaces of the components revealed that none of the cracks had penetrated through to the internal surfaces and that the cracks grew along the external surface from the ends of the notches. With experiment #5, two cracks propagated from the corners at each end of the notch. Each grew at an angle less than 45° to the longitudinal direction. However, one crack at each end arrested before they were 0.5mm long while the other two straightened to the longitudinal while propagating along the surface away from the notch. A similar behaviour was observed from the 1mm radius notch in experiment #8 with the cracks growing away from the notch at an angle to different lengths between 1 and 2mm long.

In experiment #13 the surface cracking was very short, $<0.5\text{mm}$, while in experiment #19, both the 1mm and the 2mm radius notches displayed cracking at an angle from the corners at the ends of the notches. From the 1mm radius notch cracks grew to an average length of 1mm from the notch while from the 2mm radius notch the cracks propagated to 5mm from the notch, as shown in Figure 3.4.44.

If two cracks had propagated from the notch to nearly equal lengths, then the average of the two lengths was taken as the crack surface length from the notch. Following surface measurement the components were sectioned across the notches, polished and etched to observe the depth and the nature of the crack growth across the p.d. probe positions. In experiment #8 a number of cracks initiated at the root of the notch and either arrested by a depth of 0.01mm or coalesced with other cracks to form one dominant crack. Both the 1mm and the 2mm notches in experiment #13 displayed a more rounded notch root than that in experiment #8, consequently multiple initiation led to two dominant cracks in each case. From the root of the 1mm radius notch both cracks grew to depths of 0.4mm and 0.5mm respectively, while one of the cracks from the 2mm radius notch arrested at a depth of 0.14mm from the notch root and the other propagated to a depth of 0.86mm from the notch, Figure 3.4.45. Short secondary cracking occurred, however, in general the crack growth was predominately transgranular in a straight line from the notch root

towards the internal surface.

The crack growth rate from semi-circular notches is greatly reduced in comparison to that from rectangular notches of the same depth. For a similar number of thermal cycles, the resultant crack depths were far shorter than those observed from rectangular notches of the same depth. Both the overall decrease in final crack depth and the tendency for two surface cracks to grow from the corners of the semi-circular notch, suggests that with short notches, the crack growth begins at the stress concentrating corners of the notch, on the external surface, before major penetration in depth has occurred. This would control the crack propagation plane as is the case for the rectangular notches. It may also be possible that the semi-circular shape of the notch does not concentrate the stress at the notch root to the same effect as the longer rectangular notch. Therefore the number of cycles spent in both crack initiation and the resultant propagation is greatly increased with a semi-circular shaped notch.

The microstructural features of the cracking displayed a reduction in the width of the cracks with a decrease in the length of secondary cracks. However, for short cracks, of similar depths, from either rectangular notches, (expt.#24, at 4,000 cycles), or semi-circular notches, (expt.#13, at 31,000 cycles), the features of the cracks are very similar. Cracking from both experiments appears to be narrow and slightly meanders which is typical of crack initiation.

For each of the experiments with semi-circular notches the deepest section of the crack was observed across the p.d. probes at the centre of the notch. The crack depths at these positions were measured to relate to the corresponding normalized potential difference. Equations to represent the calibrated crack depth, a_{cal} , (in mm), in terms of the normalized potential, V^* , (non-dimensional), were developed, using the Tablecurve software package, for the 1mm and the 2mm deep notches respectively:

$$a_{cal} = 0.98 + 12.52(V^*)^{0.68} \quad (3.4.4.5)$$

$$a_{cal} = 1.98 + 8.87(V^*) - 9.97(V^*)^2 + 2.91\sqrt{V^*} \quad (3.4.4.6)$$

Equations 3.4.4.5 and 3.4.4.6 were applied to the normalized potential development curves for the central positioned p.d. probe pairs in each of the experiments to develop the calibrated crack depth with the number of thermal cycles, Figure 3.4.46. For each experiment the cracks were observed to initially grow slowly in depth with a slight increase with continuous thermal cycles. Crack growth rates were greater with cracks from 2mm radius notches, although the general trend was for slower cracking than

previously observed, sections 3.4.4.1 and 3.4.4.2.

From surface and sectioned measurements it can be assumed that the short cracks from both 1mm and 2mm radius notches remained semi-circular in shape. When the cracks propagated to depths greater than half the notch depths then the tendency was for the cracks to propagate along the surface and develop as semi-ellipses with decreasing aspect ratios towards 0.5. It is possible that with short notches the crack growth begins at the ends of the notch on the external surface before major penetration in the depth has taken place. this would control the crack propagation plane, as is the case for the rectangular notches.

3.4.4.4. External Surface Notches in the Circumferential Plane.

Thermal fatigue experiments were performed on components with a machined notch around the circumference on the external surface to investigate the crack growth behaviour in the cyclic axial stress field and to compare the crack growth rate with the external surface longitudinal results. Two experiments, (expt.#3 and expt.#15), were performed with external circumferential notches which had a semi-circular cross section with a 1mm deep radius. A deeper section was electro-eroded into the notch in experiment #3 to investigate the development of the circumferential crack shape. Each component was instrumented with pairs of p.d. probes, positioned across the notch at intervals around the circumference. The component in experiment #3 had eight probe pairs across the notch while the component in experiment #15 had seven probe pairs across the notch. Another pair were positioned within the constant current field above the notch to measure change in the potential which were not related to the crack growth. After 26,300 cycles in experiment #3 the component was held at 500°C for 1 minute to mark the corresponding fracture surface. Values of the both the heat tinted and the final notch and crack depths, a_r , and the corresponding normalized potential difference, $V^*=(V-V_0)/V_0$, at each of the probe pairs positioned across the notches are presented in Table 3.4.5.

Expt. Number p.d. Probe Number	Notch Depth a_o , (mm)	Notch and Crack Depth a_r , (mm)	Max. Depth p.d. $(V-V_o)/V_o$	Number of Thermal Cycles
3, CH1	0.94	2.41	0.1802	26,300
3, CH2	0.96	2.84	0.1356	26,300
3, CH3	0.98	3.23	0.1842	26,300
3, CH4	0.95	2.47	0.1997	26,300
3, CH5	1.00	2.90	0.1662	26,300
3, CH6	2.15	3.81	0.1840	26,300
3, CH7	2.44	4.10	0.2040	26,300
3, CH8	2.14	3.87	0.2260	26,300
3, CH1	0.94	3.42	0.3921	39,300
3, CH2	0.96	4.42	0.3162	39,300
3, CH3	0.98	4.33	0.3960	39,300
3, CH4	0.95	3.27	0.4323	39,300
3, CH5	1.00	3.90	0.3992	39,300
3, CH6	2.15	5.15	0.3763	39,300
3, CH7	2.44	5.09	0.4164	39,300
3, CH8	2.14	4.72	0.4347	39,300
15, CH1	0.98	4.27	0.4944	81,600
15, CH2	0.98	4.69	0.5379	81,600
15, CH3	1.00	4.10	0.4787	81,600
15, CH4	1.02	3.88	0.4289	81,600
15, CH5	1.02	5.06	0.6590	81,600
15, CH6	1.00	6.33	0.8700	81,600
15, CH7	1.00	4.11	0.4727	81,600

**Table 3.4.5. External Surface Notches in the Circumferential Plane:
Experimental Results.**

The development of the potential measurements with continuous thermal cycling were very similar during both experiments as shown for a number of channels from each experiment in Figure 3.4.47. A slight decrease in potential was measured over the initial 500 cycles, however this decrease was insignificant in comparison to both the magnitude of the p.d. measurements and the resultant change in p.d. The lowest value of p.d. during the initial 500 cycles was taken as the initial notch p.d., V_o , as with the longitudinal notches. Following the initial decrease, constant p.d. measurements were recorded for a period of 3000 to 6000 cycles which varied from channel to channel. This region of constant p.d. was far longer than that observed with external surface rectangular longitudinal notches, although not as long as that observed with the external

longitudinal semi-circular shaped notches. In the remainder of the experiments, the p.d. measurements increased with an increasing number of thermal cycles. The magnitude of the p.d. measurements were almost eight times as large as the measurements over the external longitudinal notches, due to the strength of the direct current field over the circumferential notch in comparison to the field over the longitudinal notch.

Very little change occurred over the reference potential measurement probes, therefore the normalized potential differences, V^* , were calculated and plotted against the number of thermal cycles producing a continuous estimation of the crack depth from the aluminium foil calibration curve. The aluminium foil calibration curve was employed to estimate the desired crack depth at which to stop the experiment. The development of the normalized potential, at selected p.d. probe positions in both components, throughout the course of the experiments is shown in Figure 3.4.48. A large range of final normalized p.d. values is observed in experiment #15, with the greatest change in p.d. at the channel which first recorded an initial increase, at 3000 cycles. The channel which was last to record an increase in p.d., at 7000 cycles, displayed the lowest normalized p.d. value. The normalized p.d. measurements from experiment #3 sit between the limits in the range of values from experiment #15, with an increase in the rate of change of normalized p.d. at each of the eight channels following the period of constant temperature.

At the end of each experiment, the root of the notch, the external surface and the internal surface of the components were inspected for signs of crack growth. Cracking was limited to the root of the notch around the circumference of the components in both experiments, while no cracks were observed on the free surfaces.

The components were sectioned across the notches, polished and etched to reveal the nature and depth of crack growth adjacent to the p.d. probe positions. The initiation and resultant crack growth resembled that from the semi-circular external surface longitudinal notches more than the cracking from the rectangular external surface longitudinal notches. At each section a large number of crack initiation sites produced short cracks which arrested within 0.2mm length, while one dominant crack propagated from the middle of the notch root, Figure 3.4.49. The cracking was narrow in comparison to the cracking from the rectangular longitudinal notches and had a tendency to meander transgranularly through the material with only a small number of secondary cracks, which arrested within one grain diameter from the main crack. The general direction of the crack propagation was in a direct line from the root of the notch towards the internal surface. The depth of cracking from the 1mm section of the circumferential notch in experiment #3 varied from 3.27mm to 4.75mm while the cracking from the

deep electro-eroded sections propagated to depths of 5.15mm through the 9.5mm thickness of the component.

From the longer experiment #15, (81,600 cycles), the range of total notch and crack depths, in the etched sections, varied from 3.88mm to 6.33mm, the later of which is very comparable with the largest crack depths from external rectangular notches over a similar number of thermal cycles.

From a comparison of the etched sections with the normalized potential difference development plots it was observed that the circumferential crack initiated from an initiation point in the circumferential notch and the crack propagated from that point before it initiated at other sites around the notch. The initiation and early propagation at a single site within a circumferential notch may be related to local material, temperature and stress effects. This localised crack initiation did not occur in the components which contained two identical longitudinal 1mm deep notches, positioned 180° from each other around the component. The crack initiated from each of the notches after a similar number of cycles and propagated at the same rate to similar crack depths, (expt.#4). When the crack initiated from the last site in the circumference notch, the difference between the deepest point and the initiation site was too large for the crack front ever to be circular. The varied nature of the final crack fronts was observed when the notched pieces which did not contain a pair of p.d. probes were exposed to liquid nitrogen, fractured and remounted to represent a fracture surface around the circumference of each component, Figures 3.4.50 and 3.4.51. From measurements of the crack depth at the heat tint, Figure 3.4.51, estimations were made of the corresponding crack depths in the sections over the p.d. probes.

The measurements of both the heat tinted and the total notch and crack depths through the p.d. probe sections with the approximately 1mm deep notches, Table 3.4.5, were plotted against the corresponding values of normalized potential difference for comparison with the calibration data from the aluminium foil calibration curve, Figure 3.4.52. Surprisingly, the circumferential crack data compared well with the aluminium foil calibration curve, which was not observed with the foil calibration and the longitudinal crack data, Figure 3.4.27a. In the circumferential calibration, it is possible that the aluminium foil model of a longitudinal section of the component could be more realistic since the current inputs are at the exact position with regard to distance from the cracked plane which was not the case for the longitudinal crack foil calibration model. Differences were observed between the calibration curve and a best-fit curve through the experimental data at low values of V^* , as there were no experimental data points between the original notch depths and total notch and crack depths of 2.4mm.

From a combination of the experimental results and the aluminium foil calibration data, an equation was developed to represent the calibrated crack depth, a_{cal} , (in units of mm), in terms of the normalized, non-dimensional, potential, V^* , using the Tablecurve software package:

$$a_{cal} = 0.903 + 1.22(V^*)^{\frac{3}{2}} + 4.73\sqrt{V^*} \quad (3.4.4.7)$$

Equation 3.4.4.7 was applied to the normalized potential development curves for the p.d. probe pairs in both experiments to produce plots of the calibration crack depth development with the number of thermal cycles. Typical values from three of the p.d. probe sections over 1mm deep notches from both experiments are shown in Figure 3.4.53.

The initial surprising feature of Figure 3.4.53 is that no region of non-growth appears at the original notch depths as was expected following the normalized potential drop development plots, Figure 3.4.49. This was probably due to inaccuracies in the calibration fit at low V^* values. However, by 4,000 cycles each channel displayed a period of fast crack growth which decreased in growth rate beyond 20,000 cycles. The data from experiment #3 sits perfectly between the fastest and the slowest crack growth data from experiment #15. The slowest crack growth data, which corresponds to the shortest final crack depth in experiment #15, increased at a steady rate from 4,000 cycles to 30,000 cycles. Beyond which the crack growth continued at a steady decreased rate until 50,000 cycles, about which time the growth rate once again decreased and the crack continued to propagate at this reduced rate until the end of the experiment, at 81,600 cycles.

The deepest calibrated crack data initially displayed the fastest crack depth growth rate, which decreased after 14,000 cycles. However propagation continued at the fastest rate in comparison to the growth rate at other channels. At 39,000 cycles the value of calibrated crack depth is similar to the deepest crack depth from a 1mm deep notch in experiment #3. Beyond 39,000 cycles the crack continued to propagate at a steady fast rate until 60,000 cycles at which point the growth rate slightly decreased but still remained greater than that observed at any other channel. The final calibrated crack depth was 6.2mm which is very similar to the measured depth, Table 3.4.7.

3.4.4.5. Internal Surface Notches in the Circumferential Plane.

Thermal fatigue experiments were performed on components with a machined notch

around the circumference on the internal surface to investigate the crack growth behaviour in the cyclic axial stress field and to compare the crack growth rate with the internal surface longitudinal results. Two experiments, (expt.#6 and expt.#20), were performed with internal circumferential notches which had a semi-circular cross section with a 1mm deep radius. Each component was instrumented with pairs of p.d. probes, positioned across the plane of the notch at intervals around the circumference of the external surface. Experiment #6 had eight probe pairs positioned 10mm apart across the plane of the notch with two reference probe pairs, also 10mm apart, positioned within the constant current field above the plane of the notch to measure change in the potential which was not related to the crack growth. By the time experiment #20 was performed, the control programme had been developed to incorporate seven probe pairs measuring p.d. across the plane of the notch with another pair positioned above the notch to measure the reference potential. Values of the final notch and crack depths, a_f , and the final normalized potential difference, $V^*=(V-V_0)/V_0$, at each of the probe positions are given in Table 3.4.6.

Expt. Number p.d. Probe Number	Notch Depth a_n , (mm)	Notch and Crack Depth a_c , (mm)	Max. Depth p.d. (V-V ₀)/V ₀	Number of Thermal Cycles
6, CH1	0.85	3.50	0.0904	72,785
6, CH2	0.89	1.49	0.0367	72,785
6, CH3	0.89	2.00	0.0303	72,785
6, CH4	0.94	2.14	0.0308	72,785
6, CH5	0.89	3.16	0.0791	72,785
6, CH6	0.87	4.90	0.1543	72,785
6, CH7	0.96	4.26	0.1376	72,785
6, CH8	0.87	4.24	0.1160	72,785
20, CH1	0.98	0.98	0.0020	52,000
20, CH2	0.98	0.98	0.0008	52,000
20, CH3	1.00	1.00	0.0052	52,000
20, CH4	1.02	1.02	0.0011	52,000
20, CH5	1.02	1.02	0.0015	52,000
20, CH6	1.00	1.00	0.0075	52,000
20, CH7	1.00	1.00	0.0021	52,000
25, CH1	1.00	1.00	0.0022	27,000
25, CH2	1.00	1.00	0.0016	27,000
25, CH3	1.00	1.00	0.0028	27,000
25, CH4	1.00	1.00	0.0009	27,000
25, CH5	1.00	1.00	0.0014	27,000
25, CH6	1.00	1.00	0.0020	27,000
25, CH7	1.00	1.00	0.0031	27,000

Table 3.4.6. Internal Surface Notches in the Circumferential Plane: Experimental Results.

The development of the potential measurements with continuous thermal cycling for a number of channels from each experiment are shown in Figures 3.4.54. In experiment #6 a slight decrease in potential was measured over the initial 6000 cycles, however this decrease was insignificant in comparison to both the magnitude of the p.d. measurements and the resultant change in p.d. The lowest value of p.d. during the initial 6000 cycles was taken as the initial notch p.d., V₀. Following the initial decrease, constant p.d. measurements were recorded up to 40,000 cycles, beyond which channels 6, 7 and 8 displayed an increase in p.d. measurement. By 60,000 cycles channels 1 and 5 increased in p.d. measurement and were followed by channels 2, 3 and 4 at 65,000 cycles. Apart from the initial decrease in the measurements, no obvious changes were observed at the reference channels. During both experiment #20 and experiment #25, all eight channels

measured constant potential for the entire duration of the experiments. Both were stopped earlier than experiment #6 in order to check for crack initiation, with a similar magnitude to the initial potential measurements to those measured during experiment #6.

Estimations of the experimental crack depths were made during the experiments by comparing the normalized potential differences, V^* , with the aluminium foil calibration curve. Only in experiment #6 was V^* great enough for an estimation of the crack depth and the experiment was terminated when the crack depth was calculated to be approximately half-way through the thickness of the component. The development of the normalized potential, at selected p.d. probe positions in both components, throughout the course of the experiments #6 and #20 are shown in Figure 3.4.55. The channels, in experiment #6, which display an initial increase in normalized potential were all on the same side of the component. At the opposite side of the component, a change in p.d. was not observed at channels 2, 3, and 4 until 45,000 cycles and the rate of change in normalized p.d. remained less than that at channels 1, 5, 6, 7, and 8 to the end of the experiment. There was no change in normalized potential at all seven channels in experiment #20 all of which compared well with the data from channels 2, 3 and 4 in experiment #3 over the entire 52,000 cycles of the experiment.

At the end of each experiment, the external surface, the root of the notch in the internal surface and the internal surface of the components were inspected for signs of crack growth. Cracking was observed only at the root of the notch around the circumference of the component from experiment #3, while no cracks were observed on the component from experiment #20.

The components were sectioned across the notches, polished and etched to reveal the nature and depth of crack growth adjacent to the p.d. probe positions. No crack initiation from either the notch, the internal surface or the external surface was observed in any of the sections from experiment #20. Crack initiation was observed from each of the sections of the notch from experiment #6, with the deepest crack having propagated 4.03mm from the root of the notch to a depth of 4.90mm from the internal surface. The values of combined notch and crack depths are presented in Table 3.4.6. At each section initiation was limited to one site which propagated in a generally straight direction from the root of the notch towards the centre of the component wall. The transgranular nature of the cracking within the section from p.d. probe pair #6.8 is shown in Figure 3.4.56. The cracking was narrow in comparison to the cracking from the rectangular longitudinal internal notches with very few secondary cracks, all of which arrested within one grain diameter from the main crack. The combined depth of cracking and circumferential notch varied from 1.49mm to 4.90mm through the 9.5mm thickness of the component.

A combination of the measured sections and the normalized potential difference development plots seem to indicate that a circumferential crack initiates at one site within a component which concentrates the stress and continues to grow before the crack initiates at other sites around the component. With no great thermal change at the internal surface, this phenomena of crack initiation must be linked to local material differences around the circumferential notch root. When the crack initiated at the last site around the circumference then the difference between the deepest point and the initiation site was too large for the crack front ever to be circular. The varied nature of the final crack fronts was observed when the notched pieces which did not contain a pair of p.d. probes were exposed to liquid nitrogen, fractured and remounted to represent a fracture surface around the circumference of each component, Figures 3.4.57.

The measurements of the total notch and crack depths through the p.d. probe sections with the approximately 1mm deep notches, Table 3.4.6, were plotted against the corresponding final values of normalized potential difference for comparison with the calibration data from the aluminium foil calibration curve, Figure 3.4.58.

The experimental data compared well with the aluminium foil calibration curve for calibrated notch and crack depths of 3mm, beyond which the calibration curve displayed higher values of normalized potential difference than those observed in experiment #6. It is possible that the cracks in the experiment were so narrow that the current flowed across the crack for some distance behind the crack tip therefore the magnitude of the potential measurement was less than that in the foil calibration for the same depth of crack. Enough data points were obtained from the experiments to develop a relationship between the calibrated crack depth, a_{cal} , (in mm), and the normalized, non-dimensional, potential, V^* , using the Tablecurve software package:

$$a_{cal} = 57.78 - 42.81(V^*)^{3/2} - 4.3\sqrt{V^*} - 56.8e^{-V^*} \quad (3.4.4.8)$$

Equation 3.4.4.8 was applied to the normalized potential development curves for the p.d. probe pairs in both experiments to produce plots of the calibration crack depth development with the number of thermal cycles. Typical values from the eight channels in experiment #6 and two channels in experiment #20 are shown in Figure 3.4.59.

Each channel displayed a period of constant crack depth from which initiation occurred initially from channel 6 in experiment #6 at 30,000 cycles. The greatest calibrated crack depth growth rate was at channel 6 and remained so for the duration of the experiment. The two probe pair positions close to channel 6, also initiated within 40,000 cycles and

displayed similar calibrated crack depth growth rates to the end of the experiments. The smallest crack growth rates were observed at channels 2, 3 and 4 which did not display a change in calibrated crack depth until 50,000 thermal cycles. The calibrated crack depths from experiment #20 compared well with the values from channels 2, 3 and 4 as no increase in crack depth was monitored during the 52,000 cycles of the experiment.

3.4.4.6. Miscellaneous Experiments: Results Section.

A number of miscellaneous experiments were performed to investigate the effects of increasing the maximum temperature of the thermal cycle, to determine if cracks could be initiated from an area of the material welded by a laser beam, thus simulating plasma disruption damage, and to investigate which direction a crack would grow from a circular hole in the mid-section of the material. The experimental conditions and the resultant crack depths are given in Table 3.4.8.

Expt. Number	Experimental Conditions	Crack Depth a_c (mm)	# Thermal Cycles
7	External Surface Cycled Between 80°C and 600°C. One Spot Weld on the External Surface.	3 Longitudinal Cracks From The External Surface: 7.32mm DEEP, 7.24mm DEEP, 7.28mm DEEP.	16,700
10	External Surface Cycled Between 80°C and 350°C. Laser Welds on the External Surface: Spots and a Longitudinal Line.	No Cracking	55,100
14	External Surface Cycled Between 80°C and 450°C. Laser Welds on the External Surface: Spots and a Longitudinal Line.	No Cracking	14,010
21	External Surface Cycled Between 80°C and 350°C. Laser Welded Spots on the External Surface, Plus Two Machined Holes: a) 2mm Diameter, 1mm Deep. b) 4mm Diameter 2mm Deep.	Spot Weld Cracks: 0.6mm, 1mm Deep Machined Holes: 1mm, 2.78mm Deep.	65,105

Table 3.4.7. Miscellaneous Experimental Results.

In experiment #7, three cracks initiated from individual sites around the oxide covered external surface. The deepest crack, 7.32mm, grew 25.4mm in length along the longitudinal direction from a deliberately placed spot weld, Figure 3.4.60. Another two longitudinal cracks were observed at different positions within the thermally cycled region around the external surface. One had a surface length of 10.79mm and the other was 13.06mm long. The component was sectioned across the centre of the spot weld and across the centre of the 13.06mm long crack. Both sections were polished and etched to display cracks which had propagated from the external surface to depths of 7.3mm and

7.2mm respectively. Crack initiation was observed from the internal surface with propagation to a depth of 1.2mm in both sections. The other longitudinal crack was exposed to liquid nitrogen and fractured to reveal a semi-elliptical crack shape.

The component in experiment #10 had laser welded zones in either 1mm or 2mm diameter spots or a 15mm long, 1mm wide strip on the external surface. The laser was directed at the component at a power level and period of time to produce a 1mm deep bead into the external surface of the component. The welded strip and spots were monitored using the potential drop system however no indication of cracking appeared during experiment #10. The welded zones were inspected under a microscope but no visible signs of crack growth were detected. The same component was replaced in the rig and cycled as experiment #14 with a higher maximum temperature range. with no change in the potential signal, the component was removed and inspected for crack growth. When no crack growth was detected, the experiment was abandoned.

Another component was subjected to a high powered laser beam for a very short period of time, 0.5 seconds, to produce laser spots, which contained small cracks, on the external surface. The four "defective" laser spot welds were inspected under a microscope before testing to measure the length of the surface cracks, one of which is shown in Figure 3.4.61.

At 120° around the component, on either side from the row of laser spot welds, two holes were machined into the external surface. One hole was 2mm in diameter and 1mm deep while the other was 4mm in diameter and 2mm deep. Following 65,105 cycles, the cracks in the laser spots had grown in length along the surface although they had not propagated out of the welds and along the external surface. The extension in the crack within the laser welded spot in Figure 3.4.61, is clearly shown in Figure 3.4.62. Cracks had grown in the longitudinal direction from both the machined holes. From the large hole the cracks had propagated 7.76mm and 2.95mm from either side of the hole, while from the small hole the crack growth was limited to 0.97mm and 0.44mm in length.

The component was sectioned through the laser spots and the machined holes and the crack depths were measured. With the largest two laser spot welds, the cracks had penetrated into the base material of the component, Figure 3.4.63. The total crack depths, including the depth of the laser spots, were 0.6mm and 1.00mm, while the cracking although short, was generally transgranular through both the welded and the base material.

From the 2mm deep hole the crack had grown a further 0.88mm in depth while the crack

extension from the smaller 0.88mm deep hole was 0.12mm in depth. From both machined holes, the crack growth was greater along the surface than in depth, as the cracks tended to grow semi-elliptical in shape.

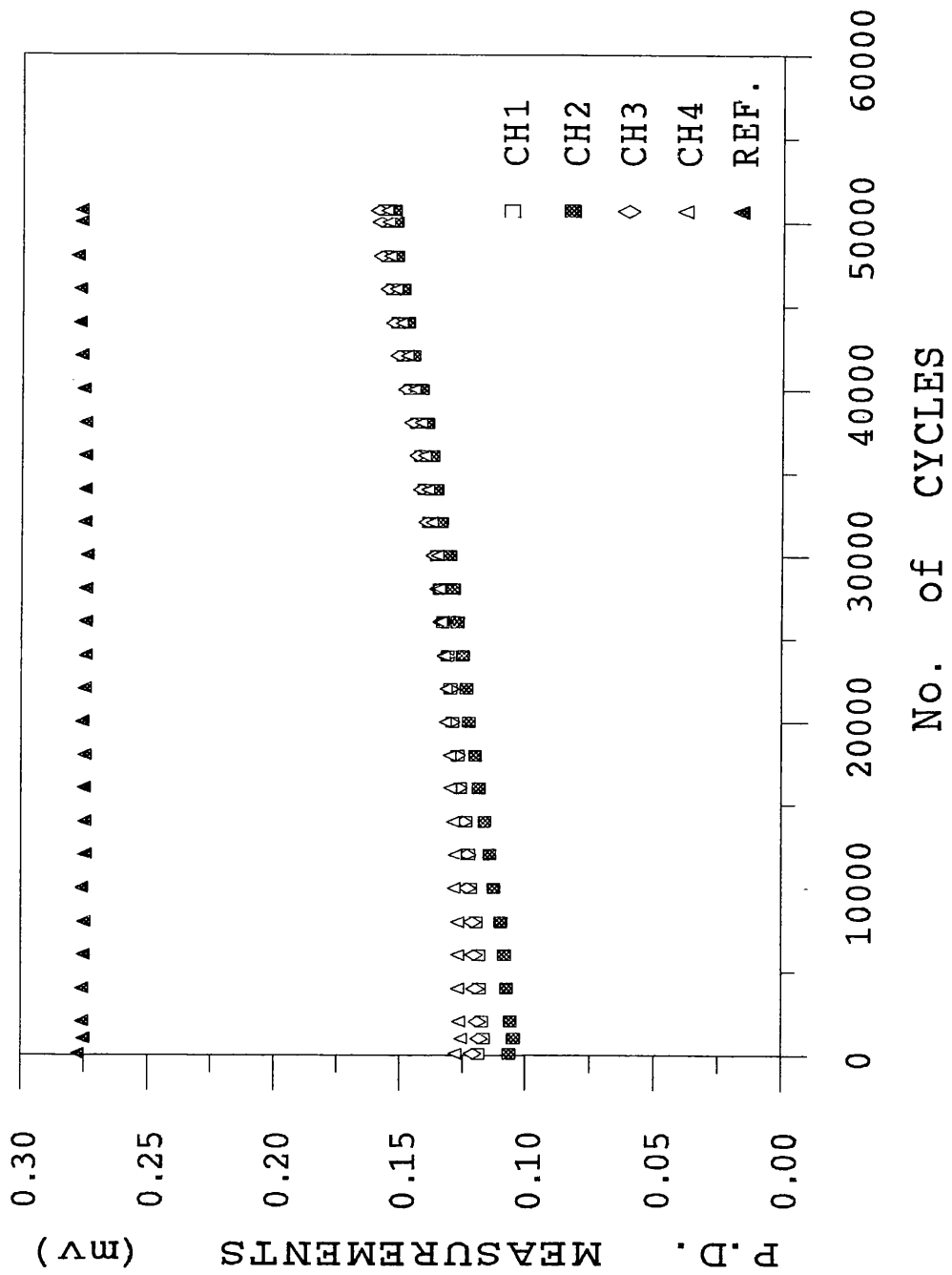


Figure 3.4.18. Potential Measurements in Expt.#4.

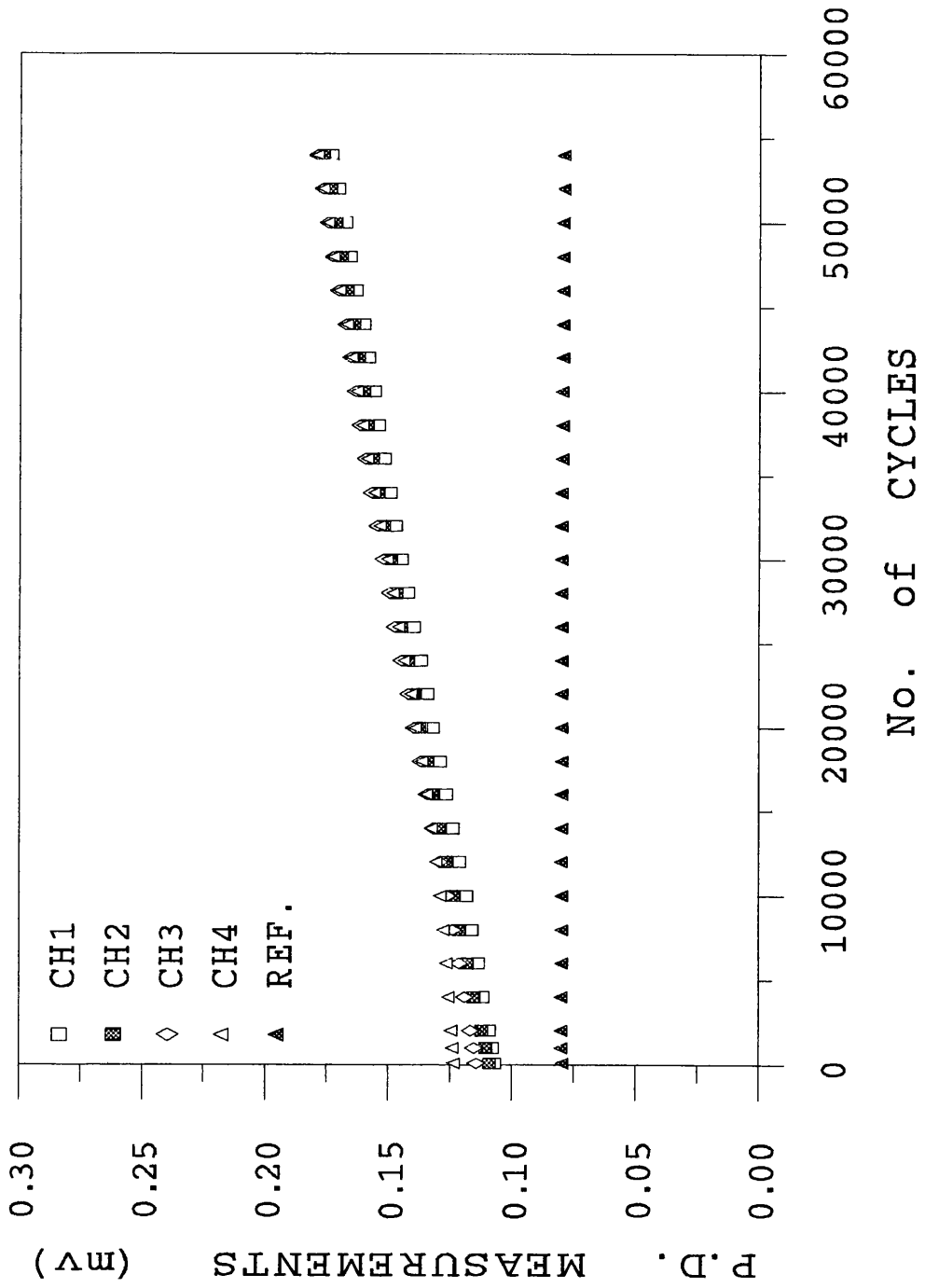


Figure 3.4.19. Potential Measurements in Expt.#12.

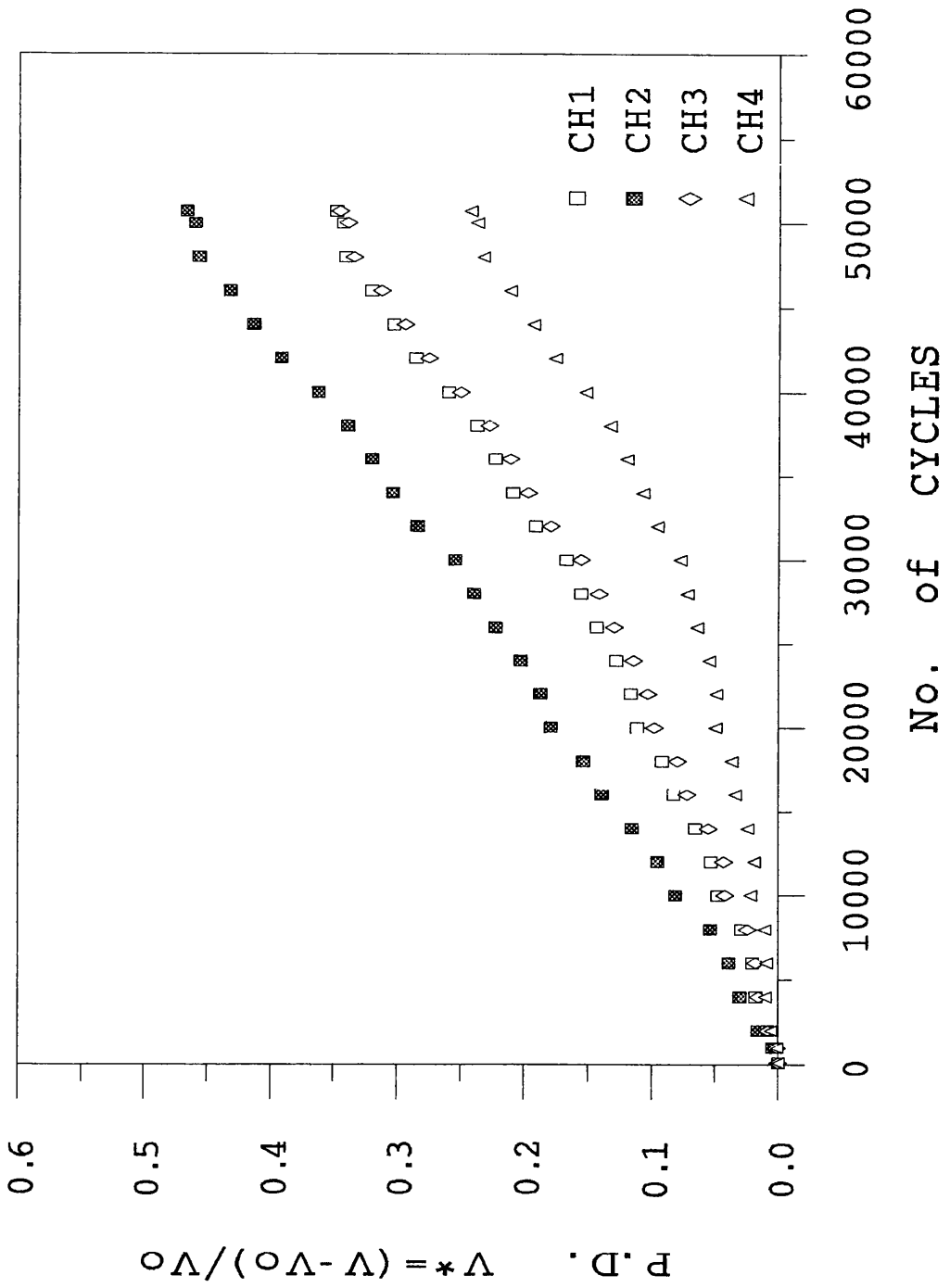


Figure 3.4.20. Normalized Potential Measurements in Expt.#4.

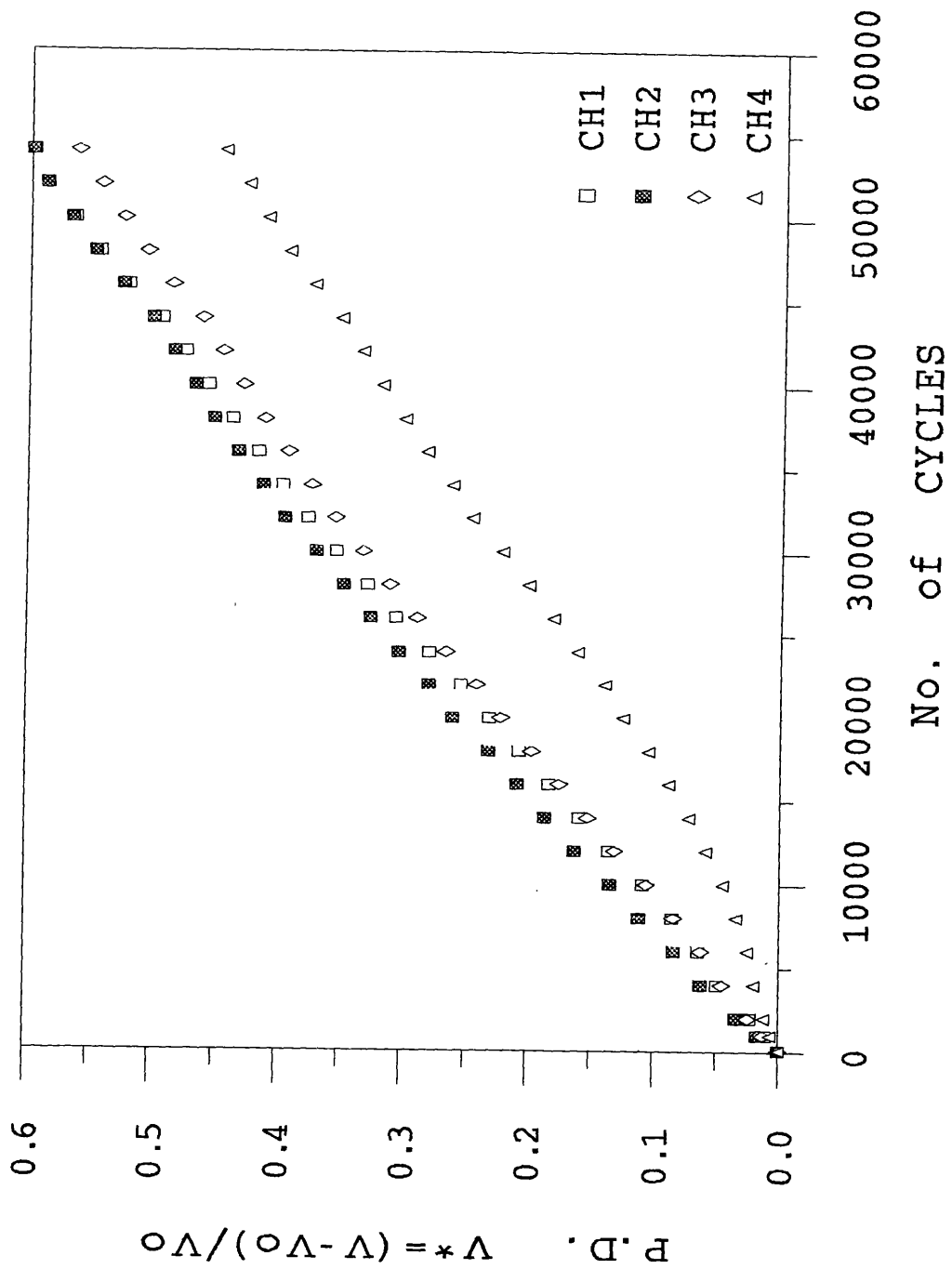


Figure 3.4.21. Normalized Potential Measurements in Expt.#12.

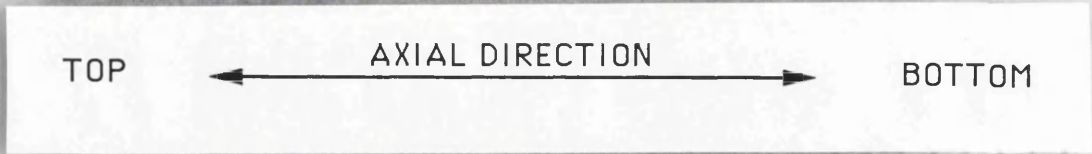


Figure 11. (Caption text is faint and partially obscured)

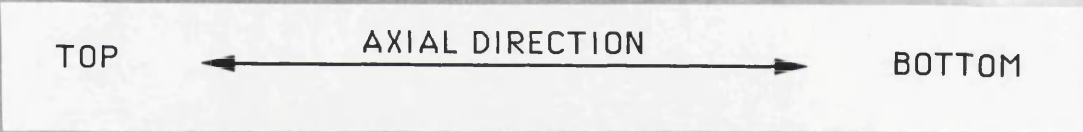


Figure 12. (Caption text is faint and partially obscured)

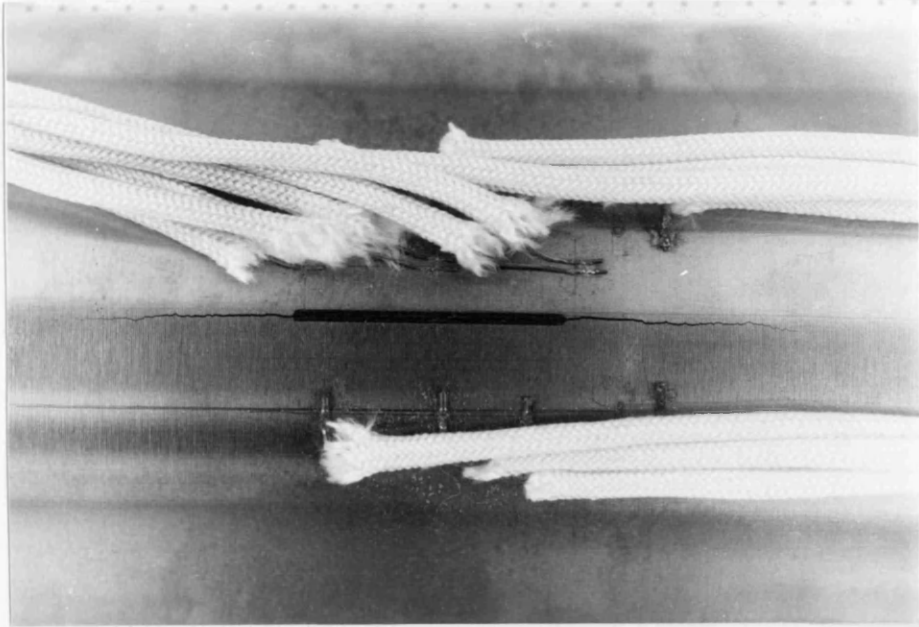


Figure 3.4.22. Crack Growth along the External Surface from the Notch, Expt.#11, (Mag.X2.4).

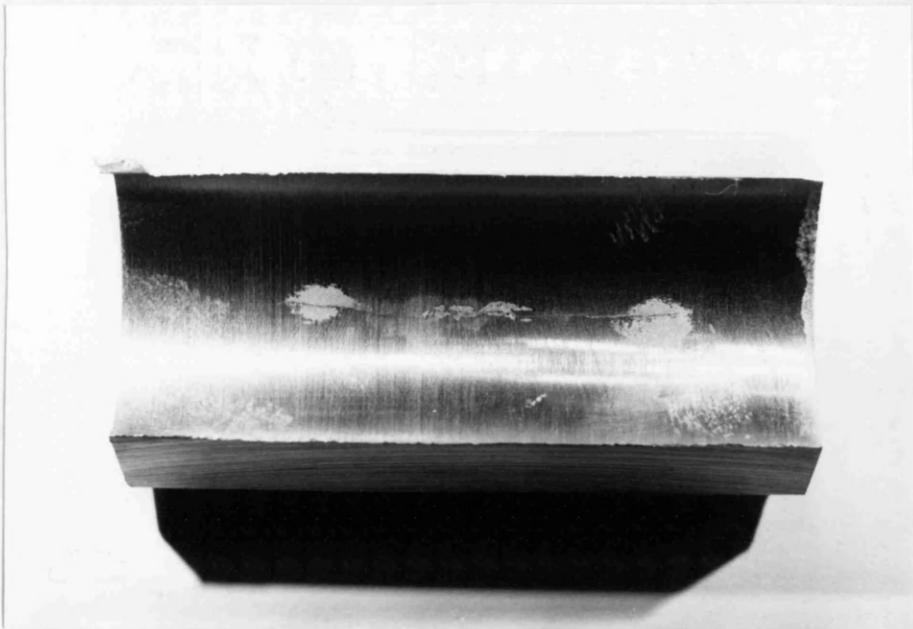


Figure 3.4.23. Crack Growth along the Internal Surface, Expt.#23, (Mag.X1.8).

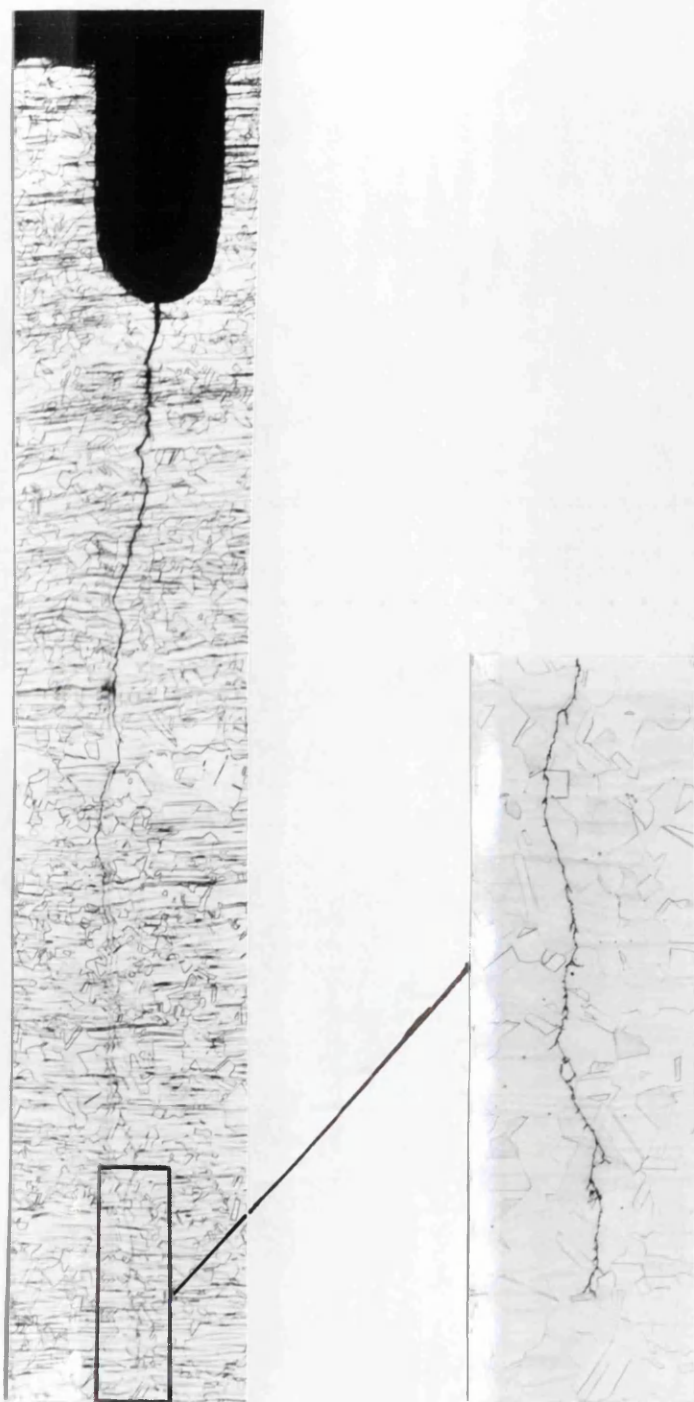


Figure 3.4.24. Transgranular Crack from External Longitudinal Notch, Expt.#4,
(Mag.X32), Insert Photograph, (Mag.X100).

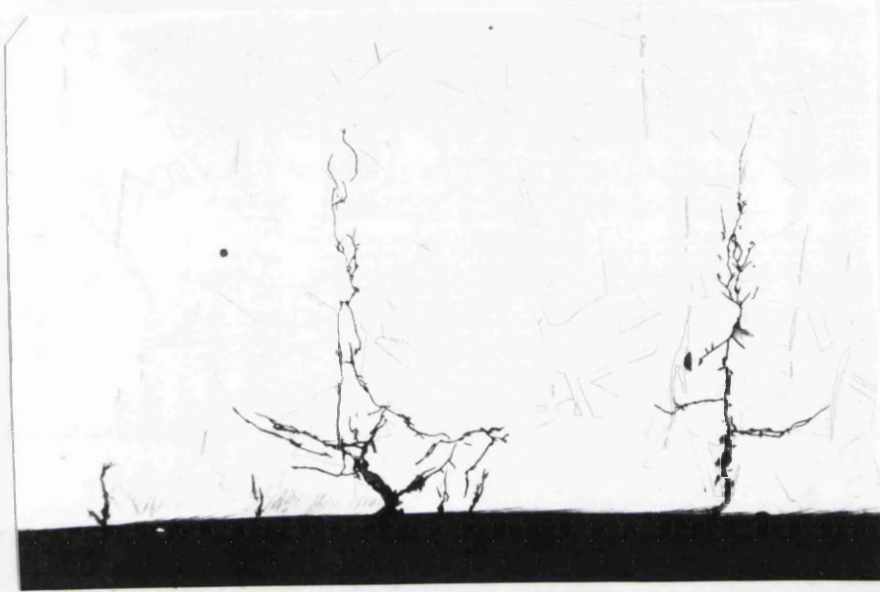


Figure 3.4.25. Internal Surface Crack Initiation, Expt.#5, (Mag.X200).

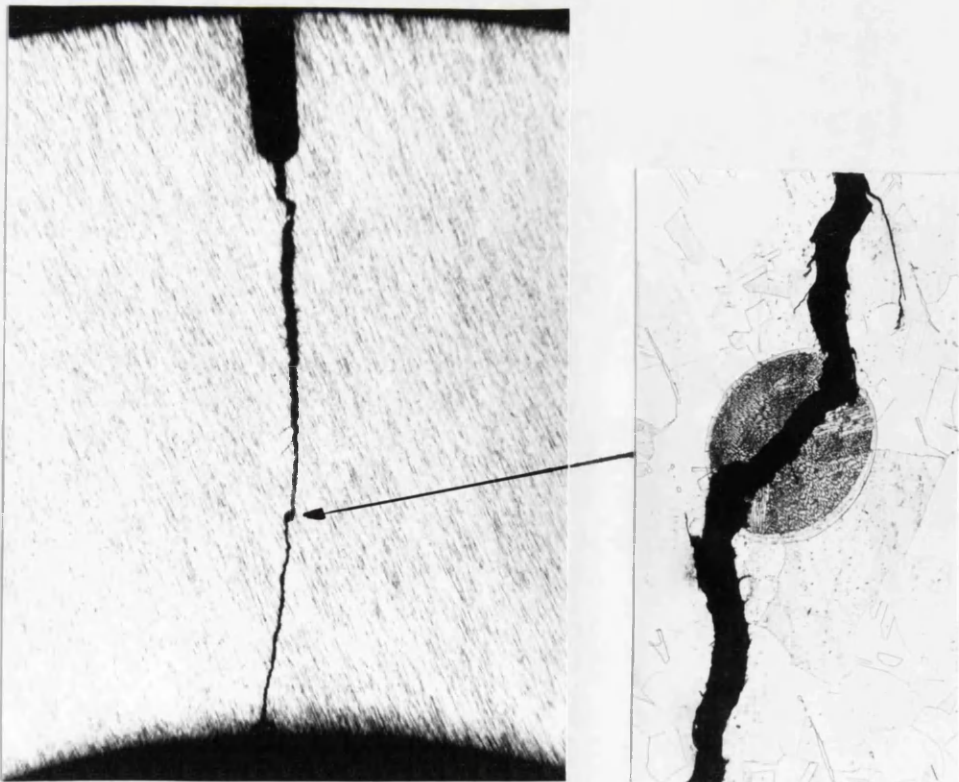


Figure 3.4.26. External and Internal Crack Coalescence, Expt.#23, (Mag.X10), Insert, (Mag.X160).

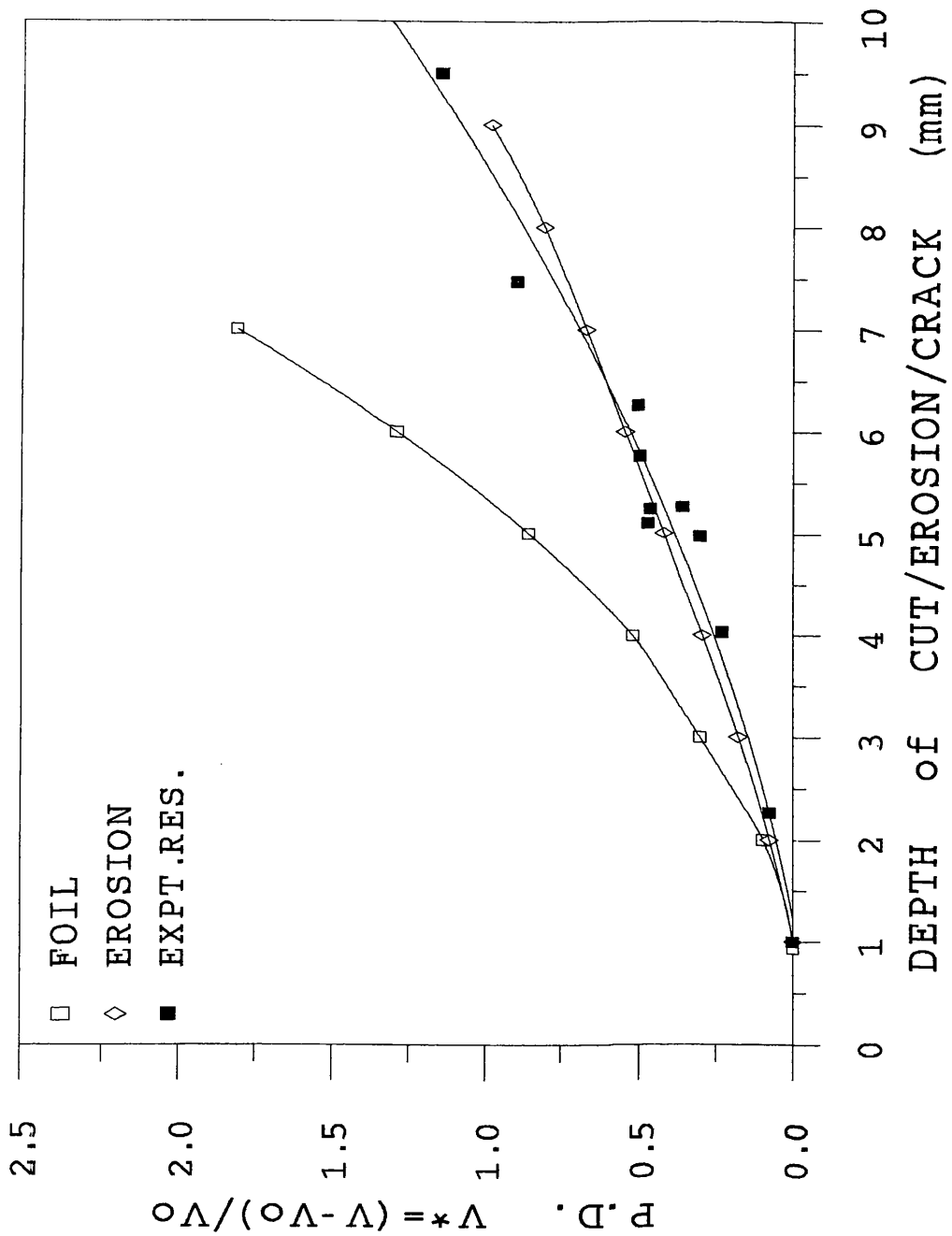


Figure 3.4.27a Calibration Curves for 1mm Deep External Longitudinal Notched Components: Established by Different Methods.

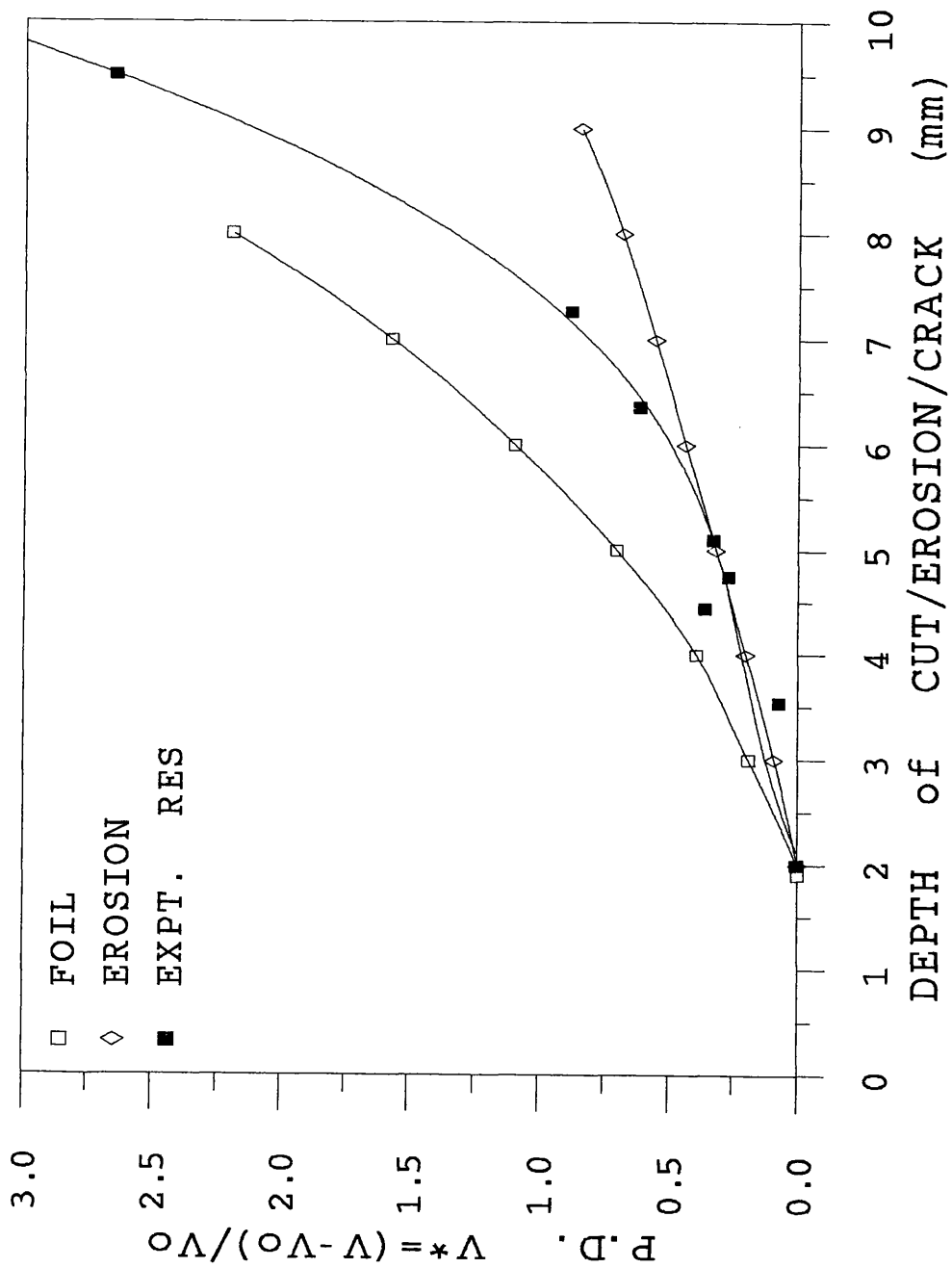


Figure 3.4.27b. Calibration Curves for 2mm Deep External Longitudinal Notched Components: Established by Different Methods.

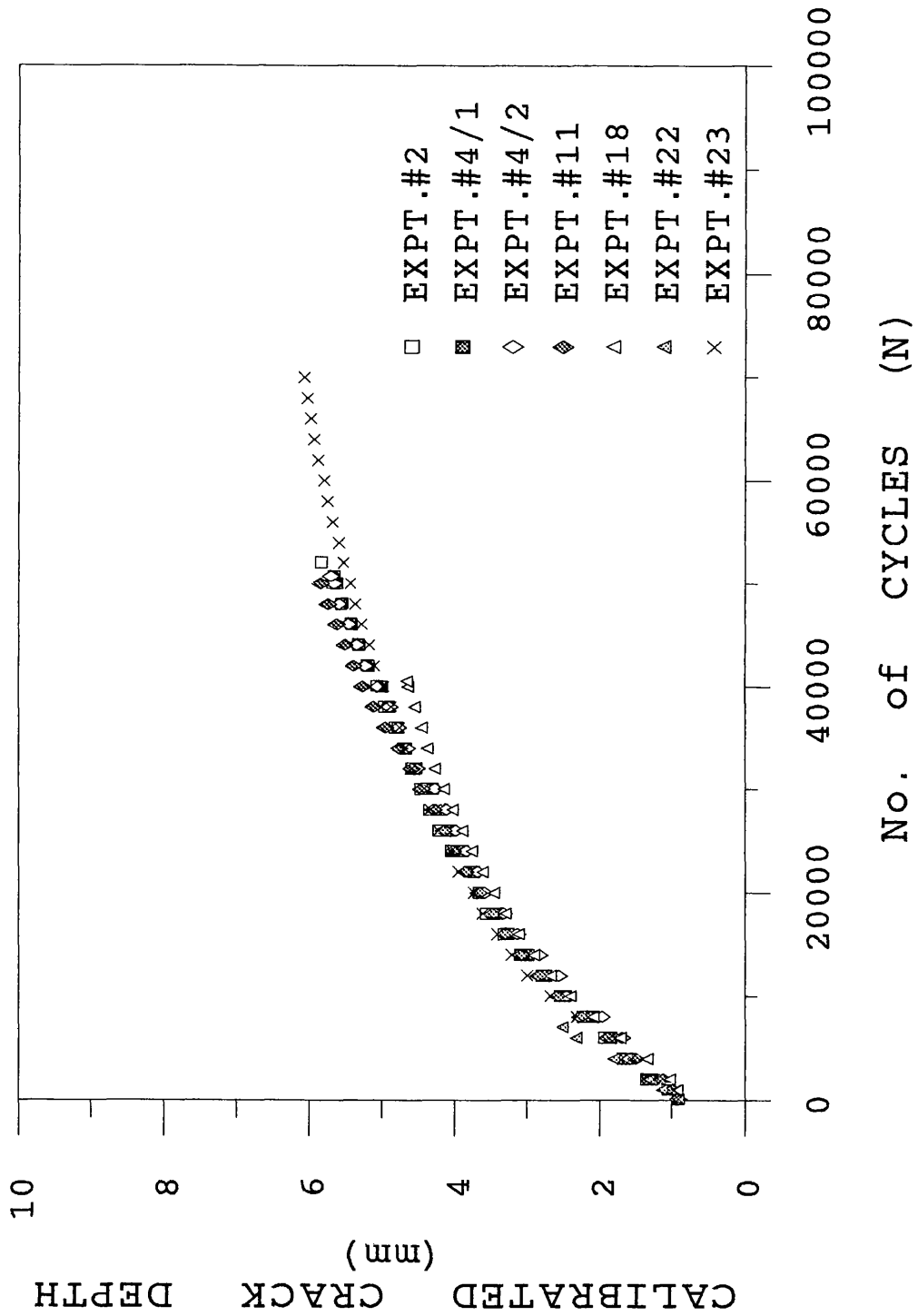


Figure 3.4.28a. Calibrated Crack Depths in 1mm Deep External Longitudinal Notched Components.

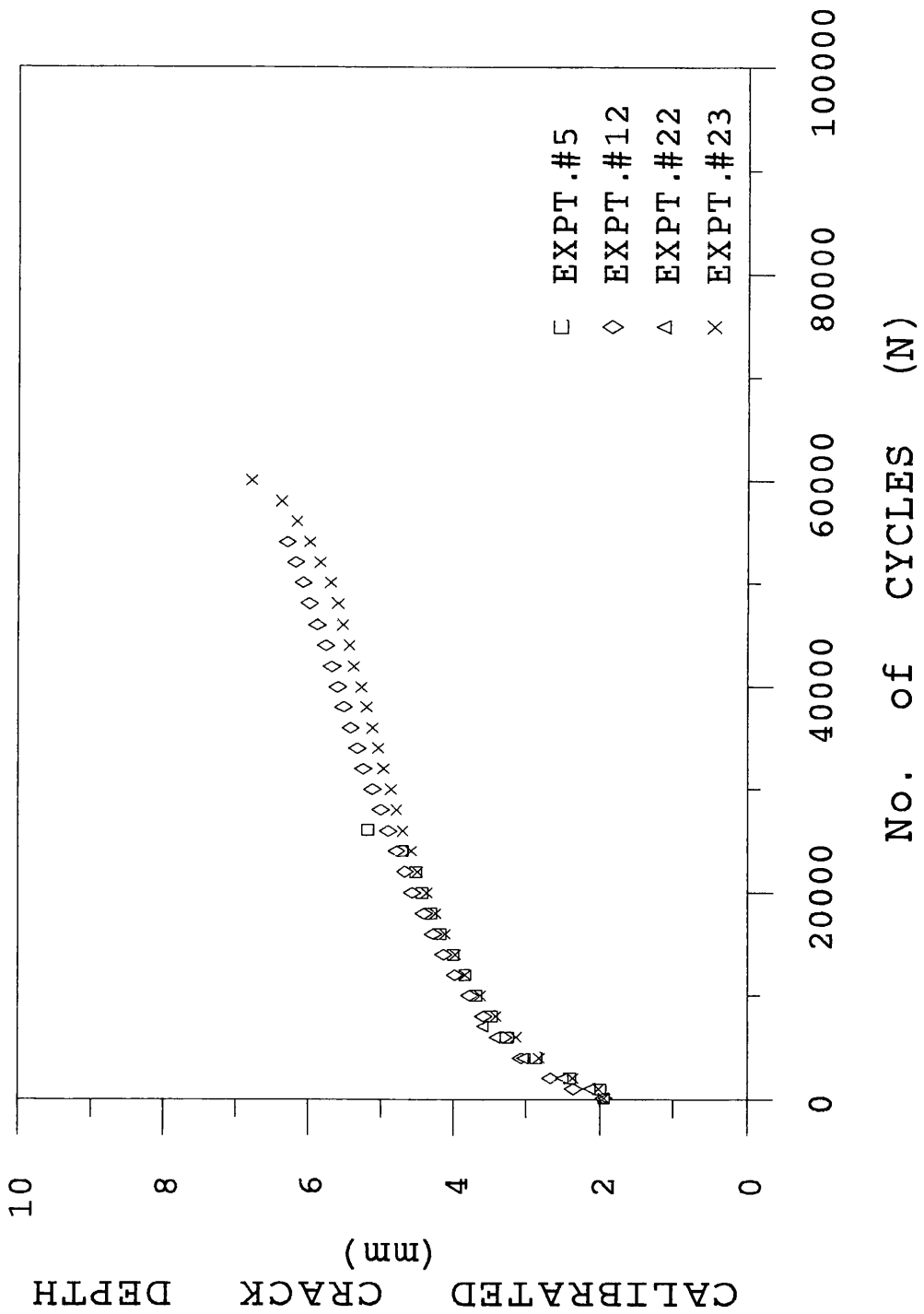


Figure 3.4.28b. Calibrated Crack Depths in 2mm Deep External Longitudinal Notched Components.

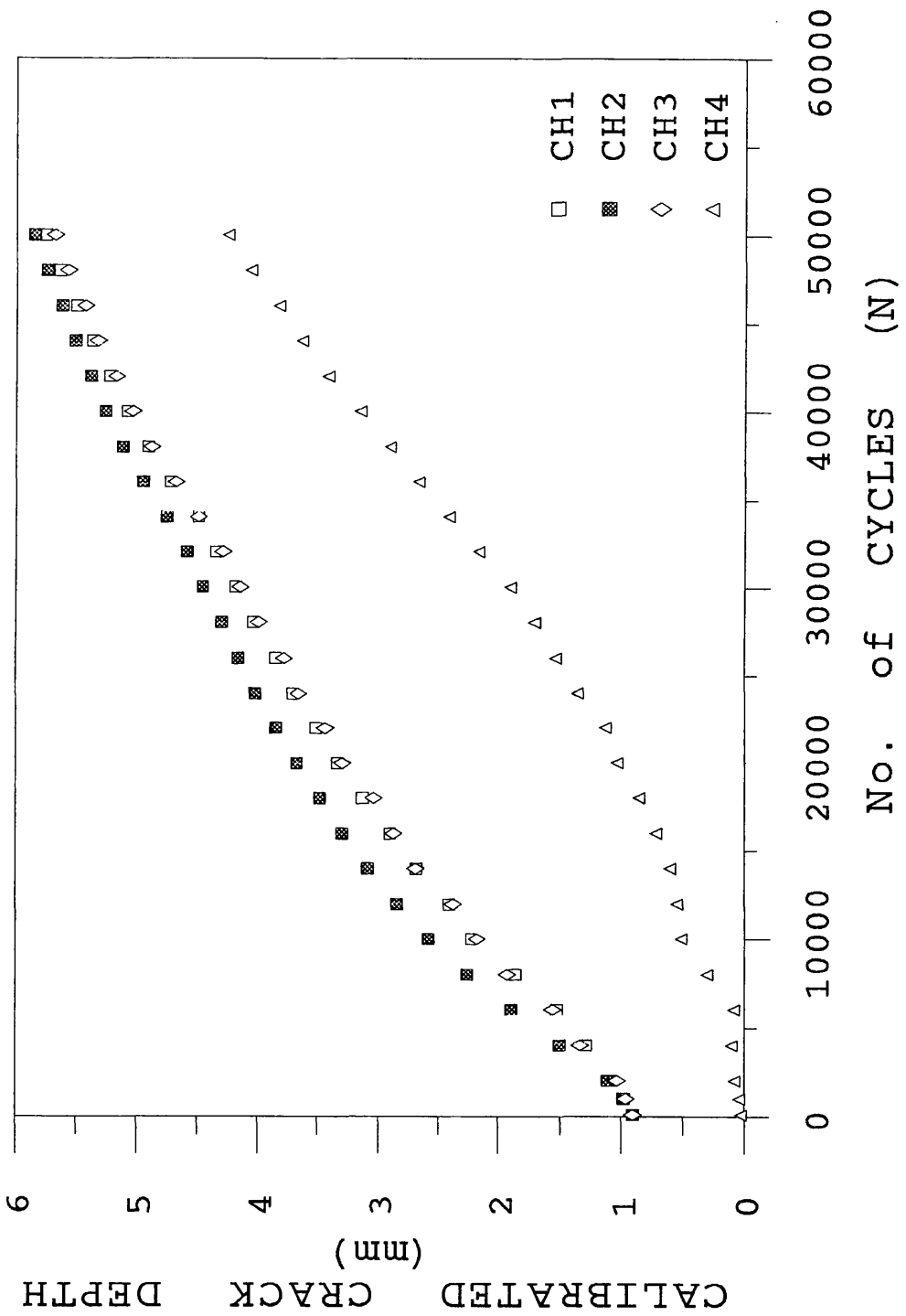
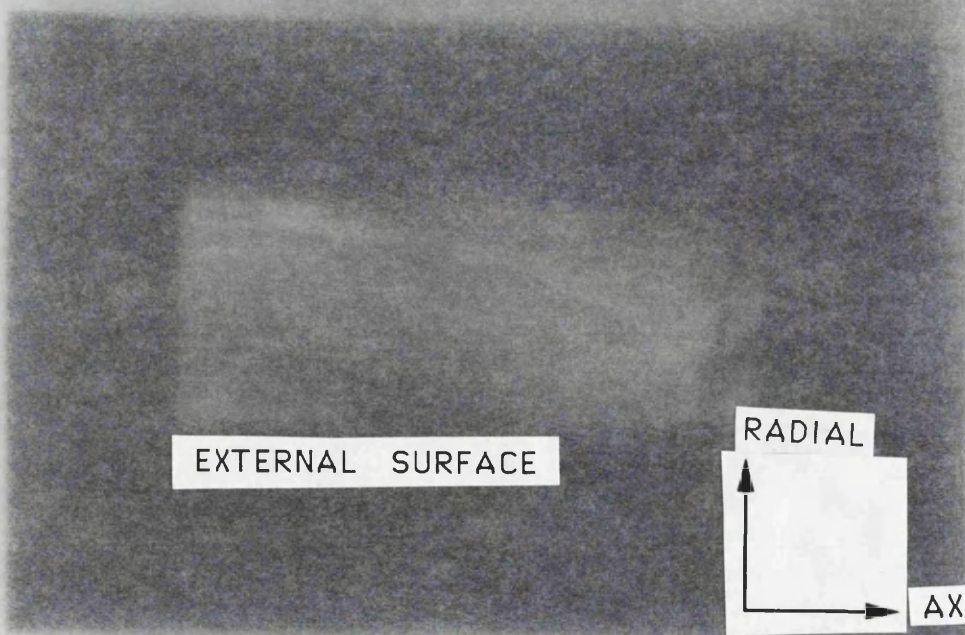


Figure 3.4.29. Development of Calibrated Crack Depths in Expt.#11.



EXTERNAL SURFACE

RADIAL

AXIAL

Figure 3.4.24. (a) Cross-section of a cylindrical component showing the external surface and the radial and axial directions.

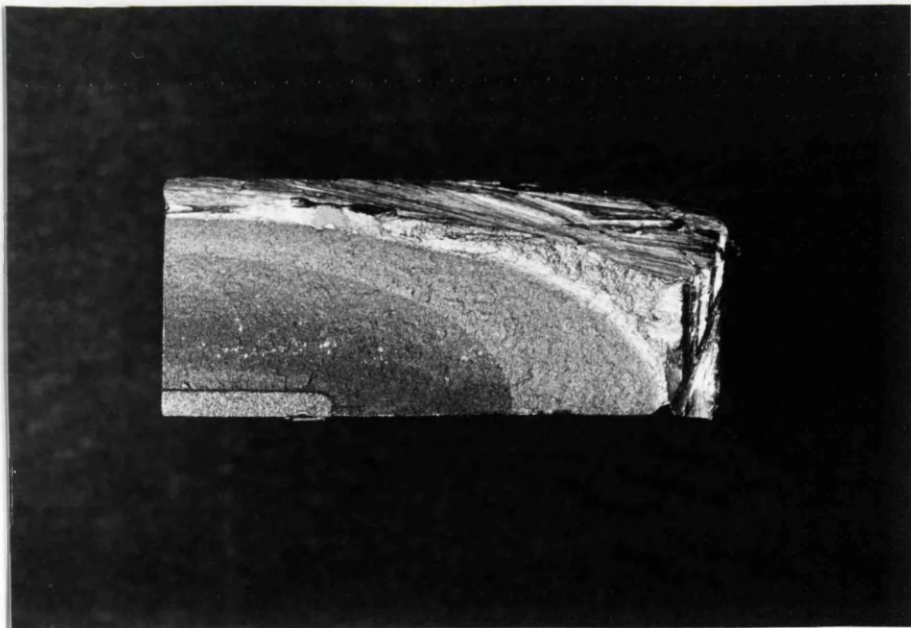


Figure 3.4.30. Heat Tinted Half Fracture Surface, Expt.#11,(Mag. X3.5).

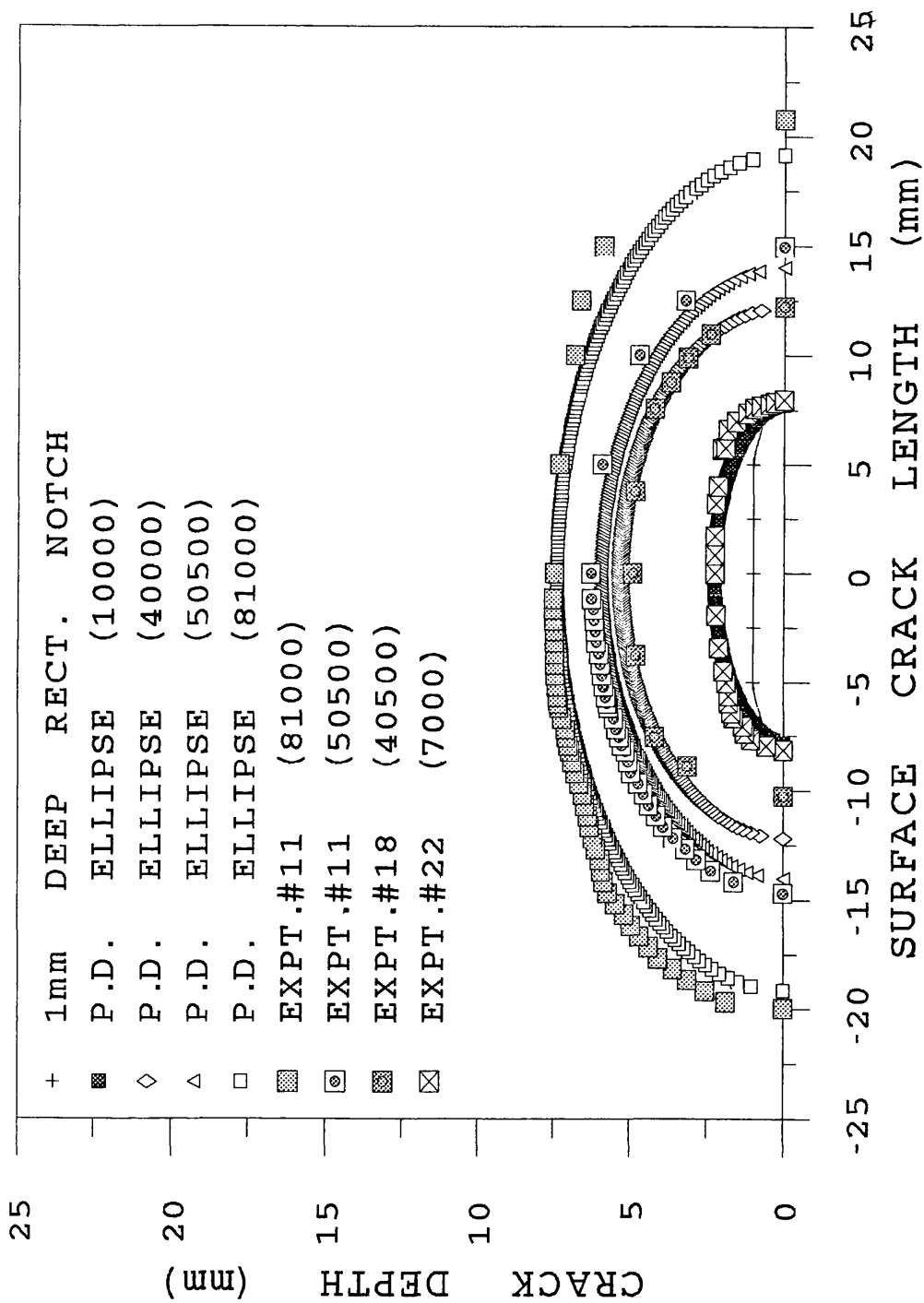


Figure 3.4.31. Crack Front Development and Experimental Results, Expt.#11.

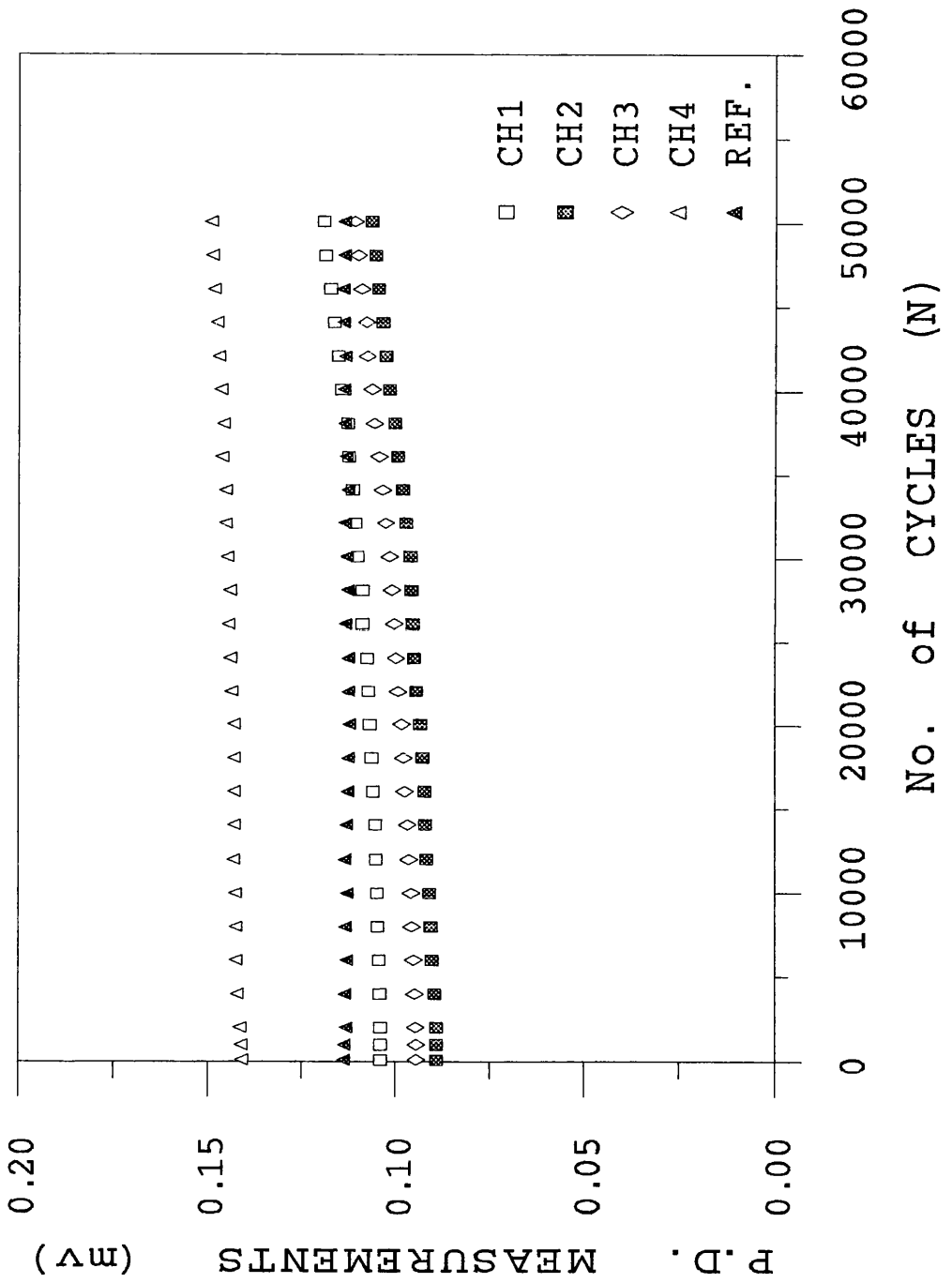


Figure 3.4.32. Potential Measurements in Expt.#9.

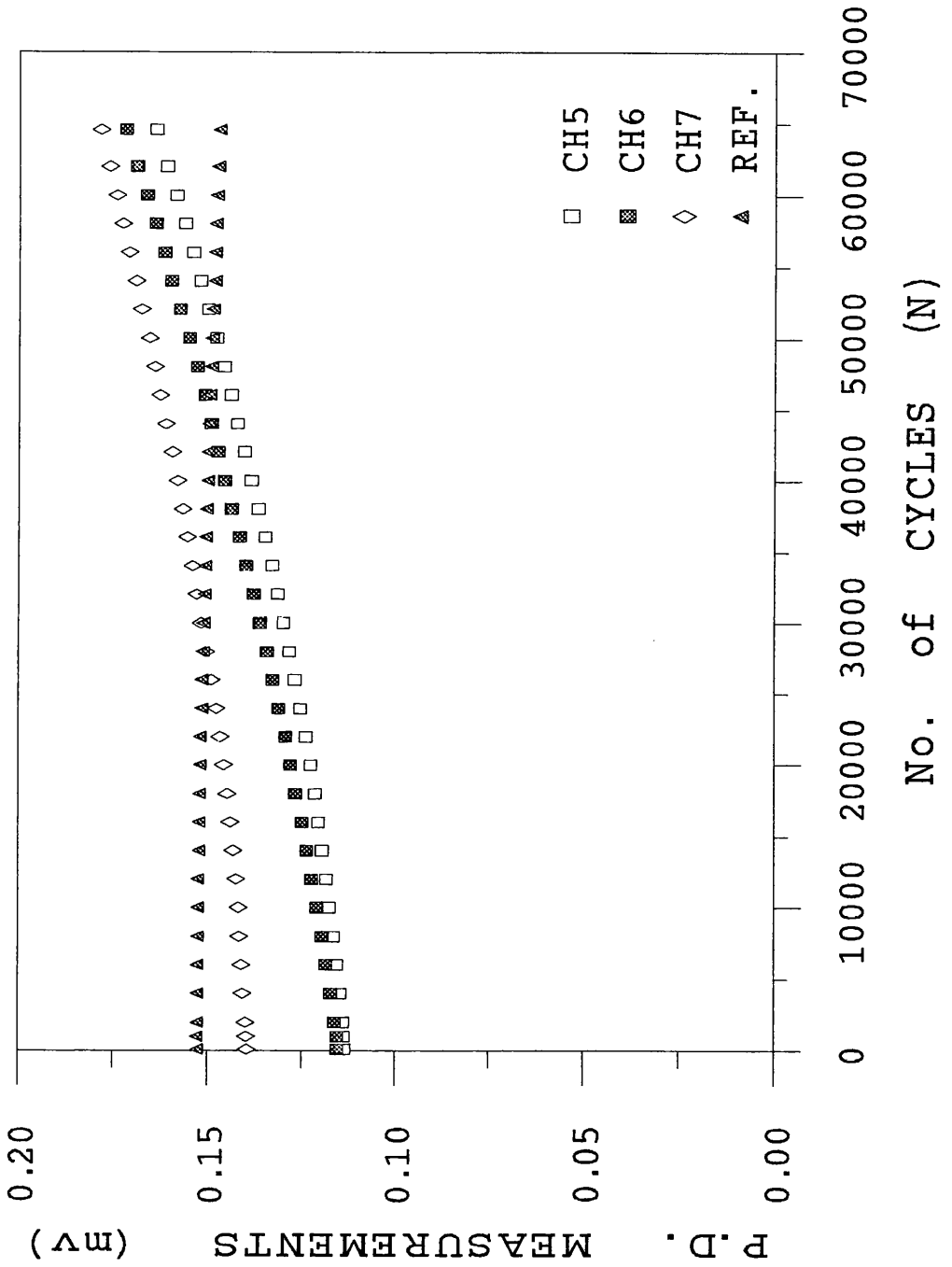


Figure 3.4.33. Potential Measurements in Expt.#17.

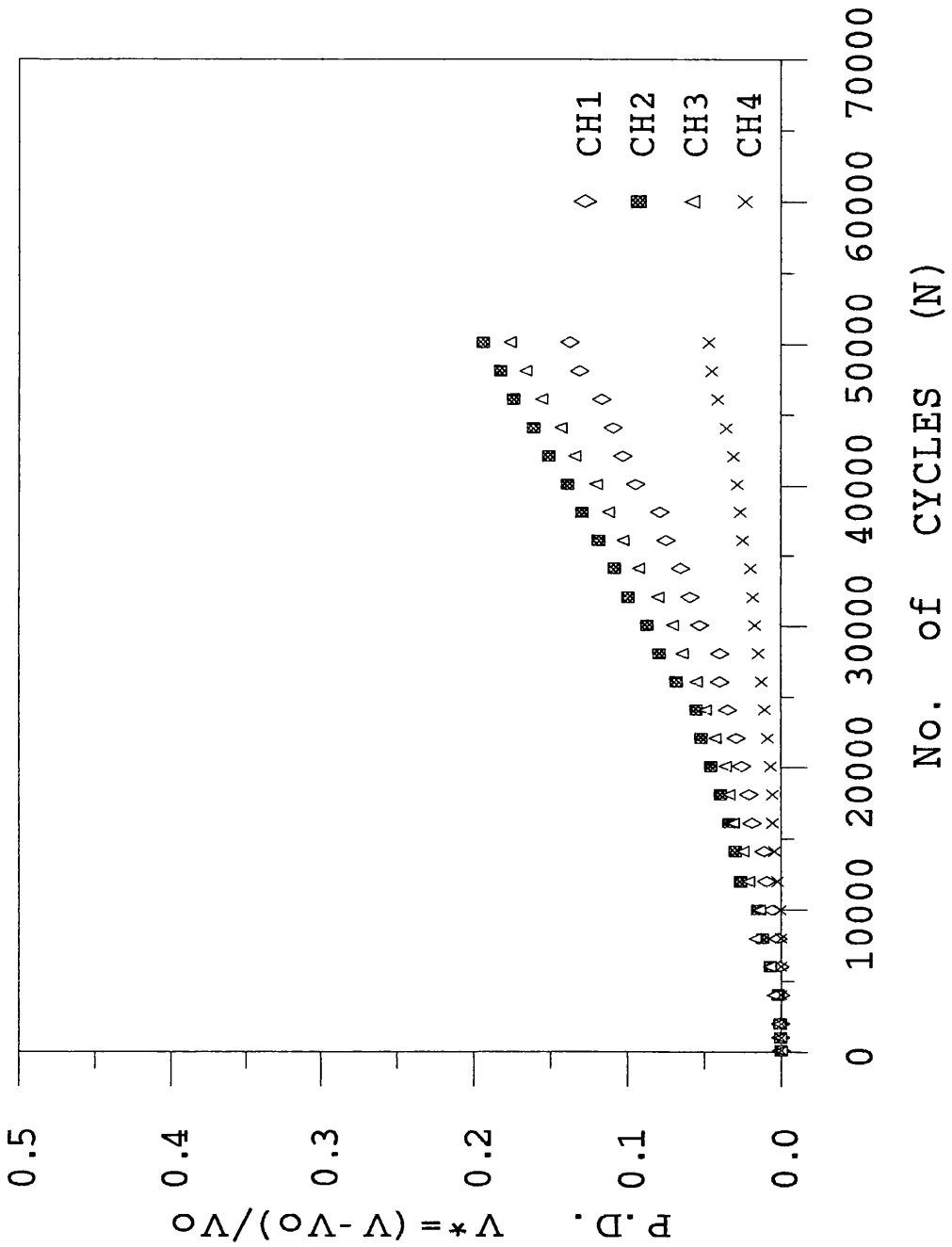


Figure 3.4.34. Normalized Potential Measurements in Expt.#9.

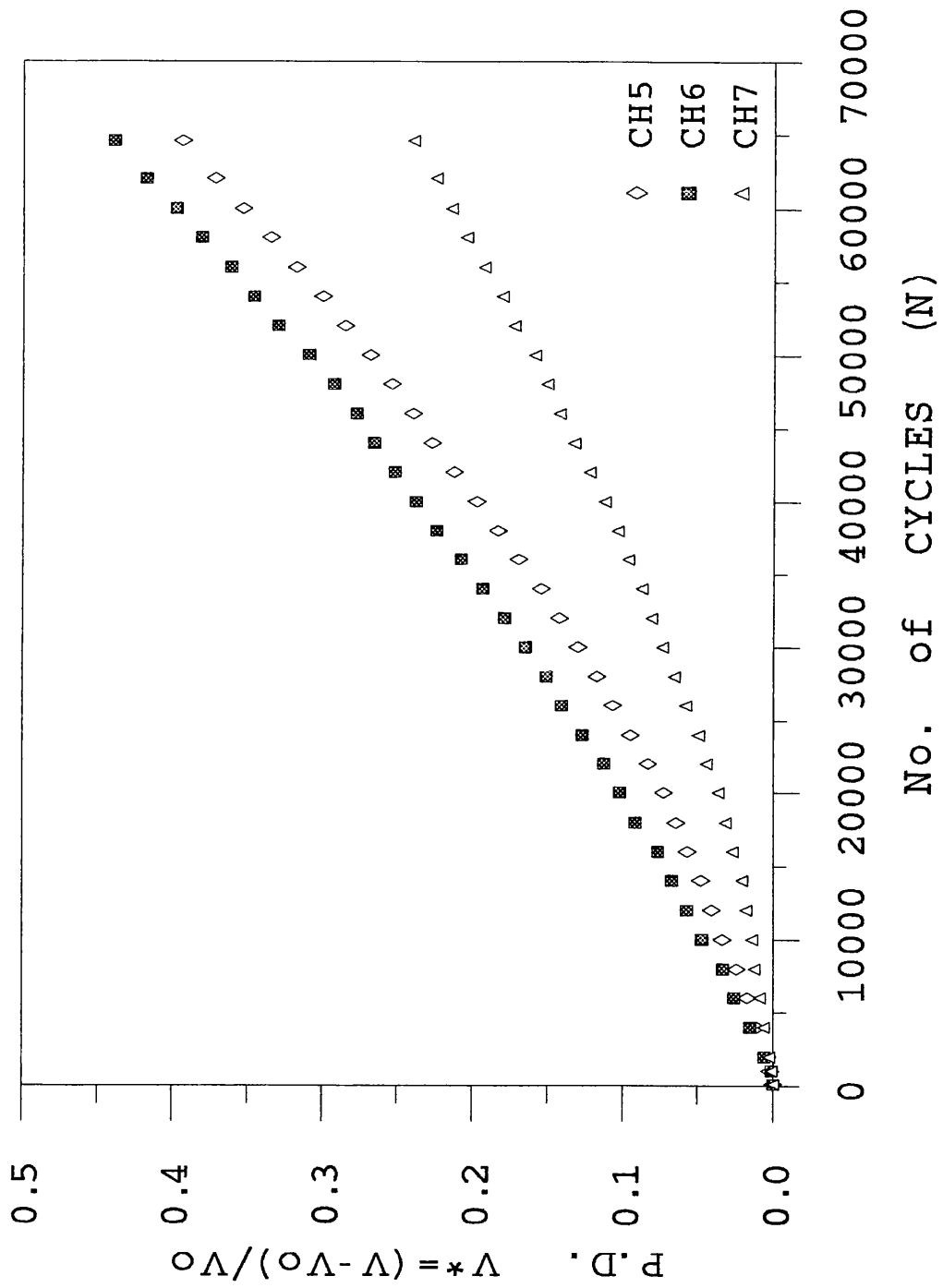


Figure 3.4.35. Normalized Potential Measurements in Expt.#17.



Figure 3.4.36. Transgranular Crack from an Internal Longitudinal Notch, Expt.#2, (Mag.X50).

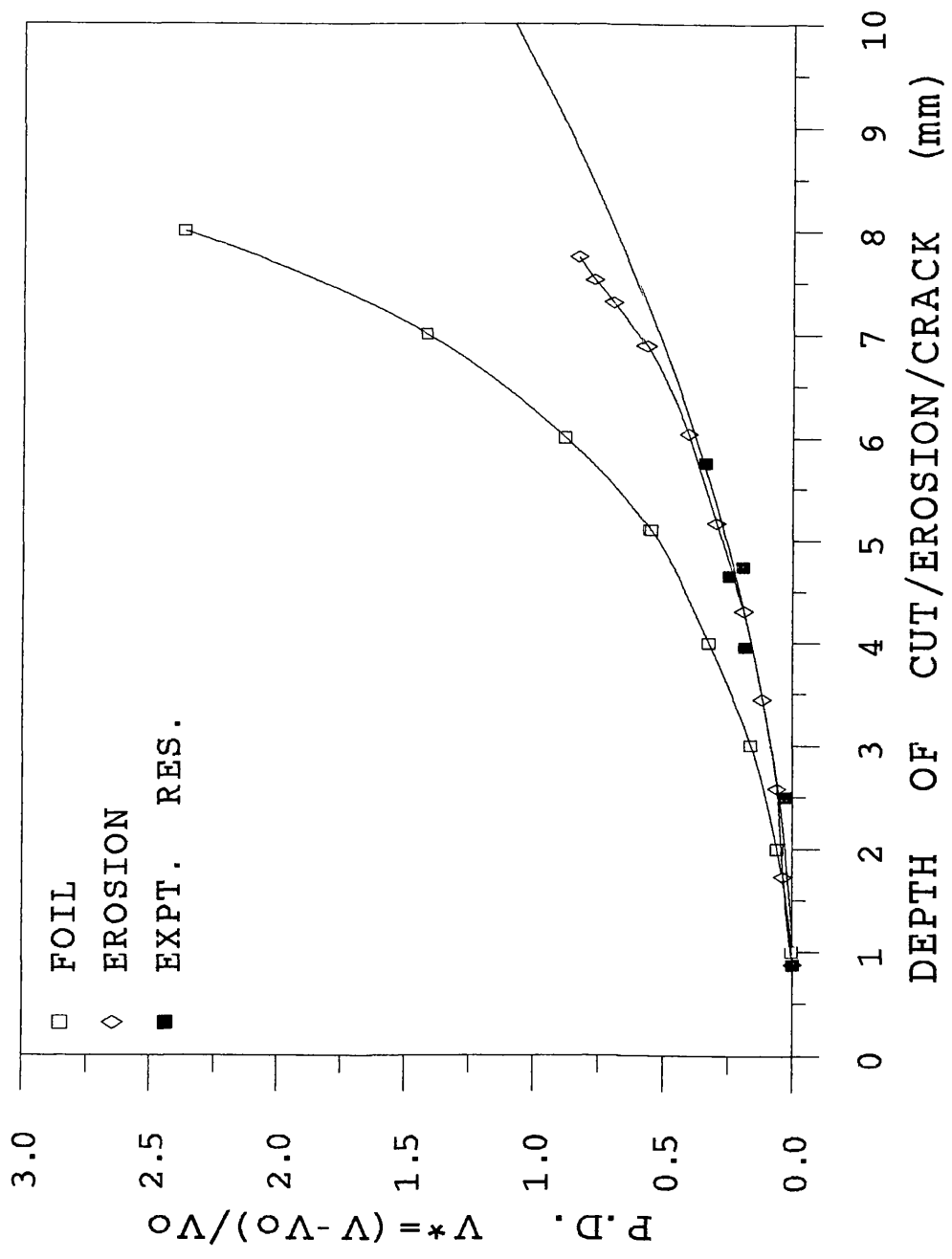


Figure 3.4.37a. Calibration Curves for 1mm Deep Internal Longitudinal Notched Components: Established by Different Methods.

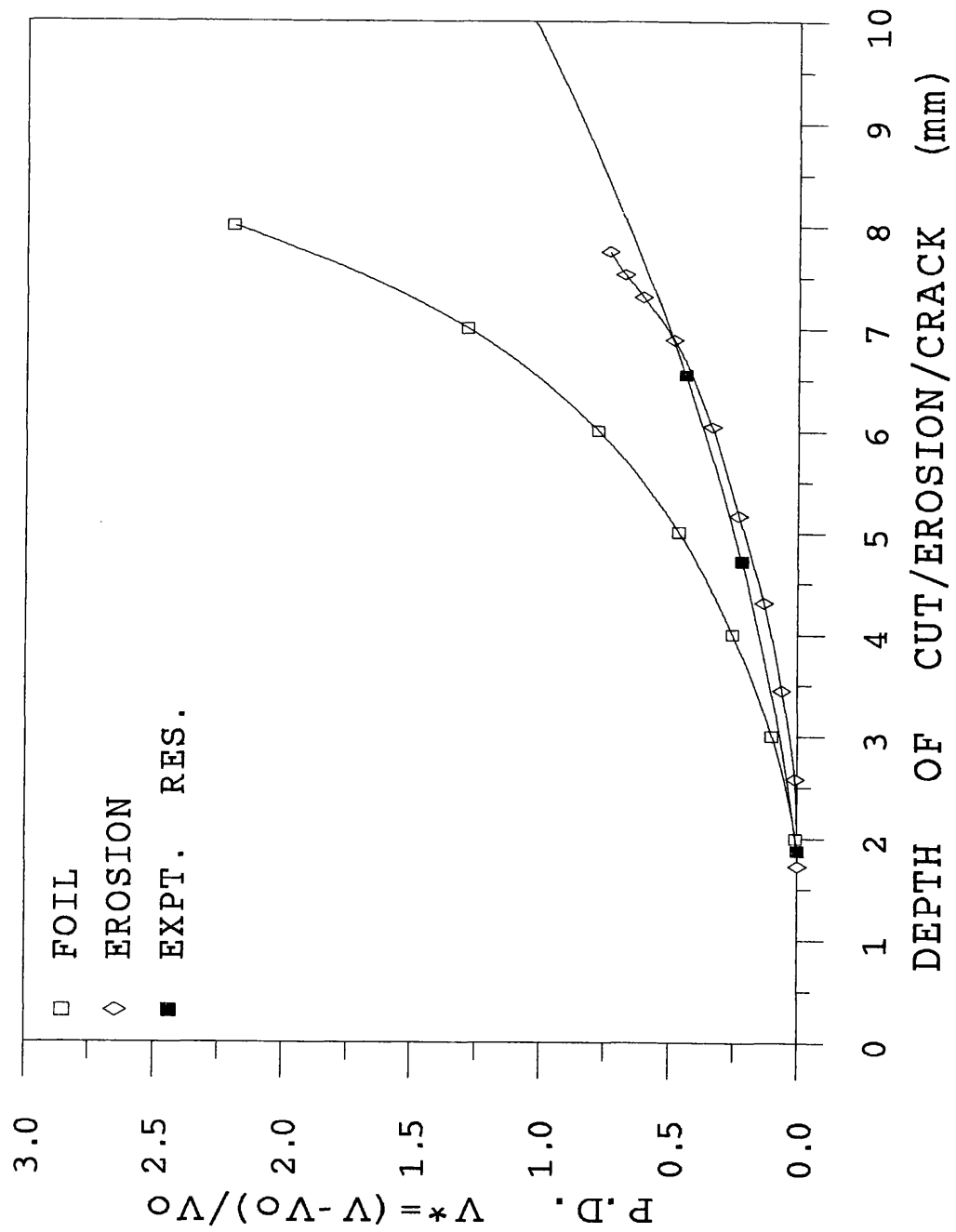


Figure 3.4.37b. Calibration Curves for 2mm Deep Internal Longitudinal Notched Components: Established by Different Methods.

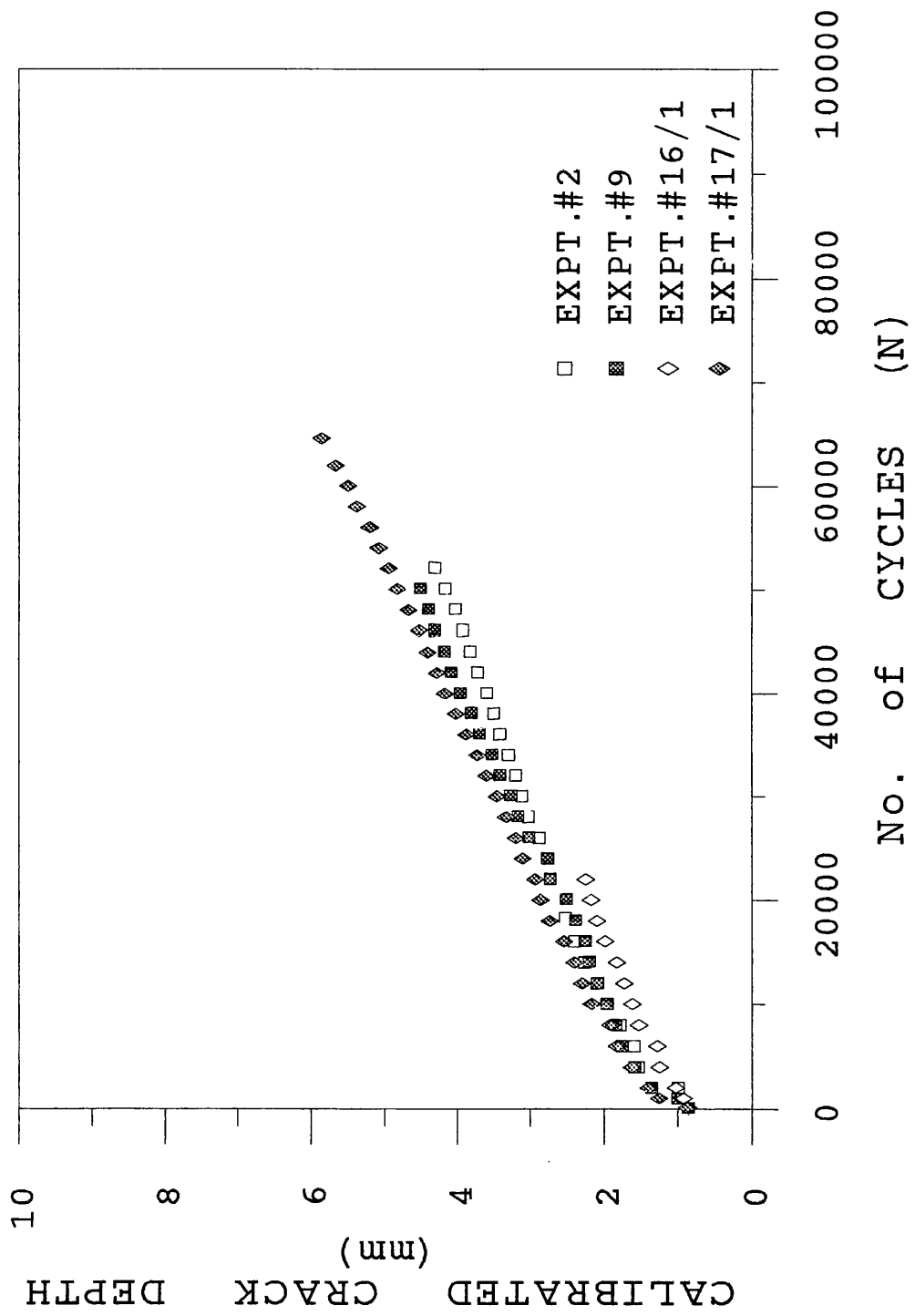


Figure 3.4.38a. Calibrated Crack Depths in 1mm Deep Internal Longitudinal Notched Components.

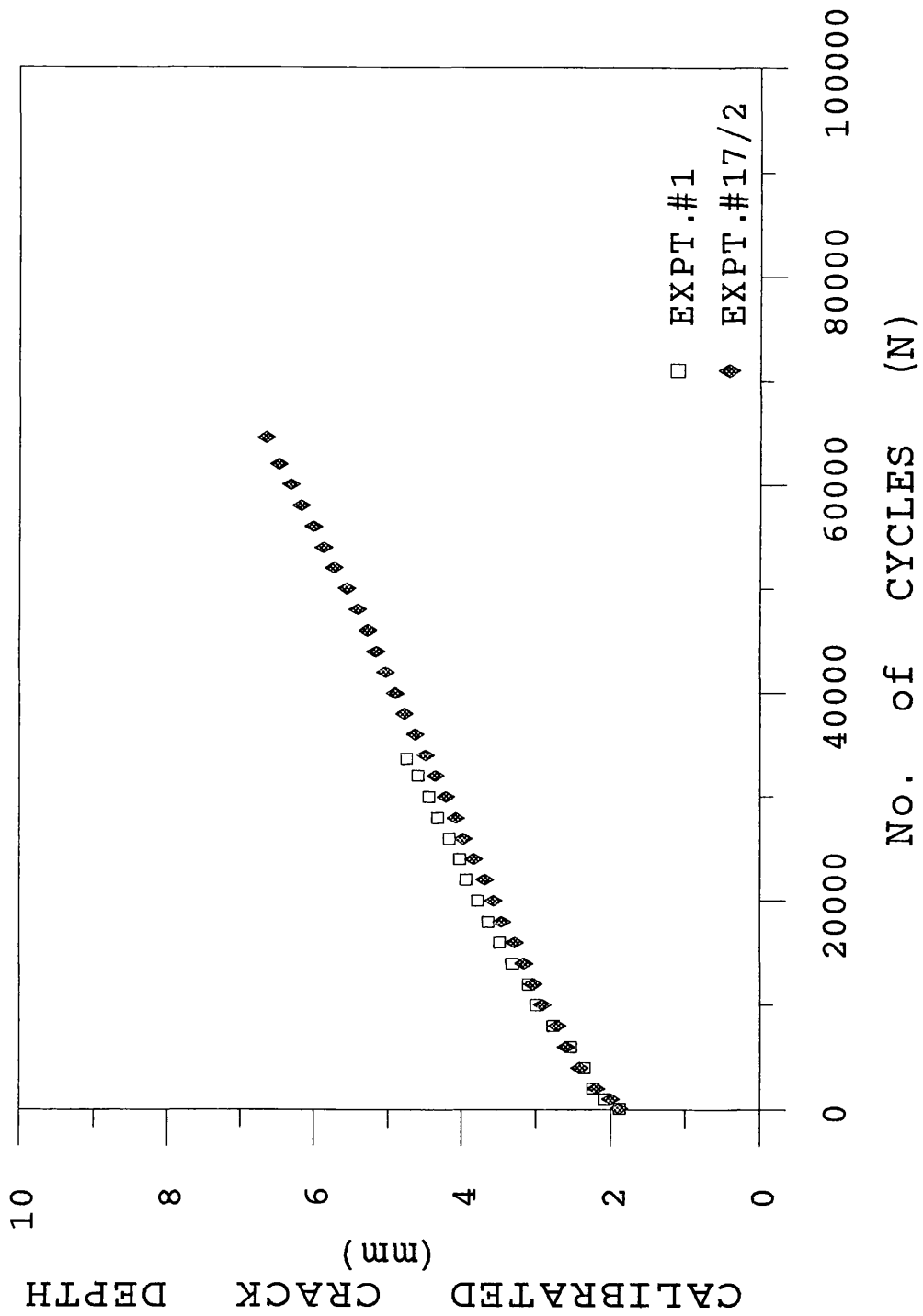


Figure 3.4.38b. Calibrated Crack Depths in 2mm Deep Internal Longitudinal Notched Components.

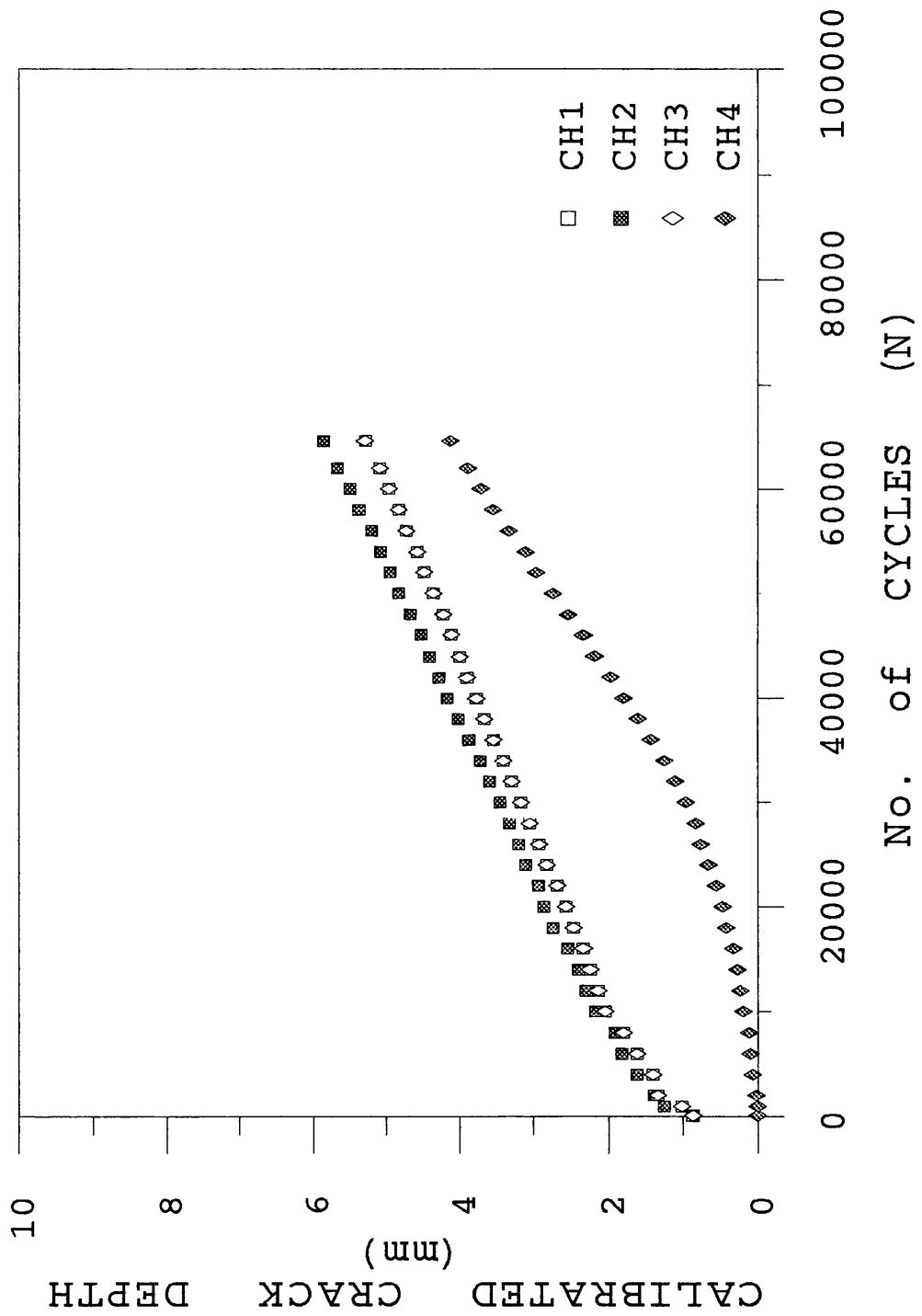


Figure 3.4.39. Calibrated Crack Depths in Expt.#17.

Faint, illegible text, possibly bleed-through from the reverse side of the page.

INTERNAL SURFACE

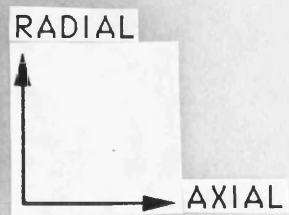




Figure 3.4.40. Half Fracture Surface, Expt.#2, (Mag.X3.5).

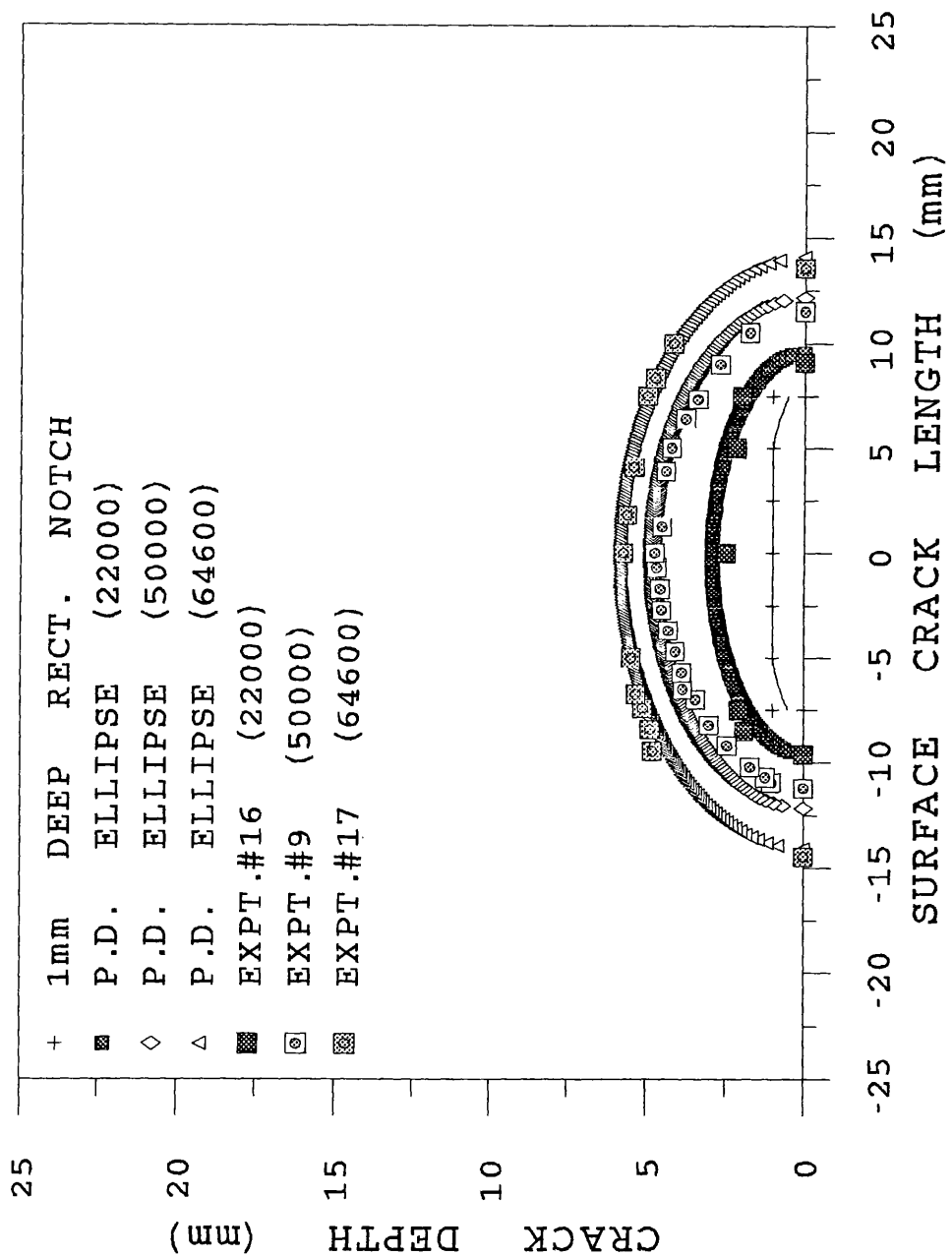


Figure 3.4.41. Crack Front Development and Experimental Results from Expt.#17.

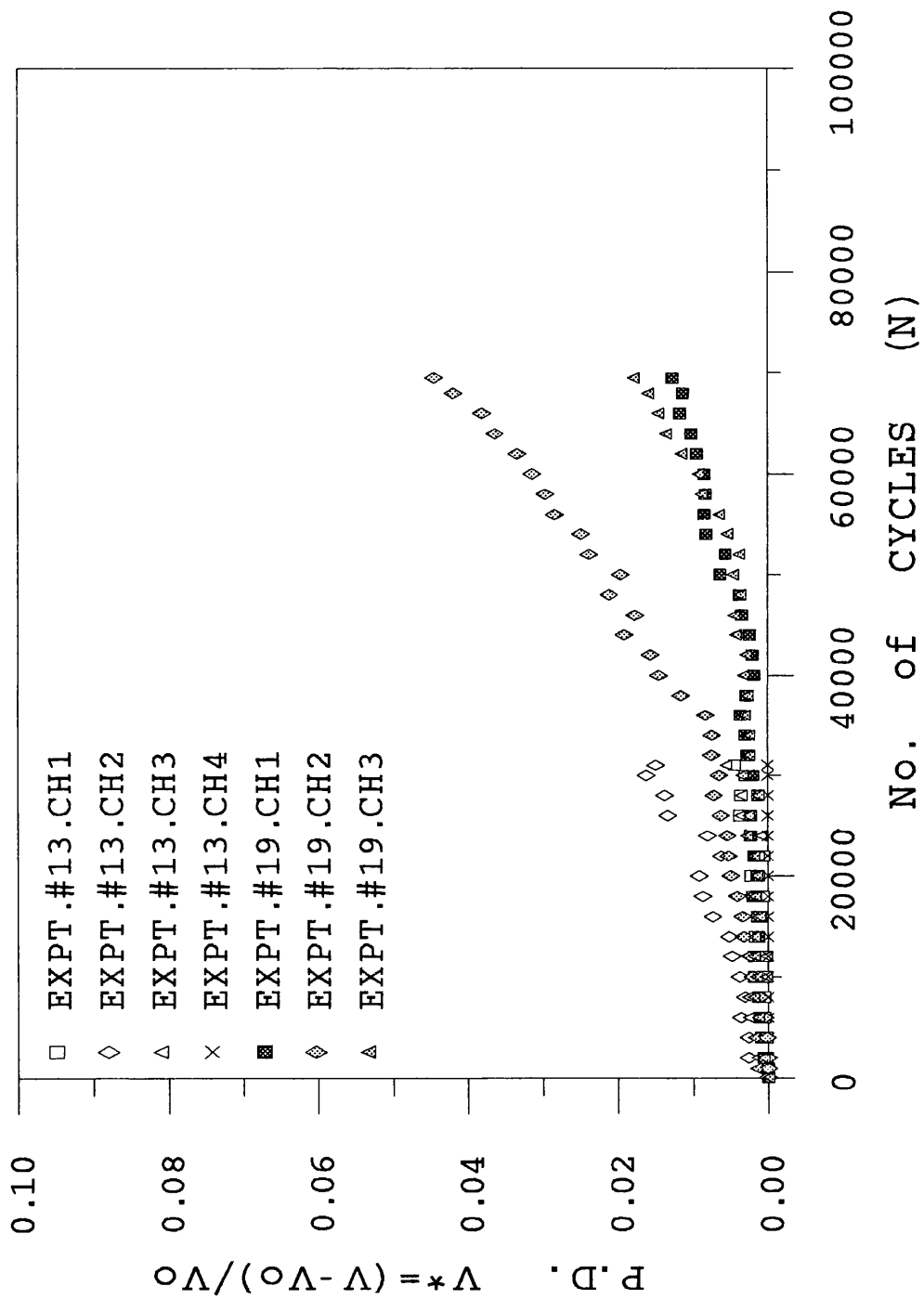


Figure 3.4.42. Normalized Potential Difference for 1mm Deep External Longitudinal Semi-Circular Notched Components.

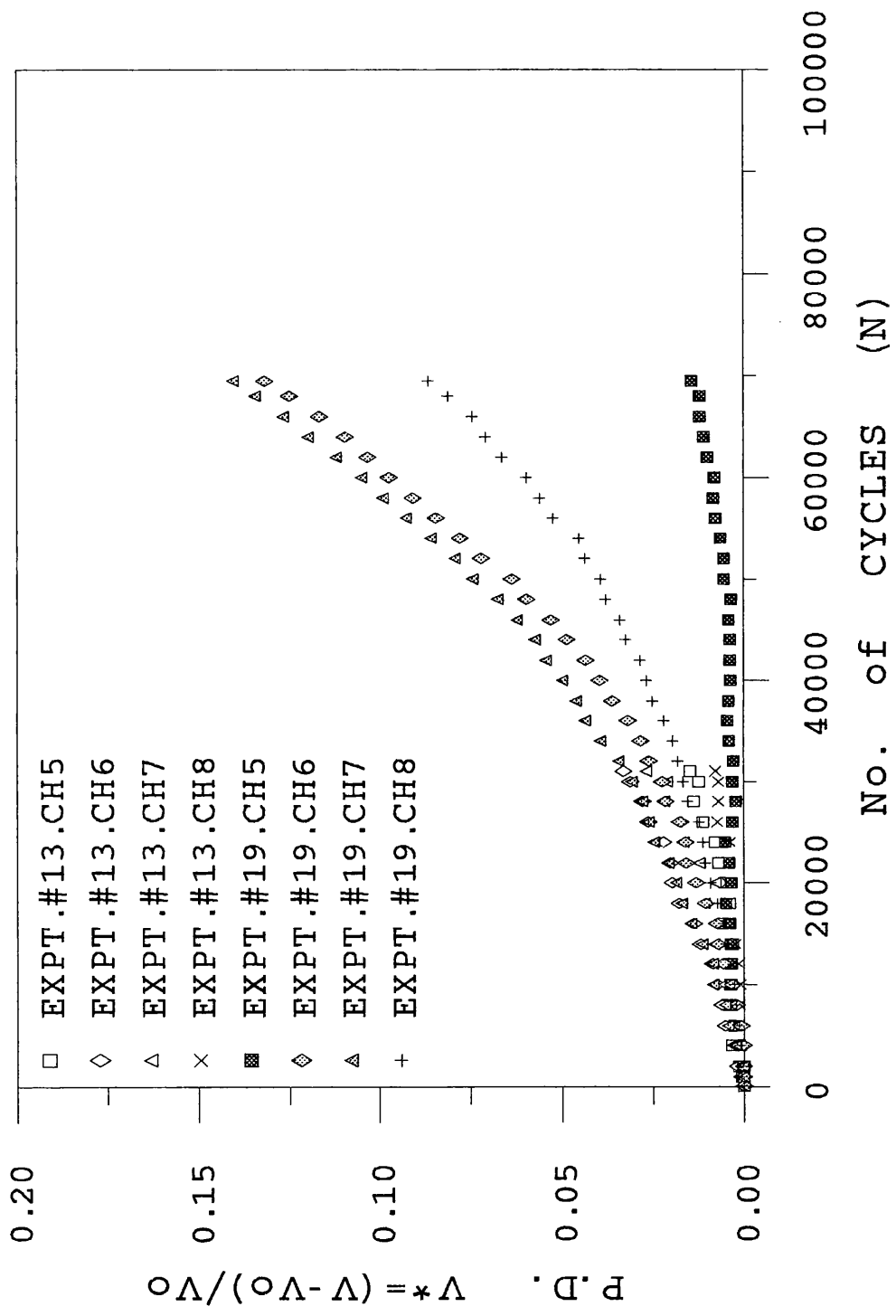
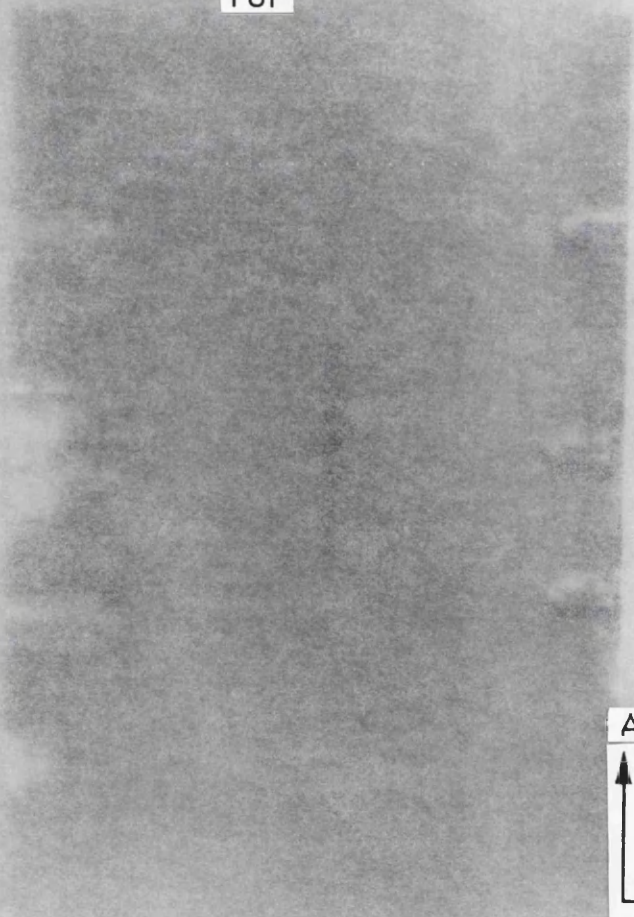


Figure 3.4.43. Normalized Potential Difference for 2mm Deep External Longitudinal Semi-Circular Notched Components.

TOP



BOTTOM

AXIAL



CIRCUMFERENTIAL

Figure 2. Micrograph showing crack in steel specimen No. 19, (Mag. X6.5).

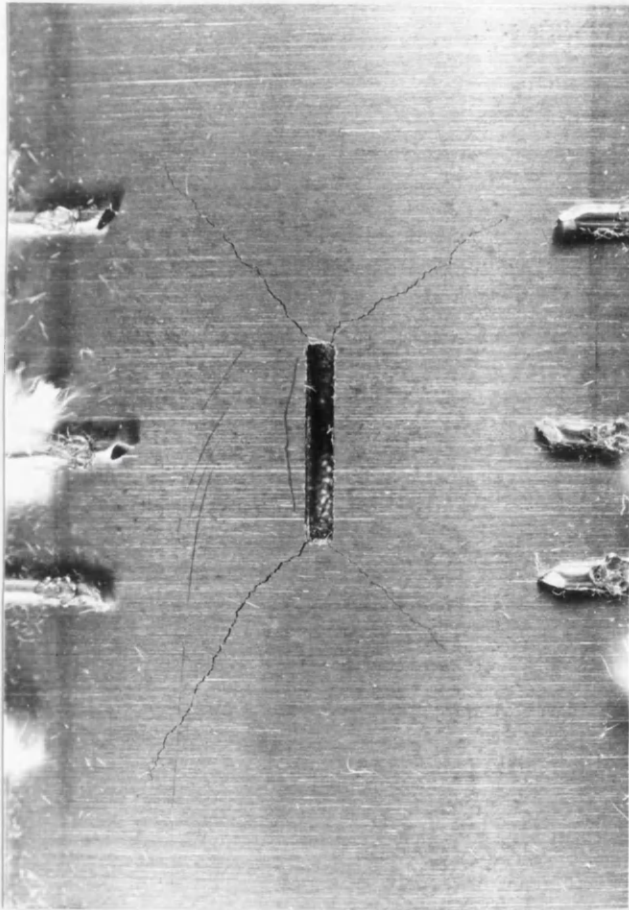


Figure 3.4.44. Surface Cracking from 2mm Radius Notch, Expt.#19, (Mag.X6.5).

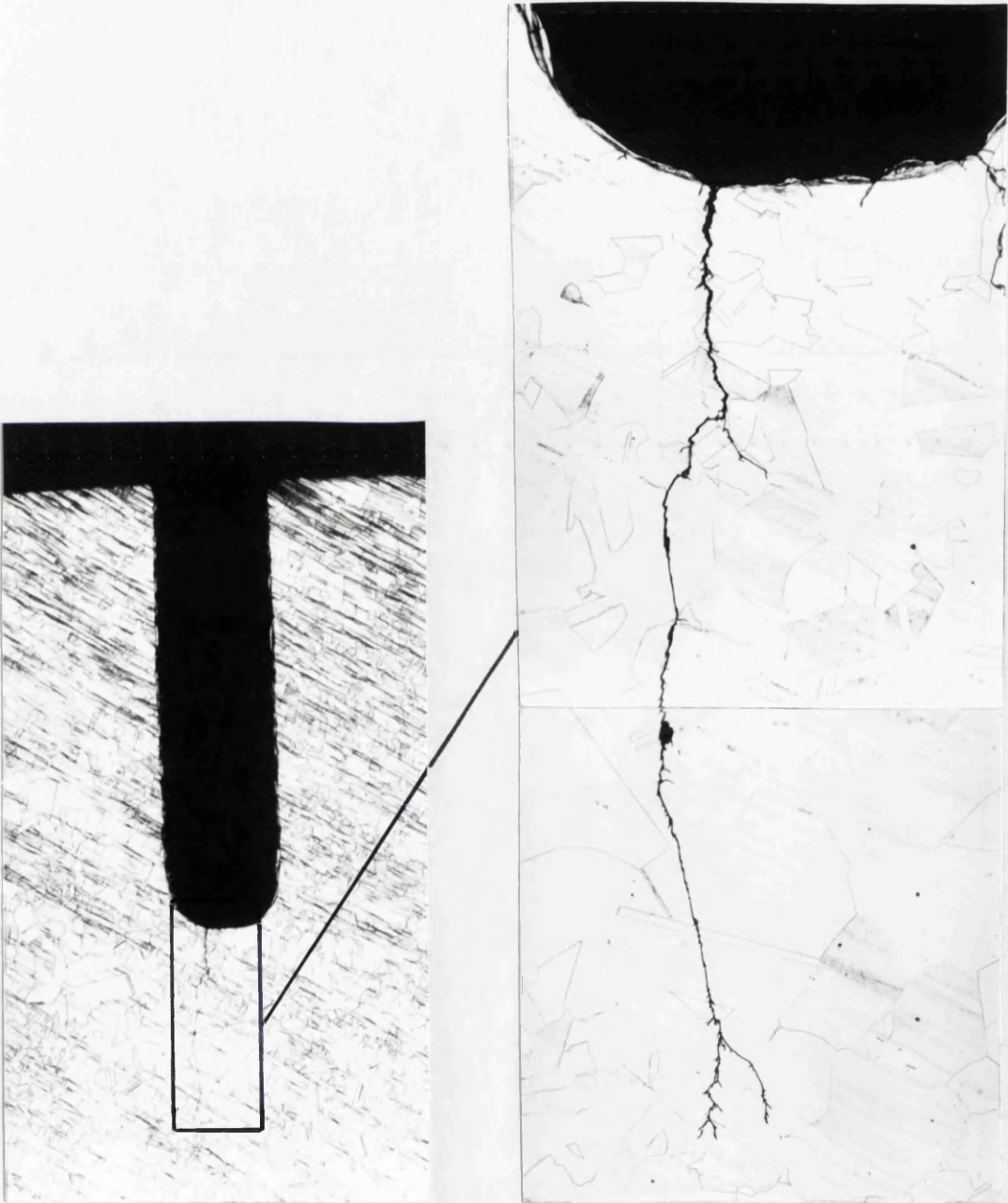


Figure 3.4.45. Transgranular Crack from 2mm Deep Semi-Circular Notch, Expt.#13.
(Mag.X30), Insert, (Mag.X160).

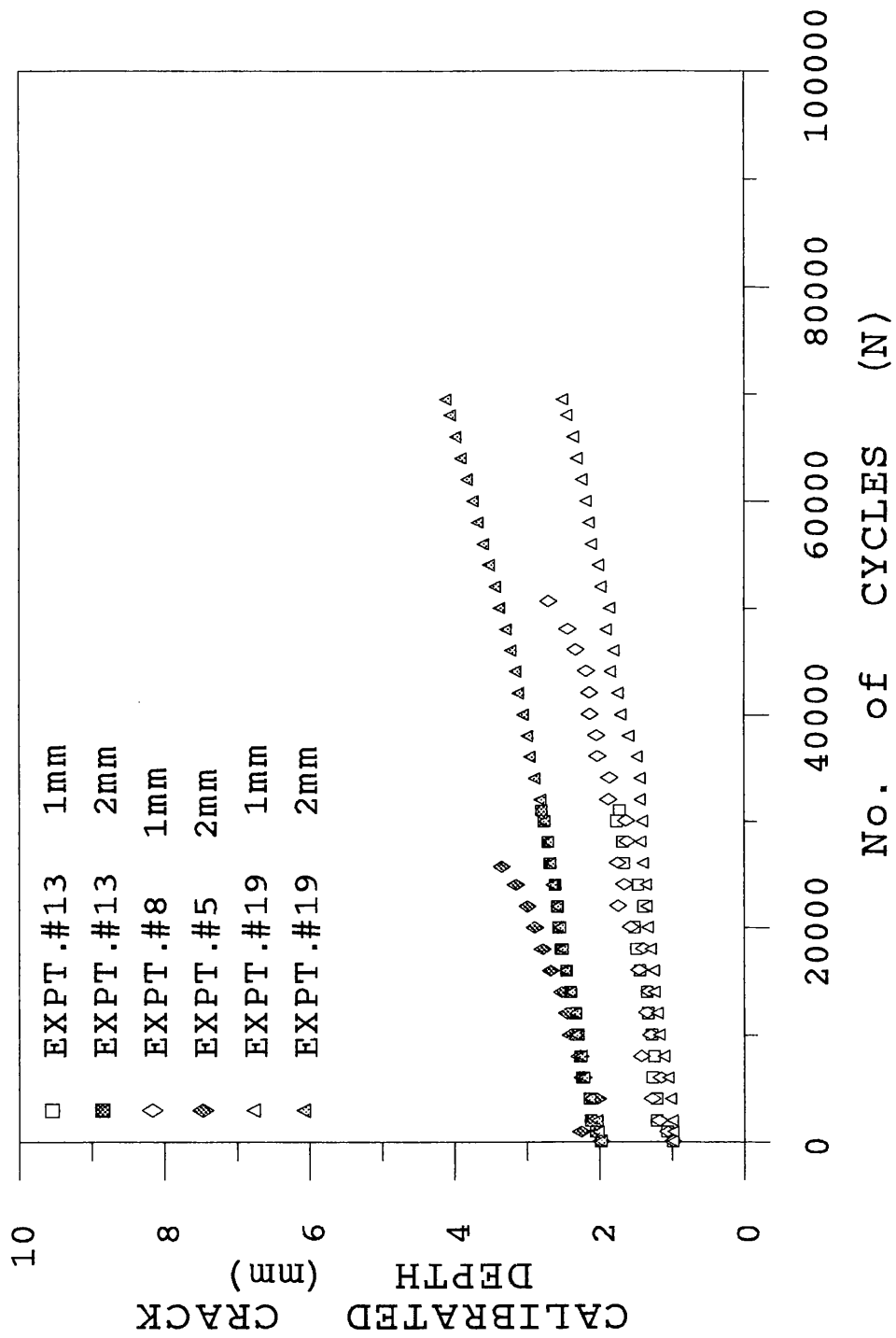


Figure 3.4.46. Calibrated Crack Depths in External Longitudinal Semi-Circular Notched Components.

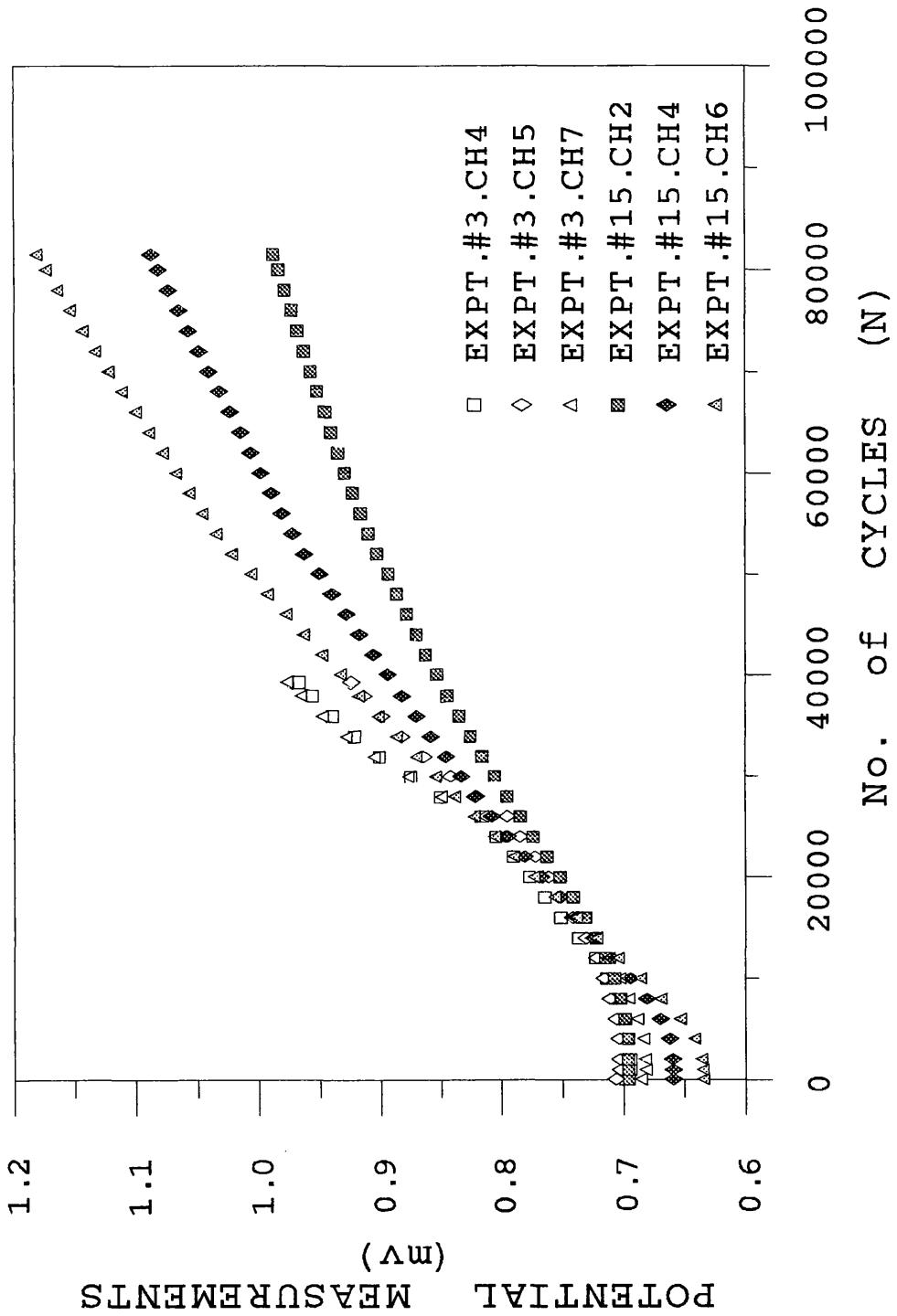


Figure 3.4.47. Potential Measurements During Expt.#3 and Expt.#15.

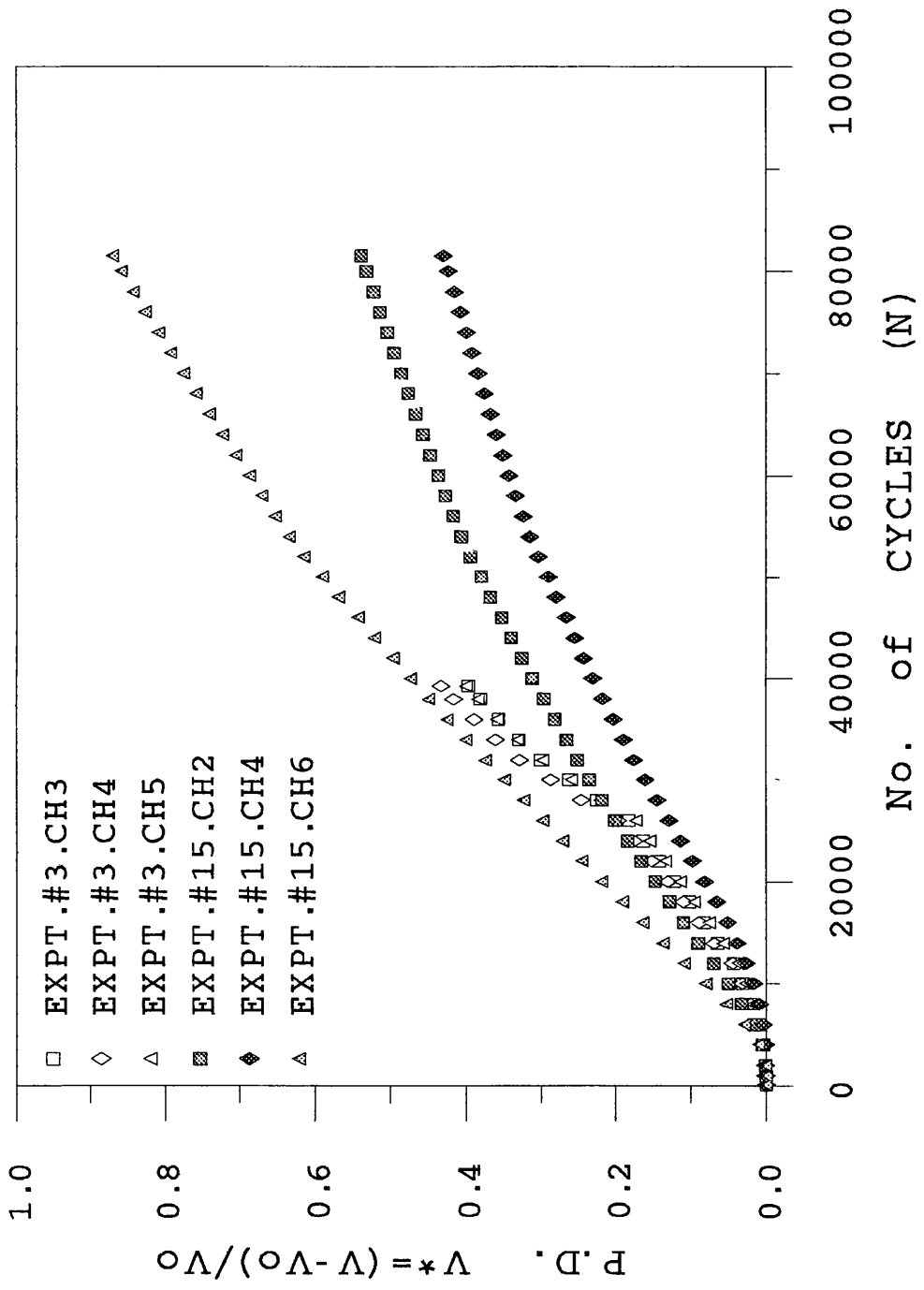


Figure 3.4.48. Normalized Potential Measurements in Expt.#3 and Expt.#15.

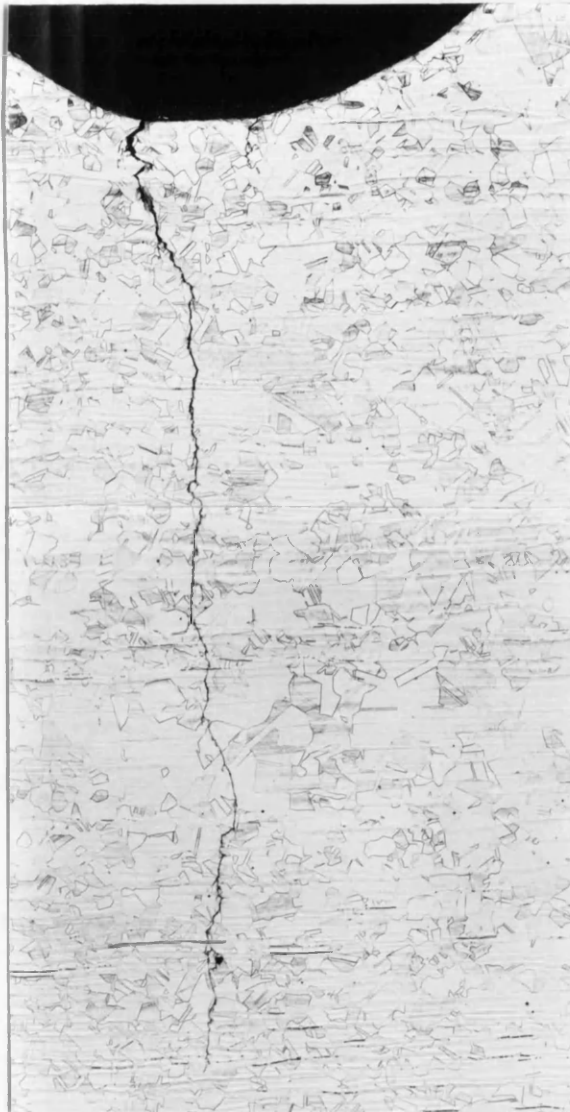


Figure 3.4.49. Transgranular Crack in 1mm Deep External Circumferential Notched Component, Expt.#3, (Mag.X50).



Figure 3.4.50. Circumferential Crack Fracture Surface, Expt.#3, (Mag.X1.3).

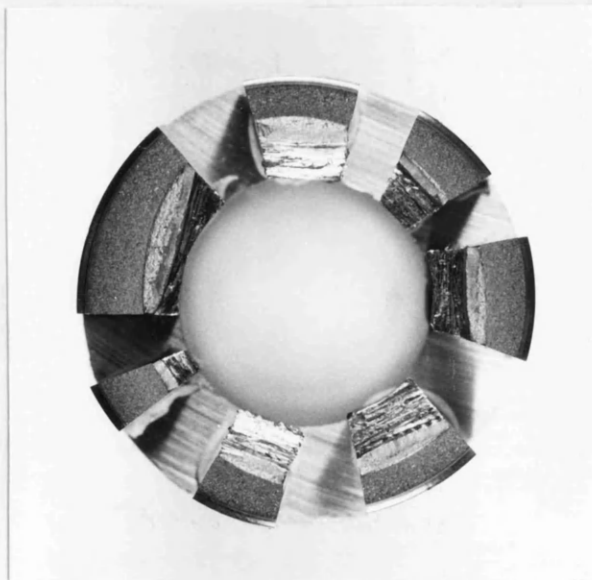


Figure 3.4.51. Circumferential Crack Fracture Surface, Expt.#15, (Mag.X1.3).

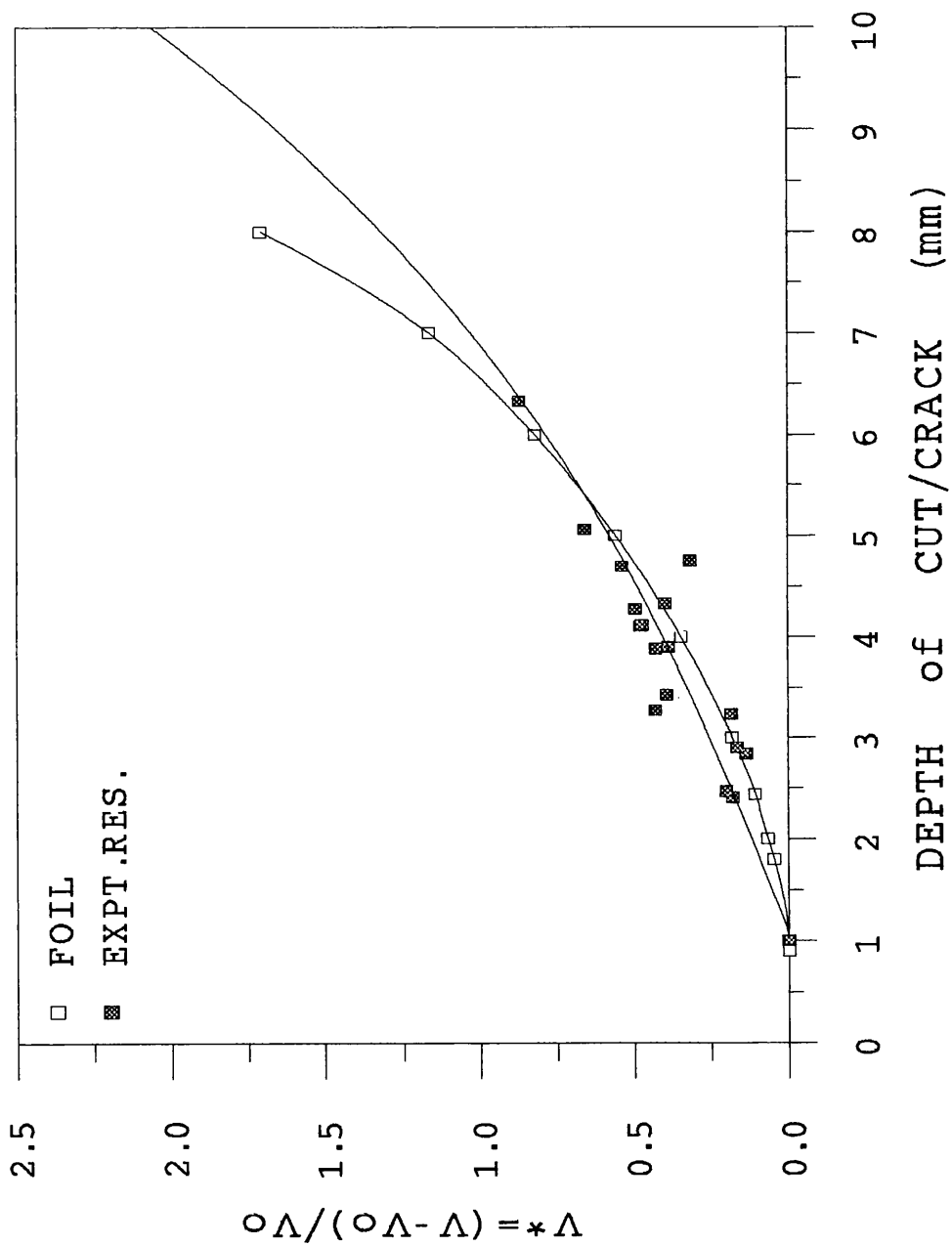


Figure 3.4.52. Calibration Curves for 1mm Deep External Circumferential Notched Components: Established by Different Methods.

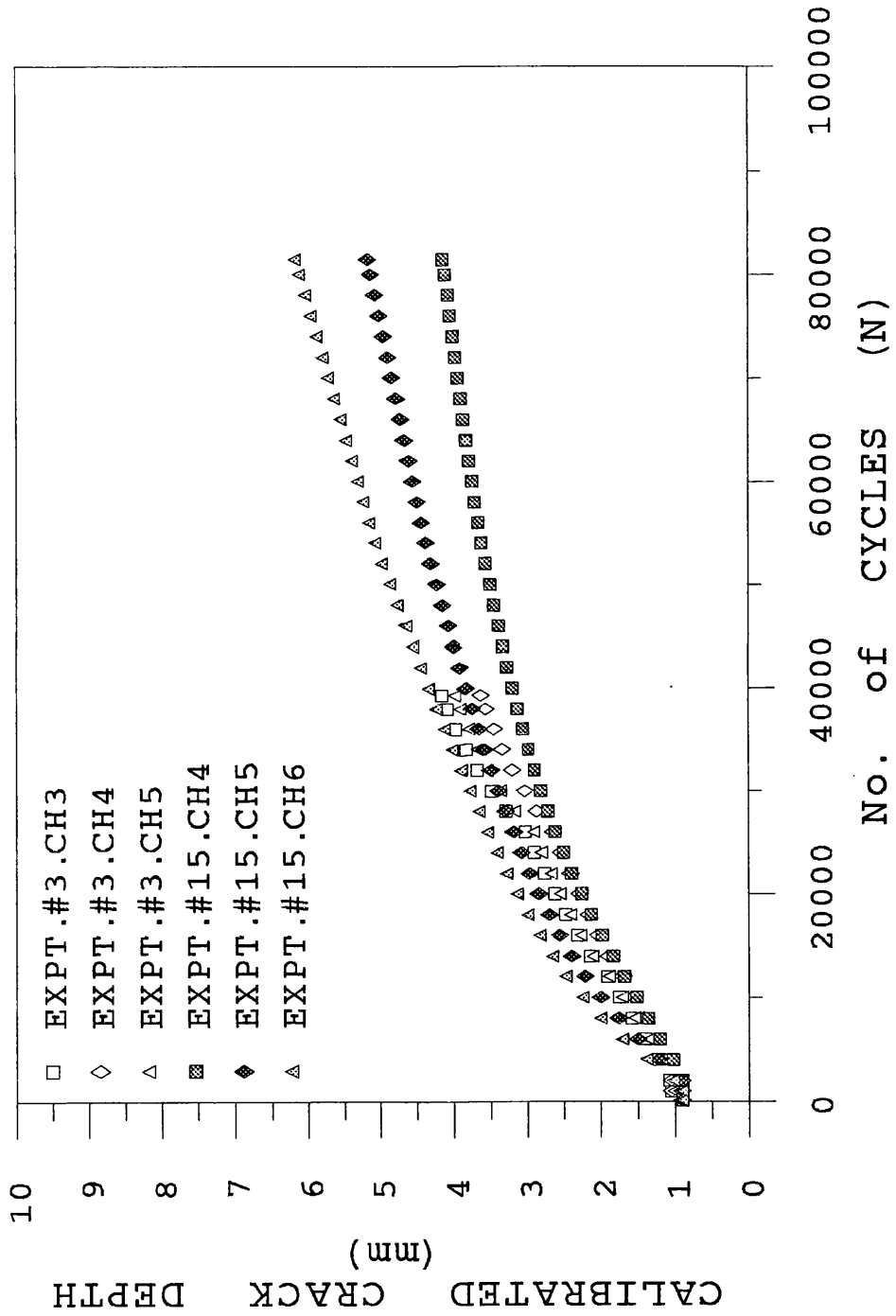


Figure 3.4.53. Calibrated Crack Depths in 1mm Deep External Circumferential Notched Components.

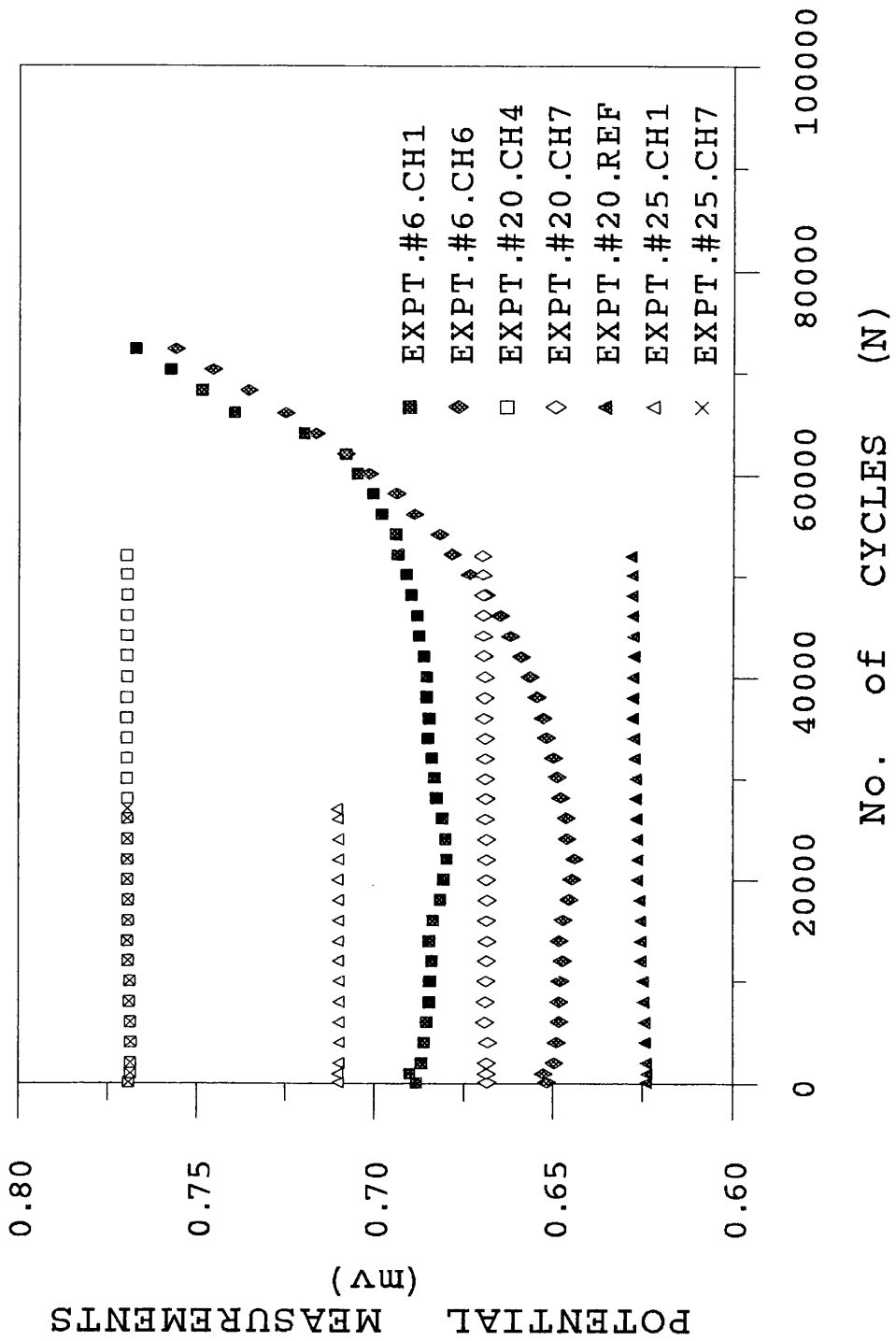


Figure 3.4.54. Potential Measurements in 1mm Deep Internal Circumferential Notched Components.

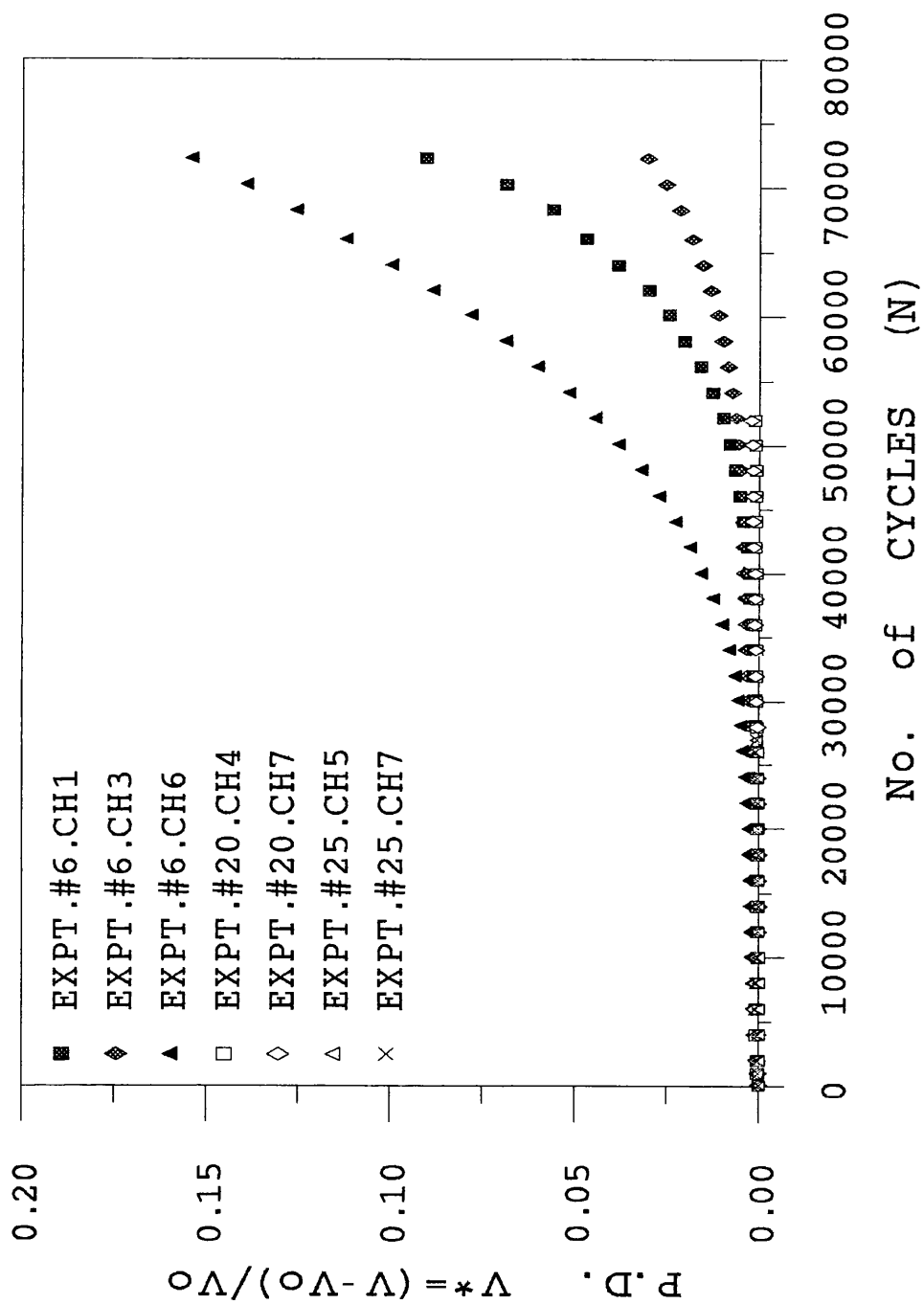


Figure 3.4.55. Normalized Potential Measurements in 1mm Deep Internal Circumferential Notched Components.



Figure 3.4.56. Transgranular Crack in 1mm Deep Internal Circumferential Notched Component, Expt.#6, (Mag.X50).



Figure 3.4.57. Circumferential Crack Fracture Surface, Expt.#6, (Mag.X1.3).

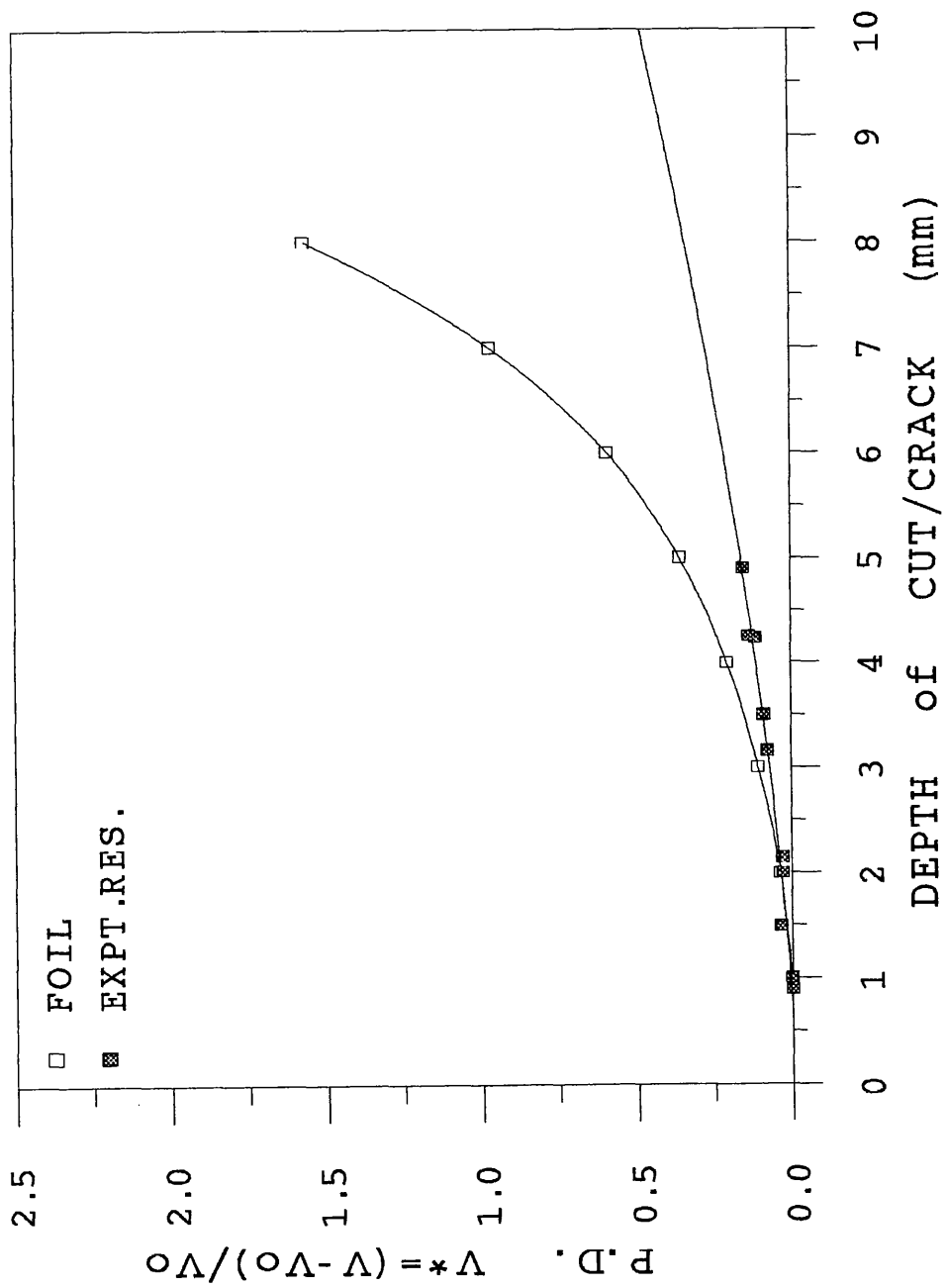


Figure 3.4.58. Calibration Curves for 1mm Deep Internal Circumferential Notched Components: Established by Different Methods.

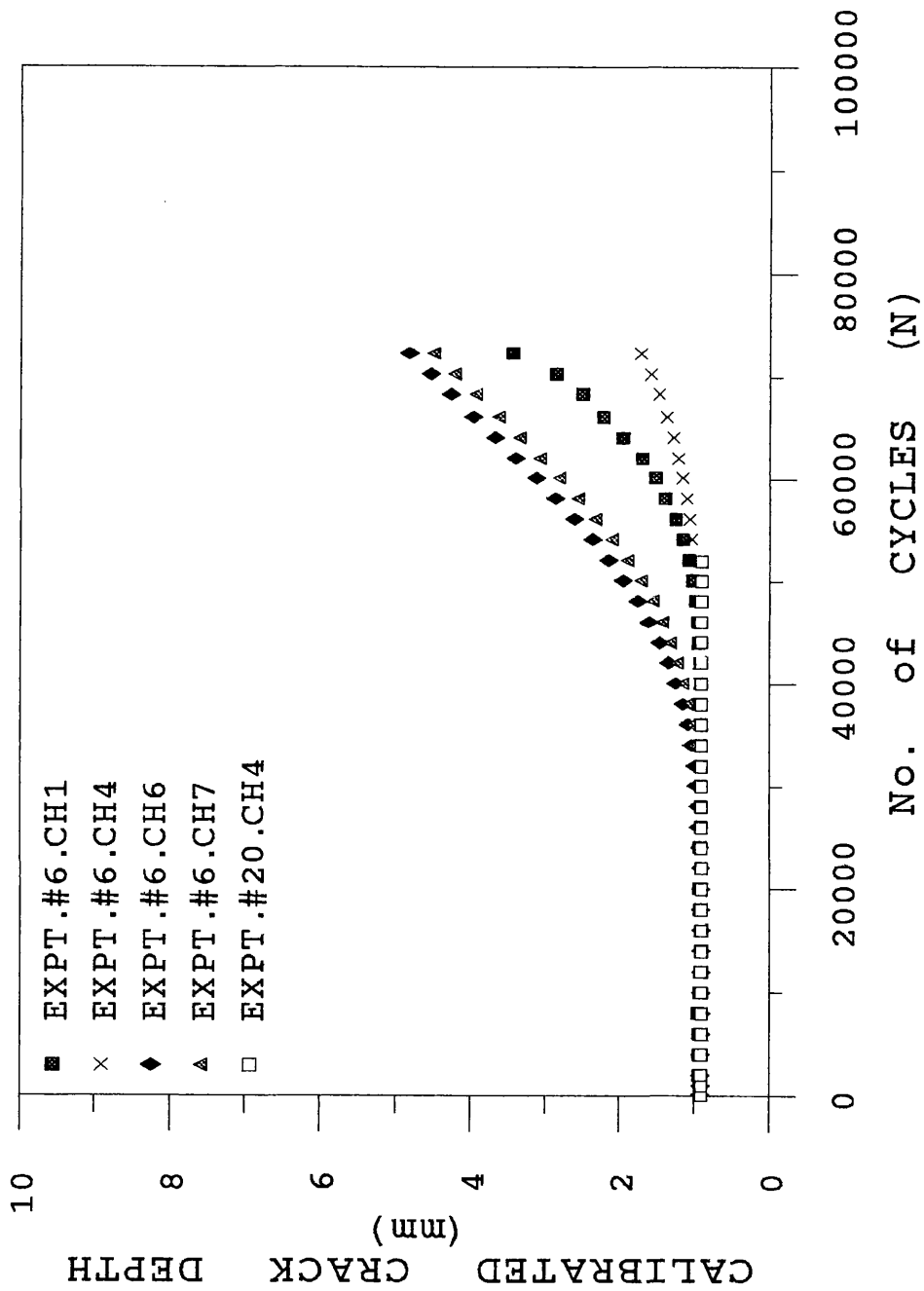


Figure 3.4.59. Calibrated Crack Depths in 1mm Deep Internal Circumferential Notched Components.



Figure 3.4.50. External Surface Crack across a Spot Weld, Expt #7, (Mag. X32).

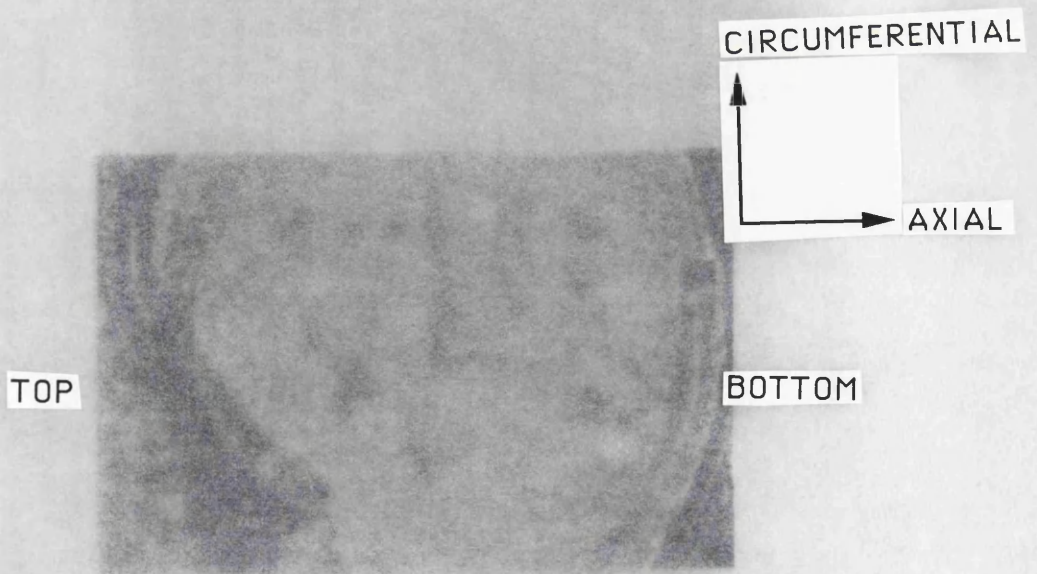


Figure 3.4.51. Pre-Test Laser Welded Spot with a Surface Crack, Expt.#21, Mag.X32).

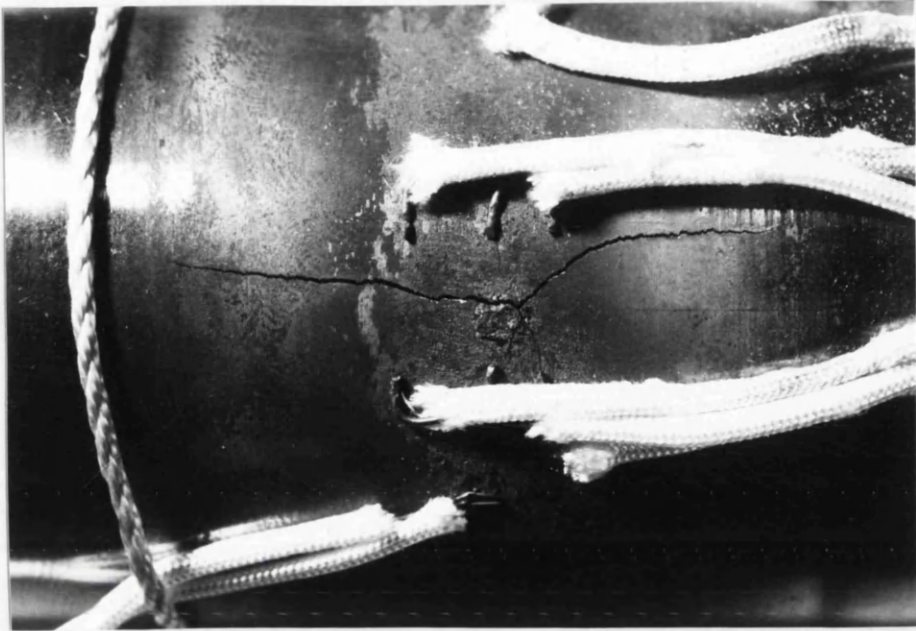


Figure.3.4.60. External Surface Crack from a Spot Weld, Expt.#7, (Mag.X3.2).

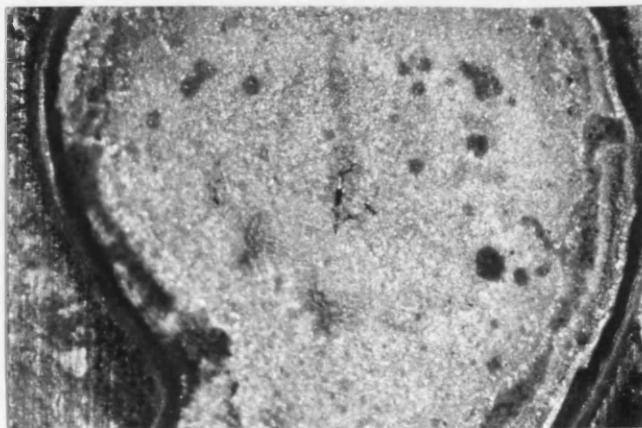


Figure 3.4.61. Pre-Test Laser Welded Spot with a Short Crack, Expt.#21, (Mag.X32).

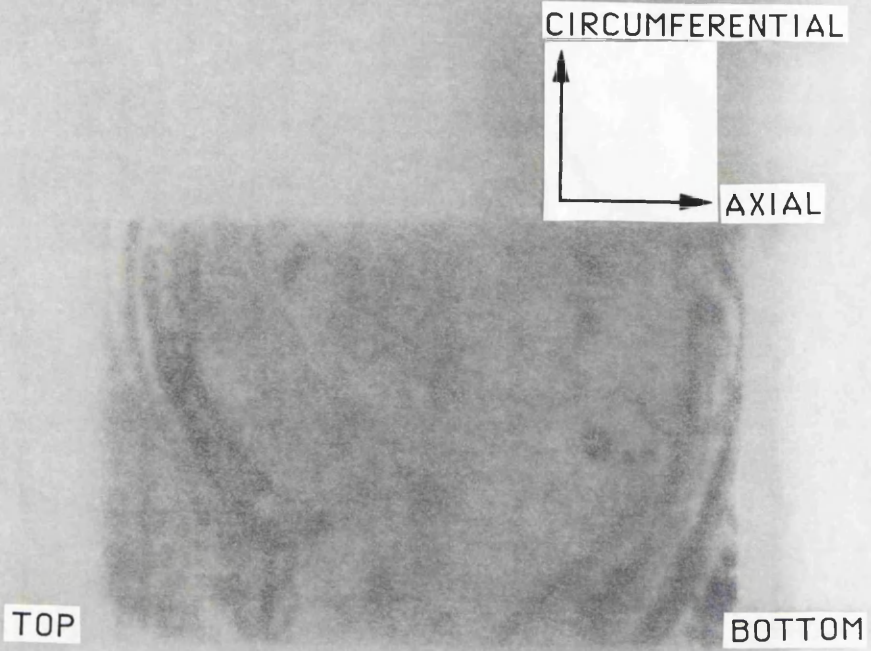


Figure 3.4.52. Post-Fatigue Laser-Welded Spot with a Longer Crack, Expt.#21, (Mag.X32).

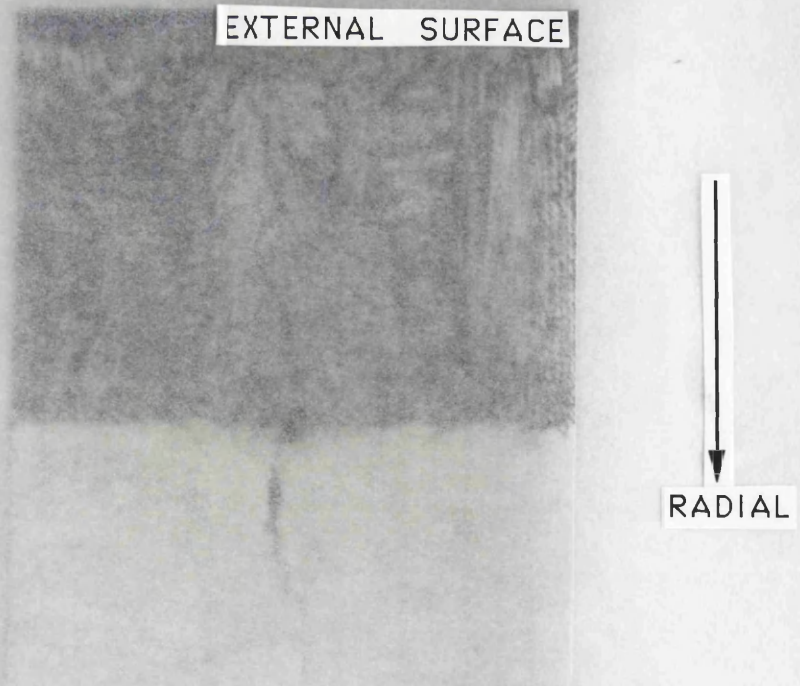


Figure 3.4.53. Crack Growth from Laser-Welded Spot, Expt.#21, (Mag.X100).

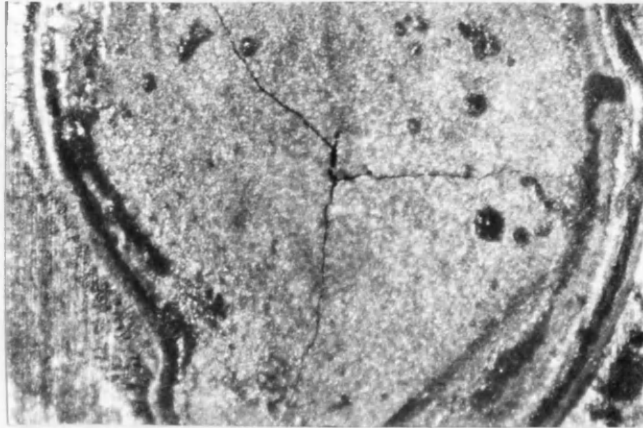


Figure 3.4.62. Post-Test Laser Welded Spot with a Longer Crack, Expt.#21, (Mag.X32).



Figure 3.4.63. Crack Growth from Laser Welded Spot, Expt.#21, (Mag.X100).

4.0. Analysis and Discussion Section.

4.1. Thermal Fatigue Crack Growth.

The crack growth rates measured in the thermal fatigue experiments will be discussed with reference to the effects of the location, position, depth and shape of the notch on the crack initiation. Plots of the crack depth development were produced from the series of experiments on each of the identically notched components, Figs. 3.4.28a-b, 3.4.38a-b, 3.4.47, 3.4.53 and 3.4.59. Equations to describe the best-fit relationships of the calibrated crack depth vs. number of thermal cycles were developed for each of the data sets which correspond to the potential drop readings across the position of maximum crack growth. Polynomial equations of varying degrees were used to describe the development of the crack depths. Data was selected from only one experiment as representative of the crack growth from each of the different starter notch depths and locations. Each equation was differentiated to describe the change in calibrated crack depth in terms of the change in number of cycles. Substituting the values of the number of thermal cycles into each equation produced the corresponding values of the crack growth rate, da/dN . The corresponding values of crack growth rate were plotted against both the number of cycles and the position through the component wall for each of the series of experiments, Figs 4.1.1(a-l).

The crack growth rate data from the rectangular shaped, 1mm deep, longitudinal notch in the external surface, (expt.#23), is illustrated in Figures 4.1.1(a-b). The initial crack growth rate was 1.93×10^{-4} mm/cycle which decreased, within the initial 10,000 cycles, to a value of 1.55×10^{-4} mm/cycle at $a/t=0.2$. A steady decrease in crack growth rate continued until after 60,000 cycles at which point the crack depth was $a/t=0.66$. Towards the end of the experiment, at 79,000 cycles, the crack growth rate continued to decrease at a slower rate. to 1.75×10^{-5} mm/cycle, which was above the threshold crack growth rates reported in section 3.3. The range in thermal fatigue crack growth rates compared well with the range in mechanical fatigue crack growth rates which were described by the Paris Law in section 3.3.

Similar trends were observed with the development of the fatigue crack growth rate from a 2mm deep, rectangular shaped notch in the external surface of the component, (expt.#12), Figures 4.1.1(c-d). The initial crack growth rate, 2.13×10^{-4} mm/cycle, was of similar magnitude to the initial crack growth rate from the 1mm notch. A decrease in crack growth rate was observed until $a/t=0.5$, which corresponded to the initial 20,000 thermal cycles. During the following 20,000 cycles, the crack growth rate was in the region of 4.9×10^{-5} mm/cycle while the crack propagated to 60% of the component wall.

Finally, there was a slight decrease in the crack growth rate measurement until the experiment was terminated after 55,000 cycles when the crack depth was $a/t=0.66$. Once again, the thermal fatigue crack growth rates were in the range of the mechanical fatigue crack growth rates of section 3.3.

The development of the crack growth rate, from rectangular shaped, longitudinal notches in the internal surface of the components, with respect to both the crack depth, a/t , and the number of thermal cycles, is illustrated in Figures 4.1.1(e-f). During the initial 25,000 cycles the initial crack growth rate from the 1mm deep notch decreased from 1.21×10^{-4} to 6.24×10^{-5} mm/cycle, which corresponded to an increase in crack depth from $a/t=0.09$ to $a/t=0.35$. For the remaining 36,000 thermal cycles, the crack growth rate was in the region of 6.5×10^{-5} mm/cycle. The crack depth at the end of the experiment was $a/t=0.62$.

A similar behaviour in crack growth rate development was measured from the 2mm deep, rectangular shaped, longitudinal notch in the internal surface, Figures 4.1.1(g-h). During the initial 22,000 cycles, ($0.2 \leq a/t \leq 0.42$), the crack growth rate decreased from 1.05×10^{-4} to 6.32×10^{-5} mm/cycle. Over the following 28,000 cycles the crack propagated through the mid-thickness region, ($0.424 \leq a/t \leq 0.636$), at a negligible increase in crack growth rate from 6.32×10^{-5} to 7.4×10^{-5} mm/cycle. As the crack extended, ($0.636 \leq a/t \leq 0.701$), towards the end of the experiment, after 63,000 thermal cycles, the crack growth rate decreased slightly from 7.4×10^{-5} to 7.09×10^{-5} mm/cycle.

Clear differences were observed between the calculated development of the thermal fatigue crack growth rate from the notches in the longitudinal plane, in comparison to those in the circumferential plane of the components.

For a 1mm deep, circumferential notch, in the external surface, the calibrated crack depth data from experiment #15, p.d. channel 6, was chosen as this was the deepest cracked section in an uninterrupted experiment. The development of the crack growth rates with respect to the number of thermal cycles and the position through the thickness of the component, is shown in Figures 4.1.1(i-j). Following crack initiation, the crack growth rate decreased from 1.39×10^{-4} to 4.25×10^{-5} mm/cycle, while the crack propagated to a depth of $a/t=0.51$. This occurred during the initial 40000 cycles. For the remaining 41,000 cycles the crack grew at the reduced rate of 4.5×10^{-5} mm/cycle to a depth of $a/t=0.64$.

For a 1mm deep, circumferential notch, in the internal surface, the calibrated crack depth data from experiment #6, p.d. channel 6, was chosen as this was the deepest

cracked section in the only experiment in which a crack initiated from an internal, circumferential notch. Initiation did not occur until 21,000 thermal cycles therefore the 4th order polynomial equations, which best described the development of the calibrated crack depth, were limited between 21,000 and 72,000 cycles. The resultant crack growth rates have been described in terms of both the number of thermal cycles and the position through the thickness of the component, as illustrated in Figures 4.1.1(k-l). During the 39,000 cycles following crack initiation, the crack growth rate increased to 1.35×10^{-4} mm/cycle while the crack propagated to a depth of $a/t=0.34$. Over the remaining 12,000 cycles to the end of the experiment, the crack propagated to a depth of $a/t=0.49$) at a stabilised growth rate of 1.4×10^{-4} mm/cycle, with a slight decrease to 1.3×10^{-4} mm/cycle.

In general, following initiation, the cracks from each of the differently notched components have displayed similar resultant crack growth rates, with exception of the components which contained a circumferential notch in the internal surface, as illustrated in Figure 4.1.2. If the initial crack growth, corresponding to a distance of $a/t=0.1$ ahead of the notch root, is neglected, then the majority of the crack growth rates fall in between the range of 1.5×10^{-4} and 0.5×10^{-4} mm/cycle. The general trend was for initially high crack growth rates which decreased rapidly to a crack depth of $a/t \geq 0.35$, followed by continued crack growth at a stable rate in the region of 4×10^{-5} mm/cycle. The similarities in the thermal fatigue crack growth rates, beyond the influence of the notches, were observed until the experiments were concluded. It was also observed from Figure 4.1.2, that the greater initial crack growth rates were from the notches in the external surface positioned in either the longitudinal or the circumferential planes. Both the magnitude and the range of temperatures, throughout the thermal cycles, were greater at the external surface than at the internal surface. Therefore the lower yield stress at the external surface would have an effect on the initial crack growth rates. At the external surface, the magnitude of the initial crack growth rate increased with increasing notch depth and decreased from longitudinal notches to that from a notch in the circumferential plane. It appears that both the shape and the position of the notch have an important effect on the resultant thermal stress field and the resultant early crack growth rates. The magnitude of the corresponding initial crack growth rates from internal notches were reduced, in comparison, with little influence of the notch depth, as the initial crack growth rates from both the 1mm and the 2mm notches were similar. The stress field at the internal surface would have been greatly reduced due to the smaller range in cyclic temperatures, therefore the depth of the notch has negligible effect. Similarly, the increased yield stress, corresponding to the lower temperatures may have restricted the mechanisms of the fatigue crack process from occurring. The delayed crack initiation from the circumferential notch in the

internal surface combined with the reduced initial crack growth rate raises questions over both the magnitude of the axial stress field at the internal surface in comparison to the hoop stress field and influence of the smoother, circular shaped notch which was machined into the circumferential plane in comparison to the sharper 1mm and 2mm deep notches in the longitudinal plane. In an attempt to verify the observations made from Figure 4.1.2, the contents of section 4.2 will concentrate on the development of the thermal cyclic stress fields in the experimental component, with and without a machined notch.

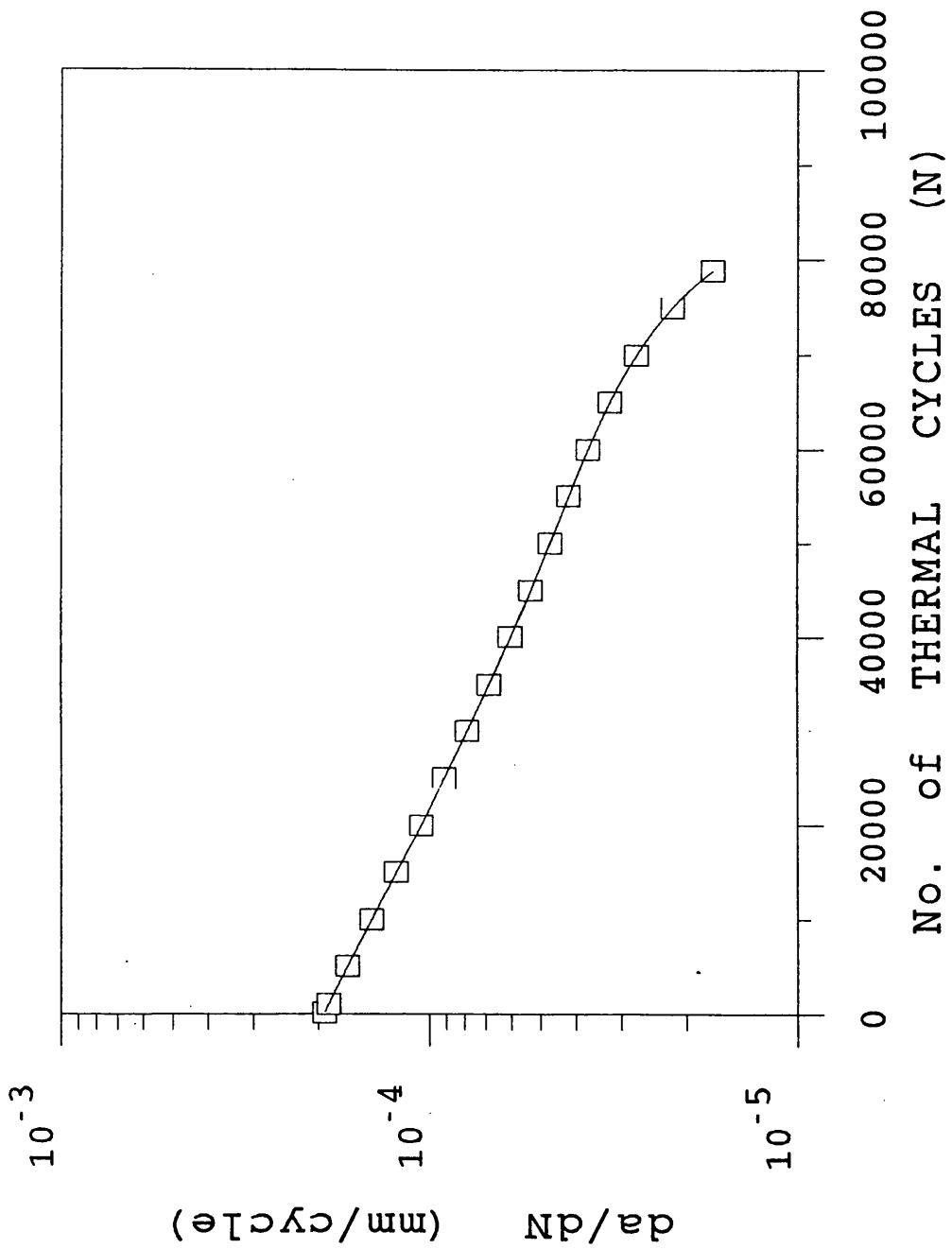


Figure 4.1.1a. Thermal Fatigue Crack Growth Rates in a 1mm Deep External Longitudinal Notched Component.

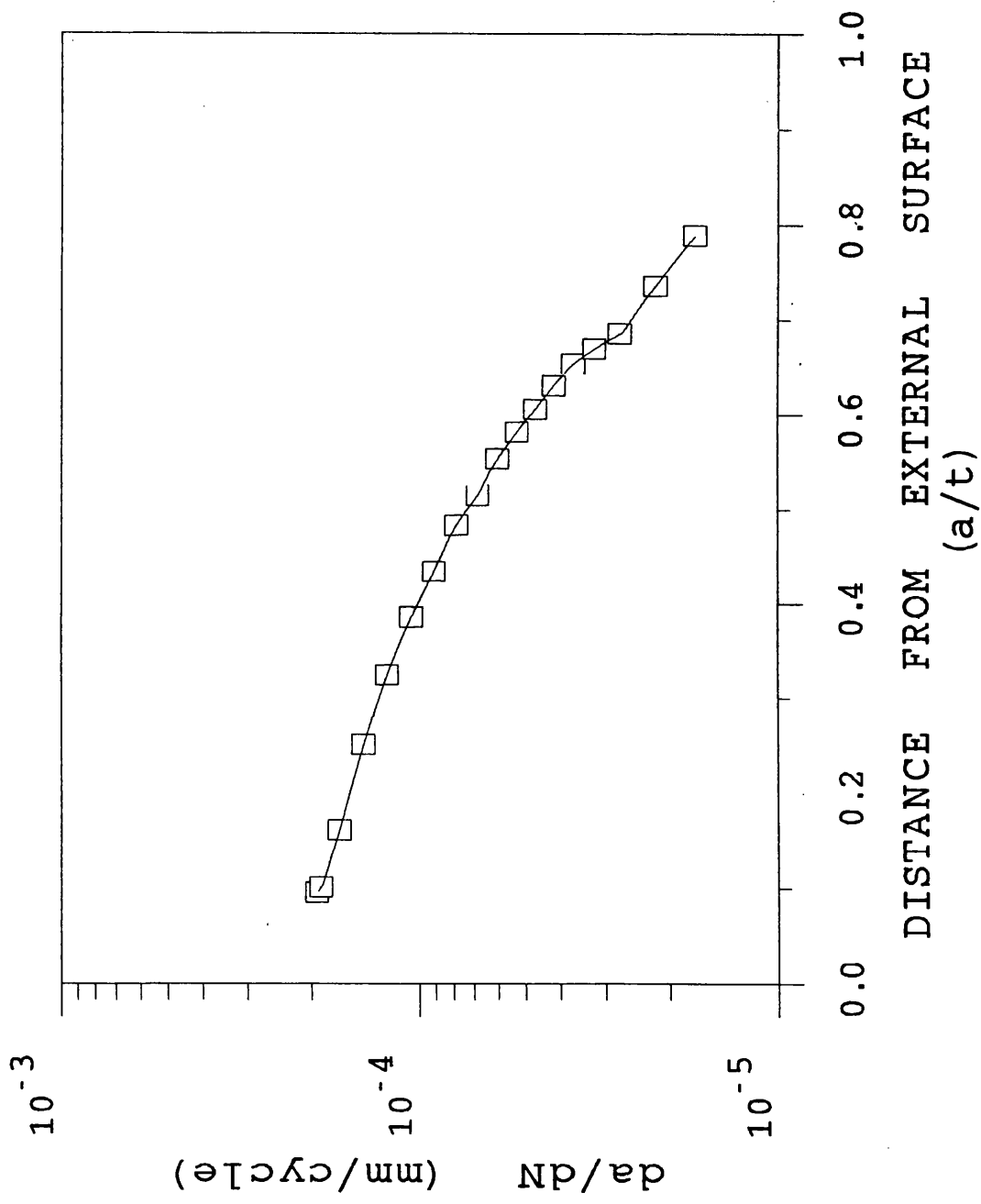


Figure 4.1.1b. Thermal Fatigue Crack Growth Rates Through a 1mm Deep External Longitudinal Notched Component.

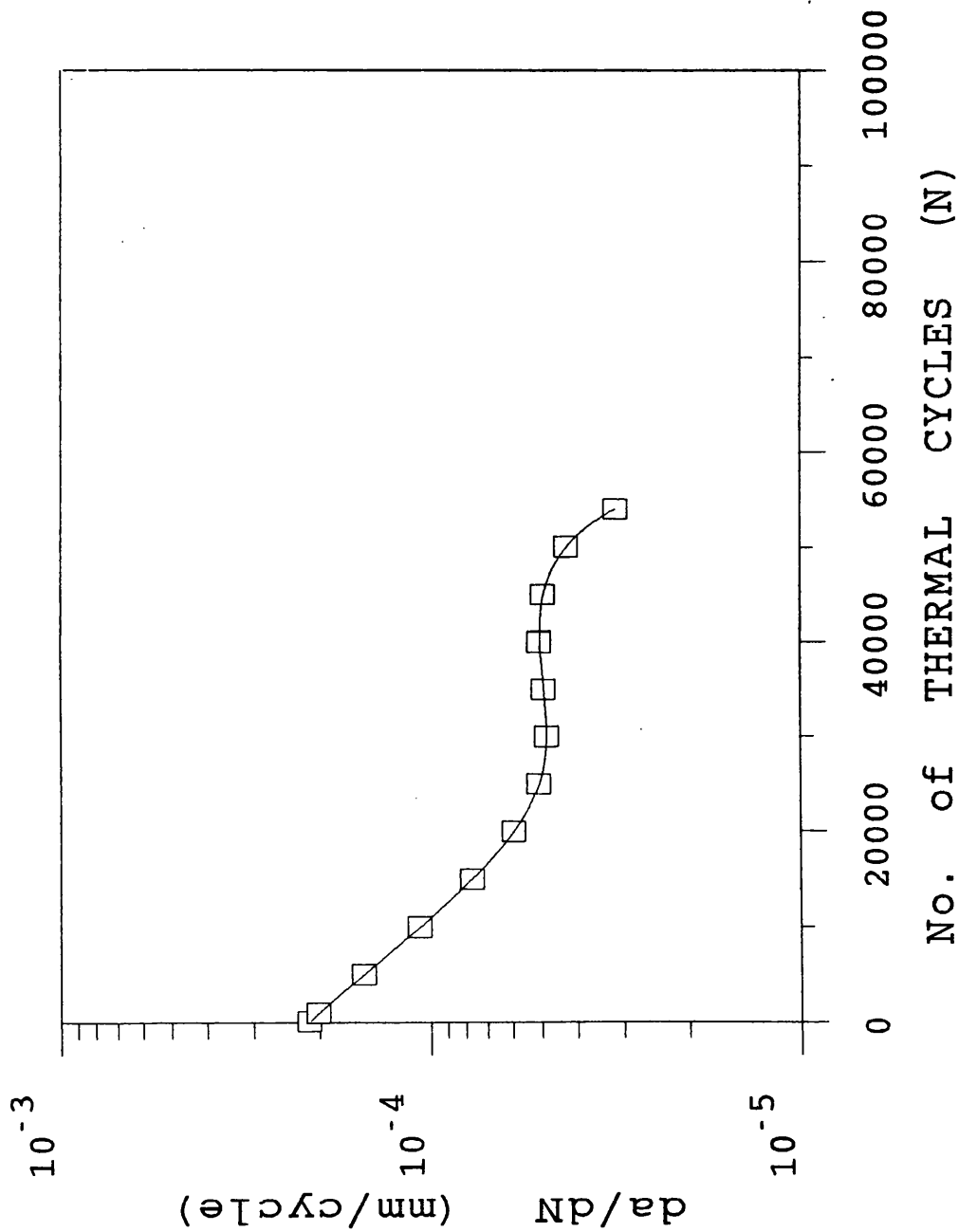


Figure 4.1.1c. Thermal Fatigue Crack Growth Rates in a 2mm Deep External Longitudinal Notched Component.

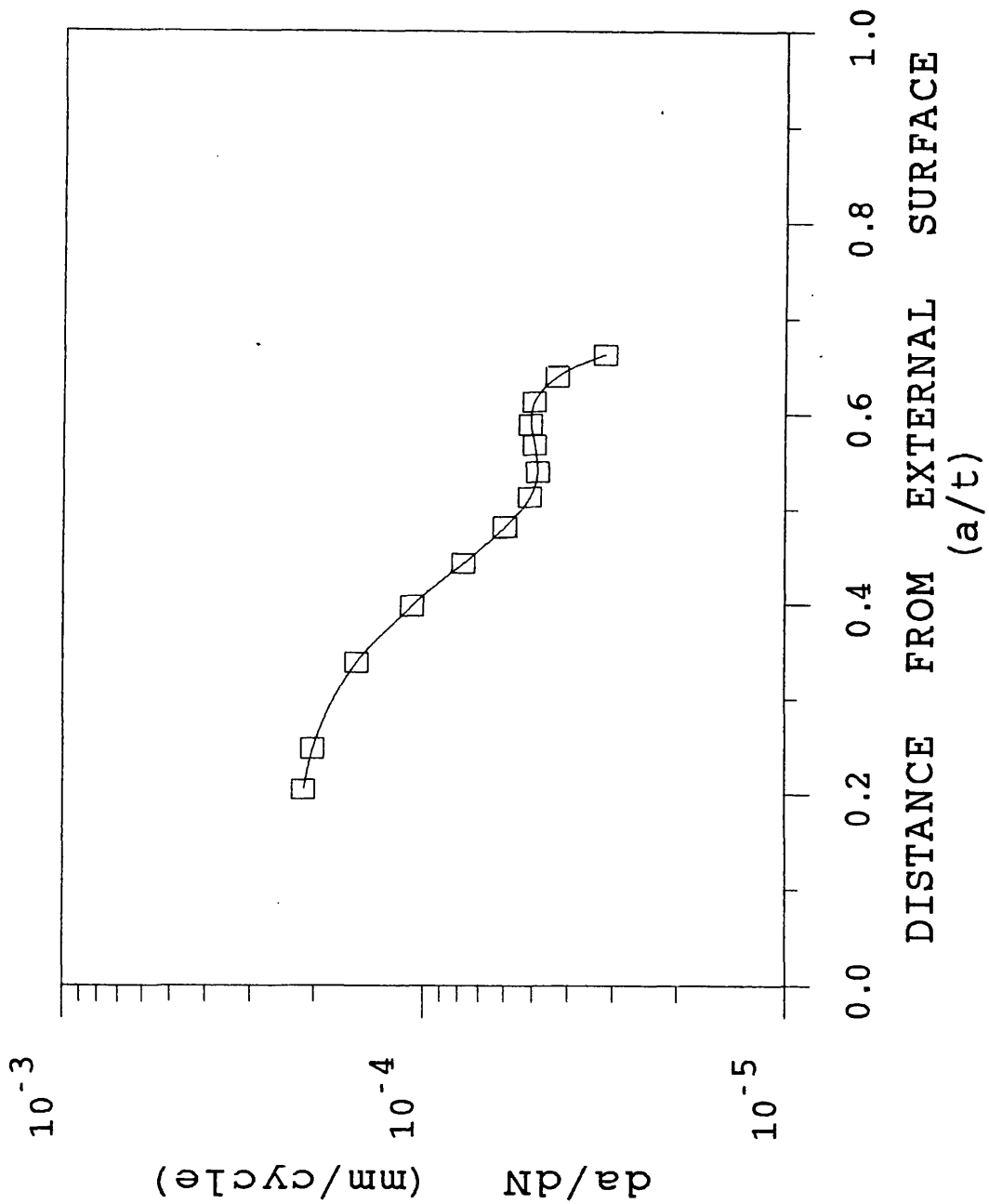


Figure 4.1.1d. Thermal Fatigue Crack Growth Rates Through a 2mm Deep External Longitudinal Notched Component.

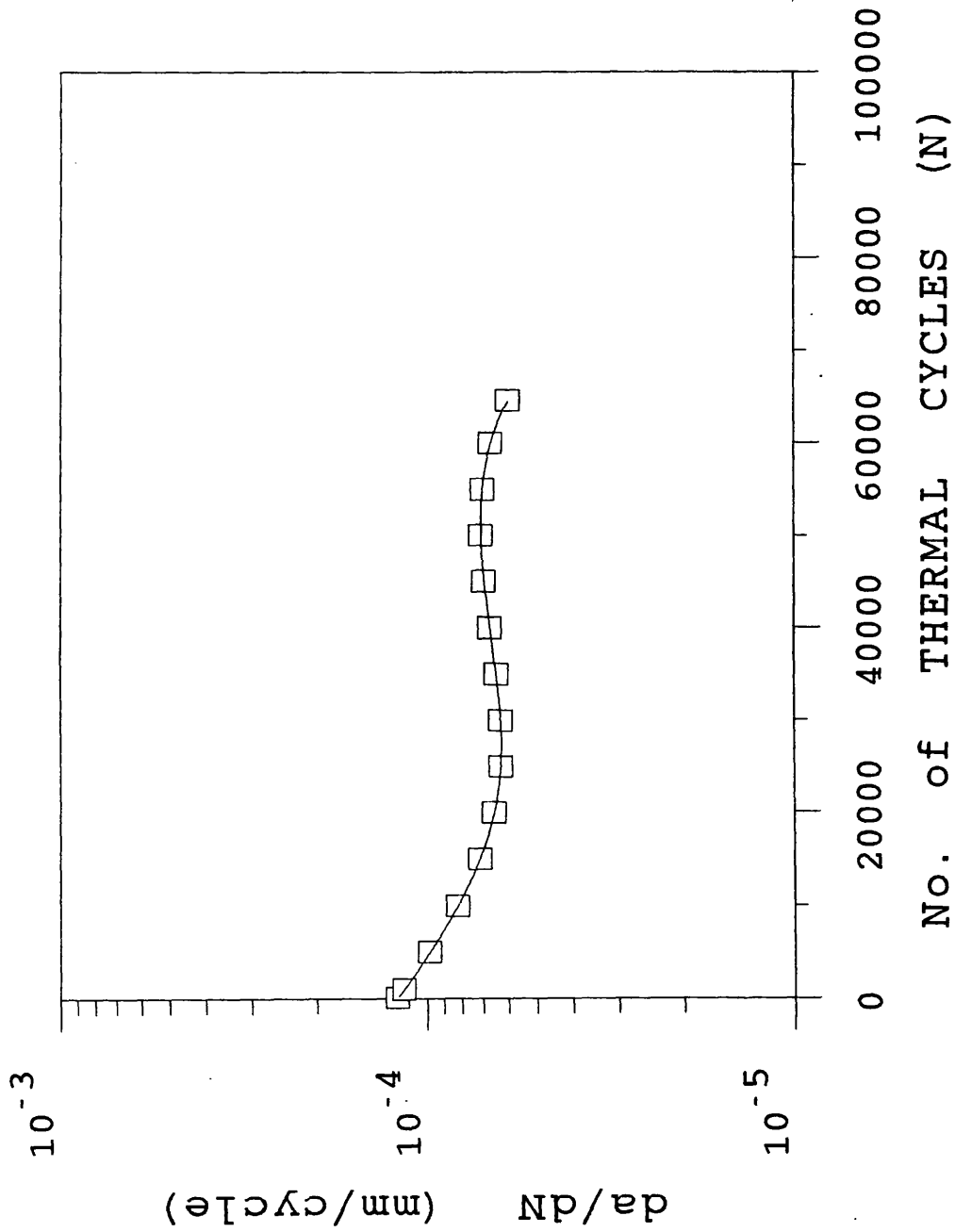


Figure 4.1.1e. Thermal Fatigue Crack Growth Rates in a 1mm Deep Internal Longitudinal Notched Component.

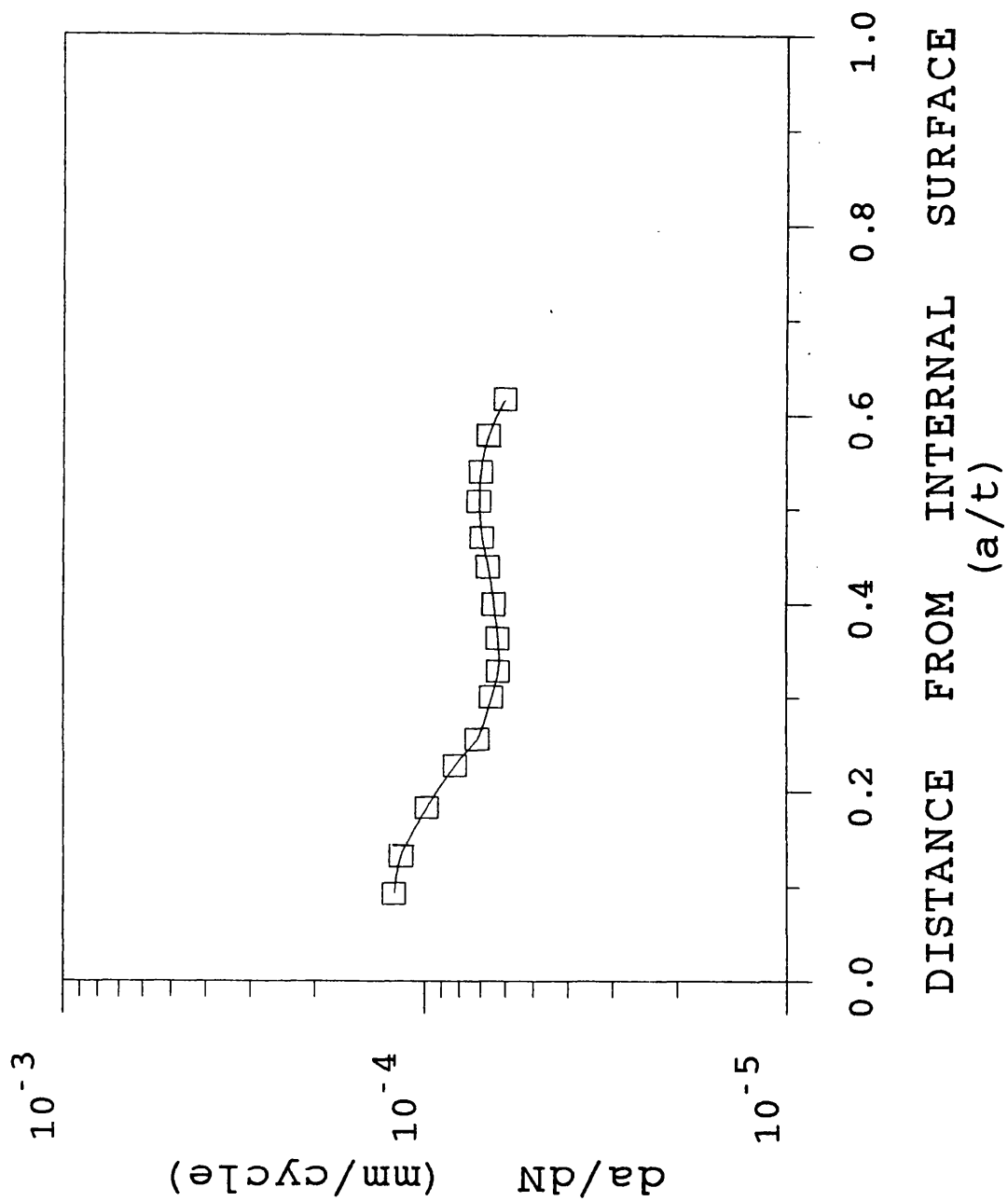


Figure 4.1.1f. Thermal Fatigue Crack Growth Rates Through a 1mm Deep Internal Longitudinal Notched Component.

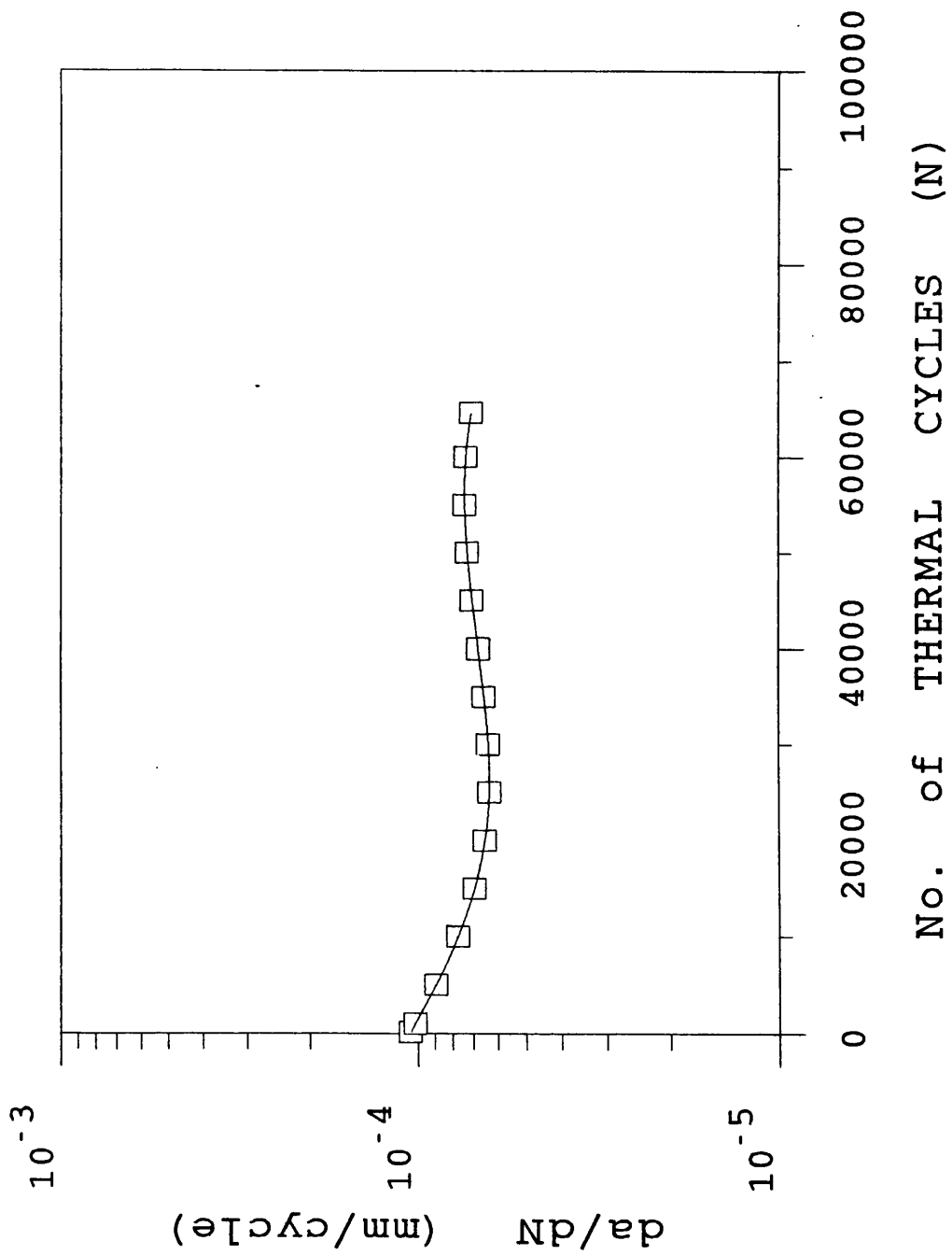


Figure 4.1.1g. Thermal Fatigue Crack Growth Rates in a 2mm Deep Internal Longitudinal Notched Component.

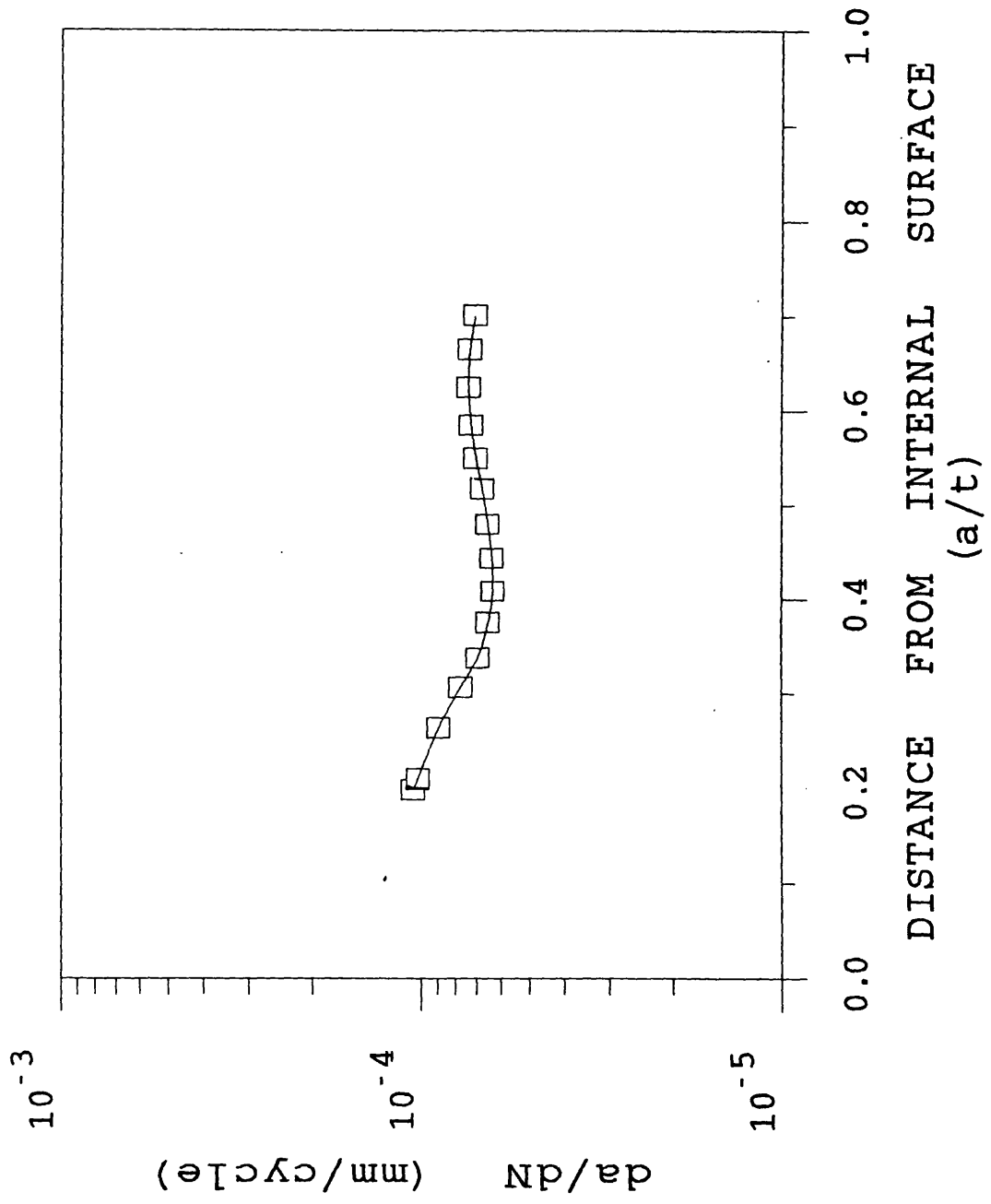


Figure 4.1.1h. Thermal Fatigue Crack Growth Rates Through a 2mm Deep Internal Longitudinal Notched Component.

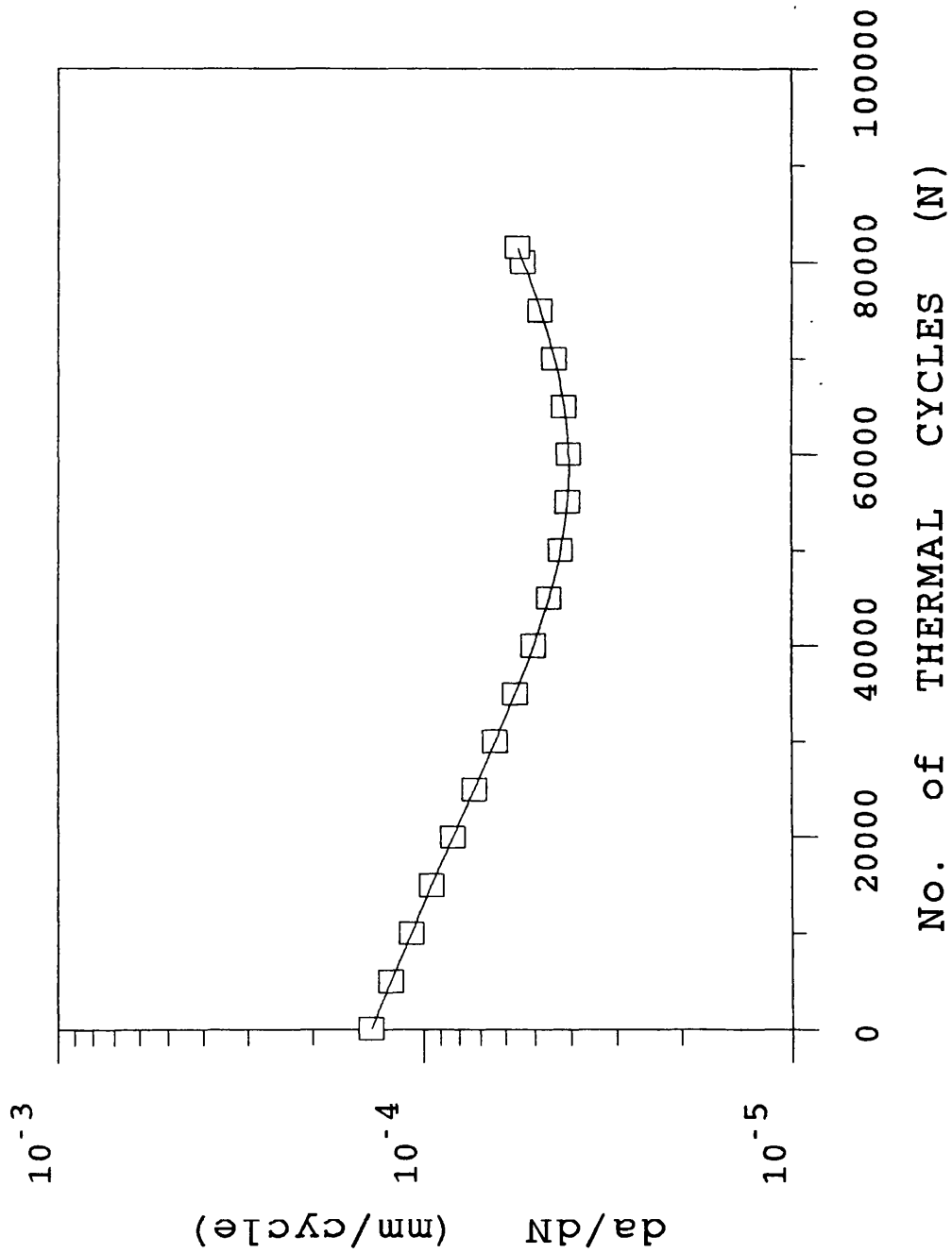


Figure 4.1.1i. Thermal Fatigue Crack Growth Rates in an External Circumferential Notched Component.

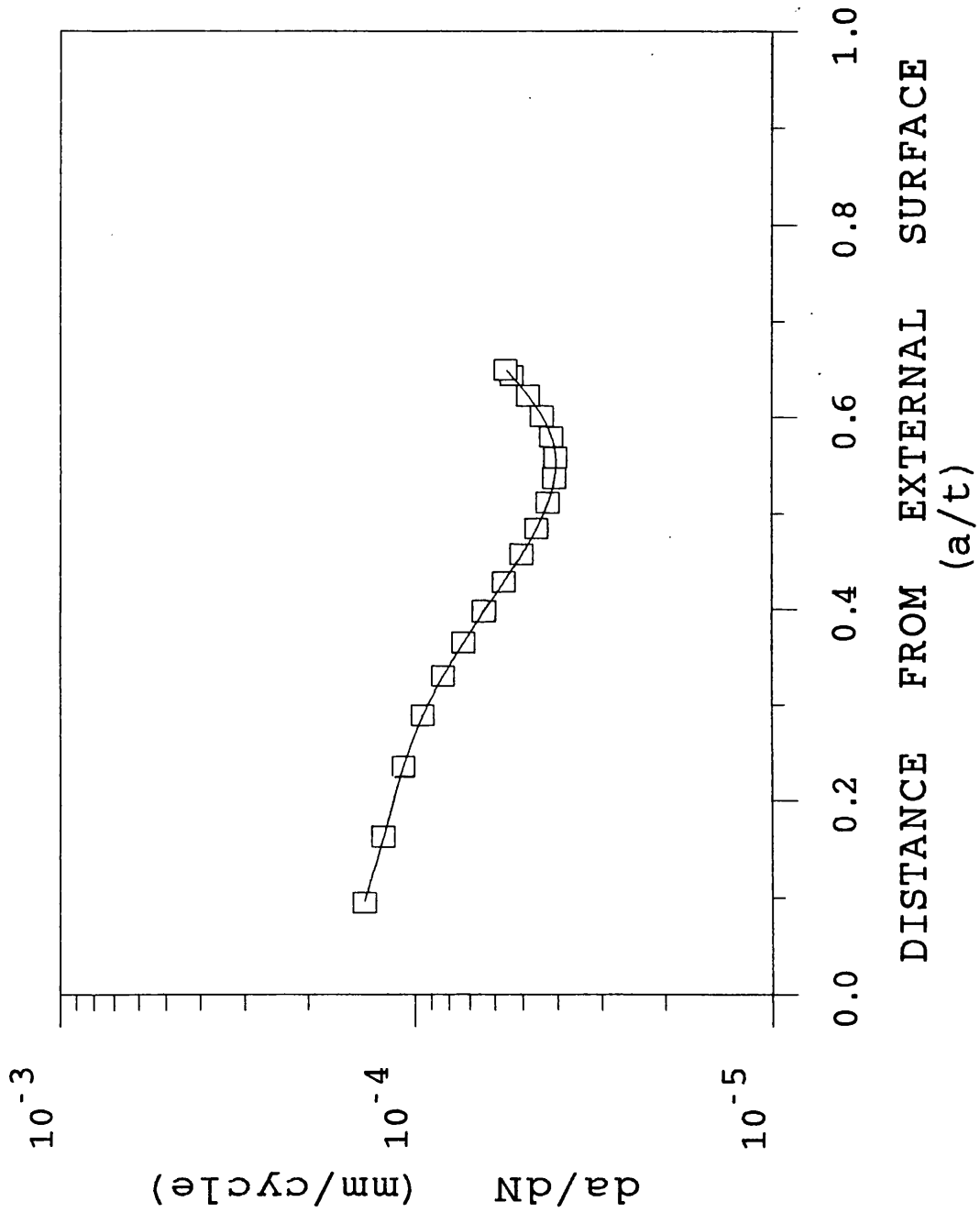


Figure 4.1.1j. Thermal Fatigue Crack Growth Rates Through an External Circumferential Notched Component.

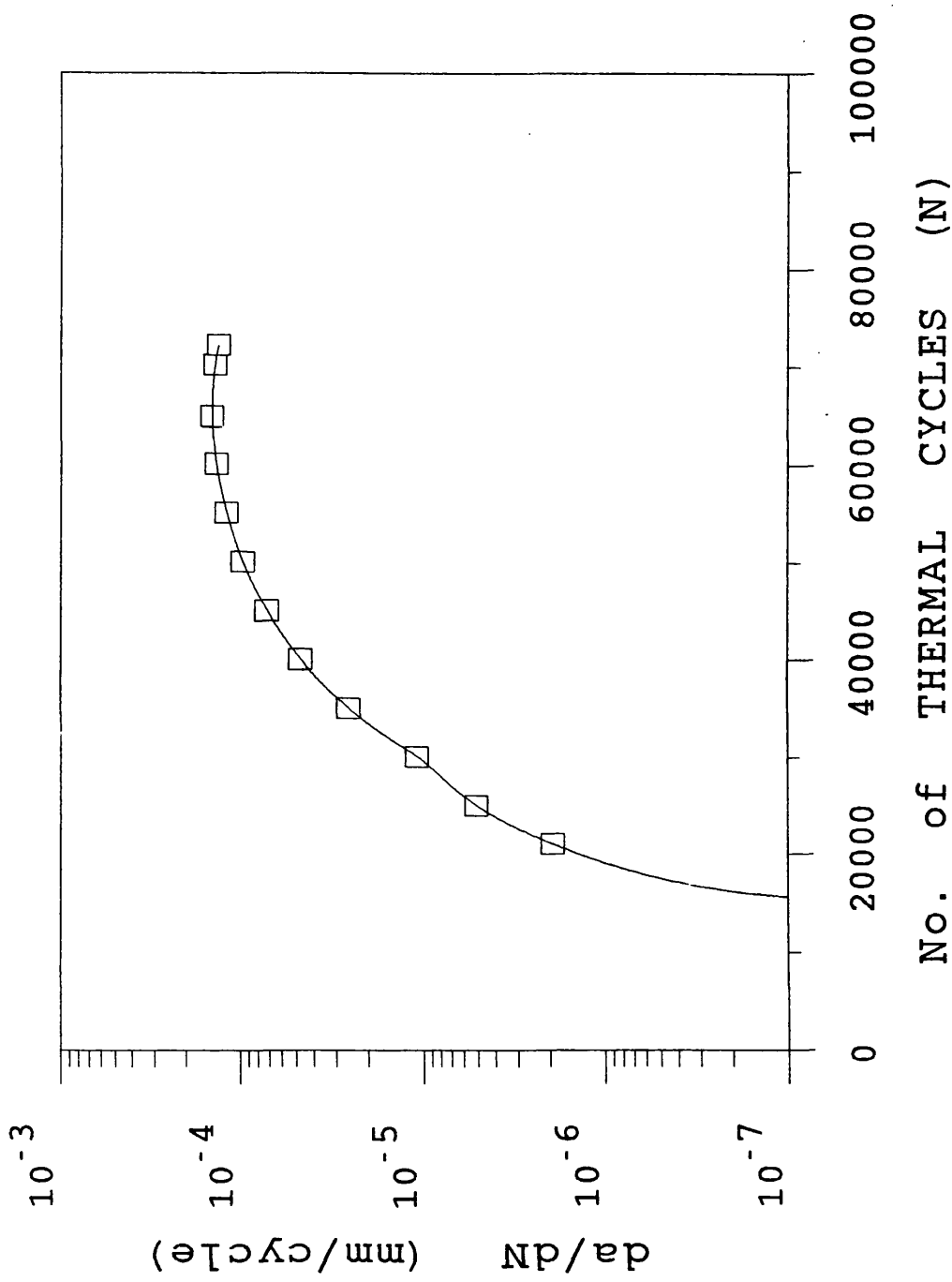


Figure 4.1.1k. Thermal Fatigue Crack Growth Rates in an Internal Circumferential Notched Component.

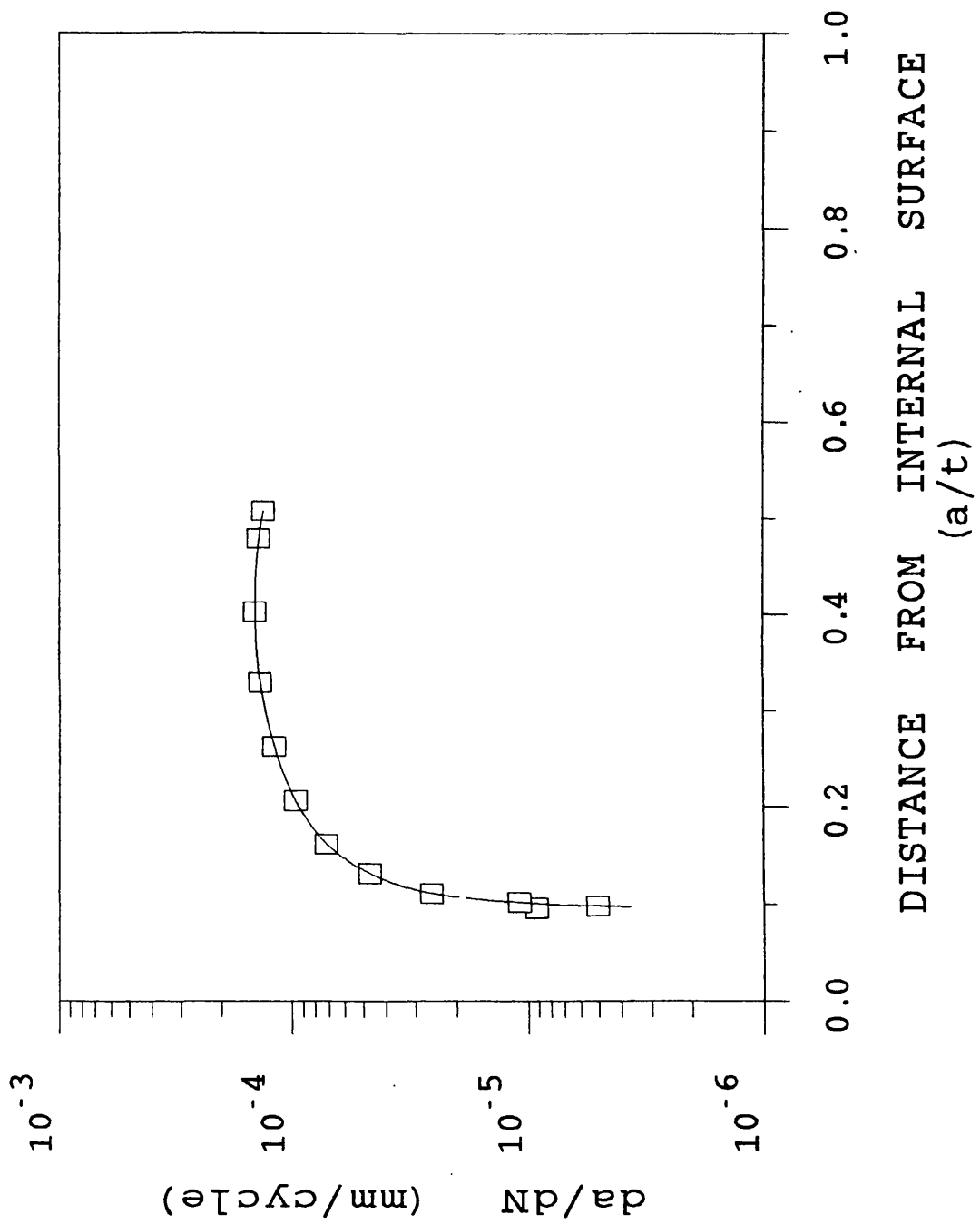


Figure 4.1.11. Thermal Fatigue Crack Growth Rates Through an Internal Circumferential Notched Component.

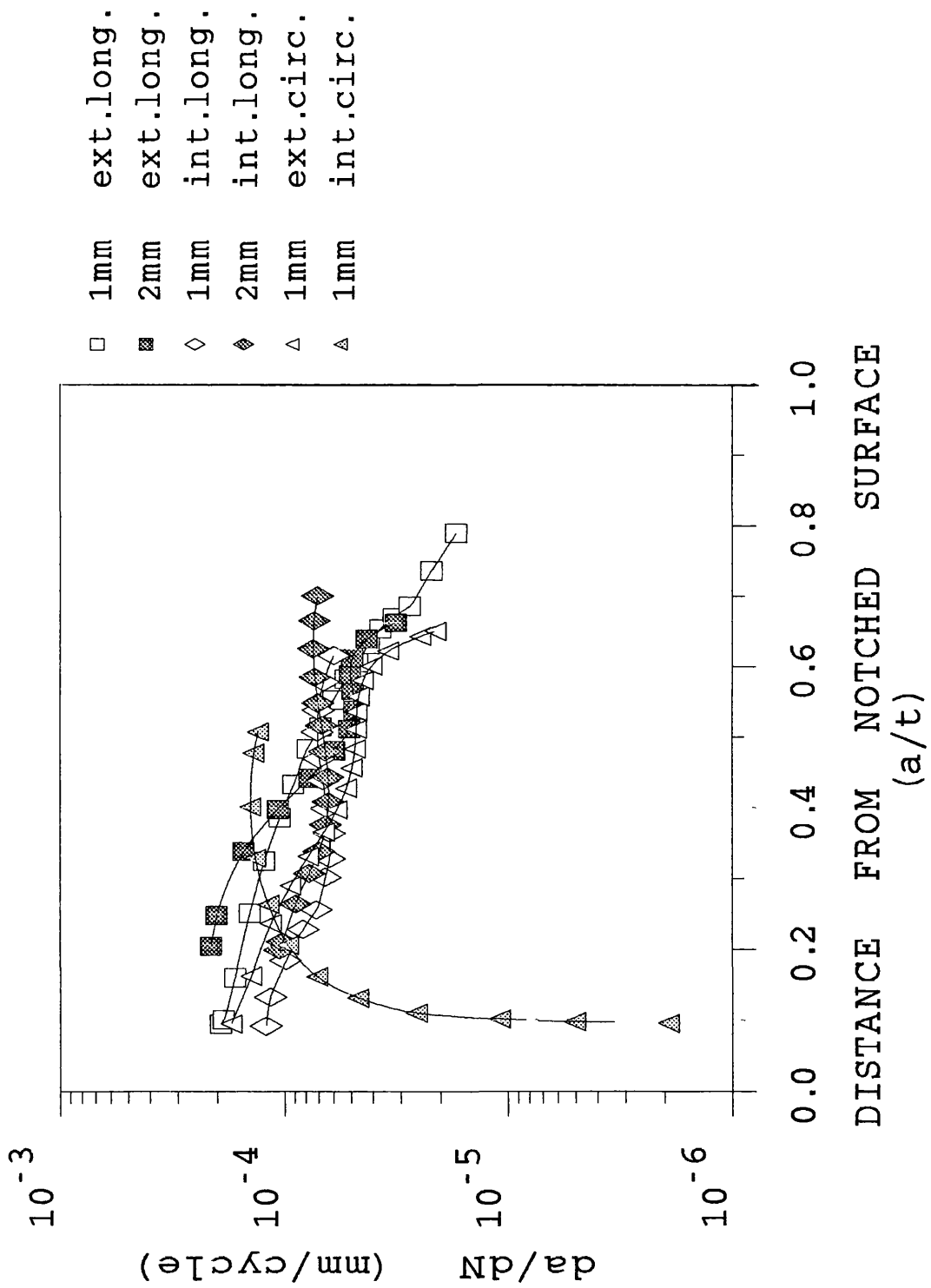


Figure 4.1.2. Thermal Fatigue Crack Growth Rates Through Each of the Notched Components.

4.2. Calculation of Cyclic Stress/Strain Field.

To explain both the similar da/dt for crack propagation from different notches and the delayed initiation from the internal circumferential notches, values of the cyclic thermal stresses and strains are required. Unfortunately, throughout the experimental programme, measurements of stress, strain and crack opening displacement could not be recorded, due to the complexity of the experimental set-up. Therefore values of the thermal stress/strain gradients have to be calculated from numerical methods.

In thermal shock testing, the elastic stress field is developed according to equation 2.1.25, [Skelton,1990], for the most damaging thermal gradient in an axisymmetric component. The peak thermal stresses were calculated at the moment a change in temperature was observed at the unshocked surface of the component. At the beginning of each thermal cycle, the component was initially at uniform temperature and experienced a sudden change in temperature at the shocked surface. With rapid thermal cycles both upshocks and downshocks were produced to such an extent that the component never experienced a uniform temperature, following the initial heat-up, and equation 2.1.25 could not be used to determine the thermal stresses. Consequently, a numerical method, such as the finite element method, has to be used to calculate the stress-strain fields resulting from the cyclic temperature gradients, [Burllet et al.,1989].

A model of the unnotched tubular component in the present analysis was generated using the Patran graphics package and was written to the input file of the Abaqus finite element analysis package. The model, Figure 4.2.1, consisted of 427 nodes which were assembled into 124 eight noded, axisymmetric, solid elements. Both radial and axial reductions were made in the element size at the central section of the component to produce greater accuracy in results. Type DCAX8 heat transfer elements were used for the thermal analysis, in which the temperature histories during the initial two cycles were specified at sets of selected nodes throughout the component. The material characteristics, density, specific heat, thermal expansion and thermal conductivity, as presented in Table 2.3.3, (section 2.3), were specified as a function of temperature over the range of interest. The resultant files of cyclic temperature gradients were produced at specified increments of the thermal cycles and were used as input files for the thermal stress/strain analysis.

The same model was used for the stress/strain analysis with type CAX8R eight noded axisymmetric solid elements which contain only four integration points for reduced stiffness to prevent shear locking. The material characteristics were specified, as a function of temperature, in the Abaqus input files. Initially, an elastic analysis was

performed, with the elastic parameters, Young's modulus and Poisson's ratio, specified as a function of temperature. Boundary conditions were specified to allow expansion of the component in the axial direction while a set of nodes were constrained from expansion in the radial direction to model the Leybold flange clamped ends of the component. The resultant values of axial stress, hoop stress, axial total strain, hoop total strain, axial elastic strain and hoop elastic strain were generated at selected element sets while values of displacement and temperature were generated at selected nodes for specified increments of the thermal cycles.

The results of the elastic finite element analysis are presented as graphs of both the hoop stress and the axial stress, Figure 4.2.2a and Figure 4.2.2b, respectively. Each of the stress graphs display the stress gradient through the thickness of the component, from the external surface, at both the heating and the cooling limits of the thermal cycle. The corresponding yield stress gradients have been plotted for comparison. At the maximum external surface temperature, marked heat, the internal surface was subjected to maximum the tensile yield stress While the external surface experienced the maximum compressive yield stress. Both the external and internal surfaces experienced stresses well above the yield stresses previously determined for the material at temperatures between 20°C and 350°C, [Tartaglia,1989]. The total strain graph, Figure 4.2.2c, displays high values of strain, $> 2 \times 10^{-3}$, at both surfaces, when the external surface was subjected to the maximum temperature during the cycle. The range of total strain values throughout the component was greatly reduced to $< 1 \times 10^{-3}$ while the component was subjected to the minimum temperature during the cycle. These results indicated the requirement of an elastic-plastic analysis which required cards in the Abaqus input file which described the temperature dependent yield stresses and corresponding values of plastic strain.

A plastic stress/strain analysis was performed on the same model with the results from the temperature analysis used as the thermal gradient input file. Plastic parameters were added to the material characteristic input cards to describe both the yield stress and a greater value of stress and plastic strain to describe the cyclic stress-strain behaviour of the material as a function of temperature. The resultant components of axial and hoop plastic strain were generated along with the previously mentioned stresses and strains. A variation in the material characteristics input cards enabled the analysis to be performed taking into account the cyclic hardening behaviour of the material. Values of yield stress and a greater value of stress and corresponding plastic strain were specified in the ORNL cyclic plastic card in the Abaqus input file to describe the cyclic stress-strain behaviour at both the initial and the tenth cycle. The cyclic stress-strain parameters were described at the three temperatures of interest, 20°C, 80°C and 350°C. All values

of Young's modulus, yield stress and plastic strain were determined from the solid specimen experiments in section 3.2. The main assumptions for the calculations were that there was no axial constraint on the component and the loading was purely thermal.

The resultant axial and hoop stress gradients through a radial section of the mid-thickness of the components were compared for over twenty increments a cycle corresponding to the mechanical steady state, Figures 4.2.3(a-b). The data at 4.9 seconds and 25 seconds, marked heat and cool, refer to the points of the thermal cycle corresponding to maximum heating temperature and minimum cooling temperature at the external surface. The increments of interest were identified at 1.2 seconds and 3.5 seconds as well as the increments at which the induction heating was switched off, 4.9 seconds, and switched on, at 25 seconds of the thermal cycle. A combination of the stress gradients at these selected increments produced a tensile stress profile through the thickness of the uncracked component. Maximum and minimum stress profiles were selected and plotted against the normalised component thickness, Figs. 4.2.4(a-d).

The maximum hoop stress was 264MPa at the external surface, as illustrated in Figure 4.2.4a, and occurred at the end of each cycle. The hoop stress remained above the yield stress to a depth of $x/t=0.12$ from the surface where the stress was 200MPa. The stress profile sharply decreased to a compressive value of -42.6MPa at $x/t=0.32$ and on to a value of -131MPa at $x/t=0.54$. The stress remained compressive, although never yielding, to a value of -96MPa at the internal surface. The maximum hoop stress at the internal surface occurred after 5 seconds of each cycle when the temperature at the external surface was 350°C, Figure 4.2.4b. The maximum value of hoop stress was 255MPa at the internal surface and remained above the yield stress of 195MPa to a depth of $x/t=0.2$. The stress then fell to 3.06MPa at $x/t=0.4$ and then on to a compressive yield value of -223MPa at $x/t=0.9$. Therefore yielding occurred at a region below the external surface during both the heating and cooling parts of the cycle while the internal surface experienced yielding only during the heating part of the cycle. However, the internal surface did experience tensile stress over a greater region below the surface, be it of a reduced magnitude compared to that at the external surface.

The maximum axial stress at the external surface also occurred at the end of each cycle, when the temperature was 80°C, Figure 4.2.4c. The maximum value was 210MPa, at the external surface, and remained above the yield stress to a depth of $x/t=0.1$ when the axial stress was 195.8MPa. By a depth of $x/t=0.27$ the axial stress value was -21.1MPa and remained compressive to a value of -35MPa at the internal surface. The maximum compressive stress was -122.4MPa, at a depth of $x/t=0.46$ which was below the yield stress. At the end of the heating part of the cycle, the internal surface was

subjected to a tensile stress of 235MPa, Figure 4.2.4d. The region of yielding continued to a depth of $x/t=0.19$ where the axial stress peaked at 253.6MPa. The stress profile decreased to a compressive value of -27.9MPa at $x/t=0.54$ and on to a region of compressive yielding from $x/t=0.9$ to the external surface, where the value of axial stress was -215MPa. Similar regions of yielding were observed with the axial stress profiles as were observed with the hoop stress profiles. Similar behaviours in the depths of tensile loading were observed with the region below the internal surface experiencing a tensile load to $x/t=0.53$ while the region below the external surface was under tension to only $x/t=0.23$.

Values of plastic strain were calculated and plotted in Figure 4.2.5. The magnitude of the hoop plastic strain was greater than the axial plastic strain at regions next to both the external surface, $x/t < 0.46$, and the internal surface, $x/t > 0.85$, where x/t was measured from the external surface. A region of zero plastic strain was observed in the centre of the component, ($0.46 \leq x/t \leq 0.73$), while the components of both axial and hoop plastic strain did not change between the mid-thickness of the component and the internal surface. Only a region below the external surface, ($0 \leq x/t \leq 0.1$), experienced cyclic plastic strain, with both the axial and the hoop values displaying a maximum change in plastic strain, $\Delta \epsilon_p = 5 \times 10^{-4}$. The unnotched component was subjected to three different strain states, for both the axial and the hoop strain components, as illustrated in Figure 4.2.5. Both the axial and the hoop loading have produced a region of cyclic plastic strain over a depth of $x/t \leq 0.1$ from the external surface. It is assumed that this region would be subject to cyclic plastic loading for the duration of the experiment since the strain hardening behaviour of the material had been taken into account during the calculation. A region of elastic straining existed in the centre of the component, ($0.5 \leq x/t \leq 0.75$), in which no plastic straining occurred. Finally, two regions of the component exhibited elastic shakedown after initial plasticity within the first half cycle. This is observed in Figure 4.2.5. over both of the regions, ($0.1 \leq x/t \leq 0.5$) and ($0.75 \leq x/t \leq 1.0$), at the internal surface, where the plastic strain remains constant throughout the thermal cycle. Similar magnitudes of hoop stress and both hoop and axial plastic strains were developed from an elastic-plastic finite element analysis on a similar model in which slightly different material plastic properties were specified, [Andritsos,1991a].

Skelton and Miles,[1984], stated that equation 2.2.32 could be used to apply uniaxial stress/strain data to thermal cycling applications, however, in the present analysis it was assumed that only one of the components of stress controlled the corresponding crack propagation, (hoop stress for a longitudinal crack). Further developments of the stress fields were proposed, [Skelton,1983], to take into account the region of cyclic plastic strain, equation 2.2.33. This method has produced equivalent stress intensity values

which sit well within a large scatter of experimental thermal fatigue results, [Burllet et al.,1989]. However equation 2.2.33 does involve multiplying the plastic strain range with the corresponding value of Young's elastic modulus which is not a regular practice in linear elastic fracture mechanics.

The calculations from the present finite element analysis for an unnotched component, in combination with the findings of the miscellaneous experiments in section 3.4, can now be used to explain the thermal fatigue crack growth rate behaviour from the various notched components. In each of the 80°C to 350°C experiments, no crack initiation was observed from either the free surface or the uncracked laser welded regions, expt.#10. However a small degree of cracking was observed, Figure 4.2.6, along the axial direction from a deliberately damaged spot weld on the external surface of a component, expt#11. Crack initiation occasionally occurred from the spot-welded p.d. probes on the external surface while limited crack growth was observed only from small laser welds which contained surface cracks, expt.#21. In this experiment, the total crack depth was less than 1mm in 65,000 cycles. The different characteristics of the welded material also produced difficulties in the comparison of the crack initiation. Experiments with machined round holes, expt.#21, favoured longitudinal cracking, which indicated that the hoop stress/strain was greater than the corresponding axial stress/strain, as confirmed in Figures 4.2.4(a and c). Furthermore, the higher temperature cycling test, expt.#7, produced a higher stress gradient, giving crack initiation from three regions around the external surface including one at a deliberately damaged spot weld. The resultant crack propagation was along the axial direction on the external surface, Figure 4.2.7, which indicates that with this component geometry, thermal fatigue loading produces higher magnitudes of cyclic hoop stress than axial stress while favouring crack initiation at the external surface in preference to the internal surface. Crack initiation at the internal surface only occurred when the component had been either accidentally overheated, expt.#5, or when the cracks from the external surface had grown to depths greater than $a/t=0.65$, expt.#8 and expt.#24. However it must be noted that there were much fewer spot welds on the internal surface than on the external surface and hence this conclusion cannot be compared.

The shape of the notch also had a large effect on both the initiation and resultant crack growth rate. In experiments #5, #8, #13 and #19, semi-circular shaped notches were electro-eroded into the external surface of the components, in the longitudinal plane, for comparison with the findings from the longer rectangular shaped notches of similar depths. With notches of similar depths and surface lengths and different notch shapes, both the crack growth rates and the final crack depths were reduced when the cracks propagated from semi-circular rather than rectangular shaped notches, during

experiments of similar number of cycles and test conditions. Apart from expt.#5, which was subjected to overheating, none of the cracks from the semi-circular shaped notches extended to depths greater than $a/t=0.44$, while experiments with rectangular notches and similar number of cycles, produced crack depths of $a/t=0.74$. An even greater trend was observed with shallower cracks. A total of 31,000 cycles were required to grow cracks 0.59mm and 0.86mm deep from a 1mm and a 2mm deep semi-circular notch respectively in expt.#13. Greater crack depths were obtained after only 7,000 cycles from rectangular notches of similar depths, (expt.#22). The final crack shapes from all semi-circular and rectangular notches were always semi-elliptical. Using the definitions of section 3.4.4, the final aspect ratios, (a/c), of the deeper cracks from the semi-circular notches tended to have a semi-elliptical aspect ratio towards 0.5 while the cracks of similar depths from the rectangular notches had aspect ratios between 0.35 and 0.45. The potential drop measurements suggested that the cracks from the semi-circular notches spent a larger number of cycles in initiation and the consequent crack growth was greater in the direction along the axial length of the component than through the thickness. Crack initiation from the longer, rectangular notches, was immediate and the cracks extended in depth in a semi-elliptical shape. Therefore the crack growth rate was initially greater through the thickness of the component than along the axial length, as illustrated in Figure 3.4.31, in section 3.4.4.1.

Although the crack growth rates from rectangular shaped longitudinal notches and circumferential notches were greater than those measured from the shorter semi-circular shaped notches, similarities in crack growth behaviour were observed. Similar differences in the development of a crack from a shorter longitudinal notch in comparison to a greater longitudinal notch, were made in expt.#12. Two notches, each 2mm deep, were electro-eroded 180° apart in the middle of the gauge section of the external surface of a component. Both notches were rectangular in shape although one had a total surface length of 15mm while the other was 4mm long. The resultant cracks were both semi-elliptical in shape, although the final crack depths after 55,000 cycles were $a/t=0.67$ from the longer notch in comparison to $a/t=0.54$ from the shorter notch.

Another factor that had an effect on both the rate of crack initiation and, thus, the fatigue lifetime, was the curvature of the cross sectional shape of the notch. From both the internal and external surfaces, the initial crack growth rates were greater from 2mm deep longitudinal notches than from 1mm deep notches. Both the notch width and the curvature of the notch root were similar, across the width, for both notch depths. The effect of the presence of an electro-eroded longitudinal notch on the hoop stress was derived from a thermal strain finite element analysis with the component modelled as a

circular cross section containing a 0.5mm wide and either 1mm or 2mm deep notch, positioned in either the internal or external surface, [Andritsos,1991b]. The stress gradients were developed for the sections at both the maximum and minimum temperature gradients. The maximum values of hoop stress at both surfaces of the unnotched sections of the component were surprisingly lower, 197MPa compared to 254MPa, than those previously calculated, [Andritsos,1991a]. Furthermore, the root of the notch was modelled as rectangular in shape, which led to very high stress concentrations at the bottom corner of the notch, while the root of the longitudinal notches in the experimental components were shaped with a radius of 0.25mm. Another difference from the present analysis was in the use of different plastic characteristics to describe the cyclic stress/strain behaviour of the material. However, the results from Andritsos' analysis are useful as they display the general effects of a notch on the maximum stress profiles throughout the thickness of the component.

In these calculations, a 2mm deep notch in the external surface was found to increase the magnitude of the hoop stress, at the end of the cooling part of the cycle, from 90MPa to 310MPa, at a depth of $x/t=0.2$, as illustrated in Figure 4.2.8a. The increase in hoop stress continued to a depth of 1.7mm ahead of the notch while the depth of the tube under compression remained about 4.8mm from the internal surface, which was similar to the calculation with an unnotched component. At the end of the heating part of the cycle, the presence of a 2mm deep notch in the internal surface increased the region of tensile stress to a depth of 4.8mm from the internal surface in comparison to 3.4mm in an unnotched component, as illustrated in Figure 4.2.8b. To compensate for the increased region of tensile stress, a region at the external surface was subjected to increased magnitudes of compressive stress values, -130MPa, in comparison to only -110MPa in the unnotched component.

Calculations of the effect of a 1mm deep notch on the hoop stress field were limited to the increment of the thermal cycle when the temperature at the external surface was 350 °C. The stress at the root of the internal notch increased by 50MPa to 233MPa and this effect continued to a depth of $x/t=0.47$ at which point the notch affected stress was 16MPa in comparison to -20MPa in the unnotched section. For a region of 1.5mm from the external surface the magnitude of compressive stress increased from -110MPa to -124MPa which compensated for the increased tensile stress in the notch effected zone.

Another method to determine the effect of the notch on the unnotched stress profile was to use available information from literature. Under purely elastic loading, the stress at the notch tip is raised by the stress concentration factor, $[1+2\sqrt{(L/r)}]$, where L is the depth of the notch and r is the notch root radius. Similar relationships have been

developed for elastic fatigue loading, [Rice et al,1989], which specified that an increase in notch depth increases the magnitude of stress at the notch tip. Furthermore, an area of plastic straining, in addition to an area of increased elastic stress, must be expected to develop for a short distance ahead of the root of the notch, since this area of material was already strained slightly below yielding. Expressions for stress, strain and plastic strain concentration factors have been developed and incorporated into an equation which described the decrease in notch effect with increasing distance ahead of the notch, [Skelton, 1983], Table 4.2.1. Therefore as a crack propagates away from the notch it will reach a depth which is beyond the influence of the notch and the crack will be subjected to the same stress field regardless of the shape of the notch. This was observed in the similarity in crack growth rates at depths greater than $a/t=0.4$ from both 1mm and 2mm deep external longitudinal notches. Similar crack growth rates were measured from both 1mm and 2mm deep internal longitudinal notches after the cracks had propagated beyond $a/t=0.33$.

Distance From Notch Root (mm)	Longitudinal k_{σ} 1mm deep, 0.5mm wide	Longitudinal k_{σ} 2mm deep, 0.5mm wide	Circumferential k_{σ} 1mm deep, 1mm wide
0.00	2.25	2.60	1.74
0.10	1.456	1.583	1.269
0.25	1.156	1.20	1.093
0.50	1.046	1.059	1.027
0.75	1.019	1.025	1.012
1.00	1.01	1.013	1.006

Table 4.2.1 Reduction In Stress Concentration Factors From Notch Root.

Although the finite element analysis was performed to produce stress profiles for the calculation of the stress intensity factors through the thickness of the cracked components, (see section 4.3), it is still of general interest to look at the influence of the stresses on the cracking from each of the different notches in the tubular components.

The resultant axial and hoop stresses were calculated for the presence of either a longitudinal or a circumferential notch, by applying the stress concentration factors, k_{σ} , to the results of the ORNL elastic-plastic thermal stress-strain finite element analysis, Figure 4.2.9(a-d). The maximum tensile hoop stresses are shown in Figures 4.2.9(a and b) when the external surface temperature was 80°C and 350°C respectively. Likewise

the maximum tensile axial stresses at external surface temperatures of 80°C and 350°C are shown in Figures 4.2.9(c and d).

The magnitude of maximum hoop stress at the root of the notches was greater than the corresponding components of axial stress. Very conservative values of stress were calculated using the equations which contained elastic stress concentration factors to calculate the increased stress values due to the influence of a notch in a yielded zone. However, the immediate crack initiation from rectangular shaped longitudinal notches positioned in either the external or internal surface of the tube and the corresponding initially high crack growth rates indicate that very high levels of hoop stress were developed. The yield stress profile through the thickness of the components were plotted in Figures 4.2.9(a-d) at the temperatures of interest to highlight the yielded regions ahead of the notch root. In general, the longitudinal notches had a greater influence on the local stress both in magnitude and in distance ahead of the notch. Therefore the component was subject to larger regions of yield when a longitudinal notch was present than with a circumferential notch. Beyond the influence of the notches, the values of hoop stress fell sharply such that compressive stresses were dominant at depths of $x/t=0.4$, from the external surface, and $x/t=0.5$ from the internal surface. Similar decreases with increasing crack depth were observed in the values of crack growth rate, although cracks propagated beyond $x/t=0.6$ from both surfaces. These extended crack depths were unexpected since previous investigations had revealed cracks to arrest at the mid-thickness of thick-walled tubular components subject to only cyclic thermal stresses, [Burlet et al.,1989]. It is possible that the actual stress field is different from the stress field calculated in the present investigation, especially with the inclusion of a deep longitudinal notch. Another reason for the increased depth of crack propagation is that once the crack had propagated beyond mid-thickness then the propagation may have been controlled by the tensile stresses developed within the component throughout the thermal cycle, as illustrated in Figure 4.2.3a. As previously shown for unnotched components, Figures 4.2.4(a-b), regions beyond $x/t=0.45$ from the external surface and $x/t=0.6$ from the internal surface were subjected to a range of tensile stresses during the heating and the cooling part of the thermal cycle respectively. Therefore it might have been possible for the tip of a long crack to be subject to tensile stresses while the mouth of the crack at the notch was subjected to a compressive stress.

Greater differences were observed in both the initiation and the crack propagation behaviour from the circumferential notches in comparison to that from the longitudinal notches. The external circumferential notches had a semi-circular cross section which produced a lower stress concentration at the notch root compared to that at the root of

the rectangular longitudinal notch, as shown in Table 4.2.1. The reduced stress concentration was a result of the smooth shape of the circumferential notches which were similar in both width and depth, while the depth of the sharper longitudinal notches were at least twice the width. Although the initial crack growth rate from the 1mm deep external circumferential notches was slightly less than that from the 1mm deep longitudinal notches, the large degree of yielding ensured that crack initiation was almost immediate and similar crack growth rates were measured at crack depths beyond the influence of the notch. Tensile stresses which develop at depths beyond $x/t=0.45$, as illustrated in Figure 4.2.4c, during the heating part of the cycle should contribute towards steady crack growth rates beyond the influence of the notch to crack depths of $a/t=0.64$, (expt#15). In expt.#3 a short section of the 1mm deep notch was electro-eroded to a depth of 2.4mm. Following initiation, the crack propagated completely around the circumference from the notch root and remained deeper at the region corresponding to the deepest section of the notch. However the final depths of crack propagation from the root of the notch were very similar around the entire circumference of the cracked section. Therefore it can be assumed that beyond the influence of the notch and initiation, the cracks grew at a specific growth rate with respect to the position of the crack tip within the thickness of the component section.

From the three experiments performed with a 1mm deep internal circumferential notch, crack initiation from the notch occurred in only expt.#6 and only after 29,000 cycles. The maximum calculated axial stress at the internal surface was greater than the yield stress at 60°C, at the end of the heating part of the cycle, although it was not as great as the corresponding value of maximum hoop stress. The reduced rate of crack initiation from the circumferential notch must have been due to a combination of no cyclic plastic deformation, both with and without a notch, at the internal surface, combined with the reduced stress concentrating effect of the cross sectional shape across the width of the circumferential notch. When crack initiation occurred, the crack growth rate increased rapidly as the crack propagated through a region of high tensile stress, greater than 200MPa, and then decreased as the stress approached zero at a depth of $x/t=0.55$ from the internal surface. The similar crack growth rates beyond the influence of the various shaped notches, indicates that similar stress fields are developed in both the longitudinal and the circumferential directions within the components during the thermal cycles. Therefore if the crack depth could be measured or determined to be beyond the yielded region of the notch, then the crack growth rate and the effective life of the thermally cycled component may be calculated. This would be very beneficial to both the designer and the operator of the first wall components.

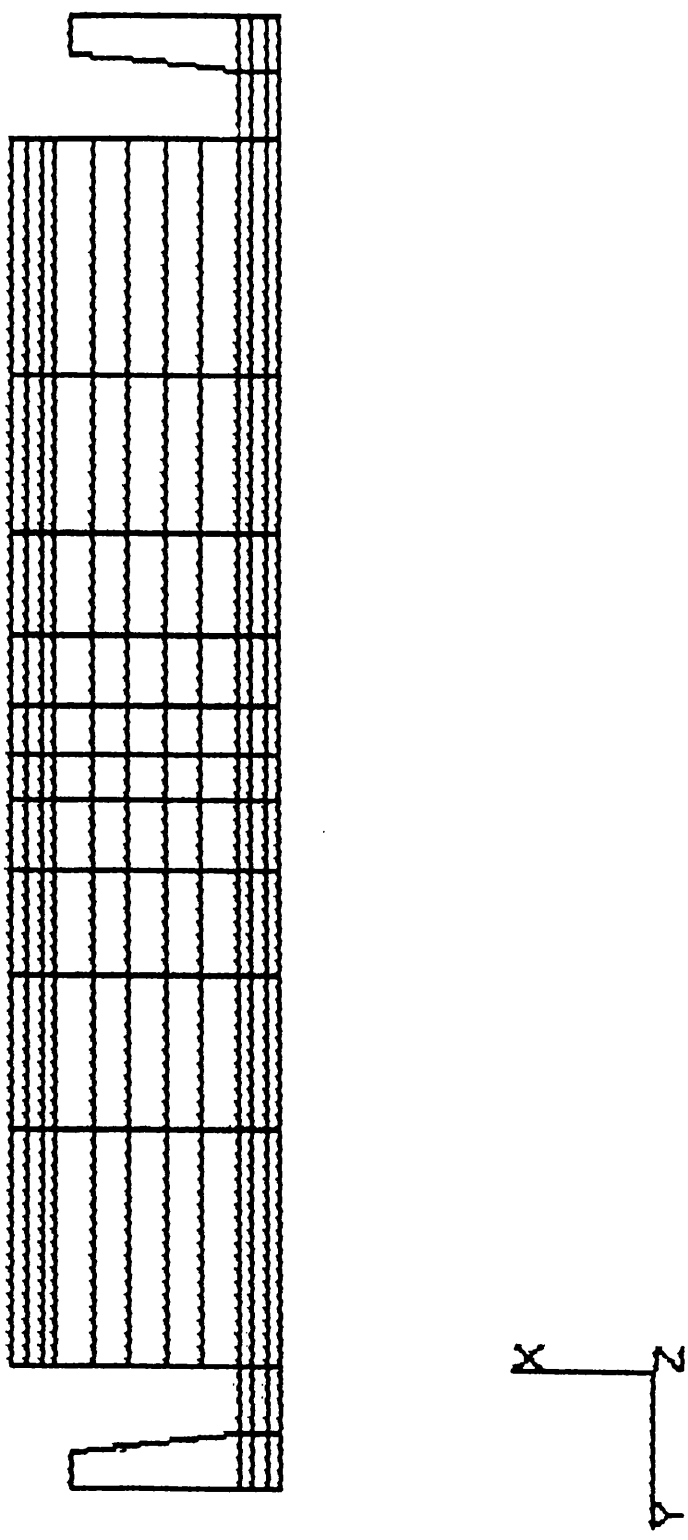


Figure 4.2.1. Model of Tubular Component for Finite Element Analysis.

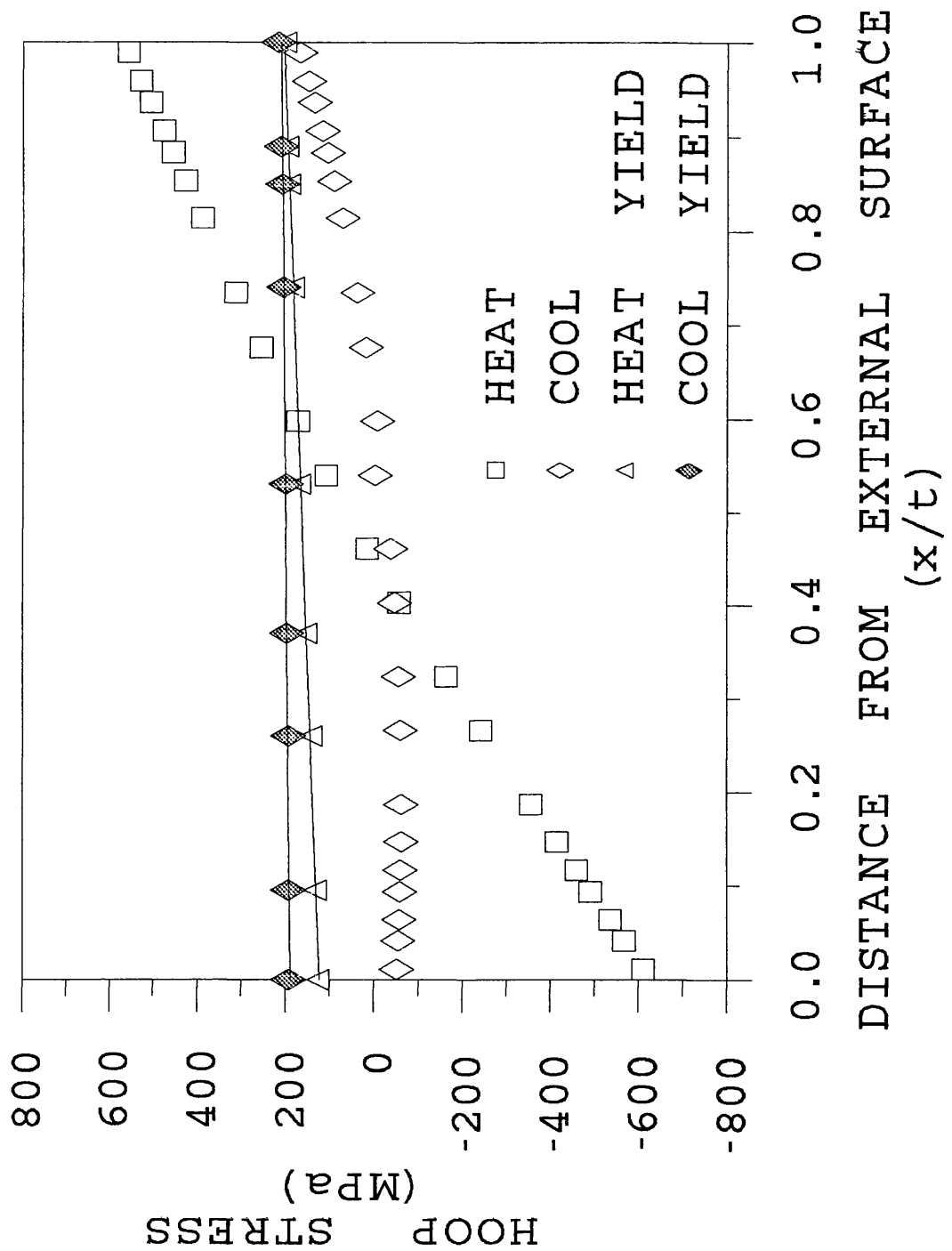


Figure 4.2.2a. Hoop Stress Through a Section of an Unnotched Component.

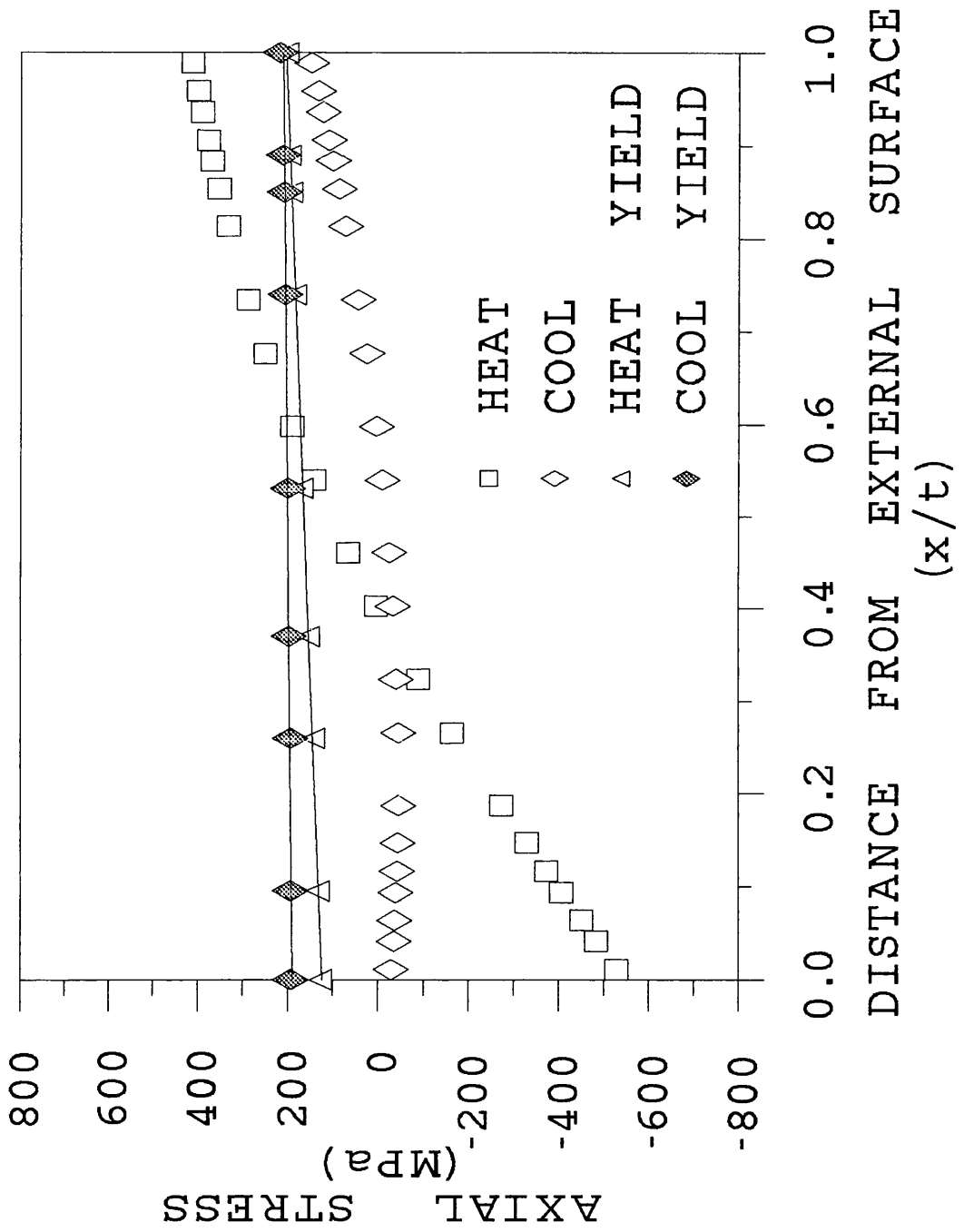


Figure 4.2.2b. Axial Stress Through a Section of an Unnotched Component.

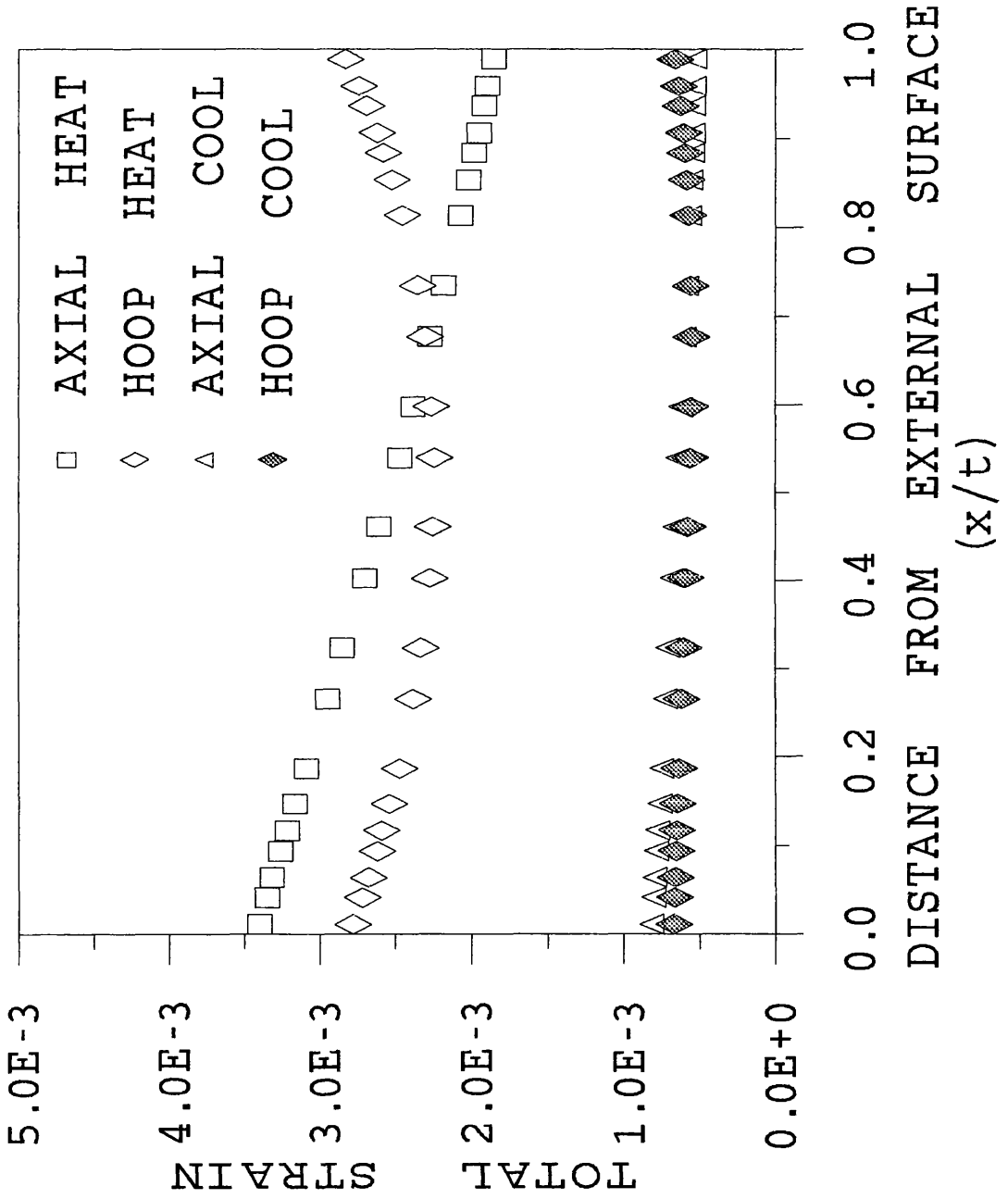


Figure 4.2.2c. Total Strain Through a Section of an Unnotched Component.

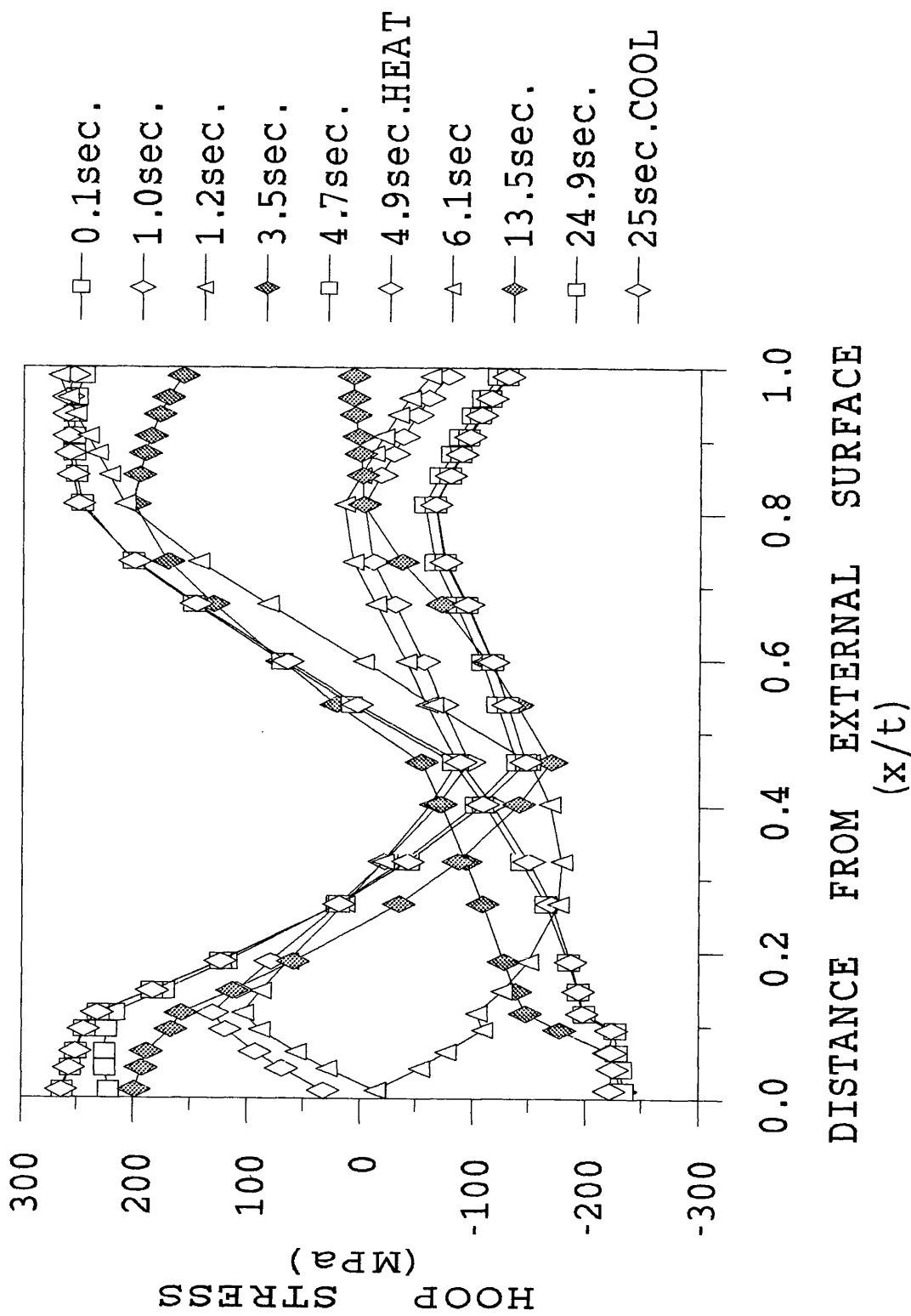


Figure 4.2.3a. Stress Distribution Through an Unnotched Component During a Thermal Cycle.

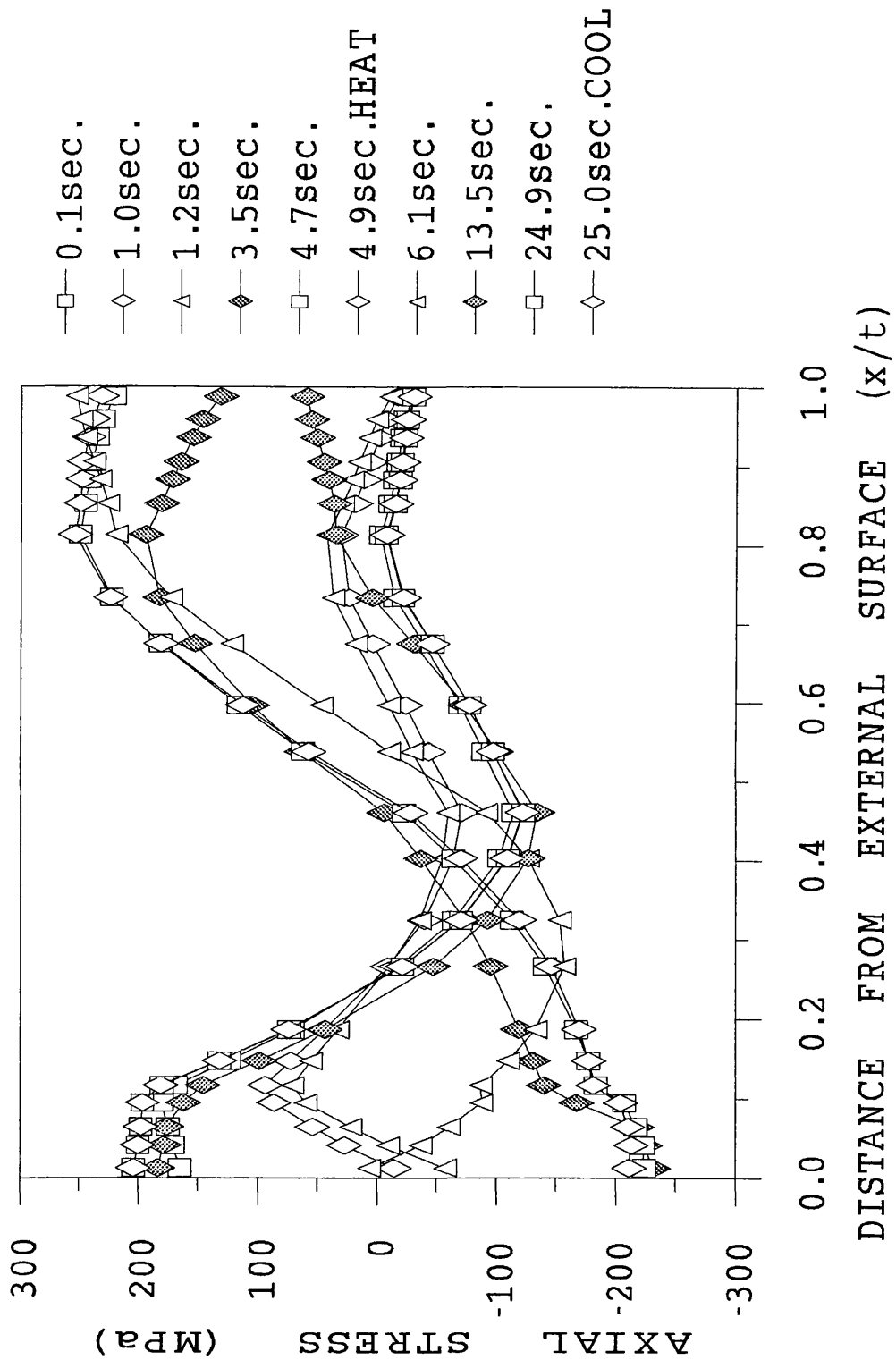


Figure 4.2.3b. Stress Distribution Through an Unnotched Component During a Thermal Cycle.

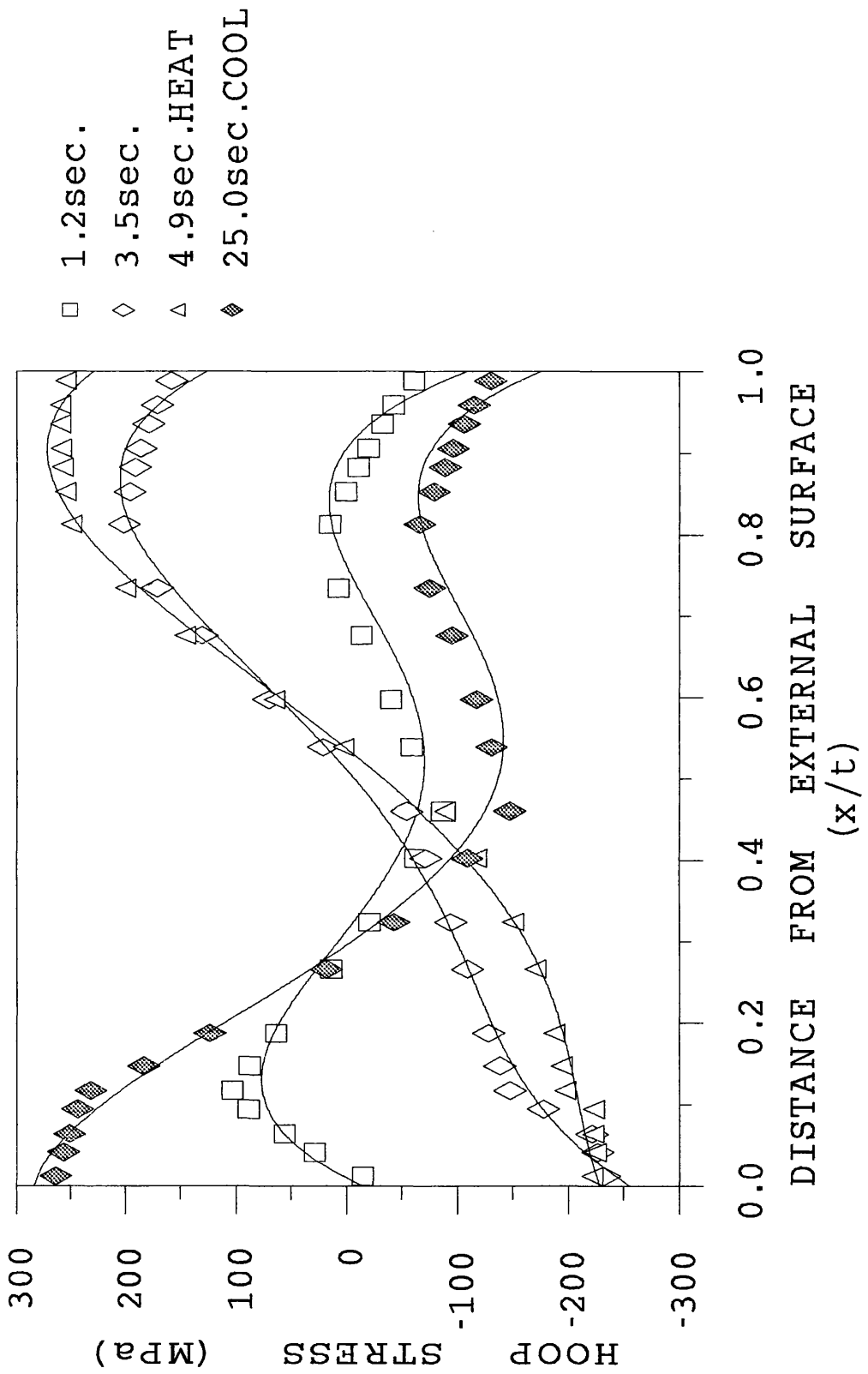


Figure 4.2.4a. Stress Distribution Through an Unnotched Component During a Thermal Cycle.

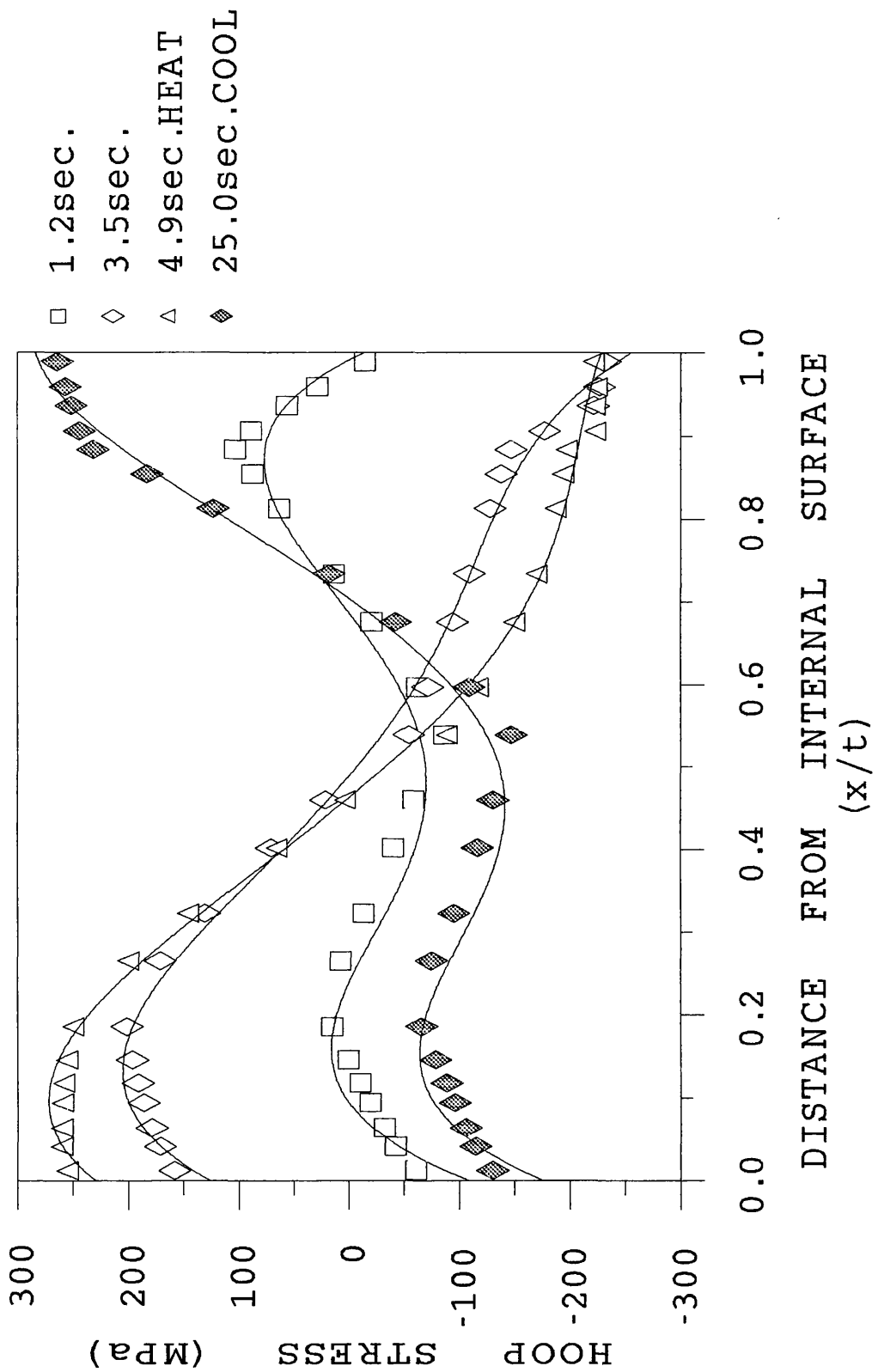


Figure 4.2.4b. Stress Distribution Through an Unnotched Component During a Thermal Cycle.

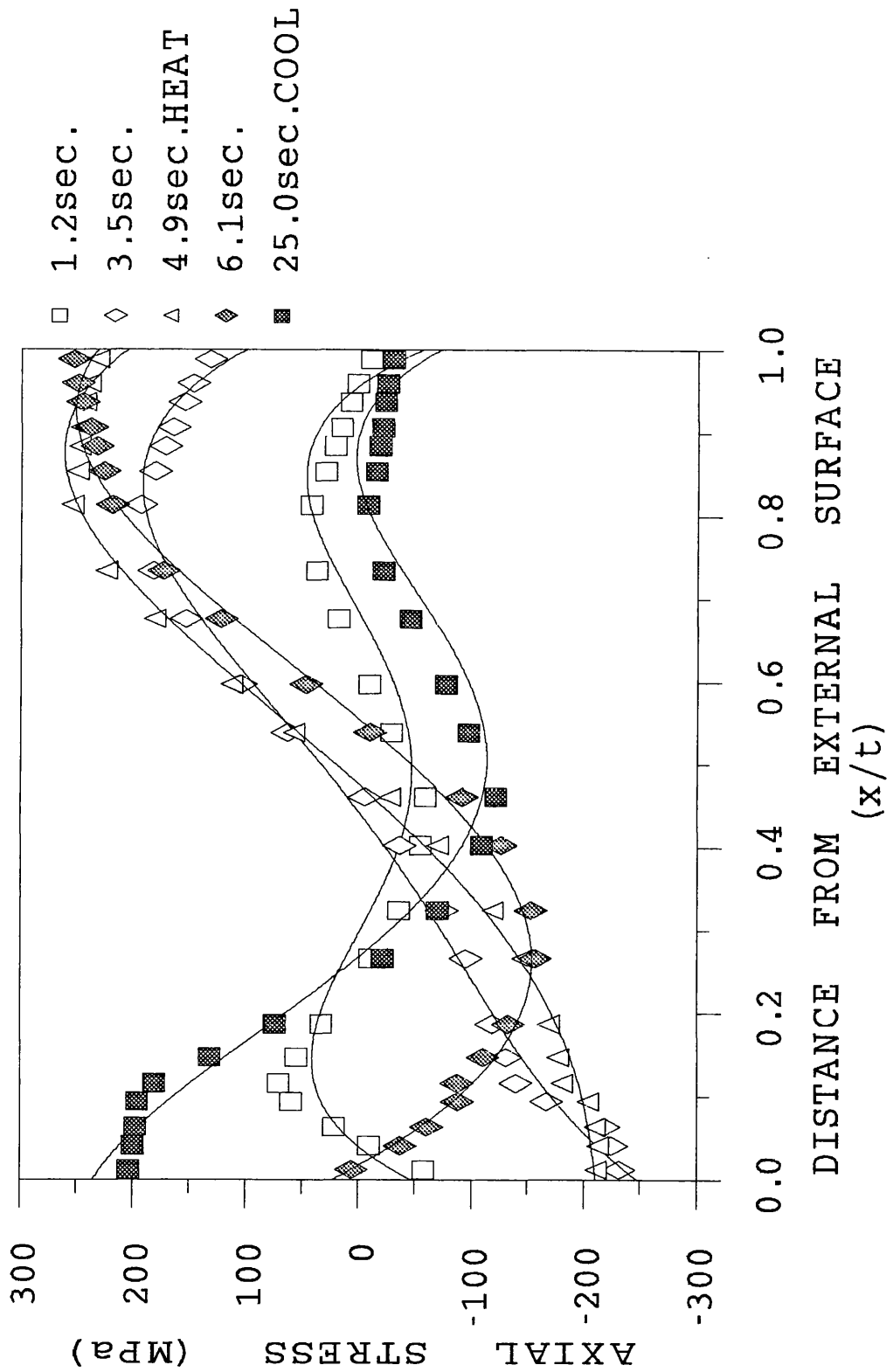


Figure 4.2.4c. Stress Distribution Through an Unnotched Component During a Thermal Cycle.

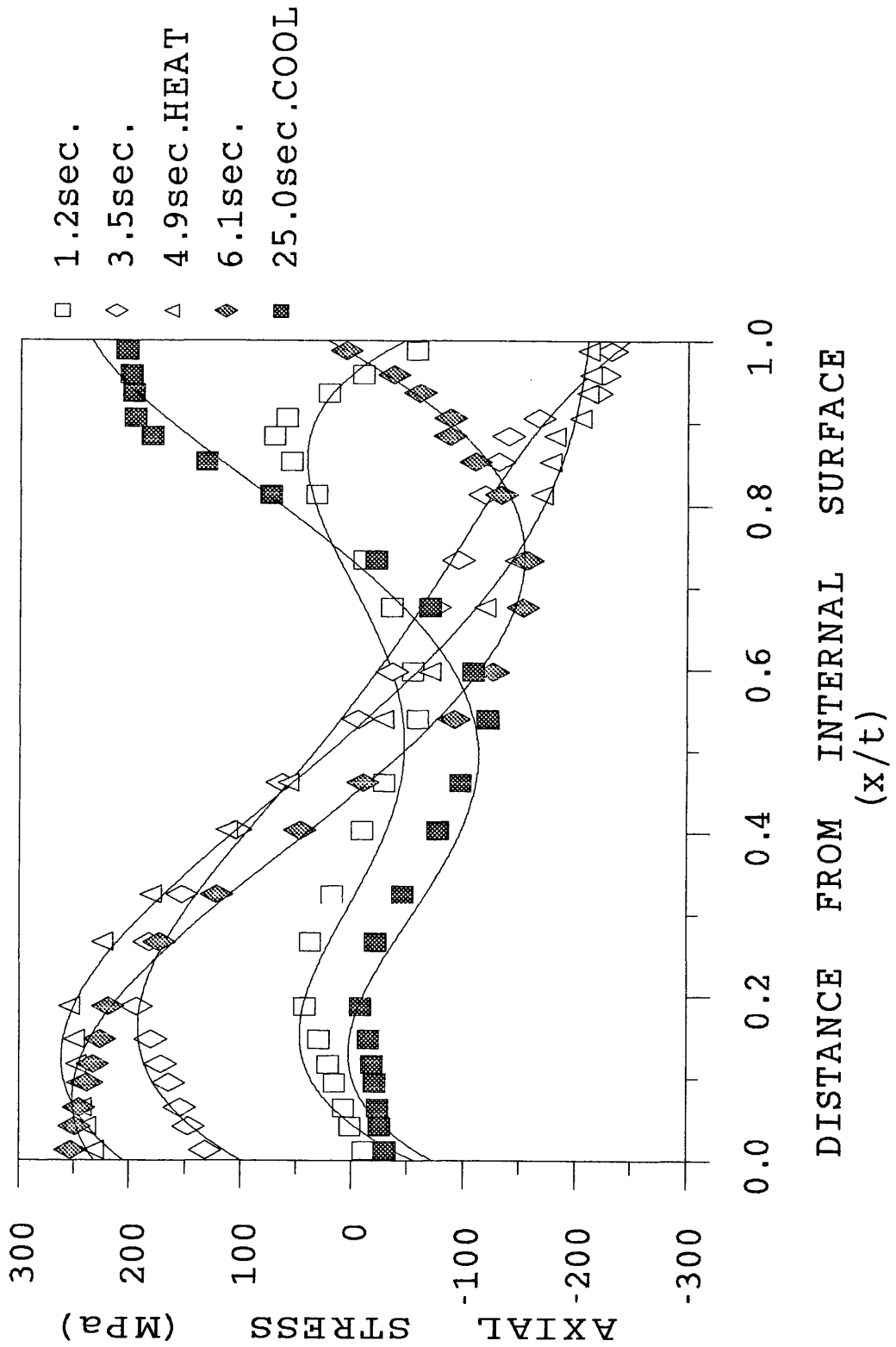


Figure 4.2.4d. Stress Distribution Through an Unnotched Component During a Thermal Cycle.

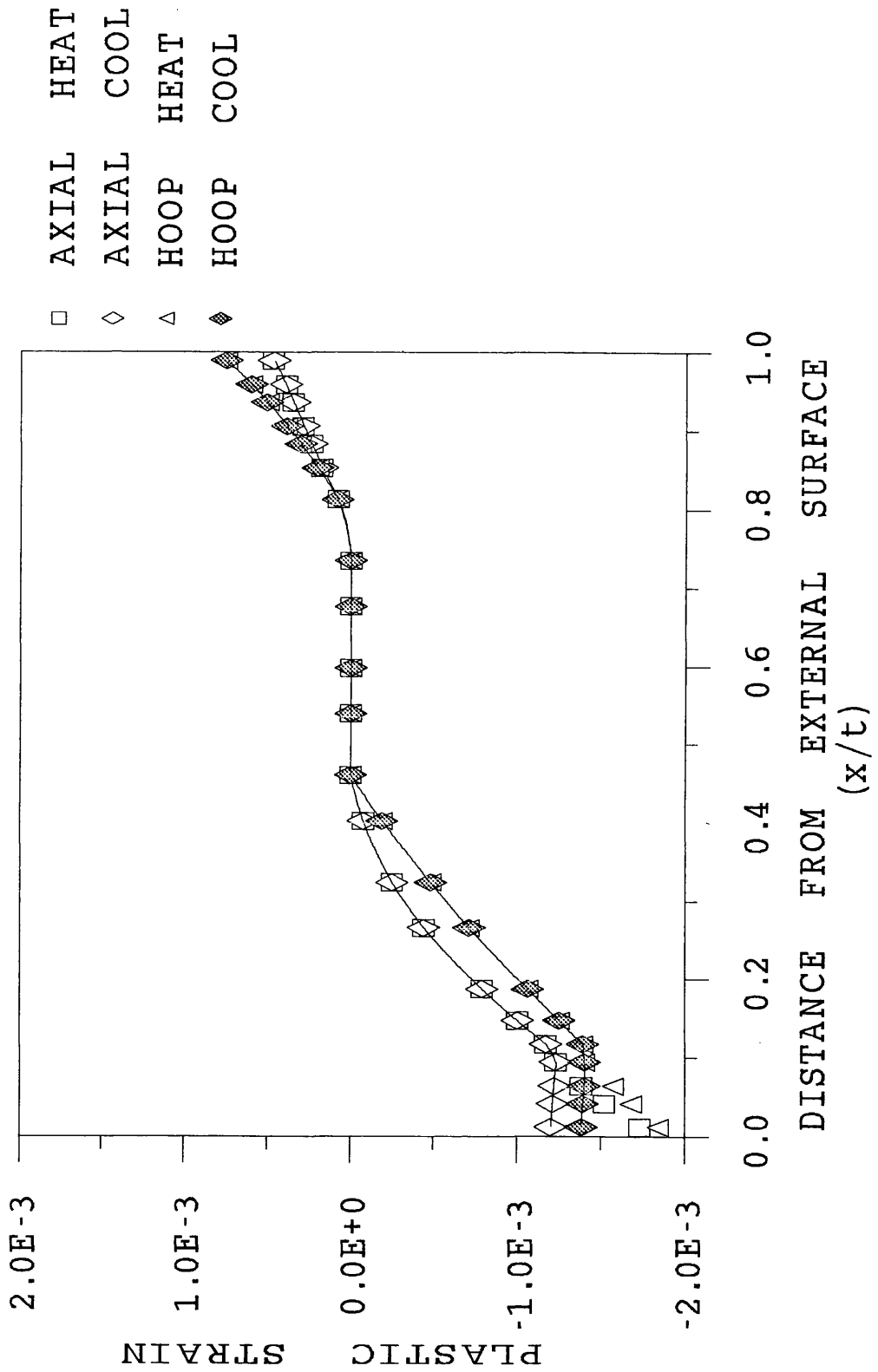


Figure 4.2.5. Plastic Strain Distribution Through an Unnotched Component During a Thermal Cycle.

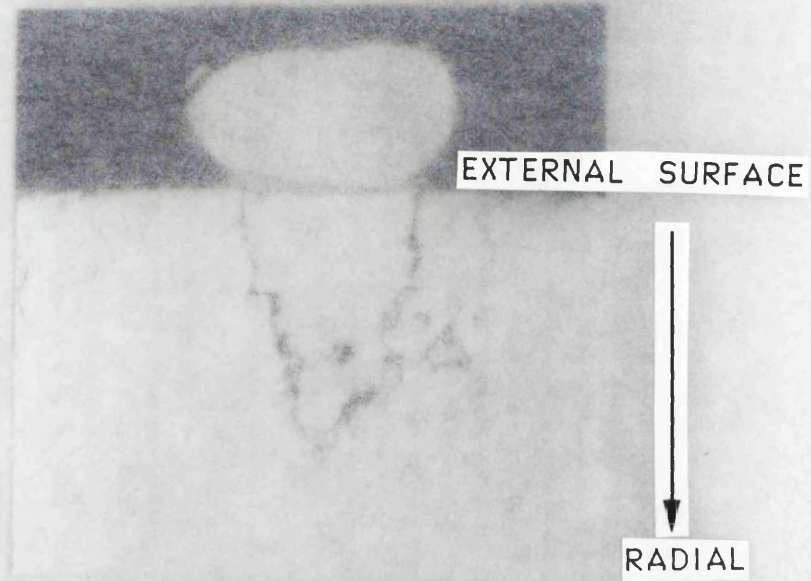


Figure 4.2.6. Fatigue Crack Growth From a Spot Weld in Expt. #11, (Mag. X50).

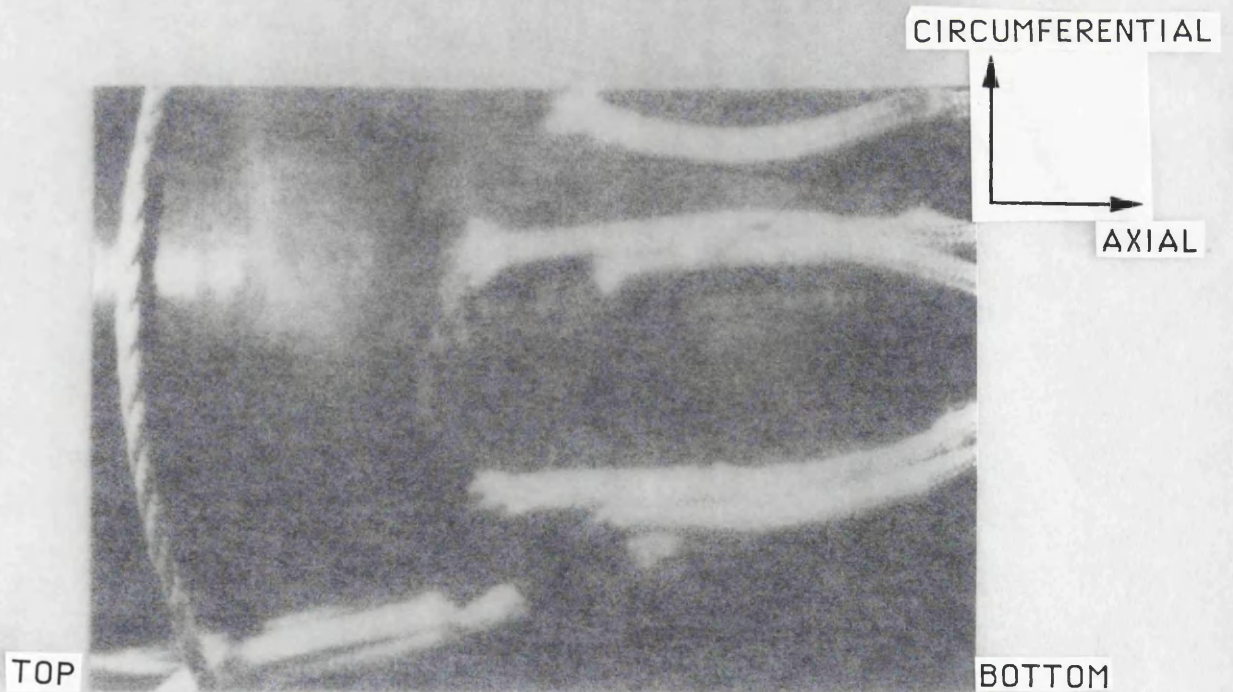


Figure 4.2.7. Surface Cracking from a Spot Weld in Expt. #7, (Mag. X3.2).

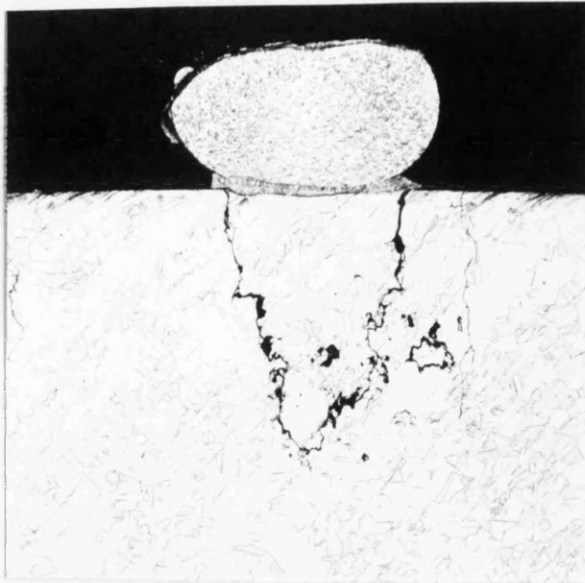


Figure 4.2.6. Fatigue Crack Growth From a Spot Weld in Expt.#11, (Mag.X50).

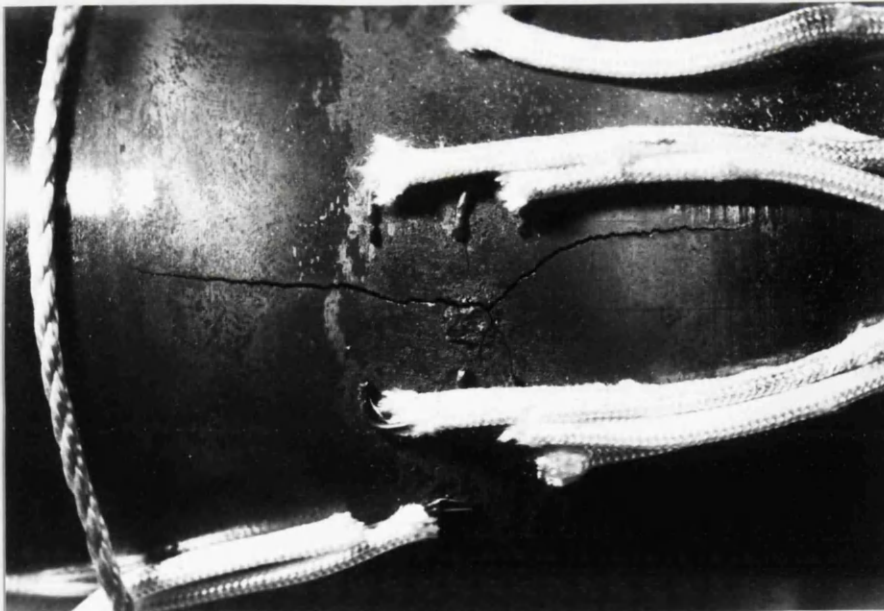


Figure 4.2.7. Surface Cracking from a Spot Weld in Expt.#7, (Mag.X3.2).

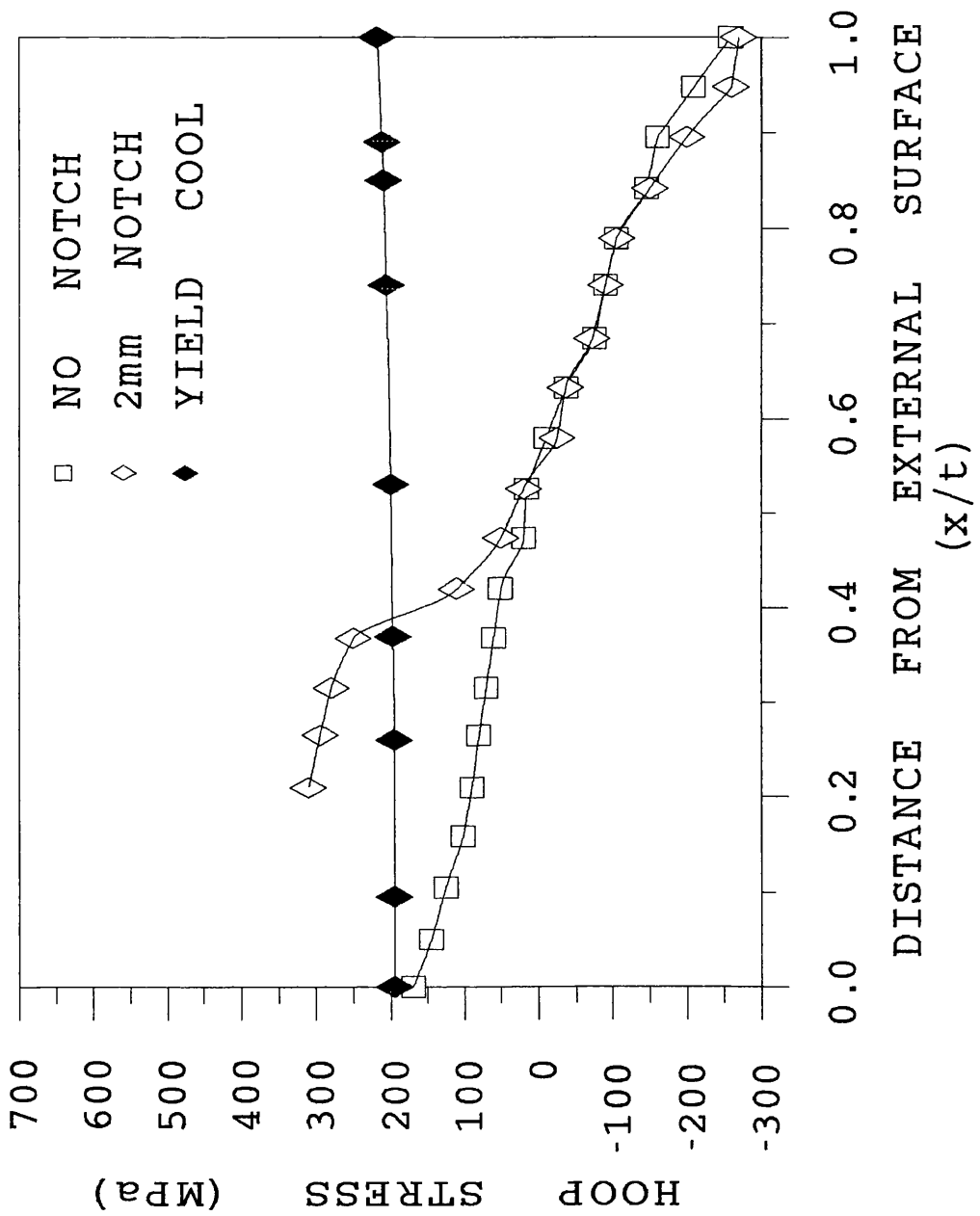


Figure 4.2.8a. Notch Effect on Hoop Stress Profile, (after Andritsos,1991[a-b]).

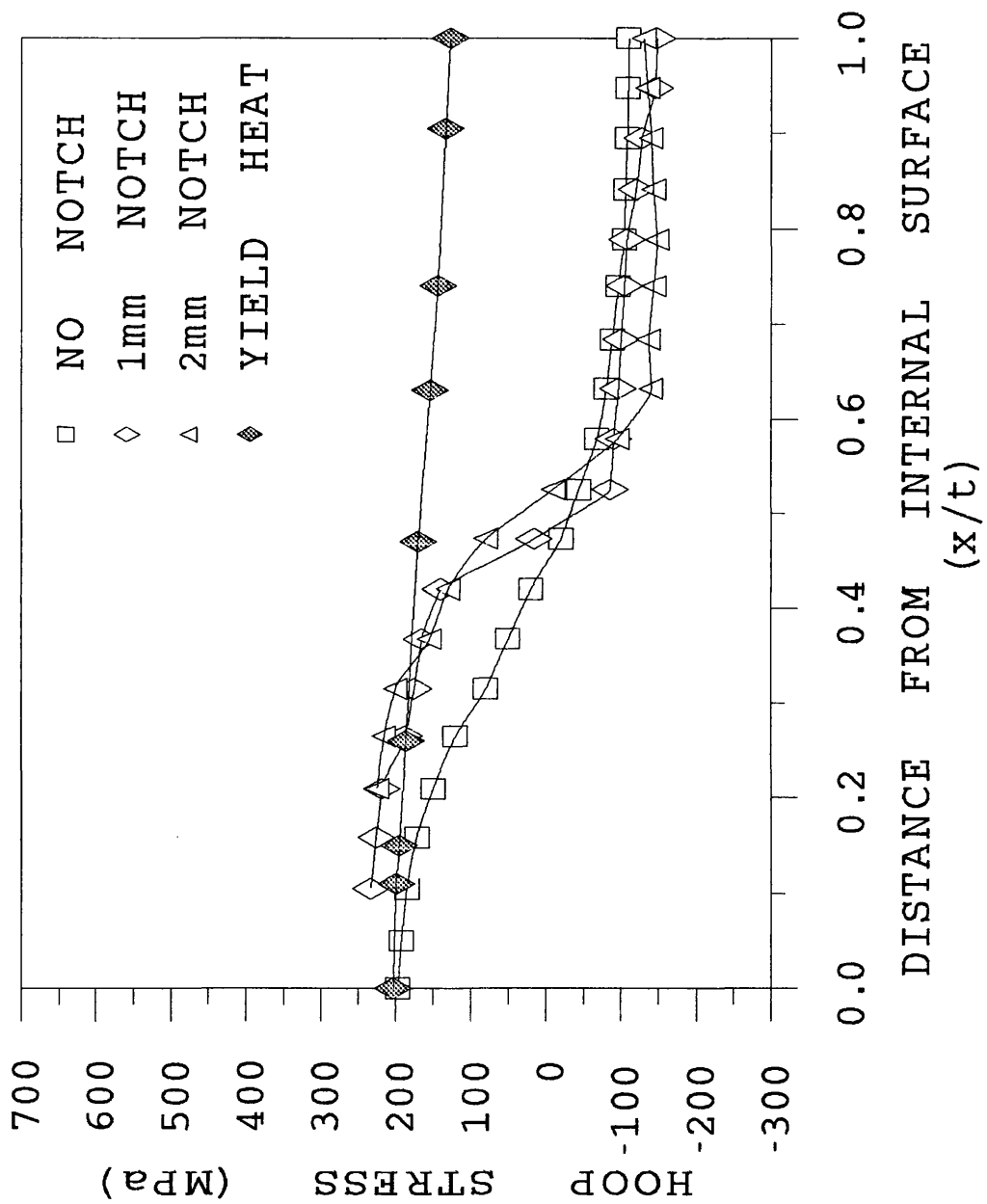


Figure 4.2.8b. Notch Effect on Hoop Stress Profile, (after Andritsos, 1991[a-b]).

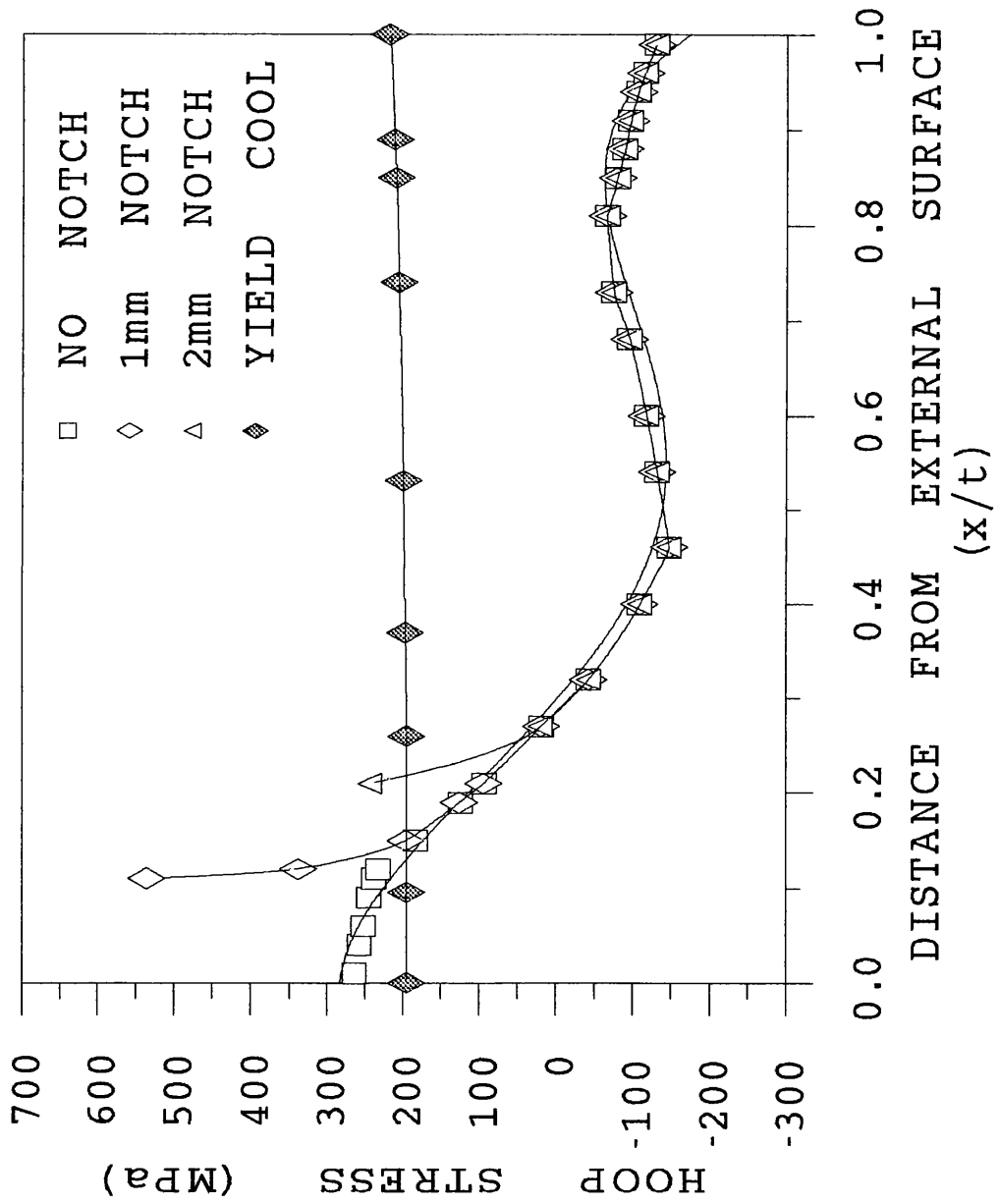


Figure 4.2.9a. Notch Effect on Maximum Stress Profiles During a Thermal Cycle.

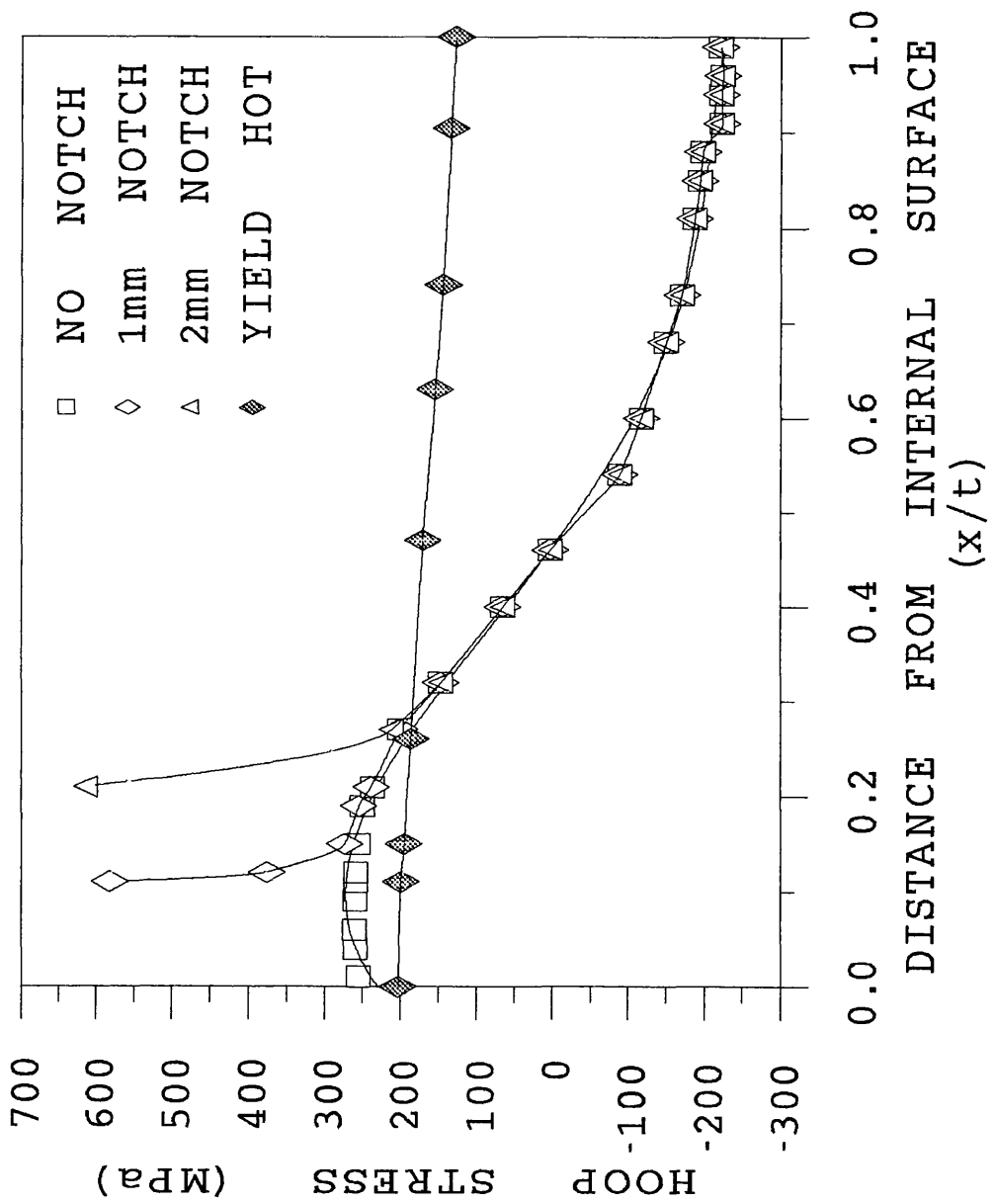


Figure 4.2.9b. Notch Effect on Maximum Stress Profiles During a Thermal Cycle.

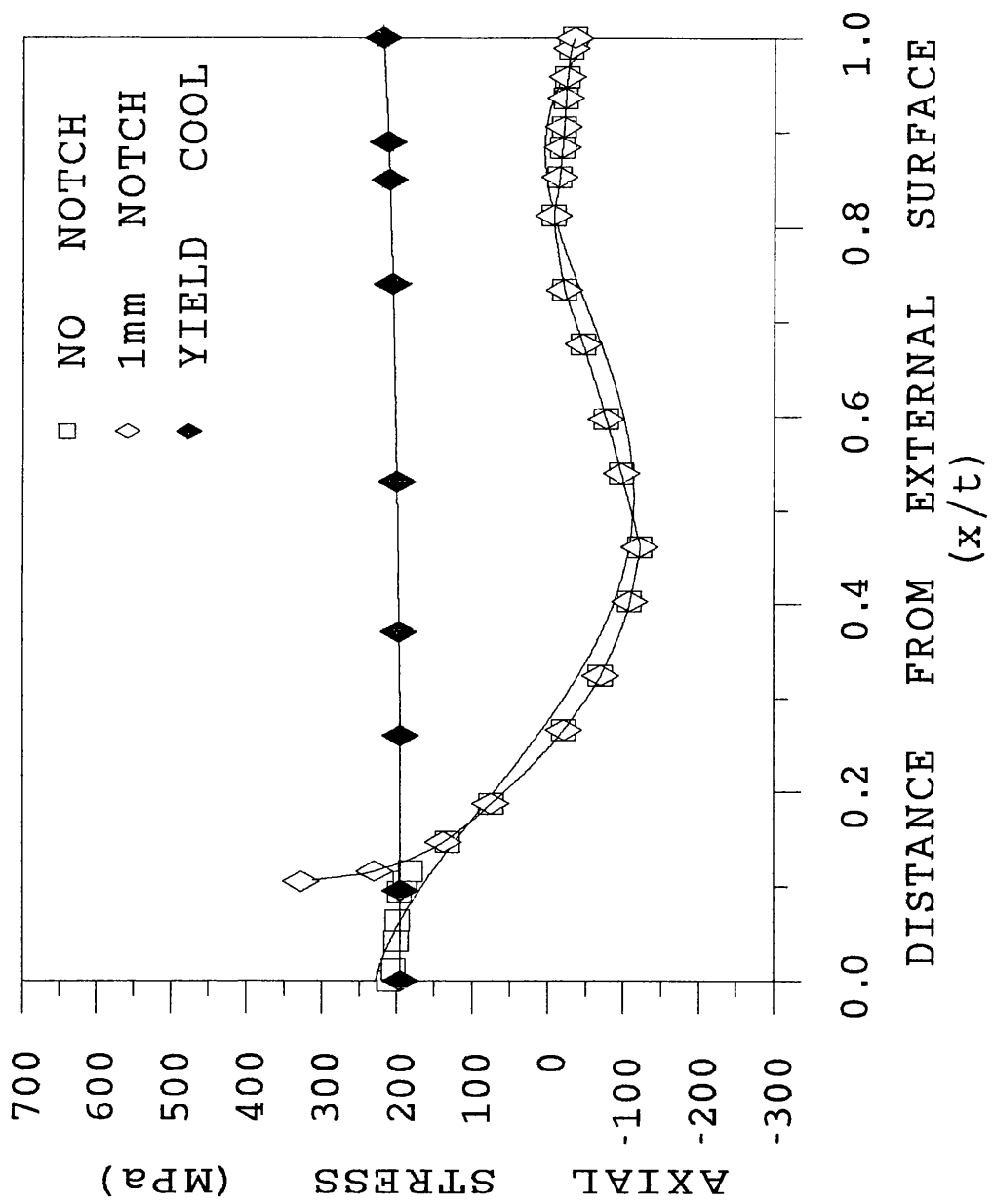


Figure 4.2.9c. Notch Effect on Maximum Stress Profiles During a Thermal Cycle.

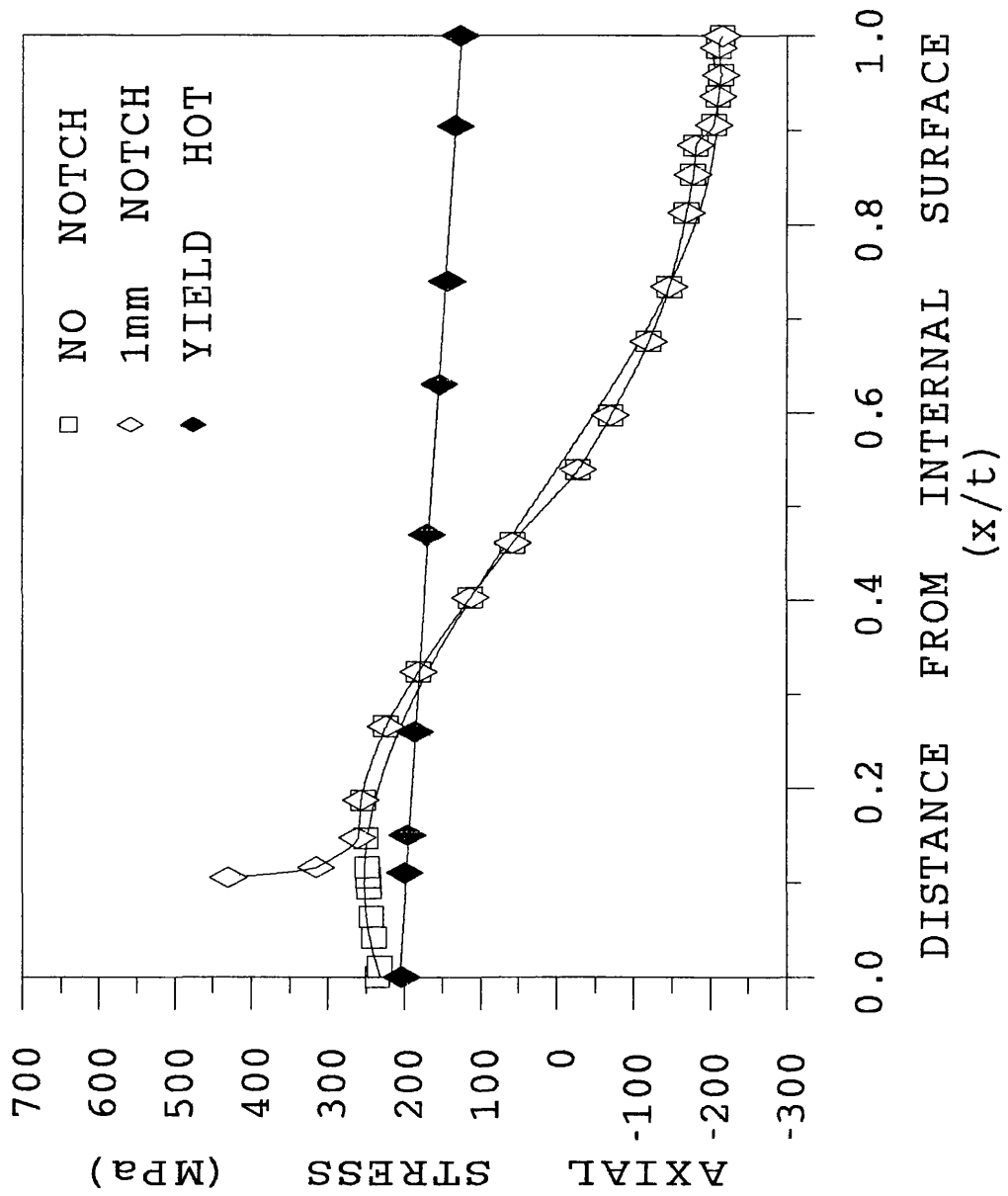


Figure 4.2.9d. Notch Effect on Maximum Stress Profiles During a Thermal Cycle.

4.3. Development of the Thermal Fatigue Stress Intensity Factors.

To compare the measured thermal fatigue crack growth rates in the components with the Paris Law data, which was developed in section 3.3, values of the crack tip stress intensity factors throughout the thickness of the thermally cycled component are required. In section 4.2, the component was shown to be subjected to both a maximum tensile stress profile and a maximum compressive stress profile throughout the course of a thermal cycle. The maximum stress intensity factors at the tip of a crack propagating through the component are determined by representing the maximum stress profile through the uncracked component as a polynomial function of the normalised depth, a/t , equation 2.2.30, and using the superposition method, [Buchalet and Bamford,1976], equation 2.2.31. The resultant values of maximum stress intensity factor are equivalent to the range in stress intensity factors since the component is subjected to both tensile and compressive stress profile, therefore for fatigue analysis, the values of minimum stress intensity factors were taken to be zero.

The thermal stress/strain analysis, Figures 4.2.4(a-d), indicated that the cracks would propagate from a cyclic yielded zone into an elastic domain, therefore the classic concept of linear elastic fracture mechanics cannot be applied over the entire thickness of the component. A number of parameters have been developed to account for the effect of the components of elastic and plastic strain on fatigue crack growth rates. An effective stress intensity factor, [Haigh and Skelton,1978], is one of these parameters while others include the crack tip opening displacement, CTOD, and the cyclic J-integral, both of which have been shown to relate to the effective stress intensity factor. A greater scatter in results was observed when the cyclic J-integral was used to describe mechanical fatigue crack growth data in comparison to using the strain based intensity relationship, [Brown,1988]. Furthermore the effective, or equivalent, stress intensity factor has been shown to agree well with thermal fatigue crack growth data which display a large degree of scatter due to the limited techniques which were employed to measure the crack propagation, [Burlét et al.,1989].

The superposition method is a convenient way to estimate ΔK in the cracked component without performing a complicated three dimensional brick finite element analysis. In the present analysis, a fourth order polynomial equation was used to describe each of the stress fields in Figures 4.2.8(a-d), as a function of the normalised distance from the tensile stressed surface. This method may be used to calculate the stress intensity factors at the tip of a crack propagating from either the internal or the external surface of a tube, whether the crack is in the longitudinal or the circumferential plane. The coefficients of the equations were used in equation 2.2.31 along with the magnification

factors, Y_n , which were determined, using weight functions, for an unnotched tubular component with radial dimensions $r_o/r_i=1.75$, and a longitudinal crack from either the internal or external surface, [Parker and Andrasic, 1984]. Values of Y_n , for circumferential cracks were calculated from the longitudinal crack values with comparison to the differences between those of longitudinal and circumferential cracks in thin tubular components, [Buchalet and Bamford,1976]. Attention was paid to the decrease in magnitude of the magnification factor with both increasing thickness of the component and in the change in crack orientation.

It is assumed in the superposition method that the cracks are infinitely long at the surface with a straight crack front. However, the longitudinal cracks were observed to grow in a changing semi-elliptical shape with increasing crack depth. Therefore a correction factor, termed the crack shape development factor, ω , was introduced to take into account the influence of the crack shape development on the crack tip stress intensity factor. Values of the crack shape development factor are presented in Table 4.3.1, as a function of both a/t and a/c , where c is the half-length of the semi-ellipse and t is the component thickness, [Rees,1980, Lamain,1992, Cesari and Hellen,1979].

Rectangular 1mm Deep Notch		Rectangular 2mm Deep Notch	
$a/t=f(a/c)$	ω	$a/t=f(a/c)$	ω
0.095	1.00	0.2	0.717
0.2	0.755	0.295	0.624
0.295	0.6298	0.4	0.5348
0.4	0.5318	0.495	0.4197
0.495	0.4130	0.611	0.2579
0.611	0.2445	0.695	0.2032
0.695	0.2	0.8	0.2
0.8	0.2	0.895	0.2
0.895	0.2	0.921	0.2
0.921	0.2	0.947	0.2
0.947	0.2	1.00	0.2
1.00	0.2		

Table 4.3.1. Correction Factor, ω , as a Function of a/t and a/c

The maximum stress intensity profiles for infinitely long surface longitudinal cracks in unnotched components were plotted against a/t from the cracked surface, Figures

4.3.1(a-b). During the calculation of the stress intensity factors at the tip of a crack from either the free surface, (internal or external), or the circumferential notches, it was assumed that the crack was infinitely long with a straight crack front. The crack shape development observed in section 3.4.4, with cracks from longitudinal notches, was taken into account using the correction factors presented in Table 4.3.1., during the calculation of the stress intensity factors. These results display the well documented trend in stress intensity factors calculated from the thermal shock testing of tubular components, [Burlet et al.,1989]. The magnitude of the stress intensity factor increases rapidly with the initial increase in crack depth through the region of high tensile stress below the surface of initiation. The stress intensity factor peaks at a depth which primarily depends upon the magnitude of the maximum tensile stress combined with the depth of the region under tension. Thereafter the stress intensity factor decreases with increasing crack depth.

With the introduction of a 1mm deep notch, the initial K_{max} values at the root of the notch were over twice the magnitude of the stress intensity factor at the corresponding depth in an unnotched component, as illustrated in Figure 4.3.1a. The maximum value was $33\text{MPa}\sqrt{\text{m}}$ at the root of the 1mm deep notch in the external surface. A similar behaviour was observed in the stress intensity factors from a 2mm deep notch in the external surface. A maximum value of $36\text{MPa}\sqrt{\text{m}}$ at the root of the notch decreased at a similar rate to that observed from the 1mm deep notch. The inclusion of the notches increased the stress intensity factor for a depth of $a/t \leq 0.2$ from both notches in comparison to the calculated stress intensity factors for the crack in an unnotched component. Beyond the influence of the notch, the stress intensity factors decreased rapidly as the crack shape correction factor influenced the calculations. The stress intensity factors were similar for all crack depths beyond mid-thickness and were always above threshold values.

The effect of the crack shape development correction factor were clearly observed in comparison between the stress intensity factors for cracks from the internal surface and those for cracks from notches in the internal surface, as illustrated in Figure 4.3.1b. The introduction of stress concentrating longitudinal notches from the internal surface produced similar trends in the behaviour of the stress intensity factors with increasing crack depth, as observed with external longitudinal crack calculations. A similar magnitude of maximum stress intensity factor, $32\text{MPa}\sqrt{\text{m}}$, was calculated at the root of the 1mm deep notch. Differences from the profile observed with the external notch were that the stress intensity factor remained at a peak value for a greater depth and then it decreased from the internal notch at a slower rate. A similar trend was observed from the 2mm deep notch except that the magnitude of the peak stress intensity factor

was $43\text{MPa}\sqrt{\text{m}}$, at $a/t=0.3$, and the stress intensity factor decreased at a slightly faster rate. The magnitude of stress intensity factor at the tip of a crack propagating from a 2mm deep notch was always greater than that from a 1mm deep notch and the values were similar to those for cracks from external longitudinal notches at depths beyond the mid-thickness of the component.

The circumferential cracks are assumed to be infinitely long, therefore no correction factors were applied to the calculated K_{max} values, which are plotted against a/t in Figures 4.3.2(a-b). The stress intensity factors from the external surface, Figure 4.3.2a, reflect the observed reduction in both the magnitude of tensile axial stress and the proportion of the component subjected to it. The introduction of a 1mm deep notch doubled the stress intensity value to a maximum value of $20\text{MPa}\sqrt{\text{m}}$ at the root of the notch. The introduction of the notch into the component increased the stress intensity factor through the thickness of the component to a crack depth of $a/t=0.5$. In comparison to the longitudinal crack stress intensity factors, the values corresponding to the circumferential crack were lower throughout the thickness of the component, with the influence of the notch restricted to crack depths less than the mid-thickness of the component.

A very different development of the stress intensity factor was observed for the circumferential cracks from the internal surface, Figure 4.3.2b. The stress intensity factor peaked at a higher value than those calculated at the tip of a circumferential crack from the external surface. A plateau of the stress intensity factor above $20\text{MPa}\sqrt{\text{m}}$ extended from the root of the notch until a crack depth of $a/t=0.7$, following which point the stress intensity factor decreased rapidly to a value of $10\text{MPa}\sqrt{\text{m}}$. With the introduction of a 1mm deep circumferential notch, the magnitude of the stress intensity factor increased to a maximum value of $31\text{MPa}\sqrt{\text{m}}$ at a crack depth of $a/t=0.3$. Thereafter the stress intensity factor decreased with increasing crack depth to a value of $25\text{MPa}\sqrt{\text{m}}$ at $a/t=0.7$ and then decreased rapidly. The maximum values of stress intensity factors were similar to those calculated for cracks propagating from a 1mm deep longitudinal notch in either the external or internal surface. This would imply that a crack growing from either of these notches would grow at similar crack growth rates.

The effects of multiple cracking, [Parker and Farrow,1981], were taken into account and displayed a negligible effect of two longitudinal cracks on the values of stress intensity factor. The two longitudinal notches and resultant cracks were far enough apart, 180° around the circumference from each other, to have no influence on the stress fields that developed around each other during the thermal cycles. The presence of four longitudinal cracks slightly reduced the stress intensity factor especially with

increasing crack depths, expt.#18. The circumferential distance between each crack tip decreased as the cracks propagated through the decreasing volume of uncracked tube. The stress would have been redistributed between the four cracks with one crack dominating. The deepest crack initiated from a notch which was positioned 90° from the notch from which the shortest crack initiated. The maximum and minimum crack depths were 5.26mm and 3.9mm respectively. The crack growth rates were lower at crack depths greater than $a/t=0.4$, as measured for two of the four cracks in expt.#18, in comparison to the crack growth rates from components with only one, or two, 1mm deep longitudinal notches on the external surface.

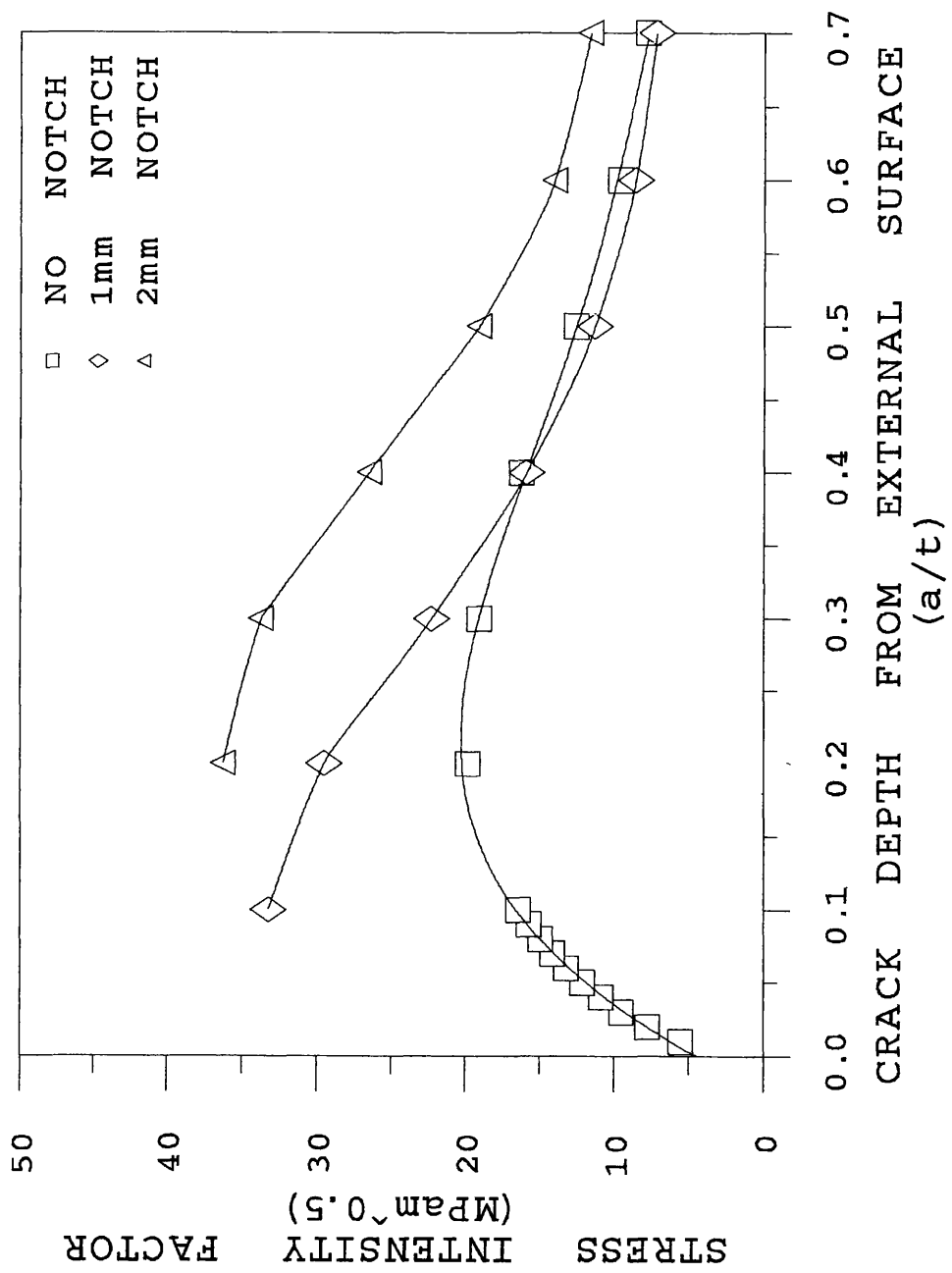


Figure 4.3.1a. Stress Intensity Factors for Longitudinal Cracked Components.

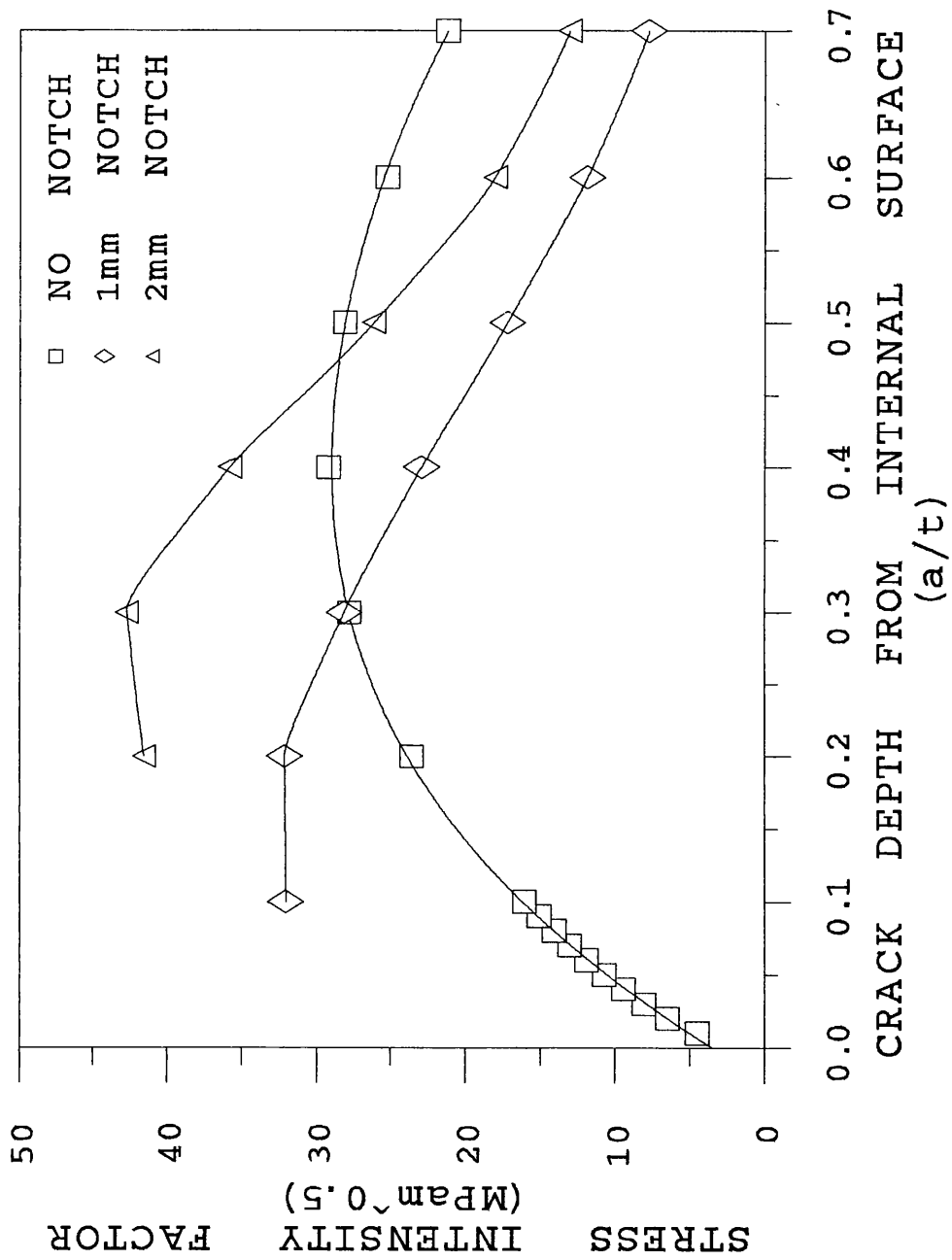


Figure 4.3.1b. Stress Intensity Factors for Longitudinal Cracked Components.

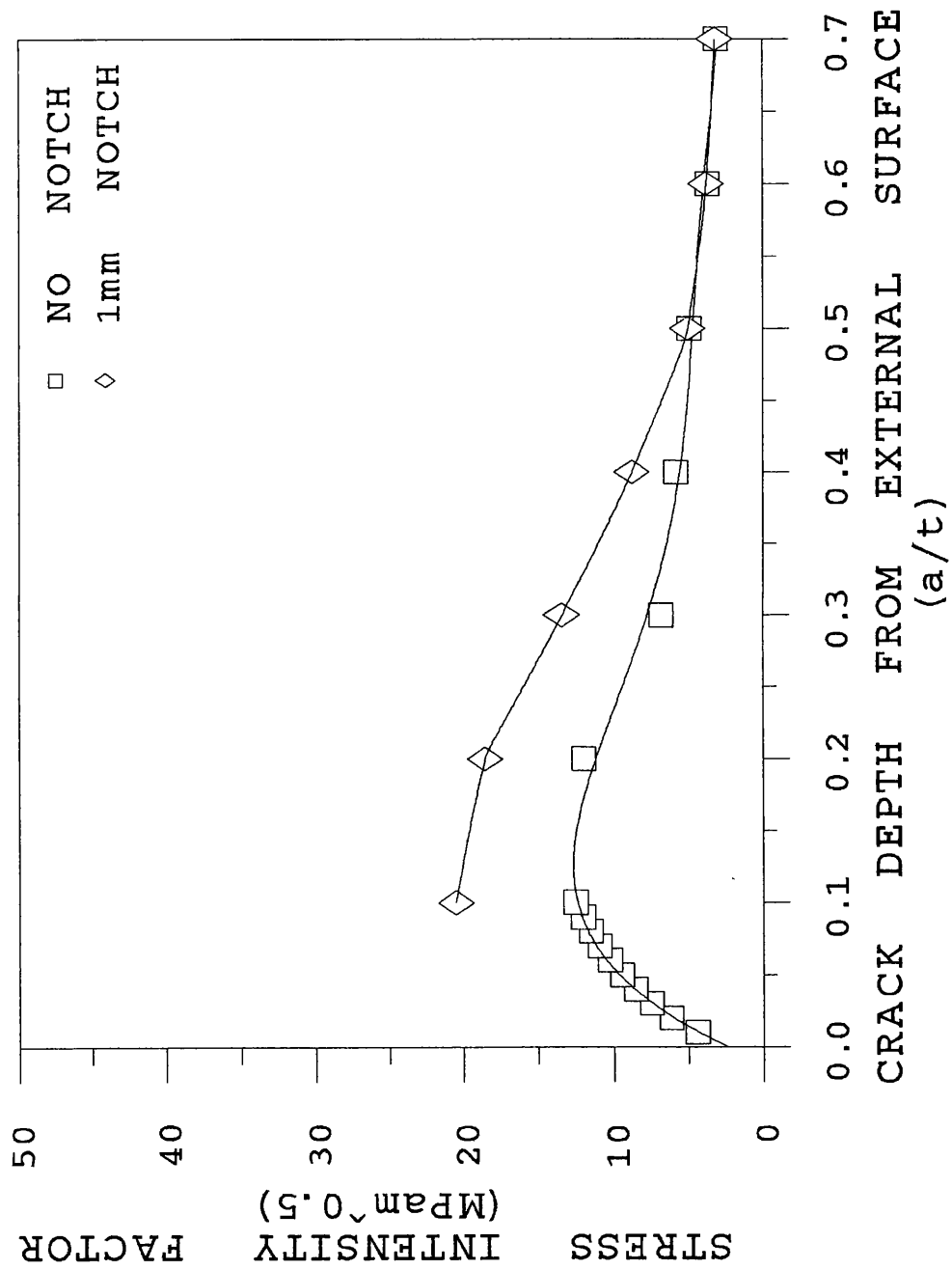


Figure 4.3.2a. Stress Intensity Factors for Circumferential Cracked Components.

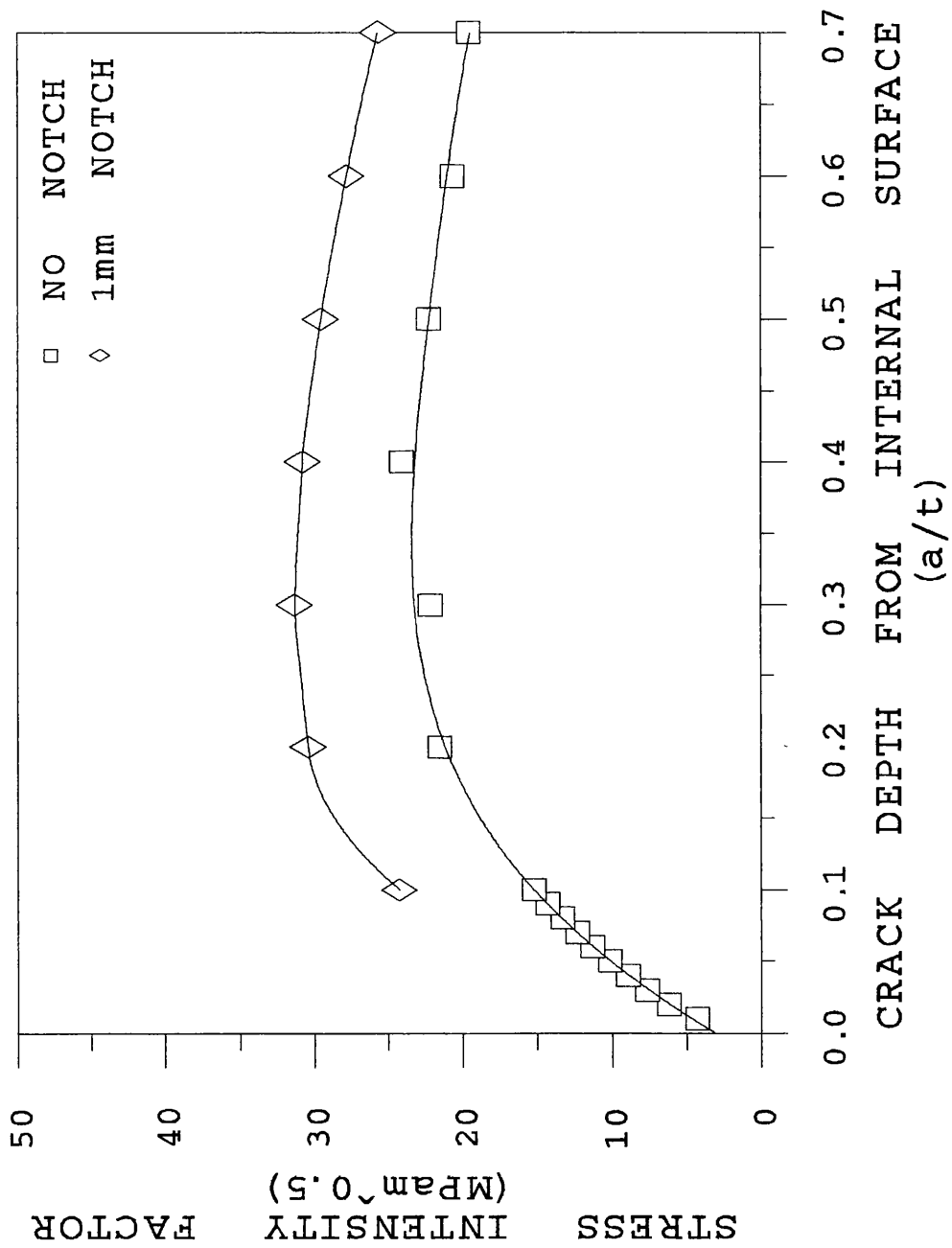


Figure 4.3.2b. Stress Intensity Factors for Circumferential Cracked Components.

4.4. Mechanical and the Thermal Fatigue Crack Growth Rates.

The thermal cycling component experiments were performed to simulate the thermal fatigue conditions that are likely to occur in actual first wall components of a fusion reactor. The actual behaviour of the component material is difficult to analyse, however the development of the p.d. measurement technique has produced crack growth data which when compared with mechanical fatigue crack growth data should determine the accuracy of the simulation experiments. This can only be achieved for crack growth through the parts of the component subject to elastic loading. The mechanical fatigue crack growth rate is represented by the Paris Law which describes da/dN in terms of the range in crack tip stress intensity factor, ΔK , during a cycle, as presented in section 3.3. The range in stress intensity factors that control the thermal fatigue crack growth were calculated with increasing normalised crack depth in section 4.3. The corresponding thermal fatigue crack growth rates were determined for an example of each of the differently notched component tests, section 4.1. Neglecting the notch influenced regions in which yielding occurred, as displayed in Figures 4.2.8 and 4.2.9, values of the stress intensity factors have been paired with the corresponding thermal fatigue crack growth rates for each increment of crack depth, $a/t=0.05$. Comparisons between the results from the thermally loaded component testing and the standard specimen experiments are displayed in Figures 4.4.1(a-d).

In general, the comparisons between the thermal fatigue data and the LEFM fatigue data are very good, especially at the beginning of the thermal fatigue tests, when the cracks were at a depth beyond the influence of the notch but still within the range of accuracy of the superposition method. The thermal fatigue data, for all cracks from the external surface notches and the longitudinal notches at the internal surface, initially display high crack growth rates matched with high stress intensity factors which correspond well with the upper right region in the plots of the Paris Law data, as illustrated in Figures 4.4.1(a-d).. With increasing crack depths, the thermal fatigue crack growth data tends towards the lower ranges in both stress intensity factor and crack growth rates, which corresponds to the lower left of the plots in Figures 4.4.1(a-d). The calculated values of stress intensity, at crack depths of $a/t \geq 0.5$, predict lower crack growth rates from the Paris Law data than were measured during the thermal cycling experiments. This was observed more for crack growth rates from 1mm deep notches in the external surface.

The range in thermal fatigue crack growth rates were very similar for crack propagation from either a 1mm or 2mm deep longitudinal notch in the external surface. However the calculated range in stress intensity factors differs considerably. The stress intensity

values accurately predict the initially high crack growth rates from both depth of notch, Fig.4.4.1a, with good agreement with the predicted crack growth rates from the 80°C Paris Law data. However the rapid decrease in stress intensity factors for crack depths greater than $a/t=0.4$, from a 1mm deep notch, produces non-conservative crack growth rates from both the 80°C and the 350°C Paris Law relationships in comparison to the thermal cycling results. Similar differences between experimental and calculated data have previously been attributed to a combination of the limited accuracy of the superposition method polynomial function to describe the stress profile for crack depths larger than $a/t=0.4$ and a large scatter band of experimental results, [Burllet et al.,1989]. The accuracy of the potential drop technique to measure the thermal fatigue crack depths in the present analysis has limited the scatter in results and the subsequent field of agreeable data. However, the worst case prediction of a crack growth rate of 7×10^{-6} mm/cycle, from the 80°C Paris Law data, when the measured crack growth rate was 6×10^{-5} mm/cycle, is brought into perspective when the fatigue crack growth data from the centred-cracked tension specimen tests are brought into consideration, Fig.4.4.1b. The CCT specimen fatigue crack growth rate data was rejected in section 3.3 because of increased crack tip plasticity which resulted in greater crack growth rates than those obtained from both literature and the CT specimen tests. The increased crack growth rates throughout the reduced range in stress intensity factors from the CCT specimen results display a better agreement with the decreasing stress intensity factors which correspond to the measured growth rates at the deeper crack depths from the 1mm deep notches. This agreement indicates that the crack growing through the thermally cycled component is subjected to a greater magnitude in tensile stress than that determined for the 1mm deep notch influenced, stress profile from the finite element analysis calculations. Such an increase in tensile stress profile was obtained when the inclusion of a 2mm deep notch was taken into consideration. The resultant range in stress intensity factors agree favourably with the corresponding values from the 80°C Paris Law data over the entire range of measured thermal fatigue crack growth rates.

Although the magnitudes of maximum tensile stresses at the roots of the internal longitudinal notches were similar to those at the root of the external longitudinal notches, the cracks propagating from the internal surface notches were subjected to a greater region of tensile stress. Consequently the calculated stress intensity factors were initially high and compared well with the 80°C Paris Law data for the decreasing crack growth rates from the 1mm deep notch to a crack depth of $a/t=0.5$, Fig.4.4.1c. Continuous comparison to the Paris Law data would underestimate the constant thermal fatigue crack growth rate due to the rapid decrease in stress intensity factor with increasing crack depth. A similar behaviour was observed with the calculated stress

intensity factors and the thermal fatigue crack growth rates from the 2mm deep notched component. Differences occur at very short crack depths when the calculated stress intensity factors were greater. Consequently, the predicted crack growth rates were almost three times those measured in the thermal fatigue experiments. The similar range in stress intensity factors and crack growth rates at deeper crack depths with those from the external longitudinal experimental results indicates that the resultant thermal fatigue crack growth rates were partly due to increased tensile stresses beyond the mid-thickness of the component. The increased tensile stresses were not taken into account during the calculation of the corresponding stress intensity factors.

Greater differences were observed between the calculated stress intensity factors and the measured thermal fatigue crack growth rates in the components that contained a circumferential notch in either the external or internal surface, Fig.4.4.1d. A combination of the reduced magnitude of maximum tensile axial stress, the reduced influence of the semi-circular shaped notch and the small region of tensile axial stress from the external surface resulted in the lowest calculated value of maximum stress intensity factor. Thus agreement with the 350°C Paris Law data occurred only for the initial stress intensity values when the thermal fatigue crack growth rates were greater than 1×10^{-4} mm/cycle. Thereafter the rapid decrease in calculated stress intensity factor with the increasing crack depth, continuously results in non-conservative predictions of the thermal fatigue crack growth rates using either the 80°C or the 350°C Paris Law data. The similarity in crack growth rates with increasing crack depths illustrate that the deeper cracks must have been subjected to a greater tensile stress field than that used in the superposition method.

Both the magnitude of the maximum axial tensile stress and the depth of the component subjected to tensile stress were greater for the presence of a circumferential notch in the internal surface than that calculated for the external surface. Consequently, the initial stress intensity factors were only slightly greater than those calculated for a crack at the root of the external notch. Crack initiation from the internal notch was not immediate, however, following initiation the crack growth rate increased with crack depth. By a crack depth of $a/t=0.15$, the crack growth rate had rapidly increased and is very accurately described by the calculated stress intensity factor in reference to the 80°C Paris Law data. The calculated stress intensity factor continues to accurately describe the increasing thermal fatigue crack growth rate to $a/t=0.5$, at which point the experiment was stopped. Unfortunately no crack initiation occurred in a further two thermal cycling experiments on a component containing an internal circumferential notch. This was unexpected, since the calculated tensile stress at the tip of the notch, (Fig.4.2.9d), was similar in magnitude to the corresponding stress at the root of the

identical circumferential notch in the external surface, (Fig.4.2.9c). in comparison to the calculated tensile stresses at the tip of the longitudinal notches, the maximum axial stresses at the root of the circumferential notches were greatly reduced and were greater than the yield stress over a shorter distance from the notch tip. However, crack initiation always occurred from the external circumferential notches. This may be explained from the calculations of the cyclic plastic strain from the finite element analysis in an un-notched component, the results of which were shown in Figure 4.2.5. A region of continuous cyclic axial plastic strain occurred at the external surface, while the internal surface was subjected to plastic strain during the initial thermal cycle with a region of shakedown elastic loading. With the circumferential notches having a limited influence on the stress/strain field it may be assumed that the tip of the circumferential notch was subjected to a greater magnitude of cyclic plastic strain than that at the tip of the internal circumferential notch, which may have been subjected to cyclic elastic strain following the initial cycle. The number of cycles for a crack to initiate would be reduced when the notched region was subjected to reduction in the magnitude of cyclic plastic strain.

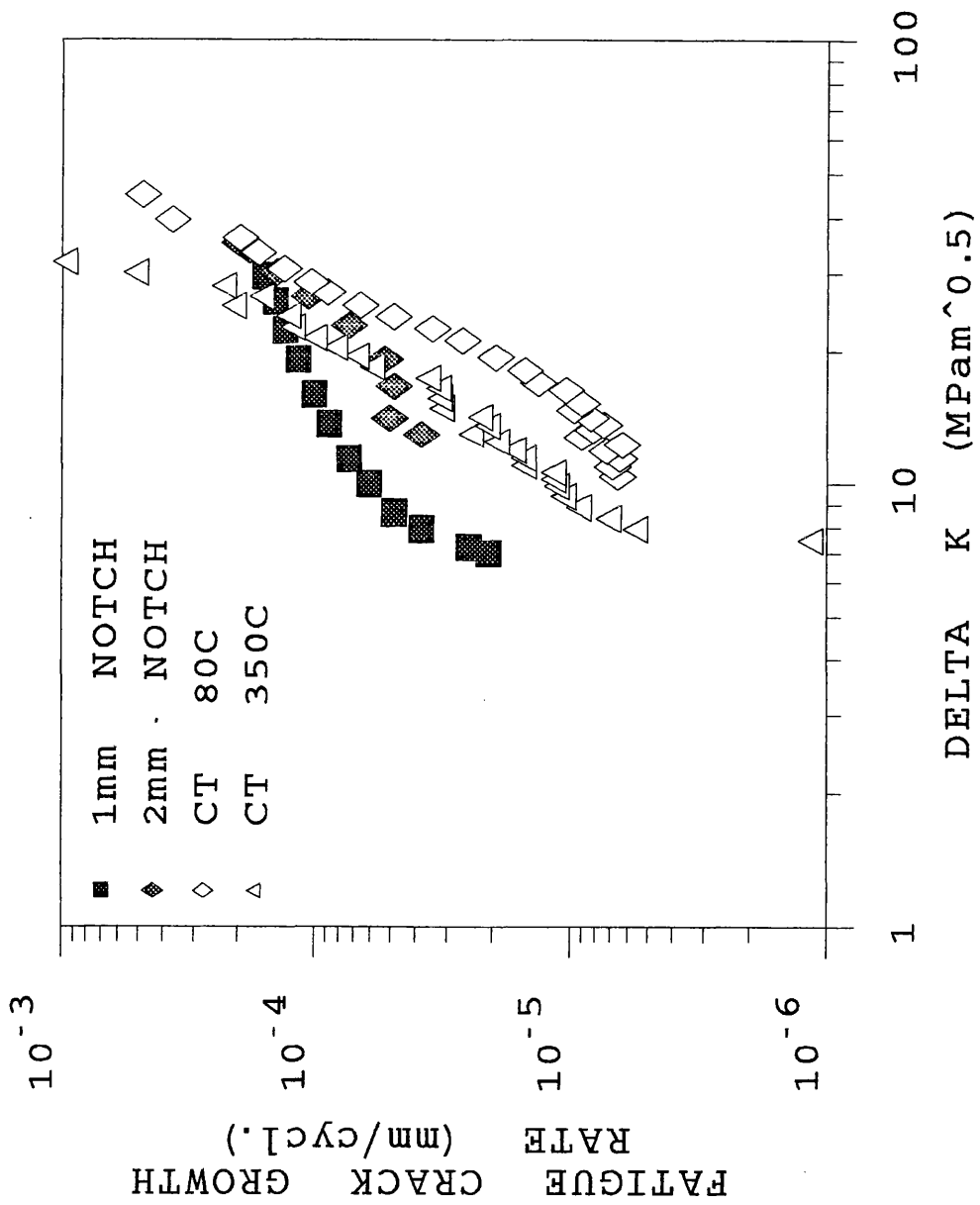


Figure 4.4.1a. Thermal Fatigue Crack Growth Rates in External Longitudinal Notched Components.

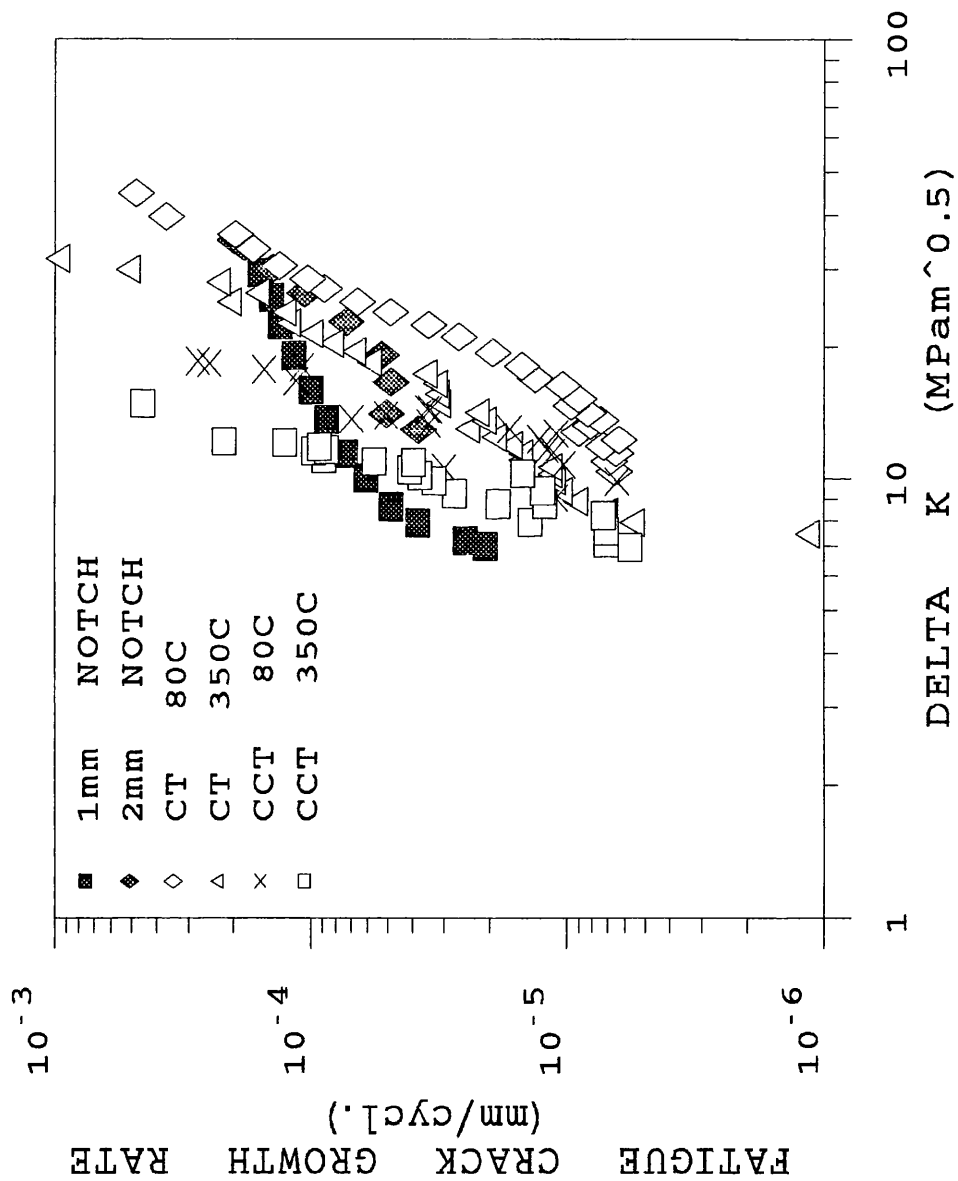


Figure 4.4.1b. Thermal Fatigue Crack Growth Rates in External Longitudinal Notched Components.

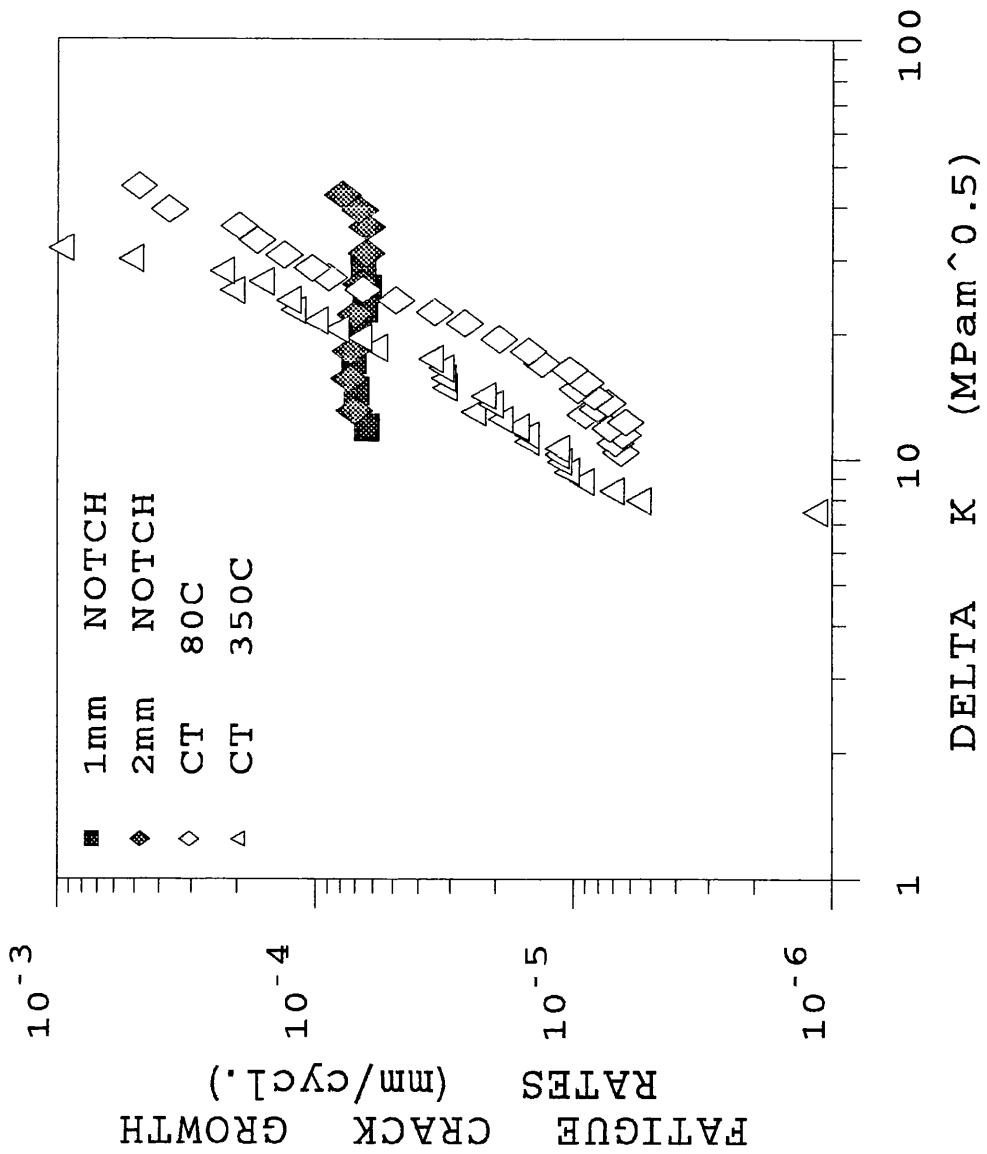


Figure 4.4.1c. Thermal Fatigue Crack Growth Rates in Internal Longitudinal Notched Components.

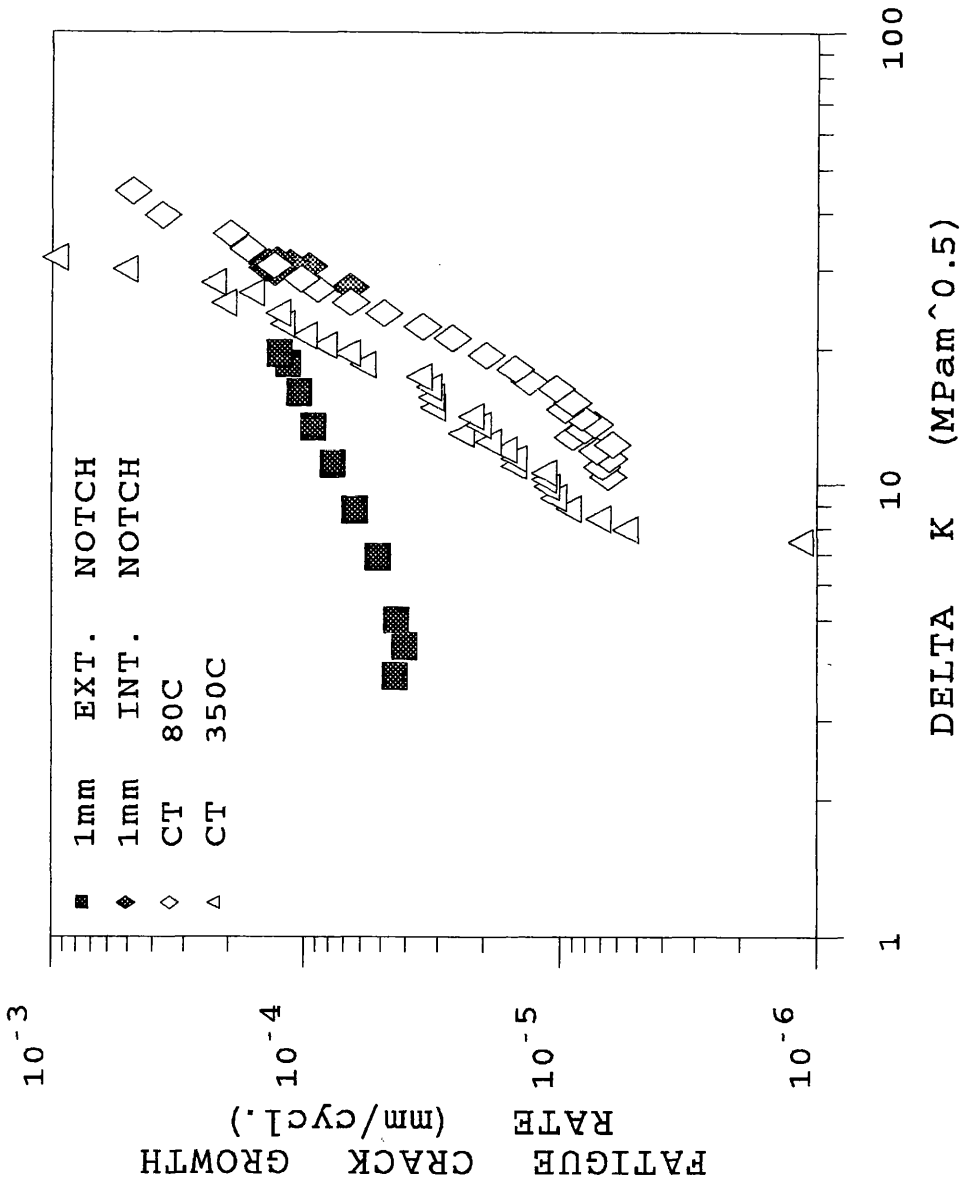


Figure 4.4.1d. Thermal Fatigue Crack Growth Rates in Circumferential Notched Components.

5.0. Conclusions.

1. A unique experimental rig has been designed and developed to produce the thermal cycles and the resulting thermal gradients that are expected during in-service conditions in first wall components of a nuclear fusion reactor. Twenty-four thermal fatigue experiments were performed on tubular components which were manufactured from the austenitic stainless steel, ICL 167 SPH. The experiments were carried out on tubular components containing fully circumferential semi-circular notches and longitudinal notches. The notches were either machined or electro-eroded into the internal or the external surface of the components with the intention of increasing the local cyclic thermal stresses. The consequent thermal fatigue crack growth was monitored using the direct current potential drop technique, which was developed for the specific specimen geometry and starter notch position.

2. The cracked ligaments were sectioned, polished and etched for measurement of the crack depth across the potential drop probes. Cracking was transgranular with short secondary cracks and little deviation in the direction of propagation at grain boundaries. Separation of the cracked ligaments in liquid nitrogen displayed fracture surfaces that tended toward a semi-elliptical shape with increasing crack depth from the longitudinal notches. Both the large number of experiments performed on components with two or more notches and the consistently similar potential drop development curves encouraged the use of the interrupted experimental results to develop the potential drop/crack growth calibration curves. Similar crack growth rates were measured through each of the components as the cracks propagated through the thickness, beyond the influence of the notch. A small number of experiments were performed with components that contained spot welded and laser welded defects instead of machined notches. The standard of the laser weld had to be deliberately poor before crack growth into the parent material was possible. Overall, the crack growth from both laser welded regions and spot welds was greatly reduced in comparison to that from machined notches.

3. Mechanical fatigue crack growth experiments were performed on compact tension specimens at the temperatures of interest. A combinations of visual inspection and the direct current potential drop method were used to measure the crack growth. The resultant crack growth rates compared well with data for similar Type 316L stainless steels and were described using the Paris Law with different coefficients for each of the experimental temperatures.

4. The cyclic strain hardening properties of the material were determined from uniaxial, strain controlled low cycle fatigue experiments on smooth solid specimens

under isothermal conditions at either 20°C, 80°C or 350°C. Values of the Elastic Modulus and the 0.2% proof stress were determined at each of the temperatures of interest.

5. The material characteristics generated from the low cycle fatigue experiments were employed in a thermal strain finite element analysis which was performed to determine the stress/strain field across the unnotched tube wall. The elastic-plastic analysis produced hoop and axial stress distributions which displayed a region of cyclic plastic strain at the external surface of the component, two regions of elastic shakedown following initial plasticity, one of which was at the internal surface, and a large region of purely elastic loading at the mid-thickness. The presence of a notch increased the maximum tensile stress beyond the yield stress of the material which produced a region, ahead of each notch, that was subjected to plastic loading during the thermal cycling.

6. The superposition method was used to determine the stress intensity factor at the tip of a crack at various increments of crack depth through a component which was subjected to the stress fields developed from the finite element analysis. The stress intensity factors were greatest at the tip of the notches and remained large up to the mid-thickness of the component. Beyond the mid-thickness, the stress intensity factors decreased rapidly to values similar to those calculated for unnotched components.

7. By neglecting the yielded regions in the notched components, the stress intensity factors in the elastic shakedown and elastic loaded regions were paired with the corresponding thermal fatigue crack growth rates for comparison with the Paris Law data. Even though the stress intensity factor decreased with increasing crack depth through the thickness of the components, the thermal fatigue crack growth data, compared well with the mechanical fatigue crack growth data. The decrease in stress intensity factor for crack depths beyond $a/t=0.6$ displayed the inaccuracy of the stress profile which was used in the superposition method. However, the component testing in the present study can be regarded as a success as it demonstrated that under the thermal cyclic loading conditions of first wall components, cracks will grow from all types of defects and at high rates in the region of 10^{-4} mm/cycle. Finally, the results from the component tests can be used as a guideline and comparison to future experiments on the same material subjected to irradiation or different thermal cycles.

6.0. Suggestions For Further Work.

During the performance of the present investigation, a number of topics, both experimental and analytical, have emerged and although considered, were never developed any further than that of a rough sketch. A brief description of these ideas is now presented with the intention of continued development in the study of thermal fatigue crack growth in tubular components.

For a greater understanding of the crack growth behaviour in the notched region of the tubular component, high strain fatigue, HSF, experiments could be performed on push-pull specimens. The experiments would be performed under plastic strain loading at plastic strain ranges which correspond to those calculated in the finite element analysis, Figure 4.2.5. Crack propagation rates could be measured by introducing a short starter notch and monitoring the crack propagation using the potential drop technique. The short crack growth data may be described in terms of HSF growth relationships, [Skelton,1983], and the thermal fatigue crack growth rates, through the entire thickness of the tubular components, may be compared with a combination of both HSF and LEFM crack growth data.

The thermal cycling rig can be adapted for investigation into thermal fatigue loading in other practical applications and materials. It may be used to grow short starter cracks in tubular components that will be tested under other loading conditions, such as combined internal pressure and tensile loading creep at a temperature above the maximum in the thermal cycle. Thermal cycle experiments may also be developed to include hold times at temperatures above the creep strain threshold temperature or even be performed as a series of decreasing maximum temperatures in an attempt to mark regions of growth on the fracture surface of the crack. Longer experiments may be performed to investigate the crack growth in components that contain cracked laser welded spots to give a better representation of the damaging effect of plasma bombardment. Without the presence of stress concentrating notches, the initial crack growth rate may be greatly reduced, thus increasing the useful life of the component. Similarly, an extension of the present project may be to perform experiments on components with no manufactured defects, for a longer number of thermal cycles. This may give a greater perception of the process of crack initiation under cyclic thermal loading.

The instrumentation of the thermal cycling rig can be further developed. Variations in the induction heating coil design can produce a more even temperature distribution over a greater test region while larger spaces between consecutive turns of the coil will produce space for viewing the crack surface during the cooling part of the cycle.

Furthermore, a ceramic extensometer could possibly be designed to measure the crack tip opening displacement from across the machined notch. The range in crack tip opening displacement could then be used in conjunction with an elastic-plastic analysis.

An improvement in the calculation of the range in stress intensity factor, ΔK , at the tip of a crack propagating through thermally cycled component, may occur if the effects of crack opening and closure, during the compressive part of the thermal cycle, were taken into consideration. In the present analysis, it was assumed that crack propagation occurred under tensile loading, $P > 0$. However it has been observed that crack opening occurs during the tension-going phase of the compressive part of a fatigue crack, with $R < 0$, [Skelton, 1983]. Therefore the load range that controls the crack propagation is greater than the tensile load amplitude, $\Delta P/2$, and less than the total load range, ΔP . Equations for a crack opening factor, q_0 , with respect to a/W , could be multiplied to the total thermal stress range, at increments of x/t , to calculate the equivalent stress intensity range through the thickness of the component. The resultant da/dN vs. ΔK_{eq} data could be plotted against the CT data and the thermal fatigue results from the present analysis.

A three-dimensional model finite element analysis would generate stress magnitudes and plastic strain values at regions ahead of the crack tip for cracks of increasing lengths in a tubular component subject to thermal cycles. If crack tip opening displacements were calculated then comparisons with the experimental values would display the accuracy of the finite element analysis thermal model. Variations could be made to the model until the predicted crack growth rates are similar to those measured during a single long experiment. Therefore the development of a crack could be predicted from only one experiment with greater emphasis on the analytical analysis. The range of temperatures could be changed to produce crack growth data as a function of the applied temperature range. This would help plant operators in predicting the operational life of a component during in-service loading.

7.0. References.

Abdel-Raouf et al.,[1973], Abdel-Raouf, H., Plumtree, A., Topper, T.H., *Effects of Temperature and Deformation Rate on Cyclic Strength and Fracture of Low-Carbon Steel, Cyclic Stress-Strain Behaviour-Analysis, Experimentation, and Failure Prediction*, ASTM STP 519, American Society for Testing and Materials, pp28-57, 1973.

Amzallag et al.,[1981], Amzallag, C., Rabbe, P., Bathias, C., Beniot, D., Truchon, M., *Influence of Various Parameters on the Determination of the Fatigue Crack Arrest Threshold, Fatigue Crack Growth Measurement and Data Analysis*, ASTM STP 738, eds. Hudak, Jr., S.J., Bucci, R.J., American Society for Testing and Materials, pp.29-44, 1981.

Andritsos,[1991a], Andritsos, A., *Thermal Stress Distribution in a Cylindrical Test Specimen*, Technical Note No. I.91.01, JRC Ispra, January 1991.

Andritsos,[1991b], Andritsos, A., Personal Communication over unpublished work, JRC Ispra 1991.

Ardellier,[1981], Ardellier, A., *Fatigue and Creep-Fatigue In Sodium of 316L Stainless Steel*, Material Behaviour and Physical Chemistry in Liquid Metal Systems, pp.165-173, Karlsruhe, March 1981.

Aronson and Ritchie,[1979], Aronson G.H., Ritchie, R.O., *Optimisation of the Electrical Potential Technique for Crack Growth monitoring in Compact Test Pieces Using Finite Element Analysis*, Journal of Testing and Evaluation, JTEVA, Vol.7, No.4, pp.208-215, July 1979.

ASTM E399,[1978], *Standard Test Method for Plane-Strain Fracture Toughness of Metallic Materials*, Annual Book of ASTM Standards, American Society for Testing and Materials, pp.580-601, 1978.

ASTM E647,[1988], *Standard Test Method for Measurement of Fatigue Crack Growth Rates*, Annual Book of ASTM Standards, American Society for Testing and Materials, pp.646-666, 1988.

Bairstow,[1911], Bairstow, L., *The Elastic Limits of Iron and Steel under Cyclical Variations of Stress*, Phil. Trans. Royal Soc., Vol.210, pp.35-55, 1911.

- Barker,[1927], Barker, L.H., *The Calculation of Temperature Stresses in Tubes*, Engineering, pp.443-444, October 7th 1927.
- Basquin,[1910], Basquin, H.O., *The Exponential Law of Endurance Tests*, Proc. ASTM, Vol.10, pp.625-630, 1910
- Bauschinger,[1886], Bauschinger, J., *On the Change of the Position of the Elastic Limit of Iron and Steel under Cyclic Variations of Stress*, Mitt. Mech.-Tech. Lab., Munich, Vol.1, No.1, 1886.
- Beer,[1971], Beer, F.J., *Plastic Growth of Pressurized Shell Through Interaction of Steady Pressure with Cyclic Thermal Stresses*, Thermal Stress and Thermal Fatigue, ed. D.J. Littler, Butterworth Publishers, London, pp.340-367, 1971.
- Berling and Slot,[1969], Berling, J.T., Slot, T., *Effect of Temperature and Strain Rate on Low-Cycle Fatigue Resistance of AISI 304, 316 and 348 Stainless Steels*, Fatigue at High Temperatures, ASTM STP 459, American Society of testing and Materials, pp.3-30, 1969.
- Bethge et al.,[1988], Bethge, K., Munz, D., Stamm, H., *Growth of Semi-Elliptical Surface Cracks in Ferritic Steel Plates Under Cyclic Thermal Shock Loading*, Fatigue and Fracture in Engineering Materials and Structures, Vol.11, No.6, pp.467-482, 1988.
- Bilby, Cottrell and Swinden,[1963], Bilby, B.A., Cottrell, A.H., Swinden, K.H., *The Spread of Plastic Strip from a Notch*, Proceedings of the Royal Society of London, Series A, Vol.272, pp.304-314, 1963.
- Boettner, Laird and McEvily,[1965], Boettner, R.C., Laird, C., McEvily, A.J., *Crack Nucleation and Growth in High Strain, Low-Cycle Fatigue*, Transactions of the Metallurgy Society, AIME, Vol.233, pp.379-387, 1965.
- Braithwaite,[1854], Braithwaite, F., *On the Fatigue and Consequent Fracture of Metals*, Minutes of Proc. Inst. Civil Engineers, No.915, pp.463-475, 1854.
- Brinkman and Korth,[1974], Brinkman C.R., Korth, G.E., *Low Cycle Fatigue and Hold Time Comparisons of Irradiated and Unirradiated Type 316 Stainless Steel*, Metallurgical Transactions, Vol.5, pp.792-794, March 1974.

Brown,[1988], Brown, M.W., *Aspects of Fatigue Crack Growth*, Proceedings of a Conference of the Institute of Mechanical Engineers, Vol.202, No.C1, pp.19-29, 1988.

Brown and Miller,[1985], Brown, M.W., Miller, K.J., *Mode I Fatigue Crack Growth Under Biaxial Stress at Room and Elevated Temperature*, Multi-Axial Fatigue, ASTM STP 853, pp.135-152, 1985.

Brown et al.,[1988], Brown, M.W., de los Rios, E.R., Miller, K.J., *A Critical Comparison of Proposed Parameters for High-Strain Fatigue Crack Growth*, Basic Questions in Fatigue, Vol.1, ASTM STP 924, eds., Fong, J.T., Fields, R.J., American Society for Testing and Materials, Philadelphia, pp.23-259, 1988.

Brun et al.,[1976], Brun, G., Gauthier, J.P., Petrequin, P., *Etude de la Fatigue Oligocyclique d'un Acier Z2 CND 17-12 (Type AISI 316L)*, Memoires Scientifiques Revue Metallurgie, pp.461-483, (in French), August 1976.

Bucci,[1981], Bucci, R.J., *Effect of Residual Stress on Fatigue Crack Growth Rate Measurement*, Fracture Mechanics (13th Conference), ASTM STP 743, pp.28-47, 1981.

Buchalet and Bamford,[1976], Buchalet, C.B., Bamford, W.H., *Stress Intensity Factor Solutions for Continuous Surface Flaws in Reactor Pressure Vessels*, Mechanics of Crack Growth, ASTM STP 590, American Society for Testing and Materials, pp.385-402, 1976.

Budynas,[1977], Budynas, G., *Advanced Strength and Applied Stress Analysis*, McGraw-Hill Kogabusha Ltd., pp285-292, Tokyo, 1977.

Burlet et al.,[1989], Burlet, H., Vasseur, S., Besson, J., Pineau, A., *Crack Growth Behaviour in a Thermal Fatigue Test-Experiments and Calculations*, Fatigue and Fracture of Engineering Materials and Structures, Vol.12, No.2, pp.123-133, 1989.

Cesari and Hellen,[1979], Cesari, F., Hellen, T.K., *Evaluation of Stress Intensity Factors For Internally Pressurised Cylinders With Surface Flaws*, Int. J. Pres. Ves. & Piping, (7), pp199-227, Applied Science Publishers Ltd., England, 1979.

Chell,[1981], Chell, G.G., *Some Subcritical Crack Growth Parameters and their Evaluation*, Proceedings of Subcritical Crack Growth due to Fatigue, Stress Corrosion and Creep, ed. Larsson, L.H., J.R.C. Ispra, Elsevier Applied Science Publishers, pp.1-29, October 1981.

Chipperfield,[1978], Chipperfield, C.G., *A Summary and Comparison of J Estimation Procedures*, Journal of Testing and Evaluation, JTEVA, Vol.6, No.4, pp.253-259, July 1978.

Clark,[1971], Clark Jr, W.G., *Fracture Mechanics in Fatigue*, Experimental Mechanics, pp.421-428, September 1971.

Clark and Knott,[1975], Clark, G., Knott, J.F., *Measurement of Fatigue Cracks in Notched Specimens By Means of Theoretical Electrical Potential Calibrations*, J. Mech. Phys. Solids, Vol.23, pp.265-276, 1975.

Clavel et al.,[1979], Clavel, M., Levailant, C., Pineau, A., *Influence of Micromechanisms of Cyclic Deformation at Elevated Temperature on Fatigue Behaviour*, Creep-Fatigue Environment Interactions, TMS AIME, pp.24-45, Milwaukee, Wis., 1979.

Coffin,[1954], Coffin, Jr., L.F., *A Study of the Effects of Cyclic Thermal Stresses on a Ductile Metal*, Trans. ASME, Vol. 16, pp931-950, New York, 1954.

Coffin,[1972], Coffin, Jr., L.F., *Fatigue*, Annual Review of Material Science, Vol.2, pp.313-348, 1972.

Coffin,[1974], Coffin, Jr., L.F., *Fatigue at High Temperatures-Prediction and Interpretation*, James Clayton Lecture, Proc. Instn. Mech. Engrs., Vol.188, No.9/74, pp.109-127, 1974.

Coffin,[1977], Coffin, Jr., L.F., *Fatigue at High Temperature*, Fracture 1977, Vol.1, ICF4, Waterloo Canada, pp.263-292, June 1977.

Coles et al.,[1967], Coles, A., Hill, G.J., Dawson, R.A.T., Watson, S.J., *The High Strain Fatigue Properties of Low-alloy Creep Resisting Steels*, International Conference on Thermal and High Strain Fatigue, Monograph and Report Series 32, Institute of Metals and the Iron and Steel Institution, pp.270-294, London 1967.

Colangelo and Heiser,[1974], Colangelo, V.J., Heiser, F.A., *Analysis of Metallurgical Failures*, Wiley-Interscience Publications, London, 1974.

Cordwell,[1990], Cordwell, J.E., *Thermal Shock Testing of Type 316 Stainless Steel Using Sodium*, High Temperature Technology, Vol.8, No.2, pp.158-168, May 1990.

Cottrell,[1961], Cottrell, A.H., *Introductory Review of the Basic Mechanisms of Crack Propagation*, Proceedings of Crack Propagation Symposium, pp.1-7, Cranfield, 1961.

Creusot-Loire Industrie,[1984], Manufacturers Information on Supplied Material, Le Creusot, France, December 1984.

Degallaix et al.,[1988], Degallaix, S., Degallaix, G., Foct, J., *Influence of Nitrogen Solutes and Precipitates on Low Cycle Fatigue of 316L Stainless Steels*, Low Cycle Fatigue ASTM STP 942, eds. Solomon, H.D., Halford, G.R., Kaisand, L.R., Leis, B.N., American Society for Testing and Materials, pp.798-811, Philadelphia, 1988.

Degallaix et al.,[1990], Degallaix, G., Korn, C., Pluvinage, G., *Lifetime Predictions on Cr-Mo-V and 316L Steels Under Thermal and Mechanical Cycling*, Fatigue and Fracture in Engineering Materials and Structures, Vol.13, No.5, pp.473-485, 1990.

Diegele et al.,[1991], Diegele, E., Jakeman, R., Klischenko, A., Matera, R., Merola, M., Munz, D., Suzuki, S., *Structural Analysis of a First Wall Component-Results and Benchmark Calculations*, 5th International Conference on Fusion Reactor Materials, pp.1-25, Clearwater, Florida, USA, November 1991.

Dowling,[1976], Dowling, N.E., *Geometry Effects and the J-Integral Approach to Elastic-Plastic Fatigue Crack Growth*, ASTM STP 601, pp.19-32, 1976.

Driver,[1971], Driver, J.H., *The Effect of Boundary Precipitates on the High-Temperature Fatigue Strength of Austenitic Stainless Steels*, Metal Science Journal, Vol.5, pp.47-50, 1971.

Driver et al.,[1988], Driver, J.H., Gorlier, C., Belrami, C., Violan, P., Amzallag, C., *Influence of Temperature and Environment on the Fatigue Mechanisms of Single-Crystal and Polycrystal 316L*, Low Cycle Fatigue, ASTM STP 942, eds. Solomon, H.D., Halford, G.R., Kaisand, L.R., Leis, B.N., American Society for Testing and Materials, pp.438-455, Philadelphia, 1988.

Dugdale,[1960], Dugdale, D.S., *Yielding of Steel Sheets Containing Slits*, Journal of Mech. Phys. Solids, Vol.8, pp.100-104, 1960.

Edmunds and White,[1966], Edmunds, H.G., White, D.J., *Observations of the Effect of Creep Relaxation on High Strain Fatigue*, Journal of Mechanical Engineering and Science, Vol.8, pp310-321 ,1966.

Ermi et al.,[1981], Ermi, A.M., Bauer, R.E., Chin, B.A., Straalsund, J.L., *Multispecimen Fatigue Crack Propagation Testing*, Journal of Engineering Materials and Technology, Trans. ASME, Vol.103, pp.240-245, July 1981.

Ewing and Humfrey,[1903], Ewing, J.A., Humfrey, J.C.W., *The Fracture of Metals Under Repeated Alternations of Stress*, Phil. Trans. Royal Soc., Vol.200, pp.241-253, 1903.

Feltner and Laird,[1967], Feltner, C.E., Laird, C., *Cyclic Stress-Strain Response of F.C.C. Metals and Alloys-II: Dislocation Structures and Mechanisms*, ACTA Metallurgica, Vol.15, pp.1633-1653, October 1967.

Fenici and Suolang,[1991], Fenici, P., Suolang, S., *Fatigue Crack Growth in 316 Type Stainless Steel at Temperatures and Displacement Damage Rates Representative for the NET First Wall Loading*, Internal Report, C.E.C. Joint Research Centre, Ispra, Italy, November 1991.

Gangloff,[1981], Gangloff, R.P., *Electrical Potential Monitoring of Crack Formation and Subcritical Growth From Small Defects*, Fatigue of Engineering Materials and Structures, Vol.4, No.1, pp.15-33, 1981.

Gerland et al.,[1989a], Gerland, M., Mendez, J., Ait Saadi, B., Violan P., *Evolution of Dislocation Structures and Cyclic Behaviour of a 316L-Type Austenitic Stainless Steel Cycled in Vacuo at Room Temperature*, Materials Science and Engineering, A118, pp.83-95, 1989.

Gerland et al.,[1989b], Gerland, M., Ait Saadi, B., Violan P., *Evolutions of Dislocation Structures in Type 316L Stainless Steel During Plastic Fatigue at 20, 300 and 600 °C in Vacuum*, pp.671-676, 1989.

Gilbey and Pearson,[1966], Gilbey, D.M., Pearson, S., *Measurement of the Length of a Central or Edge Crack in a Sheet of Metal by an Electrical Resistance Method*, Royal Aircraft Establishment, Technical Report No.66402, December 1966.

Goodier,[1937], Goodier, J.N., *Thermal Stress and Deformation*, Journal of Applied Mechanics, Vol.59, pp.A33-A36, March 1937.

Gorlier et al.,[1984], Gorlier, C., Amzallag, C., Rieux, P., Driver, J.H., *The Cyclic Plastic Behaviour of a 316 Steel at 20 to 600 °C*, Conf. Proc. Fatigue 84, pp.41-48, Birmingham September 1984.

Granville,[1991], Granville, R.K., *In-Service Eddy Current Examination of Non-Ferrous Industrial Heat Exchanger Tubing*, British Journal of NDT, Vol.33, No.8, pp.403-408, August 1991.

Griffith,[1921], Griffith, A.A., *The Phenomena of Rupture and Flow in Solids*, Phil. Trans. Royal Soc., Section A, Vol.221, pp.163-198, 1921.

Grossbeck and Liu,[1981], Grossbeck, M.L., Liu, K.C., *High-Temperature Fatigue Life of Type 316 Stainless Steel Containing Irradiation Induced Helium*, Journal of Nuclear Materials, Nos. 103 &104, pp.853-858, 1981.

Grossbeck and Liu,[1982], Grossbeck, M.L., Liu, K.C., *Fatigue Behaviour of Type 316 Stainless Steel Irradiated in a Mixed Spectrum Fission Reactor Forming Helium*, Nuclear Technology, Vol.58, No.3, pp.538-547, September 1982.

Grossbeck and Liu,[1985], Grossbeck, M.L., Liu, K.C., *Fatigue Behaviour at 650 °C of 20% Cold-Worked Type 316 Stainless Steel Irradiated at 550 °C in the High-Flux Isotope Reactor (HFIR)*, Effects of Radiation on Materials: Twelfth International Symposium, ASTM STP 870, eds. Garner, F.A., Perrin, J.S., American Society for Testing and Materials, pp.732-744, Philadelphia, 1985.

Grosskeutz,[1971], Grosskeutz, J.C., *Fatigue Mechanisms in the Sub-Creep Range, Metal Fatigue Damage-Mechanisms. Detection, Avoidance, and Repair*, ASTM STP 495, American Society for Testing and Materials, pp.5-60, 1971.

Grosskeutz and Hancock,[1969], Hancock, J.R., Grosskeutz, J.C., *Mechanisms of Fatigue Hardening in Copper Single Crystals*, ACTA Metallurgica, Vol.17, pp.77-93, 1969.

Haigh and Skelton,[1978], Haigh, J.R., Skelton, R.P., *A Strain Intensity Approach to High Temperature Fatigue Crack Growth and Failure*, Materials Science and Engineering, 36, pp133-137, 1978.

Ham,[1967], Ham, R.K., *The Metallurgy of Transition-Life Fatigue*, Proceedings of Conference on Thermal and High-Strain Fatigue, The Institute of Metals, pp55-79, London, 1967.

Harries,[1986], Harries, D.R., *The Material Requirements for NET*, Radiation Effects, Vol.101, Gordon and Breach Science Publishers, pp.3-19, 1986.

Harries and Zolti,[1986], Harries, D.R., Zolti, E., *Structural Mechanics and Material Aspects of the Next European Torus*, Nuclear Engineering and Design Fusion, Vol.3, pp.331-344, Amsterdam 1986.

Hatanaka,[1990], Hatanaka, K., *Cyclic Stress-Strain Response and Low-Cycle Fatigue Life in Metallic Materials*, JSME International Journal, Series I, Vol.33, No.1, pp.13-25, January 1990.

Hatanaka and Fujimitsu,[1984], Hatanaka, K., Fujimitsu, T., *The Cyclic Stress-Strain Response and Strain Life Behaviour of Metallic Materials*, Proceedings of Fatigue '84, Vol.I. pp.93-110, 1984

Hatanaka et al.,[1989], Hatanaka, K., Fujimitsu, T., Shiraishi, S., *An Analysis of Surface Crack Growth in Circumferential Grooved Components under Low-Cycle Fatigue*, JSME International Journal, Series I, Vol. 32, No. 2, pp245-255, 1989.

Hayashi et al.,[1985], Hayashi, M., Ohtaka, M., Kanno, S., Shimizu, T., *D.C. Potential Crack Detection System For Single Edge Crack*, pp.245-252, 1985.

Hunter,[1990], Hunter, C.P., *Creep and Creep Crack Growth in Alloy 800H Tubes at 800 °C*, PhD thesis, Trinity College, Dublin, 1990.

Hunter et al.,[1992], Hunter, C.P., Hurst, R.C., Taplin, D.M.R., *Creep Crack Growth Studies on Alloy 800H Tubes Under Complex Loading Conditions*, Materials at High Temperatures, Vol.10, No.2, pp.144-149, May 1992.

Irwin,[1960], Irwin, G.R., *Fracture Mechanics*, in *Structural Mechanics*: Proceedings of the 1st Symposium on Naval Structural Mechanics, 1958, eds. Goodier, J.N., Hoff, N.J., pp.557-591, Pergamon Press, New York, 1960.

- Jaeger,[1945], Jaeger, J.C., *On Thermal Stresses In Circular Cylinders*, Phil. Mag., Vol.36, pp.414-428, 1945.
- James et al.,[1989], James, M.N., Dimitriou, C., Chandler, H.D., *Low Cycle Fatigue Lives of Notched Components*, Fatigue Fract. Engng. Mater. Struct., Vol. 12, No. 3, pp213-225, 1989.
- Jaske and Leis,[1979], Jaske, C.E., Leis, B.N., *Important Considerations in Thermal-Mechanical Fatigue Evolution of Metallic Materials*, Proceedings of Corrosion '79, pp.18-27, March 1979.
- Jaske et al.,[1973], Jaske, C.E., Mindlin, H., Perrin, J.S., *Development of Elevated Temperature Fatigue Design Information for Type 316 Stainless Steel*, Instn. Mech. Engineers, Conference Publication 13, Paper C163/73, pp.163.1-163.7, 1973.
- Jenkins,[1923], Jenkins, C.F., *The Fatigue Failure of Metals*, Proc. Royal Soc., Series A, Vol.102, pp.121-138, 1923.
- Jones, Bourcier and Van Avyle,[1988], Jones, W.B., Bourcier, R.J., Van Avyle, J.A.D., *Thermal Fatigue of Stainless Steel*, Effects of Load and Thermal Histories on Mechanical Behaviour of Materials, pp.153-178, Denver USA, February 1987.
- Kanawaza and Yoshida,[1973], Kanawaza, K., Yoshida, S., *Effect of Temperature and Strain Rate on the High Temperature, Low Cycle Fatigue Behaviour of Austenitic Stainless Steels*, Institute of Mechanical Engineers Conference Publication 13, Paper C226/73, pp.226.1-226.10, 1973.
- Kawamoto et al.,[1966], Kawamoto, M., Tanaka, T., Nakajima, H., *Effects of Several Factors on Thermal Fatigue*, Journal of Materials, Vol.1, pp.719-758, 1966.
- Kent,[1932], Kent, C.H., *Thermal Stresses in Spheres and Cylinders Produced by Temperatures Varying With Time*, Transactions of the American Society of Mechanical Engineers, Vol.54, No.18, pp.185-196, 1932.
- Kerr,[1988], Kerr, D.C., *Integrity Assessment Procedures for the Tubular Joints of Offshore Structures*, Final Year B.Eng. Project, Department of Mechanical Engineering, University of Glasgow, 1988.

Klesnil and Lukas,[1980], Klesnil, M., Lukas, P., *Fatigue of Metallic Materials*, Elsevier Scientific Publishing Co., Amsterdam, 1980.

Knott,[1973], Knott, J.F., *Fundamentals of Fracture Mechanics*, Butterworth and Co (Publishers) Ltd., London, 1973.

Kusmaul and Stegmeyer,[1989], Kusmaul, K., Stegmeyer, R., *The Thermal Fatigue Behaviour of a Thick-Walled, Notched Hollow Cylinder*, Biaxial and Multiaxial Fatigue, eds. Brown, M.W., Miller, K.J., Mechanical Engineering Publications, pp.301-315, London 1989.

Laird,[1967], Laird, C., *Fatigue Crack Propagation*, ASTM STP 415, American Society of Testing and Materials, pp.131-140, Philadelphia, 1967.

Lamain,[1992], Lamain L.G., *A Computer Code to Analyse Fatigue Behaviour of Tubes: Theory and Application*, Internal Report, C.E.C. Institute For Advanced Materials, Petten, The Netherlands, 1992

Landgraf et al.,[1969], Landgraf, R.W., Morrow, J-D., Endo, T., *Determination of the Cyclic Stress-Strain Curve*, Journal of Materials, JMLSA, VOL. 4, No. 1, pp176-188, March 1969.

Leis,[1982], Leis, B.N., *Fatigue Crack Propagation Through Inelastic Gradient Fields*, International Journal of Pressure Vessels and Piping, Vol. 10, pp141-158, 1982.

Levaillant and Pineau,[1982], Levaillant, C., Pineau, A., *Assessment of High-Temperature Low-Cycle Fatigue Life of Austenitic Stainless Steels by Using Intergranular Damage as a Correlating Parameter*, Low-Cycle Fatigue and Life Prediction, ASTM STP 770, eds. Amzallag, C., Leis, B.N., Rabbe, P., American Society for Testing and Materials, pp.169-193, 1982.

Li and Wei,[1966], Li, C-Y, Wei, R.P., *Calibrating the Electrical Potential Method for Studying Slow Crack Growth*, Materials Research and Standards, Vol.6, No.8, pp.392-394, August 1966.

Lieurade et al.,[1986], Lieurade, H.P., Ribes, A., Dias, A., Leburn, J.L. *Influence of a Cold Working on the Behaviour of a AISI 316L Stainless Steel*, Low Cycle Fatigue, pp.707-712, 1986.

Lord and Coffin,[1973], Lord D.C., Coffin, Jr., L.F., *Low Cycle Fatigue Hold Time Behaviour of Cast Rene 80*, Metallurgical Transactions, Vol.4, pp1647-1654, July 1973.

Love,[1990], Love, J.B., *The Use of RF Heating for Cyclic Thermal Shock Testing*, High Temperature Technology, Vol.8, No.2, pp.146-152, May 1990.

Love and Hoddinott,[1983], Love, J.B., Hoddinott, D.S., *Endurance of Type 316 Stainless Steel Subjected to Cyclic Thermal Shock-an Experimental and Theoretical Investigation*, Trans. of 7th International Conference on Structural Mechanics in Reactor Technology, Vol.G, Paper G/F1/10, pp.157-164, 1983.

Lukas, Klesnil and Polak,[1974], Lukas, P., Klesnil M., Polak, J., *High Cycle Fatigue Life of Metals*, Materials Science and Engineering, vol.15, p239-245, 1974

Lukas and Klesnil,[1973], Lukas, P., Klesnil, M., *Cyclic Stress-Strain Response and Fatigue Life of Metals in Low Amplitude Range*, Materials Science and Engineering, 11, pp.345-346, 1973.

Lundberg and Sandström,[1982], Lundberg, L., Sandström, R., *Application of Low Cycle Fatigue Data to Thermal Fatigue Cracking*, Scandinavian Journal of Metallurgy, Vol.11, pp.85-104, 1982.

Magnin et al.,[1988], Magnin, T., Lardon, J.M., Coudreuse, L., *A New Approach to Low Cycle Fatigue Behaviour of a Duplex Stainless Steel Based on the Deformation Mechanisms of the Individual Phases*, Low Cycle Fatigue, ASTM STP 942, eds. Solomon, H.D., Halford, G.R., Kaisand, L.R., Leis, B.N., American Society for Testing and Materials, pp.812-823, Philadelphia, 1988.

Magnin et al.,[1989], Magnin, T., Ramade, C., Lepinoux, J., Kubin, L.P., *Low-Cycle Fatigue Damage Mechanisms of F.C.C. and B.C.C. Polycrystals: Homologous Behaviour*, Materials Science and Engineering, A118, pp.41-51, 1989.

Mahoney and Paton,[1974], Mahoney, M.W., Paton, N.E., *The Effect of Carbide Precipitation on Fatigue Crack Propagation in Type 316 Stainless Steel*, Nuclear Technology, Vol.23, pp.53-62, July 1974.

Manjoine and Landerman,[1982], Manjoine, M.J., Landerman, E.I., *Techniques for Fatigue Testing and Extrapolation of Fatigue Life for Austenitic Stainless Steels*, Journal of Testing and Evaluation, JTEVA, Vol.10, No.3, pp.115-120, May 1982.

Manson,[1954], Manson, S.S., *Behaviour of Materials Under Conditions of Thermal Stress*, National Advisory Committee For Aeronautics, Report 1170, Washington D.C., USA, p.2933, 1954.

Manson and Hirschberg,[1965], Manson, S.S., Hirschberg, M.H., *Crack Initiation and Propagation in Notched Fatigue Specimens*, Proceedings of the 1st International Conference on Fracture, Vol.1, pp.479-498, Sendai, Japan, 1965.

Manson and Muralidharan,[1988], Muralidharan, U., Manson, S.S., *A Modified Universal Slopes Equation for Estimation of Fatigue Characteristics of Metals*, Journal of Engineering Materials and Technology, Vol.110, pp55-58, January 1988.

Marchand, Dorner and Ilschner,[1988], Marchand, N.J., Dorner, W., Ilschner, B., *Crack Initiation and Growth in Thermal Fatigue Testing*, Proc. of the ASTM Conf. on Surface Crack Growth: Models, Experiment and Structures, pp.1-33, April 1988.

Marsh,[1981], Marsh, D.J., *A Thermal Shock Fatigue Study of Type 304 and 316 Stainless Steels*, Fatigue of Engineering Materials and Structures, Vol.4, No.2, pp.179-195, 1981.

Merola,[1991], Merola, M., *Numerical Analysis and Nuclear Standard Code Application to Thermal Fatigue*, C.E.C. Institute for Advanced Materials, J.R.C. Ispra Internal Report EUR 14028 EN, pp.1-45, Ispra 1991.

Merola and Matera,[1991], Merola, M., Matera, R., *Design Problems of the NET/ITER Experimental Reactor First Wall*, Energia Nucleare, Vol.8, No.1, pp.42-54, April 1991.

Miller,[1980], Miller, K.J., *An Introductory Lecture on Fatigue of Metals*, Unpublished, University of Sheffield, pp.1-11, 1980.

Morrow,[1965], Morrow, J., *Cyclic Plastic Strain Energy and Fatigue of Metals*, ASTM STP 378, pp.45-87, 1965.

Morrow et al.,[1969], Morrow, J., Wetzel, R.M., Topper, T.H., *Neuber's Rule Applied to fatigue of Notched Specimens*, JMLSA, ASTM, Vol.4, No.1, pp.200-209, March 1969.

Mowbray and McConnelee,[1973], Mowbray, D.F., McConnelee, J.E., *Applications of Finite Element Stress Analysis and Stress-Strain Properties in Determining Notch Fatigue Specimen Deformation and Life*, Cyclic Stress-Strain Behaviour-Analysis, Experimentation, and Failure Prediction, ASTM STP 519, American Society for Testing and Materials, pp151-169, 1973.

Mowbray and Trantina,[1978], Mowbray, D.F., Trantina, G.G., *Thermal Fatigue Analysis, Fatigue: Environment and Temperature Effects*, Sagamore Army Materials Research Conference Proceedings, No.27, Plenum Publications, 1978.

Neuber,[1961], Neuber, H., *Theory of Stress Concentration for Shear-Strained Prismatical Bodies With Arbitrary Non-Linear Stress-Strain Laws*, Transactions of the American Society of Mechanical Engineering, Series E, Vol.28, No.4, pp.544-550, December 1961.

Newton,[1976], Newton, J.D., *Thermal Fatigue Cracking of 2¼%Cr-1%Mo Steel Caused by Repeated Quenching From Elevated Temperatures*, Journal of the Australian Institute of Metals, Vol.21, Nos.2&3, pp.94-102, June-September 1976.

Okazaki and Koizumi,[1983], Okazaki, M., Koizumi, T., *Crack Propagation of Steels During Low Cycle Thermal-Mechanical and Isothermal Fatigue at Elevated Temperatures*, Metallurgical Transactions A, Vol.14A, pp.1641-1648, August 1983.

Oliveira and Wu,[1987], Oliveira, R., Wu, X.R., *Stress Intensity Factors for Axial Cracks in Hollow Cylinders Subjected to Thermal Shock*, Engineering Fracture Mechanics, Vol.27, No.2, pp.185-197, 1987.

Paris,[1964], Paris, P.C., *The Fracture Mechanics Approach to Fatigue*, Fatigue-An Interdisciplinary Approach, Syracuse University Press, pp.107-132, 1964.

Paris and Erodogan,[1963], Paris, P.C., Erodogan, F., *A Critical Analysis of Crack Propagation Laws*, Journal of Basic Engineering, Trans. of American Society of Mechanical Engineers, Series D, Vol.85, No.4, pp.525-543, December 1963.

Parker and Andrasic,[1984], Andrasic, C.P., Parker, A.P., *Technical Note: Dimensionless Stress Intensity Factors For Cracked Thick Cylinders Under Polynomial Crack Face Loadings*, Engineering Fracture Mechanics, Vol.19, No.1, pp187-193, 1984.

Parker and Farrow,[1981], Parker, A.P., Farrow, J.R., Technical Note: *Stress Intensity Factors For Multiple Radial Cracks Emanating From the Bore of an Autofrettaged or Thermally Stressed, Thick Cylinder*, Engineering Fracture Mechanics, Vol.14, Pergamon Press Ltd., pp237-241, 1981.

Peckner and Bernstein,[1977], Peckner, D., Bernstein, I.M., *Handbook of Stainless Steels*, McGraw-Hill, Inc., New York, USA, 1977.

Pickard et al.,[1975], Pickard, A.C., Ritchie, R.O., Knott, J.F., *Fatigue Crack Propagation in a Type 316 Stainless Steel Weldment*, Metals Technology, MT/178, pp.253-263, June 1975.

Plumbridge et al.,[1980], Plumbridge, W.J., Dalski, M.E., Castle, P.J., *High Strain Fatigue of a Type 316 Stainless Steel*, Fatigue of Engineering Materials and Structures, Vol.3, pp.177-188, 1980.

Potter,[1973], Potter, J.M., *The Effect of Load Interaction and Sequence on the Fatigue Behaviour of Notched Coupons*, Cyclic Stress-Strain Behaviour-Analysis, Experimentation, and Failure Prediction, ASTM STP 519, American Society for Testing and Materials, pp109-132, 1973.

Raju and Newman,[1979], Raju, I.S., Newman, Jr., J.C., *Stress-Intensity Factors for a Wide Range of Semi-Elliptical Surface Cracks in Finite Thickness Plates*, Engineering Fracture Mechanics, Vol.11, No.4, pp817-829, 1979.

Rees,[1989], Rees, D.W.A., *Fatigue Crack Growth In Thick-Walled Cylinders Under Pulsating Internal Pressure*, Engineering Fracture Mechanics, Vol.33, No.6, pp.927-940, 1989.

Rice,[1968], Rice, J.R., *A Path Independent Integral and the Approximate Analysis of Strain Concentrations by Notches and Cracks*, Journal of Applied Mechanics, Vol.35, pp.379-386,1968.

Rice and Rosengren,[1968], Rice, J.R., Rosengren, G.F., *Plane Strain Deformation Near a Crack Tip in a Power Law Hardening Material*, J. Mech. Phys. Solids, Vol.16, pp.1-12, 1968.

Rice et al.,[1973], Rice, J.R., Paris, P.C., Merkle, J.G., *Some Further Results of J-Integral Analysis and Estimates, Progress in Flaw Growth and Fracture Toughness Testing*, ASTM STP 536, American Society for Testing and Materials, pp.231-245, 1973.

Rice et al.,[1989], Rice, R.C., Leis, B.N., Nelson, D.V., Berns, H.D., Mitchell, M.R., Lingenfelter, D., *Fatigue Design Handbook*, 2nd Edition, Society of Automotive Engineers, Inc., Warrendale, PA, USA, 1989.

Rickerby et al.,[1984], Rickerby, D.G., Fenici, P., *Fatigue Crack Growth in Thin Section Type 316 Stainless Steel*, Engineering Fracture Mechanics, Vol.19, No.4, Pergamon press Ltd., pp585-599, 1984.

Ritchie,[1986], Ritchie R.O., *Fatigue Crack Growth: Mechanistic Aspects*, Encyclopaedia of Material Science and Engineering, Vol.3, pp.1650-1666, Pergamon Press, 1986.

Rooke and Cartwright,[1976], Rooke, D.P., Cartwright, D.J., *A Compendium of Stress Intensity Factors*, HMSO, London, 1976.

Rose and White,[1987], Rose, R.T., White, P.S., *Shakedown Design Methods for High Temperatures*, pp.1-5, 1987.

Sadananda and Shahinian,[1980], Sadananda, K., Shahinian, P., *Effect of Environment on Crack Growth Behaviour in Austenitic Stainless Steels Under Creep and Fatigue Conditions*, Metallurgical Transactions, Vol.11A, American Soc. for Metals and the Metallurgical Soc. of AIME, pp,267-276, February 1980.

Shahinian et al.,[1973], Shahinian, P., Smith, H.H., Watson, H.E., *Fatigue Crack Growth Characteristics of Several Austenitic Stainless Steels at High Temperature*, Fatigue at Elevated Temperatures, ASTM STP 520, American Society for Testing and Materials, pp.387-400, 1973.

Shimizu et al.,[1983], Shimizu, M., Brown, M.W., Miller, K.J., *Fatigue Crack Propagation in Stainless Steel Subjected to Repeated Thermal Shock*, Proc. 4th International Conference on the Mechanical Behaviour of Materials, eds. Carlsson, J., Ohlson, N.G., Vol.1, pp.207-213, Stockholm 1983.

Skelton,[1983], Skelton, R.P., *Crack Initiation and Growth in Simple Components During Thermal Cycling*, Fatigue at High Temperatures, Applied Science Publishers, London, pp1-62, 1983.

Skelton,[1982], Skelton, R.P., *Growth of Short Cracks During High Strain Fatigue and Thermal Cycling*, Low-Cycle Fatigue and Life Prediction, ASTM STP 770, American Society of Testing and Materials, pp337-381, 1982.

Skelton,[1979], Skelton, R.P., *Crack Propagation in Metals During Thermal Shock*, Proc. 3rd International Conference on Mechanical Behaviour of Metals, Vol.2, pp.13-22, 1979.

Skelton,[1990], Skelton R.P., *Introduction to Thermal Shock*, High Temperature Technology, Vol.8, No.2, pp.75-89, May 1990.

Skelton and Miles,[1984], Skelton, R.P., Miles, L., *Crack Propagation in Thick Cylinders of ½CrMoV Steel During Thermal Shock*, High Temperature Technology, Vol.2, No.1, pp.23-34, February 1984.

Skelton and Nix,[1987], Skelton, R.P., Nix, K.J., *Crack Growth Behaviour in Austenitic and Ferritic Steels During Thermal Quenching Form 550 °C*, High Temperature Technology, Vol.5, No.1, pp.3-12, February 1987.

Smith and Wedgewood,[1915], Smith J.H., Wedgewood, G.A., *Stress-Strain Loops for Steel in the Cyclic State*, J. Iron and Steel Inst., Vol.91, No.1, pp.365-397, 1915.

Speidel,[1975], Speidel, M.O., *Fatigue Crack Growth at High Temperatures*, High Temperature Materials in Gas Turbines, eds., Salum, P.R., Speidel, M.O., Elsevier Scientific Publishing Co., pp.207-255, 1975

Stadnick and Morrow,[1972], Stadnick, S.J., Morrow, J., *Techniques for Smooth Specimen Simulation of the Fatigue Behaviour of Notched Members*, ASTM STP 515, pp.229-252, 1972.

Tada et al.,[1985], Tada, H., Paris, P.C., Irwin, G.R., *The Stress Analysis of Cracks Handbook*, 2nd Edition, Paris Productions Inc. and Del Research Corporation, St. Louis, Missouri, USA, 1985.

Taira et al.,[1979], Taira, S., Ryuichi, O., Komatsu, T., *Application of J-Integral to High-Temperature Crack Propagation: Part II-Fatigue Crack Propagation*, Journal of Engineering Materials and Technology, Vol.101, pp162-167, April 1979.

Tartaglia,[1989], Tartaglia, G.P., *Temperature and Stress Distributions in Cylindrical Samples*, Technical Note P/F1/89/12, C.E.C. Joint Research Centre, Petten, The Netherlands, June 1989.

Tomkins,[1968], Tomkins, B., *Fatigue Crack Propagation-An Analysis*, Phil. Mag., Vol.18, pp.1041-1066, 1968.

Tomkins,[1984], Tomkins, B., *Fatigue Failure and the Integrity of Structures*, Fatigue 84, pp.1-11, 1984.

Tomkins,[1981], Tomkins, B., *High Strain Fatigue*, Proceedings of a Conference on Subcritical Crack growth due to Fatigue, Stress Corrosion and Creep, JRC Ispra, Italy, Elsevier Applied Science Publishers, pp.239-266, October 1981.

Udoguchi et al.,[1973], Udoguchi, T., Yasuhide, A., Ichino, I., *A Frequency Interpretation of Hold-Time Experiments on High Temperature Low-Cycle Fatigue of Steels for LMFBR*, Institute of Mechanical Engineers Conference Publication 13, Paper C211/73, pp.211.1-211.9, 1973.

Vandermeulen et al.,[1988], Vandermeulen, W., Hendrix, W., Massaut, V., Van de Velde, J., *Influence of Neutron Irradiation at 430 °C on the Fatigue Properties of SA 316L Steel*, Journal of Nuclear Materials, Vols.155-157, pp.953-956, 1988.

Vogt et al.,[1984], Vogt J.B., Degallaix, S., Foct, J., *Low Cycle Fatigue Life Enhancement of 316L Stainless Steel by Nitrogen Alloying*, International Journal of Fatigue, Vol.6, No.4, pp.211-215, October 1984.

Wareing and Vaughan,[1979], Wareing, J., Vaughan, H.G., *Influence of Surface Finish on Low-Cycle Fatigue Characteristics of Type 316 Stainless Steel at 400 °C*, Metal Science, pp.1-8, January 1979.

Webster,[1989], Webster, G.A., *Fracture Mechanics Concepts*, A Course on High Temperature Component Life Assessment, Imperial College of Science, Technology and Medicine, London, pp.2.1-2.22, May 1989.

Wei and Brazill,[1981], Wei, R.P., Brazill, R.L., *An Assessment of A.C. and D.C. Potential Systems for Monitoring Fatigue Crack Growth*, Fatigue Crack Growth Measurement and Data Analysis, ASTM STP 738, eds. Hudak, Jr., S.J., Bucci, R.J., American Society for Testing and Materials, pp.103-119, 1981.

Westwood,[1979], Westwood, H.J., *Tensile Hold Time Effects on Isothermal and Thermal Low-Cycle Fatigue of 304 Stainless Steel*, Proc. International Conference ICM 3, pp.59-67, Cambridge England, August 1979.

White,[1970], White, D.J., *Some Contributions to British Work on Thermal and High Strain Fatigue*, Materials Under Cyclic Loading at High Temperature, pp.3-26, 1970.

Wöhler,[1871] Wöhler, A., *Tests to Determine the Forces Acting on Railway Carriage Axles and the Capacity of Resistance of the Axles*, Engineering, Vo.,11, pp199-210, 1871.

Wood et al.,[1977], Wood, D.S., Slattery, G., Wynn, J., Connaughton, D., Lambert, M.E., *Preliminary Results of Effect of Environment on the Low Cycle Fatigue Behaviour of Type 316 Stainless Steel and 9%Cr Ferritic Steel*, Institute of Mechanic Engineers: Conference Publication C99/77, pp.11-19, 1977.

Yamaguchi and Kanazawa,[1980], Yamaguchi, K., Kanazawa, K., *Effect of Strain Wave Shape on High Temperature Fatigue Life of a Type 316 Steel and Application of the Strain Range Partitioning Method*, Metallurgical Transactions A, Vol.11A, pp.2019-2027, December 1980.

Yamaguchi et al.,[1978], Yamaguchi, K., Kanazawa, K., Yoshida, S., *Crack Propagation in Low-Cycle Fatigue of Type 316 Stainless Steel at Temperatures Below 600°C Observed by Scanning Electron Microscopy*, Material Science and Engineering, Vol.33, pp.175-181, 1978.

Yoshida et al.,[1977] Yoshida, S., Kanawaza, K., Yamaguchi, K., Sasaki, M., Kobayashi, K., Sato, M., *Elevated Temperature Fatigue Properties of Engineering Materials: Part 1*, Transactions of National Research Institute for Metals, Vol.19, No.5, pp.2-27, September 1977.